Mathematical modelling of mammalian mitochondrial metabolism

Amar Suresh Ghaisas

A thesis submitted in partial fulfilment of the requirements of
Oxford Brookes University
for the award of the degree Doctor of Philosophy

Cell Systems Modelling Group
School of Life Sciences

December 2015

Contents

List of Figures

List of Tables

Acronyms

α-KGDH	α-ketoglutarate dehydrogenase
AcCoA	Acetyl-CoA
ACS	acetyl-CoA synthetase
ACO	aconitate hydratase
$AcCoA_m$	acetyl-CoA
ADP	adenosine diphosphate
ADP_c	free cytosolic ADP
ADP_m	magnesium-bound mitochondrial ADP
ATPhyd	ATP hydrolysis
αKG_c	cytosolic α-ketoglutarate
α-KGDH	α-ketoglutarate dehydrogenase
α-KG_{exp}	α-ketoglutarate transporter
αKG_m	α-ketoglutarate
αKG_m	mitochondrial α-ketoglutarate
ALD	aldolase
AMP	adenosine monophosphate
ANT	adenine-nucleotide translocase
Asp	aspartate
Asp_c	cytosolic aspartate
Asp_m	mitochondrial aspartate
ATPsynth	ATP synthase
ATP_c	free cytosolic ATP
ATP_m	magnesium-bound mitochondrial ATP
HCO_3^-	bicarbonate
13BPG	1,3-bisphosphoglycerate
Ca^{2+}	mitochondrial free divalent calcium ions
CO_2	carbon dioxide
C^S	concentration control coefficient
$\mathcal{E}_S$	elasticity coefficient
C^J	flux control coefficient
cGOT	cytosolic glutamate-oxoglutarate transaminase
Cit_m	citrate

cMDH . . . . . cytosolic malate dehydrogenase
CoA_m . . . . . coenzyme A
CoA . . . . . external coenzyme A
CS . . . . . Citrate synthase
CS . . . . . citrate synthase
CSMG . . . . . Cell Systems Modelling Group
CSMG . . . . . Cell Systems Modelling Group
$cAdN_{csum}$ . . . . . conserved total of cytosolic adenine nucleotides

DHAP . . . . . dihydroxyacetone phosphate

ElMo . . . . . elementary modes
ENO . . . . . enolase
ESS . . . . . enzyme subsets
ETC . . . . . electron transport chain

FAD . . . . . flavin adenine dinucleotide (oxidized)
$FADH_2$ . . . . . flavin adenine dinucleotide (reduced)
FFAs . . . . . Free Fatty acids
FM . . . . . fumarate hydratase
F16BP . . . . . fructose 1,6-bisphosphate
F6P . . . . . fructose 6-phosphate
Fum_m . . . . . fumarate

GATx . . . . . glutamate-aspartate transporter
Glc . . . . . glucose
Glc_{bL} . . . . . blood glucose
$G6P_{exp}$ . . . . . glucose 6-phosphate export
G6Px . . . . . glucose 6-phosphate (external)
G6P . . . . . glucose 6-phosphate
GLUT4 . . . . . glucose transporter type 4
Glut . . . . . glutamate
$Glut_c$ . . . . . cytosolic glutamate
$Glut_m$ . . . . . mitochondrial glutamate
GAPDH . . . . . glyceraldehyde phosphate dehydrogenase
GAP . . . . . glyceraldehyde 3-phosphate
α-GLYp . . . . . α-glycerol 3-phosphate
cGPD1 . . . . . cytosolic α-glycerol phosphate dehydrogenase type 1

HRT_{Glc} . . . . . heart glycolysis model
HRT_{TCA+} . . . . . heart integrated TCA cycle model
HRT_{MAS} . . . . . malate-aspartate shuttle model
HRT_{TCA} . . . . . heart TCA cycle model
HK . . . . . hexokinase
OH^- . . . . . hydroxyl ion

IDH . . . . . Isocitrate dehydrogenase
IDH . . . . . isocitrate dehydrogenase

IDHa . . . . . NAD^+-dependent isocitrate dehydrogenase
IDHb . . . . . $NADP^+$-dependent isocitrate dehydrogenase
$Isocit_m$ . . . . . isocitrate

Lac . . . . . lactate
Lac_{bL} . . . . . blood lactate
LDH . . . . . lactate dehydrogenase
$LVR_{TCA}{}^{OGI}$ . . . . . original liver TCA cycle model
PC_{kd} . . . . . *"PC knock-down"* model
PC_{ko} . . . . . *"PC knock-out"* model
PC_{wt} . . . . . *"PC wild-type"* model
$LVR_{TCA}{}^{UPD}$ . . . . . updated liver TCA cycle model

Mg^{2+} . . . . . mitochondrial free divalent magnesium ions
Mal_c . . . . . cytosolic malate
Mal_m . . . . . malate
Mal_m . . . . . mitochondrial malate
MAS . . . . . malate-aspartate shuttle
MC . . . . . malate carrier (malate-phosphate transporter)
MCA . . . . . Metabolic Control Analysis
MDH . . . . . mitochondrial malate dehydrogenase
mGOT . . . . . mitochondrial glutamate-oxoglutarate transaminase
mMDH . . . . . mitochondrial malate dehydrogenase
MCT1 . . . . . monocarboxylate transporter type 1
MCT1Pm . . . . . monocarboxylate transporter type 1 (cell memb.)
MCT1Mm . . . . . monocarboxylate transporter type 1 (mito. memb.)
MOTx . . . . . malate-oxoglutarate transporter

NAD^+_m . . . . . nicotinamide adenine dinucleotide (oxidized)
NAD^+_c . . . . . cytosolic nicotinamide adenine dinucleotide (oxidized)
NAD^+_m . . . . . mitochondrial nicotinamide adenine dinucleotide (oxidized)
$NADH_m$ . . . . . nicotinamide adenine dinucleotide (reduced)
$NADH_c$ . . . . . cytosolic nicotinamide adenine dinucleotide (reduced)
$NADH_m$ . . . . . mitochondrial nicotinamide adenine dinucleotide (reduced)
$NADP^+$ . . . . . nicotinamide adenine dinucleotide phosphate (oxidized)
NADPH . . . . . nicotinamide adenine dinucleotide phosphate (reduced)

OAA_m . . . . . oxaloacetate
OAA_c . . . . . cytosolic oxaloacetate
OAA_m . . . . . mitochondrial oxaloacetate

PC . . . . . pyruvate carboxylase
PDH . . . . . Pyruvate dehydrogenase
PDH . . . . . pyruvate dehydrogenase
PDHK . . . . . pyruvate dehydrogenase kinase
PDHP . . . . . pyruvate dehydrogenase phosphatase
PEP . . . . . phosphoenolpyruvate

PFK . . . . . phosphofructokinase
PGI . . . . . phosphoglucose isomerase
PGK . . . . . phosphoglycerate kinase
PGM . . . . . phosphoglycerate mutase
Pi . . . . . inorganic phosphate
Pi_c . . . . . cytosolic inorganic phosphate
Pi_m . . . . . mitochondrial inorganic phosphate
PiHt . . . . . Pi-H^+ translocator
Pps . . . . . pyruvate, water dikinase (phosphoenolpyruvate synthase)
H^+ . . . . . proton
Pyk . . . . . pyruvate kinase
Pyr . . . . . Pyruvate
Pyr_m . . . . . pyruvate
Pyr_{bL} . . . . . blood pyruvate
Pyr_c . . . . . cytosolic pyruvate
PK . . . . . pyruvate kinase

$SCoA_m$ . . . . . succinyl-CoA
SCS . . . . . succinyl-CoA synthetase
SDH . . . . . succinate dehydrogenase
Suc_m . . . . . succinate

TCA . . . . . tricarboxylic acid cycle
TCAi . . . . . TCA intermediate metabolites
TCAi . . . . . TCA cycle intermediate metabolites
3PG 3-phosphoglycerate
TPI . . . . . triosephosphate isomerase
2PG 2-phosphoglycerate

QH_2 . . . . . ubiquinol (reduced)
Q . . . . . ubiquinone (oxidized)

V_{app}^{PC} . . . . . apparent maximal activity of PC

H_2O . . . . . water

Abstract

This project is in the area of "Computational Biology" or "Systems Biology". Mathematical modelling is a method to study a biological system using computer-aided tools. A mathematical model of any biological system consists of a set of biochemical (or other) reactions – complete with reaction mechanisms, substrate, product, and effector concentrations, enzyme activities *etc.*, specific to the system. Such models utilize relevant experimental data as parameters and/or variables in the reaction equations.

In heart, mitochondrial energy metabolism involving utilization of dietary carbohydrates and fats bears a crucial importance for the normal physiological function of the cardiac muscle. The mammalian liver-specific tricarboxylic acid cycle (TCA) model developed within the Cell Systems Modelling Group (CSMG) was used to study and understand the basic functional properties of a tissue-specific TCA cycle model system and to form a knowledge base. Based on this knowledge, we successfully constructed a mammalian heart-specific TCA cycle model using heart-specific enzyme kinetics data from published literature. Analysis of the heart TCA cycle model ($\mathrm{HRT}_{\mathrm{TCA}}$) showed that it needs an input from the malate-aspartate shuttle reactions and therefore a mammalian heart-specific malate-aspartate shuttle model was built. Analysis of the malate-aspartate shuttle model revealed that in order to supply the heart TCA cycle with anaplerotic input, the cytosolic NADH/NAD^+ couple must vary dynamically and therefore a glycolysis model was built. Once, all the models were studied in detail, the three were combined to form a fully extended model of heart TCA cycle. Structural analysis of the fully extended model shows that there are more than 278 elementary modes in the extended model that use different combinations of 37 reactions. Kinetic analysis of the model shows significant findings that reveal its response to changes in various enzyme activities.

This project will lead to improved understanding of the responses of mammalian heart mitochondrial metabolism to perturbations such as varying cellular demand for energy (ATP) and substrates (*e.g.* Pyruvate (Pyr)). The invaluable addition of Malate (Mal)-Aspartate (Asp) shuttle reactions as well as glucolysis reactions has hopefully generated a more physiologically relevant model system. In future, we plan to adapt the simulation to represent the dynamics of hyperpolarized ^{13}C labelling, using the experimental data generated with hyperpolarized ^{13}C Pyr as a metabolic tracer. This enables non-invasive, real-time visualization of the biochemical mechanisms under normal as well as abnormal conditions.

Chapter 1

Introduction/ Literature Review

1.1 Metabolism

Mitochondria are sub-cellular membrane-enclosed organelles found in most eukaryotic cells and are responsible for most of cellular energy production. In humans, mitochondria found in different tissues vary in number and size. Many cells have only a single mitochondrion, whereas others can contain several thousand mitochondria, *e.g.* muscle cells. There are three major types of muscles in the human body – skeletal, smooth, and cardiac. Skeletal is a voluntary muscle whereas smooth muscle and cardiac are involuntary. Although functionally, all the three muscle types have significant differences, all three use the movement of actin against myosin to generate contraction. In skeletal and smooth muscles, contraction is stimulated by electrical impulses transmitted by the motor nerves; whereas, in cardiac muscles, internal pacemaker cells initiate the contractions and propagate the stimuli for contractions to the neighbouring cells they are in contact with.

In muscle cells, mitochondrial function is vital as muscles require a constant supply of ATP for their contractile activity (Williamson, 1979). In order to respond quickly to the changes in stimulus levels, muscle cells effectively utilize the creatine-creatine kinase (CK) shuttle to buffer the ATP content and this allows rapid regeneration of ATP when demand spikes up. Muscles also store glucose in the form of glycogen and this enables sufficient supply of substrates for oxidation when required. In the case of cardiac muscle, the cellular energetics operates primarily by oxidation of carbohydrates and fatty acids via the TCA cycle and β-oxidation, respectively (Bing, 1965).

The TCA cycle (also known as - citric acid cycle and Krebs cycle) – is a set of reactions that is involved in the conversion of acetyl-CoA into CO_2 and H_2O to generate

free chemical energy by transferring high-energy electrons to NAD^+ to form NADH. In most eukaryotic organisms, the TCA cycle is of central importance and it occurs in the mitochondrial matrix. The TCA cycle is fuelled by $AcCoA_m$ derived from oxidation of Free Fatty acids (FFAs) and oxidative decarboxylation of pyruvate. The NADH produced in the TCA cycle contains high-energy electrons, that are passed on to the electron acceptor, O_2, through a series of redox reactions to generate ATP (Lehninger et al., 1993).

β-oxidation is a catabolic process by which FFAs are broken down in mitochondria to generate Acetyl-CoA, which can then enter the TCA cycle. β-oxidation of fatty acids involves activation of fatty acids in cytosol, transport into mitochondria, and the actual set of reactions converting fatty acyl-CoA esters to acetyl-CoA (AcCoA) in mitochondria. Oxidation of fatty acids represents another important source for the generation of ATP and NADH (Kiens, 2006; Rasmussen and Wolfe, 1999).

These redox reactions occur inside a series of closely associated protein complexes in the inner mitochondrial membrane (IMM) that constitute the electron transport chain (ETC). This entire process of generating energy-rich electrons from carbon substrates by oxidation and passing them on to an electron acceptor through a series of coupled redox reactions to generate ATP is known as oxidative phosphorylation. According to the chemiosmotic hypothesis of oxidative phosphorylation proposed by Peter Mitchell in 1966, the energy produced by electrons flowing through the ETC protein complexes is used to pump protons out of the mitochondria across the IMM and thereby generating a pH gradient and electrical potential difference across IMM. This resultant electrochemical gradient (pH gradient and electrical potential difference) – also referred to as the protonmotive force (PMF), is utilized by the F_o-F_1–ATPase to pump H^+ into the mitochondria, generating ATP in the process through change in its conformation (Lehninger et al., 1993).

Under certain conditions, protons can re-enter the mitochondrial matrix without contributing to ATP synthesis. This process is known as proton leak and is due to the facilitated diffusion of protons into the matrix. The process results in the unharnessed potential energy of the proton electrochemical gradient being released as heat. In normal physiology, this phenomenon is primarily found in brown adipose tissue, or brown fat of new born babies and hibernating animals. The heat generated during this process is dissipated throughout the body and helps to maintain the core temperature. In muscle cells, under normal physiological conditions, the proton leak is negligible and can be safely assumed to be equal to zero. Under certain disease conditions or with exposure to certain respiratory inhibitors (e.g. 2,4-dinitrophenol), the mitochondrial proton leak may increase, reducing the total yield of ATP generated under such conditions (Lehninger et al., 1993).

1.1.1 Heart mitochondrial metabolism

In this project, we propose to study the properties of mammalian heart mitochondrial energy metabolism using a mathematical model.

The heart functions as a pump and requires energy to propel sufficient blood through the vascular system to sustain life. The heart is capable of adjusting its pump performance to meet various demands by adjusting its elastic and contractile properties and excitation-contractile coupling. Myocardium is adapted to be highly resistant to fatigue by an increased number of mitochondria per cell, enabling continuous aerobic respiration via oxidative phosphorylation, and an enriched blood supply, which provides nutrients and O_2 (Opie, 1998).

Under basal aerobic conditions, 60% of total energy produced is derived from lipids, 35% from carbohydrates, and 5% from amino acids and ketone bodies. However, these proportions vary widely according to the nutritional state. Since aerobic respiration is the predominant mode in the myocardium, the total O_2 consumption by the myocardium is a good overall indicator of the metabolic rate. O_2 consumption by an organ is usually expressed as a volume of O_2 consumed per 100 g of tissue per minute. During resting conditions the O_2 consumption of the heart is about 8 ml of O_2 per 100 g of tissue*min^{-1} (Neely and Morgan, 1974; Stanley et al., 2005; Taegtmeyer et al., 2005).

The O_2 consumption of the heart has implications for cardio-respiratory fitness and it refers to the ability of the circulatory and respiratory systems to supply oxygen to skeletal muscles during sustained physical activity. Sustained levels of sufficient O_2 consumption can reduce the risk of heart disease, type 2 diabetes, stroke, and other illnesses.

1.2 Control of TCA cycle

Four major mechanisms mediating regulation of TCA cycle reactions may be considered:

1. Regulation of the dehydrogenase reactions of the TCA cycle by ATP or ADP levels (LaNoue et al., 1970),
2. Regulation of the dehydrogenase reactions of the TCA cycle by Ca^{2+} levels (Denton et al., 1980),
3. Regulation by the oxidation-reduction state of the flavin and pyridine nucleotides (LaNoue et al., 1970), and
4. Regulation of the transport of TCA intermediate metabolites (TCAi) across the mitochondrial membrane (LaNoue et al., 1970).

The major sites in the TCA cycle where feedback control from the respiratory chain may be exerted are at Pyruvate dehydrogenase (PDH), Citrate synthase (CS), Isocitrate dehydrogenase (IDH), and α-ketoglutarate dehydrogenase (α-KGDH) (LaNoue et al., 1970). The feedback control at these reactions is imparted in through the regulation of mitochondrial NAD^+/NADH, ATP/ADP, and AcCoA/CoA ratios and the concentrations of their substrate and products. Since there are a number of enzyme-regulatory mechanisms, it is difficult to ascertain the relative contribution of each of these mechanisms due to their large number and inter-dependence.

The transport of molecules across the inner membrane of mitochondria is controlled by several small-molecule transporters and carriers. Also, the inner mitochondrial membrane is impermeable to free carnitine, free CoA and their derivatives (Bremer, 1967; Brosnan and Fritz, 1971; Garland et al., 1969; Haddock et al., 1970; Oram et al., 1973; Parsons et al., 1966; Sottocasa et al., 1967; Yates and Garland, 1966), as well as other low-molecular-weight solutes (Chappell, 1968; Klingenberg, 1970; Klingenberg and Pfaff, 1966; Pfaff et al., 1968; Williamson et al., 1968). In terms of transport of TCAi – adenine-nucleotide translocase (ANT), malate carrier (malate-phosphate transporter) (MC), OH^--Pyr antiport carrier, Pi-H^+ translocator (PiHt), malate-oxoglutarate transporter (MOTx), and glutamate-aspartate transporter (GATx); are some of the important transporters which may share a variable amount of control over the rate of TCA cycle, depending on the physiological conditions (Stryer, 2002).

1.2.1 Anaplerotic reactions

Pyruvate carboxylase (PC) is an *anaplerotic* reaction in the liver TCA cycle model. The term, *'Anaplerosis'* refers to the entry of carbon into the TCA cycle, by routes other than $AcCoA_m$ entry via the citrate synthase (CS) reaction. While, *'Cataplerosis'* refers to the exit of carbon from the TCA cycle by routes other than CO_2 production (Bowtell et al., 2007). The expression *'anaplerotic sequences'* was a term used in biochemistry by Sir Hans Kornberg (Kornberg, 1966) to describe a series of enzymatic reactions or pathways that replenish the pools of metabolic intermediates in the TCA cycle (Gibala, 2003; Gibala et al., 2000; Owen et al., 2002). Ambient levels of TCA cycle intermediate metabolites are controlled by various carboxylation and decarboxylation reactions which regulate carbon flux into and out of the cycle (Lee and Davis, 1979). Under normal conditions the cataplerotic removal of TCAi's is counteracted by anaplerotic processes so that the absolute concentration of TCAi's remains constant (Gibala et al., 1997; Lehninger et al., 1993).

The first reaction of the TCA cycle, citrate synthase, catalyses the condensation of oxaloacetate (OAA_m) with $AcCoA_m$; the oxaloacetate is subsequently regenerated by the reactions of the cycle and condenses with another molecule of $AcCoA_m$. However, in gluconeogenic tissue like liver, TCA cycle also functions in biosynthetic processes in which TCAi's are removed from the cycle; which necessitates anaplerotic reactions to replenish TCAi's to ensure its continued function. Pyruvate carboxylase, which synthesizes oxaloacetate from Pyruvate in the mitochondrial matrix, is the archetypical anaplerotic enzyme. The activity of this enzyme is high in many tissues (e.g. 10–12 units/g of liver); $AcCoA_m$ is a positive allosteric regulator of the enzyme. Anaplerosis is obligatory during both gluconeogenesis (hepatocytes in liver) and lipogenesis (adipocytes in adipose tissue) when malate (gluconeogenesis) or citrate (lipogenesis) leaves the mitochondria and is further metabolized to form glucose or fatty acids, respectively (Owen et al., 2002).

1.2.2 TCA cycle unspanning

Although, the accumulation of TCA cycle intermediate metabolites (TCAi)'s is quite extreme as seen in the results shown later (see, pg. 55), the peculiar divisioning of the TCA cycle observed therein calls for a further discussion. In 1970, Randle, England, and Denton observed a similar sort of division in rat heart TCA cycle, under conditions of acetate perfusion and since then this property has been referred to as the *"unspanning of TCA cycle"*. Owing to this finding, such a scheme of the TCA cycle, which is physiologically relevant as well, appears to be the polar-opposite of the idealised *'circular pathway'* notion used throughout several leading biochemistry textbooks. Indeed, this may only be of academic importance, but an essential aspect to point out, nonetheless.

Randle et al. suggested that the TCA cycle may operate as two 'spans': $AcCoA_m \rightarrow \alpha KG_{mit}$, controlled by citrate synthase, and $\alpha KG_{mit} \rightarrow OAA_m$, controlled by α-ketoglutarate dehydrogenase. This proposal was brought on by the fact that they observed accumulation of Cit_m & αKG_m along with transient differences between the rates of certain TCA cycle reactions during acetate perfusion of rat heart. They also observed that since acetate increased the concentration of $AcCoA_m$ from 40 µM to 400 µM, changes in $AcCoA_m$ concentration along with that of CoA_m & AMP, brought about by acetyl-CoA synthetase (ACS), could act as the initiating factors for such *unspanning* of the TCA cycle (Randle et al., 1970).

Therefore, the *"unspanning of TCA cycle"* is a phenomenon wherein, different TCA cycle reactions operate at distinctly different rates, in turn resulting in accumulation of several of the TCAi's. The unspanning phenomenon permits a redistribution of carbons between TCAi's during transition states of heart workload, which does happen physiologically, and might be expected for other such changes (Achs and Garfinkel, 1977; Ng et al., 1994; O'Donnell et al., 1998; Peuhkurinen et al., 1983; Randle et al., 1970; Safer and Williamson, 1973). Furthermore, *unspanning* of the TCA cycle was shown in isolated rat heart mitochondria (LaNoue and Williamson, 1971; LaNoue et al., 1970; LaNoue et al., 1972), in perfused rat heart (Randle et al., 1970; Safer and Williamson, 1973; Safer et al., 1971; Williamson et al., 1973) and *in vivo* for liver (Jucker et al., 1998). (LaNoue et al., 1973) Also, and more importantly, from Depre et al. (1999); Griffin et al. (2000); O'Donnell et al. (1998); Russell and Taegtmeyer (1991), it appears that anaplerotic reactions like the pyruvate carboxylase or transaminase reactions from the malate-aspartate shuttle (MAS), may also play a pivotal role in mitochondrial carbon metabolism by causing the *unspanning* of the TCA cycle at their respective intersection points with the TCA cycle through competition for common pools of TCAi's.

1.2.3 Metabolic homeostasis & TCA cycle

ATP synthesis is a consumer of NADH generated by the cycle, and as such also occupies a unique position within the system. As discussed by Hofmeyr and Cornish-Bowden, metabolism can be viewed as a network of functionally discrete supply and demand blocks, which are linked by common intermediates (Hofmeyr and Cornish-Bowden, 2000). Metabolic supply-demand analysis (Hofmeyr and Cornish-Bowden, 2000) shows that in order for supply to efficiently meet changes in demand, while preserving common intermediates at relatively constant levels far from equilibrium, the demand block controls the flux through the system whereas the supply block is responsible for maintaining intermediate concentrations. Furthermore, rather than feedback regulation of allosteric enzymes being a means of controlling flux, as is often believed to be the case, the analysis instead indicates that this brings about homeostasis of metabolites. Within the TCA cycle model, ATP synthesis forms the demand block, whereas the supply block is represented by the reactions of the cycle. As shown later in the results (see, pg. 74), the relatively high flux control coefficient of ATP synthesis and minimal coefficients of enzymes within the cycle, even though some (e.g. IDH and α-KGDH) are highly regulated and commonly viewed as key rate-controlling enzymes, are therefore in keeping with this view of metabolic control and regulation.

1.3 Mathematical modelling

In the Cell Systems Modelling Group, we use ScrumPy, a modelling software written in the Python programming language and developed in the group (Poolman, 2006). Python (http://www.python.org/) is a general-purpose, high-level programming language whose design philosophy emphasizes code readability. ScrumPy provides tools for model definition, model interrogation as well as data analysis. ScrumPy model files are plain ASCII files with an extension ".spy".

Using a programming language for the above mentioned activities offers flexibility in data handling. The model definition and data analysis can be maintained separately and it yields an easily manageable data structure. It becomes easy to create, append, modify and read the datasets without having to use any other special tools.

1.3.1 Need for mathematical models

At the system level, the responsiveness of ATP producing reactions is a result of the total sum of effects caused by several factors, internal as well as external. In effect, the emergent behaviour of any metabolic system is a function of manifold interactions between its individual components. Such emergent behaviour is subject to change with change in the environmental conditions. In order to study the local as well as systemic effects caused by several factors simultaneously, a well defined quantitative description of such a system is required. Conventional experimental approaches are often limited to studying the local effects and prove difficult to be used for studying and analysing multiple effects simultaneously. Therefore, if a comprehensive view of the quantitative kinetic behaviour of any metabolic system is to be achieved, reliable mathematical models representing such a system are essential.

The process of constructing quantitative models of metabolism can help in several ways:

(i) It can help identify whether the individual components of a system have been adequately characterized and whether available data are complete and consistent.

(ii) It can be used to qualitatively investigate and compare the model results with that of the observed behaviour exhibited by the real system.

(iii) It can be utilized to assess the validity of the experimental values for the components' properties based on whether one can make accurate predictions of the system's *in vivo* responses using those values.

1.3.2 Model definition and formulation

A detailed mathematical description of any dynamic biological system is called a model. In a metabolic context, a metabolic model would include a set of balanced biochemical reactions with details about the proportions of reactants and products in each reaction, concentrations and constants. A metabolic model is a simplified mathematical representation of the observed system or process. The term *modelling* refers to establishing a formal representation of the system under observation, and the term *simulation* refers to the numerical calculations performed using the model. Heinrich and Schuster discuss the aspects of modelling and theory in biochemistry in great detail (Heinrich and Schuster, 1996).

1.3.2.1 Stoichiometry

The stoichiometry of a reaction expresses the proportions of changes in mole numbers of the reactants and products involved. Metabolic models consist of more than one biochemical reaction. A concise way of representing the stoichiometric coefficients is to compile them in a matrix. In this matrix, the rows correspond to metabolites and columns correspond to reactions. Such a matrix is called a Stoichiometry matrix. Using such a model, metabolic pathways can be found, if any, within a metabolic network. Then, if the routes exist, it is possible to calculate the overall stoichiometries for each metabolic conversion and to find the most efficient route to produce a certain metabolite. This has a potential application in genetic engineering, *e.g.* Genetically modified crops or genetically modified bacteria producing ethanol.

1.3.2.2 Classification of metabolites

In order to apply the principles of mass conservation in a meaningful way, the distinction is made between two types of metabolites. *Internal metabolites* are those metabolites that are internal to the model and their dynamics can be explained based on the restriction imposed by the mass conservation relationship. That is, the concentration of an internal metabolite depends on the difference between the rates of formation and utilization. On the other hand, *External metabolites* are those that form the *boundaries* of the system, *i.e.* they participate both in reactions involved in the model and in additional (external) reactions that are outside the scope of the model. External metabolites are sometimes also known as source and sink, as they define the points in the system that remain constant over time acting as a source to generate a metabolite or as a sink to destroy one.

1.3.2.3 Rate equations

The rate equation for a chemical reaction is an equation that links the reaction rate with concentrations of reactants and constant parameters (*e.g.* rate coefficients and equilibrium constants). The rate equation is a differential equation, and it can be integrated to obtain an integrated rate equation that links concentrations of reactants or products with time. In metabolic models, the rate equations take different forms depending on the nature of enzyme mechanism. Widely used forms of the rate equations include first order mass balance rate equations, Michaelis-Menton enzyme kinetics, modified Michaelis-Menton enzyme kinetics *etc.*

Equation 1.2 shows a simplified, generic, reversible bi-substrate equation (Chassagnole et al., 2001b; Rohwer et al., 2006), modified where necessary to account for more than two substrates and/ or products. Equation 1.2 shows an example of such a simplified bi-substrate equation for a generic reaction (see, eq. 1.1). Equations of this form are simple enough to include a limited number of parameters that are easily determined, and do not require additional explicit assumptions to be made, yet adequately describe the response of an enzyme to changes in both substrate and product concentrations within the physiological range (Chassagnole et al., 2001b).

$$\mathrm{A} + \mathrm{B} \rightleftharpoons \mathrm{P} + \mathrm{Q} \tag{1.1}$$

$$\nu = \frac{V_\mathrm{f}\left[[\mathrm{A}]\cdot[\mathrm{B}] - \left(\frac{[\mathrm{P}]\cdot[\mathrm{Q}]}{K_\mathrm{eq}}\right)\right]}{\left[K_\mathrm{A}\left(1+\frac{[\mathrm{P}]}{K_\mathrm{P}}\right)+[\mathrm{A}]\right]\left[K_\mathrm{B}\left(1+\frac{[\mathrm{Q}]}{K_\mathrm{Q}}\right)+[\mathrm{B}]\right]} \tag{1.2}$$

By default, this equation assumes competitive product inhibition with respect to the corresponding substrate (*e.g.* ADP competitive with ATP), and non-competitive inhibition for unrelated substrate-product pairs in multi-substrate reactions. Additional effector interactions are also considered when necessary. In all cases, the simplest expression that adequately represents the key kinetic properties of the enzyme is used.

Throughout the models described in this work, nearly all rate equations are based on such a simplified bi-substrate equation, as it allowed us to maintain the model complexity to a bare minimum, while making the models neither too complicated nor overly simplified.

1.3.3 Models of TCA cycle

Over the years, several research groups have attempted modelling different aspects of TCA cycle. Kohn et al. built a TCA cycle model for pyruvate perfused rat heart (Kohn et al., 1979a,b). Cortassa et al. attempted to study an integrated model of cardiac mitochondrial energy metabolism that included regulation of TCA cycle dehydrogenases by calcium (Cortassa et al., 2003). Mogilevskaya et al. studied a kinetic model of the TCA cycle for the salicylate hepatotoxic effects (Mogilevskaya et al., 2006). Wu et al. built a TCA cycle model integrated with oxidative phosphorylation and metabolite transport and also included the aspects of electrophysiology (Wu et al., 2007). Nazaret et al. investigated the properties of a simplified model of TCA cycle with ATP production (Nazaret et al., 2009). In CSMG, we are trying to build a heart-specific model of TCA cycle that attempts to address certain limitations posed by these earlier published models.

1.3.4 Different types of model analyses

Model analysis involves exploring the mathematical model and its response to varying conditions using mathematical and computer programming tools. Model analysis is categorized as Structural and Kinetic analysis. The distinction is made at the level of analysis and not the model because it is the type of analysis and tools used to characterize the model responses that changes according to aim of study and not the model itself.

1. **Structural analysis:** The models used for this type of analysis are comparatively simple in their construction and do not need no more than a reaction list. Such models require all the metabolic intermediates to be exactly balanced with respect to their respective rates of formation and utilization at metabolic steady state. In other words, at steady state, these types of models require all of their intermediate metabolites to be stoichiometrically balanced and therefore emphasize on stoichiometry. Apart from the stoichiometry, the other important aspect in these models are the mass conservation relationships between metabolites. The conservation relationships between metabolites imply that the temporal change in the concentration of each metabolite equals the sum of all reaction rates producing that metabolite minus all reaction rates consuming it. In fact, it is because of the restrictions imposed by the mass conservation of metabolites that we can express them in terms of meaningful equations that make the mathematical modelling of metabolic systems possible.

2. **Kinetic analysis:** A model used for kinetic analysis requires a full kinetic description of each enzyme or step of the reaction list. Therefore, essentially, all kinetic models

are structural models containing kinetic details of every reaction. This means that these models will comprise detailed reaction equations representing the enzyme reaction mechanism observed in physiology. Such equations consider the effects of all the substrates, the products, the reverse reaction and any effectors, with all the corresponding parameters such as the limiting rate and K_m values. These kinetic details are subject to change depending on the experimental conditions, species of the organism used for experiments, methods etc. Although, obtaining such large array of information is often a cumbersome task, once utilized appropriately, it can lead to important predictions with respect to time courses and steady states, as well as the control distribution, for a wide range of different conditions. In time course simulations, dynamic changes in concentrations of metabolites are monitored against time. Time course simulations can help in understanding temporal effects of perturbations to the system. Steady state simulations show the information related to the reaction rate and metabolite concentrations, when there is no net flow of mass in the system. Steady state simulations help in determining the structural properties of the system. Models used for the kinetic analysis can also be used for Metabolic Control Analysis (MCA) of the system for determining the different types of sensitivities associated with individual enzymes, concentrations, and fluxes in the system.

1.3.4.1 Discussion on the identicalness of elementary modes

For the sake of clarity in this discussion, let us briefly consider a hypothetical system with **r** reactions (say, **j** in number), as shown in fig. 1.1 (see Schuster et al., 2002a, fig. 2.1).

This system comprises internal metabolites (**i** and **k** in number), that have variable concentrations and external metabolites (**X** and **p** in number) with fixed concentrations (*i.e.* they can act as sinks or sources), for example due to regulated supply. As seen in fig. 1.1, **N** denotes the stoichiometry matrix of the system. Many biochemical systems achieve an asymptotically stable steady-state, in such a way that the vector of reaction rates, **V**, fulfils the condition (Reder, 1988; Schilling et al., 1999; Schuster and Hilgetag, 1994; Schuster et al., 2002a; Trinh et al., 2009):

$$\mathbf{N}.\mathbf{V} = \mathbf{0} \tag{1.3}$$

As shown in the fig. 1.1, rows of **N** represent the internal metabolite s (i_k) only, as the steady-state condition (eq. 1.3) applies only to the internal metabolite s (Reder,

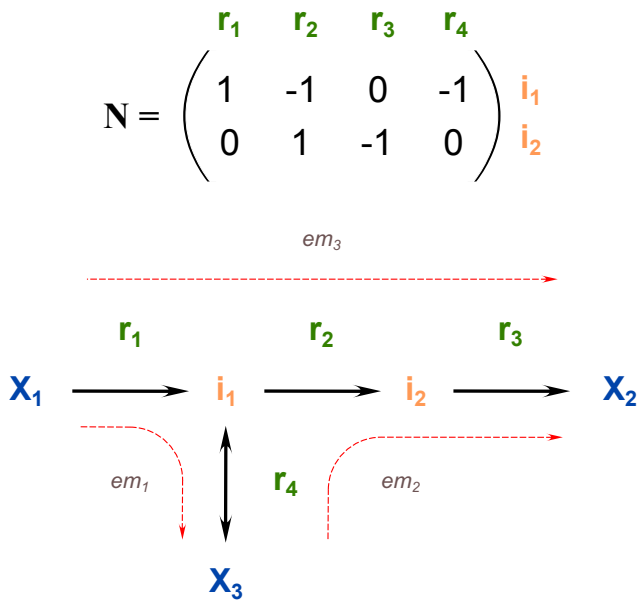

- **Figure 1.1.**

A hypothetical reaction scheme showing elementary modes and stoichiometry matrix.

i_k: internal metabolites; X_p: external metabolites; r_j: reactions. The reaction with double arrowheads is assumed to be reversible. Dashed lines denote elementary modes. Let **N** denote the stoichiometry matrix of the system. In **N**, column **j** denotes reaction **j** (r_j) and row **k** denotes internal metabolite **k** (i_k).

The value at $N_{(k,j)}$ is a stoichiometric coefficient (α) of i_k in reaction r_j.

For α:

if, $\alpha = +\alpha$, reaction r_j produces α molecules of i_k;
if, $\alpha = -\alpha$, reaction r_j consumes α molecules of i_k; and
if, $\alpha = 0$, reaction r_j neither produces nor consumes i_k.

1988; Schilling et al., 1999; Schuster and Hilgetag, 1994; Schuster et al., 2002a; Trinh et al., 2009). This means that the stoichiometry matrix **N** is independent of the status of external metabolite s (**X**). In that case, if we were to internalise, say external metabolite-X_3, then the value of α at $N_{(k,j)}$ is likely to vary due to the change in topology of said metabolic network* and also the elementary mode ($\mathbf{em_3}$) would disappear; but the length of **N** (total number of rows & columns) would remain constant.

While discussing how the elementary modes could behave if additional reactions are included, Schuster et al. say that the invariance in elementary modes after additional reactions are included, only holds, if the status of the metabolites (internal or external) remains unchanged. If the metabolite status is indeed changed, the modes could vary in a complicated way (Schuster et al., 2000). Furthermore, Schuster et al. state that sometimes in simple systems, however, the number of modes does not increase but some of the modes are increased in length (Schuster et al., 2000). For example, if in an

* ***Topology of a metabolic network:*** *Set of enzymes and metabolites, their connections and the stoichiometry and directionality of the reactions.* (see Schuster et al., 1999, Glossary on pg. 2)

unbranched reaction chain, a reaction removing the product is added and the former product if now considered as an internal metabolite, the mode representing this pathway is simply enlarged by one reaction. The system shown in fig. 1.1, is a branched reaction chain, so although we may not be able to comment on how its modes could behave if an additional reaction was included, but we can give an example of an additional reaction removing the product from this system. Reaction r_3 and r_4 (in forward direction, from i_1 to X_3) are two examples of reactions removing the product from the system.

In the study of biochemical systems, generally, such reactions are differentiated from internal reactions and termed as *'boundary reactions'*. Schuster and Hilgetag, discuss the properties of boundary reactions, in detail (Schuster and Hilgetag, 1994). They mention that it is the property of boundary reactions that all the reactants utilised or all the products formed by such reactions are external (i.e. their concentrations are fixed). In the example shown in fig. 1.1, reactions r_1, r_3, and r_4 are boundary reactions, while reaction r_2 is internal. Schuster and Hilgetag also mention that this distinction between boundary reactions & internal reactions can be made by investigating the stoichiometry matrix. In the stoichiometry matrix, boundary reactions are represented by those columns that only contain elements of the same sign or zeros, while internal reactions are represented by columns that contain elements of opposite sign. From the corresponding stoichiometry matrix of the system shown in fig. 1.1, we can conclude that columns **1**, **3**, and **4** represent boundary reactions and **2** represents the only internal reactions in this system.

In theory, it is possible to have same length for two modes and correspondingly, different overall (net) stoichiometries. From Schuster et al. (2000), consider the case of inclusion of pyruvate, water dikinase (phosphoenolpyruvate synthase) (Pps) to the reaction scheme representing a part of monosaccharide metabolism (*see, Fig. 1 & Table 1* from Schuster et al.). When this (reversible) enzyme is considered in addition to the other E.coli enzymes, all the 13 modes, plus eight additional modes are obtained (see Schuster et al., 2000, Table 2). These eight modes comprise seven modes that coincide with the seven modes producing pyruvate except that pyruvate kinase (Pyk) is replaced by Pps in the reverse direction and in the overall stoichiometry, ADP is partially replaced by AMP plus inorganic phosphate. The eighth additional mode is the futile cycle made up of Pyk and Pps.

1.3.4.2 Physiological relevance of elementary modes

Before we discuss each elementary modes (ElMo) in detail later on in the results section, we must keep in mind that they represent idealised situations and a single ElMo may therefore, represent the cellular physiology, at given initial conditions, in part. Usually, in living cells, demands are mixed so that the flux distribution specific to that state of

cellular physiology is a superposition* of several modes. However, cellular metabolism can sustain potentially different flux distributions in response to different environmental stimuli (Stephanopoulos and Vallino, 1991). For instance, in muscle tissue, post rigorous exercise, aerobic metabolism is noticeably repressed. This indicates a switch between markedly different metabolic modes, which are likely to be superpositions of a limited number of elementary modes. Specific metabolic pathways dominate in certain stress conditions. For example, catabolic modes predominate during prolonged starvation. (Schuster et al., 1999, 2000)

1.4 Concepts in metabolic regulation

The *'regulation'* of an enzyme in a set of reactions is how its activity is increased or decreased in response to a change in stimulus. Regulation refers to a biological phenomena of specific alteration of enzyme activity by other molecules or their properties. Enzymes can be regulated by altering the level of gene transcripts, compartmentalization, effectors, post-translational modification. Therefore, it can be said that *'regulation'* implies a qualitative relationship between enzymes and effectors.

Control, as used in a biological context, is a vague term and unless defined appropriately, may lead to false interpretations. *'Control'* should be distinguished from *'regulation'*. For example, *'X controls respiration'*, in this report, only means that the change in the level of X will cause a change in the rate of respiration, and does not necessarily imply that respiration is regulated by X *in vivo*. According to Kacser and Burns, control implies simply a quantitative relationship between components of a system. To say A controls B means that altering the amount or activity of A causes a change in the amount or activity of B (Kacser and Burns, 1973). We will follow the same distinction between these two terms in the discussion to follow.

Metabolic regulation allows the organism to respond optimally to change in its environment and variations in stimuli levels. Metabolic regulation can be divided further into intrinsic regulation and extrinsic regulation. In intrinsic regulation, metabolic pathways appear to self-regulate to respond to changes in levels of substrates and products, often by means of allosteric regulation of enzyme activities in the pathway.

Extrinsic regulation involves a cell in a multicellular organism altering its metabolism in response to stimuli from the neighbouring cells. Regulation of glucose metabolism by insulin is a very well studied example for the extrinsic regulation. Enzyme activity can

*__Linear combination (superposition):__ *Sum of several terms, each of which may be weighted by an appropriate coefficient. (see Schuster et al., 1999, Glossary on pg. 2)*

also be altered by reversible covalent modification of the enzyme and this mechanism represents another level of metabolic regulation. The catalytic properties of many enzymes are markedly altered by the covalent attachment of a modifying moiety, most commonly a phosphoryl group. ATP serves as the phosphoryl donor in these reactions, which are catalyzed by protein kinases and on the other hand the removal of the phosphoryl group is catalyzed by protein phosphatases, thereby altering the enzyme between active and inactive states. The covalent attachment or removal of the phosphoryl group causes a conformational change in the enzyme structure and thereby altering its activity. Activation of PDH by pyruvate dehydrogenase phosphatase (PDP)-mediated dephosphorylation and inactivation by pyruvate dehydrogenase kinase (PDK)-mediated phosphorylation is a well understood example of reversible covalent modification of enzyme activity.

Allosteric regulation is the regulation of an enzyme activity by an effector molecule binding to the enzyme. Effector molecules that enhance enzyme activity are referred to as allosteric activators, whereas those that decrease the enzyme activity are called allosteric inhibitors. Ca^{2+}, Mg^{2+} are some of the important examples of allosteric activators of metabolic enzyme activity.

1.4.1 Metabolic Control Analysis

In an attempt to provide a reliable quantitative description of control of metabolic flux, the theory of *'Metabolic Control Analysis'* (MCA) arose from two independent approaches by Kacser and Burns (1973) and Heinrich and Rapoport (1974). MCA is a form of sensitivity analysis; that is, the magnitude of the effect of small change in a parameter (such as an enzyme activity) on a metabolic system property (such as the flux or the concentration of a metabolite) is mathematically related to the properties of the components of the system (Fell, 1997).

Metabolic Control Analysis attempts to relate the systemic properties of a metabolic system to the properties of its component parts, in particular, the enzymes. Control coefficients are the system properties that are at the centre of this theory. These describe how a variable or property of the system, typically a metabolic flux or the concentration of a metabolite, will respond to variation of a parameter, typically enzyme concentration. Thus, MCA defines four types of control coefficients, *viz.*– flux control coefficient (C^J), response coefficient, concentration control coefficient (C^S) and elasticity coefficient (ε_S). For further explanation of control coefficients let us consider the following specimen pathway:

$$X_0 \quad \underset{J_{xase}}{\xrightarrow{xase}} \quad S_1 \ \rightarrow \cdots Y \quad \underset{J_{ydh}}{\xrightarrow{ydh}} \quad S_6 \cdots \rightarrow \quad X_1$$

1. Flux Control Coefficient (C^J) : Suppose that if a small change, δE_{xase}, is made in the amount of enzyme E_{xase}, and that this produces a small change, δJ_{ydh}, in the steady state pathway flux, J, measured at the step catalyzed by ydh, then the flux control coefficient, $C_{xase}^{J_{ydh}}$, is defined as:

$$C_{xase}^{J_{ydh}} = \frac{\delta J_{ydh}}{\delta E_{xase}} \cdot \frac{E_{xase}}{J_{ydh}}$$

2. Elasticity Coefficient (ε_{S}): Unlike control coefficients, elasticities are properties of individual enzymes and not of the metabolic system. The elasticity coefficient for the effect of metabolite S on the velocity υ of enzyme $xase$ is the fractional change in rate of the isolated enzyme for a fractional change in substrate S, with all other effectors of the enzyme held constant at their respective values:

$$\varepsilon_S^{xase} = \frac{\delta \upsilon_{xase}}{\delta S} \cdot \frac{S}{\upsilon_{xase}}$$

   Elasticities have positive values for metabolites that stimulate the rate of a reaction (substrates, activators) and negative values for those, like products and inhibitors, that slow the reaction.

3. The summation theorem: When Kacser and Burns first developed MCA, they found that, if all the enzymes that can affect a particular metabolic flux in a cell or a metabolic system are taken and the values of their control coefficients on that flux added up, the sum comes to 1. Thus if we number all the enzymes involved from 1 to n, then:

$$C_1^J + C_2^J + \cdots + C_n^J = 1$$

   This relationship is known as the summation theorem for flux control coefficients, and in mathematical notation can be expressed as:

$$\sum_{i=1}^{n} C_i^J = 1$$

   Therefore, the summation theorem shows that the enzymes of the pathway can share the control of flux. The summation theorem also shows that the flux control coefficient of an enzyme is a system property. Therefore, the value of a flux control coefficient cannot be determined by considering the properties of the enzyme in isolation; the characteristics and amounts of the other enzymes in the metabolic system will affect the result.

4. The connectivity theorem: Suppose we choose one pathway metabolite S and find all the enzymes in the given metabolic system whose rates respond to it; further suppose that we find there are three and let us lable these enzymes i, j, and k. The connectivity theorem states that, for each of these enzymes, if we form a term by taking its flux control coefficient on a particular flux J and multiplying by its elasticity with respect to S, then the sum of the terms is zero, i.e. :

$$C_i^J \varepsilon_S^i + C_j^J \varepsilon_S^j + C_k^J \varepsilon_S^k = 0$$

In mathematical notation can be expressed as:

$$\sum_{i=1}^{n} C_i^J \varepsilon_S^i = 0$$

Metabolic Control Analysis shows that neither the degree of displacement of a reaction from equillibrium nor the relative value of the limiting rate of an enzyme is a reliable guide to the degree of control an enzyme can exert on a flux and therefore quantifying these effects in terms of control coefficients is essential for reliable analysis.

Chapter 2

Modification of the existing liver TCA cycle model

2.1 Overview

The biochemical background of mitochondrial carbon metabolism in mammalian cells was reviewed in the introductory chapter. Furthermore, the basic techniques involved in the construction and analysis of kinetic metabolic models were also described in the introductory chapter. A major objective of this study is to investigate the basic functional characteristics of the tricarboxylic acid cycle (TCA) and its interactions with other mitochondrial metabolic pathways, in response to changes in cellular energy demand at the systemic level, in specific mammalian tissues such as the cardiac or skeletal muscle; using kinetic as well as structural modelling and analysis techniques.

However, before defining a heart or skeletal muscle-specific TCA cycle model, at the beginning stages of this project, it was essential to study an existing tissue-specific model, to understand the basic functional properties of a tissue-specific TCA cycle, as well as to learn the processes involved in properly defining and analysing such a model. The mammalian liver-specific tricarboxylic acid cycle model developed within the Cell Systems Modelling Group (CSMG) was used for this purpose (Brightman et al., 2010, *unpublished manuscript*). This model was developed using COPASI (A COmplex PAthway SImulator; see, `http://www.copasi.org/`; Hoops et al., 2006), as part of a larger-scale project, to investigate the systemic consequences of molecular defects in mitochondrial energy metabolism. For the work described here, the COPASI -based model was manually converted into a ScrumPy -based model, henceforth referred to as the – ***Original liver TCA cycle model (LVR$_{TCA}^{OGI}$)***. ScrumPy is a metabolic modelling tool written in

Python (see, Poolman 2006; also, Poolman et al. 2003, *Modelling software, pg.3*; and http://www.python.org).

Detailed analysis of this model revealed that CoA–related metabolites were not conserved within this system, because coenzyme A (CoA_m) was defined as a fixed parameter of the model (external metabolite), instead of being defined as a model variable (internal metabolite), the value of which would be determined dynamically at model simulation. Therefore, the ScrumPy -based original liver TCA cycle model was developed further to include the conservation relationship involving CoA_m, acetyl-CoA ($AcCoA_m$), & succinyl-CoA ($SCoA_m$), by redefining CoA_m as a model variable. Henceforth, this updated model will be referred to as – ***Updated liver TCA cycle model*** ($\boldsymbol{LVR_{TCA}^{UPD}}$). Just to reiterate, the *'original'* & the *'updated'* liver TCA cycle models differ from each other *only* in terms of the model definition of coenzyme A; otherwise, the two models are identical with respect to their individual model definitions. Although, upon model simulation, such a change in the model definition might cause some alteration in its dynamic properties; for the purposes of discussing how these models are defined in terms of their individual reaction rate equations *etc.*, there is absolutely no need to treat them separately. Therefore, in the following section, we shall discuss the definition & construction of updated liver TCA cycle model, as a common example. Section 2.3: Results for the liver TCA cycle models on pg. 32, describes an in-depth analysis of the plausible differences in the dynamic properties of the two models.

2.2 Methods: Model design and definition

As mentioned earlier, the updated liver TCA cycle model (LVR_{TCA}^{UPD}) representing the operation of mammalian liver-specific TCA cycle was manually constructed using ScrumPy. The model in ScrumPy format is available in Appendix C (see, pg. 233) and is illustrated in fig. 2.1 (see, pg. 21). The final version of the updated model contains 15 reactions and 28 metabolites.

2.2.1 Choice of model design

For any particular mathematical model, its design choices and other design-related requirements are mainly determined by the specific questions that it aims to address. The original large-scale project for which the liver TCA cycle model was developed, required a model of mitochondrial carbon metabolism in a specific mammalian tissue, in which the individual enzyme rate equations exhibit certain key properties, such as – enzyme saturation, product inhibition and reversibility (where appropriate); since all

of these specific enzyme characteristics are known *a priori* for their potential effects on the overall distribution of control in a given metabolic system (Cornish-Bowden and Cárdenas, 2001; Fell and Sauro, 1985). There are a number of existing models of mitochondrial energy metabolism that include varying representations of the TCA cycle (Bazil et al., 2010; Cortassa et al., 2003; Kohn et al., 1979a; Mogilevskaya et al., 2006; Nazaret et al., 2009; Stucki and Walter, 1972; Tran-Dinh et al., 1997; Wu et al., 2007; Yugi and Tomita, 2004). However, none of these models both exhibit the scope and properties required, and operate at appropriate concentrations of mitochondrial metabolites; which prompted the development of this novel, mammalian liver-specific model of the TCA cycle in our group. *We continued to follow the same modelling strategy for the development of other models presented as a part of this work.*

The liver TCA cycle model is constructed using saturable kinetics to represent 14 out of 15 reactions in the model and most of these processes are assumed to be reversible. All of these 15 enzyme-catalysed reactions, including those considered to be effectively irreversible, are modelled considering the effects of product inhibition as well as other additional effector interactions, as appropriate. Except one reaction, all of the single substrate/ product processes are assumed to follow a simple uni-uni kinetic model (Segel, 1993). The remaining reactions are represented using the simplified, generic, reversible bi-substrate equation (Chassagnole et al., 2001b; Rohwer et al., 2006), modified where necessary to account for more than two substrates and/ or products. Equation 2.2 shows an example of such a simplified bi-substrate equation for a generic reaction (see, eq. 2.1). Equations of this form are simple enough to include a limited number of parameters that are easily determined, and do not require additional explicit assumptions to be made, yet adequately describe the response of an enzyme to changes in both substrate and product concentrations within the physiological range (Chassagnole et al., 2001b).

$$\mathrm{A} + \mathrm{B} \rightleftharpoons \mathrm{P} + \mathrm{Q} \tag{2.1}$$

$$\nu = \frac{V_\mathrm{f}\left[[\mathrm{A}]\cdot[\mathrm{B}] - \left(\frac{[\mathrm{P}]\cdot[\mathrm{Q}]}{K_\mathrm{eq}}\right)\right]}{\left[K_\mathrm{A}\left(1+\frac{[\mathrm{P}]}{K_\mathrm{P}}\right)+[\mathrm{A}]\right]\left[K_\mathrm{B}\left(1+\frac{[\mathrm{Q}]}{K_\mathrm{Q}}\right)+[\mathrm{B}]\right]} \tag{2.2}$$

By default, this equation assumes competitive product inhibition with respect to the corresponding substrate (*e.g.* ADP competitive with ATP), and non-competitive inhibition for unrelated substrate-product pairs in multi-substrate reactions. Additional effector interactions are also considered when necessary. In all cases, the simplest expression that adequately represents the key kinetic properties of the enzyme is used.

2.2.2 Model definition

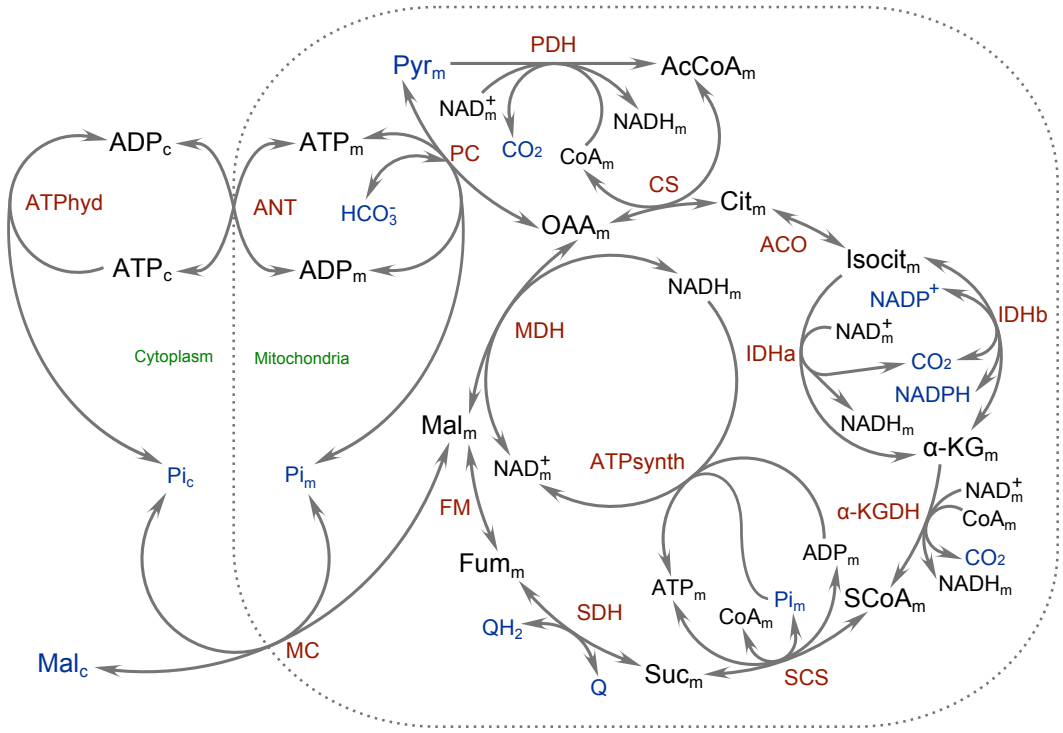

Figure 2.1.
Schematic illustrating the TCA cycle reactions in the updated liver TCA cycle model.

- The original liver TCA cycle model is also defined as illustrated in the above shown schematic, with the exception of CoA_m; which is a fixed parameter (external metabolite) in the original model.
- Internal metabolites: in *Black*; external metabolites: in *Blue*; reaction/ enzyme names: in *Red*.
- Reaction with double arrowheads is assumed to be reversible and reaction with single arrowhead is assumed to be irreversible.

As illustrated in Figure 2.1, the model includes nine canonical (non-tissue-specific) TCA cycle reactions including the reaction catalysed by pyruvate dehydrogenase (PDH), two liver tissue-specific reactions (malate carrier (malate-phosphate transporter) (MC) & pyruvate carboxylase (PC)), a reaction catalysed by the $NADP^+$-dependent isocitrate dehydrogenase (IDHb), and three ATP/ADP–linked reactions that include an abstracted representation of oxidative phosphorylation, cytosolic ATP hydrolysis (ATPhyd), along with an adenine-nucleotide exchange with the cytosol catalysed by ANT. The major outflow from the TCA cycle in liver mitochondria is via malate (Baranyai and Blum, 1989; Des Rosiers et al., 1995; Rabkin and Blum, 1985) and despite the existence of several mitochondrial metabolite transporters in liver cells, malate carrier (malate-phosphate transporter) is the only transporter considered in the model to represent this outflow (Lehninger, 1977); since other transporter systems, such as the Malate-Aspartate shuttle, do not achieve a net export of carbon from the cycle.

In this model , except pyruvate dehydrogenase, NAD^+-dependent isocitrate dehydrogenase, α-ketoglutarate dehydrogenase, & ATP hydrolysis, all other enzyme-catalysed steps are modelled using reversible form of the simplified, generic, saturable rate equation. While, the aforementioned reactions (except ATPhyd) are modelled using the irreversible form. The ATP hydrolysis reaction is represented using an irreversible, first-order flux. All other single substrate/ product reactions are assumed to follow a simple uni-uni kinetic model (Segel, 1993). Table 2.1 (see, pg. 24) gives a brief overview of the liver TCA cycle reactions. Also, complete details regarding net stoichiometric equations as well as enzyme rate equations used in the liver TCA cycle model are included in Appendix B (see eqs. B.1 to B.38 on pgs. 221 to 232, respectively).

The liver TCA cycle model comprises 16 variables that describe the concentrations of TCA cycle intermediates, and of acetyl-CoA, CoA_m, adenine nucleotides, NAD^+_m, & $NADH_m$. In other words, these 16 metabolites are *'internal'* to the system described by the liver TCA cycle model and their respective values are computed at model simulation. Each of these variables in the model is assigned an initial value, based on literature data. Also, this model includes 12 parameters that describe fixed quantities of model inputs (pyruvate & HCO_3^-), enzyme cofactors (Q/ QH_2, $NADP^+$, & NADPH), effectors (Ca^{2+} & Mg^{2+}), inorganic phosphates (Pi_m & Pi_c), and system outputs (CO_2 & Mal_c); *i.e.* they are *'external'* to the system under consideration, since the *in vivo* processes that determine these concentrations are beyond its scope.

The updated liver TCA cycle model ($LVR_{TCA}{}^{UPD}$) consists of a system of 12 non-linear ordinary differential equations, each of which describes the evolution of one of the model variables (concentrations of internal metabolites) over time, from their respective initial model values. This system also contains 4 algebraic expressions that define the concentrations of conserved moieties in terms of their total quantities, whereby the total is a sum all concentrations in a given conservation relationship (*e.g.* in eq. A.14 on pg. 220, $[N_{Tot}]$ is a conserved total of $[NAD^+_m]$ & $[NADH_m]$). The decision to include such algebraic expressions in the original COPASI -based model, might have been made in light of certain limitations in COPASI *.

In ScrumPy however, an internal, global parameter (in the form: `CSUM_<name>`) is assigned to each of the conserved totals in the model, by default, at model simulation.

*In COPASI, moieties are the result of stoichiometric analysis and the result of this analysis is not unique, as it depends on the algorithm chosen (*e.g.* the Householder reduction method described by Vallabhajosyula et al., 2006). Therefore, in order to compute the conserved totals in an algorithm-independent manner, COPASI requires the declaration of a global quantity of type *'assignment'* (COPASI project, 2009a). Global quantities with assignment require a mathematical expression to be specified (which can involve other variable or parameter values from the model) and their value is always the value of this expression. These assigned quantities could be used as model input/ output only or both (COPASI project, 2009b). The 4 algebraic expressions in the liver TCA cycle model are actually such *'globally assigned quantities'* that originated in the COPASI -based version of the model.

For instance, every conservation relationship described in Results (see tbl. 2.5 on pg. 34) points to a unique internal parameter generated at model simulation, with a constant value, for a given conserved total (*e.g.* `CSUM_NAD = 2.1`). During model analysis, it is possible to change the value of these internally generated parameters, without applying any permanent changes to the model, since they are generated by default at model simulation. However, the respective algebraic function/ expression for a given conservation relationship, can not be changed manually in ScrumPy, since it is a direct result of the structural definition of a given mathematical model. Nonetheless, these manually defined algebraic expressions (see, eqs. A.13 to A.16 on pg. 220) have been maintained even in the ScrumPy -based model, since they are more accessible than the internal parameters, and their value as well as the mathematical expression can both be changed, if necessary. This model also includes a function that dynamically calculates the apparent maximal activity of PC (see, eqs. B.3 to B.5 on pg. 222). The non-linear ordinary differential equations as well as the algebraic expressions used in the liver TCA cycle model are described in Appendix A (see, eqs. A.1 to A.16 on pg. 220).

The values of the model parameters (kinetic and thermodynamic constants, plus concentrations of external metabolites and constants describing the total quantities of the conserved moieties), and the initial concentrations of the variables, were derived almost exclusively from experimental studies reported in the literature. The main exceptions are the activities of adenine-nucleotide translocase (ANT), malate carrier (malate-phosphate transporter) (MC), ATP synthase and ATP hydrolysis, for which satisfactory estimates were not available. These quantities were fitted to the representative experimental data taken from a number of sources, using the *genetic algorithm for parameter estimation* in COPASI 4.5. Briefly, the representative experimental data was obtained by extensively surveying the literature for experimental measurements of TCA cycle flux (flux through CS) and mitochondrial metabolite concentrations in mammalian tissues. For most metabolites, a range of values, largely from rat liver tissue, were found. However, fumarate was the only metabolite for which mitochondrial concentration data were not available. Table 2.2 (see, pg. 25) shows the values of TCA cycle variables (internal metabolites & key fluxes) in liver tissue taken from the literature and compares them to corresponding values predicted by the model at initial steady-state. The values of all the model parameters (external metabolites & kinetic/ thermodynamic constants) are provided in the supplementary material, in Table I.2 (see, pg. III).

Table 2.1. Overview of the liver TCA cycle reactions in the model [a]

Eqn. No.	Enzyme	Inhibitors [h]	Additional effectors	Reversibility in the model	No. of substrates
B.11	ACO [b]	Isocit	–	Reversible	1
B.24	FM [b]	Mal	–		
B.9	CS [c]	Citrate	SCoA [i] & ATP [i]		2
B.16	IDHb [c]	αKG & NADPH	CO_2 [l]		
B.22	SDH [d]	Fum & QH_2	OAA [p]		
B.26	MDH [d]	OAA & NADH	–		
B.28	ANT [d]	ADP & ATP_c	–		
B.34	MC [d]	Pi_m & Mal_c	–		
B.2	PC [c]	OAA, ADP, & Pi_m	AcCoA [g] & Mg^{2+} [g]		3
B.20	SCS [c]	Suc & CoA	GTP [o] & Pi_m [o]		
B.38	ATPhyd [e]	–	–	Irreversible	1
B.13	IDHa [f]	NADH & ATP [j]	ADP [k] & Ca^{2+} [k]		2
B.7	PDH [f]	AcCoA & NADH	–		3
B.18	α-KGDH [f]	ATP [m], SCoA, & NADH [n]	ADP [k] & Ca^{2+} [k]		
B.36	ATPsynth [f]	NAD & ATP	ATP & Pi_m		

[a] For further details regarding each enzyme-catalysed reaction, please refer to the detailed account given in the Appendix B (see, pg. 221).

[b] A reversible uni-uni rate law is used to represent this step (Segel, 1993).

[c] The extended, reversible form of the generic rate equation is used to represent this step.

[d] The simplified, generic, reversible bi-substrate rate equation (see, Equation 2.2 on pg. 20) is used to represent this step.

[e] This step is modelled as a simple first-order flux.

[f] The extended, irreversible form of the generic rate equation is used to represent this step.

[g] Apparent maximal activity of PC is a function of AcCoA & Mg^{2+}.

[h] Product inhibition, competitive with respect to corresponding substrate(s); unless stated otherwise.

[i] Inhibitor, competitive with respect to AcCoA (Shepherd and Garland, 1969; Smith and Williamson, 1971).

[j] Inhibitor, competitive with respect to NAD^+_m (Chen and Plaut, 1963; Plaut and Aogaichi, 1968).

[k] Activator.

[l] Inhibitor, non-competitive.

[m] Inhibitor, competitive with respect to αKG (McCormack and Denton, 1979).

[n] Mixed inhibition with respect to NAD^+_m.

[o] Competitive binding between GTP & Pi has been reported (Cha and Parks, 1964). Also, ADP and ATP are substituted for GDP and GTP in the expression, according to (Alberty, 2003b).

[p] Inhibitor, competitive with respect to succinate (Hatefi and Stiggall, 1976).

Table 2.2. Values of TCA cycle variables in liver tissue taken from the literature and predicted by the model [d,e]

Fluxes are in units of mmol/sec and concentrations in mM.

Variable	Literature Values		Model Values
	Range	Median	
TCA cycle (CS) flux	0.04 – 0.48	0.24	0.27
PC flux	0.05 – 4.5	0.70	0.82
MDH flux	−0.63 – −4.0E-04	−0.07	−0.55
MC flux	0.03 – 1.0	0.34	0.82
$[CoA_m]$ [a]	0.31 – 1.93	1.92	1.67
$[AcCoA_m]$	0.14 – 0.49	0.25	0.35
$[Cit_m]$	1.7 – 5.5	3.73	3.57
$[Isocit_m]$	0.14 – 0.62	0.15	0.19
$[\alpha KG_m]$	0.38 – 2.8	1.3	1.34
$[Suc_m]$	1.5	– [b]	1.64
$[SCoA_m]$	0.30 – 1.4	– [b]	0.68
$[Fum_m]$	–	– [b]	0.34
$[Mal_m]$	0.23 – 2.5	1.26	1.41
$[OAA_m]$	4.0E-05 – 2.71E-02	2.26E-03	4.05E-04
$[NAD^+_m]$	0.41 – 1.93	1.25	1.22
$[NADH_m]$	0.20 – 1.25	0.51	0.88
$[ADP_m]$	3.11 – 9.0	6.12	3.06
$[ATP_m]$	3.19 – 13.65	7.64	7.34
Free [c] $[ADP_c]$	0.04 – 0.20	0.17	0.14
Free [c] $[ATP_c]$	2.62 – 7.4	4.76	4.67

[a] In the original liver TCA cycle model, CoA_m was a fixed parameter. In the updated liver TCA cycle model, it has been correctly re-defined as a model variable.

[b] Fewer than three reported values, hence a median value was not determined.

[c] Not bound to fixed sites.

[d] The predicted model values are obtained at steady-state, upon simulating the updated liver TCA cycle model. These are the same values shown in the analysis of initial steady-state of the model, in the results section.

[e] An expanded version of this table, containing details of the source references for the literature data, is provided in the supplementary material (see, Table I.1 on pg. I).

2.2.3 Special Cases: Alternative model definitions & other models

Later on, as the different analyses evolved, we were required to construct alternative variations of the updated liver TCA cycle model, as well as other simple models for testing purposes. Here, we shall discuss the respective definitions of these custom-built models. Further details regarding each of these different analyses can be found in the Section 2.3: Results for the liver TCA cycle models on pg. 32.

2.2.3.1 The [Pi] -variation of the updated liver TCA cycle model

During the elementary modes analysis, we needed to experiment with the the basic structure of the updated model to validate or reject a specific hypothesis regarding the possibility of an alternative outcome of this analysis. Here, we describe the specifically altered structure of the existing updated liver TCA cycle model and full details of its elementary modes analysis can be found in Results (see, pgs. 39 to 42).

As illustrated in Figure 2.1 (see, pg. 21), the inorganic phosphate metabolites (Pi_m & Pi_c) are defined as *'external metabolites'* in the existing updated liver TCA cycle model. From fig. 2.1, we may also note that both these metabolites are involved in at least two reactions in the model, either as co-substrate(s) or co-product(s) and that these reactions represent key enzyme-catalysed processes in this system. Our investigation with the existing model structure revealed that a desired, alternative outcome of the elementary modes analysis is a distinct possibility if the existing boundary conditions of the model are extended to include the external inorganic phosphate metabolites (Pi_m & Pi_c) as internal species. Originally, from a modelling standpoint, they were defined as *external metabolites* to avoid the additional complexity involved in balancing the total phosphate content of the system, as well as to maintain the simplified framework of the model by holding off on all such dynamic interactions that are secondary to the central liver TCA cycle dynamics (*e.g.* the effect of mitochondrial free divalent calcium ions (Ca^{2+}) on TCA cycle dehydrogenases).

From the literature, we know that the total phosphate content of an intact cell is held essentially constant in a *"metabolic homoeostasis"* in relation with the varying energy demands of the cell (Balaban, 2002; Bose et al., 2003; Connett, 1988; From et al., 1990; Katz et al., 1989a; Korzeniewski et al., 2008). Therefore, to generate this new structural model, the inorganic phosphate metabolites (Pi_m & Pi_c) were redefined as *'internal metabolites'*, as illustrated in Figure 2.2 (see, pg. 27). Internalisation of inorganic phosphates in this model, forms a new conservation relationship involving the inorganic phosphates, as shown in tbl. 2.7 (see, pg. 40) from Results.

Also, for the scope of this experiment, a reaction representing the cytosolic inorganic phosphate (Pi_c) influx into the mitochondria via the Pi-H^+ translocator (PiHt) was introduced in the liver TCA cycle model. Cytosolic inorganic phosphate is believed to enter the mitochondria via a neutral phosphate transporter (PiHt) in exchange for a hydroxyl ion (OH^-) or by co-transport with a proton (H^+) (Bose et al., 2003; Chappell and Crofts, 1966; Chappell and Haarhoff, 1967; Greenbaum and Wilson, 1985; Hoek et al., 1971; Wohlrab, 1986). However, the OH^- efflux or the H^+ influx part of the PiHt reaction was excluded from the model; since in these models, it is implicitly assumed that water (H_2O) and thereby its ionised products (OH^- & H^+) are present in excess. Moreover, the OH^- & H^+ dynamics has not been considered in any of the other liver TCA cycle reactions as well.

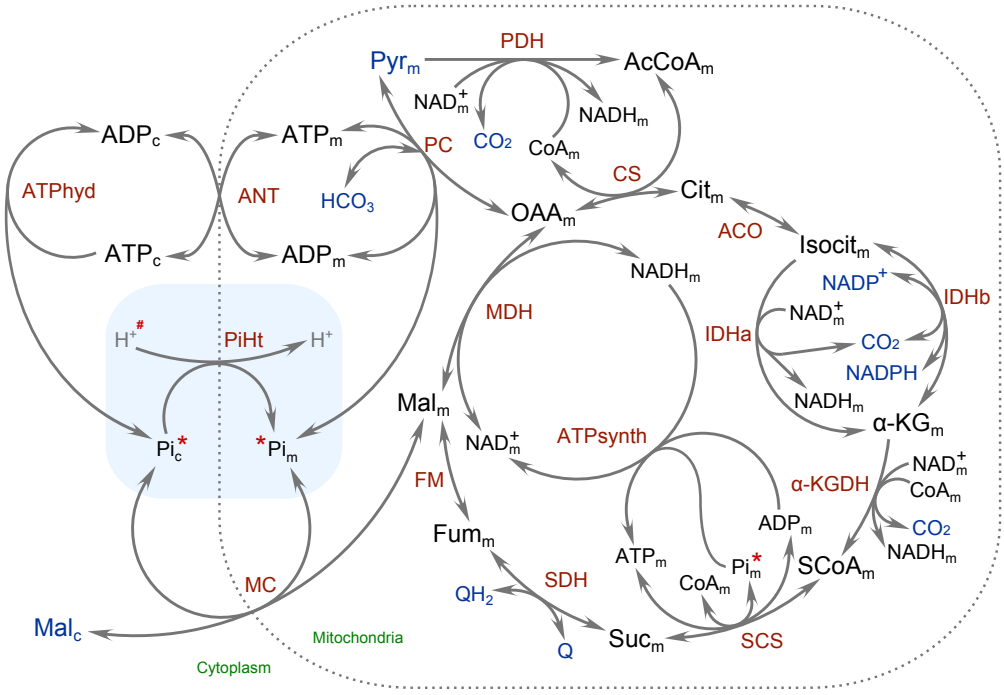

- **Figure 2.2.**

Schematic illustrating the [Pi] -variation of the updated liver TCA cycle model.

- Newly added Pi-H^+ translocator (PiHt) is shown here against a bluish background.
- #, in Red : Protons (H^+) are implicitly assumed to be in excess and therefore their co-transport via PiHt has not been included in the model.
- ∗, in Red : In this [Pi] variant model, the inorganic phosphate metabolites (Pi_m & Pi_c) were redefined as *internal metabolites* and therefore shown in *Black*.
- Other conditions as shown in fig. 2.1 on pg. 21.

However, later on this [Pi] variant model appeared to be kinetically unstable and could not be readily stabilised. Therefore, due to its kinetic instability, any changes made to this variation of the updated liver TCA cycle model, were not implemented during further development towards the Heart TCA cycle model.

2.2.3.2 The apparent maximal activity of PC and evolution of the *"PC knock-down"* model (PC_{kd})

As shown in eqs. B.2 to B.5 (see, pg. 222), we know that the updated liver TCA cycle model comprises a separate algebraic expression that dynamically calculates the apparent maximal activity of PC, at model simulation. As shown in eq. B.3 (see, pg. 222), the apparent maximal activity of PC (V_{app}^{PC}) is modelled as a function of acetyl-CoA & Mg^{2+} concentrations; where, α is an acetyl-CoA dependent activation term; and β is a Mg^{2+} dependent activation term. At model simulation, this algebraic expression is evaluated dynamically and substituted into the rate equation. In other words, unlike the maximal activity parameters of other enzyme catalysed reactions, V_{app}^{PC} is a *'variable'* of the model. In liver TCA cycle models, Mg^{2+} is an external metabolite and therefore in the context of this function, its effect is a constant. The other effector in this function, acetyl-CoA, is an internal metabolite and its concentration varies significantly with change in enzyme maximal activity, as shown using the steady-state analysis data in Results (see figs. 2.13 to 2.15 on pgs. 50 to 52, respectively). Therefore, compared to the constant effect of Mg^{2+}, change in acetyl-CoA concentration could significantly affect the resultant *variable* value of PC apparent maximal activity, as well as the net flux through PC.

In Results, the steady-state analysis data shows the dynamically changing concentration of acetyl-CoA against increasing maximal activity of PDH, across consecutive steady-state solutions of the updated liver TCA cycle model (see fig. 2.13b on pg. 50). In such a situation, the value of α from eq. B.3 would vary, with respect to a change in steady-state concentration of acetyl-CoA. As a result, the value of V_{app}^{PC} would change as well, thereby causing a change in the pyruvate carboxylase flux. In other words, if a change in enzyme activity alters the acetyl-CoA concentration, then the activity of that enzyme is also likely to change the value of V_{app}^{PC}.

While analysing the complex patterns of flux control coefficient distribution in the updated liver TCA cycle model (see sec. 2.3.5.2 on pg. 80), we wanted to evaluate the impact of such dynamic variability in pyruvate carboxylase activity on the distribution of flux control in liver TCA cycle models. However, before proceeding with any such analysis, we first had to determine the possible range of V_{app}^{PC} variability, when key enzyme activities/ metabolite concentrations are changed in liver TCA cycle models. Ideally, we wanted to generate a single plot containing all computed variations in the apparent maximal activity of PC against change in key TCA cycle enzyme activities/ metabolite concentrations. Therefore, in order to generate such a plot, we designed a specifically-modified *Python* function, which allowed us to combine all possible variations of the V_{app}^{PC} value in a single dataset. In Appendix D (see, pg. 237), we have described the working of this function in brief, along with the actual code written in Python (see listing D.1 on pg. 238).

Negative control condition for the V_{app}^{PC} variability analysis

Furthermore, to provide a valid negative control for the V_{app}^{PC} variability analysis, as well as to show that the value of V_{app}^{PC} stays constant in the absence of variability in the acetyl-CoA concentration, we computed the value of PC apparent maximal activity using a specific control condition.

In this control condition, the updated liver TCA cycle model was modified by redefining all three CoA–related metabolites (*i.e.*, CoA_m, $AcCoA_m$, & $SCoA_m$), as external metabolites. In this modified control condition model, the CoA–related metabolites are no longer conserved and their respective concentrations remain constant over time. Therefore, using this modified system, if the V_{app}^{PC} value is computed in response to changes in key enzyme activities/ metabolite concentrations, we expect its value to remain constant regardless of any perturbation in this system.

As the final output shown in the Results section shows, the V_{app}^{PC} value computed under these control conditions, serves as a *'control value'* against which, the V_{app}^{PC} variability seen in the updated liver TCA cycle model can be compared (see, pg. 86).

The *"PC knock-down"* model (PC_{kd})

Thus, the V_{app}^{PC} variability analysis raised an interesting question — does the C^J distribution pattern in the updated liver TCA cycle model differ when the V_{app}^{PC} value is a *constant* against when it is a *variable*? In order to answer this question, we required a model system which is nearly identical to the existing one, except for the definition of V_{app}^{PC}. The modified control condition model described above, in which all 3 CoA–related metabolites are defined as *external*, did not fit these requirements, due to its significantly altered structural properties.

Hence, as a minor variation of the existing model, we created a test model system, in which the original algebraic expression describing the V_{app}^{PC} (see, pg. 222) was replaced with a constant value of 2.26 mM/sec. This particular value was chosen based on the following — *(a.)* in the modified control condition model described above, wherein the respective concentrations of CoA–related metabolites are kept *constant*, V_{app}^{PC} is equal to 2.26 mM/sec; and *(b.)* in the existing updated liver TCA cycle model, at *initial conditions,* the V_{app}^{PC} algebraic expression equates to the exact same value and also at *initial steady-state conditions,* the V_{app}^{PC} value is nearly the same (*i.e.* 2.28 mM/sec). Therefore in this altered system, apart from this one minor change, everything else, including the model's structural properties, remains identical to the updated liver TCA cycle model system.

Thus, for this altered model, also known as the *"PC knock-down"* model (PC_{kd}), the flux control coefficients were computed and subsequently compared with the corresponding coefficients from the existing updated model (see pgs. 86 to 88).

2.2.3.3 A reduced version of the updated liver TCA cycle model

While analysing the complex patterns of flux control coefficient distribution in the updated liver TCA cycle model (see, pg. 88), we wanted to determine which features of these control distribution patterns might be due to kinetic or thermodynamic characteristics of the model and which are influenced by the model's structural characteristics. However, since the structure of the updated liver TCA cycle model involves branching of the TCA cycle (see, pgs. 32 and 43), it proved to be quite a complex problem to solve.

Therefore, to eliminate possible effects due to the structural properties of the model, the control distribution patterns were studied using a reduced version of the model, consisting of only the 9 canonical TCA cycle reactions, plus PDH (see fig. 2.1 on pg. 21). In this reduced version, all adenine and nicotinamide nucleotide concentrations (*i.e.* ATP_m, ADP_m, NAD^+_m, & $NADH_m$) were redefined as external metabolites, *i.e.* their respective quantities were fixed. By virtue of these modifications, we were able to reduce this system to contain only two conservation relationships, one involving the 3 CoA–related metabolites and the other involving all TCA cycle intermediates, except $SCoA_m$. Thus, the full version of the liver TCA cycle model was successfully scaled down to a canonical, textbook version of the TCA cycle, which includes PDH as an input reaction. Figure 2.3 illustrates this reduced version of the updated liver TCA cycle model.

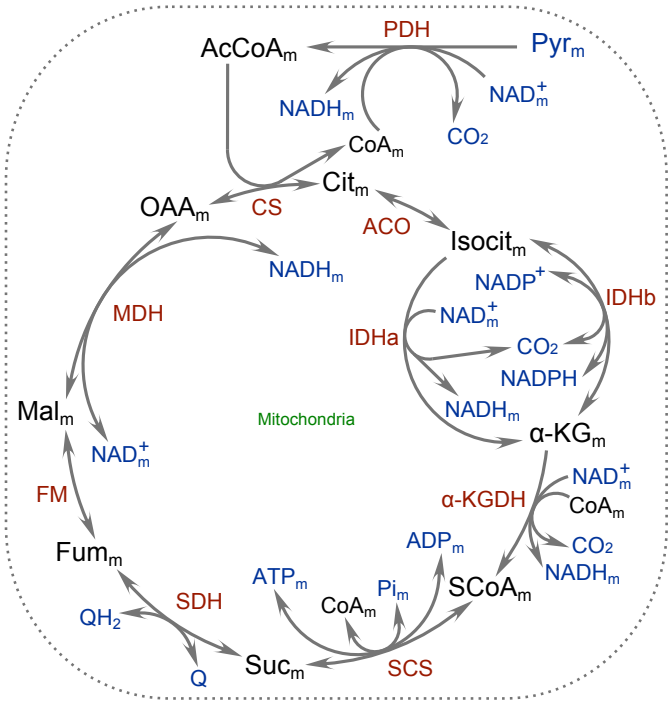

- **Figure 2.3.**

Schematic illustrating the reduced version of the updated liver TCA cycle model.

- Other conditions as shown in fig. 2.1 on pg. 21.
- Please note that in this reduced model, all adenine and nicotinamide nucleotide concentrations are redefined as external metabolites and therefore are shown in *Blue*.

2.2.3.4 Simple Test Models

While analysing the complex patterns of flux control coefficient distribution in the updated liver TCA cycle model (see sec. 2.3.5.3 on pg. 88), we discovered that the *substrate-dependent enzyme saturation* is likely to be the most important factor responsible for the characteristic sigmoidal C^J distribution curves in metabolic systems with saturable enzyme kinetics. However, we still needed to show whether it is a *general property* of all saturable metabolic systems and not just the system described by the updated liver TCA cycle model.

Therefore, to explore the control properties of some simple models, we built 4-step simple test models, both linear and cyclical, and containing four reactions in series, that are based on the simplest, reversible Michaelis-Menton kinetic equations. In addition, except the *input* & *output* reactions comprising the external *'source'* and *'sink'* metabolites, all other reactions involve a single substrate/ product interconversions. All internal as well as external metabolites (*'source'* and *'sink'* metabolites) are set to unity. The schematic in fig. 2.4, shows a general composition of a 4-step cyclical model. Using both the test models, flux control coefficients were computed at different levels of enzyme saturation. Please refer to Results for further information (see sec. 2.3.5.3 on pg. 88).

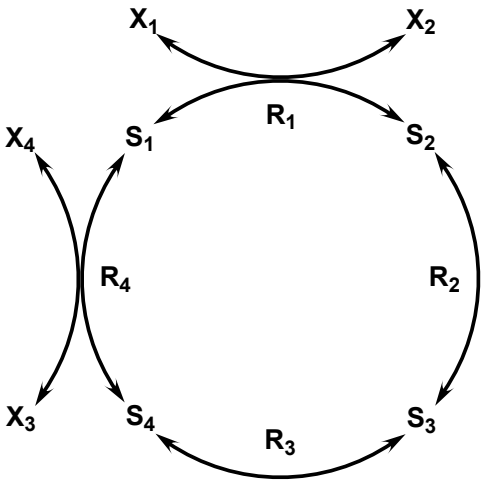

- **Figure 2.4. Composition of the cyclical test model containing four reactions**
  - Reactions are: **R1** to **R4**;
  - Internal metabolites are: **S1** to **S4**;
  - External metabolites are: **X1** to **X4**

2.3 Results for the liver TCA cycle models

Earlier, in Methods (see, pg. 19), we described the *'model design & definitions'* for a couple of liver TCA cycle models as well as other accessory models. In this section, various kinetic as well as structural properties of the liver TCA cycle models are studied using various methods of analysis, such as – *'Elementary modes analysis', 'Enzyme subset analysis', 'Steady-state analysis', 'Metabolic Control Analysis', etc.* Due to the large volume of data available for each model, in this section, we will primarily focus on physiologically significant key findings, in order to present a more thorough discussion of the presented data.

As shown earlier in Methods (see, pg. 19), there are two liver TCA cycle models, one that comprises CoA as an external metabolite (*original liver TCA cycle model* – $\mathrm{LVR_{TCA}}^{\mathrm{OGI}}$) and the other which includes CoA as an internal metabolite (*updated liver TCA cycle model* – $\mathrm{LVR_{TCA}}^{\mathrm{UPD}}$). Here, we shall present, compare and analyse the results for both these models. Due to the difference in their respective definitions, the two models could possibly exhibit different properties and therefore comparing the two sets of data, could prove beneficial towards the overall understanding of similar dynamic systems.

Briefly, the following types of results will be presented for each model:

1. Elementary modes analysis (see sec. 2.3.1 on pg. 32)
2. Enzyme subset analysis (see sec. 2.3.2 on pg. 43)
3. Initial steady-state data & Steady-state analysis (see sec. 2.3.3 on pg. 46)
4. Metabolic Control Analysis (MCA) results (see sec. 2.3.5 on pg. 73)

2.3.1 Elementary modes analysis of liver TCA cycle models

Both liver TCA cycle models have 9 possible elementary modes that are identical in terms of their composition. Elementary modes (ElMo) are presented in tbl. 2.3 (see, pg. 33) and corresponding elementary mode stoichiometries are presented in tbl. 2.4 (see, pg. 33); both of which are common between the two models. So, why are the two models identical with respect to their structural properties?

	Liver TCA cycle reactions												ATP/ ADP- linked reactions		
Modes	PDH	CS	ACO	IDHa	IDHb	α-KGDH	SCS	SDH	FM	MDH	MC	PC	ATPsynth	ATPhyd	ANT
EIMo 0	0	0	0	1.4	-1.4	0	0	0	0	-1	1	1	0.1	0	0
EIMo 1	0	0	0	0	0	0	0	0	0	1	-1	-1	0.25	3.5	3.5
EIMo 2	1	1	1	0	1	1	1	1	1	1	0	0	0.75	8.5	8.5
EIMo 3	1	1	1	1	0	1	1	1	1	1	0	0	1	11	11
EIMo 4	1	1	1	0	1	1	1	1	1	0	1	1	0.5	5	5
EIMo 5	1	1	1	1	0	1	1	1	1	0	1	1	0.75	7.5	7.5
EIMo 6	0	0	0	1	-1	0	0	0	0	0	0	0	0.25	2.5	2.5
EIMo 7	0.7	0.7	0.7	0	0.7	0.7	0.7	0.7	0.7	-1	1.7	1.7	0.1	0	0
EIMo 8	0.35	0.35	0.35	0.35	0	0.35	0.35	0.35	0.35	-0.75	1.1	1.1	0.075	0	0

- **Table 2.3.** A table showing elementary modes for liver TCA cycle models.

- For each mode, fractions have been converted to decimals. - Key: NAD^+-dependent isocitrate dehydrogenase (IDHa), $NADP^+$-dependent isocitrate dehydrogenase (IDHb), and malate carrier (MC).

	Reactants		Products	
EIMo 0 :	HCO_3^- + 1.4 NADPH + Pi_c + Pyr_m	⟶	Mal_c + Pi_m + 1.4 $NADP^+$	(1)
EIMo 1 :	Mal_c + 4.5 Pi_m	⟶	HCO_3^- + 4.5 Pi_c + Pyr_m	(2)
EIMo 2 :	8.5 Pi_m + Pyr_m + $NADP^+$ + Q	⟶	3 CO_2 + NADPH + QH_2 + 8.5 Pi_c	(3)
EIMo 3 :	11 Pi_m + Pyr_m + Q	⟶	3 CO_2 + QH_2 + 11 Pi_c	(4)
EIMo 4 :	4 Pi_m + HCO_3^- + 2 Pyr_m + $NADP^+$ + Q	⟶	3 CO_2 + Mal_c + QH_2 + 4 Pi_c + NADPH	(5)
EIMo 5 :	6.5 Pi_m + HCO_3^- + 2 Pyr_m + Q	⟶	3 CO_2 + Mal_c + QH_2 + 6.5 Pi_c	(6)
EIMo 6 :	2.5 Pi_m + NADPH	⟶	$NADP^+$ + 2.5 Pi_c	(7)
EIMo 7 :	1.7 HCO_3^- + 0.7 $NADP^+$ + 1.7 Pi_c + 2.4 Pyr_m + 0.7 Q	⟶	2.1 CO_2 + 1.7 Mal_c + 1.7 Pi_m + 0.7 QH_2 + 0.7 NADPH	(8)
EIMo 8 :	1.1 HCO_3^- + 1.1 Pi_c + 1.45 Pyr_m + 0.35 Q	⟶	1.05 CO_2 + 1.1 Mal_c + 1.1 Pi_m + 0.35 QH_2	(9)

- **Table 2.4.** Net stoichiometries for elementary modes presented in tbl. 2.3.

- Since the elementary modes for both liver TCA cycle models are identical, a common list of elementary mode stoichiometries is presented here.
- All metabolites in this table are, by necessity, external in the modelling sense.
- For each net stoichiometric equation, fractions have been converted to decimals.

As seen earlier in the introductory chapter, we know that the stoichiometry matrix ($\mathbf{N}$) is independent of the status of external metabolites ($\mathbf{X}$) (Reder, 1988; Schilling et al., 1999; Schuster and Hilgetag, 1994; Schuster et al., 2002a; Trinh et al., 2009). Moreover, in both liver TCA cycle models, there are equal number of reactions that either produce (citrate synthase (CS) & succinyl-CoA synthetase (SCS)) or consume (pyruvate dehydrogenase (PDH) & α-ketoglutarate dehydrogenase (α-KGDH)) CoA_m

and all of these reactions are part of a common "enzyme subset" *. We also know that in resulting elementary modes, all reactions of a given enzyme subset exist in "all-or-none" fashion (Klamt and Gilles, 2004; Pfeiffer et al., 1999). Therefore, irrespective of whether CoA_m is defined as an internal or an external metabolite in liver TCA cycle models, any change in the length of the stoichiometry matrix, elementary mode lengths, or mode stoichiometries between the two models is not feasible.

Having said that, the change in the metabolic status of CoA in liver TCA cycle models does however affect an important structural property of metabolic systems – the property of "moiety conservation". With internalisation of CoA, an additional but necessary conservation relationship involving CoA_m, $AcCoA_m$, & $SCoA_m$ is introduced in the $LVR_{TCA}{}^{UPD}$ model. Apart from their structural significance, conservation relationships also affect the kinetic properties of a metabolic system, as they form an inherent relationship between the constituent metabolite concentrations. Table 2.5 shows the individual conservation relationships that exist in liver TCA cycle models.

	Original liver TCA cycle model	Updated liver TCA cycle model
1	ATP_c : ADP_c	ATP_c : ADP_c
2	ATP_m : ADP_m	ATP_m : ADP_m
3	$NADH_m$: NAD_m	$NADH_m$: NAD_m
4	--- N.A. ---	$AcCoA_m$: ($SCoA_m$, CoA_m)

Table 2.5. Moiety conservation in liver TCA cycle models

Thus, elementary modes analysis of the two liver TCA cycle models shows that irrespective of the metabolic status of CoA in these models, there is no significant structural difference between the two; indeed apart from the change in the moiety conservation of CoA–related metabolites. Hence, the significance may lie in the kinetics and metabolite concentrations; which shall be discussed later in Section 2.3.3 : Steady-state analysis of the Liver TCA cycle kinetic models on pg. 46.

*Enzyme subset analysis results for liver TCA cycle models are discussed on pg. 43.

2.3.1.1 Properties of the elementary modes for Liver TCA cycle models

Length	Modes	Non-participating reactions
13	Mode 5	IDHb & MDH
13	Mode 4	IDHa & MDH
12	Mode 8	IDHb, ATPhyd & ANT
12	Mode 7	IDHa, ATPhyd & ANT
12	Mode 3	IDHb, MC & PC
12	Mode 2	IDHa, MC & PC
6	Mode 1	PDH, CS, ACO, IDHa, IDHb, α-KGDH, SCS, SDH, & FM
6	Mode 6	PDH, CS, ACO, α-KGDH, SCS, SDH, FM, MDH, MC, & PC
6	Mode 0	PDH, CS, ACO, α-KGDH, SCS, SDH, FM, ATPhyd, & ANT

- **Table 2.6.** Resulting lengths of the elementary modes presented in tbl. 2.3.

1st column : total no. of reactions in each ElMo; 3rd column : non-participating reactions in each ElMo.

1. In liver TCA cycle models there are 15 reactions in total. 9 canonical (non-tissue-specific) reactions, 3 ATP/ADP−linked reactions, 2 liver tissue-specific reactions (MC & pyruvate carboxylase (PC)), and $NADP^+$-dependent isocitrate dehydrogenase. From tbl. 2.6, we can observe that in any given ElMo, the total number of participating reactions is always less than 15.

2. Except for three ElMos (*i.e.* $ElMo_{[0]}$, $ElMo_{[6]}$ & $ElMo_{[1]}$), IDHa & IDHb function in a mutually exclusive manner (see, tbl. 2.3). In $ElMo_{[0]}$ & $ElMo_{[6]}$, both these reactions participate and they balance each other by carrying fluxes in opposite directions; wherein, IDHa works in its forward direction and IDHb acts in its reverse direction. Whereas, in $ElMo_{[1]}$ both reactions are absent along with most other canonical TCA cycle reactions.

3. Due to the mutual exclusivity of IDHa & IDHb in liver TCA cycle models, the remaining six elementary modes can be divided into modes that comprise IDHa and those that contain IDHb, instead. $ElMo_{[3]}$, $ElMo_{[5]}$ & $ElMo_{[8]}$ are IDHa -based and $ElMo_{[2]}$, $ElMo_{[4]}$ & $ElMo_{[7]}$ are their respective IDHb -based counterparts. Functionally, elementary modes that comprise only IDHb produce 2.5 ATP_m molecules fewer than the modes that contain only IDHa; provided that mitochondrial malate

dehydrogenase (MDH) functions in its respective forward direction. $ElMo_{[7]}$ & $ElMo_{[8]}$ are two such modes that are inconsistent with this observation as they contain MDH in its reverse direction.

4. As explained earlier in Methods (see, pg. 19), the mammalian liver-specific TCA cycle includes additional reactions such as PC & MC; whereas, in mammalian heart as well as skeletal muscle-specific TCA cycle, the anaplerotic contribution of PC to the total TCA cycle flux is disputable (Gibala, 2003; Gibala et al., 2000; Owen et al., 2002; Scrutton and Utter, 1968). Therefore, we may classify the 9 elementary modes of liver TCA cycle models into 3 separate categories as follows:

4.(*a.*) **$ElMo_{[4]}$, $ElMo_{[5]}$, $ElMo_{[7]}$, & $ElMo_{[8]}$:** Modes that contain all the canonical TCA cycle reactions along with mammalian liver-specific reactions (*viz.*– PC & MC). These modes describe the complete structural aspect of mammalian liver-specific TCA cycle (see fig. 2.5 on pg. 37).

4.(*b.*) **$ElMo_{[2]}$, & $ElMo_{[3]}$:** Modes that contain only the canonical TCA cycle reactions and lack the mammalian liver-specific reactions. These modes can be assumed to describe the structural framework of mammalian heart or skeletal muscle-specific TCA cycle (see fig. 2.6 on pg. 38).

4.(*c.*) **$ElMo_{[0]}$, $ElMo_{[1]}$, & $ElMo_{[6]}$:** Modes that contain a partial list of reactions, in this case, only 6 out of possible 15 reactions. These modes describe either the internal cycles within a system or a particular span of TCA cycle (see fig. 2.7 on pg. 38).

5. Having said that, we must remember that elementary modes represent certain idealised situations and therefore, a single elementary mode is only a partial representation of the cellular physiology, under a given set of initial conditions. Most often, a superposition of several elementary modes is required to adequately describe the flux distribution in a specific state of cellular physiology; due to mixed energy demands in living cells (Schuster et al., 1999, 2000; Stephanopoulos and Vallino, 1991). Therefore in mathematical models, it is possible that a combination of several elementary modes is required to explain the kinetic behaviour of a specific steady-state.

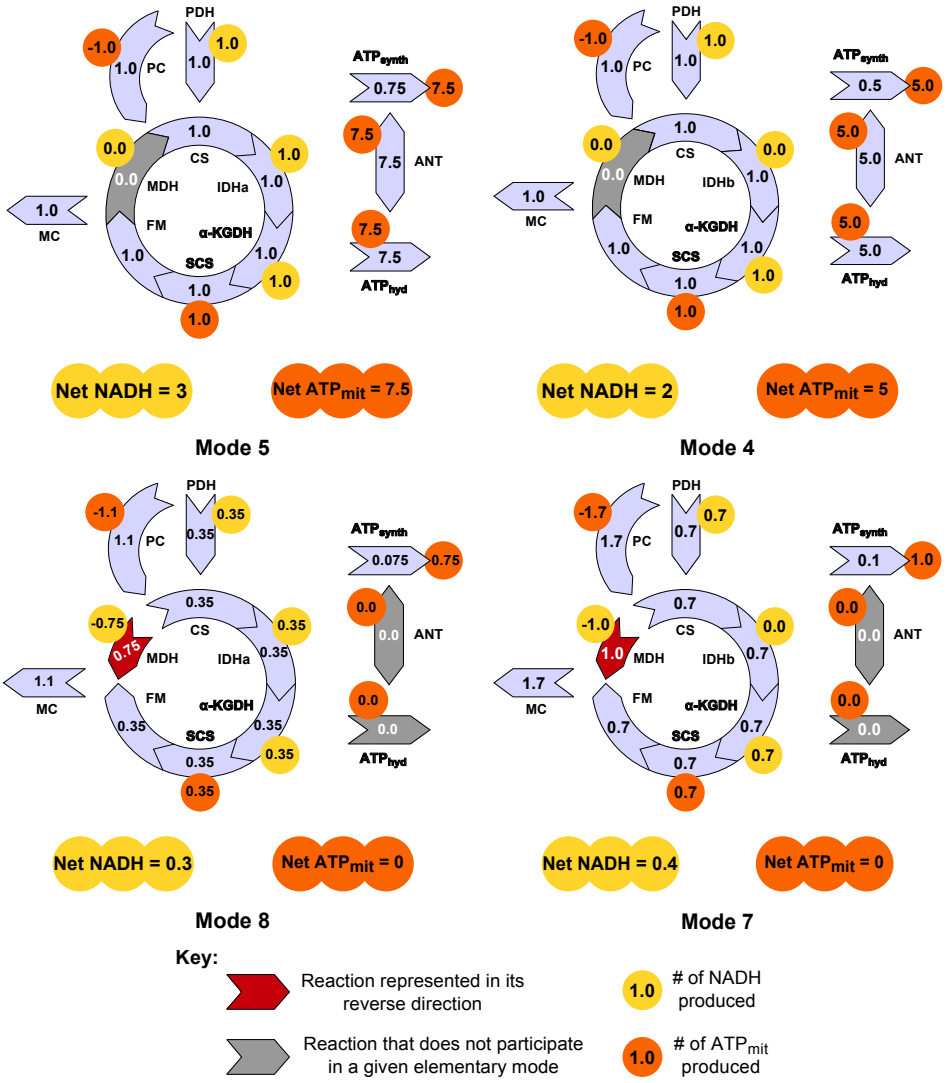

- **Figure 2.5.**

Infographics showing the stoichiometric account of the net mitochondrial ATP_m and $NADH_m$ production for elementary modes of group (a) — the TCA cycle with PC & MC.

- All the liver TCA cycle model reactions are represented in their minimal form. Only the absolutely essential metabolites & co-factors are included in this diagram.
- In this figure, the arrowheads point towards the respective forward or reverse directions of the participating reactions, specific to each elementary mode.
- Reactions shown in Red, function in their respective reverse directions. Also, those shown in Grey, do not participate in that elementary mode. Whereas, reactions shown in light Blue, function in their respective forward directions.
- For a given elementary mode, numbers within the arrows represent the respective reaction strengths (see tbl. 2.3 on pg. 33). Also, all reactions that act in the reverse direction are shown using positive numbers; since, the arrowheads point towards their true direction.
- ATP_m is represented by a small Yellow circle and $NADH_m$ by a small Orange circle. Numbers within these circles represent the number of molecules produced by the corresponding reaction. For any reaction, the production of a metabolite is shown using a positive number and the consumption using a negative number. For IDHb containing modes, the $NADH_m$ production for IDHb is shown to be zero; since, it is a $NADP^+$ -dependent enzyme.
- Net $NADH_m$ production = ${NADH_m}^{PDH} + {NADH_m}^{IDHa} + {NADH_m}^{\alpha\text{-}KGDH} + {NADH_m}^{MDH}$
- Net ATP_m production = ${ATP_m}^{ATPsynth} + {ATP_m}^{SCS} + {ATP_m}^{PC}$

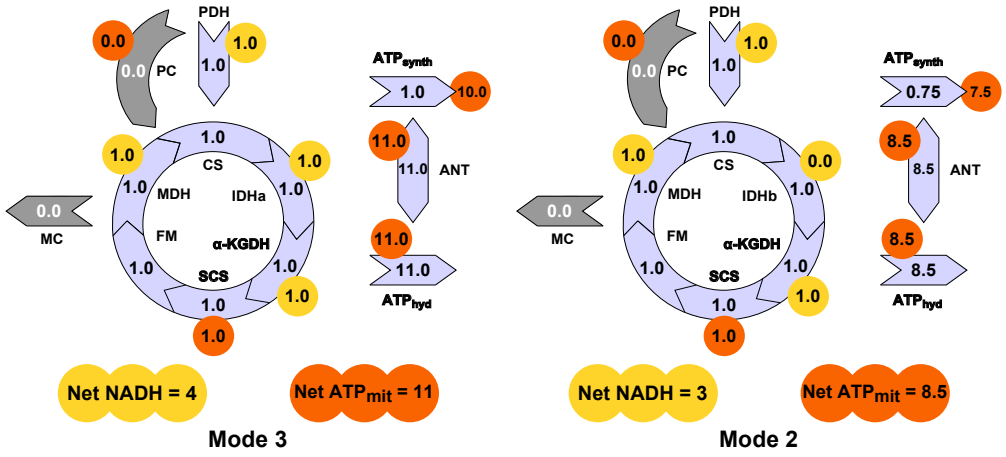

▪ **Figure 2.6.**
Infographics showing the stoichiometric account of the net mitochondrial ATP_m and $NADH_m$ production for elementary modes of group (b) — the canonical TCA cycle.

▪ Key, symbols and representation as shown in fig. 2.5 on pg. 37.

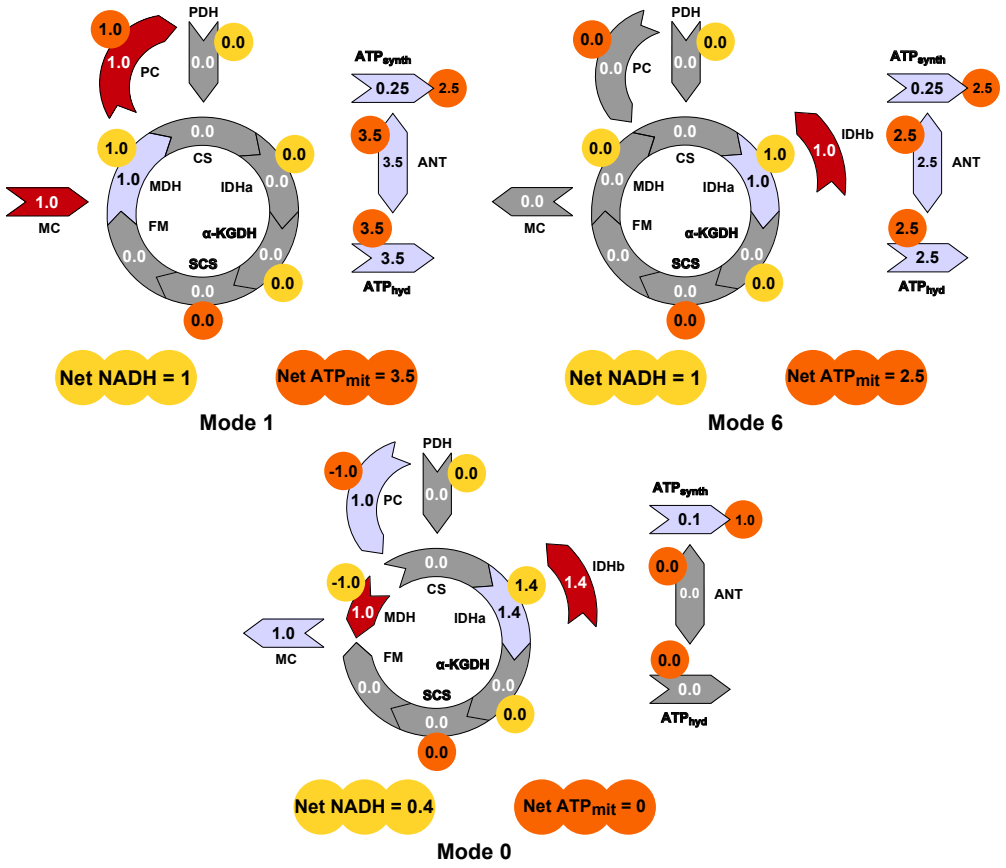

▪ **Figure 2.7.** Infographics showing the stoichiometric account of the net mitochondrial ATP_m and $NADH_m$ production for elementary modes of group (c) — subsets of the full set of liver TCA cycle reactions.

▪ Key, symbols and representation as shown in fig. 2.5 on pg. 37.

As seen in fig. 2.5 (see, pg. 37), $ElMo_{[4]}$ & $ElMo_{[5]}$ lack MDH; whereas, $ElMo_{[7]}$ & $ElMo_{[8]}$ lack adenine-nucleotide translocase (ANT) & ATP hydrolysis (ATPhyd) but include MDH, albeit in reverse direction. It means that in liver TCA cycle models, MDH

can function either in its reverse direction or not at all, provided that PC & MC both act in their respective forward directions. Other modes of liver TCA cycle models (*viz.*– $ElMo_{[1]}$, $ElMo_{[2]}$, & $ElMo_{[3]}$) show that the converse is also true; that is, for MDH to function in its forward direction, both PC & MC must act in their respective reverse directions or not at all. Also, though $ElMo_{[1]}$ shows the possibility of producing external pyruvate (Pyr_m) from external cytosolic malate (Mal_c); only the net forward reaction of PC is likely to occur in cells, at physiological concentrations of reactants & products (K_{eq} = 10.98 unitless; Wood et al., 1966).

In an ideal and physiologically correct representation of the liver TCA cycle, the required combination of elementary modes must exist in such a fashion, so that the resultant state of the model should include MDH (in either direction) and PC/ MC in their respective forward directions. As shown later in fig. 2.18 (see, pg. 59), the steady-state data for these models show that MDH operates in its reverse direction, PC & MC in their respective forward directions, and IDHa/ IDHb function as an internal cycle, balancing each other by carrying fluxes in opposite directions; wherein, IDHa works in its forward direction and IDHb acts in its reverse direction. Logically, it points towards 2 possible sets of superpositions of individual elementary modes – a set containing $ElMo_{[0]}$ & $ElMo_{[5]}$; and another containing $ElMo_{[6]}$ & $ElMo_{[8]}$ (see figs. 2.5 to 2.7 on pgs. 37 to 38, respectively).

Table 2.6 (see, pg. 35) shows that in liver TCA cycle models, the maximum number of participating reactions is 13. Thus raising the question that whether the same liver TCA cycle model can exist in such a way that one or more of its resultant elementary modes include 14 or even all (*i.e.* 15) of its possible reactions; where, PC & MC act in their respective forward directions and MDH functions in either forward or reverse direction? In other words, could the existing structure of this model be altered in order to meet all the requirements mentioned earlier? Further investigation with the [Pi] -variation of the updated liver TCA cycle model described in Methods (see, pg. 26), revealed that such a structure is a distinct possibility if the existing boundary conditions of the model are extended to include the external inorganic phosphate metabolites (Pi_m & Pi_c) as internal species.

At least structurally, such a variation of the liver TCA cycle model is worth looking into; however, later it appeared to be kinetically unstable and could not be readily stabilised. Internalisation of inorganic phosphates in the model, forms a new conservation relationship involving the inorganic phosphates (see tbl. 2.7 on pg. 40); which, in effect, maintains the total phosphate content of the system constant. Table 2.8 (see, pg. 40) shows the 9 possible elementary modes for such a structural variation of the liver TCA cycle model and tbl. 2.9 (see, pg. 40) shows the corresponding overall (net) stoichiometries for the same.

	Updated liver TCA cycle model	[Pi] variation of the updated model
1	ATP_c : ADP_c	ATP_c : ADP_c
2	ATP_m : ADP_m	ATP_m : ADP_m
3	$NADH_m$: NAD_m	NAD_m : $NADH_m$
4	$AcCoA_m$: ($SCoA_m$, CoA_m)	CoA_m : ($AcCoA_m$, $SCoA_m$)
5	--- N.A. ---	Pi_m : (ADP_m, ADP_c, Pi_c)

- **Table 2.7.** Moiety conservation in the [Pi] variant model

Table 2.8 shows that in liver TCA cycle models, if indeed the inorganic phosphate metabolites (Pi_m & Pi_c) are made internal, then 2 out of 9 resulting elementary modes satisfy the earlier mentioned requirements for an ideal and physiologically correct representation of the liver TCA cycle function. Both these modes, *viz.*– $ElMo_{[0]}$ & $ElMo_{[7]}$, include 14 out of 16 possible reactions from the [Pi] variation of the liver TCA cycle model: PC & MC in their respective forward directions, MDH in its respective reverse direction and all the other 9 canonical TCA cycle reactions along with the 3 ATP/ADP–linked reactions.

	Liver TCA cycle reactions												*ATP/ ADP- linked reactions*		
Modes	**PDH**	**CS**	**ACO**	**IDHa**	**IDHb**	**α-KGDH**	**SCS**	**SDH**	**FM**	**MDH**	**MC**	**PC**	**PiHt**	**ATPsynth**	**ATPhyd**	**ANT**
ElMo 0	4.5	4.5	4.5	4.5	0	4.5	4.5	4.5	4.5	-6.5	11	11	0	1.75	11	11
ElMo 1	1	1	1	0	1	1	1	1	1	0	1	1	4	0.5	5	5
ElMo 2	0	0	0	1	-1	0	0	0	0	0	0	0	2.5	0.25	2.5	2.5
ElMo 3	1	1	1	0	1	1	1	1	1	1	0	0	8.5	0.75	8.5	8.5
ElMo 4	1	1	1	1	0	1	1	1	1	0	1	1	6.5	0.75	7.5	7.5
ElMo 5	0	0	0	0	0	0	0	0	0	1	-1	-1	4.5	0.25	3.5	3.5
ElMo 6	0	0	0	1.8	-1.8	0	0	0	0	-1	1	1	0	0.2	1	1
ElMo 7	4.5	4.5	4.5	0	4.5	4.5	4.5	4.5	4.5	-4	8.5	8.5	0	1.25	8.5	8.5
ElMo 8	1	1	1	1	0	1	1	1	1	1	0	0	11	1	11	11

- **Table 2.8.** Elementary modes for the [Pi] variation of the liver TCA cycle model.
  - Other conditions as shown in tbl. 2.3 on pg. 33.
  - Key: Pi-H^+ translocator (PiHt).

	Reactants		Products	
ElMo 0 :	11 HCO_3^- + 15.5 Pyr_m + 4.5 Q	⟶	13.5 CO_2 + 11 Mal_c + 4.5 QH_2	(1)
ElMo 1 :	HCO_3^- + 2 Pyr_m + $NADP^+$ + Q	⟶	3 CO_2 + Mal_c + QH_2 + NADPH	(2)
ElMo 2 :	NADPH	⟶	$NADP^+$	(3)
ElMo 3 :	Pyr_m + $NADP^+$ + Q	⟶	3 CO_2 + NADPH + QH_2	(4)
ElMo 4 :	HCO_3^- + 2 Pyr_m + Q	⟶	3 CO_2 + Mal_c + QH_2	(5)
ElMo 5 :	Mal_c	⟶	HCO_3^- + Pyr_m	(6)
ElMo 6 :	HCO_3^- + 1.8 NADPH + Pyr_m	⟶	Mal_c + 1.8 $NADP^+$	(7)
ElMo 7 :	8.5 HCO_3^- + 4.5 $NADP^+$ + 13 Pyr_m + 4.5 Q	⟶	13.5 CO_2 + 8.5 Mal_c + 4.5 QH_2 + 4.5 NADPH	(8)
ElMo 8 :	Pyr_m + Q	⟶	3 CO_2 + QH_2	(9)

- **Table 2.9.** Net stoichiometries for elementary modes presented in tbl. 2.8.
  - Other conditions as shown in tbl. 2.4 on pg. 33.

In fact, the 9 resultant elementary modes for the [Pi] variant model shown in tbl. 2.8 are quite similar to the 9 modes of the existing liver TCA cycle model shown in tbl. 2.3 (see, pg. 33), barring a few exceptions. Table 2.10 shows how the two sets of elementary modes map with reference to each other.

Models	Group A						Group B		
Existing Liver TCA cycle model	ElMo 1	ElMo 2	ElMo 3	ElMo 4	ElMo 5	ElMo 6	ElMo 0	ElMo 7	ElMo 8
[Pi] variant of the Liver TCA cycle model	ElMo 5	ElMo 3	ElMo 8	ElMo 1	ElMo 4	ElMo 2	ElMo 6	ElMo 7	ElMo 0

- **Table 2.10.** Mapping the ElMo's between the existing and the [Pi] variant model.

This table maps out the elementary modes between tbl. 2.3 (see, pg. 33) and tbl. 2.8 (see, pg. 40).

As shown in Table 2.10, all the *Group A* elementary modes are exactly the same, except for the inclusion of PiHt, in the [Pi] variant model. Also, all the *Group B* elementary modes are exactly the same, except that modes corresponding to the [Pi] variant model include the involvement of ATPhyd & ANT, with comparatively higher stoichiometric coefficients than that of the existing model.

In the case of [Pi] variant model, 6 elementary modes that belong to *Group A* ($ElMo_{[1]}$, $ElMo_{[2]}$, $ElMo_{[3]}$, $ElMo_{[4]}$, $ElMo_{[5]}$, $ElMo_{[8]}$), include the PiHt reaction; which in turn indicates that in these modes, PiHt recycles the additional cytosolic inorganic phosphate back to the mitochondria. If both MC & PiHt are present in a given mode, as seen in $ElMo_{[1]}$, $ElMo_{[4]}$ & $ElMo_{[5]}$, then PiHt would import the remaining cytosolic inorganic phosphate generated by ATPhyd into the mitochondria; since, stoichiometrically, MC can only exchange a single molecule of cytosolic inorganic phosphate for a molecule of Mal_m.

The 3 *Group B* elementary modes of the [Pi] variant model ($ElMo_{[0]}$, $ElMo_{[6]}$, $ElMo_{[7]}$), generate *approx.* 2 to 2.5 times more $NADH_m$ & ATP_m, compared to corresponding modes of the existing liver TCA cycle model. This comparison shows that the [Pi] variant model is capable of producing sufficient ATP_m to be transported into cytosol using ANT and subsequently hydrolysed to ADP_c & Pi_c via ATPhyd; whereas, the existing liver TCA cycle model produces just enough ATP_m to be consumed by PC in the mitochondria. We believe that this could be a direct effect of the internalisation of inorganic phosphate metabolites in the [Pi] variant model, since the additional recycling of inorganic phosphates via PiHt does not occur in these three modes. Although, most classical hypotheses concerning the regulation of oxidative phosphorylation have now been proven to be inadequate; the present experimental observations strongly suggest that among other regulatory factors, the rate of oxidative phosphorylation is kinetically regulated by the availability of its substrates, NADH, ADP, and Pi in the presence of

abundant O_2 (Balaban, 2002; Erecinska et al., 1977, 1978; From et al., 1990; Katz et al., 1989a). In this context, as a result of the internalisation of inorganic phosphates in liver TCA cycle models, a relative increase in the capacity of $NADH_m$ & ATP_m synthesis, is therefore a significant structural outcome in the right direction.

Also, from the corresponding stoichiometries shown in tbl. 2.9 (see, pg. 40) we can observe that external inorganic phosphate metabolites are absent from the net equations due to their internalisation in the [Pi] variant model, compared to those from tbl. 2.4 (see, pg. 33). Whereas, tbl. 2.4 shows the lack of recycling for cytosolic inorganic phosphate in the existing liver TCA cycle model; since it tends to accumulate in the model, in response to the consumption of its mitochondrial counterpart during ATP synthesis. Internalisation of inorganic phosphates and the inclusion of PiHt in the [Pi] variant model, addresses such apparent inconsistencies in the existing liver TCA cycle model by allowing the excess cytosolic inorganic phosphate to be recycled back to the mitochondria.

Having said that, as already mentioned, due to kinetic instability of the [Pi] variant model, we decided to consider the existing updated Liver TCA cycle model as a starting point for further development towards the Heart TCA cycle model.

Table 2.6 (see, pg. 35) shows that in the updated liver TCA cycle model, $ElMo_{[2]}$ & $ElMo_{[3]}$ lack the mammalian liver-specific reactions and only contain 9 canonical TCA cycle reactions along with 3 ATP/ADP−linked reactions. In mammalian heart as well as skeletal muscle tissue, evidence suggests that the anaplerotic contribution of PC to the total flux through the TCA cycle is insignificant as compared to that in liver (*for refs., please see earlier*). Also, there is very little evidence that would suggest any significant activity of MC in heart or skeletal muscle tissue (Chappell, 1968; Fiermonte et al., 1999; Klingenberg, 1970; LaNoue and Schoolwerth, 1979; Palmieri, 1994; Sluse et al., 1971). Therefore, if we were to isolate these 12 reactions, the resulting structural framework would appropriately define a mammalian heart or skeletal muscle-specific TCA cycle model.

$ElMo_{[0]}$ & $ElMo_{[6]}$ contain only a partial list of liver TCA cycle reactions and mostly describe an internal substrate cycle in which α-ketoglutarate (αKG_m) generated by IDHa is converted back to isocitrate by IDHb. In fact, as we already know from Methods (see, pg. 19), the $NADP^+$-dependent isocitrate dehydrogenase was introduced in the model for the same purpose. This idea is supported based on the original proposal put forward by Sazanov and Jackson (1994, 1995). Furthermore, conclusive evidence for the existence of such a cycle has been provided by several studies in both heart and liver (Ernster and Navazio, 1957; Huang and Colman, 2005; Londesborough and Dalziel, 1968; McCormack and Denton, 1981; Rutter and Denton, 1988; Sazanov and Jackson, 1993). Also, Comte et al. (1997, 2002) observed a reverse flux through $NADP^+$

-dependent isocitrate dehydrogenase under normoxia as well as ischemia in perfused rat hearts. Therefore, existence of such a substrate cycle in these liver TCA cycle models is a significant structural outcome.

2.3.2 Enzyme subset analysis of liver TCA cycle models

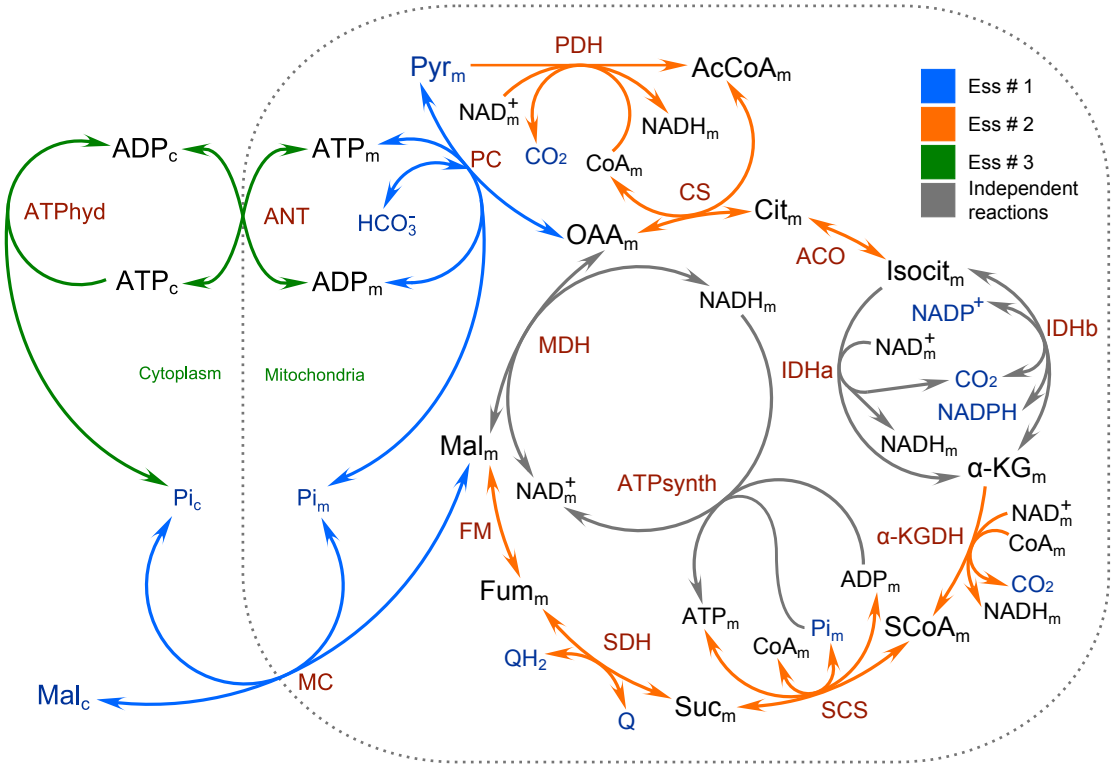

- **Figure 2.8.** Schematic showing the enzyme subsets for both the liver TCA cycle models.
  - Internal metabolites: in *Black*; external metabolites: in *Blue*; reaction/ enzyme names: in *Red*.
    - Reversible reactions: double arrowheads and irreversible reactions: single arrowhead.

Figure 2.8 shows a common theme for "Enzyme subsets (ESS)" of the two liver TCA cycle models. Since, the elementary modes (Heinrich and Schuster, 1998; Schilling et al., 1999; Schuster and Hilgetag, 1994; Schuster et al., 2000, 2002a) as well as enzyme subsets (Pfeiffer et al., 1999; Poolman et al., 2007; Schuster et al., 2002b) can be readily calculated from the stoichiometry matrix of a model, it is not entirely unexpected that the two liver TCA cycle models share identical elementary modes as well as enzyme subsets.

From Figure 2.8, the following observations can be made to elaborate the significance of identifying the enzyme subsets of a mathematical model:

1. **ESS #2:**

   This subset comprises most of the canonical TCA cycle reactions from liver TCA cycle models, *viz.*– PDH, CS, aconitate hydratase (ACO), α-KGDH, SCS, succinate dehydrogenase (SDH), and fumarate hydratase (FM); except for MDH, IDHa, and IDHb. The latter three act as "independent reactions" and break the subset into two halves; with the top/ upper-half containing PDH, CS, & ACO and the bottom/ lower-half containing α-KGDH, SCS, SDH, & FM. 'ESS #2' can be viewed as a set of reactions that along with both the independent reactions, allow for the complete functioning of a generic (tissue non-specific) TCA cycle.

2. **ESS #1:**

   This subset comprises two distant reactions, PC & MC, interrupted by MDH that acts as an independent reaction.

   As seen earlier (see, pgs. 37 and 38), this subset is functional in the forward direction in $\text{ElMo}_{[0]}$, $\text{ElMo}_{[4]}$, $\text{ElMo}_{[5]}$, $\text{ElMo}_{[7]}$ & $\text{ElMo}_{[8]}$; in the reverse direction in $\text{ElMo}_{[1]}$; and is completely absent in $\text{ElMo}_{[2]}$, $\text{ElMo}_{[3]}$ & $\text{ElMo}_{[6]}$.

   We have already discussed $\text{ElMo}_{[1]}$ earlier at length. In $\text{ElMo}_{[0]}$, $\text{ElMo}_{[7]}$ & $\text{ElMo}_{[8]}$ 'ESS #1' operates in the forward direction and MDH acts in its reverse direction, thus separating PC & MC within 'ESS #1'. Their net stoichiometries (see, pg. 33) suggest that 'ESS #1' along with MDH working in its reverse direction, futilely adds anaplerotic carbon into the TCA cycle, only to remove most of it in the form of Mal_{c}. Also, these 3 elementary modes result in zero net production of mitochondrial ATP (see, pgs. 37 and 38). The significance of 'ESS #1', MDH, & $\text{ElMo}_{[8]}$ is discussed in further detail with respect to the steady-state analysis results (see, pgs. 58 to 60).

   In contrast, in $\text{ElMo}_{[4]}$ & $\text{ElMo}_{[5]}$, 'ESS #1' participates in the absence of MDH and thus provides sufficient oxaloacetate (OAA_{m}) for the system to produce the theoretically maximal amount of mitochondrial ATP possible under these conditions.

   As noted earlier, whether we consider the original system represented by liver TCA cycle models or the [Pi] variant model, it appears that the two reactions that comprise 'ESS #1' and the independent reaction – MDH, can not all simultaneously operate in their respective forward directions in any given elementary mode of the liver TCA cycle models presented here.

   Thus, for the system represented by liver TCA cycle models, structurally, there are 3 viable modes of operation in terms of the combination of 'ESS #1' and MDH:

2.(***a.***) Futilely add anaplerotic carbon into the TCA cycle via PC and later remove most of it via MC and reverse acting MDH; as well as effect a suboptimal production of mitochondrial ATP, as seen in $\text{ElMo}_{[7]}$ & $\text{ElMo}_{[8]}$ (see fig. 2.5 on pg. 37).

2.(***b.***) Allow 'ESS #1' to function in absence of MDH and consequently result in the near-to-optimal production of mitochondrial ATP, as seen in $\text{ElMo}_{[4]}$ & $\text{ElMo}_{[5]}$ (see fig. 2.5 on pg. 37).

2.(***c.***) Completely remove the anaplerotic component of the system via deletion of 'ESS #1', thereby converting the system back to its canonical form and consequently effect a theoretically optimal production of mitochondrial ATP, as seen in $\text{ElMo}_{[2]}$ & $\text{ElMo}_{[3]}$ (see fig. 2.6 on pg. 38).

Hence, in liver TCA cycle models, depending on the exact flux distribution of a given steady-state, a specific superposition (linear combination) of suitable elementary modes may exist and in that resultant superposition of elementary modes, MDH and the two 'ESS #1' reactions are likely to be operational in one of these 3 possible ways, as described above.

3. ESS #3:

This enzyme subset includes ANT & ATPhyd, two reactions that share most of their reactants & products (*i.e.* ATP_m, ADP_m, ADP_c & ATP_c), except of course, Pi_c, which is external to the system. Curiously, ATP synthase (ATPsynth), another ATP/ADP–linked reaction, is excluded from this subset; perhaps, due to its tight coupling with the 4 NADH -producing dehydrogenases of the TCA cycle.

'ESS #3' remains absent in $\text{ElMo}_{[0]}$, $\text{ElMo}_{[7]}$ & $\text{ElMo}_{[8]}$, since their net mitochondrial ATP production is zero. As seen earlier (see, pg. 45), these are the same modes that operate with MDH in its reverse direction. On the other hand, corresponding modes of the [Pi] variant model ($\text{ElMo}_{[6]}$, $\text{ElMo}_{[7]}$ & $\text{ElMo}_{[0]}$; see tbl. 2.10 on pg. 41), show both 'ESS #3' reactions to be functional, due to the near-to-optimal production of mitochondrial ATP via ATPsynth, which could be a direct consequence of the internalisation of the inorganic phosphate metabolites in the system. Interestingly, such relative increase in the net production of mitochondrial ATP is observed despite the reversal of MDH in these modes.

In the following sections, we look at the kinetic/ dynamic properties of liver TCA cycle models and in some cases establish appropriate links with its structural properties as well.

2.3.3 Steady-state analysis of the Liver TCA cycle kinetic models

To compare the steady-states of the two liver TCA cycle models, both were solved with the 'initially defined' values of all the parameters & variables presented in Methods (see tbl. 2.2 on pg. 25 & tbl. I.2 on pg. III in supplementary material).

At first, let us begin by comparing the compositions of *"Initial steady-states"* for the two liver TCA cycle models. The reaction fluxes are shown in fig. 2.9 and metabolite concentrations in fig. 2.10 (see, pg. 47), respectively.

Figures 2.11 and 2.12 (see, pgs. 47 and 48) show the comparison of individual reaction fluxes (Δ Flux) and metabolite concentrations (Δ Conc.) between the two liver TCA cycle models at steady-state; with reactions & metabolites arranged in the descending order of Δ Flux & Δ Conc, respectively.

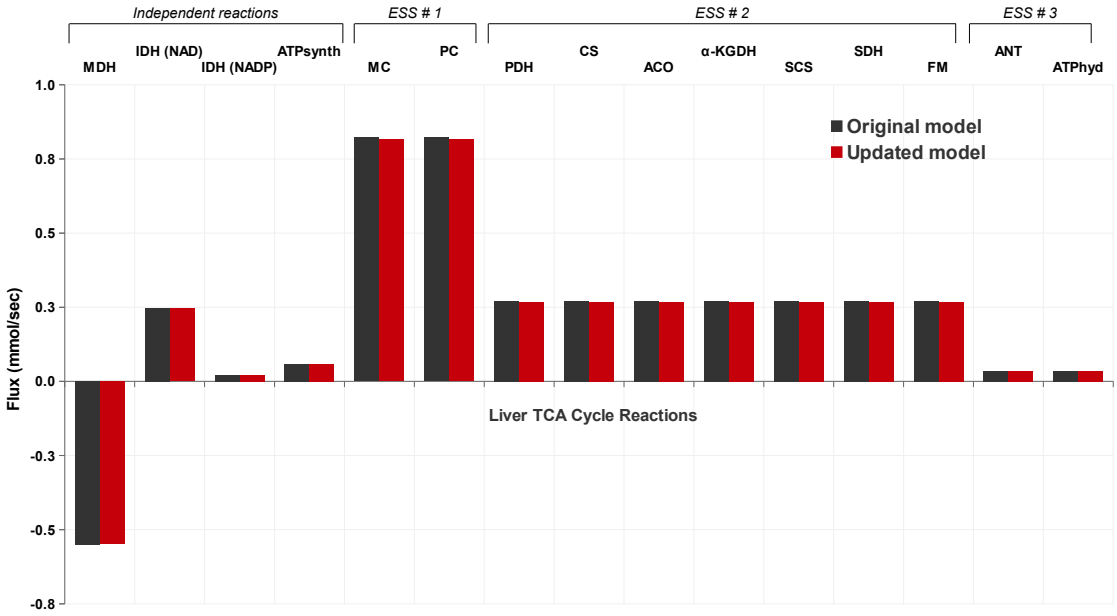

- **Figure 2.9.** Fluxes for the $LVR_{TCA}{}^{OGI}$ & $LVR_{TCA}{}^{UPD}$ models, at initial steady-state.
  - Dark Grey: $LVR_{TCA}{}^{OGI}$ data;
  - Red: $LVR_{TCA}{}^{UPD}$ data
- The difference through the individual reaction fluxes between the two models (Δ Flux) is shown separately in fig. 2.11 (see, pg. 47).

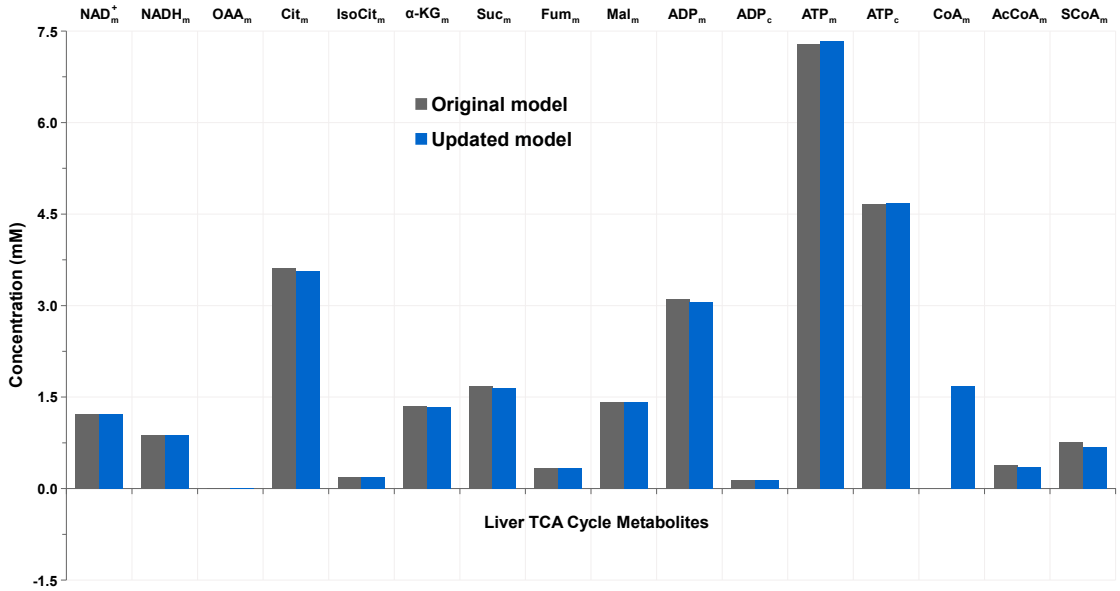

▪ **Figure 2.10.** A bar graph showing the metabolites for the $LVR_{TCA}{}^{OGI}$ & $LVR_{TCA}{}^{UPD}$ models, at initial steady-state.

▪ Dark Grey: $LVR_{TCA}{}^{OGI}$ data; ▪ Blue: $LVR_{TCA}{}^{UPD}$ data

▪ In liver TCA cycle models, [oxaloacetate] is in submicromolar range and therefore it is particularly mentioned in this figure.

▪ The difference through the individual metabolite concentrations between the two models (Δ Conc.) is shown separately in fig. 2.12 (see, pg. 48).

▪ **Figure 2.11.** Δ Flux through the individual reaction fluxes between the two liver TCA cycle models, at steady-state.

▪ **Δ Flux, at steady-state = [Value in $LVR_{TCA}{}^{OGI}$] – [Value in $LVR_{TCA}{}^{UPD}$]**

▪ 'ESS #1': Sea Blue; ▪ 'ESS #3': Deep Blue; ▪ 'ESS #2': Yellow

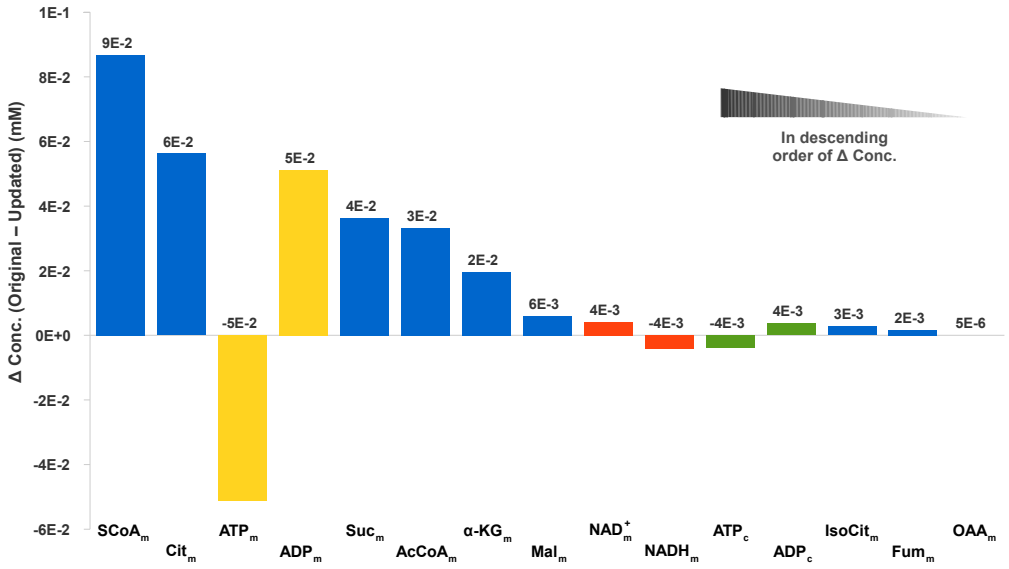

- **Figure 2.12.** Δ Conc. through the individual metabolite concentrations between the two liver TCA cycle models, at steady-state.
- CoA_m is not included in this figure; since, it is an external metabolite in LVR_{TCA}^{OGI}.
- **Δ Conc., at steady-state = [Value in LVR_{TCA}^{OGI}] − [Value in LVR_{TCA}^{UPD}]**
- All metabolites are shown in Blue; except for the conserved pairs. ATP_m & ADP_m are shown in Yellow; NAD^+_m & $NADH_m$ are shown in Orange; and ATP_c & ADP_c are shown in Green.

From figs. 2.9 to 2.12 (see, pgs. 46 to 48), we can observe the following:

1. Between the steady-states of two liver TCA cycle models, the difference in fluxes (Δ Flux, in mmol/sec) ranges from 3.0E-05 to 6.0E-03; whereas, the difference in metabolite concentrations (Δ Conc., in mM) ranges from 5.0E-06 to 9.0E-02.
2. The Δ Flux for 11 out of 15 reactions falls in the range of 2.0E-03 to 6.0E-03 and the remaining 4 reactions are within a much lower range of 3.0E-05 to 4.0E-04. All 'ESS #1', 'ESS #2' reactions, IDHa, & MDH fall under the earlier category; whereas the 'ESS #3' reactions, IDHb, & ATPsynth are in the latter category. Since the enzyme subsets are common between the two liver TCA cycle models, all respective subset reactions necessarily exhibit the same Δ Flux value.
3. Three reactions with the largest changes in their fluxes between the two models are – PC, MC, & MDH. PC & MC have a comparatively larger flux in the original liver TCA cycle model; whereas, MDH carries a relatively greater flux in the updated model.
4. The Δ Conc. for 7 out of 15 metabolites falls in the range of 2.0E-02 to 9.0E-02 and remaining 8 metabolites are within a lower range of 5.0E-06 to 6.0E-03. $SCoA_m$, citrate (Cit_m), ATP_m, ADP_m, succinate (Suc_m), $AcCoA_m$, & αKG_m fall under the earlier category; whereas, malate (Mal_m), NAD^+_m, $NADH_m$, ATP_c, ADP_c, isocitrate ($Isocit_m$), fumarate (Fum_m), & OAA_m are in the latter category.
5. In the original liver TCA cycle model, relatively higher concentrations of TCA cycle intermediate metabolites (TCAi) such as, Cit_m, Suc_m, & αKG_m, could result from the continuous supply of external CoA and a comparatively higher flux through PC.

In the updated liver TCA cycle model, a conserved CoA content and a much lower flux through PC is likely to limit such increases in TCAi's.

6. In the updated liver TCA cycle model, a relatively higher flux through MDH translates to a slightly higher concentration of $NADH_m$, which in turn causes a comparatively higher concentration of ATP_m. Thus, the updated model could possibly produce a comparatively higher mitochondrial ATP than the original model.
7. As shown earlier in fig. 2.9 (see, pg. 46), MDH functions in its reverse direction in both models. Also, in both models, IDHa is in the forward direction; whereas, IDHb in the reverse direction.
8. From the literature, we know that in liver mitochondria, Pyruvate carboxylase flux apparently ranges from 1.3 to 9.4 times the TCA cycle flux (flux through CS), and is on average around 3 times the TCA cycle flux (Baranyai and Blum, 1989; Beylot et al., 1995; Des Rosiers et al., 1995; Di Donato et al., 1993; Magnusson et al., 1991; Rabkin and Blum, 1985). At steady-state, both liver TCA cycle models are in agreement with this average value (see, fig. 2.9).
9. Overall, the respective compositions of initial steady-states for the two liver TCA cycle models are very similar and yet, not identical, unlike their corresponding elementary modes. Sizeable differences in 2–3 out of 15 possible fluxes give rise to substantial differences in 6–7 out of 15 possible metabolite concentrations, between the two models. Therefore, it would be particularly interesting to study whether, across several different steady-states, such differences in fluxes and metabolite concentrations between the two models actually translate to significant differences in, for example, the net ATP_m production or the net anaplerotic contribution by PC.

2.3.4 Dynamic responses of the two liver TCA cycle models to the variations in TCA cycle enzyme activities

Observations made earlier regarding the differences between initial steady-states of the two liver TCA cycle models, suggest a further analysis of these models to determine whether these differences are genuine or just an isolated consequence of a particular set of parameters used. Therefore, in response to variations in the TCA cycle enzyme activities, successive steady-states of both liver TCA cycle models are analysed in detail. From this analysis, data for the specific reaction fluxes & metabolite concentrations is presented here, with an emphasis on the two key aspects that emerge entirely due to the change in metabolic status of CoA between the two liver TCA cycle models. They are as follows:

1. Conservation of CoA_m, $SCoA_m$, & $AcCoA_m$.
2. Effect of CoA_m conservation relationship on rest of the liver TCA cycle system.

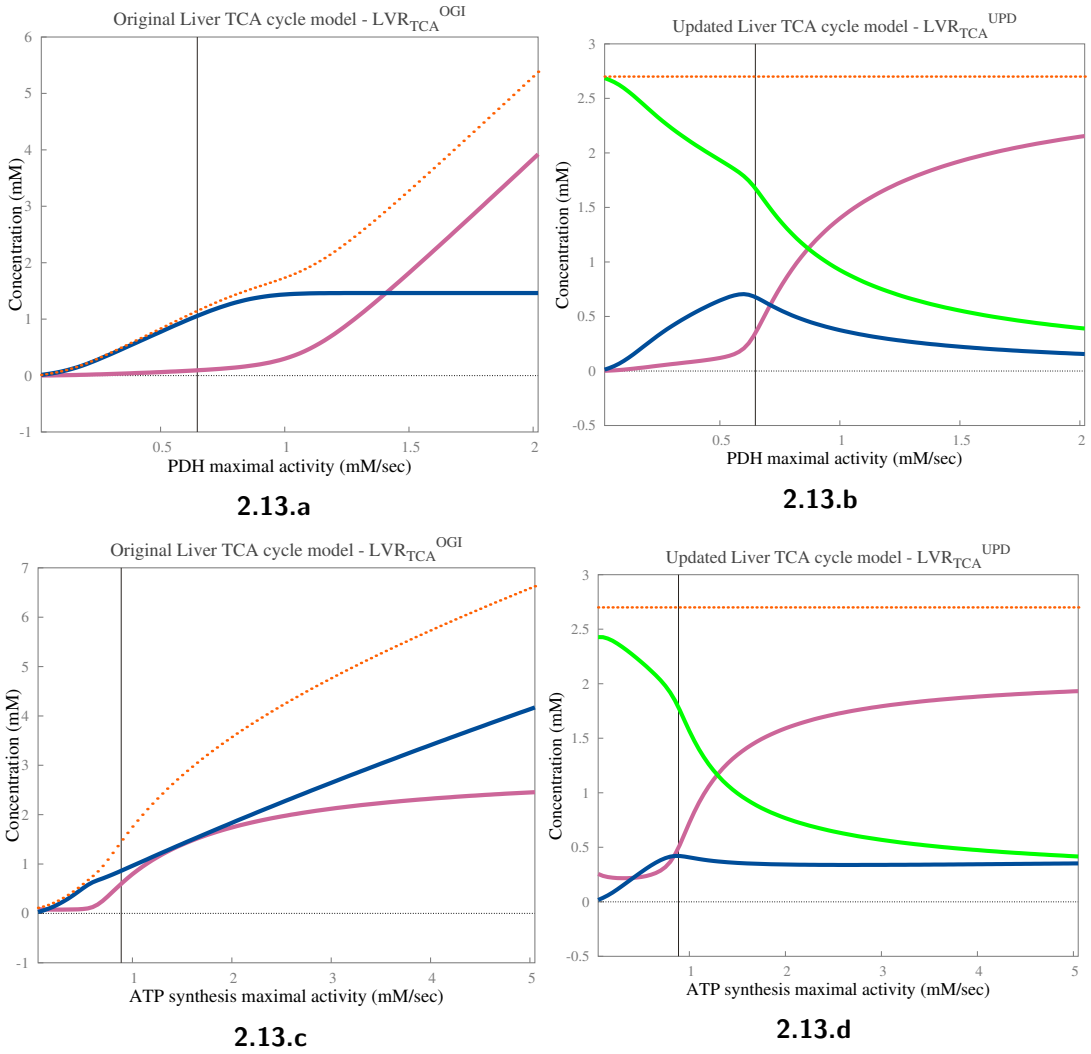

▪ **Figure 2.13. Change in the metabolic status of CoA between the two liver TCA cycle models:** Effect on [AcCoA], [SCoA] & [CoA] of changes in the maximal activities of PDH & ATPsynth, respectively.

$AcCoA_m$; CoA_m ; $SCoA_m$; *Total CoA content*

- The vertical black line represents the initial model value. At this point, in figs. 2.13a and 2.13b, $V_{max}^{PDH} = 0.648$ mM/sec and in figs. 2.13c and 2.13d, $V_{max}^{ATP_{synth}} = 0.886637$ mM/sec, respectively.
- *Total CoA content* for $LVR_{TCA}{}^{OGI} = [AcCoA_m] + [SCoA_m] =$ *variable*; & for $LVR_{TCA}{}^{UPD} = [AcCoA_m] + [SCoA_m] + [CoA_m] =$ *constant* $= 2.7$ mM.
- Since, CoA_m is an *external metabolite* in $LVR_{TCA}{}^{OGI}$, it is absent from figs. 2.13a and 2.13c, unlike in corresponding plots for $LVR_{TCA}{}^{UPD}$.
- Note the different *Y-axis* scales between figs. 2.13a and 2.13c compared with figs. 2.13b and 2.13d, respectively.

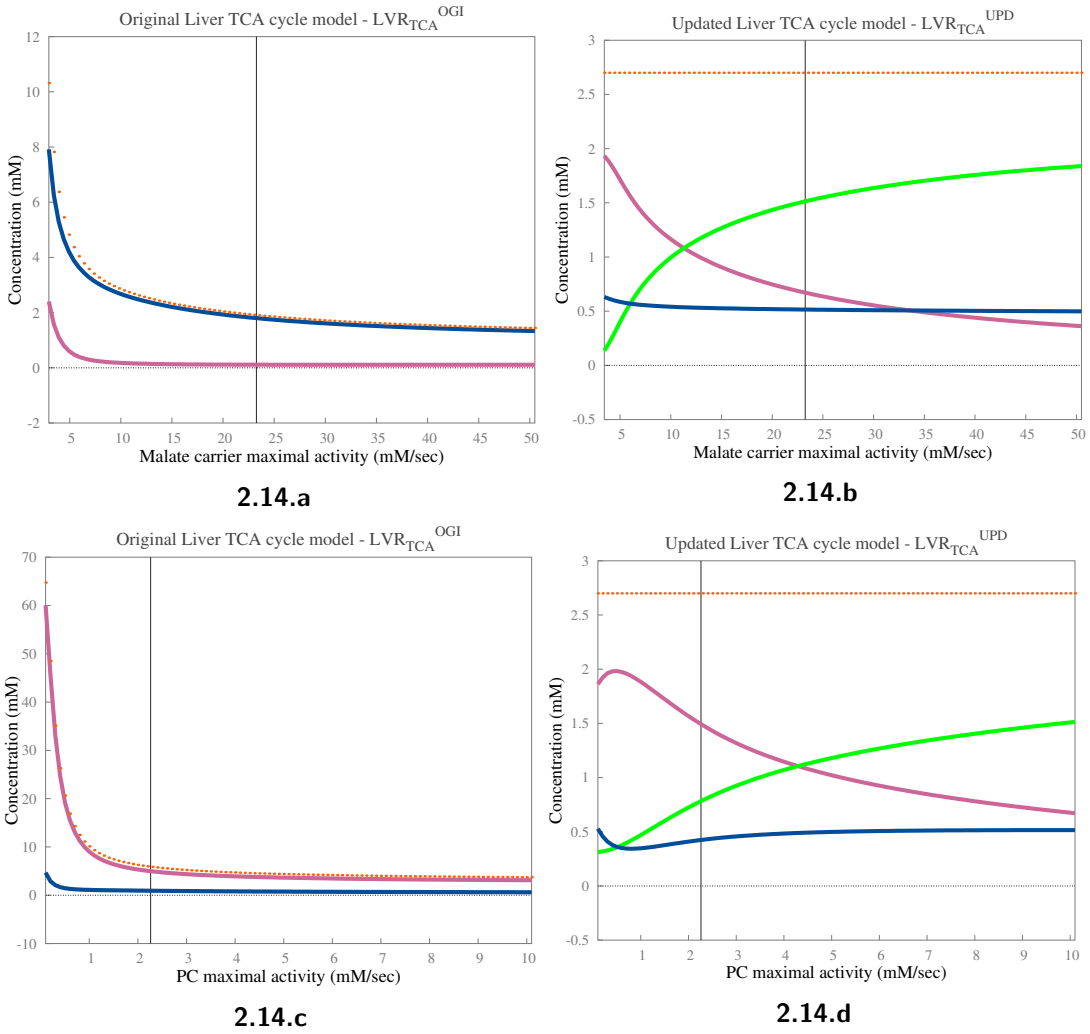

▪ **Figure 2.14. Change in the metabolic status of CoA between the two liver TCA cycle models:** Effect on [AcCoA], [SCoA] & [CoA] of change in the maximal activities of MC & PC, respectively.

AcCoA$_m$; CoA$_m$; SCoA$_m$; *Total CoA content*

- The vertical black line represents the initial model value. At this point, in figs. 2.14a and 2.14b, $V_{max}^{MC} = 23.2574$ mM/sec and in figs. 2.14c and 2.14d, $V_{max}^{PC} = 2.26234$ mM/sec (apparent velocity), respectively.
- Note the substantially different *Y-axis* scales between figs. 2.14a and 2.14c compared with figs. 2.14b and 2.14d, respectively.
- Other conditions as shown in fig. 2.13 on pg. 50.

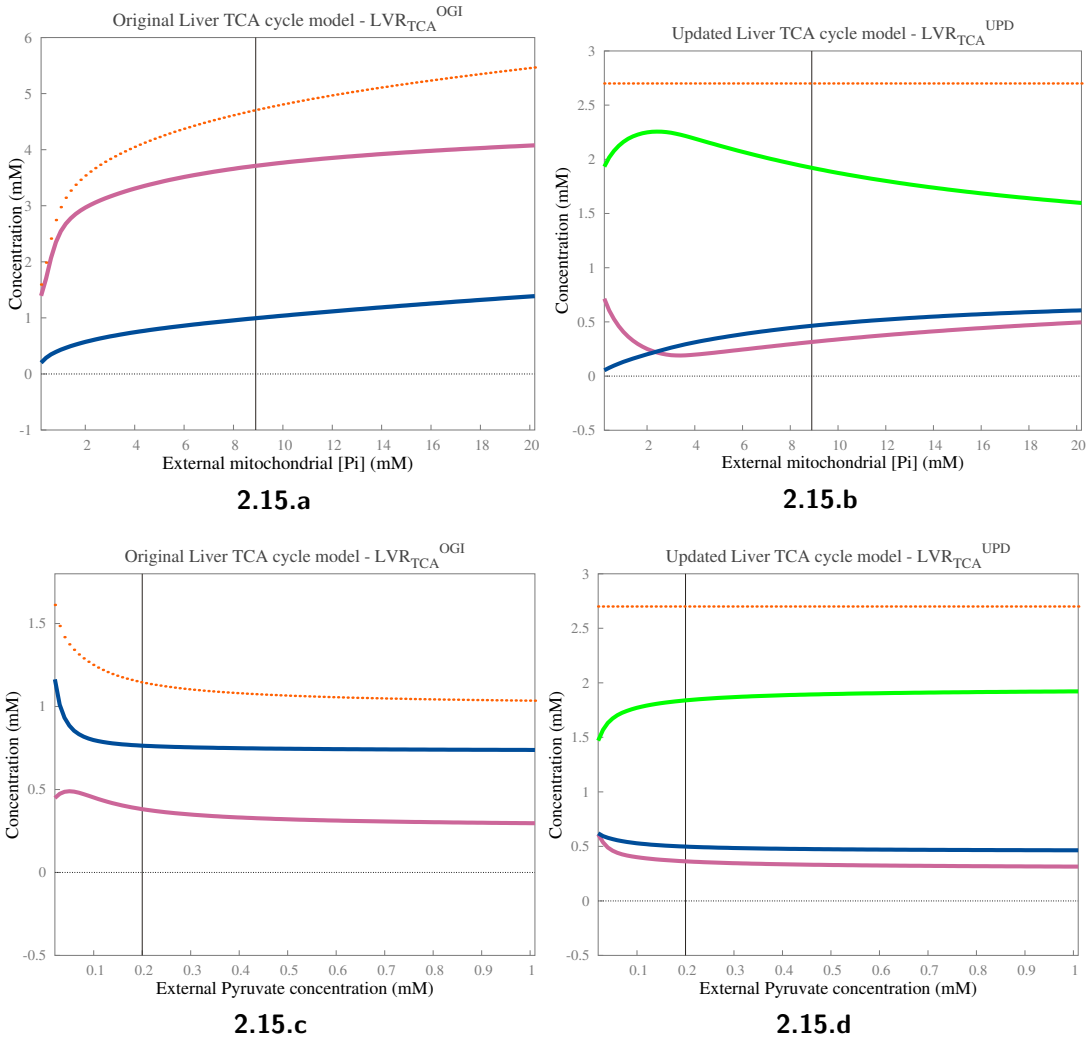

▪ **Figure 2.15. Change in the metabolic status of CoA between the two liver TCA cycle models:** Effect on [AcCoA], [SCoA] & [CoA] of change in the concentrations of Pi_m & Pyr_m, respectively.

AcCoA$_m$; CoA$_m$; SCoA$_m$; *Total CoA content*

▪ The vertical black line represents the initial model value. At this point, in figs. 2.15a and 2.15b, [Pi_m] = 8.9 mM and in figs. 2.15c and 2.15d, [Pyr_m] = 0.2 mM, respectively.

▪ Note the substantially different *Y-axis* scales between figs. 2.15a and 2.15c compared with figs. 2.15b and 2.15d, respectively.

▪ Other conditions as shown in fig. 2.13 on pg. 50.

Figures 2.13 to 2.15 (see, pgs. 50 to 52), describe the effect of CoA internalisation on the steady-state concentrations of CoA–related metabolites against a change in enzyme activity (V_{max}) or metabolite concentration. These figures clearly show a significant difference in total CoA content of the two liver TCA cycle models. In the original liver TCA cycle model, which contains CoA as an *external metabolite*, total CoA content is a *'variable'* and varies with the AcCoA$_m$ & SCoA$_m$ concentrations (see figures, *a.* & *c.* from figs. 2.13 to 2.15). Moreover, in the original model, total CoA content can vary within a wide range of values due to a constant supply of an external CoA in this

model. For example, in figs. 2.13a and 2.13c, total CoA content varies between 0.0–7.0 mM; whereas, in fig. 2.14a its value decreases from *approx.* 8.0 mM to 2.0 mM and in fig. 2.14c its value drops from almost 65.0 mM to 2.0 mM. On the other hand, in the updated liver TCA cycle model, which contains CoA_m as an *internal metabolite*, total CoA content is a *'constant'* at 2.7 mM; which is due to the conservation relationship involving CoA_m, $AcCoA_m$ & $SCoA_m$ that arises as a result of the change in metabolic status of CoA (*external*) to CoA_m (*internal*).

Therefore, based on the following reasons, we believe that behaviour exhibited by the Updated liver TCA cycle model is more realistic —

1. Due to the conservation relationship involving CoA_m, $SCoA_m$, & $AcCoA_m$, total CoA content in the updated model remains constant at 2.7 mM; whereas in the original model, in the absence of such a moiety conservation, it increases to unlikely levels. In rat liver mitochondria, CoA ranges from 0.3 mM to 2.0 mM (Hansford and Johnson, 1975; Mogilevskaya et al., 2006; Williamson and Brosnan, 1974; Williamson and Corkey, 1969; Williamson et al., 1968), AcCoA from 0.1 mM to 1.0 mM (Garland et al., 1965; McClure and Lardy, 1971; Williamson, 1969; Williamson et al., 1968, 1972), and SCoA from 0.3 mM to 1.4 mM (Hansford and Johnson, 1975; LaNoue et al., 1972; Mogilevskaya et al., 2006; Smith and Williamson, 1971; Williamson et al., 1972). Also, the inner mitochondrial membrane is impermeable to free carnitine, free CoA and their derivatives (Bremer, 1967; Brosnan and Fritz, 1971; Garland et al., 1969; Haddock et al., 1970; Oram et al., 1973; Parsons et al., 1966; Sottocasa et al., 1967; Yates and Garland, 1966), as well as other low-molecular-weight solutes (Chappell, 1968; Klingenberg, 1970; Klingenberg and Pfaff, 1966; Pfaff et al., 1968; Williamson et al., 1968). It means that *in vivo*, the total mitochondrial CoA content is in limited supply and remains fairly constant, which is appropriately shown in the updated liver TCA cycle model by the internalisation of CoA.

2. Although the variation in enzyme activity (V_{max}) or metabolite concentration shown here is above the physiological range, *in vivo*, it would be particularly unusual for metabolites such as $AcCoA_m$ to vary to the extent it does in the original liver TCA cycle model. On the other hand, in the updated liver TCA cycle model, such variations in the CoA–related metabolites are within physiological range, considering the concentration of $AcCoA_m$ in rat liver mitochondria and the fact that the inner mitochondrial membrane is impermeable to CoA–related metabolites.

Now, let us look at how the internalisation of CoA affects other metabolites and reaction fluxes.

Note: The relative change in TCAi's and fluxes is mostly quantitative in nature and hence presented here as bar graphs. The original steady-state analysis plots are included in the supplementary material. Details are given in the figures.

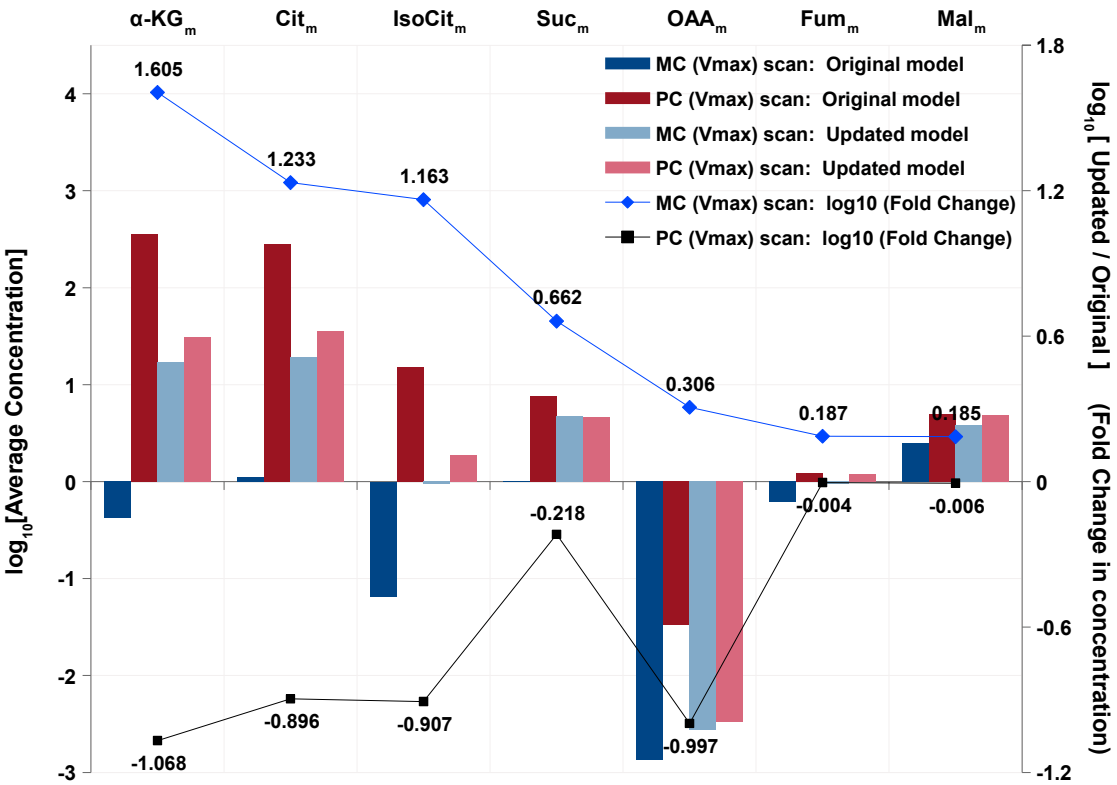

2.16.a. TCA cycle intermediate metabolites (TCAi)

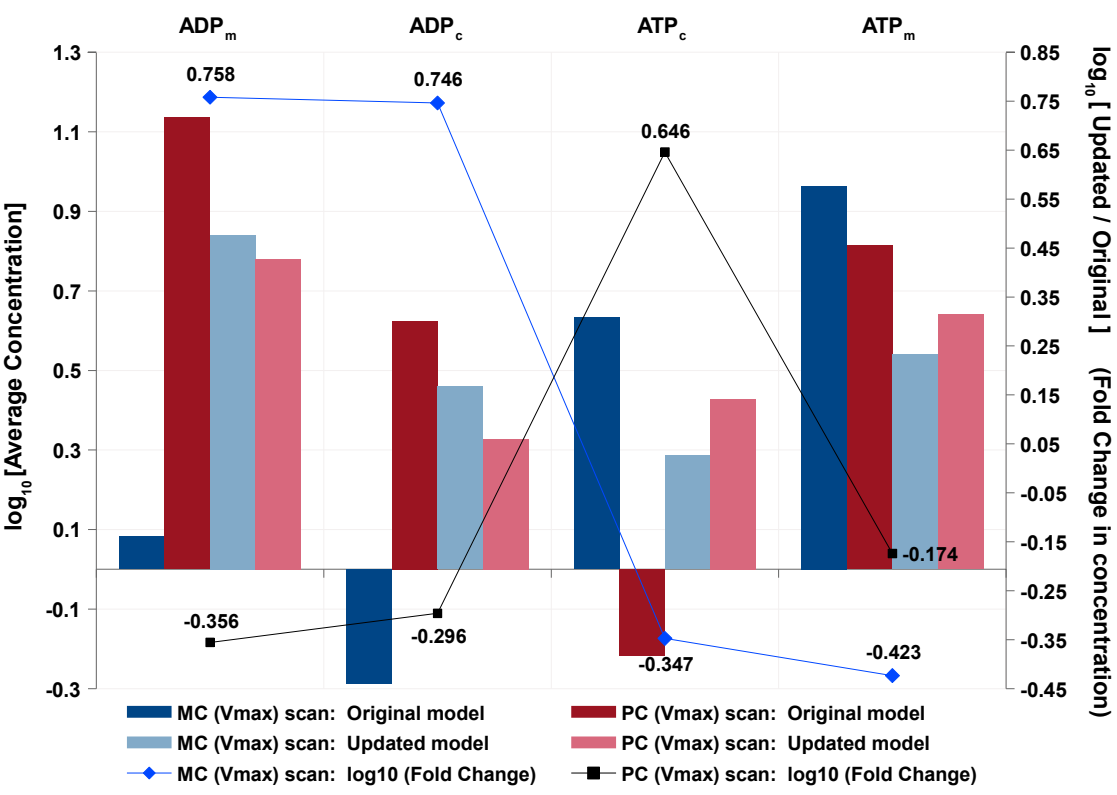

2.16.b. ATP−related metabolites

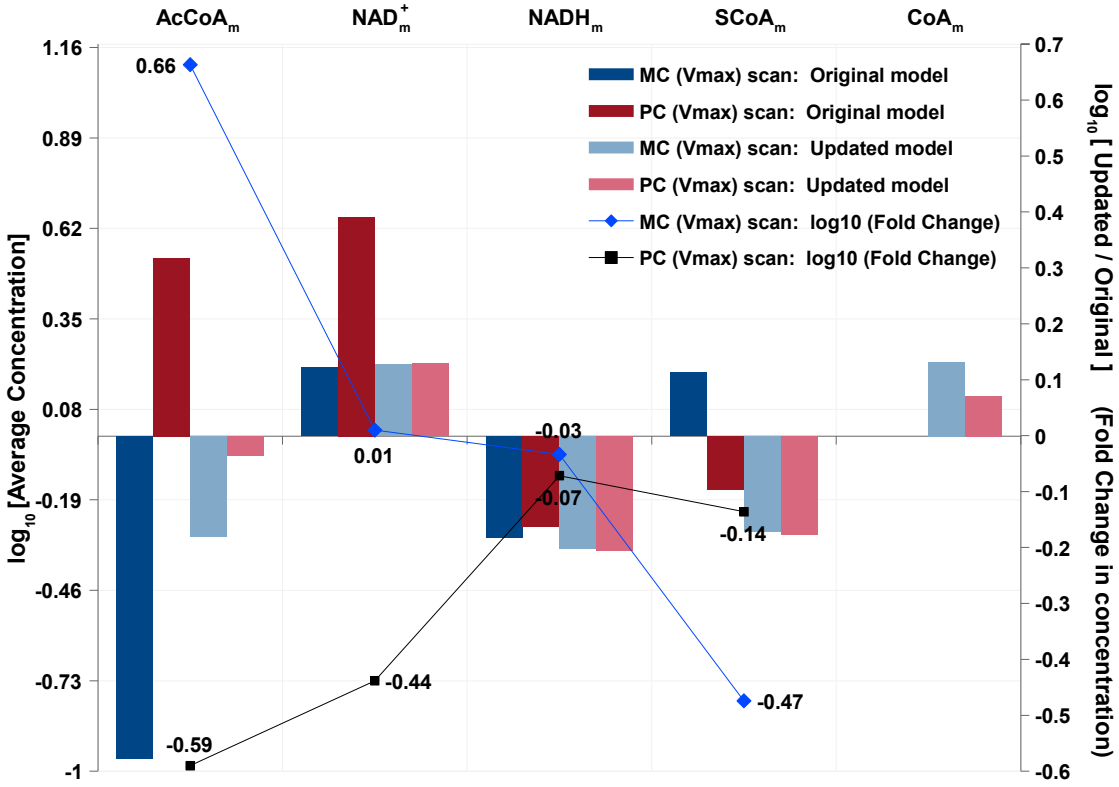

2.16.c. NAD- & CoA−related metabolites

▪ **Figure 2.16. Change in the metabolic status of CoA between the two liver TCA cycle models:** Effect on the TCAi concentrations against the change in the maximal activities of MC & PC, respectively.

▪ **Combined bar graphs against the change in maximal activities of MC (V^{MC}_{max}) & PC (V^{PC}_{max}), for the change in concentrations of — (a.) TCAi's, (b.) ATP−related metabolites, and (c.) NAD & CoA−related metabolites, respectively. 4 different bars represent 4 separate piece of data from 2 liver TCA cycle models – 2 each for MC & PC.**

▪ **Red bars** represent the steady-state data for change in V^{PC}_{max}; whereas, **Blue bars** show the data for change in V^{MC}_{max}. In both colours, *darker* bars represent the Original liver TCA cycle model ($LVR_{TCA}{}^{OGI}$) and *lighter* bars represent the Updated liver TCA cycle model ($LVR_{TCA}{}^{UPD}$), respectively.

▪ An average concentration value was calculated for each metabolite from all consecutive steady-state values per dataset. These were then used in the form of ***log$_{10}$*** values to generate the actual bar graph. For each common parameter, *i.e.*, MC or PC; a fold difference was calculated as –
[(avg. conc. in updated model)/(avg. conc. in original model)]
and represented in the graph as –
log$_{10}$[(avg. conc. in updated model)/(avg. conc. in original model)].

▪ **Blue points** represents the *log$_{10}$[Fold difference] w.r.t.* the change in V^{MC}_{max} and **Black points** represents the *log$_{10}$[Fold difference] w.r.t.* the change in V^{PC}_{max}. *Points in both colours are drawn aligned to the 'Secondary Y-axis'.*

▪ **Lines in both colours are drawn only to connect two consecutive points, otherwise they do not hold any significance to the data presented here.**

▪ In each subfigure, the metabolites are arranged in a descending order of log$_{10}$[Fold difference] values, calculated for the change in V^{MC}_{max}.

▪ ***Supplementary data for figs. 2.16a, 2.16b and 2.16c is shown in figs. I.1, I.2 and I.3 on pgs. IX to XI, respectively.***

▪ ***Figure 2.16c includes the same CoA/ AcCoA/ SCoA data presented earlier in fig. 2.14 on pg. 51.***

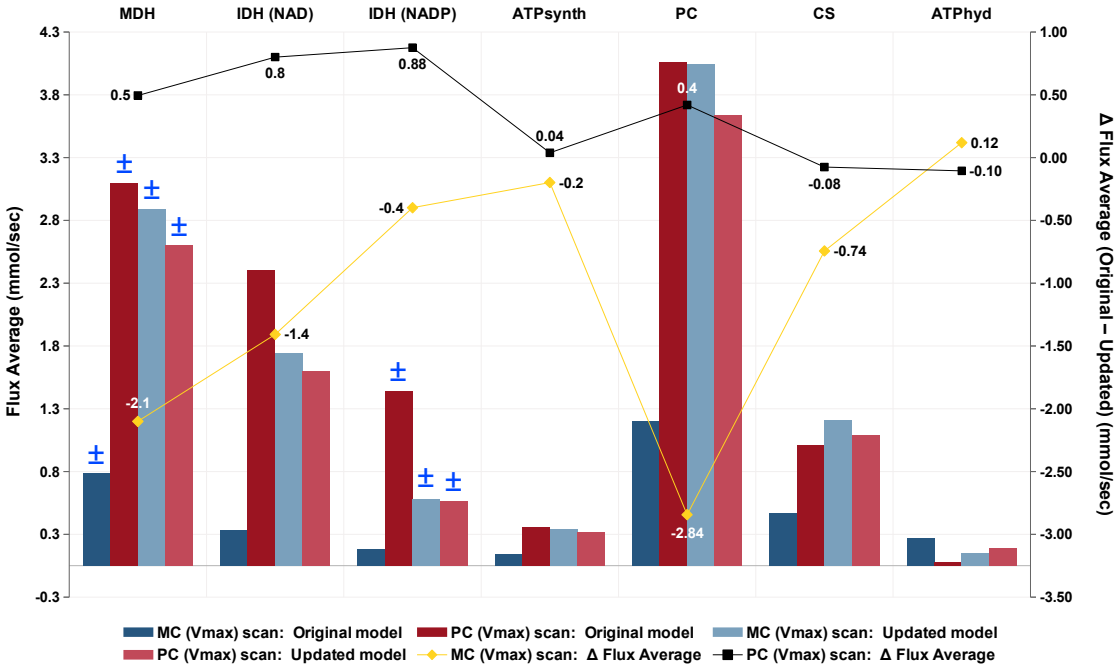

▪ **Figure 2.17. Change in the metabolic status of CoA between the two liver TCA cycle models:** Effect on the key liver TCA cycle reaction fluxes against change in the maximal activities of MC & PC, respectively.

▪ **This is a combined bar graph for change in key liver TCA cycle reaction fluxes against the change in maximal activities of MC (V_{max}^{MC}) & PC (V_{max}^{PC}), respectively. 4 different bars represent 4 separate piece of data from 2 liver TCA cycle models, 2 each for MC & PC.**

▪ **Red bars** represent the steady-state data for change in V_{max}^{PC}; whereas, **Blue bars** show the data for change in V_{max}^{MC}. In both colours, *darker* bars represent the Original liver TCA cycle model ($LVR_{TCA}{}^{OGI}$) and *lighter* bars represent the Updated liver TCA cycle model ($LVR_{TCA}{}^{UPD}$), respectively.

▪ An average flux value was calculated for each reaction from all consecutive steady-state values per dataset. These were then used to generate the actual bar graph. For each common parameter, *i.e.*, MC or PC; a difference of respective average flux values was calculated between the two liver TCA cycle models and was termed as **Δ Flux Average (Original – Updated)**.

▪ Since, in the case of a reaction flux, the negative sign signifies only the direction taken by a reaction in a steady-state; in this graph, the average flux value was considered as a positive number for those reactions that function in their respective reverse directions. **All such reactions are denoted by ±** .

▪ ***X-axis:*** Key liver TCA cycle reaction fluxes as data categories. These 7 reactions were chosen as representatives of three enzyme subsets as well as all the independent reactions from liver TCA cycle models.

▪ **Yellow points** represents the Δ Flux Average (Original – Updated) *w.r.t.* the change in V_{max}^{MC} and **Black points** represents the Δ Flux Average (Original – Updated) *w.r.t.* the change in V_{max}^{PC}. *Points in both colours are drawn aligned to the 'Secondary Y-axis'.* **Actual lines are inconsequential.**

▪ ***Supplementary data shown in fig. I.4 on pg. XII.***

From figs. 2.16 and 2.17 (see, pgs. 55 and 56) following observations can be made:

1. In the updated model, across increasing maximal activity of MC (V_{max}^{MC} scan), respective average concentrations of αKG_m, Cit_m, & $Isocit_m$ show the largest fold change in the range of *approx.* 15 to 40 folds, when compared to the original model (see, fig. 2.16a). Whereas, other TCAi concentrations show only a moderate increase in the range of *approx.* 2 to 6–folds. Noticeably, NAD_m^+ & $NADH_m$ levels remain fairly stable between the two models (see, fig. 2.16c). Compared to the original, ATP_c, ATP_m, & $SCoA_m$ show a slight decrease (by *approx.* 0.5–fold) in the updated model (see, figs. 2.16b and 2.16c). Across the V_{max}^{MC} scan, the average fold change in all TCAi concentrations is *approx.* 7.0–fold *w.r.t.* the original model. On the other hand, across increasing maximal activity of PC (V_{max}^{PC} scan), most TCAi concentrations in the updated model decrease significantly compared to the original; except for an increase in ATP_c by *approx.* 3.0–folds (see, fig. 2.16b). As a result, the overall variation observed in all TCAi's is quite moderate (*approx.* 0.75–fold) compared to that seen in the V_{max}^{MC} scan.

Across the V_{max}^{MC} scan, most liver TCA cycle fluxes in the updated model increase significantly in the range of *approx.* 3.0 to 6.0–folds relative to the original model; except for a slight drop in the ATPhyd flux (see, fig. 2.17). The overall fold change in TCA cycle fluxes is *approx.* 3.4–fold *w.r.t.* the original model. On the other hand, across increasing maximal activity of PC, key liver TCA cycle fluxes in the updated model decrease significantly compared to the original model; similar to the trend displayed by most TCAi concentrations. However, in this scan, CS, & ATPsynth remain nearly constant between the two models. For this scan, similar to TCAi's, the average fold change in all TCA cycle fluxes is quite moderate as well (*approx.* 1.3–fold) compared to that seen in the MC scan.

The log_{10}*[Fold difference]* values included in these graphs provide a clear indication of the comparative course taken by the metabolite concentrations and reaction fluxes between the two liver TCA cycle models.

2. In the case of V_{max}^{PC} scan, a significant reduction in most TCAi concentrations shows that the internalisation of CoA brings about a desired change in the updated liver TCA cycle model, in such a way that the overall TCA cycle metabolite content is kept relatively close to the physiological range. In this model, the newly established conservation relationship between CoA–related metabolites forces the system to maintain its total metabolite content within physiological range, in accordance with a set of constraints imposed by mass conservation and available external *'sources'*, in the absence of CoA as an external metabolite. As a result, this model is able to maintain the total CoA content at a *constant* value, as well as limit the degree of

variation in the overall metabolite content of the TCA cycle. Such reduction in the metabolite concentrations is a result of lower flux through the TCA cycle reactions and a relatively higher flux through 'ESS #1' that constitutes PC & MC. In both liver TCA cycle models, the flux through 'ESS #1' is at least 4 times more than the TCA cycle flux (flux through CS), as shown in fig. 2.17 (see, pg. 56). In the updated liver TCA cycle model, for V_{max}^{PC} scan, most reaction fluxes drop by *approx.* 0.4–0.9 mmol/sec compared to the original model; except CS & ATPhyd, which tend to compensate by increasing their flux slightly, especially ATPhyd.

The role of 'ESS #1' in varying the overall TCA cycle metabolic content is discussed at length in the following point.

3. In the case of V_{max}^{MC} scan, most TCAi concentrations increase significantly in the updated model as compared to that of the original. In liver TCA cycle models, although MC & PC constitute 'ESS #1'; intrinsically their roles differ in that, PC introduces the anaplerotic carbon into the TCA cycle and MC transports that carbon into the cytosol in a 1:1 exchange with Pi_c to the mitochondria. More importantly, there are 2 reactions in these models that introduce carbon into the TCA cycle, *viz.*– PDH & PC; whereas, only a single reaction, *i.e.* MC, which removes that carbon from the TCA cycle. Therefore, increase in V_{max}^{MC} causes the MC flux to increase, thus removing the TCA cycle carbon at a higher rate and imposing an enhanced demand on the two input reactions (*viz.*– PDH & PC) to maintain TCA cycle homoeostasis by increasing their flux.

As seen earlier, fig. 2.17 (see, pg. 56) shows that in liver TCA cycle models, the TCA cycle flux is *approx.* $1/4^{th}$ the flux through PC. Also, MDH functions in its reverse direction and is *approx.* 3 times the TCA cycle flux; which means that a large portion of the TCA cycle carbon is routed via: PC $\rightarrow$ $MDH_{(reverse)}$ $\rightarrow$ MC ; and only a smaller fraction of the TCA cycle carbon comes from the rest of TCA cycle to MC. This idea is supported further on the basis of elasticity coefficients of the updated liver TCA cycle model (see, pg. 108). It is likely that both these factors along with the conservation of CoA–related metabolites, would cause the observed build-up of most TCAi's in the updated liver TCA cycle model, despite the increased demand set by MC. Figure 2.18 (see, pg. 59) describes the aforementioned flux distribution pattern using the approximated flux data from fig. 2.17 and the enzyme subsets from fig. 2.8 (see, pg. 43).

4. When we compare the individual flux values from both liver TCA cycle models, at initial steady-state (see fig. 2.9 on pg. 46), to the values across consecutive steady-states (see, fig. 2.17), the relative impact of increasing V_{max}^{MC} or V_{max}^{PC} becomes more evident.

5. In fig. 2.16a (see, pg. 55), we can also observe that regardless of the model version or the scanning parameter, Cit_m, αKG_m & $Isocit_m$ (to some extent), tend to accumulate in the system compared to other TCAi's. The following factors could be responsible for such a selective accumulation of TCA cycle metabolites in liver TCA cycle models:

a) As shown earlier (see, fig. 2.8), 'ESS #2' is divided into two halves (top/ upper-half & bottom/ lower-half) as the 3 independent reactions (MDH, IDHa, & IDHb) break this subset at different junctions. It means that isocitrate is at a junction between the top-half of 'ESS #2' and IDHa/ IDHb; whereas, α-ketoglutarate is at a junction between IDHa/ IDHb and the bottom-half of 'ESS #2'.

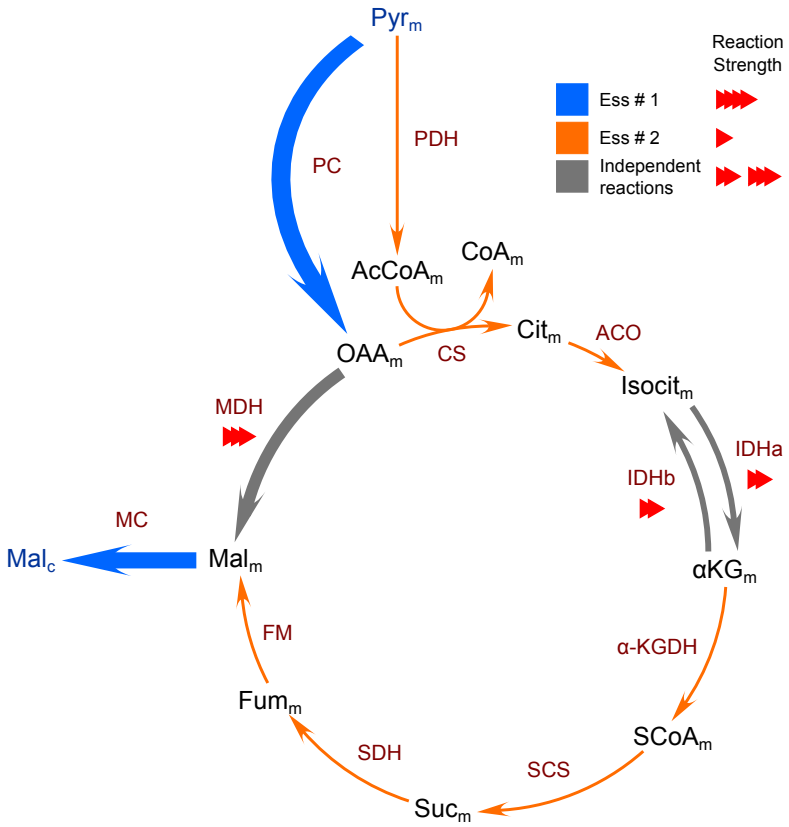

▪ **Figure 2.18.** A generalised flux distribution pattern observed for liver TCA cycle models against the increasing maximal activities of MC (V^{MC}_{max}) or PC (V^{PC}_{max}).

▪ Since, in this schematic the flux information of ATP/ADP−linked reactions is of little importance, ATPsynth, ANT, & ATPhyd are excluded. Also, all reactions are shown in their minimal form. Only the absolutely essential metabolites & co-factors are included in this diagram.

▪ The *arrow-line thickness* varies according to the respective strength of every flux.

▪ In this figure, the arrowheads point towards the respective forward or reverse directions of the participating reactions, specific to the flux data. For actual reaction definitions, please refer to fig. 2.1 from Methods (see, pg. 21).

▪ internal metabolites: in *Black*; external metabolites: in *Blue*; reaction/ enzyme names: in *Red*; "Independent reactions": in *Grey*.

b) From figs. 2.17 and 2.18, we know that the flux through IDHa is *approx.* 0.8–2.5 times greater than the TCA cycle flux and that in most situations IDHb operates in its reverse direction, thereby producing isocitrate at the expense of α-ketoglutarate, CO_2 & NADPH.

Therefore, in demanding situations such as represented by the V_{max}^{MC} or V_{max}^{PC} scans; there are 2 input reactions (PC & PDH) that can push the Cit_m concentration upward via OAA_m & $AcCoA_m$; whereas, there is only one reaction (IDHa) that can directly reduce the Cit_m concentration by producing $Isocit_m$. On the other hand, the reverse acting IDHb could effectively counteract any such reduction in Cit_m by partially replenishing the $Isocit_m$ concentration. Moreover, aconitate hydratase (ACO) is assumed to be operating reversibly at equilibrium, (Cortassa et al., 2003; Kohn et al., 1979a) characterised by an equilibrium constant (K_{eq}) of 0.0685 (dimensionless) (Alberty, 2003a).

c) Also, in such situations, it is now evident that the accumulation of αKG_m could be a direct result of it being produced faster by the independent reaction (IDHa) and consumed at a slower rate by the reactions constituting the bottom-half of 'ESS #2', especially α-KGDH.

d) From Methods (see, pg. 223), we know that the activity of citrate synthase is inhibited by physiological concentrations of $SCoA_m$ (Smith and Williamson, 1971) and ATP (Shepherd and Garland, 1969). Whereas, PDH is allosterically inhibited by increase in mitochondrial ATP/ADP, NADH/NAD^+ & AcCoA/CoA ratios (Lehninger et al., 1993; Tsai et al., 1973). We also know that α-KGDH is inhibited by $SCoA_m$, NADH, & ATP and activated by ADP (Smith et al., 1974). Also, IDHa is activated by ADP and inhibited by ATP as well as its products, αKG_m, NADH & CO_2 (Colman, 1975). *Since, the allosteric interactions of all TCA cycle enzymes are described in detail in the Methods section (see Appendix B on pg. 221), please refer to it for further details as well as references.*

Also, Williamson and Cooper, observed an energy-dependent link between CS, α-KGDH, & SCS, via succinyl-CoA & ATP/ADP -mediated inhibition and based on such a link, suggested a concerted regulation of these enzymes (Williamson and Cooper, 1980). In liver TCA cycle models, all of the above effector interactions are considered, alongside the substitution of GDP & GTP with ATP & ADP in the SCS rate equation (Alberty, 2003a). Therefore, in liver TCA cycle models, such inhibitory interactions are likely to cause an accumulation of citrate, isocitrate, & α-ketoglutarate, due to reductions in consuming fluxes, particularly when either of the ATP/ADP, AcCoA/SCoA, or NADH/NAD^+ ratios are significantly altered; which is the case, against change in PC or MC maximal activity (see, fig. 2.14d for AcCoA/SCoA on pg. 51 and figs. 2.22a and 2.22c for ATP/ADP & NADH/NAD^+ on pg. 68).

Once again, Williamson and Cooper, observed that the mitochondrial citrate concentration in turn is dependent on the IDHa activity and the effect of this interaction is to allow an increase of flux despite a fall in the isocitrate concentration. As the citrate is converted to isocitrate, falling citrate concentration lowers the apparent K_m of CS for oxaloacetate; which together with the direct effect of rising oxaloacetate levels (see fig. 2.39b on pg. 101) that result from the adjustment of malate/oxaloacetate ratio due to the falling NADH/NAD^+ (see fig. 2.22c on pg. 68), permits increased flux through CS, thereby increasing the citrate concentration further (Williamson and Cooper, 1980; and in supplementary material, see figs. I.1d and I.11c on pg. IX & pg. XIX, respectively).

Therefore, in liver TCA cycle models, as a consequence of the combined effect of all or some of the aforementioned regulatory interactions involving key 'ESS #2' enzymes, an average increase in the respective concentrations of citrate, isocitrate, and α-ketoglutarate appears distinctly possible, especially in the absence of mono-, di-, tricarboxylate transporter reactions; which when present, could possibly reduce the mitochondrial metabolite concentrations (Chappell, 1968; Klingenberg, 1970; LaNoue and Schoolwerth, 1979; Passarella et al., 2003; Williamson et al., 1968, 1969a).

Thus, in conclusion, along with the contribution of regulatory effector interactions of TCA cycle enzymes, the difference between respective fluxes of different TCA cycle *'spans'* and that of the independent reactions is responsible for such a bipartite response; wherein, some TCAi's decrease while others accumulate.

In the introductory chapter we have already discussed the *unspanning of TCA cycle* in detail along with several examples from the literature. Here, in the case of liver TCA cycle models, the *unspanning* is somewhat similar to the suggestion made by Randle et al. in that, the bottom half of liver TCA cycle, from α-KGDH to FM, forms a single 'span' (Randle et al., 1970). The exclusion of MDH, IDHa, and IDHb from the enzyme subsets is very specific to the structure of the models described here and as such can not be held against the aforementioned claim.

Now, we'll see the effect of increasing the TCA cycle inputs, such as Pyr_m & Pi_m, on various metabolite concentrations & reaction fluxes and whether the change in metabolic status of CoA (external) causes any variation in behaviour between the two models.

Note: As seen earlier, the relative change in TCAi's and fluxes is mostly quantitative in nature and hence presented here as bar graphs. The original steady-state analysis plots are included in the supplementary material. Details are given in the figures.

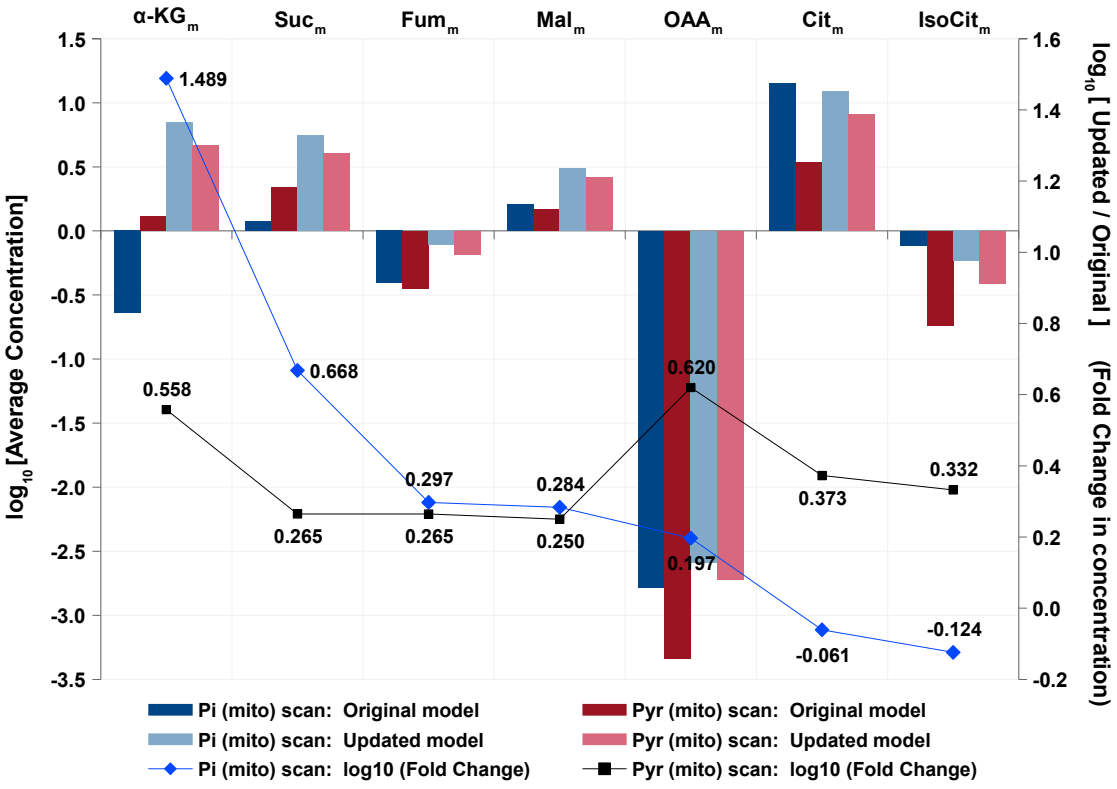

2.19.a. TCA cycle intermediate metabolites (TCAi)

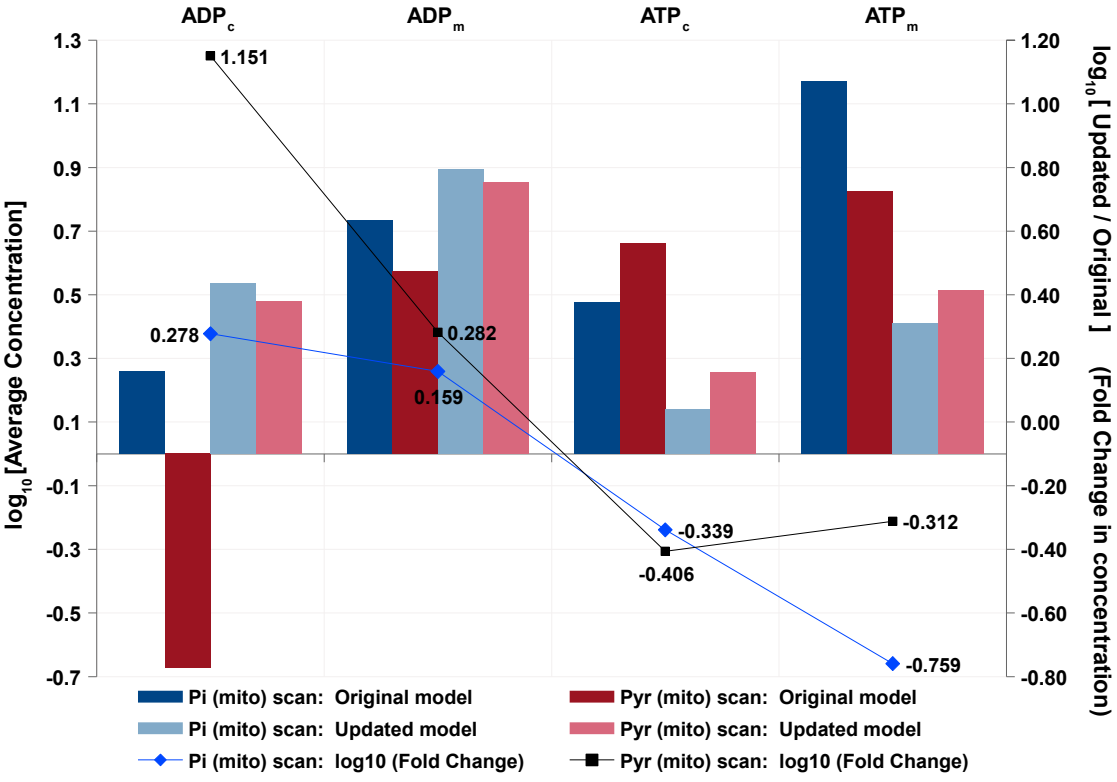

2.19.b. ATP−related metabolites

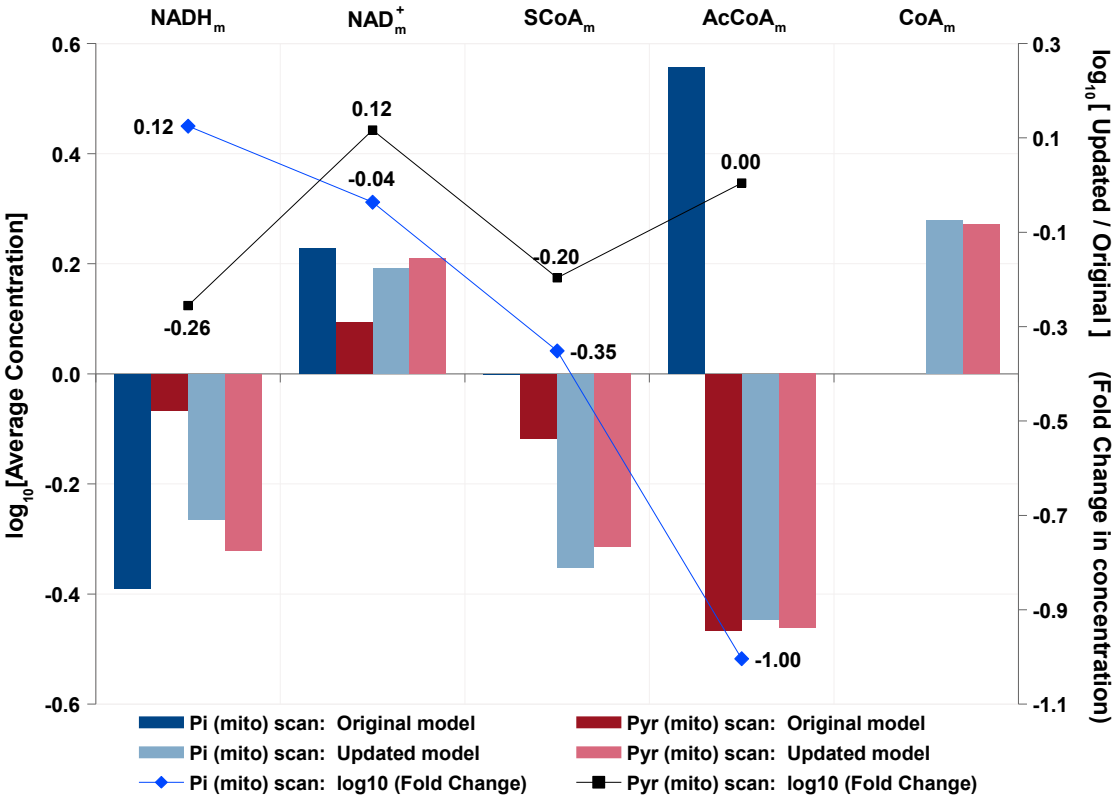

2.19.c. NAD- & CoA−related metabolites

▪ **Figure 2.19. Change in the metabolic status of CoA between the two liver TCA cycle models:** Effect on the TCAi concentrations against change in the concentrations of Pi_m & Pyr_m, respectively.

▪ **Combined bar graphs against the increasing concentrations of [Pi_m] & [Pyr_m] respectively, for the change in concentrations of — (a.) TCAi's, (b.) ATP−related metabolites, and (c.) NAD & CoA−related metabolites. 4 different bars represent 4 separate piece of data from 2 liver TCA cycle models, 2 each for [Pi_m] & [Pyr_m].**

▪ **Red bars** represent the steady-state data for change in [Pyr_m]; whereas, **Blue bars** show the data for change in [Pi_m]. In both colours, *darker* bars represent the Original liver TCA cycle model ($LVR_{TCA}{}^{OGI}$) and *lighter* bars represent the Updated liver TCA cycle model ($LVR_{TCA}{}^{UPD}$), respectively.

▪ An average concentration value was calculated for each metabolite from all consecutive steady-state values per dataset. These were then used in the form of ***log$_{10}$*** values to generate the actual bar graph. For each common parameter, *i.e.*, [Pi_m] or [Pyr_m]; a fold difference was calculated as –
[(avg. conc. in updated model)/(avg. conc. in original model)]
and represented in the graph as –
log$_{10}$[(avg. conc. in updated model)/(avg. conc. in original model)].

▪ **Blue points** represents the *log$_{10}$[Fold difference] w.r.t.* the change in [Pi_m] and **Black points** represents the *log$_{10}$[Fold difference] w.r.t.* the change in [Pyr_m]. *Points in both colours are drawn aligned to the 'Secondary Y-axis'.*

▪ **Lines in both colours are drawn only to connect two consecutive points, otherwise they do not hold any significance to the data presented here.**

▪ In each subfigure, the metabolites are arranged in a descending order of log$_{10}$[Fold difference] values, calculated for the change in V^{MC}_{max}.

▪ ***Supplementary data for figs. 2.19a, 2.19b and 2.19c is shown in figs. I.5, I.6 and I.7 on pgs. XIII to XV, respectively.***

▪ ***Figure 2.19c includes the same CoA/ AcCoA/ SCoA data presented earlier in fig. 2.15 on pg. 52.***

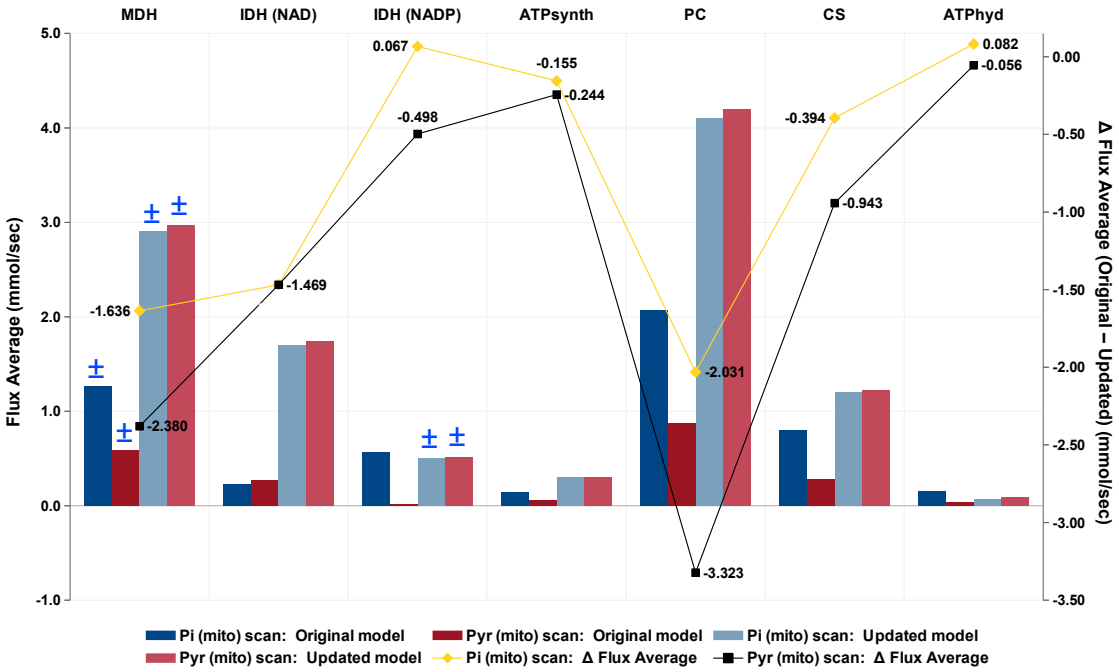

▪ **Figure 2.20. Change in the metabolic status of CoA between the two liver TCA cycle models:** Effect on the key liver TCA cycle reaction fluxes against change in the concentrations of Pi_m & Pyr_m, respectively.

▪ **This is a combined bar graph for change in key liver TCA cycle reaction fluxes against the change in respective concentrations of [Pi_m] & [Pyr_m]. 4 different bars represent 4 separate piece of data from 2 liver TCA cycle models, 2 each for [Pi_m] & [Pyr_m].**

▪ **Red bars** represent the steady-state data for change in [Pyr_m]; whereas, **Blue bars** show the data for change in [Pi_m]. In both colours, *darker* bars represent the Original liver TCA cycle model ($LVR_{TCA}{}^{OGI}$) and *lighter* bars represent the Updated liver TCA cycle model ($LVR_{TCA}{}^{UPD}$), respectively.

▪ An average flux value was calculated for each reaction from all consecutive steady-state values per dataset. These were then used to generate the actual bar graph. For each common parameter, *i.e.*, MC or PC; a difference of respective average flux values was calculated between the two liver TCA cycle models and was termed as **Δ Flux Average (Original − Updated)**.

▪ Since, in the case of a reaction flux, the negative sign signifies only the direction taken by a reaction in a steady-state; in this graph, the average flux value was considered as a positive number for those reactions that function in their respective reverse directions. **All such reactions are denoted by ±** .

▪ ***X-axis:*** Key liver TCA cycle reaction fluxes as data categories. These 7 reactions were chosen as representatives of three enzyme subsets as well as all the independent reactions from liver TCA cycle models.

▪ **Yellow points** represents the Δ Flux Average (Original − Updated) *w.r.t.* the change in [Pi_m] and **Black points** represents the Δ Flux Average (Original − Updated) *w.r.t.* the change in [Pyr_m]. *Points in both colours are drawn aligned to the 'Secondary Y-axis'.*

▪ **Lines in both colours are drawn only to connect two consecutive points, otherwise they do not hold any significance to the data presented here.**

▪ ***Supplementary data shown in fig. I.8 on pg. XVI.***

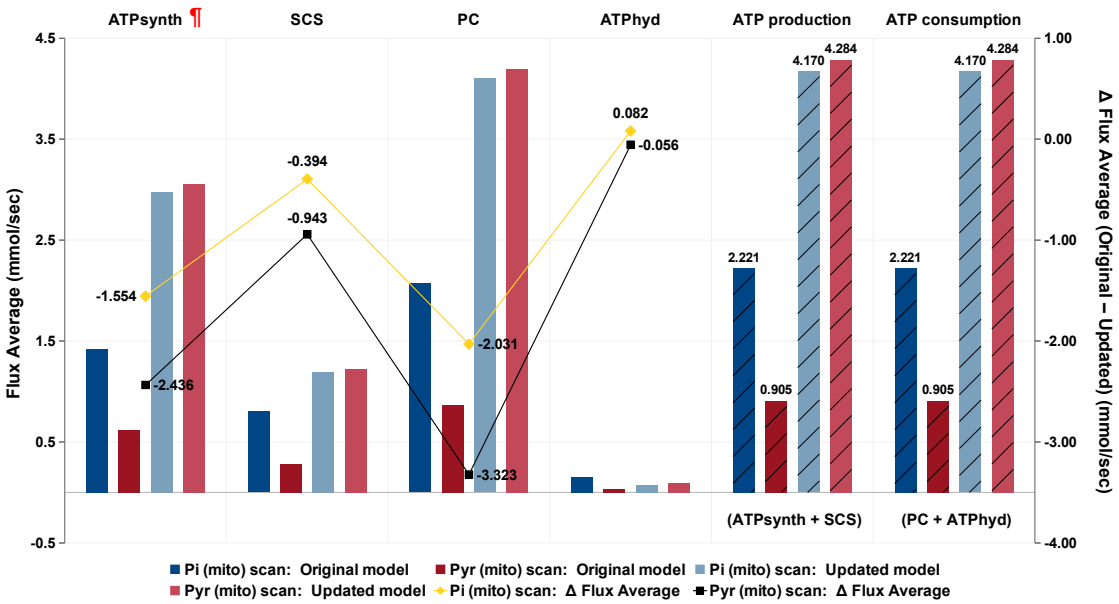

▪ **Figure 2.21. Change in the metabolic status of CoA between the two liver TCA cycle models:** Effect on the ATP/ADP-linked reaction fluxes against change in the concentrations of Pi_m & Pyr_m, respectively.

▪ **This is a combined bar graph for change in the ATP/ADP-linked reaction fluxes against the change in respective concentrations of [Pi_m] & [Pyr_m]. 4 different bars represent 4 separate piece of data from 2 liver TCA cycle models, 2 each for [Pi_m] & [Pyr_m].**

▪ **Red bars** represent the steady-state data for change in [Pyr_m]; whereas, **Blue bars** show the data for change in [Pi_m]. In both colours, *darker* bars represent the Original liver TCA cycle model ($LVR_{TCA}{}^{OGI}$) and *lighter* bars represent the Updated liver TCA cycle model ($LVR_{TCA}{}^{UPD}$), respectively.

▪ An average flux value was calculated for each reaction from all consecutive steady-state values per dataset. These were then used to generate the actual bar graph. For each common parameter, *i.e.*, Pi_m or Pyr_m; a difference of respective average flux values was calculated between the two liver TCA cycle models and was termed as **Δ Flux Average (Original − Updated)**.

▪ In this graph, a set of hatched bars in the same colour key show the total ATP_m production or consumption by the respective liver TCA cycle models, for respective scans.

▪ ***X-axis:*** pyruvate carboxylase (PC) is included alongside other ATP/ADP−linked reactions to maintain the balance between ATP-consuming reactions (ATPhyd & PC) and ATP-producing reactions (ATPsynth & SCS).

▪ **Yellow points** represents the Δ Flux Average (Original − Updated) *w.r.t.* the change in [Pi_m] and **Black points** represents the Δ Flux Average (Original − Updated) *w.r.t.* the change in [Pyr_m]. *Points in both colours are drawn aligned to the 'Secondary Y-axis'.*

▪ **Lines in both colours are drawn only to connect two consecutive points, otherwise they do not hold any significance to the data presented here.**

▪ ¶ : In this figure, the average values for ATP synthase (ATPsynth) flux have been scaled by a factor of 10; due to the difference in respective reaction stoichiometries between ATPsynth (in mitochondria) and ATPhyd (in cytosol).

▪ ***Supplementary data shown in fig. I.9 on pg. XVII.***

From figs. 2.19 to 2.21 (see, pgs. 63 to 65) following observations can be made:

1. Across increasing [Pi_m], compared to the original model, the TCA cycle flux increases by *approx.* 0.5–fold in the updated model; whereas, across increasing [Pyr_m], it increases by *approx.* 3–fold. Increase in IDHa flux is nearly the same in both scans (by about 6–fold). MDH, PC, & ATPsynth are *approx.* twice the original in the [Pi_m] scan; whereas, across increasing [Pyr_m], these fluxes increase by *approx.* 4–fold compared to the original model. In both scans, IDHb operates in its reverse direction. Its flux remains virtually unaffected across increasing [Pi_m]; whereas, it increases by *approx.* 35–fold across increasing [Pyr_m].

As seen earlier in the case of MC/ PC scans, flux data for both these scans suggest the same flux distribution pattern as shown in fig. 2.18 (see, pg. 59).

2. Across increasing [Pyr_m], the overall flux carrying capacity of the updated liver TCA cycle model is on an average 5 times the original; whereas, it is about thrice the original across increasing [Pi_m]. Original plots given in the supplementary material clearly show that even within a physiological range of Pi_m/ Pyr_m concentrations, such an increase in the overall flux carrying capacity is quite plausible for liver TCA cycle models (see figs. I.8 and I.9 on pg. XVI and pg. XVII, respectively).

In systems built using saturable kinetics, the responsiveness of a system to an increase or decrease in its primary inputs (in this case, Pyr_m & Pi_m) depends on the substrate saturation of enzymes. A substrate present at a concentration greater than the corresponding K_m is generally considered to be saturating. However, in the case of liver TCA cycle models, since the effects of competitive product inhibition are also factored in for several enzymes; the overall reaction rate can still be responsive to changes in substrate concentration, regardless of the extent of substrate saturation (*i.e.* $K_{m,S} \ll$ [substrate]). In such systems, calculation of enzyme elasticities can help to study the sensitivity of a reaction rate to a change in substrate concentration.

In the updated liver TCA cycle model, some of the elasticity coefficients of PDH & PC, calculated for pyruvate (0.05 & 0.41, respectively) and those of SCS & ATPsynth for Pi_m (-3.35 & 0.61, respectively) were found to be high enough to conclude that the observed increase in the total flux carrying capacity is due to the responsiveness of some of these reactions towards the primary inputs to the TCA cycle. Subsequently, the elasticities of remaining liver TCA cycle enzymes towards other metabolites could also play a role in increasing the overall flux capacity (*e.g.* elasticity coefficients of citrate synthase : 0.95 for oxaloacetate & 0.70 for acetyl-CoA). For further discussion on elasticities, please see, pg. 108.

Compared to the original model, fold increase in the total flux carrying capacity is significantly more in the updated model; which could primarily be due to the internalisation of CoA. As seen earlier, reassignment of external CoA as an internal metabolite, maintains the total metabolite content of a system within physiological range. Figure 2.19c (see, pg. 63) shows that the average concentration of $SCoA_m$ is reduced by about 55% across $[Pi_m]$ and by about 36% across $[Pyr_m]$ compared to the original model. Also, $AcCoA_m$ is reduced by *approx.* 90% across increasing $[Pi_m]$, but remains nearly unchanged across increasing $[Pyr_m]$.

As mentioned earlier on pg. 61, the allosteric inhibitory interactions of PDH, CS, IDHa, & α-KGDH are appropriately considered while defining the respective rate equations in liver TCA cycle models. *Since, the allosteric interactions of all TCA cycle enzymes are described in detail in the Methods section (see Appendix B on pg. 221), please refer to it for further details as well as references.*

Therefore, compared to the original liver TCA cycle model, significantly reduced $SCoA_m$ concentration in the updated model lowers its CS and α-KGDH inhibition, thereby contributing towards the higher flux carrying capacity of the model. Also, across increasing $[Pi_m]$, a significant 90% reduction in $AcCoA_m$ concentration could play a role as well, by lowering its inhibition of PDH via a possible decrease in the AcCoA/CoA ratio. Moreover, across increasing $[Pi_m]$ as well as $[Pyr_m]$, a significantly lower $[ATP/ADP]_m$ ratio also helps to increase the flux carrying capacity by reducing the ATP-induced inhibition of CS, IDHa, & α-KGDH. The individual ratio profiles are presented later in figs. 2.23 and 2.24 (see, pgs. 69 and 70).

3. Across increasing $[Pi_m]$, compared to the original model, most TCAi concentrations from the bottom-half of 'ESS #2' show a significant increase in the range of 1.5 to 5.0–folds. α-ketoglutarate increases by *approx.* 30–fold than that in the original model, due to the same flux distribution pattern explained earlier in the case of MC/ PC scans (see fig. 2.18 on pg. 59). Increase in Suc_m and decrease in $SCoA_m$ are as a result of 1.5–fold increase in the substrate-level phosphorylation via SCS, as the availability of its co-substrate (Pi_m) increases. Whereas, across increasing $[Pyr_m]$, the relative change in TCAi concentrations is spread throughout 'ESS #2', perhaps due to the significant increases in key TCA cycle fluxes as well as the reversal of IDHb.

In the updated liver TCA cycle model, although the actual scale of relative change in TCA metabolite concentrations is very large, original plots provided in the supplementary material suggest that qualitatively such changes in TCAi levels are valid to some extent within a much smaller range that includes the physiological concentrations of Pi_m/ Pyr_m (see fig. I.5 on pg. XIII).

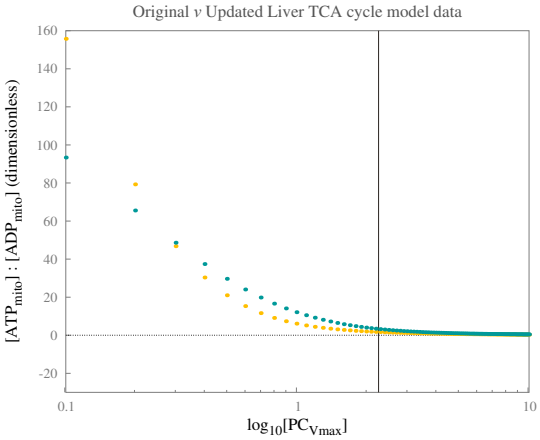

2.22.a. $[ATP/ADP]_m$

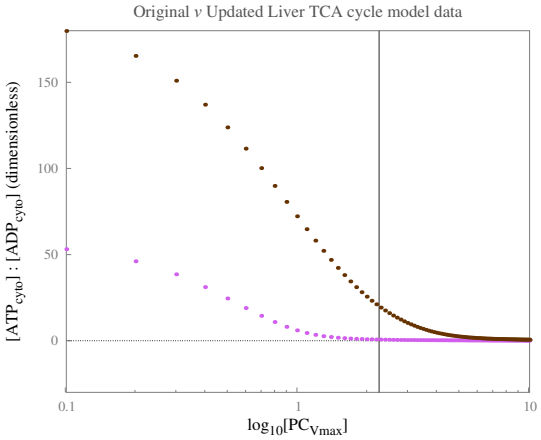

2.22.b. $[ATP/ADP]_c$

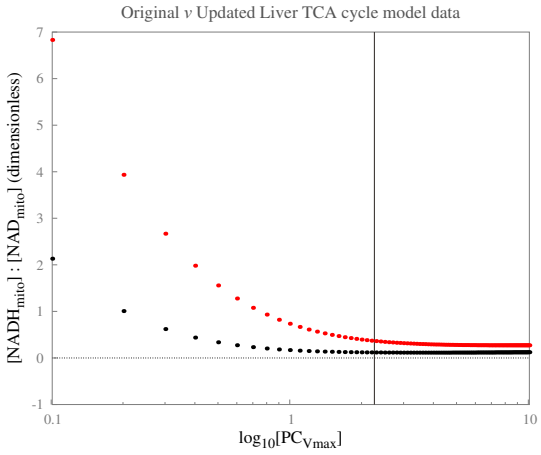

2.22.c. $[NADH/NAD^+]_m$

Median values		
$NADH_m / NAD_m$	Updated model	0.3
	Original model	0.1
ATP_m / ADP_m	Updated model	1.0
	Original model	0.6
ATP_c / ADP_c	Updated model	2.3
	Original model	0.2

2.22.d. Median values

▪ **Figure 2.22. Variations in the 'Energy status' of liver TCA cycle models:** $[ATP/ADP]$ & $[NADH/NAD^+]$ ratios across the increasing maximal activity of PC (V_{max}^{PC}).

▪ Key for figs. 2.22a to 2.22c is as follows :

- **$[ATP/ADP]_m$:** Original model ; Updated model
- **$[ATP/ADP]_c$:** Original model ; Updated model
- **$[NADH/NAD^+]_m$:** Original model ; Updated model

For figs. 2.22a to 2.22c :

▪ *X-axis* : $\log_{10}[V_{max}^{PC}]$ – PC maximal activity in logarithmic scale.

▪ *Y-axis* : Ratio of concentrations (dimensionless).

▪ The vertical black line represents the initial model value. At this point on the *X-axis*, V_{max}^{PC} = 2.26234 mM/sec (apparent velocity) in logarithmic scale.

▪ A dotted, black, horizontal line represents the *"zero-axis"* in each figure.

▪ ***Supplementary data for figs. 2.22a, 2.22b and 2.22c is shown in figs. I.2c, I.2d, I.3c and I.3d on pg. X & pg. XI, respectively.***

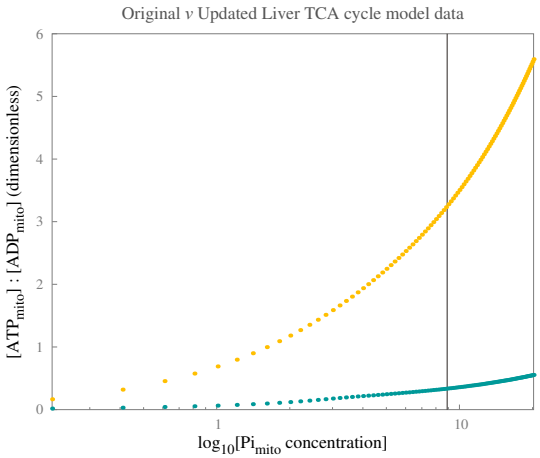

2.23.a. $[ATP/ADP]_m$

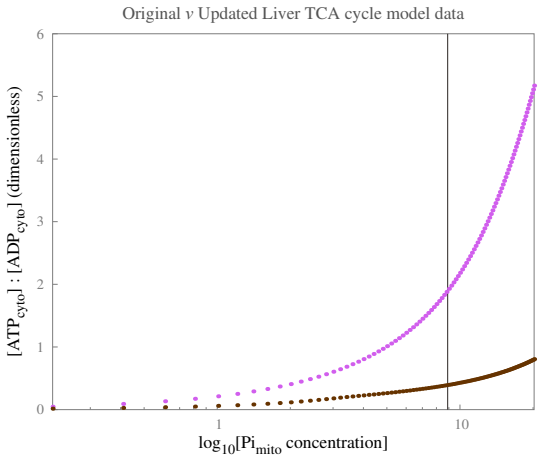

2.23.b. $[ATP/ADP]_c$

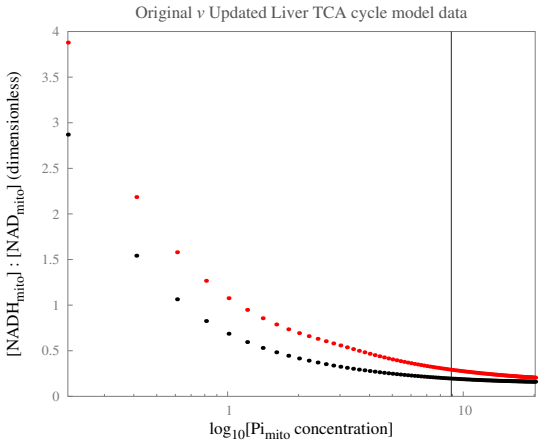

2.23.c. $[NADH/NAD^+]_m$

Median values		
$NADH_m$ / NAD_m	Updated model	0.3
	Original model	0.2
ATP_m / ADP_m	Updated model	0.4
	Original model	3.5
ATP_c / ADP_c	Updated model	0.4
	Original model	2.2

2.23.d. Median values

▪ **Figure 2.23. Variations in the 'Energy status' of liver TCA cycle models:** $[ATP/ADP]$ & $[NADH/NAD^+]$ ratios across the increasing concentration of $[Pi_m]$.

- Key for figs. 2.23a to 2.23c is as follows :
  - **$[ATP/ADP]_m$:** Original model ; Updated model
  - **$[ATP/ADP]_c$:** Original model ; Updated model
  - **$[NADH/NAD^+]_m$:** Original model ; Updated model

For figs. 2.23a to 2.23c :

- *X-axis* : $\log_{10}[Pi_m]$ – concentration of mitochondrial inorganic phosphate (Pi_m) in logarithmic scale.
- *Y-axis* : Ratio of concentrations (dimensionless).
- The vertical black line represents the initial model value. At this point on the *X-axis*, $[Pi_m] = 8.9$ mM in logarithmic scale.
- A dotted, black, horizontal line represents the *"zero-axis"* in each figure.
- ***Supplementary data for figs. 2.23a, 2.23b and 2.23c is shown in figs. I.6a, I.6b, I.7a and I.7b on pg. XIV & pg. XV, respectively.***

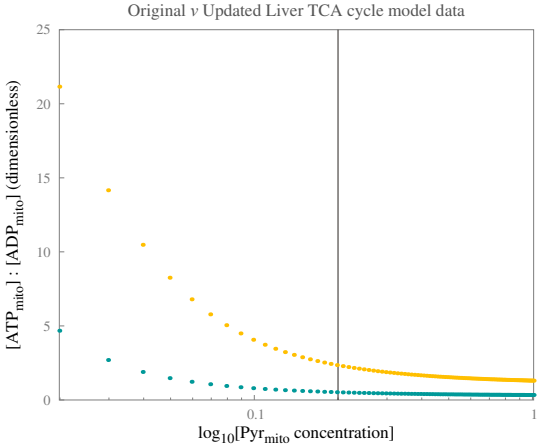

2.24.a. $[ATP/ADP]_m$

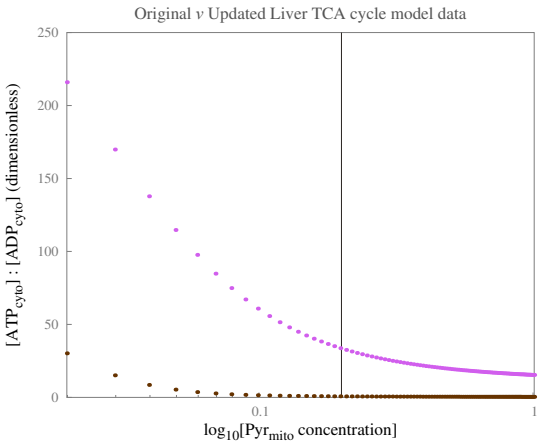

2.24.b. $[ATP/ADP]_c$

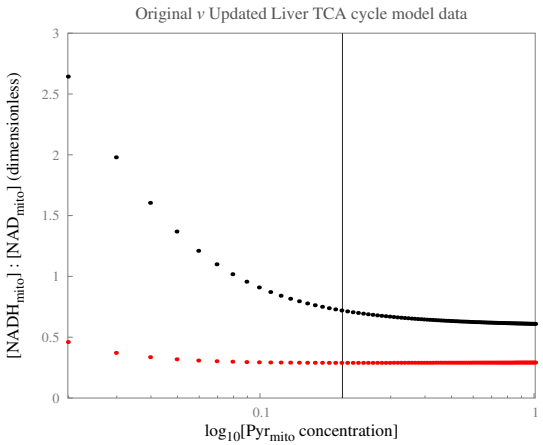

2.24.c. $[NADH/NAD^+]_m$

Median values		
$NADH_m$ / NAD_m	Updated model	0.3
	Original model	0.6
ATP_m / ADP_m	Updated model	0.4
	Original model	1.5
ATP_c / ADP_c	Updated model	0.5
	Original model	19.3

2.24.d. Median values

▪ **Figure 2.24. Variations in the 'Energy status' of liver TCA cycle models:** $[ATP/ADP]$ & $[NADH/NAD^+]$ ratios across increasing concentration of $[Pyr_m]$.

- Key for figs. 2.24a to 2.24c is as follows :
  - **$[ATP/ADP]_m$:** Original model ; Updated model
  - **$[ATP/ADP]_c$:** Original model ; Updated model
  - **$[NADH/NAD^+]_m$:** Original model ; Updated model

For figs. 2.24a to 2.24c :

- *X-axis* : $\log_{10}[Pyr_m]$ – concentration of pyruvate (Pyr_m) in logarithmic scale.
- *Y-axis* : Ratio of concentrations (dimensionless).
- The vertical black line represents the initial model value. At this point on the *X-axis*, $[Pyr_m] = 0.2$ mM in logarithmic scale.
- A dotted, black, horizontal line represents the *"zero-axis"* in each figure.
- ***Supplementary data for figs. 2.24a, 2.24b and 2.24c is shown in figs. I.6c, I.6d, I.7c and I.7d on pg. XIV & pg. XV, respectively.***

Figures 2.22 to 2.24 (see, pgs. 68 to 70) describe the *'energy status'* of liver TCA cycle models in terms of key ratios like – $[ATP/ADP]_m$, $[ATP/ADP]_c$ & $[NADH/NAD^+]_m$, across increasing maximal activity of PC and across increasing concentrations of Pi_m & Pyr_m, respectively. Figures 2.22d, 2.23d and 2.24d provide a list of median values for these ratios. *Before we inspect the differences in ratio profiles between the two models, it is important to note that the initial concentrations of ADP_m, ATP_m, ADP_c, ATP_c, $NADH_m$, & NAD^+_m are identical in both models. Moreover, the individual conservation relationships among these metabolites between the two models are identical as well.*

Although, both liver TCA cycle models appear to follow a similar course qualitatively, there is a distinct quantitative gap between their respective ratio profiles, as shown by their corresponding median values.

Across increasing $[Pyr_m]$, the $[NADH/NAD^+]_m$ ratio between the two models is noticeably different (see fig. 2.24c on pg. 70) in that, the original model appears to be more reduced (median = 0.6) than the updated model (median = 0.3). Whereas, across increasing maximal activity of PC (see fig. 2.22c on pg. 68) and across increasing $[Pi_m]$ (see fig. 2.23c on pg. 69), the median redox ratio values for the two models are relatively similar. The respective redox states between the two models are quantitatively similar even within a much narrower range of a given scanning parameter, where the given range includes its initial model value; with the exception of $[Pyr_m]$ scan.

The mitochondrial redox ratio reported for control rat livers varies from 0.01 (Siess et al., 1976, 1982b; Soboll et al., 1978; von Glutz and Walter, 1975; Williamson et al., 1969a,b) to 0.1 (Krebs and Veech, 1969; Stubbs et al., 1972; Veech et al., 1969; Williamson et al., 1967a), depending on the experimental conditions, diet, *etc.* In livers from rats that are starved for 48 hrs., the mitochondrial redox ratio is 0.2 (Krebs and Veech, 1969; Veech et al., 1969; Williamson et al., 1967a). In rats fed on a high-sucrose diet for 3–5 days, the ratio is 0.15–0.2 and in rats fed on low-carbohydrate diet for 3–5 days, it is 0.2–0.3 (Krebs and Veech, 1969; Veech et al., 1969). In ethanol treated rat livers the mitochondrial redox ratio is 0.4; whereas, in L-ethionine treated livers it is 0.15 (Stubbs et al., 1972). On the other hand, in isolated rat hepatocytes, depending on the experimental conditions, the mitochondrial redox ratio varies between 0.2 to 0.65, upon the direct estimation of mitochondrial NAD & NADH (Tischler et al., 1977). Therefore, it appears that within physiological range, the redox ratios for both models are in good agreement with the published data and that the two models differ only qualitatively, in terms of their respective $[NADH/NAD^+]_m$ profiles. The mitochondrial redox ratios are discussed further with respect to elasticity coefficients on pg. 108.

Across all 3 scanning parameters, the mitochondrial as well as cytosolic ATP/ADP ratios are distinctly different between the two models. Even within physiological range,

a qualitative difference between the two ATP/ADP ratio profiles is quite noticeable. Across V_{max}^{PC}, both the mitochondrial as well as cytosolic ATP/ADP ratio median values are significantly higher in the updated model (1.0 & 2.3, respectively), compared to the original model (0.6 & 0.2, respectively). On the other hand, across increasing $[Pi_m]$ as well as $[Pyr_m]$, both ratio medians are significantly lower in the updated model than the original.

Qualitatively, the ATP/ADP ratio can be seen as a preliminary indicator of system's *'energy-yielding readiness'* in energy demanding situations. Whether a high or a low ATP/ADP ratio is preferable, depends entirely on the given metabolic state of a cell. For example, from *in vitro* studies, we know that pyruvate dehydrogenase is inhibited by a high ATP/ADP ratio (Siess and Wieland, 1975); whereas, pyruvate carboxylase is activated by a high ATP/ADP ratio (Stucki et al., 1972; von Glutz and Walter, 1976). Therefore, pyruvate oxidation in the fed state would require an active PDH and low ATP/ADP ratios; whereas, gluconeogenesis in the starved state would require an activation of PC and an inactivation of PDH favoured by high ATP/ADP ratios (Soboll et al., 1978). Therefore, it appears that the ATP/ADP ratios in the updated liver TCA cycle model are in good agreement with this observation.

The ATP/ADP ratios in isolated mitochondria, under control conditions, vary between 0.4 (von Glutz and Walter, 1975) to 0.6 (Stucki and Walter, 1972). In rat liver *in situ*, the mitochondrial ATP/ADP ratio is 0.9 in fed rats and 1.0 in starved rats; whereas, the cytosolic ATP/ADP ratio is 6.9 in fed rats and 5.9 in starved rats (Schwenke et al., 1981). In perfused rat livers, the mitochondrial ATP/ADP ratio is 0.2 in fed rats and 0.7 in starved rats; whereas, the cytosolic ATP/ADP ratio is 10.3 in fed rats and 2.6 in starved rats (Soboll et al., 1978). In isolated hepatocytes, the mitochondrial ATP/ADP ratio is 2.3 in fed rats and 1.5 in starved rats; whereas, the cytosolic ATP/ADP ratio is between 5–12 in fed rats and 9.1 in starved rats (Akerboom et al., 1978; Siess and Wieland, 1976; Soboll et al., 1980). Within physiological range, the ATP/ADP ratios are well inside the reported range; except across increasing V_{max}^{PC}.

In conclusion, key metabolic ratios between the two models show significant qualitative differences. The significance of their quantitative differences, if any, is subjective to the available experimental data and therefore, as such, can not be properly assessed, at present.

Now, in the following sections, we shall discuss the control properties of the two models, in terms of the *flux control coefficients, concentration control coefficients, & elasticity coefficients*. Also, in these sections we shall revisit some of the special cases we have seen so far and discuss them with respect to the emergent control properties of the two liver TCA cycle models.

2.3.5 Metabolic Control Analysis (MCA) of the Liver TCA cycle models

In the introductory chapter, we discussed the theory of *"Metabolic Control Analysis (MCA)"*, at length. In this section, we'll see the results of such analysis, when applied to liver TCA cycle models by observing the distribution of flux control coefficient (C^J), concentration control coefficient (C^S) and elasticity coefficient (ε_S).

'Flux control coefficient scans', a method of obtaining the flux control coefficient data, is already explained in the global Methods chapter.

2.3.5.1 Flux control coefficient analysis for Liver TCA cycle models

In this section, we will first analyse the control of flux through citrate synthase (CS), using the flux control coefficients of all liver TCA cycle enzymes. Later, we'll also analyse the control of flux through other liver TCA cycle reactions, such as – independent reactions (*e.g.* IDHa) & other enzyme subset reactions (*e.g.* PC). Since, we have already established that the updated liver TCA cycle model is a qualitatively better version of the liver TCA cycle, going forward, we will only focus on the updated model. *Between two parameter datasets, if required, one of the qualitatively similar flux control coefficient plots are included in the supplementary material .*

As the enzyme activities or metabolite concentrations vary, their corresponding degree of control varies as well. Hence, we examined how the pattern of control changed as these parameters were varied over a fixed range. Figure 2.25 (see, pg. 74) and figs. I.10 and I.11 in supplementary material (see, pg. XVIII & pg. XIX) show the flux control coefficients calculated with respect to TCA cycle flux (flux through CS), for all enzymes in the liver TCA cycle model, across a fixed range of increasing maximal activities (ATPsynth, PDH, PC & MC) or metabolite concentrations ($\mathrm{Pi_m}$ & $\mathrm{Pyr_m}$). These C^J plots are presented alongside a corresponding steady-state plot of citrate synthase (CS) flux across the same fixed range of a given parameter (*here, CS is the reaction* 'J' *on which the flux control coefficient, 'C^J' is calculated*). In each plot, result of the *summation theorem* is also included using a dotted line. In these plots, the flux control coefficients are distributed between the range of -0.6 to 1.2 (unitless).

A plot of C^J against the enzyme maximal activity or concentration would normally be expected to be hyperbolic however, for ATPsynth (see, fig. 2.25a), PDH (see, fig. 2.25b), PC (see, fig. I.11a), and $\mathrm{Pi_m}$ (see, fig. I.10a), a complex pattern of C^J variation can be observed. For $\mathrm{Pyr_m}$ (see, fig. I.10b) and MC (see, fig. I.11b) however, the observed C^J pattern is comparatively more simpler. *The emergence of complex pattern of variation in flux control coefficients is discussed later, on pg. 80.*

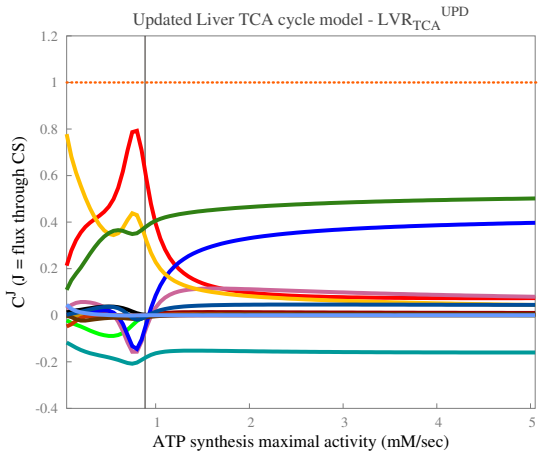

2.25.a. C^J, Updated model

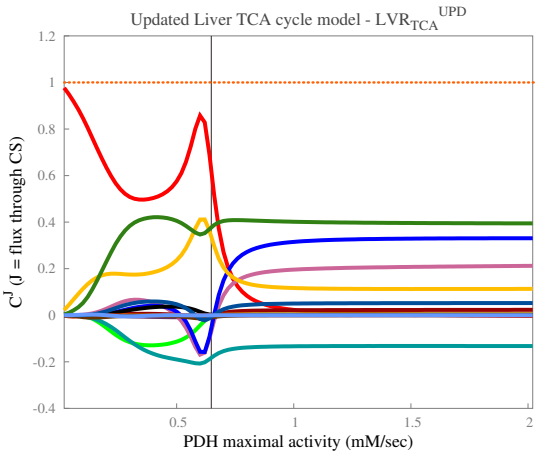

2.25.b. C^J, Updated model

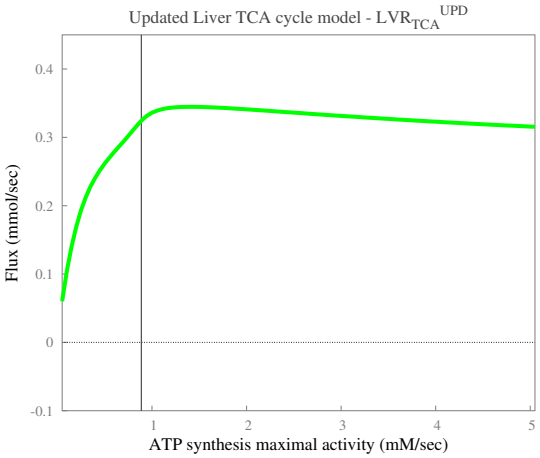

2.25.c. CS flux, Updated model

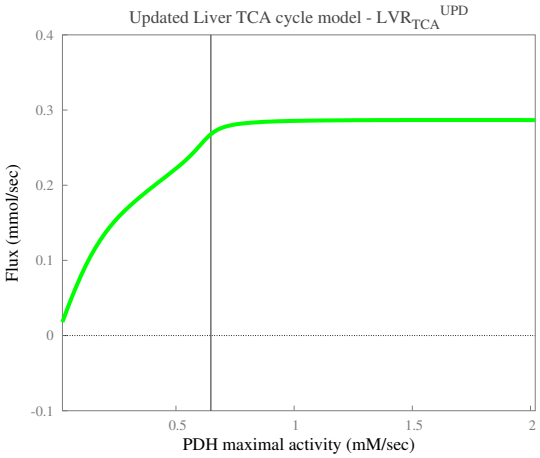

2.25.d. CS flux, Updated model

▪ **Figure 2.25. Control of TCA cycle flux in the updated liver TCA cycle model:** against the changing activities of ATPsynth & PDH.

▪ Key for figs. 2.25a and 2.25b is as follows :

PDH ;	CS ;	ACO ;	IDHa ;	α-KGDH ;	SCS;
SDH ;	FM ;	MDH ;	ATPsynth ;	ANT ;	ATPhyd;
PC ;	MC ;	IDHb ;	Total Sum (dotted line)		

▪ The vertical black line represents the initial model value. At this point, in figs. 2.25a and 2.25c, $V_{max}^{ATP_{synth}} = 0.886637$ mM/sec and in figs. 2.25b and 2.25d, $V_{max}^{PDH} = 0.648$ mM/sec, respectively.

▪ ***Orange dotted line*** shows the *Summation theorem* result across the entire range.

▪ ***Corresponding flux control coefficient plots for the original liver TCA cycle model are both qualitatively as well as quantitatively similar to the data shown above and therefore not included here.***

From fig. 2.25 and figs. I.10 and I.11 in supplementary material, it is evident that pyruvate dehydrogenase has a relatively greater control of the TCA cycle flux; however, the control is also distributed between PDH and two other enzymes: pyruvate carboxylase & ATP synthase. While the popular notion of a single *'rate limiting'* step in a pathway has been shown both theoretically as well as experimentally to be erroneous (Fell, 1997), the first enzyme in a linear pathway often does possess a higher degree of control of the pathway flux, with declining extent of control for the consecutive enzyme reactions along the rest of the pathway length. This can be explained on the basis of the relationship between individual flux control coefficients and the disequilibrium ratio (ρ) of each enzyme reaction (Kacser and Burns, 1973). The liver TCA cycle model represents a cyclical, branched metabolic system and the actual factors that affect the distribution of control in such a system are more complex than the theoretical linear pathway considered by Kacser and Burns, 1973. However, PDH & PC, two of the most controlling enzymes, are a set of connected reactions in the initial linear portion of the liver TCA cycle pathway, and therefore can be expected to exhibit a relatively higher degree of control, particularly in the absence of any feedback regulation (or *'closed' regulatory sequences*, see Crabtree and Newsholme, 1987) other than a direct product inhibition.

Based on the concepts – *'organisation of metabolic networks as functionally discrete supply & demand blocks' and 'supply-demand analysis'*, put forward by Hofmeyr and Cornish-Bowden (2000), we may say that ATP synthase forms a demand block within liver TCA cycle, whereas other reactions of the cycle represent the supply block and they are linked via a common intermediate, $NADH_m$, which is produced by the TCA cycle dehydrogenases and consumed by ATPsynth. Therefore, a comparatively high C^J of ATPsynth and minimal coefficients of enzymes within the cycle, for the control of TCA cycle flux, is in good agreement with the *'molecular economy'* –based view of Hofmeyr and Cornish-Bowden (2000). Although, PDH is in fact a part of the supply block, its position in the initial linear portion of the pathway automatically tends to allow a higher C^J than the successive reactions.

A small but notable negative flux control coefficient for IDHa indicates that an increase in the IDHa activity causes a modest decrease in the TCA cycle flux. This may initially seem counter-intuitive, but an increase in the IDHa activity increases the α-ketoglutarate concentration and thus its availability for the IDHb; which in turn increases the IDHb reverse flux, thereby counteracting and occasionally, even over-compensating for the greater IDHa activity. SDH is one of the four dehydrogenase reactions within liver TCA cycle and yet it shares a relatively high degree of control for the TCA cycle flux along with ATPsynth. Although, initially it may appear to contradict with our earlier view of the distribution of control, it can be explained as follows:

1. We know that in liver TCA cycle models, 'ESS #2' is broken into two halves by the presence of independent reactions on both ends. In these halves, α-KGDH, SCS, SDH form a linear portion; whereas, due to the reverse direction of MDH, FM, MC & MDH form a branched reaction sequence.

2. Within this linear reaction sequence, α-KGDH & SCS are – (a.) highly regulated and (b.) share their co-substrate/ co-product – CoA_m, with PDH & CS, two enzymes from the top/ upper-half of 'ESS #2'; thereby adding onto their existing level of complexity.

3. On the other hand, SDH is regulated by a direct product inhibition by Fum_m & QH_2 and an inhibition by OAA_m (competitive to Suc_m).

Therefore, a high C^J for SDH does not seem to be counter-intuitive after all. Moreover, in situations where MDH acts in its respective forward direction, SDH is likely to exhibit a minimal coefficient value.

Also, C^J for SDH is transiently negative just *before* the respective initial model value of a given scanning parameter, as well as it mirrors the complex pattern of variation in C^J for PDH. This pattern is also shared to some degree by ATPsynth, and mirrored by other enzymes as well, most notably α-KGDH and IDHa. A transiently negative C^J for SDH translates to a transient & modest decrease in the TCA cycle flux, effectively reducing the efflux of TCA cycle carbon via MC. This view is further supported by fig. I.11b (see, pg. XIX), which shows that at activities higher than the initial model value of V_{max}^{MC} (23.3 mM/sec), the system attempts to restrict the efflux of TCA cycle carbon by limiting the TCA cycle flux through a negative C^J for SDH. Interestingly, the negative coefficient of SDH never exceeds the negative value of C^J for IDHa, thereby limiting its reductive effect on the TCA cycle flux within the upper (negative) bound set by the transiently negative C^J for IDHa. α-KGDH, despite being highly regulated, shares a small but notable flux control coefficient with SDH and follows the SDH coefficient pattern throughout the given parameter range. Therefore, in the liver TCA cycle model, the transiently negative flux control coefficients for enzymes within the cycle, such as – IDHa, α-KGDH, & SDH, together can be considered as a mechanism to limit the extent TCA cycle carbon efflux, under demanding situations.

Here, we have been able to reproduce, both qualitatively as well as quantitatively, the same distribution pattern of flux control coefficients for the liver TCA cycle model that was originally developed within our group using COPASI (see, `http://www.copasi.org/`). These original results are a part of the *unpublished manuscript* (Brightman et al., 2010). In particular, the complex distribution pattern of C^J against the PDH maximal activity (see fig. 2.25b on pg. 74), matches exactly with that shown in Brightman et al., *see figure 3A*.

Figure 2.25 showed the distribution of control for the overall TCA cycle flux (flux through CS) or the flux through 'ESS #2'. Now, let us investigate the distribution of control for the flux through other enzyme subsets and independent reactions in the updated liver TCA cycle model. Figure 2.26 (see, pg. 77) shows the distribution of control for the flux through IDHa and PC ('ESS #1'), against the change in PDH maximal activity. Figure 2.27 (see, pg. 78) shows the distribution of control for the flux through MDH and ANT ('ESS #3'), against the change in PDH maximal activity.

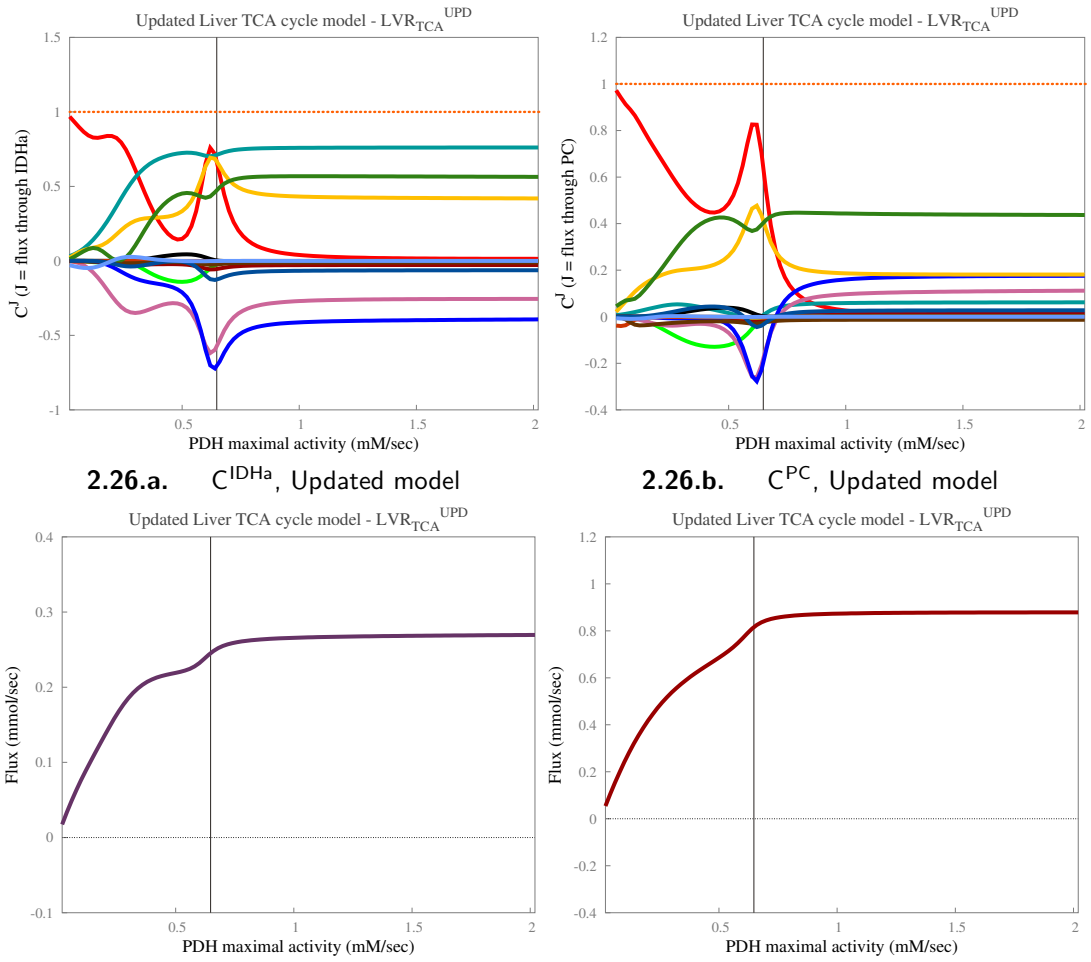

2.26.a. C^{IDHa}, Updated model **2.26.b.** C^{PC}, Updated model

2.26.c. IDHa flux, Updated model **2.26.d.** PC flux, Updated model

- **Figure 2.26. Control of flux through IDHa & PC in the updated liver TCA cycle model:** against the PDH maximal activity.

- Key for figs. 2.26a and 2.26b is as follows :

PDH ;	CS ;	ACO ;	IDHa ;	α-KGDH ;	SCS;
SDH ;	FM ;	MDH ;	ATPsynth ;	ANT ;	ATPhyd;
PC ;	MC ;	IDHb ;	Total Sum (dotted line)		

- The vertical black line represents the initial model value. At this point, in figs. 2.26a to 2.26d, $V_{max}^{PDH} = 0.648$ mM/sec.
- ***Orange dotted line*** shows the *Summation theorem* result across the entire range.
- ***Corresponding flux control coefficient plots for the original liver TCA cycle model are both qualitatively as well as quantitatively similar to the data shown above and therefore not included here.***

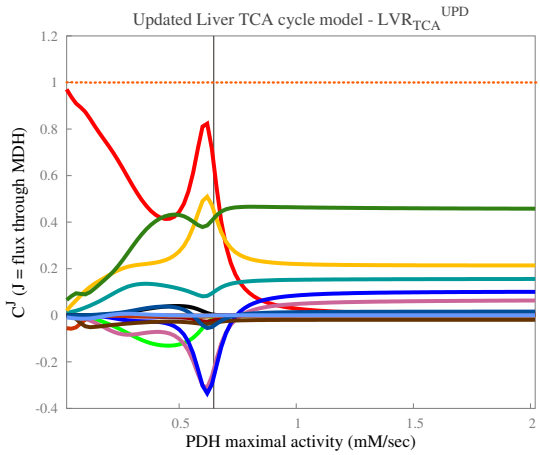

2.27.a. C^{MDH}, Updated model

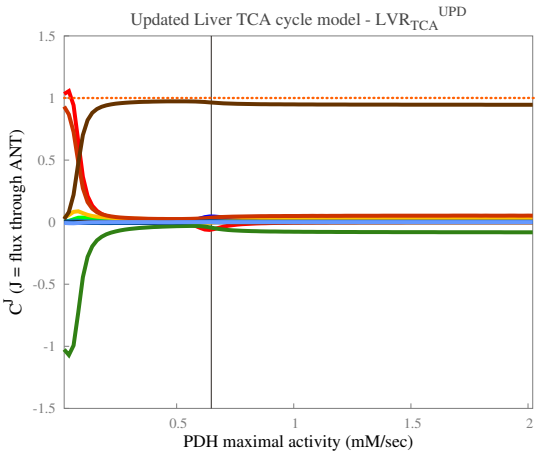

2.27.b. C^{ANT}, Updated model

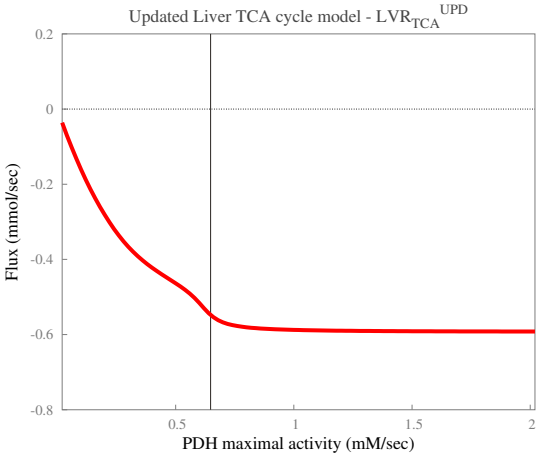

2.27.c. MDH flux, Updated model

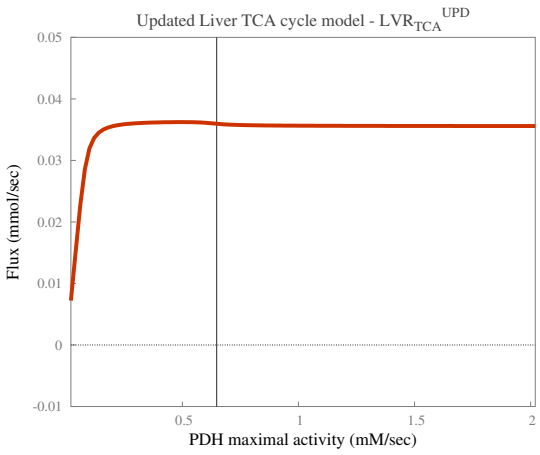

2.27.d. ANT flux, Updated model

▪ **Figure 2.27. Control of flux through MDH & ANT in the updated liver TCA cycle model:** Distribution of flux control coefficients calculated for the flux through MDH & ANT, against the PDH maximal activity.

▪ Key and other conditions are as shown in fig. 2.26 on pg. 77.

Figures 2.26 and 2.27 (see, pgs. 77 and 78) show a complex pattern of control distribution for the flux through IDHa, PC & MDH, similar to that shown in fig. 2.25 (see, pg. 74), for the control of TCA cycle flux. On the other hand, control distribution for the flux through ANT (see, fig. 2.27b) is distinctly simple and shows signs of sigmoidal C^J transition curves.

From figs. 2.26 and 2.27 it is evident that at lower PDH activities, PDH has a relatively greater control of flux; whereas, at higher activities, the control is rapidly exchanged and distributed between PDH and other TCA cycle enzymes, similar to that observed in fig. 2.25. However, for the control of IDHa flux (see, fig. 2.26a), the control is more widely distributed between PDH and other TCA cycle enzymes and the exchange phase is notably different than that observed in other cases.

In fig. 2.26a, the control of IDHa flux is evenly distributed between PDH, ATPsynth, IDHa, PC, α-KGDH, & SDH throughout the given range of PDH maximal activity, except at very low activity values. In this case, IDHa has a majority of the control of its own flux and C^J for IDHa is positive throughout the given range, unlike in fig. 2.25, where it is negative. Also in this case, the respective coefficients for α-KGDH & SDH remain negative throughout the given range, whereas in fig. 2.25 they are positive for the most part and become transiently negative near the initial model value of PDH maximal activity. Therefore, for the control of IDHa flux, IDHa, PC, ATPsynth, & PDH are the most-controlling enzymes that would increase the flux through IDHa as their individual activities are increased; whereas, α-KGDH & SDH would decrease its flux moderately with any increase in their individual activities.

The C^J distribution patterns for the flux through PC (see, fig. 2.26b) & MDH (see, fig. 2.27a) are almost identical to each other and closely resemble the control distribution pattern for the TCA cycle flux (see, fig. 2.25). In both cases, PDH has most of the control, before it is rapidly exchanged and distributed between PC, ATPsynth, SDH, IDHa, & α-KGDH. C^J for IDHa is distinctly positive in both these cases, whereas it is distinctly negative for the control of TCA cycle flux; which means that while an increase in the IDHa activity causes a moderate decrease in the TCA cycle flux, it would also increase the MDH & PC fluxes moderately.

Figure 2.27b shows the control distribution pattern for the flux through ANT and it stands out due to its distinctively simple C^J transition curves. The rapid exchange of control between two enzymes seems to be a central feature of the control distribution in liver TCA cycle models, as it exists even in this comparatively uncomplicated pattern of control distribution. In this case, the flux through ANT is controlled mostly by ATPhyd and to a small extent by PC, after a rapid exchange of control with PDH & SCS. Therefore, for PDH maximal activity values between 0.3 to 2.0 mM/sec, an increase in the ATPhyd activity will increase the flux through ANT; whereas, any increase in the PC activity will marginally decrease the ANT flux. ANT carries out a 1:1 exchange of mitochondrial ATP and cytosolic ADP. ATPhyd in the cytosol and pyruvate carboxylase in the mitochondria both compete for the mitochondrial ATP. Therefore, the control distribution for ANT flux suggests that ATPhyd ensures an efficient ANT mediated transfer of mitochondrial ATP to cytosol, by gaining maximal control of the ANT flux; whereas, a small negative C^J for PC reduces the ANT flux fractionally with any increase in the PC activity, in order to maintain a sufficient supply of mitochondrial ATP that is required for the carboxylation of pyruvate.

Therefore, figs. 2.26 and 2.27 show that in the updated liver TCA cycle model, reactions that were classified as structurally distinct, are also discrete in terms of their kinetic control properties. This observation provides further support to the *'unspanning'* of TCA cycle, as seen earlier in pg. 59 and suggested by Randle et al., 1970.

2.3.5.2 The complex pattern of variation in flux control coefficients of Liver TCA cycle models: Impact of enzyme kinetics

A plot of C^J against the enzyme maximal activity or concentration is expected to be hyperbolic; instead, in fig. 2.25, fig. I.10 & fig. I.11, the emerging pattern of variation in C^J is mostly *'multiphasic'*.

In literature, there are known examples of *'biphasic'* C^J curves. For example, in rat liver mitochondria, for the control of oxidative phosphorylation and respiration (Brand et al., 1993; Brown, 1992; Fell, 1997; Groen et al., 1982b; Hafner et al., 1990; Korzeniewski and Mazat, 1996a); also, for control of glycolysis in *T. brucei* (Bakker et al., 1999), & *S. cerevisiae* (Pritchard and Kell, 2002). Whereas, specific examples of *'multiphasic'* C^J curves are rare (Chassagnole et al., 2001a; Giersch, 1995a; Liguzinski and Korzeniewski, 2006) [*]. It could be due to the fact that in most studies, a single C^J value per enzyme is computed; which corresponds to either a unique physiological state (Fritzen et al., 2007; Giersch, 1995b; Kashiwaya et al., 1994; Moreno-Sánchez et al., 2008; Torres et al., 1986, 1989) or a unique steady-state solution of a mathematical model (Albe and Wright, 1992; Cortassa et al., 2003, 2009; Dzbek and Korzeniewski, 2007, 2008; Korzeniewski and Froncisz, 1991; Moreno-Sánchez et al., 2008; Rohwer and Botha, 2001).

As a representative case of the complex pattern, let's focus on fig. 2.25b (see, pg. 74), which shows the variation in C^J against PDH activity. Although these patterns are not easy to interpret, it is clear that within a very narrow range of activities around the initial model value (0.65 mM/sec), the distribution of control shifts abruptly between PDH and the other enzymes. Thus, C^J for PDH varies from almost unity to approaching zero, between 0.6 to 1.0 mM/sec, *i.e.* with a less than 25% change in PDH activity. The initial model value of PDH V_{max} (0.65 mM/sec; Fahien and Teller, 1992 [†]) is assumed to represent the PDH active fraction under physiological conditions, which has been reported to be between 50% and 100% in perfused rat heart (Dennis et al., 1979; Olson et al., 1978; Reed et al., 1972). Therefore, it suggests that the abrupt shift in the distribution of C^J across a fixed range of PDH activity, apparently occurs within the physiological range of PDH activation. However, fig. 2.25d (see, pg. 74) shows that large increases in PDH activity, particularly between 0.6 to 1.0 mM/sec and beyond, cause only a minimal net increase in the TCA cycle flux (flux through CS).

Figure 2.25, fig. I.10 & fig. I.11 show that the model is poised in such a way that control over the TCA cycle flux is distributed largely between PDH, PC & ATPsynth; wherein the system is maximally responsive to the activity changes in each of these

[*] In Giersch 1995a, the C^J curves are against simulated time and comparatively simpler and in Chassagnole et al. 2001a, the C^J curves are across successive steady-states and comparatively simpler.

[†] Calculated from the reported mitochondrial concentration and specific activity, taking into account the number of active sites within the holoenzyme.

key enzymes with minimal influence of the liver TCA cycle reactions (with the notable exceptions of SDH, IDHa & α-KGDH). Therefore, we investigated the effect of changing respective initial model values of PDH, PC & ATPsynth V_{max}'s, on the complex pattern of C^J distribution against enzyme maximal activities. Figures 2.28 to 2.30 (see, pgs. 81 to 83) show this effect on C^J for PDH, against a fixed range of PDH & ATPsynth activities.

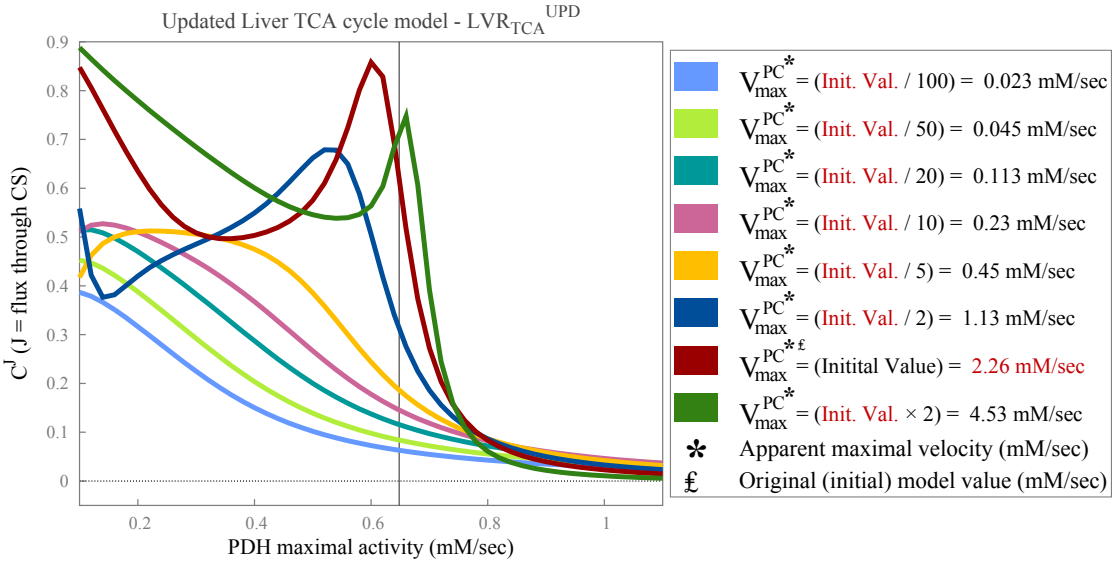

2.28.a. C^J for PDH at different maximal activities of PC

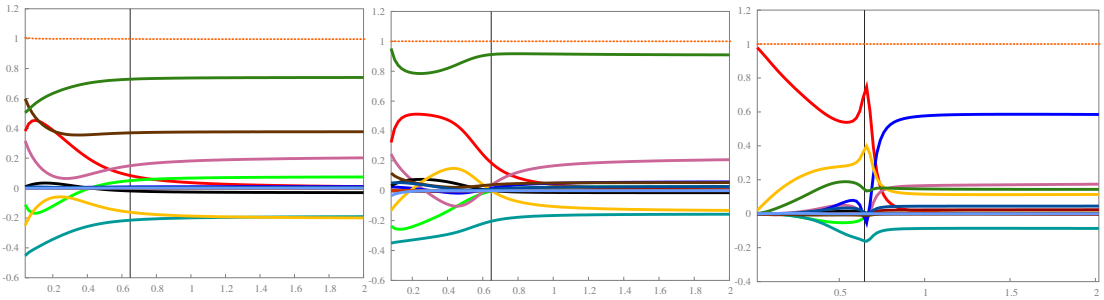

2.28.b. at PC V_{max} = 0.045 mM/sec **2.28.c.** at PC V_{max} = 0.45 mM/sec **2.28.d.** at PC V_{max} = 4.53 mM/sec

▪ **Figure 2.28. Effect of different PC activities on the flux control coefficient of PDH:** plotted against a fixed range of PDH maximal activity.

▪ Key for figs. 2.28b to 2.28d (only for enzymes with most control; for the rest, refer to: pg. 74) :

PDH ; CS ; IDHa ; α-KGDH ; SDH ; PC ; ATPsynth ; ATPhyd

▪ Figure 2.28a is a result of 8 simulations at different PC activities. Figures 2.28b to 2.28d describe the complete flux control distribution at specific values of PC activities used in fig. 2.28a.

- Figure 2.28b includes C^J for PDH shown in fig. 2.28a using at V_{max}^{PC} = 0.045 mM/sec
- Figure 2.28c includes C^J for PDH shown in fig. 2.28a using at V_{max}^{PC} = 0.45 mM/sec
- Figure 2.28d includes C^J for PDH shown in fig. 2.28a using at V_{max}^{PC} = 4.53 mM/sec

▪ *X & Y-axes* for figs. 2.28b to 2.28d : Range of PDH maximal activity: 0.0 – 2.0 mM/sec and flux control coefficient for the flux through CS (C^{CS}) (unitless), respectively.

▪ The vertical black line represents the initial model value. At this point, in figs. 2.28b to 2.28d, V_{max}^{PDH} = 0.648 mM/sec.

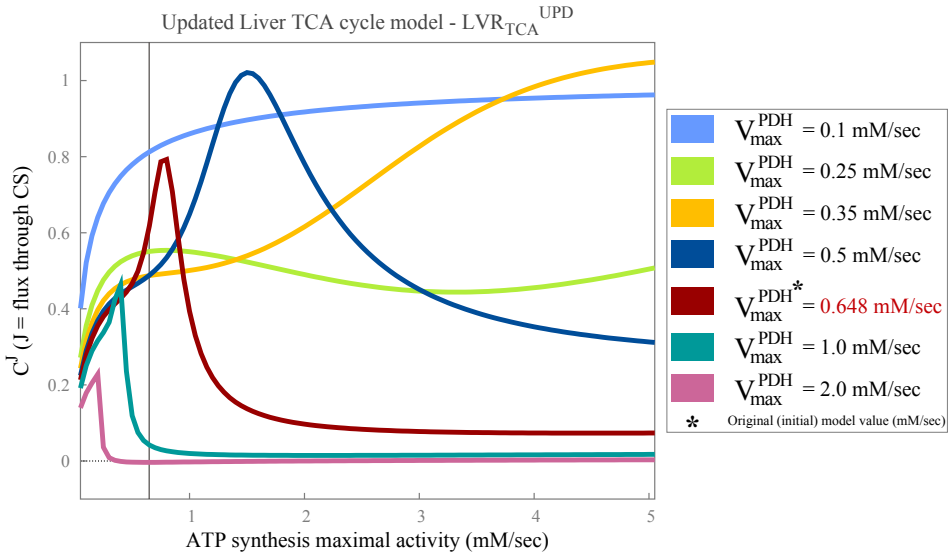

2.29.a. C^J for PDH at different maximal activities of PDH

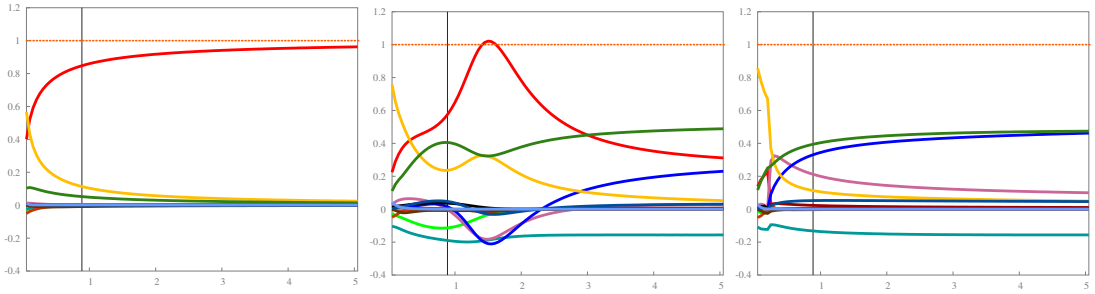

2.29.b. at PDH V_{max} = 0.1 mM/sec

2.29.c. at PDH V_{max} = 0.5 mM/sec

2.29.d. at PDH V_{max} = 2.0 mM/sec

▪ **Figure 2.29. Effect of different PDH activities on the flux control coefficient of PDH:** plotted against a fixed range of ATPsynth maximal activity.

▪ Key for figs. 2.29b to 2.29d (only for enzymes with most control; for the rest, refer to: pg. 74) :

PDH ; CS ; IDHa ; α-KGDH ; SDH ; PC ; ATPsynth ; ATPhyd

▪ Figure 2.29a is a result of 7 simulations at different PDH activities. Figures 2.29b to 2.29d describe the complete flux control distribution at specific activities of PDH used in fig. 2.29a.

- Figure 2.29b includes C^J for PDH shown in fig. 2.29a using at V_{max}^{PDH} = 0.1 mM/sec
- Figure 2.29c includes C^J for PDH shown in fig. 2.29a using at V_{max}^{PDH} = 0.5 mM/sec
- Figure 2.29d includes C^J for PDH shown in fig. 2.29a using at V_{max}^{PDH} = 2.0 mM/sec

▪ *X & Y-axes* for figs. 2.29b to 2.29d : Range of ATPsynth maximal activity: 0.0 – 5.0 mM/sec and flux control coefficient for the flux through CS (C^{CS}) (unitless), respectively.

▪ The vertical black line represents the initial model value. At this point, in figs. 2.29b to 2.29d, $V_{max}^{ATP_{synth}}$ = 0.886637 mM/sec.

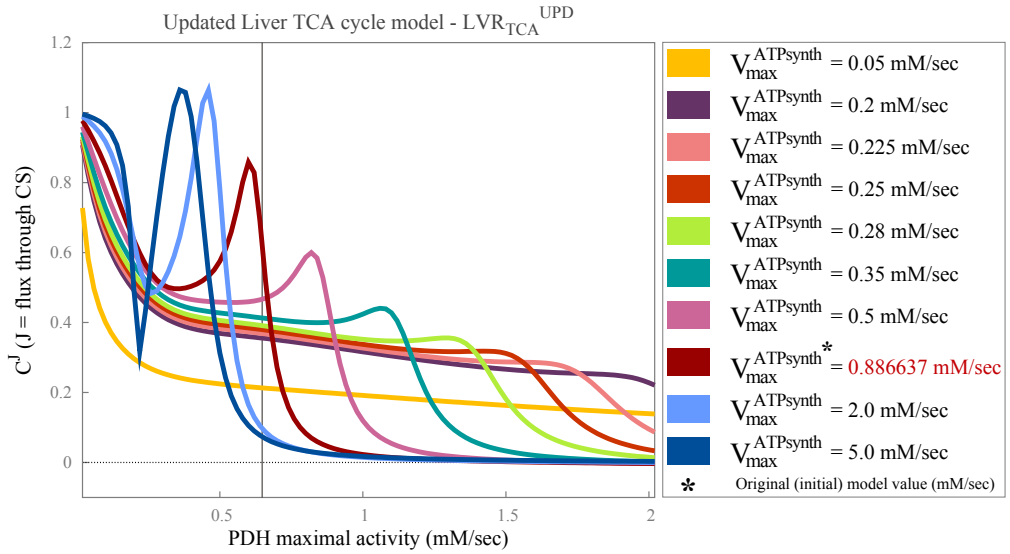

2.30.a. C^J for PDH at different maximal activities of ATPsynth

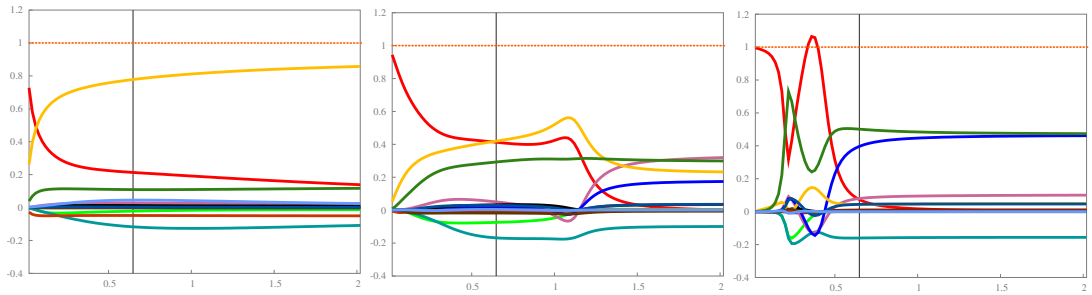

2.30.b. at ATPsynth V_{max} = 0.05 mM/sec

2.30.c. at ATPsynth V_{max} = 0.35 mM/sec

2.30.d. at ATPsynth V_{max} = 5.0 mM/sec

▪ **Figure 2.30. Effect of different ATPsynth activities on the flux control coefficient of PDH:** plotted against a fixed range of PDH maximal activity.

▪ Key for figs. 2.30b to 2.30d (only for enzymes with most control; for the rest, refer to: pg. 74) :

PDH ; CS ; IDHa ; α-KGDH ; SDH ; PC ; ATPsynth ; ATPhyd

▪ Figure 2.30a is a result of 10 simulations at different ATPsynth activities. Figures 2.30b to 2.30d describe the complete flux control distribution at specific activities of ATPsynth used in fig. 2.30a.

- Figure 2.30b includes C^J for PDH shown in fig. 2.30a using at $V_{max}^{ATP_{synth}}$ = 0.05 mM/sec
- Figure 2.30c includes C^J for PDH shown in fig. 2.30a using at $V_{max}^{ATP_{synth}}$ = 0.35 mM/sec
- Figure 2.30d includes C^J for PDH shown in fig. 2.30a using at $V_{max}^{ATP_{synth}}$ = 5.0 mM/sec

▪ *X & Y-axes* for figs. 2.30b to 2.30d : Range of PDH maximal activity: 0.0 – 2.0 mM/sec and flux control coefficient for the flux through CS (C^{CS}) (unitless), respectively.

▪ The vertical black line represents the initial model value. At this point, in figs. 2.30b to 2.30d, V_{max}^{PDH} = 0.648 mM/sec.

Figures 2.28 to 2.30 (see, pgs. 81 to 83) and observations made earlier on pg. 80 concerning the PDH maximal activity, indicate the importance of choosing physiologically relevant values for key model parameters such as enzyme activities. Figures 2.28a, 2.29a and 2.30a show that the complex pattern of C^J distribution observed earlier can become nearly hyperbolic, but only at significantly lower values of enzyme activities than those used in the model. For example, the C^J curve can become **nearly** hyperbolic when — (a.) V_{max}^{PC} is at least 10 times lower (0.23 mM/sec) than its initial model value (2.26 mM/sec; see fig. 2.28a) or (b.) V_{max}^{PDH} is at least 6 times lower (0.1 mM/sec) than its

initial model value (0.65 mM/sec; see fig. 2.29a) or (c.) $V_{max}^{ATP_{synth}}$ is at least 4 times lower (0.225 mM/sec) than its initial model value (0.9 mM/sec; see fig. 2.30a). More importantly, these figures show that the rapid transfer of control between PDH and other TCA cycle enzymes changes with change in the initial model values of enzyme activity parameters. For example, at very low $V_{max}^{ATP_{synth}}$ values (0.05 mM/sec; see fig. 2.30b), the rapid exchange of control is between PDH & ATPsynth; at 0.35 mM/sec, the exchange is between PDH & SDH plus α-KGDH (see, fig. 2.30c); and at 5.0 mM/sec, the exchange is between PDH & PC, SDH, plus α-KGDH (see, fig. 2.30d). These figures also show that the slope of C^J transition curve increases with an increase in the initial model value and *vice versa*. For example, in fig. 2.28a, as V_{max}^{PC} is increased from 1.13 to 4.53 mM/sec or in fig. 2.30a as the $V_{max}^{ATP_{synth}}$ is increased from 0.25 to 5.0 mM/sec, the steepness (slope) of the C^J curve for PDH increases.

In the case PC activity, the lower value at which the C^J curve is nearly hyperbolic (0.23 mM/sec), is at least 400% lower than the basal PC activity (1.02 mM/sec) reported in literature; which is shown to be *approx.* 20% of activity for maximally activated enzyme (Ashman et al., 1972; Fahien and Teller, 1992; Scrutton, 1974; Scrutton and White, 1972). Incidentally, fig. 2.28a includes C^J curves near to the reported values of both basal (1.02 mM/sec; shown in ■) as well as maximal activities (5.1 mM/sec; shown in ■ ; Fahien and Teller, 1992) and shows that the complex C^J pattern exists even at the physiologically relevant PC activities. For PDH activity, the lower value at which the C^J curve is nearly hyperbolic (0.1 mM/sec), is in fact within close range of the reported PDH activity in rat heart mitochondria (Kerbey et al., 1976; Kohn et al., 1979b). Therefore, at this level of PDH activity, though the observed C^J curve is hyperbolic (see, figs. 2.29a and 2.29b), the resulting flux control distribution does not correctly represent the normal physiological state of the mammalian liver-specific TCA cycle.

For ATPsynth activity, the initial model value used in the model (0.9 mM/sec), is a fitted estimate of the ATP synthase rate constant. The unidirectional rate constant (k_{fwd}) of ATP synthase (rate of Pi → ATP incorporation) calculated by ^{31}P NMR saturation-transfer measurements under varying cardiac performance conditions using Langendorff-perfused rat hearts, is seen to vary from 0.2 to 0.8 mM/sec between the data presented in Bittl and Ingwall (1985); Kingsley-Hickman et al. (1986); Spencer et al. (1988) *. Although Kingsley-Hickman et al. report this rate constant to be twice as large than the actual net rate of ATP synthase in intact rat hearts, this range gives us a good enough approximation of k_{fwd} for ATPsynth. Also, in pig hearts, k_{fwd} for ATPsynth varies between a much wider range, from 0.04 to 1.2 mM/sec (originally reported in sec^{-1}; Zweier and Jacobus, 1987). Thus, our fitted estimate for the initial model value of

*In these reports, the unidirectional rate constants (k_{fwd}) of ATP synthase are originally shown in units: sec^{-1}. The values shown here are a product of the rate constant and the concentration of F_1F_0-ATPase, in mM. Concentration of F_1F_0-ATPase was taken from Cortassa et al. (2003), originally reported by Magnus (1995); Magnus and Keizer (1997). Here, a median value of the reported range is used for these calculations.

$V_{max}^{ATP_{synth}}$ (0.9 mM/sec) appears to be within close range of the reported physiological values. For ATPsynth activity, although the lower value at which the C^J curve is nearly hyperbolic is within the reported range of k_{fwd} for ATPsynth, it is very close to the lower limit of the range (0.225 mM/sec; shown in).

However, the steady-state data at such lower values of ATPsynth activity, shows that the previously observed dynamic behaviour of this model is significantly altered at this rate of ATP synthase (data not shown). For instance, at this lower rate of ATPsynth activity, the *'redox state'* ($NADH/NAD^+$) of this model shifts from *oxidised* ($\approx 0.6 - 0.7$) to *reduced* ($\approx 4.0 - 5.0$) and its *'energy state'* (mitochondrial ATP/ADP) shifts from being 'ATP-rich' ($\approx 2.0 - 3.0$) to 'ADP-rich' ($\approx 0.7 - 0.8$). These observations confirm that although less complex, the C^J distribution at such lower values of ATPsynth activity, describes a metabolic state which is dynamically distinct from the normal physiological state of the mammalian liver-specific TCA cycle.

In liver TCA cycle models, two of the most controlling enzymes, PDH & PC, share pyruvate as a common primary substrate and acetyl-CoA as a common allosteric effector. From Methods (see pg. 223 in Appendix B), we know that pyruvate dehydrogenase is competitively inhibited by acetyl-CoA with respect to CoA_m (Bremer, 1969); whereas, for pyruvate carboxylase, acetyl-CoA is an effective allosteric activator (Scrutton and Utter, 1967; see pg. 221 in Appendix B). Therefore, in liver TCA cycle models, if the mitochondrial AcCoA/CoA ratio is increased, it would inhibit PDH and lower its flux and activate PC, thereby increasing the flux through it. It would be interesting to find out if the acetyl-CoA -induced activation of pyruvate carboxylase affects the distribution of flux control and whether it is significant enough to change the presently observed pattern of distribution.

In the liver TCA cycle model, the apparent maximal activity of PC (V_{app}^{PC}) is modelled as a function of acetyl-CoA & Mg^{2+} concentrations, which is evaluated dynamically through a separate algebraic expression (see pg. 222 in Appendix B) and substituted into the rate equation during model simulation. For further details regarding the PC rate equation, please refer to pg. 221 in Appendix B. Therefore, given the model definition of V_{app}^{PC} and the significantly changing $AcCoA_m$ concentration (as shown in, figs. 2.13 to 2.15 on pgs. 50 to 52, respectively), it is probable that the *'variable'* V_{app}^{PC} value causes the PC flux to change and thereby affects the distribution of flux control in liver TCA cycle models to some degree. However, before analysing the flux control data any further, we must determine the possible extent of V_{app}^{PC} variability in the liver TCA cycle model, as key enzyme activities/ metabolite concentrations are varied. Therefore, the limits of V_{app}^{PC} variability in the liver TCA cycle model was evaluated using a specifically-modified *Python* function, described earlier in Methods (see Appendix D on pg. 237 and Listing D.1 on pg. 238). Figure 2.31 shows the limits of V_{app}^{PC} variability in the liver TCA cycle model, in response to changes in key enzyme activities/ metabolite concentrations.

Figure 2.31 also includes the V_{app}^{PC} value for a control condition, where it was computed using a model containing all CoA−related metabolites as *external metabolites*. A (negative) control value of V_{app}^{PC}, constant at 2.26 mM/sec (shown using ∗, in Red) provides a baseline variation against which the liver TCA cycle model data can be compared. Please refer to Methods for further details of this control condition model (see, pg. 29).

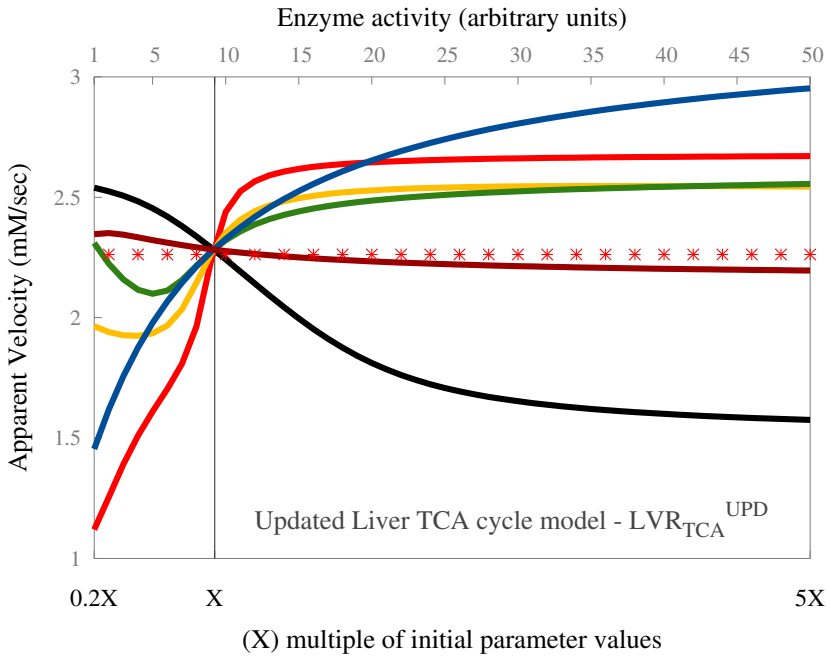

▪ **Figure 2.31. Dynamic nature of PC apparent maximal activity (V_{app}^{PC}):** against a fixed range of change in the key enzyme activities or metabolite concentrations.

▪ Key for variation in V_{app}^{PC} value against a change in maximal activity or concentration of :

PC ; MDH ; PDH ; ATPsynth ; Pi_m ; Mg^{2+} ; Pyr_m

▪ The plot shown above is a combined result of 7 different simulations, one for each enzyme activity or metabolite concentration selected.

▪ Each plot line, shown in different colours, represents the variation in V_{app}^{PC} value against a change in maximal activities of key TCA cycle enzymes or metabolite concentrations. *e.g.* line shown in Red represents variation against PDH maximal activity.

▪ **Line plotted using ∗, in Red:** represents the V_{app}^{PC} value under control conditions, computed by defining all CoA−related metabolites in the model as *'external'*. Also, this value was computed by varying the PDH maximal activity and since in this control model, all CoA−related metabolites are external, the computed value remains constant (at 2.26 mM/sec; ∗; in red); unlike the variation seen in the existing model (solid line in red), where all CoA−related metabolites are internal.

▪ The vertical black line represents the position of the respective initial model values for every selected parameter on the combined X-axis. At this point,

▪ V_{max}^{PC} = 2.26234 mM/sec (apparent velocity) ▪ V_{max}^{MDH} = 26.752 mM/sec ▪ V_{max}^{PDH} = 0.648 mM/sec

▪ $V_{max}^{ATP_{synth}}$ = 0.886637 mM/sec ▪ Pi_m, Mg^{2+} & Pyr_m conc. = 8.9, 0.37 & 0.2 mM, respectively.

▪ *In the plot shown above, though all lines appear to pass through a common point, it is simply an artefact introduced by the respective scales chosen for both axes. When the same data is observed at a higher scale, the artefact disappears to show that none of these lines pass through a common point.*

Overall, fig. 2.31 shows that in the liver TCA cycle model, the V_{app}^{PC} value can vary between 1.0 to 3.0 mM/sec, when the initial conditions are perturbed either by changing enzyme activities or metabolite concentrations. It also means that in the liver TCA cycle model, the pyruvate carboxylase flux is likely to vary similarly under these conditions, as shown in figs. 2.17 and 2.20 & also in fig. I.4 and fig. I.8 in supplementary material (see pgs. 56 and 64 & pg. XII and pg. XVI, respectively). This unique dynamic characteristic of the PC kinetics could act as one of the factors responsible for the complex nature of flux control distribution in liver TCA cycle models. Therefore, examining a direct causality between V_{app}^{PC} and the emergent complexity of flux control distributions in the updated model is essential and can be achieved by modifying the existing model definition of V_{app}^{PC} from a *'variable'* to a *'constant'*. Thus, in yet another variation of the existing updated model, the separate V_{app}^{PC} algebraic expression (see eq. B.3 on pg. 222) was replaced by a *parameter* with a value of 2.26 mM/sec and the corresponding flux control coefficients were computed using this variant model — *"PC knock-down"* model (PC_{kd}). Please refer to Methods for further details of the PC_{kd} model (see, pg. 29).

Figure 2.32 (see, pg. 88) shows the distribution of flux control coefficients in the PC_{kd} model, against the change in maximal activities of ATPsynth & PDH, respectively. Figures 2.32a and 2.32b are comparable to figs. 2.25a and 2.25b (see, pg. 74) respectively, that are computed using the updated liver TCA cycle model; wherein, V_{app}^{PC} is a variable.

Figure 2.32 shows that a deviation from the *dynamic* definition of V_{app}^{PC} to a *constant* value does significantly affect the earlier seen pattern of C^J distribution in the updated liver TCA cycle model. It is evident that the complex pattern of C^J distribution seen in fig. 2.25 becomes relatively less complex in fig. 2.32. And yet the C^J transition curves shown in fig. 2.32 are not exactly hyperbolic; which suggests that the *dynamic* definition of V_{app}^{PC} is only partially responsible for the emergence of such complex C^J distribution patterns in liver TCA cycle models.

In PC_{kd}, a constant value of V_{app}^{PC} also affects the TCA cycle flux and the sharing of control between key enzymes, quantitatively. Against the change in PDH activity, the PC_{kd} TCA cycle flux is increased by nearly 2–folds (see, fig. 2.32d), compared to that in the updated model (see, fig. 2.25d; *please note the different Y-axis scales between the two plots*). Also, in the PC_{kd} model, the sharing of control between key enzymes is comparatively more in favour of pyruvate carboxylase (see, figs. 2.32a and 2.32b) than that in the updated model (see, figs. 2.25a and 2.25b).

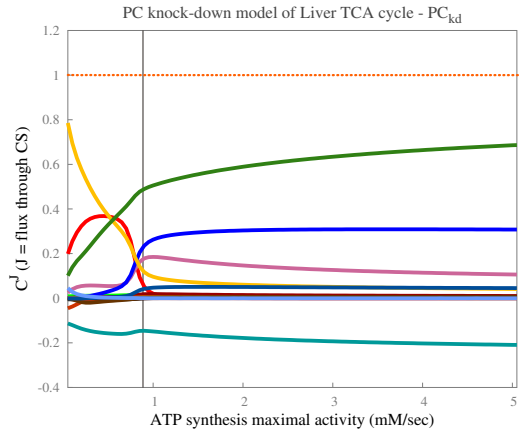

2.32.a. C^J, PC_{kd} model

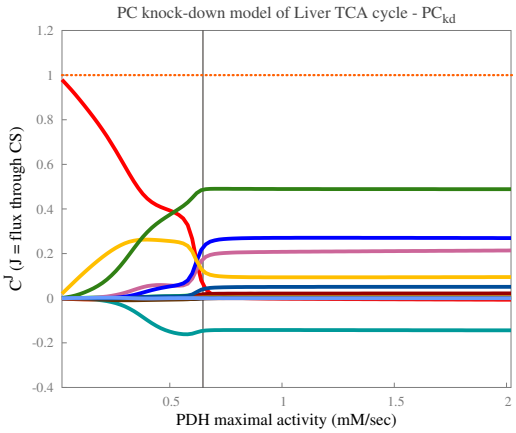

2.32.b. C^J, PC_{kd} model

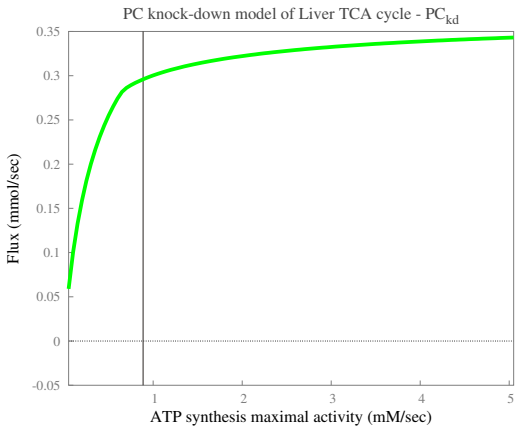

2.32.c. CS flux, PC_{kd} model

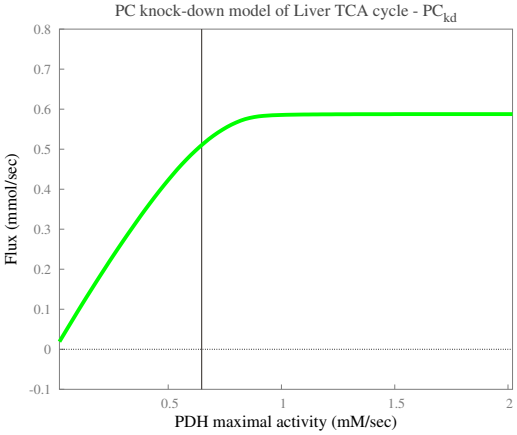

2.32.d. CS flux, PC_{kd} model

- **Figure 2.32. Control of TCA cycle flux in the PC_{kd} model:** Distribution of flux control coefficients, against the ATPsynth & PDH activities, respectively.
- Key for figs. 2.32a and 2.32b is as follows :

PDH ;	CS ;	ACO ;	IDHa ;	α-KGDH ;	SCS;
SDH ;	FM ;	MDH ;	ATPsynth ;	ANT ;	ATPhyd;
PC ;	MC ;	IDHb ;	Total Sum (dotted line)		

- ***In the PC_{kd} model, V_{app}^{PC} is a constant, at 2.26 mM/sec.***
- Other conditions as shown in fig. 2.25 on pg. 74.

2.3.5.3 The complex pattern of variation in flux control coefficients of Liver TCA cycle models: Insights from structural properties

As seen earlier, the updated liver TCA cycle model exhibits branching of the TCA cycle at various junctions. In such a systems, it is often difficult to separate between the effects caused by the kinetic or thermodynamic characteristics and those that are influenced by the structural features of the system. The evolution of complex flux control distribution patterns in the updated liver TCA cycle model is one such phenomenon. The evidence presented so far, suggests that the dynamic properties of this model do not fully explain the emergence of these complex patterns and therefore can not be deemed conclusive, unless the possible effects of the structural properties are ruled out.

Therefore, to eliminate possible effects due to the structural properties of the model, the control distribution patterns were studied using a reduced version of the model, as described in Methods (see, pg. 30). This reduced liver TCA cycle model contains a total of 10 reactions. It comprises a single enzyme subset that contains 8 out of 10 possible TCA cycle reactions, except IDHa & IDHb; which act as independent reactions. This model also results in fewer elementary modes (3 modes) compared to the full version (9 modes); where, 2 modes describe the complete TCA cycle function in this model, dependent on either IDHa or IDHb. The remaining mode is an internal cycle between IDHa (forward flux) and IDHb (reverse flux).

Figure 2.33 (see, pg. 90) describes the flux control distribution for TCA cycle flux in the reduced liver TCA cycle model, against the maximal activity of PDH.

Figure 2.33a shows that even in the reduced version of the liver TCA cycle model, a rapid exchange of control between key TCA cycle enzymes over a short range of enzyme activity, is a central feature of the evolved pattern of control distribution. In fig. 2.33a, C^J for PDH dominates and after a rapid exchange, the extent of control lost from PDH is picked up mostly by α-KGDH & SDH; which is quite similar to the distribution of control observed in the full model (see, fig. 2.25). Furthermore, fig. 2.33a shows that C^J transition curves for the reduced model are clearly sigmoidal, rather than hyperbolic. Figure 2.25b provides an indication of the sigmoidal nature of C^J transition curves in the full version of the model; however, it is partially obscured by artefacts which result from the additional structural as well as kinetic complexities that prevail in this model.

Similar rapid transfer of control between key enzymes, characterised by sigmoidal transition curves, has been observed in the Calvin cycle model (Fell et al., 1999) with experimental validations for two key enzymes involved: *rubisco* (Stitt et al., 1991) and *sedoheptulose bisphosphatase* (Poolman et al., 2001). The same phenomenon was observed in a simple model of a linear, two-step pathway (Letellier et al., 1994), as well as in more complex models of oxidative phosphorylation (Korzeniewski and Mazat, 1996b; Liguzinski and Korzeniewski, 2006), and therefore in theory, it is not limited to cyclical systems. In all cases, the effect was associated with saturating substrate concentrations (*i.e.* at $K_{m,S} \ll$ [substrate]). Comparison of the liver TCA cycle intermediate concentrations in liver mitochondria and respective K_m values of the liver TCA cycle enzymes suggests that most of these enzymes are apparently saturated with respect to their substrate(s). Hence, we studied how the saturation level of key enzymes affects the emergence of complex control distribution pattern in this system, in further detail *.

*On pg. 67, we have already clarified the actual meaning of the term *'saturated'* in the context of liver TCA cycle models. Please refer to the 2nd paragraph of itm. 2 on that page.

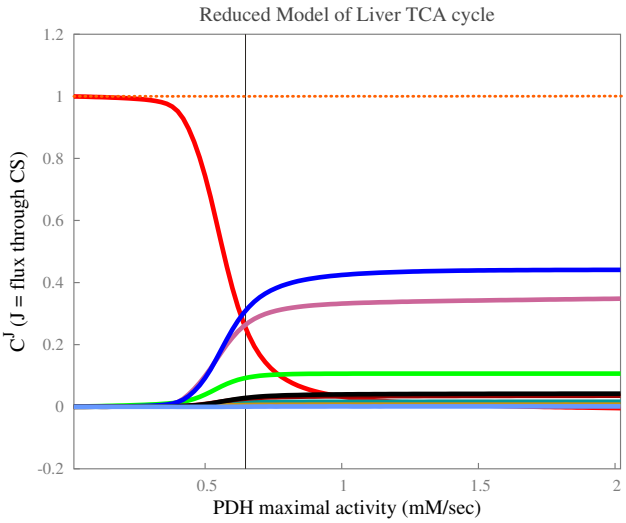

2.33.a. $K_{m,S} \ll [\text{substrate}]$; (range $\approx$ 3x)

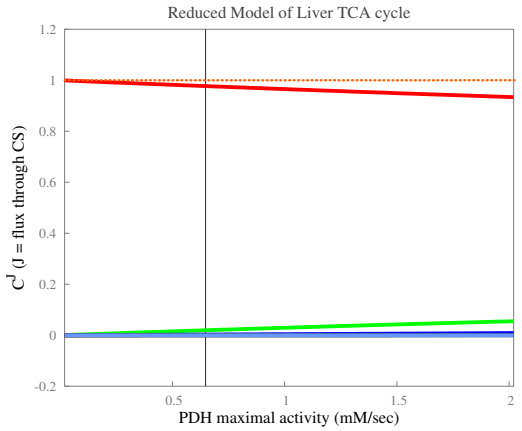

2.33.b. $K_{m,S} = [\text{substrate}]$; (range $\approx$ 3x)

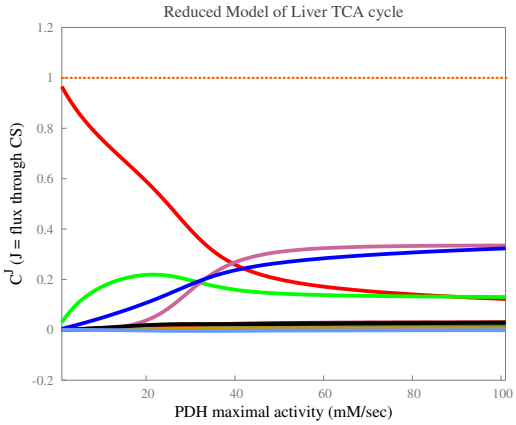

2.33.c. $K_{m,S} = [\text{substrate}]$; (range $\approx$ 150x)

▪ **Figure 2.33. Control of TCA cycle flux in the reduced liver TCA cycle model:** effect of PDH substrate saturation changes, against the PDH activity.

- Key is as follows :

PDH ; CS ; α-KGDH ; SDH ; MDH

- In fig. 2.33a, the flux control coefficients are calculated with the reduced model as is; wherein, the respective substrate concentrations for PDH far exceed their corresponding K_m values, *i.e.* at $K_{m,S} \ll [\text{substrate}]$.
- Whereas, in figs. 2.33b and 2.33c, the flux control coefficients are calculated with a modified reduced model; wherein, the respective K_m values for PDH substrates are set equal to their corresponding substrate concentrations, *i.e.* $K_{m,S} = [\text{substrate}]$.
- **X-axis:** Range of PDH maximal activity for figs. 2.33a and 2.33b: 0.0 – 2.0 mM/sec (*approx.* 3 times the initial model value of PDH maximal activity, 0.65 mM/sec).
- **X-axis:** Range of PDH maximal activity for fig. 2.33c: 0.0 – 100.0 mM/sec (*approx.* 150 times the initial model value of PDH maximal activity, 0.65 mM/sec).
- The vertical black line represents the initial model value. At this point, in figs. 2.33a and 2.33b, $V_{max}^{PDH} = 0.648$ mM/sec, respectively.
- ***Orange dotted line*** shows the *Summation theorem* result across the entire range.

Figure 2.33b (see, pg. 90) shows the distribution of flux control coefficients against PDH maximal activity, when PDH is no longer saturated with respect to its substrates (*i.e.* $K_{m,S}$ = [substrate]). The range of PDH maximal activity displayed in this plot is exactly the same as shown in fig. 2.33a — 0.0 – 2.0 mM/sec (*i.e. approx.* 3 times (3X) the initial model value of V_{max}^{PDH} (X); where, X = 0.65 mM/sec). Within this range of PDH activity, the steep C^J transition curves seen earlier in fig. 2.33a, are eliminated and the C^J for PDH remains close to unity. Therefore, the rapid transfer of control between key enzymes, characterised by sigmoidal transition curves, observed at saturating conditions for PDH (*i.e.* $K_{m,S} \ll$ [substrate]; fig. 2.33a), is completely lost with desaturation of PDH with respect to its substrates (*i.e.* $K_{m,S}$ = [substrate]; fig. 2.33b). At these conditions, flux through the system is now controlled by PDH alone, and has become virtually insensitive to changes in other enzyme activities.

As shown in fig. 2.33c (see, pg. 90), some of the central features of flux control distribution are restored even at *'non-saturating'* conditions for PDH, but only over a much wider range of PDH activity, between 0.0 – 100.0 mM/sec (*i.e. approx.* 150 times (150X) the initial model value of V_{max}^{PDH} (X); where, X = 0.65 mM/sec). In fig. 2.33c, majority of the control is eventually transferred to α-KGDH, SDH and CS; when the PDH activity is around 30 – 60 times its initial model value (*i.e.* between 20.0 – 40.0 mM/sec). Nevertheless, such a large hypothetical increase in the PDH maximal activity is unlikely to have any physiological relevance; since, in rat heart mitochondria, increases in PDH activation apparently result in at most a 5–fold increase in the total PDH activity (Dennis et al., 1979; Hutson et al., 1978).

Thus, analysis of the reduced version of liver TCA cycle model shows that the phenomenon of rapid exchange of flux control between key enzymes is independent of the structural as well as kinetic or thermodynamic complexities of liver TCA cycle models. It also suggests that the specific features of flux control transition curves, such as the slope or exact trajectory of these curves, are sensitive to change in the structural as well as kinetic properties of liver TCA cycle models; while the underlying central property of rapid exchange of control remains unaffected. Furthermore, our studies with the enzyme saturation kinetics indicate the possibility of it being the only determining factor responsible for the characteristic sigmoidal C^J distribution curves in metabolic systems with saturable enzyme kinetics. However, as a general property of all saturable metabolic systems, the enzyme saturation dependence of sigmoidal C^J curves, is still disputable, until tested against other generic, saturable metabolic systems.

Therefore, to explore the control properties of some simple models, we built 4-step simple test models, both linear and cyclical, as described in Methods (see, pg. 31). In this four-reaction cyclical test model, when at least one of the controlling enzymes is saturated with respect to its substrates, the same flux control distribution properties

are observed, as seen earlier in the reduced version of the liver TCA cycle model (see, fig. 2.33). Figure 2.34 (see, pg. 93) describes the flux control coefficient curves for a four-reaction cyclical test model.

Figure 2.34a shows that in a 4-step cyclical test model, when only one of the rate-controlling enzymes ('R_4') is saturated with respect to its substrate ('S_4') (*i.e.* at $K_m^{R_4S_4} \ll [S_4]$), the distinctive sigmoidal C^J transition curves emerge; wherein, the sharing of control between key enzymes shifts abruptly, against the 'R_4' activity. Also, it shows that as the degree of saturation is reduced, these characteristically sigmoidal C^J transition curves become increasingly more hyperbolic. On the other hand, fig. 2.34b shows that if more than a single enzyme is saturated with respect to its substrate (*i.e.* $K_m^{R_4S_4} \ll [S_4]$ & $K_m^{R_1S_1} \ll [S_1]$), the same C^J transition curves become progressively less steep as the value of $K_m^{R_4S_4}$ is increased (and as the value of $K_m^{R_1S_1}$ is kept as is). However, in this case, these curves continue to be sigmoidal in form, since the other enzymes in this system remain saturated (*i.e.* $K_m^{R_1S_1} \ll [S_1]$). This is quite similar to the situation in the reduced liver TCA cycle model. As shown earlier, at *'non-saturating'* conditions for PDH, over a narrow range, the rapid exchange of control between the key enzymes is eliminated entirely (see, fig. 2.33b); however, over a much wider range, the characteristic exchange of control between key components is restored (see, fig. 2.33c), since at least one of the remaining TCA cycle enzymes is saturated with respect to its substrates. Therefore, if all enzyme-saturation is eliminated across the entire liver TCA cycle system, the resultant C^J transition curves can be expected to be hyperbolic.

Furthermore, fig. 2.35 (see, pg. 94) shows that this phenomenon is not limited to the cyclical models, but can also exist in linear systems, as exemplified by the 4-step linear test model in this plot. Thus, our analysis of both the full and reduced versions of liver TCA cycle models, as well as the 4-step cyclical & linear test models, suggests that in saturable metabolic systems such as these, the emergence of sigmoidal C^J transition curves is symptomatic of the prevalence of enzyme saturation with respect to substrates in the system and *vice versa*. In such systems, the enzyme saturation can even be considered as the only prerequisite for the characteristic C^J patterns we have seen so far; as well as being independent of any other additional kinetic, thermodynamic or structural aspects.

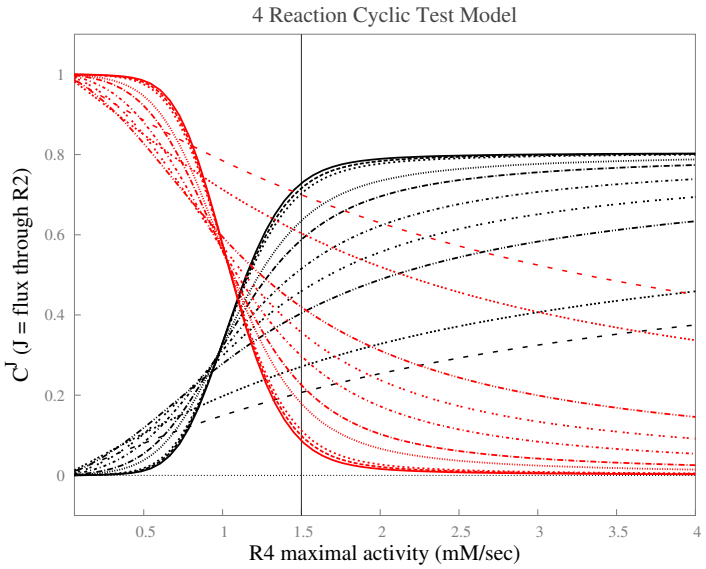

2.34.a. at $K_m^{R_4S_4} \ll [S_4]$

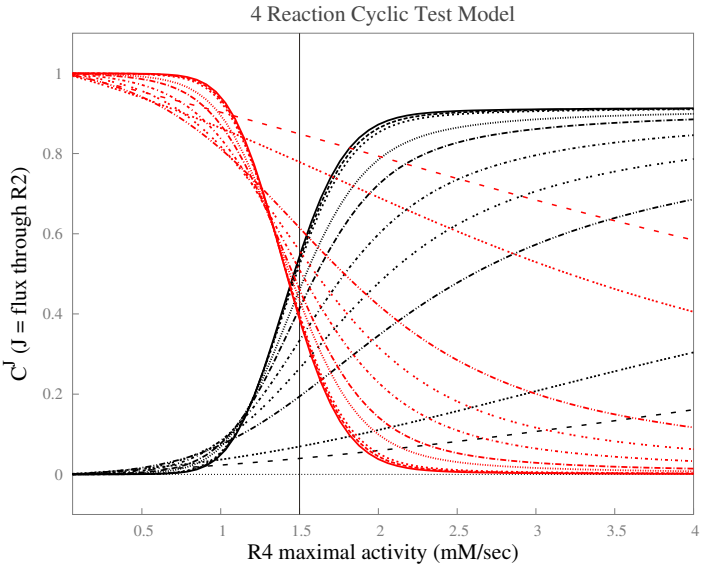

2.34.b. at $K_m^{R_4S_4} \ll [S_4]$ & at $K_m^{R_1S_1} \ll [S_1]$

- **Figure 2.34. Distribution of flux control coefficients in a cyclical test model:** effect of 'R_4' saturation variations, against the 'R_4' maximal activity.

- Plotted here are the C^J curves for 'R_1' & 'R_4', two reactions that share majority of control in this 4-step cyclical test model, against the 'R_4' maximal activity.
- Key is as follows : 'R_4' ; 'R_1'
- In this figure the flux control coefficients are calculated with variations in the $K_m^{R_4S_4}$ value; when :
  - Figure 2.34a : 'S_4' concentration far exceeds its corresponding K_m value (*i.e.* at $K_m^{R_4S_4} \ll [S_4]$); and
  - Figure 2.34b : The respective concentrations of 'S_4' & 'S_1', far exceed their corresponding K_m values (*i.e.* at $K_m^{R_4S_4} \ll [S_4]$ & at $K_m^{R_1S_1} \ll [S_1]$)
- In this 4-step cyclical test model, the initial concentrations of 'S_4' & 'S_1' are set equal to 1.0 mM and their respective initial K_m values are set equal to :
  - Figure 2.34a : $K_m^{R_4S_4} = 0.1$ mM & $K_m^{R_1S_1} = 1.0$ mM; and
  - Figure 2.34b : $K_m^{R_4S_4} = 0.1$ mM & $K_m^{R_1S_1} = 0.1$ mM.
- The flux control coefficients are calculated within a wide range of $K_m^{R_4S_4}$ values, from 0.001 to 10.0 mM.
- In these plots, matching line-types correspond to the same $K_m^{R_4S_4}$ value within the given range and the shallowest curves correspond to the highest value in that range.

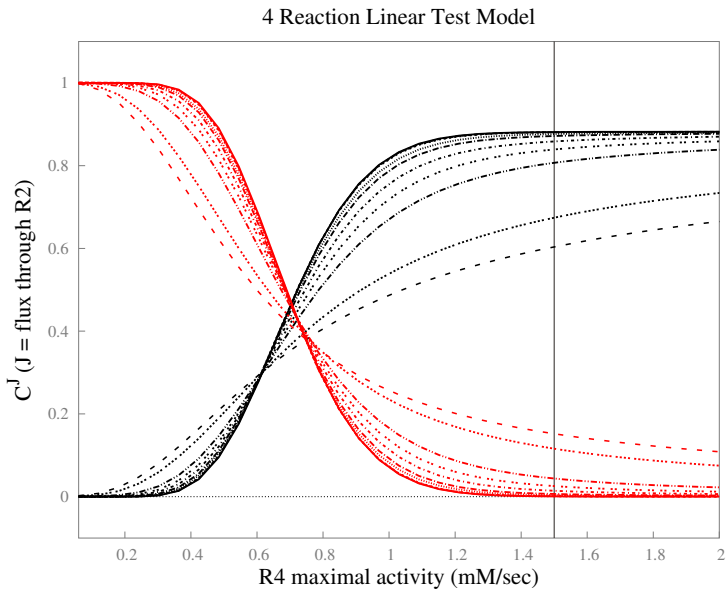

▪ **Figure 2.35. Distribution of flux control coefficients in a linear test model:** effect of 'R_4' saturation variations, against the 'R_4' maximal activity.

▪ Plotted here are the C^J curves for 'R_1' & 'R_4', two reactions that share majority of control in this 4-step linear test model, against the 'R_4' maximal activity.

▪ Key is as follows : 'R_4' ; 'R_1'

▪ In this figure the flux control coefficients are calculated with variations in the $K_m^{R_4S_4}$ value; when the respective concentrations of 'S_4' & 'S_1', far exceed their corresponding K_m values, *i.e.* $K_m^{R_4S_4} \ll [S_4]$ & $K_m^{R_1S_1} \ll [S_1]$, respectively.

▪ In this 4-step linear test model, the initial concentrations of 'S_4' & 'S_1' are set equal to 1.0 mM and their respective initial K_m values are set equal to 0.1 mM.

▪ The flux control coefficients are calculated at several different values of $K_m^{R_4S_4}$, within a wide range of values from 0.001 mM to 10.0 mM.

2.3.5.4 Distribution of flux control coefficients in the Liver TCA cycle models: Emergence of nearly-hyperbolic curves

As a further validation of our hypothesis, full version of the liver TCA cycle model was tested for the elimination of characteristic C^J transition curves by reducing the enzyme substrate saturation, similar to the analysis of reduced models. However, as a preliminary test, only PDH substrate saturation was eliminated gradually by increasing the K_m value corresponding to its primary substrate, pyruvate (*i.e.* $K_m^{PDH_{Pyr}}$). Figure 2.36 (see, pg. 95) describes the respective C^J curves for PDH, PC, SDH & ATPsynth, against V_{max}^{PDH}, at increasing values of $K_m^{PDH_{Pyr}}$.

Figure 2.36 shows that reducing the substrate saturation of PDH alone is clearly not sufficient to render hyperbolic flux control curves in the full liver TCA cycle model, unless the value of $K_m^{PDH_{Pyr}}$ is extremely high ($K_m^{PDH_{Pyr}} \gg 1.0$ mM). However, at this value, C^J for PDH is close to unity and gains nearly all control of the TCA cycle flux, rendering it insensitive to changes in the activities of other TCA cycle enzymes. At $K_m^{PDH_{Pyr}} = 1.0$ mM, although PDH is completely desaturated with respect to pyruvate (since, its

initial concentration is 0.2 mM), the resultant C^J transition curves are characteristically sigmoidal. Even a simultaneous reduction in the saturation of PDH primary as well as co-substrates (Pyr_m, CoA_m & NAD^+_m), fails to show any significant improvement in these sigmoidal curves (data not shown); since, the other TCA cycle enzymes are still saturated with respect to their corresponding substrate(s). Therefore, fig. 2.36 confirms our earlier conclusions and suggests a system-wide reduction in the substrate saturation of TCA cycle enzymes, at least with respect to key primary substrates, in order to render nearly-hyperbolic C^J transition curves in the updated liver TCA cycle model.

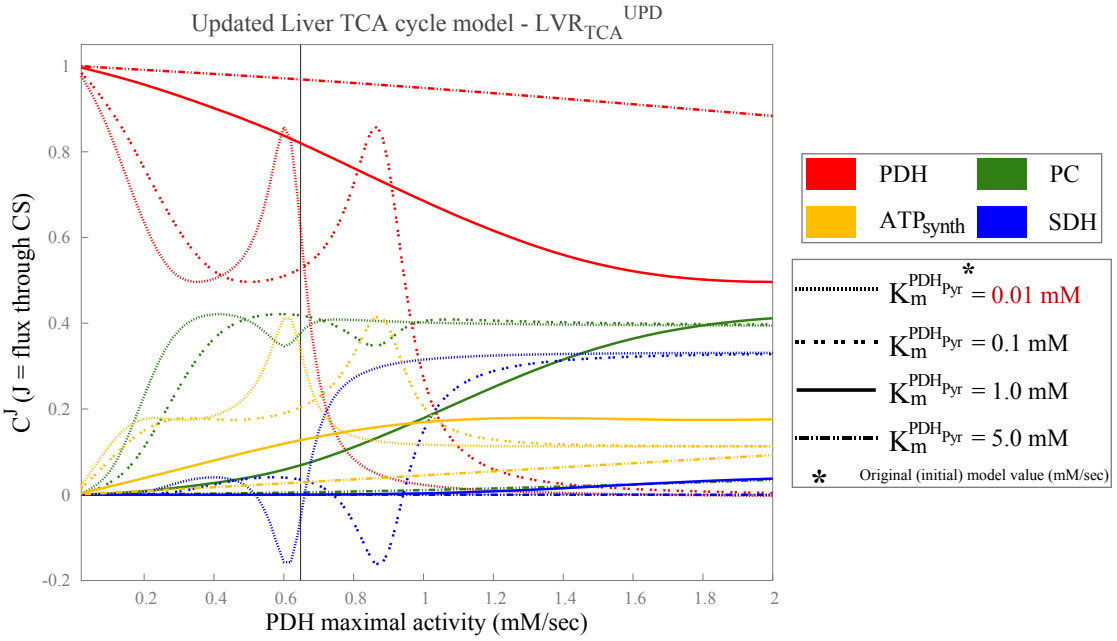

▪ **Figure 2.36. Flux control distribution for the control of TCA cycle flux in the full liver TCA cycle model:** against the maximal activity of PDH, with & without substrate saturation modifications in the PDH kinetics *w.r.t.* pyruvate.

▪ This plot is a result of 4 simulations at different values of $K_m^{PDH_{Pyr}}$, *viz.*– 0.01, 0.1, 1.0 & 5.0 mM; where, $K_m^{PDH_{Pyr}} = 0.01$ is the initial model value.

▪ **In liver TCA cycle models, the initial concentration of pyruvate (Pyr_m) is 0.2 mM.**

▪ **X-axis:** Note that the range of PDH maximal activity is exactly the same as used earlier in figs. 2.25b, 2.33a and 2.33b on pgs. 74 and 90, respectively (*i.e.* 0.0 – 2.0 mM/sec).

▪ The vertical black line represents the initial model value. At this point, $V_{max}^{PDH} = 0.648$ mM/sec.

Therefore, this test analysis was followed up by investigating the effect of a simultaneous, system-wide reduction in the substrate saturation of enzymes in the updated model, with respect to:

1. All corresponding primary substrates:

For this part of the analysis, corresponding K_m parameters for all primary substrates were replaced with a common parameter, $\mathbf{K_\alpha}$; which was then varied within a wide range between 1.0 to 10.0 mM and at each new value of $\mathbf{K_\alpha}$, the flux control coefficients were calculated for PDH & PC, two most-controlling enzymes in this model, against

the PDH maximal activity. Figure 2.37a (see, pg. 97) shows the effect of different values of $\mathbf{K_\alpha}$ on C^J for PDH & PC, respectively. Figure 2.38a (see, pg. 98) shows a complete flux control distribution for all enzymes in the updated model, against the PDH maximal activity, for a specific $\mathbf{K_\alpha}$ value (K_α = 1.6 mM), from the earlier given range of values.

2. **All corresponding primary substrates as well as key co-substrates:**

   For this part, corresponding K_m parameters for selected key co-substrates were replaced with a common parameter, $\mathbf{K_\beta}$. These key co-substrates were selected by the process of elimination, based on their degree of impact on the elimination of sigmoidal C^J transition curves. The $\mathbf{K_\alpha}$,$\mathbf{K_\beta}$ values were varied simultaneously, within a short range between 1.0 to 3.0 mM and the flux control coefficients were calculated for each new value*. Figure 2.37b (see, pg. 97) shows the effect of simultaneous change in the $\mathbf{K_\alpha}$,$\mathbf{K_\beta}$ values, on the PDH & PC coefficients, against the PDH maximal activity. Figure 2.38b (see, pg. 98) shows a complete flux control distribution for all enzymes in the updated model, against the PDH maximal activity, for a specific $\mathbf{K_\alpha}$,$\mathbf{K_\beta}$ value (K_α,K_β = 1.6 mM), from the earlier given range of values.

In the updated liver TCA cycle model, comparing all metabolite concentrations to their respective K_m values shows that 13 out of 15 TCA cycle enzymes are saturated with respect to their primary as well as co-substrates; with the exceptions of ATP synthase & ATP hydrolysis. ATPsynth is functional at nearly non-saturating conditions; while ATPhyd is modelled as a simple first-order mass-action reaction. Figures 2.37a and 2.38a (see, pgs. 97 and 98, respectively) exhibit sigmoidal C^J transition curves, as a result of varying K_α for 13 key TCA cycle enzymes. These figures also show that such a significant, system-wide reduction in the primary substrate saturation of enzymes is still insufficient to eliminate the sigmoidal C^J transition curves in the updated model and suggest that at least some of these key enzymes should be concurrently desaturated with respect to their corresponding co-substrates, as well.

A simultaneous, system-wide reduction in the saturation of all primary as well as co-substrates for all 13 enzymes in the updated liver TCA cycle model was ruled out immediately, due to the kinetic instability introduced by such system-wide changes in the model. Therefore, through the process of elimination, 9 out of 15 possible co-substrates were finalised, based on their moderate-to-high impact on the elimination of sigmoidal C^J transition curves in the updated liver TCA cycle model.

*Due to kinetic instability of the updated liver TCA cycle model for K_α,K_β values beyond 3.0 mM, a much shorter range (1.0 to 3.0 mM) was selected for their concurrent variation in the model, compared to that for the variation of K_α alone (1.0 to 10.0 mM). However, it must be noted that finding a region of kinetic instability in a model this size is not entirely unexpected, especially when the said analysis involves simultaneous variations in 22 enzyme saturation parameters of the model.

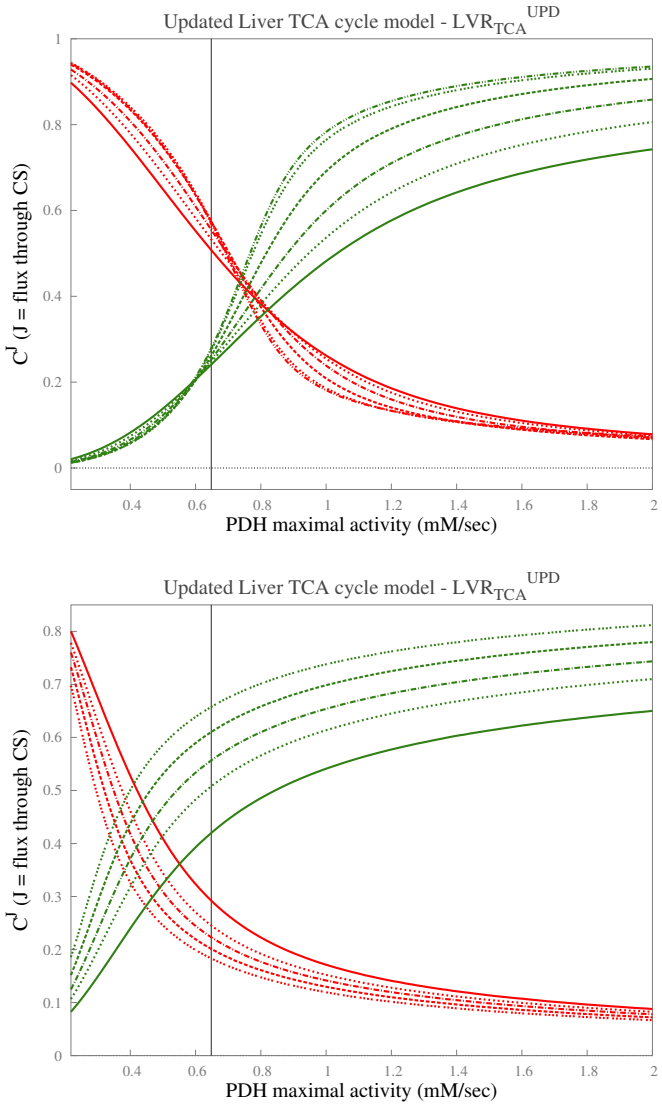

2.37.a
C^J with K_α variations

2.37.b
C^J with K_α,K_β variations

- **Figure 2.37. Flux control coefficients for PDH & PC, in the full liver TCA cycle model, against the change in PDH activity:** with modifications in the substrate saturation for all liver TCA cycle enzymes.

- Key is as follows : PDH ; PC

- Figure 2.37a: This plot is a result of 6 simulations at different values of $\mathbf{K}_\alpha$, *viz.*– 1.0, 1.6, 2.5, 4.5, 8.0 & 10.0 mM.

- Figure 2.37b: This plot is a result of 5 simulations at different values of $\mathbf{K}_\alpha$ & $\mathbf{K}_\beta$, *viz.*– 1.0, 1.6, 2.0, 2.5, & 3.0 mM; so that, for every simulation, $\mathbf{K}_\alpha = \mathbf{K}_\beta$.

- **$\mathbf{K}_\alpha$:** a common K_m parameter for all primary substrates; **$\mathbf{K}_\beta$:** a common K_m parameter for selected key co-substrates. For further details, please see pg. 96.

- **X-axis:** Note that the range of PDH maximal activity is exactly the same as used earlier in figs. 2.25b, 2.33a and 2.33b on pgs. 74 and 90, respectively (*i.e.* 0.0 – 2.0 mM/sec).

- The vertical black line represents the initial model value. At this point, $V_{max}^{PDH} = 0.648$ mM/sec.

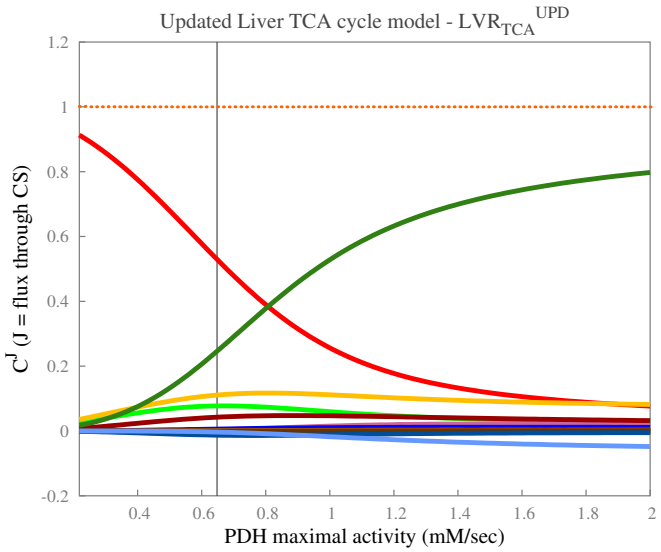

2.38.a
C^J with $K_\alpha = 1.6$ mM

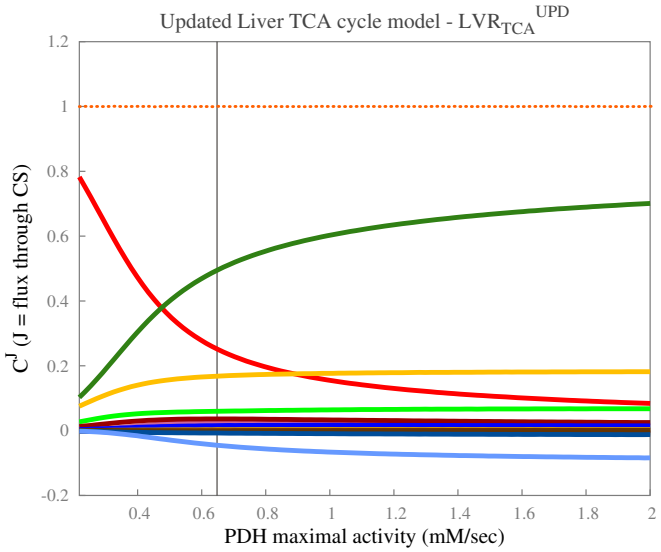

2.38.b
C^J with
K_α,$K_\beta = 1.6$ mM

- **Figure 2.38. Control of the TCA cycle flux at a specific value of K_α & K_β:** Distribution of flux control coefficients calculated for the full liver TCA cycle model, against the change in PDH maximal activity.

- Key is as follows (only for enzymes with most control; for the rest, refer to: pg. 74) :

PDH ; CS ; IDHa ; α-KGDH ; SDH ; PC ; ATPsynth ; ATPhyd

- **K_α:** a common K_m parameter for all primary substrates; **K_β:** a common K_m parameter for selected key co-substrates. For further details, please see pg. 96.

- **X-axis:** Note that the range of PDH maximal activity is exactly the same as used earlier in figs. 2.25b, 2.33a and 2.33b on pgs. 74 and 90, respectively (*i.e.* 0.0 – 2.0 mM/sec).

- The vertical black line represents the initial model value. At this point, $V_{max}^{PDH} = 0.648$ mM/sec.

- ***Orange dotted line*** shows the *Summation theorem* result across the entire range.

Figures 2.37b and 2.38b (see, pgs. 97 and 98) exhibit nearly-hyperbolic flux control curves, as a result of 4 enzymes being desaturated with respect to primary substrates alone (K_α), as well as 9 enzymes being desaturated with respect to primary as well as co-substrates (K_α,K_β), simultaneously. Therefore, within a given range of change (1.0 to 3.0 mM), using an optimal degree of system-wide enzyme desaturation in the updated liver TCA cycle model, we have successfully eliminated the sigmoidal C^J transition curves to render an overall distribution of nearly-hyperbolic C^J curves, without affecting the underlying central property of rapid exchange of control between key liver TCA cycle enzymes. (see, fig. 2.38b).

In fig. 2.38, in either case, majority of the control is shared by PDH & PC; while the remaining control is uniformly shared between ATPsynth, CS & IDHb. Also, the rapid exchange of control between key enzymes is much more gradual compared to that in fig. 2.25b (see, pg. 74). In fact, at initial conditions (*i.e.* $V_{max}^{PDH} = 0.65$ mM/sec), the gradual exchange of control between key enzymes is such that, in fig. 2.38a, PDH has majority of the control; whereas in fig. 2.38b, PC has majority of the control. Moreover, fig. 2.38 shows that a system-wide enzyme desaturation in the updated model completely destroys the significant extent of control shared by SDH, α-KGDH & IDHa in the original and far more saturated liver TCA cycle system, as seen earlier in fig. 2.25b. Instead, as seen in fig. 2.38b, CS and IDHb appear to acquire a small share of control, post system-wide enzyme desaturation.

Therefore, this analysis not only confirms that the phenomenon of rapid exchange of flux control between key enzymes is independent of the structural as well as kinetic or thermodynamic complexities of the liver TCA cycle model, it also supports our earlier hypothesis that in liver TCA cycle models, if substrate saturation for all enzymes is eliminated across the system, the resultant C^J transition curves can be expected to be hyperbolic. Also, through such comprehensive set of analyses, we have accumulated sufficient evidence to confirm that the dependence of sigmoidal flux control coefficient curves on the extent of substrate saturation of enzymes is a general property of metabolic systems with saturable enzyme kinetics.

2.3.5.5 Concentration control coefficient analysis for Liver TCA cycle models

In this section, we shall analyse the *concentration control coefficients* (C^S) of TCA cycle intermediate metabolites, calculated with respect to all enzymes in the model. For the concentration control coefficients, we will only focus on the updated liver TCA cycle model data, as mentioned earlier in the case of *flux control coefficients*. Liver TCA cycle models contain 16 internal metabolites, all of which can be analysed using the concentration control coefficients. However, in this section, we have presented data for only a selected group of metabolites. These metabolites were selected as follows —

- **Citrate :**
  - Since, it is produced by *citrate synthase*; which represents the TCA cycle flux.
  - Since, Cit_m, along with αKG_m, tends to accumulate in the system (see, pg. 59).
- **Oxaloacetate :**
  - Since, it is produced by *pyruvate carboxylase*; which has a high degree of flux control and it is a point of entry for the anaplerotic carbon into the cycle.
  - Since, $[\text{OAA}_\text{m}]$ is often a limiting factor for citrate synthesis (Olson and Williamson, 1971; Shepherd and Garland, 1969; Williamson et al., 1967a,b, 1972).
- **Acetyl-CoA :**
  - Since, it represents a point of entry for the TCA cycle carbon and acts as CS a substrate; the rate of which, represents the overall TCA cycle flux.
  - Since, $\text{V}_\text{app}^\text{PC}$ is defined as a function of $[\text{AcCoA}_\text{m}]$ (see eq. B.3 on pg. 222).
- **NADH_m, ATP_m, & ATP_c :**
  - Since, among other factors, they comprise the *'energy status'* of a cell.

Figures 2.39 to 2.41 (see pgs. 101 to 103, respectively) show the distribution of concentration control coefficients for the aforementioned TCA cycle intermediate metabolites, against the change in PC maximal activity. Also, fig. 2.42 (see, pg. 105), gives a qualitative overview of the control distribution for all 16 internal metabolites in the updated liver TCA cycle model, against the change in PC maximal activity. Moreover, other qualitatively similar concentration control coefficient plots are included in the supplementary material, in figs. I.12 to I.14 (see pgs. XX to XXII, respectively).

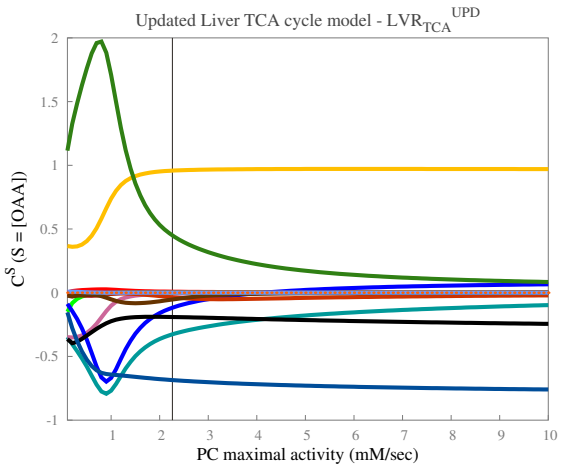

2.39.a. C^{OAA}, Updated model

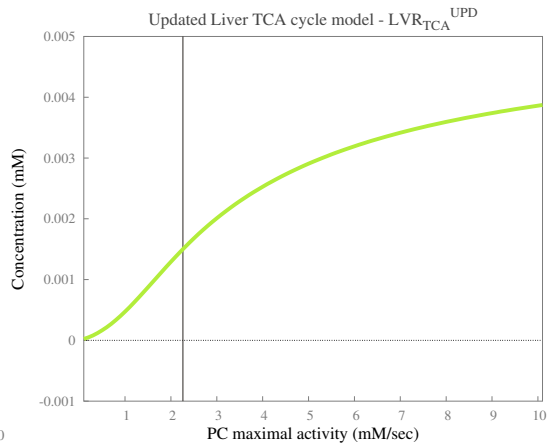

2.39.b. [OAA], Updated model

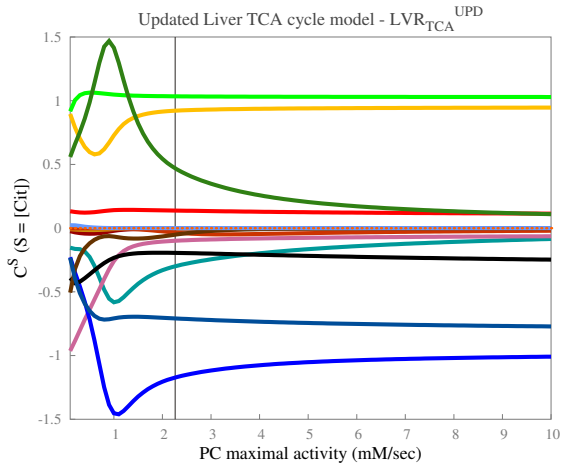

2.39.c. C^{Cit}, Updated model

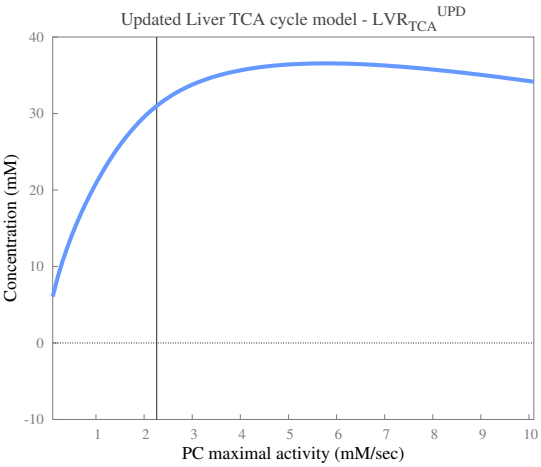

2.39.d. [Citrate], Updated model

▪ **Figure 2.39. Control of TCA cycle intermediate metabolites:** Distribution of concentration control coefficients calculated for the respective concentrations of OAA & Citrate, against the changing maximal activity of PC.

▪ Key for figs. 2.39a and 2.39c is as follows :

PDH ; CS ; ACO ; IDHa ; α-KGDH ; SCS;
SDH ; FM ; MDH ; ATPsynth ; ANT ; ATPhyd;
PC ; MC ; IDHb ; Total Sum (dotted line)

▪ The vertical black line represents the initial model value. At this point, in figs. 2.39a to 2.39d, $V_{max}^{PC} = 2.26234$ mM/sec (apparent velocity).

▪ ***Orange dotted line*** shows the *Summation theorem* result across the entire range. For concentration control coefficients, since the sum is equal to zero, the dotted line is not easily visible.

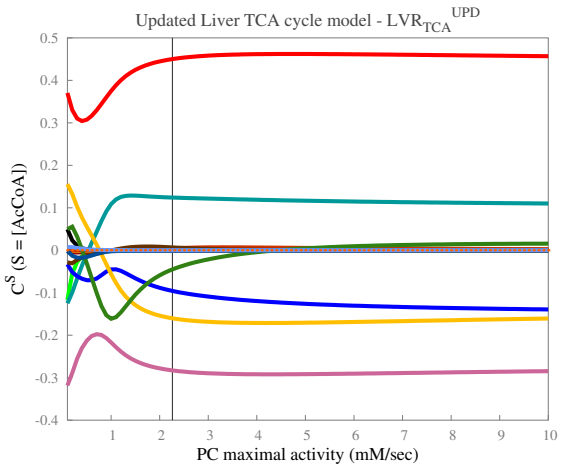

2.40.a. C^{AcCoA}, Updated model

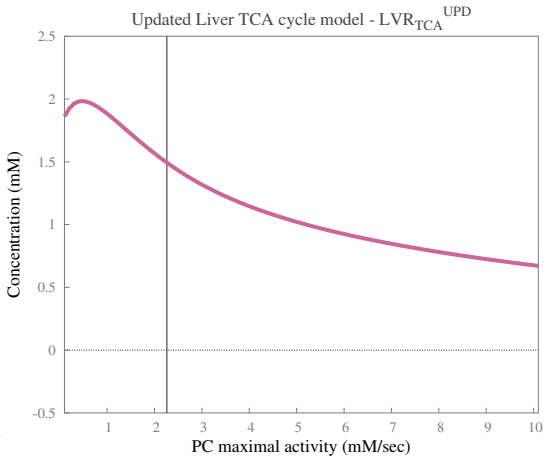

2.40.b. [AcCoA], Updated model

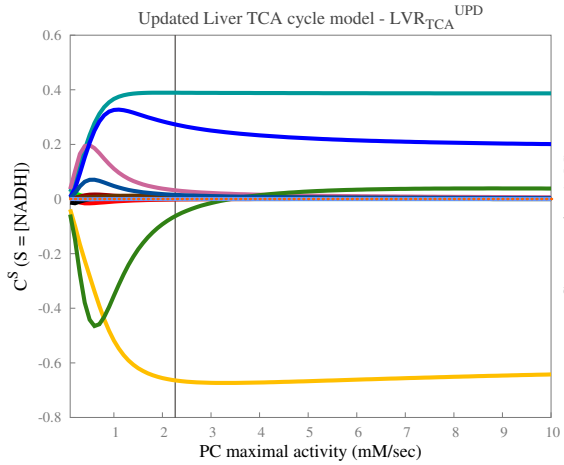

2.40.c. C^{NADH}, Updated model

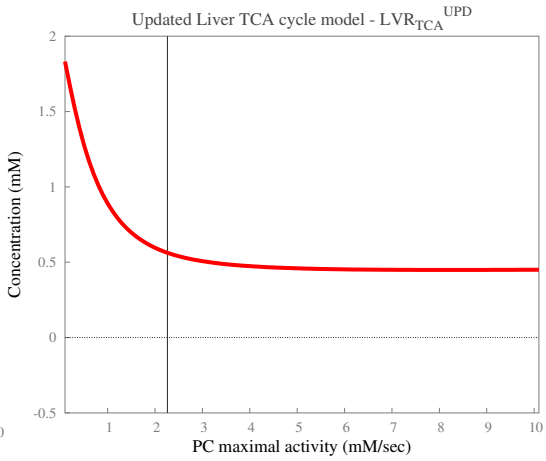

2.40.d. [NADH], Updated model

▪ **Figure 2.40. Control of CoA- & NAD− related metabolites:** Distribution of concentration control coefficients calculated for the respective concentrations of AcCoA, & NADH, against the changing maximal activity of PC.

▪ Key for figs. 2.40a and 2.40c is as follows :

PDH ; CS ; ACO ; IDHa ; α-KGDH ; SCS;
SDH ; FM ; MDH ; ATPsynth ; ANT ; ATPhyd;
PC ; MC ; IDHb ; Total Sum (dotted line)

▪ The vertical black line represents the initial model value. At this point, in figs. 2.40a to 2.40d, $V_{max}^{PC} = 2.26234$ mM/sec (apparent velocity).

▪ ***Orange dotted line*** shows the *Summation theorem* result across the entire range. For concentration control coefficients, since the sum is equal to zero, the dotted line is not easily visible.

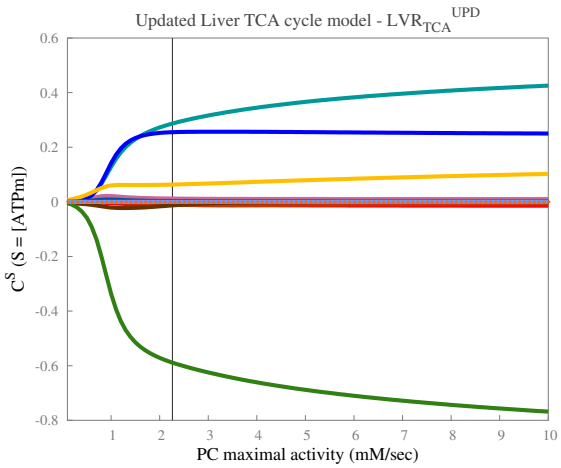

2.41.a. C^{ATP_m}, Updated model

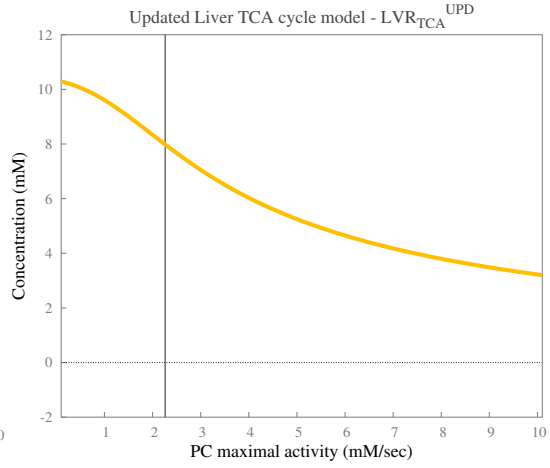

2.41.b. $[ATP_m]$, Updated model

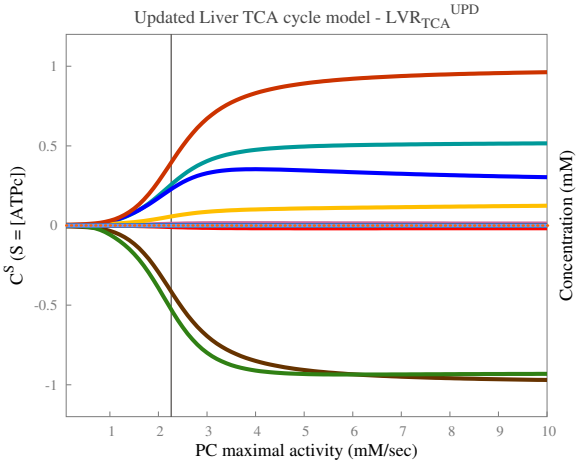

2.41.c. C^{ATP_c}, Updated model

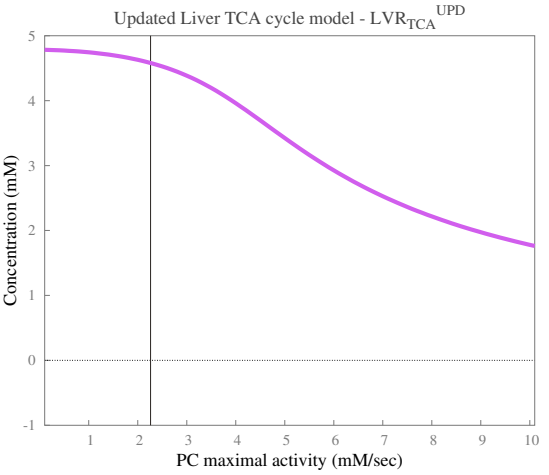

2.41.d. $[ATP_c]$, Updated model

▪ **Figure 2.41. Control of ATP−related metabolites:** Distribution of concentration control coefficients calculated for the respective concentrations of ATP_m & ATP_c, the changing maximal activity of PC.

▪ Other conditions as shown in fig. 2.39 on pg. 101.

Figures 2.39, 2.40 and 2.41 (see pgs. 101, 102 and 103, respectively), show the concentration control coefficients (C^S) of OAA_m, Cit_m, $AcCoA_m$, $NADH_m$, ATP_m, & ATP_c against the change in PC maximal activity. These concentration control coefficient plots are presented alongside a steady-state plot of the corresponding metabolite concentration, across the same parameter range (the metabolite concentration *'S'* for which the coefficient, *'C^S'* is calculated). In these plots, concentration control coefficients are distributed between the overall range of −1.5 to 2.0 (unitless). In each plot, a *summation theorem* result is also shown using a dotted line; however, for concentration control coefficients, since the sum is equal to zero, the dotted line coincides with the zero-axis and hence may not be easily visible.

As shown in figs. 2.39 to 2.41, the pattern of distribution for concentration control coefficients is distinctively sigmoidal in most cases and is not as complex as the pattern observed in the case of flux control coefficients. Also, the phenomenon of rapid exchange of control between key enzymes, is not a prominent feature of the C^S distributions, unlike that seen in the case of C^J distributions.

From these plots, it is evident that the overall control of TCA cycle intermediates is uniformly distributed between PC, ATPsynth, IDHa, SDH, & α-KGDH. Unlike in the case of flux control coefficients, PDH controls only a few TCA cycle intermediates. Figure 2.42 (see, pg. 105) provides a qualitative overview of the concentration control distribution across all 16 TCA cycle intermediate metabolites, against the change in PC maximal activity. From fig. 2.42 we may observe that, PC, ATPsynth, IDHa, SDH, & α-KGDH share a high degree of concentration control for most TCA cycle intermediates; whereas, ATPhyd, ANT, MC, & PDH share a moderate-to-high degree of control for only a few metabolites and the remaining TCA cycle enzymes control only up to 4 out of 16 TCA cycle intermediates. Later, we shall discuss this schematic in further detail.

Figure 2.39a (see, pg. 101) shows that as the PC maximal activity increases, a majority of control for oxaloacetate concentration ($[OAA_m]$) is transferred from PC to ATPsynth. To some degree, the control of $[OAA_m]$ is also distributed between IDHa, α-KGDH, SDH, MDH, & MC. In this case, PC & ATPsynth have positive C^S values; whereas, most of the other enzymes have negative C^S values. It means that any increase in the respective activities of PC & ATPsynth, would cause an increase in $[OAA_m]$; whereas, increasing the respective activities of, *e.g.* MDH & MC, would reduce its concentration. Therefore, the control distribution for oxaloacetate agrees well with the observation made by Williamson and Cooper, that the mitochondrial oxaloacetate concentration is expected to be determined by the malate concentration and the NAD^+/NADH ratio (Williamson and Cooper, 1980). Figure 2.39c shows the concentration control distribution for citrate; which, apart from its qualitative similarities to the oxaloacetate control distribution, also includes positive coefficients for CS & PDH, along with a large negative coefficient for SDH.

Figure I.12a (see, pg. XX), shows the control distribution for α-ketoglutarate concentration ($[\alpha KG_m]$) and apart from its qualitative similarities with the control distributions for Cit_m & OAA_m (see, figs. 2.39a and 2.39c), it shows a positive coefficient for IDHa as well as includes coefficients for ACO & IDHb. Figure I.12c shows the concentration control distribution for malate; where, a large negative C^S for MC counteracts a group of positive coefficients for IDHa, SDH, ATPsynth, & PC.

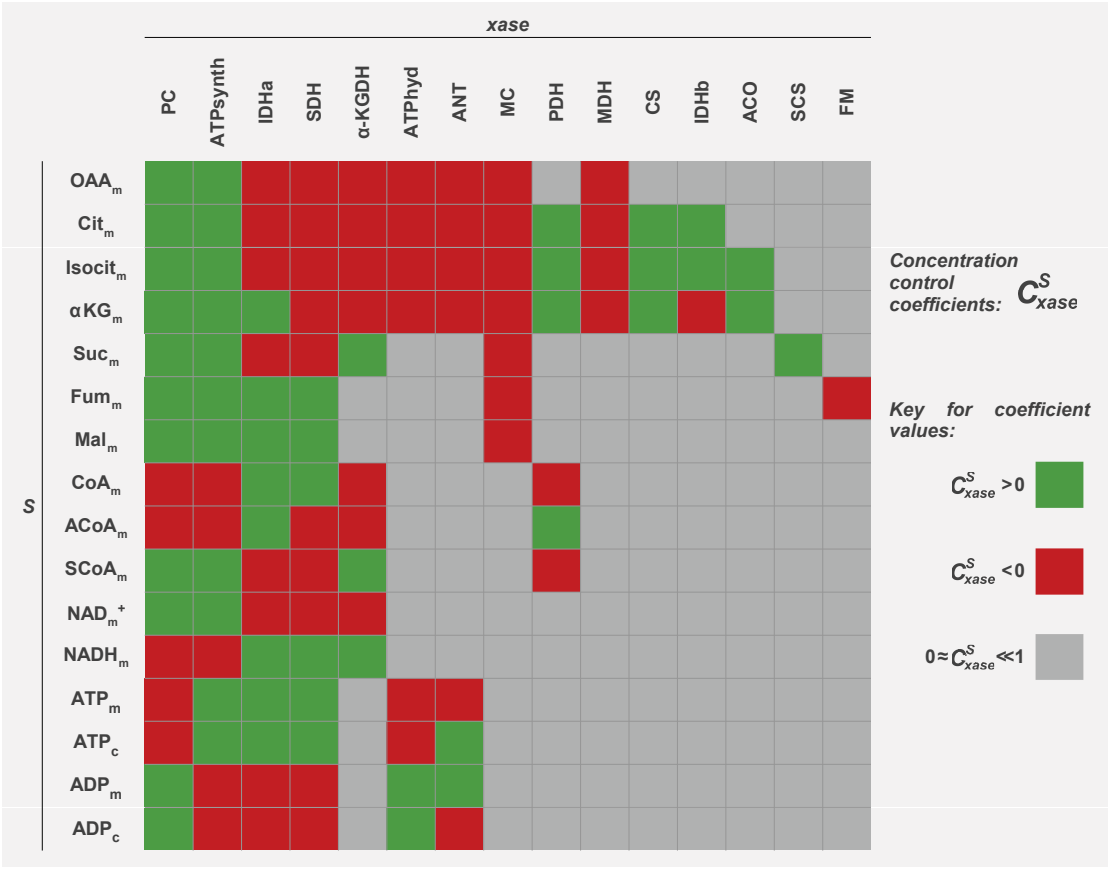

- **Figure 2.42. Control of TCA cycle intermediate metabolites:**

An overview of the distribution of concentration control coefficients in the updated liver TCA cycle model; against the changing maximal activity of pyruvate carboxylase.

- This figure shows the overall distribution of concentration control coefficients for all TCA cycle intermediate metabolites, with respect to all enzymes that share a moderate-to-high degree of control of the respective concentrations; against the change in PC maximal activity.
- Enzymes shaded in *grey* have either no control of the respective metabolite concentrations, or an infinitesimally small share of the overall control.
- This figure is based on the qualitative nature of the coefficient values (*i.e.* < 0, > 0, or ≈ 0) and does not reflect the actual quantitative data.

As mentioned earlier, ATPsynth shares a relatively high degree of control for most TCA cycle intermediates, which can be explained based on its demand for the efficient supply of NADH from TCA cycle dehydrogenases, as discussed earlier on pg. 75. Similarly, PC & PDH share a fairly high degree of control for most TCA cycle intermediates, which can be explained on the basis that these reactions form the initial linear portion of the TCA cycle pathway and therefore more likely to exhibit a higher degree of control, as discussed earlier on pg. 75. Also, a high coefficient value for citrate synthase, for the control of $\mathrm{Cit_m}$, $\mathrm{Isocit_m}$, & $\alpha\mathrm{KG_m}$, is to be expected; since, citrate is produced by CS, which is the first 6-carbon compound to be formed in the cycle and since, there are no alternative reactions in the model that can produce any of these three metabolites.

IDHa, α-KGDH, & SDH comprise the latter part of 'ESS #2', leading to the conversion of isocitrate to malate, thereby reducing the TCA cycle intermediate metabolite concentrations; which is reflected in terms of their negative coefficients for metabolites from the span between oxaloacetate to succinate. In the case of αKG_m, a positive C^S for IDHa is an exception and it arises because αKG_m is produced solely by IDHa. Also in this case, a negative C^S for IDHb can be explained based on its reverse flux in liver TCA cycle models, which converts α-ketoglutarate back to isocitrate.

Malate dehydrogenase (MDH) shows a noticeably negative coefficient for metabolites from the span between OAA_m to αKG_m; because in liver TCA cycle models, it operates in its reverse direction, thereby reducing the concentrations of oxaloacetate -dependent TCA cycle intermediates. Also, as shown earlier in fig. 2.18 (see, pg. 59), the role of MC as an exporter of TCA cycle carbon in liver TCA cycle models, is also reflected here in terms of its negative coefficient for all TCA cycle intermediate metabolites. Figure 2.42 shows that C^S for MC is negative for metabolites from the entire span between oxaloacetate to malate, which basically covers all TCA cycle intermediates.

Figures 2.40 and 2.41 (see, pgs. 102 and 103, respectively), show the distribution of concentration control coefficients for conserved metabolites in the updated liver TCA cycle model, against the change in PC maximal activity. Figure I.13 & fig. I.14 in supplementary material (see, pg. XXI & pg. XXII, respectively) show the distribution of concentration control coefficients for their corresponding counterparts from the respective conservation relationships. In fig. 2.40a & fig. I.13a, both acetyl-CoA & CoA show similar distributions of concentration control, except for the reversal of PDH & SDH coefficients. PDH produces acetyl-CoA and therefore its positive coefficient dominates the control of $AcCoA_m$ concentration ($[AcCoA_m]$); whereas, it consumes CoA_m and thus, shows a negative coefficient for the control of CoA_m concentration ($[CoA_m]$). On the other hand, any increase in the SDH activity would reduce $[AcCoA_m]$ as well as $[SCoA_m]$, thereby restoring the concentration of CoA_m via CS & SCS; which reflects in its corresponding coefficients for $AcCoA_m$ (negative) & CoA_m (positive). Overall, the control of CoA−related metabolites is uniformly distributed between PDH, PC, ATPsynth, IDHa, α-KGDH, & SDH.

The distribution of control for the conserved metabolite pairs of, *viz.*− $NAD^+_m/NADH_m$, ATP_m/ADP_m, & ATP_c/ADP_c, is a clear reflection of their counterbalancing steady-state behaviour. For $NADH_m$ (see, fig. 2.40c) & ATP_m (see, fig. 2.41a), the control is largely distributed between PC, ATPsynth, IDHa, α-KGDH, & SDH. Whereas, for ATP_c (see, fig. 2.41c), the control distributions comprise ATPhyd & ANT; plus PC, ATPsynth, IDHa, & SDH.

Pyruvate carboxylase utilises ATP_m during the carboxylation of pyruvate, thus decreasing its availability for the ANT -mediated export to cytosol and therefore, for the control of ATP_m & ATP_c concentrations, PC shows a strong negative coefficient. A large positive coefficient for SDH in this case can be explained on the basis that, any increase in the SDH activity would require a proportional increase in the 'ESS #2' flux (*i.e.* CS flux), which would ultimately increase the respective concentrations of $NADH_m$, ATP_m, & ATP_c. Also, positive coefficients for IDHa & ATPsynth can be explained in terms of the *supply & demand blocks* of the TCA cycle, as discussed earlier on pg. 75.

The control distribution of ATP_c concentration (see, fig. 2.41c), shows that ATPhyd & ANT share a large portion of control in opposite directions, with a negative C^S for ATPhyd and a positive C^S for ANT; which is due to the fact that ATP_c is produced by ANT and consumed by ATPhyd alone. Figure 2.40c, shows the distribution of control for $NADH_m$ concentration ($[NADH_m]$); where, a strong negative coefficient for ATPsynth is due to its dependence on $NADH_m$ as its substrate and indicates a key role of ATPsynth in controlling the TCA cycle dehydrogenases, via the control of $NADH_m$ concentration.

As mentioned earlier, the control distributions for NAD^+_m (see, fig. I.13c), ADP_m (see, fig. I.14a), & ADP_c (see, fig. I.14c) in supplementary material, show control properties that are exactly opposite to those observed for $NADH_m$ (see, fig. 2.40c), ATP_m (see, fig. 2.41a), & ATP_c (see, fig. 2.41c), respectively. For example, the control distribution of ATP_c shows positive coefficients for ATPsynth, SDH, IDHa, & ANT and negative coefficients for PC & ATPhyd; whereas, the control distribution of ADP_c shows positive coefficients for PC & ATPhyd and negative coefficients for ATPsynth, SDH, IDHa, & ANT.

Figure 2.42 (see, pg. 105) shows the overall distribution of concentration control coefficients across all 16 TCA cycle intermediate metabolites in the form of a *'heat-map'*, by considering all TCA cycle enzymes, for which the corresponding coefficient values are: > 0 or < 0; and not $\ll 1$ or ≈ 0. Therefore, for a given metabolite, all enzymes that have positive coefficients (> 0) are shaded in *green* and those that have negative coefficients (< 0) are shaded in *red*; whereas, enzymes with infinitesimally small coefficients ($\ll 1$ or ≈ 0) are shaded in *grey*.

From fig. 2.42, we may notice that the concentration control of Cit_m, $Isocit_m$, & αKG_m is shared by almost 12–13 TCA cycle enzymes, which suggests their significant role in the liver TCA cycle pathway. Oxaloacetate is controlled by 9 enzymes, out of which, 7 enzymes have negative coefficients; which suggests the crucial role of anaplerotic reactions

like *pyruvate carboxylase*, in maintaining an optimal level of oxaloacetate, sufficient enough to sustain the physiological rates of citrate synthesis; since, the availability of substrates, particularly, oxaloacetate, is a major regulatory factor that limits the citrate synthase activity in liver mitochondria (Garland et al., 1969; LaNoue et al., 1970; Olson and Williamson, 1971; Shepherd and Garland, 1969; Srere, 1974; Williamson and Olson, 1968; Williamson et al., 1967b, 1969a, 1972; Wojtczak, 1968). Furthermore, it indicates the need for including Malate-Aspartate shuttle reactions, particularly in the absence of PC; which is the case in mammalian heart as well as skeletal muscle (*for refs., please see earlier*). This schematic also highlights the prominent role played by PC & ATPsynth, in controlling the respective concentrations of all 16 TCA cycle intermediates; which suggests the importance of expanding the ATP synthase reaction kinetics to include an adequately detailed description of the electron transport chain (ETC) reactions.

Although, fig. 2.42 does not include data for changes in other enzyme activities, comparing such data with the data presented here (in this case, against the change in PC maximal activity), reveals that the overall distribution of concentration control against other enzyme activities, is qualitatively similar and therefore, we may conclude that fig. 2.42 shows a qualitative overview of the concentration control distribution against all enzyme activities in liver TCA cycle models.

2.3.5.6 Elasticity coefficient analysis for Liver TCA cycle models

In this section, we shall analyse the *elasticity coefficients* (ε_S) of liver TCA cycle models, calculated for all enzymes, with respect to all internal as well as external metabolites in the model. Similar to the calculation of *flux control coefficients*, we will only focus on elasticity coefficients of the updated liver TCA cycle model. Figure 2.43 (see, pg. 109) shows the distribution of elasticity coefficients for the updated liver TCA cycle model, for all 15 enzymes in the model, calculated with respect to 28 metabolites that include internal as well as external metabolites. Figure 2.45 (see, pg. 111) shows the distribution of elasticity coefficients, when most TCA cycle enzymes are desaturated with respect to primary substrates as well as co-substrates, as demonstrated earlier for the distribution of flux control coefficients using K_α,$K_\beta = 1.6$ mM (see fig. 2.38b on pg. 98). Figure 2.44 (see, pg. 110) shows the connectivity theorem result that links the elasticity coefficients ($\mathcal{E}_S^{xase}$) shown in fig. 2.43 and flux control coefficients (C_{xase}^J) computed at initial steady-state of the updated liver TCA cycle model.

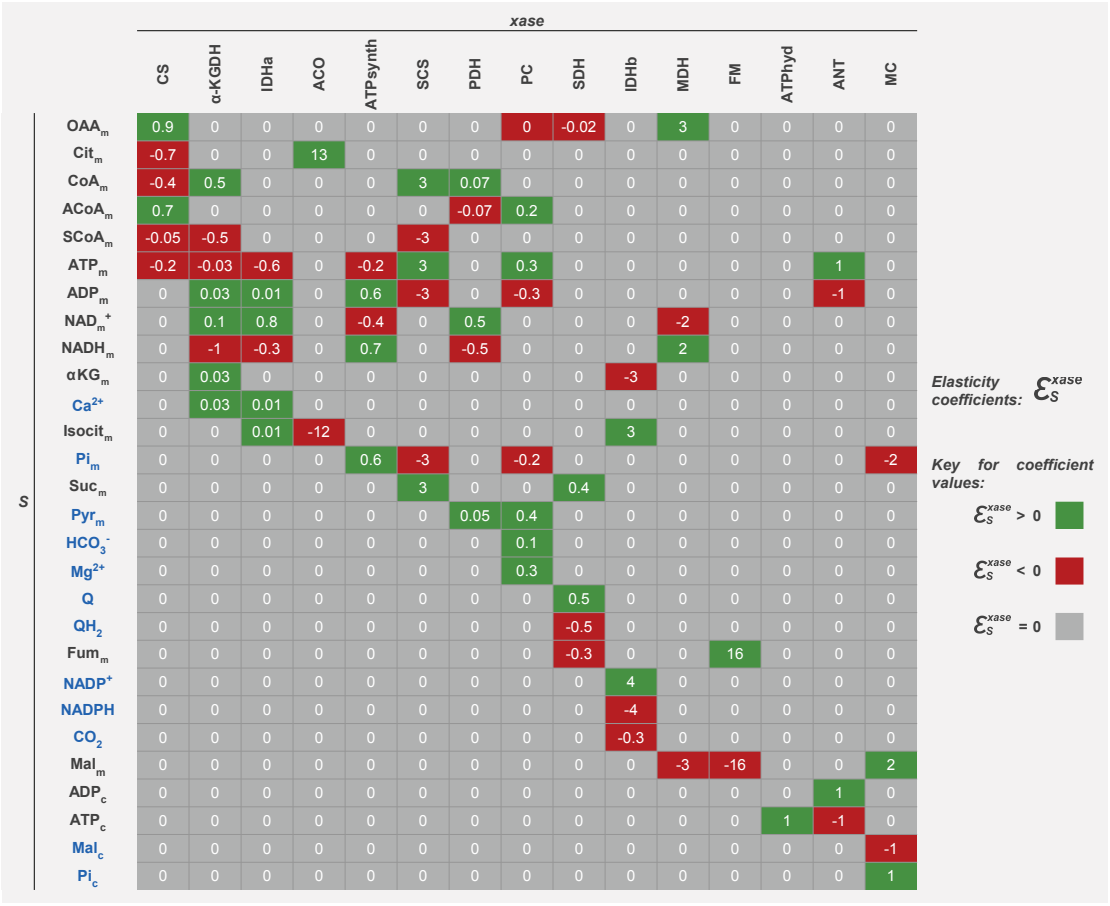

- **Figure 2.43. Local properties of the liver TCA cycle enzymes:** The distribution of elasticity coefficients in the updated liver TCA cycle model.

- In this figure, positive $\mathcal{E}_S$ values are shown in *green* and negative $\mathcal{E}_S$ values are shown in *red*.
- Enzymes that are not affected by a given metabolite ('*S*'), have elasticity values equal to zero and in this figure, they are shaded in *grey*.
- All internal metabolites are shown in *black* and external metabolites are shown in *blue*.

S \ xase	ATPhyd	ANT	α-KGDH	IDHb	CS	IDHa	ATPsynth	SCS	PDH	PC	SDH	MDH	FM	MC	ACO	Summation
¶ CoA_m	0	0	0	0	0	0	0	0	0	0	0	0	0	0	0	0
αKG_m	0	0	0	0	0	0	0	0	0	0	0	0	0	0	0	0
Ca^{2+}	0	0	0	0	0	0	0	0	0	0	0	0	0	0	0	0
$NADP^+$	0	0	0	0	0	0	0	0	0	0	0	0	0	0	0	0
NADPH	0	0	0	0	0	0	0	0	0	0	0	0	0	0	0	0
CO_2	0	0	0	0	0	0	0	0	0	0	0	0	0	0	0	0
¶ ATP_c	0	0	0	0	0	0	0	0	0	0	0	0	0	0	0	0
OAA_m	0	0	0	0	-0.01	0	0	0	0	0	0	0.01	0	0	0	0
¶ NAD^+_m	0	0	0	0	0	-0.01	-0.03	0	-0.09	0	0	0	0	0	0	-0.12
¶ ATP_m	0	0	0	0	0	0	-0.01	0	0	-0.01	0	0	0	0	0	-0.03
Pi_m	0	0	0	0	0	0	0.20	0.01	0	-0.07	0	0	0	0.01	0	0.17
Pyr_m	0	0	0	0	0	0	0	0	0.03	0.16	0	0	0	0	0	0.19
HCO_3^-	0	0	0	0	0	0	0	0	0	0.05	0	0	0	0	0	0.05
Mg^{2+}	0	0	0	0	0	0	0	0	0	0.12	0	0	0	0	0	0.12
Suc_m	0	0	0	0	0	0	0	-0.01	0	0	-0.02	0	0	0	0	-0.04
QH_2	0	0	0	0	0	0	0	0	0	0	0.03	0	0	0	0	0.03
Q	0	0	0	0	0	0	0	0	0	0	-0.03	0	0	0	0	-0.03
Fum_m	0	0	0	0	0	0	0	0	0	0	0.02	0	-0.02	0	0	0
Mal_m	0	0	0	0	0	0	0	0	0	0	0	-0.01	0.02	-0.01	0	0
Mal_c	0	0	0	0	0	0	0	0	0	0	0	0	0	0.01	0	0.01
Pi_c	0	0	0	0	0	0	0	0	0	0	0	0	0	-0.01	0	-0.01
$Isocit_m$	0	0	0	0	0	0	0	0	0	0	0	0	0	0	0.01	0.01
Cit_m	0	0	0	0	0	0	0	0	0	0	0	0	0	0	-0.01	-0.01

▪ **Figure 2.44. Connectivity relationships in the updated liver TCA cycle model:** Connectivity theorem result involving the elasticity coefficients ($\mathcal{E}_S^{xase}$) shown in fig. 2.43 (see, pg. 109) and flux control coefficients (C^J_{xase}) computed at initial steady-state, such that for a given metabolite *'S'*, the total sum of all products of $\mathcal{E}_S^{xase}$ & C^J_{xase} , calculated for each enzyme, should be equal to zero.

▪ ¶ : These metabolites are conserved within this system, which means their connectivity equations are more complicated compared to the other metabolites in the system. For further explanation, please see pg. 113. These rows represent combined connectivity equations of conserved metabolites in the liver TCA cycle models; which also means that number of individual equations are reduced compared to the total number of metabolites in the model.

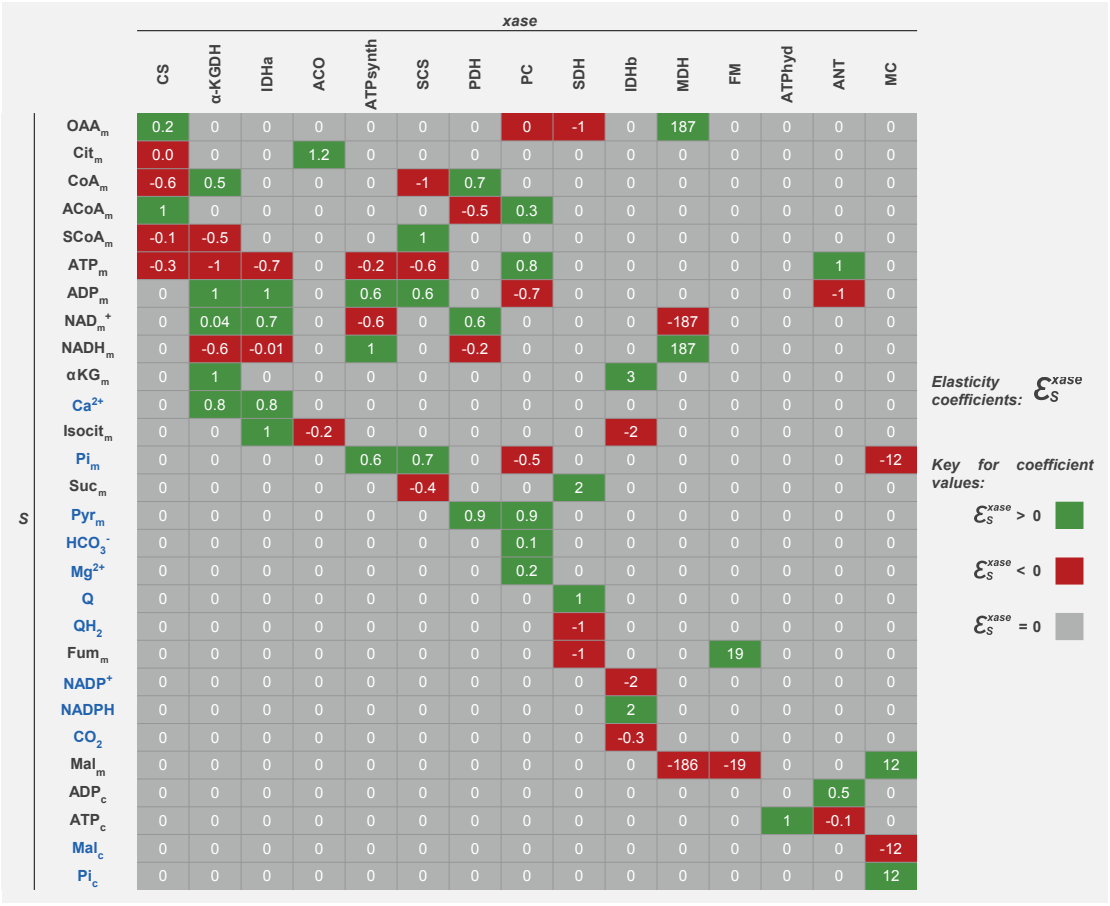

- **Figure 2.45. Local properties of the liver TCA cycle enzymes:** Elasticity coefficients of the updated liver TCA cycle model, when most enzymes are desaturated *w.r.t.* primary substrates as well as co-substrates, using K_α,K_β = 1.6 mM, as shown in fig. 2.38b (see, pg. 98).

- Other conditions as shown in fig. 2.43 on pg. 109.

From fig. 2.43, following observations can be made:

1. Link between elasticity coefficients & flux control coefficients:

Unlike control coefficients, *elasticities* represent properties of individual enzymes and not of the entire metabolic system. At the *'local'* level of individual enzymes, elasticity coefficients are a quantitative measure of how metabolite concentrations affect the enzyme activities; whereas, at the systemic level, elasticities provide a link between the kinetic properties of enzymes & their effect on the pathway flux (flux control coefficients) known as the *connectivity theorem* (Kacser and Burns, 1973). According to the connectivity theorem, flux control coefficients on a particular pathway flux (*'J'*), and elasticity coefficients on a given metabolite (*'S'*), calculated for each enzyme affected by *'S'*, are inversely proportional to each other (Fell, 1997); which means that enzymes with high flux control coefficient values have smaller elasticities and *vice versa*.

As seen earlier (see, pg. 73), the control of TCA cycle flux is distributed between PC, SDH, ATPsynth, PDH, IDHa, & α-KGDH. From fig. 2.43 (see, pg. 109), it is evident that most of these enzymes show smaller $\mathcal{E}_{S}$ values with respect to their corresponding substrates. For example, pyruvate dehydrogenase, which shows relatively high flux control coefficient values, has elasticity coefficients of 0.05, 0.07, & 0.5 for pyruvate, CoA, & NAD^{+}, respectively. Whereas, citrate synthase, which shows a minimal control of the TCA cycle flux, has elasticity coefficients of 0.7 & 0.9 for acetyl-CoA & oxaloacetate, respectively. Therefore, fig. 2.43 shows that in the absence of any information about the control of pathway flux, it is possible to predict the most-controlling pathway enzymes based on their elasticities.

Figure 2.44 (see, pg. 110) shows the result of *connectivity theorem equations* for the elasticities given in fig. 2.43. This result was obtained by multiplying flux control coefficients calculated at initial steady-state, by individual enzyme elasticities calculated for all metabolites in the model and ultimately adding all such products to get a sum total. For example, fig. 2.43 shows that oxaloacetate affects 4 enzymes – CS, PC, SDH, & MDH. For oxaloacetate, the connectivity equation would be:

$$C^{J}_{CS} \cdot \mathcal{E}^{CS}_{OAA} + C^{J}_{PC} \cdot \mathcal{E}^{PC}_{OAA} + C^{J}_{SDH} \cdot \mathcal{E}^{SDH}_{OAA} + C^{J}_{MDH} \cdot \mathcal{E}^{MDH}_{OAA} = 0 \; ; \textit{ where, } J = CS$$

For other enzymes that remain unaffected by a change in the oxaloacetate concentration, the product of $\mathcal{E}^{xase}_{S}$ & C^{J}_{xase} would be zero and therefore would not affect the total sum. Figure 2.44 shows a connectivity theorem result of zero for several metabolites and non-zero for others (shown in blue). Most of these non-zero sums are actually quite close to zero, which suggests that they might be due to numerical errors during model simulation.

In liver TCA cycle models, there are 4 conservation relationships, one involving 3 CoA –related metabolites, one each for mitochondrial ATP & NAD–related metabolites and one for cytosolic ATP metabolites (see tbl. 2.5 on pg. 34). For a conserved pair of metabolites, such as NAD^+ & NADH, there is a complication in the connectivity theorem (Fell, 1997; Fell and Sauro, 1985). Essentially, for any one of these single metabolites, the net result of the connectivity equation is no longer zero, but the equations can be combined in pairs to give a zero result, causing a reduction in the number of connectivity equations (Fell and Sauro, 1985). In liver TCA cycle models, a combined connectivity equation for each of the 4 conservation relationships causes the total number of equations to reduce by 5, thus resulting in 23 connectivity equations for 28 metabolites. In fig. 2.44, corresponding results of the combined connectivity equations are marked using ¶ (in red).

2. Elasticities as the effector impact indicators:

Elasticities have positive values for metabolites that stimulate the rate of a reaction (substrates, activators) and negative values for those that lower the reaction rate (products, inhibitors) (Fell, 1997). For example, PDH, which consumes pyruvate, CoA, & NAD^+ to generate AcCoA & NADH; shows positive values for the former and negative values for the latter. Also, for a given enzyme, based on the relative values of its positive & negative effectors, it is possible to differentiate between them, in terms of their corresponding effector strengths. For example, in the case of PDH, product inhibition by acetyl-CoA and NADH, competitive with respect to CoA & NAD^+, respectively (Tsai et al., 1973) is considered in the model. From fig. 2.43, it is clear that the elasticity of PDH for AcCoA (-0.07) is much smaller than its elasticity for NADH (-0.5); which suggests that in this model, the inhibited rate of pyruvate dehydrogenase is substantially more responsive to changes in the concentration of NADH than that of acetyl-CoA.

During a study of the kinetic properties of pig heart and kidney pyruvate dehydrogenases, it was found that PDH is only moderately inhibited by a high AcCoA/CoA ratio; whereas, it is strongly inhibited by a high NADH/NAD^+ ratio (Bremer, 1969; Strumiło, 2005; Wieland, 1983). Also, based on the increase in liver mitochondrial NADH/NAD^+ ratio in fasted animals, as well as, a lowered NADH/NAD^+ ratio (Williamson et al., 1967a) and an extremely high AcCoA/CoA ratio (Bremer and Aas, 1969) in the ketotic state of diabetic animals, Bremer suggested that in general, variations in the NADH/NAD^+ ratio might prove to be a more direct regulator of the PDH activity than the AcCoA/CoA ratio and that during the diabetic ketotic state, the latter ratio is likely to be more important (Bremer, 1969).

3. Elasticities of enzymes competing for a common substrate:

In situations where two enzymes compete for a common substrate, their responsiveness to changes in the concentration of that substrate can be assessed and differentiated using corresponding elasticities. For instance, in liver TCA cycle models, pyruvate dehydrogenase and pyruvate carboxylase compete for pyruvate as their primary substrate. For pyruvate, PDH has an elasticity coefficient of 0.05; whereas, elasticity of PC is 0.4 (see, fig. 2.43). It means that compared to PDH, pyruvate carboxylase is 35% more responsive to changes in mitochondrial pyruvate availability. This result agrees well with the observation made by Siess et al., that the PDH flux should be much less sensitive to changes in mitochondrial pyruvate availability, since the K_m of pyruvate dehydrogenase for pyruvate is much lower than that of pyruvate carboxylase (Siess et al., 1982a).

Additionally, we also know that in liver mitochondria, pyruvate carboxylase flux apparently ranges from 1.3 to 9.4 times the TCA cycle flux (flux through CS), and is on average around 3 times the TCA cycle flux (Baranyai and Blum, 1989; Beylot et al., 1995; Des Rosiers et al., 1995; Di Donato et al., 1993; Magnusson et al., 1991; Rabkin and Blum, 1985). In fact, in liver TCA cycle models, 'ESS #2' (which comprises PDH) or the TCA cycle flux is *approx.* $1/4^{th}$ the flux through 'ESS #1' (which includes PC) (see figs. 2.9 and 2.17 on pgs. 46 and 56, respectively).

In fig. 2.18 (see, pg. 59), we showed that since MDH operates in its reverse direction, a large fraction of the anaplerotic carbon introduced by PC is routed via: PC $\rightarrow$ MDH $_{(reverse)}$ $\rightarrow$ MC. Therefore, in liver TCA cycle models, Malate Dehydrogenase & citrate synthase compete for the oxaloacetate availability. Figure 2.43 shows that the elasticity of CS for OAA_m is nearly 1 (0.9) and that of MDH is 3; which not only shows the MDH reversibility in this model, but also provides an additional support to the flux distribution pattern given in fig. 2.18.

4. Elasticities of near-equilibrium reactions:

In fig. 2.43, 6 enzymes show elasticity coefficients that are greater than 1, *viz.*– ACO, SCS, IDHb, MDH, FM, & MC. In liver TCA cycle models, these enzymes represent reactions that are close to equilibrium and for such reactions, the elasticities with respect to substrate and product are mostly determined by the degree of displacement of the reaction from equilibrium (or the disequilibrium ratio (ρ)) rather than by their kinetic details, which can lead to much larger elasticity values than that of the non-equilibrium reactions (Fell, 1997; Groen et al., 1982a; Kacser and Burns, 1973; Westerhoff et al., 1984).

5. Seemingly inconsistent elasticity values:

From fig. 2.43, the corresponding elasticities of IDHb & SCS appear inconsistent compared to their earlier observed steady-state behaviour. According to fig. 2.43, IDHb and SCS appear to be operating in their forward and reverse directions, respectively. However, at steady-state, IDHb mostly functions in its reverse direction and SCS has a positive flux. In fact, the elasticities are calculated *instantaneously* (*i.e.* without simulating the model), unlike other control coefficients, which are calculated by simulating the model for a steady-state solution. In liver TCA cycle models, when the individual reaction rates are computed *instantaneously*, IDHb and SCS show positive (forward) and negative (reverse) fluxes, respectively.

Also in fig. 2.43, $\mathcal{E}^{\mathrm{PC}}_{\mathrm{OAA}}$ is shown in *red* with a value of zero; whereas, $\mathcal{E}^{\mathrm{IDHa}}_{\mathrm{\alpha KG}}$ is shown in *grey* with a value of zero. In fact, for PC, $\mathcal{E}^{\mathrm{PC}}_{\mathrm{OAA}} \approx 0$ (*i.e.* $= -2.4\text{E-}04$); which means that it has a weak product inhibition by oxaloacetate and thus its representation in the figure appears to be valid.

On the other hand, since α-ketoglutarate is a product of IDHa and this reaction is in principal reversible, one might have expected α-ketoglutarate to have some influence on reaction rate and therefore, $\mathcal{E}^{\mathrm{IDHa}}_{\mathrm{\alpha KG}}$ be shown in *red*, like other products of the reaction. However, in liver TCA cycle models, IDHa kinetics are modelled using a modified, irreversible form of the generic rate equation, while considering the product inhibition by $\mathrm{NADH_m}$ alone. In practice, the reversibility of IDHa has not been observed, possibly due to insufficient binding of both α-ketoglutarate & $\mathrm{CO_2}$ (Plaut, 1970), and hence for the purposes of modelling, α-ketoglutarate & $\mathrm{CO_2}$ are assumed to have no influence on reaction rate (Chen and Plaut, 1963; Plaut and Aogaichi, 1968), thereby making it irreversible.

The system-wide enzyme desaturation analysis performed using $\mathrm{K_\alpha}$,$\mathrm{K_\beta} = 1.6$ mM, when most enzymes are desaturated with respect to primary substrates as well as co-substrates (see, fig. 2.38b on pg. 98), presents a perfect example to demonstrate the link between elasticity coefficients and flux control coefficients. Figure 2.45 (see, pg. 111) shows the distribution of elasticity coefficients in the updated liver TCA cycle model for this analysis.

As a result of a system-wide reduction in enzyme saturation, fig. 2.45 shows significant changes in the elasticities of CS, α-KGDH, IDHa, PDH, SDH, MDH, FM, & MC, when compared to those shown in fig. 2.43. These alterations are correspondingly reflected in the distribution of flux control coefficients shown in fig. 2.38b (see, pg. 98), where the control of TCA cycle flux is shared between PDH, PC, ATPsynth, CS, & IDHb; which is significantly different from that of the saturated model (see fig. 2.25b on pg. 74).

2.4 Discussion & Conclusions

The study of liver TCA cycle model was initiated at the beginning of this project in order to gain better understanding of the modelling process as well as to understand the basic functional properties of a tissue-specific TCA cycle. Moreover, further analysis of this model showed that if modified slightly by removing pyruvate carboxylase, the resultant model is a metabolic system similar to the mammalian heart TCA cycle and the analysis of which can provide valuable insight into its dynamic properties, before actually building a proper heart-specific TCA cycle model.

The liver TCA cycle model analysis presented earlier has provided an in-depth perspective of the dynamic properties as well as the distribution of control in a tissue-specific TCA cycle model and some key aspects of this valuable analysis are as follows:

1. This model demonstrates the need of constructing simplified mathematical models that are capable of representing the fundamental physiological characteristics of real metabolic systems. The complex pattern of control distribution in this model highlights the fact that a mathematical model must not be *overloaded* with kinetic information and should be defined based on the criticality of a given process with respect to the overall biochemical function. This applies particularly well to the *kinetic/ dynamic modelling* of biochemical pathways. In kinetic metabolic models, model complexity can arise roughly due to the number of included reactions as well as the excessive enzyme kinetics data for a given process.

   The mammalian liver mitochondrial carbon metabolism is a much larger network of several biochemical processes and involves a number of smaller biochemical subsystems, such as the TCA cycle. Therefore, while modelling the mammalian liver-specific TCA cycle metabolism, embedded as it is, as a part of a much larger metabolic network, the modeller must determine which reactions or processes can be ignored based on their criticality within the network and which processes are absolutely essential for the overall biochemical function of that larger network. For example, in the case of liver TCA cycle models presented in this study, several metabolite transport reactions have been excluded (except two, *i.e.* MC & ANT), based on their criticality with respect to the overall liver TCA cycle function.

   Also, to avoid the excess use of enzyme kinetics data, most of the enzyme rate equations in liver TCA cycle models are defined using the simplified, generic, reversible bi-substrate equation (Chassagnole et al., 2001b; Rohwer et al., 2006), modified where necessary to account for more than two substrates and/ or products. In all cases, the simplest expression that adequately represents the key kinetic properties of the enzyme is used.

2. Overall, current analysis of the two liver TCA cycle models shows that a seemingly minor change, such as the *metabolic status of CoA*, can lead to significant quantitative effects in some aspects; whilst in others, it has relatively minor qualitative effects. For instance, the steady-state analysis data shows significant quantitative differences in metabolite concentrations as well as TCA cycle fluxes between the two liver TCA cycle models. On the other hand, Metabolic Control Analysis reveals that the control of TCA cycle flux between key TCA cycle enzymes is qualitatively similar between the two models.

Furthermore, this study highlights the importance of defining the *model boundary conditions* in a precise and non-conflicting manner. It shows the full extent of impact on the dynamic properties of a mathematical model caused by an ill-defined metabolite in the system (*i.e.* CoA), as a result of a simple oversight on modeller's part. More importantly, this study corrects such a significant error in the already established mammalian liver-specific TCA cycle model developed within the Cell Systems Modelling Group (CSMG) (Brightman et al., 2010, *unpublished manuscript*) and analyses the corrected/ updated model in full detail.

3. The elementary modes analysis shows that the dynamic properties of this model can arise as a result of possible linear combinations of nine elementary modes in the model. Also, the elementary modes analysis shows that we can arrive at a rough structural framework of the mammalian heart- or skeletal muscle-specific TCA cycle model, if a particular elementary mode containing only the heart-specific reactions is isolated from the model.

It also suggests that the internal substrate cycle between the NAD^+-dependent isocitrate dehydrogenase and the $NADP^+$-dependent isocitrate dehydrogenase that operates in the updated liver TCA cycle model is likely to exist in a mammalian heart-specific TCA cycle model as well, provided it follows a similar structural definition as that of the isolated elementary mode. There is sufficient literature evidence to support the existence of such a cycle in heart tissue (Huang and Colman, 2005; Londesborough and Dalziel, 1968; McCormack and Denton, 1981; Rutter and Denton, 1988; Sazanov and Jackson, 1993).

Moreover, this analysis indicates that a theoretically ideal version of TCA cycle, often described in biochemistry textbooks, that produces 11 molecules of ATP_m & 3 molecules of CO_2 per pyruvate, is a distinct possibility. PC, MC, & IDHb would be removed from the resulting model, to isolate $ElMo_{[3]}$ described in tbs. 2.3 and 2.4 (see, pg. 33). This TCA cycle model would then contain only a single elementary mode ($ElMo_{[3]}$), which would also be the only enzyme subset that comprises all 12 reactions of this model.

4. During the steady-state analysis, comparing the reported and model-predicted values of all variables for which it was possible to carry out a comparison, except fumarate (since, no literature value for its mitochondrial concentration was available) shows that the model-predicted values are all within reported ranges. This is to be expected, since four of the model parameters (see, Methods) were fitted to the *in vivo* TCA cycle intermediate concentration data.

Also, the updated liver TCA cycle model independently reproduces the behaviour observed in studies reporting TCA cycle fluxes in liver, in which the radiolabel incorporation from ^{13}C- or ^{14}C- labelled substrates into the TCA cycle intermediates was measured. Thus, PC flux is around three times the TCA cycle flux, and mitochondrial malate dehydrogenase is found to be operating in an opposite direction compared to the direction of TCA cycle flux, with PC influx into the cycle being balanced to a greater or lesser degree by an efflux via malate carrier (malate-phosphate transporter), out of the mitochondria at the level of malate (Baranyai and Blum, 1989; Beylot et al., 1995; Des Rosiers et al., 1995; Di Donato et al., 1993; Magnusson et al., 1991; Rabkin and Blum, 1985). Also, the model-predicted estimate of PC flux in relation to the overall TCA cycle flux, agrees with an average range of PC flux being 2–4 times the TCA cycle flux in liver, as reported by some of the experimental as well as model simulation studies (Nazaret et al., 2009; Stucki and Walter, 1972; Williamson et al., 1969a).

The steady-state analysis data shows that the respective magnitudes of reverse flux through MDH and the MC/ PC flux (*i.e.* 'ESS #1' flux) are rather higher in the model than would be expected, given the overall TCA cycle flux. It must be noted that the model is an abstracted representation of the real system, and that several processes have been omitted for the purposes of simplification. Amongst these are other transport processes through which material leaves the TCA cycle at the level of citrate, oxaloacetate and α-ketoglutarate, such as the mono-, di-, tricarboxylate transporters (Chappell, 1968; Klingenberg, 1970; LaNoue and Schoolwerth, 1979; Passarella et al., 2003; Williamson et al., 1968, 1969a); which, in combination with the MC efflux, balance the influx via PC into the cycle (Baranyai and Blum, 1989; Beylot et al., 1995; Des Rosiers et al., 1995; Di Donato et al., 1993; Magnusson et al., 1991; Rabkin and Blum, 1985). The model-predicted magnitude of fluxes through MDH & MC thus represent a degree of compensation for such processes absent from the liver TCA cycle model in addition to the reported estimates, and are hence greater in relation to the TCA cycle flux than reported experimentally.

5. In this study, we have analysed how flux in the mammalian liver tricarboxylic acid cycle varies with changes in the activity of its enzymes. Through the application of

Metabolic Control Analysis (MCA) to liver TCA cycle models, and also to a suite of test models, we show that the control of flux in systems containing one or more enzymes that are saturated with respect to substrate(s) displays a characteristic pattern of sharp, sigmoidal transitions between two or more key processes, with only relatively small changes in enzyme maximal activity. However, for the variation in flux control coefficients in response to a change in enzyme activity, a hyperbolic relationship would normally be expected, under ideal conditions. This characteristic pattern of sigmoidal C^J distribution is observed in both cyclical and linear systems. Moreover, although this phenomenon can allow control within the system to be dominated by a single process when maximal activity is low, MCA of the liver TCA cycle model suggests that the TCA cycle could be poised at a point where control is shared evenly between several processes. Our findings are in agreement with a theoretical analysis of another compartmentalized metabolic cycle, the Calvin cycle (Fell et al., 1999; Letellier et al., 1994). Consequently, existence of such a relationship between the control of flux and enzyme activity, establishes a strict limitation on the achievable increase in flux by activating any single enzyme; since such single-point activation results in a rapid loss of influence over flux by the given enzyme. Therefore, in order to increase the overall flux significantly, control mechanisms must act at multiple sites within the system (Fell, 1997; Fell and Thomas, 1995; Korzeniewski et al., 1995). In fact, there is indeed evidence for control mechanisms acting at multiple sites within the TCA cycle, *e.g.* through Ca^{2+}-mediated enzyme activation (Denton and McCormack, 1995) and via lysine acetylation (Zhao et al., 2010). As mentioned by Kacser and Burns, for a given metabolic system, an even distribution of flux control serves as the obvious advantage that global fluxes become relatively insensitive to large variations in enzyme concentrations (Kacser and Burns, 1981).

However, it must be noted that the liver TCA cycle models investigated in this study do not reflect the true complexity of real systems and it is possible that the properties demonstrated by these models could be suppressed *in vivo*; to our knowledge, these properties have not yet been reported in any experimental system. Indirect evidence can be found in a recent study conducted by Bennett et al.; which suggests that the potential for generating observed flux control behaviour may also exist *in vivo*, by demonstrating that the metabolite concentrations can in fact be considerably in excess of the K_m values (Bennett et al., 2009). Although, this study also implies that the TCA cycle enzymes tend not to be saturated in prokaryotes, it is not necessarily true for eukaryotic cells, due to the mitochondrial localisation of TCA cycle. Also, a comprehensive literature survey showed that several metabolite concentrations may be up to ten times higher within mammalian mitochondria than in the cytosol (or when averaged across the total cell volume), and are often found to be considerably in excess of the corresponding K_m values. For instance, a high mitochondrial concentration of

acetyl-CoA (from 0.2 to 2 mM) compared to the PC K_a value (0.06 mM) and the resulting prospect that pyruvate carboxylase is therefore likely to be saturated under mitochondrial conditions, has been noted previously (Kimmich and Rasmussen, 1969; McClure and Lardy, 1971).

Furthermore, we speculate that conserved cycles, particularly when compartmentalized, may routinely operate at near-saturation conditions; under other circumstances this situation would in fact be potentially disastrous (*e.g.* linear systems) (Cornish-Bowden, 2012). But, in a cyclical system such as the TCA cycle or the Calvin cycle, the evolution of regulatory mechanisms to prevent saturation would be redundant in the face of obligatory mass conservation imposed by the structure of the system.

Lastly, it must be noted that the saturation-dependent properties identified in the liver TCA cycle models, highlight the importance of using saturable enzyme kinetics in a mathematical model to represent the individual rate equations.

6. During the flux control analysis of liver TCA cycle models, we observed a rapid exchange of control between PDH and other key TCA cycle enzymes, as the PDH maximal activity increases. It highlights not only the importance of accurately reflecting PDH maximal activity in the model, but also has implications when considering the significance of many regulatory interactions of pyruvate dehydrogenase. For modelling purposes, we have assumed a constant PDH activity and regulation only by product inhibition. Yet, the current analysis indicates that including the PDH regulation by covalent modification in this model would be beneficial, particularly since the model variables (*i.e.*, pyruvate, acetyl-CoA, & NADH) act as allosteric effectors of pyruvate dehydrogenase kinase (PDHK) (Holness and Sugden, 2003). Moreover, if these observations are also true in the case of a real system, they could provide a slightly different perspective on the physiological significance of various PDH regulatory mechanisms. However, it is interesting to note that the liver TCA cycle model is poised at a point where the control over flux is distributed largely between PDH, PC, & ATP synthase, in such a way that the system is maximally responsive to changes in the activity of each of these key enzymes, while minimizing the influence of other TCA cycle reactions. Provided the same behaviour is also observed *in vivo*, such a phenomenon may reflect the functional organization of the system and facilitate a dynamic balance between the demands of gluconeogenesis and ATP production.

7. A high degree of control shared by SDH in liver TCA cycle models, indicates the importance of expanding the succinate dehydrogenase reaction to include the FAD/$FADH_2$ dynamics; that is to include a comprehensive representation of Complex II or

succinate-CoQ reductase (EC 1.3.5.1), an integral component of the Electron transport chain (ETC). Also, a high degree of control shared by ATP synthase indicates the importance of including fully developed modules of electron transport chain as well as ATP synthase. Such expansion would also include the oxygen consumption reaction in the form of an appropriately expanded representation of Complex IV or cytochrome c oxidase (EC 1.9.3.1); which would make the mammalian liver-specific model further aligned with the experimental observations. Moreover, including the fully developed ETC as well as ATPsynth modules has an additional significance with respect to a possible expansion of PDH kinetics that reflects its regulation by covalent modification is considered. Since, as shown earlier, ATPsynth is one of the highly controlling enzymes in the model, which acquires most of the control lost by PDH.

Therefore, this study of the liver TCA cycle models proved to be instrumental in enhancing our understanding of certain modelling fundamentals that are essential for building kinetic/ dynamic models of cellular metabolism, such as — *modelling strategy*, *model design*, *choice of rate equations*, *parameter selection*, *model boundary conditions etc.* Moreover, it informed us not only about the approximate structural aspects, but also the rough dynamic behaviour for the proposed and soon-to-be-built mammalian heart- or skeletal muscle-specificTCA cycle model. Accordingly, we followed the same modelling strategy to construct a 'consensus' kinetic model of TCA cycle in mammalian heart or skeletal muscle mitochondria, which is neither over-simplified nor too complex in terms of rate equations, reversibility of reactions and regulatory interactions.

Chapter 3

Heart TCA cycle prototype: a *"PC knock-out"* model (PC_{ko})

3.1 Overview

In this chapter we will look at a prototype of the heart TCA cycle model, which is actually a derivative of the updated liver TCA cycle model. We started studying the existing liver TCA cycle model to understand the basic functional properties of a tissue-specific TCA cycle and it provided a strong knowledge base for building a heart or skeletal muscle-specific TCA cycle model. Moreover, if modified slightly, the existing model provides an opportunity to glance at the rough qualitative nature of a heart-specific TCA cycle model, prior to building one.

As mentioned earlier in the previous chapter (see, pg. 18), in mammalian heart as well as skeletal muscle tissue, literature evidence suggests that the anaplerotic contribution of PC to the total flux through the TCA cycle is insignificant as compared to that in liver (Gibala, 2003; Gibala et al., 2000; Owen et al., 2002; Scrutton and Utter, 1968). Therefore, in order to construct a heart TCA cycle model prototype, the liver TCA cycle model needs to be modified by removing the anaplerotic contribution of pyruvate carboxylase, so that the resultant *'derivative'* system would be somewhat similar to the physiological description of a heart or skeletal muscle-specific TCA cycle model.

In Section 3.2, we shall discuss the definition & construction of a heart TCA cycle model prototype in further detail. Section 3.3 (see, pg. 124), describes an in-depth analysis of the emergent dynamic properties of this heart TCA cycle model prototype.

3.2 Methods: Model construction and definition

In a separate copy of the existing updated liver TCA cycle model, the pyruvate carboxylase (PC) reaction was *"switched off"* (*i.e.* deleted) to form a heart TCA cycle model prototype; henceforth be referred to as - ***"PC knock-out" model (PC_{ko})***. Likewise, the existing liver TCA cycle model will be referred to as - ***"PC wild-type" model (PC_{wt})***. The heart TCA cycle model prototype or the PC_{ko} model is illustrated in fig. 3.1.

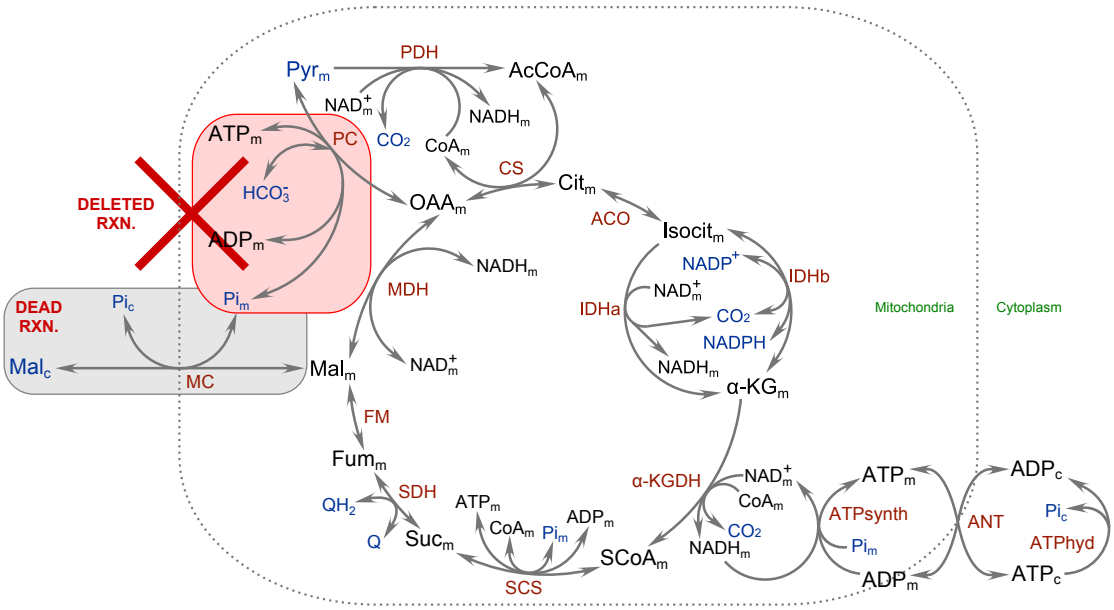

- **Figure 3.1.** Schematic illustrating the TCA cycle reactions in the PC_{ko} model.
- Internal metabolites: in *Black*; external metabolites: in *Blue*; reaction/ enzyme names: in *Red*.
- Reaction with double arrowheads is assumed to be reversible and reaction with single arrowhead is assumed to be irreversible.
- Pyruvate carboxylase (PC) reaction is deleted from the PC_{ko} model and is shown here against a red background and as a consequence, the malate carrier (malate-phosphate transporter) (MC) reaction carries infinitesimally small amount of flux and is therefore a "dead reaction" which is shown here against a grey background.

As illustrated in Figure 3.1, the PC_{ko} model only includes the heart or skeletal muscle-specific TCA cycle reactions as a result of the modifications described here. However, in spite of these modifications, PC_{ko} model is still essentially the updated liver TCA cycle model, albeit with zero pyruvate carboxylase activity. Also worth noting is that these changes do not affect the existing conservation relationships described in the earlier chapter on liver TCA cycle model (see tbl. 2.5 on pg. 34). *Apart from the changes shown here, no other reactions, variables, or parameters were modified while constructing the PC_{ko} model.*

3.3 Results for the heart TCA cycle prototype

In this section, we will take a quick look at the kinetic as well as structural properties of the PC_{ko} model in comparison with that of the PC_{wt} model. Briefly, following types of results will be presented:

1. Elementary modes analysis & Enzyme subset analysis (see, pgs. 124 and 125)

2. Initial steady-state data & Steady-state analysis (see, pg. 126)

3. Metabolic Control Analysis (MCA) results (see, pg. 139)

To begin with, in the following section, we shall establish the possible differences in structural properties between the two models.

3.3.1 Elementary modes analysis of the heart TCA cycle prototype

Since, the pyruvate carboxylase reaction is absent in the *"PC knock-out"* model, the PC containing elementary modes present in the PC_{wt} model, are no longer functional in this model. As a result, the PC_{ko} model contains only 3 elementary modes that are PC -independent and exactly identical to the corresponding modes of the PC_{wt} model (see tbs. 2.3 and 2.4 on pg. 33). The PC_{ko} elementary modes are presented in tbl. 3.1 and corresponding elementary mode stoichiometries are presented in tbl. 3.2.

	Heart TCA cycle prototype - reactions										*ATP/ ADP- linked reactions*		
Modes	**PDH**	**CS**	**ACO**	**IDHa**	**IDHb**	**α-KGDH**	**SCS**	**SDH**	**FM**	**MDH**	**ATPsynth**	**ATPhyd**	**ANT**
ElMo 0	*0*	*0*	*0*	1	**-1**	*0*	*0*	*0*	*0*	*0*	0.25	2.5	2.5
ElMo 1	1	1	1	*0*	1	1	1	1	1	1	0.75	8.5	8.5
ElMo 2	1	1	1	1	*0*	1	1	1	1	1	1	11	11

- **Table 3.1.** A table showing elementary modes for the PC_{ko} model.
- For each mode, fractions have been converted decimals.

	Reactants		Products	
ElMo 0 :	2.5 Pi_m + NADPH	⟶	$NADP^+$ + 2.5 Pi_c	(1)
ElMo 1 :	8.5 Pi_m + Pyr_m + $NADP^+$ + Q	⟶	3 CO_2 + NADPH + QH_2 + 8.5 Pi_c	(2)
ElMo 2 :	11 Pi_m + Pyr_m + Q	⟶	3 CO_2 + QH_2 + 11 Pi_c	(3)

- **Table 3.2.** Net stoichiometries for elementary modes presented in tbl. 3.1.
- All metabolites in this table are, by necessity, external in the modelling sense.
- For each net stoichiometric equation, fractions have been converted decimals.

ElMo$_{[1]}$ & ElMo$_{[2]}$ describe the structural framework of a mammalian heart or skeletal muscle-specific TCA cycle, as seen in the earlier chapter on liver TCA cycle model (see fig. 2.6 on pg. 38). These two elementary modes are actually the same mode with different isocitrate dehydrogenase (IDH) activity, where ElMo$_{[1]}$ is IDHb -dependent and ElMo$_{[2]}$ is IDHa -dependent. Due to the participation of different isocitrate dehydrogenases, these two modes also differ in terms of total amount of ATP$_m$ produced via ATP synthase reaction. For instance, the IDHb -dependent mode (ElMo$_{[1]}$) produces a total of 2.5 fewer ATP$_m$ molecules than the IDHa -dependent mode (ElMo$_{[2]}$), as it lacks one of the NADH -producing dehydrogenases (IDHa). The substrate-level phosphorylation via succinyl-CoA synthetase (SCS) accounts for the additional ATP$_m$ molecule produced by these modes.

ElMo$_{[0]}$ describes the internal substrate cycle in which α-ketoglutarate generated by IDHa is converted back to isocitrate by IDHb. In fact, literature suggests that not only such a cycle exists in both heart and liver (Huang and Colman, 2005; Londesborough and Dalziel, 1968; McCormack and Denton, 1981; Rutter and Denton, 1988; Sazanov and Jackson, 1993), but also that IDHb carries a reverse flux in perfused rat hearts under normoxia as well as ischemia (Comte et al., 1997, 2002). Further details regarding ElMo$_{[0]}$ can be seen in the earlier chapter on liver TCA cycle model (see fig. 2.7 on pg. 38).

3.3.2 Enzyme subset analysis of the heart TCA cycle prototype

The PC_{ko} enzyme subsets (ESS) are shown in fig. 3.2.

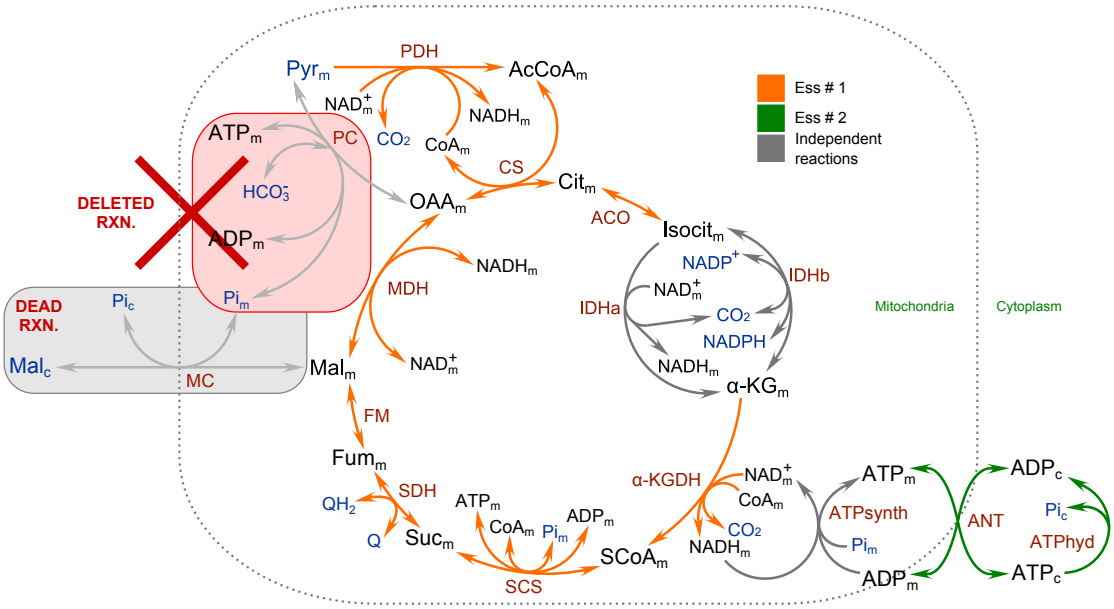

- **Figure 3.2.** Schematic showing enzyme subsets for the PC_{ko} model.
- Internal metabolites: in *Black*; external metabolites: in *Blue*; reaction/ enzyme names: in *Red*.
- Reversible reactions: double arrowheads and irreversible reactions: single arrowhead.

In the PC_{ko} model, similar to the effect observed in the case of elementary modes, the deletion or *"switching-off"* of pyruvate carboxylase reaction completely eliminates the 'ESS #1'; which is an enzyme subset originally present in the PC_{wt} model that comprised PC & MC. As a result, as illustrated in fig. 3.2 (see, pg. 125), the PC_{ko} model contains only two enzyme subsets.

'ESS #1' from the PC_{ko} model includes 8 out of 9 canonical TCA cycle reactions and is interrupted by IDHa & IDHb, which act as independent reactions. Whereas, 'ESS #2' includes ANT & ATPhyd. Also, as seen earlier in PC_{wt}, IDHa, IDHb and ATPsynth remain as independent reactions in the PC_{ko} model, as well.

Furthermore, the removal of PC, turns MC into a *"dead reaction"*, which carries an infinitesimally small amount of flux and also causes MDH to become a constituent reaction of 'ESS #1' in the PC_{ko} model. Originally, in the PC_{wt} model, MDH operated as an *'independent reaction'* along with IDHa, IDHb and ATPsynth.

3.3.3 Steady-state analysis for the heart TCA cycle prototype

In order to analyse the emergent dynamic properties of the PC_{ko} model, we begin by comparing its *"initial steady-state"* composition with that of the PC_{wt} model. The reaction fluxes are shown in fig. 3.3 and metabolite concentrations in fig. 3.4, respectively.

Note: Both the PC_{wt} & PC_{ko} models are essentially liver TCA cycle models, with different pyruvate carboxylase (PC) activities; which means that all the enzyme kinetics and metabolite concentration data applied to the PC_{ko} model is still liver tissue-specific. It is possible that in the skeletal or cardiac muscle tissue, the resting metabolite concentrations as well as the kinetics data for these same TCA cycle enzymes could differ from that in the liver tissue. ***Therefore, it is important to view the PC_{ko} results from a qualitative perspective only.***

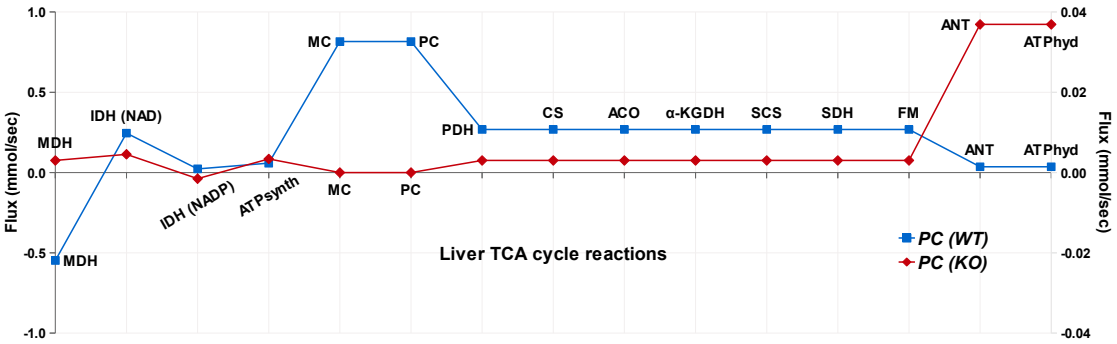

- **Figure 3.3.** Reaction fluxes of PC_{wt} & PC_{ko} models, at initial steady-state.

- **Blue line** : PC_{wt} flux data; **Red line** : PC_{ko} flux data.
- ***Primary Y-axis:*** PC_{wt} data; ***Secondary Y-axis:*** PC_{ko} data.

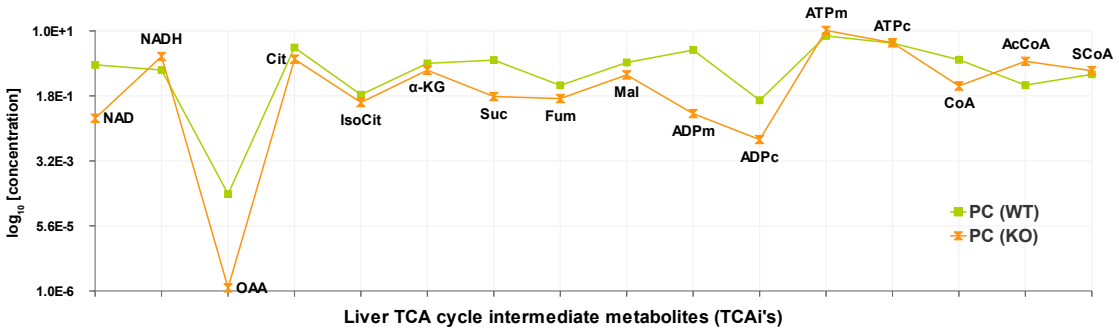

- **Figure 3.4.** TCAi concentrations of PC_{wt} & PC_{ko} models, at initial steady-state.
- **Green line** : PC_{wt} concentration data; **Orange line** : PC_{ko} concentration data.
- ***Y-axis:*** $\log_{10}$[metabolite concentration] – metabolite concentration in logarithmic scale.

From figs. 3.3 and 3.4, we can observe the following:

1. Removal of PC from the PC_{ko} model causes the the flux through malate carrier (MC) to reduce significantly to an infinitesimally small amount when compared to the PC_{wt} initial steady-state MC flux. For instance, in PC_{ko}, the MC flux equals to 3.5E-10 mmol/sec, at initial steady-state. Whereas, in the PC_{wt} model, it is nearly 3 times the TCA cycle flux. Possible factors causing MC to become a "dead reaction" in PC_{ko}, could be as follows —

(A) Complete removal of the enzyme subset that comprised PC & MC, due to the deletion of pyruvate carboxylase reaction from PC_{wt}; which essentially makes the malate carrier reaction structurally extraneous or "dead";

(B) As shown in the earlier chapter on liver TCA cycle model (see fig. 2.18 on pg. 59), some amount of oxaloacetate produced by PC flows directly out of the TCA cycle via MC; since in PC_{wt}, MDH is an *'independent reaction'* that works in a reverse direction and at a higher rate than that of the TCA cycle flux. However, in the PC_{ko} model, malate dehydrogenase functions in its forward direction, producing OAA_m from Mal_m and it also constitutes the TCA cycle enzyme subset ('ESS #1'); which means that the malate concentration is highly constrained to flow out of the TCA cycle via MC ; and

(C) In the absence of pyruvate carboxylase, the PC_{ko} TCA cycle flux is significantly reduced; which means that the TCA cycle probably produces just enough malate to help sustain that same level of flux through the cycle.

Moreover, in the PC_{ko} model, if the malate carrier (MC) would have been knocked out along with PC, then all the TCA cycle intermediates would have formed a conservation relationship; wherein, the total TCAi content would have remained constant at the start of model simulation. However, since the malate carrier was not removed from the PC_{ko} model, the conservation relationship of TCAi does not exist and the malate carrier reaches equilibrium with the cytosolic malate concentration in such a way that at steady-state, the malate carrier reaction becomes *'dead'* (as it is

structurally required to be). However, the infinitesimally small amount of flux can be observed because the malate carrier reaction allows the TCA cycle intermediates to *'equilibrate'* by exchange with the cytosolic malate pool. Physiologically, in the absence of PC, it is assumed that the cytosolic malate concentration is buffered by the amino acid metabolism and uptake of amino acids from the blood. Also, as shown in eq. B.34 from Appendix B (see, pg. 231), the malate carrier reaction comprises a single internal metabolite (mitochondrial malate) and three external metabolites of fixed concentrations (cytosolic malate & inorganic phosphate; and mitochondrial inorganic phosphate); due to which the malate carrier flux could become *zero*, given the right set of conditions.

2. *"Switching-off"* PC in the PC_{ko} model causes the TCA cycle flux (flux through CS) to reduce by *approx.* 89-fold, as compared to that in the PC_{wt} model. In mammalian liver tissue, literature suggests that the PC flux is on average around 3 times the TCA cycle flux (Baranyai and Blum, 1989; Beylot et al., 1995; Des Rosiers et al., 1995; Di Donato et al., 1993; Magnusson et al., 1991; Rabkin and Blum, 1985). Therefore, it is possible that in the absence of PC as well as any other anaplerotic mechanism, the TCA cycle flux in mammalian skeletal or cardiac muscle tissue is significantly lower than that in the hepatic tissue.

3. In the PC_{ko} model, IDHa & IDHb are reduced by *approx.* 54- & 15-fold, respectively, in comparison to the PC_{wt} model. Also, in the PC_{ko} model, IDHb acts in the reverse direction; whereas, it works in the forward direction in PC_{wt}.

4. Between the two models, the 'ESS #2' reactions, ANT & ATPhyd remain virtually unchanged. In the PC_{wt} model, PC & ATPhyd are both *ATP-hydrolysing reactions*; with PC hydrolysing ATP_m during the carboxylation of Pyr_m to OAA_m and ATPhyd hydrolysing ATP_c in to ADP_c & Pi_c. In the PC_{ko} model, in the absence of PC, ATPhyd is the only ATP-hydrolysing reaction. Since, the mitochondrial energy metabolism in skeletal and cardiac muscle tissues is highly demand-driven; the role of ATPhyd in a metabolic system like the one described by PC_{ko} thus becomes more important.

5. In the initial steady-state of the PC_{ko} model, OAA_m concentration decreases the most by *approx.* 335-fold, as compared to that in PC_{wt}. Among all TCAi's, succinate shows the next largest decrease, by *approx.* 10-fold. Whereas the remaining TCAi's, such as – Cit_m, $Isocit_m$, αKG_m, Fum_m, & Mal_m, all show relatively small reductions in their respective concentrations by *approx.* 1.5–2.0 -fold.

Figure 3.5 shows the differences in key metabolite ratios between PC_{wt} & PC_{ko} models, at initial steady-state.

NAD^+_m (by *approx.* 27-fold), ADP_m (by *approx.* 52-fold), ADP_c (by *approx.* 11-fold), & CoA_m (by *approx.* 5-fold) – all show moderate to large reductions in the PC_{ko} model,

in comparison with the PC_{wt} model. Since, these 4 metabolites form 4 separate conservation relationships in the PC_{ko} (as well as, PC_{wt}) model, corresponding members of these conservation relationships show increase in their respective concentrations. As a result, key ratios involving these metabolites change significantly between the PC_{wt} & PC_{ko} models and fig. 3.5 shows these changes in detail.

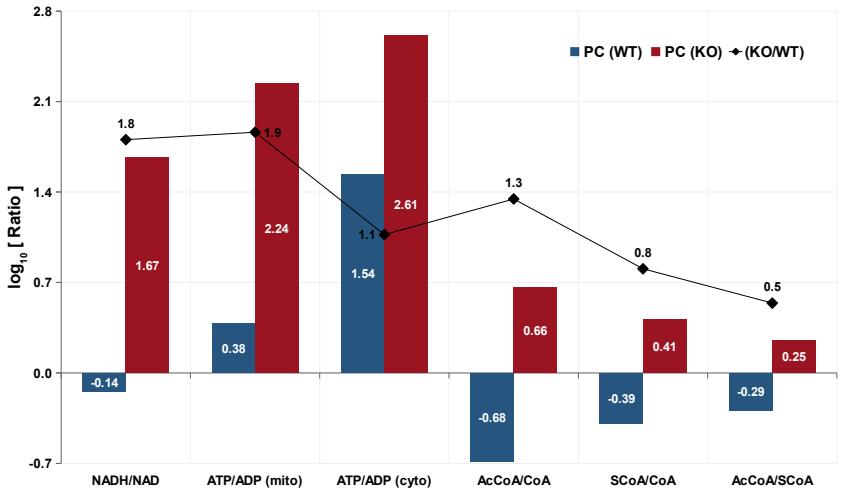

▪ **Figure 3.5.** Key metabolite ratios in PC_{wt} & PC_{ko}, at initial steady-state.

▪ **Blue bars :** PC_{wt} data; **Red bars** : PC_{ko} data. ▪ **Black line : log$_{10}$[Fold difference]** between the two models. The fold difference was calculated as – *[(Metabolite ratio in PC_{ko}) / (Metabolite ratio in PC_{wt})]*.

In fig. 3.5, difference in the $[\text{NADH}/\text{NAD}^+]_\text{m}$ ratio between the two models suggests a crucial qualitative switch in the initial redox state of these systems. PC_{wt} is an oxidised system with $[\text{NADH}/\text{NAD}^+]_\text{m}$ = *approx.* 0.7; whereas, PC_{ko} is a highly reduced system with $[\text{NADH}/\text{NAD}^+]_\text{m}$ = *approx.* 46.0. Although, in the case of mammalian skeletal or cardiac muscle mitochondria, the actual ratio may not be as high, it is still qualitatively significant; since, literature suggests that the muscle mitochondria are comparatively more reduced than the liver mitochondria (Kobayashi and Neely, 1979). Significant improvement in the $[\text{ATP}/\text{ADP}]_\text{m}$ & $[\text{ATP}/\text{ADP}]_\text{c}$ ratios in the PC_{ko} model, could be due to the PC removal and MDH operating in the forward direction, thereby producing more NADH_m than that in the PC_{wt} model.

Now, for the PC_{wt} & PC_{ko} models, let's look at the specific flux & concentration profiles using steady-state scans across a fixed range of increasing maximal activity of PDH ($\text{V}_\text{max}^\text{PDH}$ scan) and Pi_m concentration, respectively. Figure 3.6 (see, pg. 131) describes the dynamic response of TCAi's from PC_{wt} as well as PC_{ko} to changes in $\text{V}_\text{max}^\text{PDH}$ & Pi_m concentration. Figures 3.7 and 3.8 (see, pgs. 132 and 133) show the dynamic response of key TCA cycle reaction fluxes from PC_{wt} as well as PC_{ko} to changes in Pi_m concentration & $\text{V}_\text{max}^\text{PDH}$, respectively.

Note: The relative change in TCAi's and reaction fluxes is mostly quantitative in nature and hence presented here as bar graphs. The original steady-state analysis plots are included in the supplementary material. Details are given in the respective graphs.

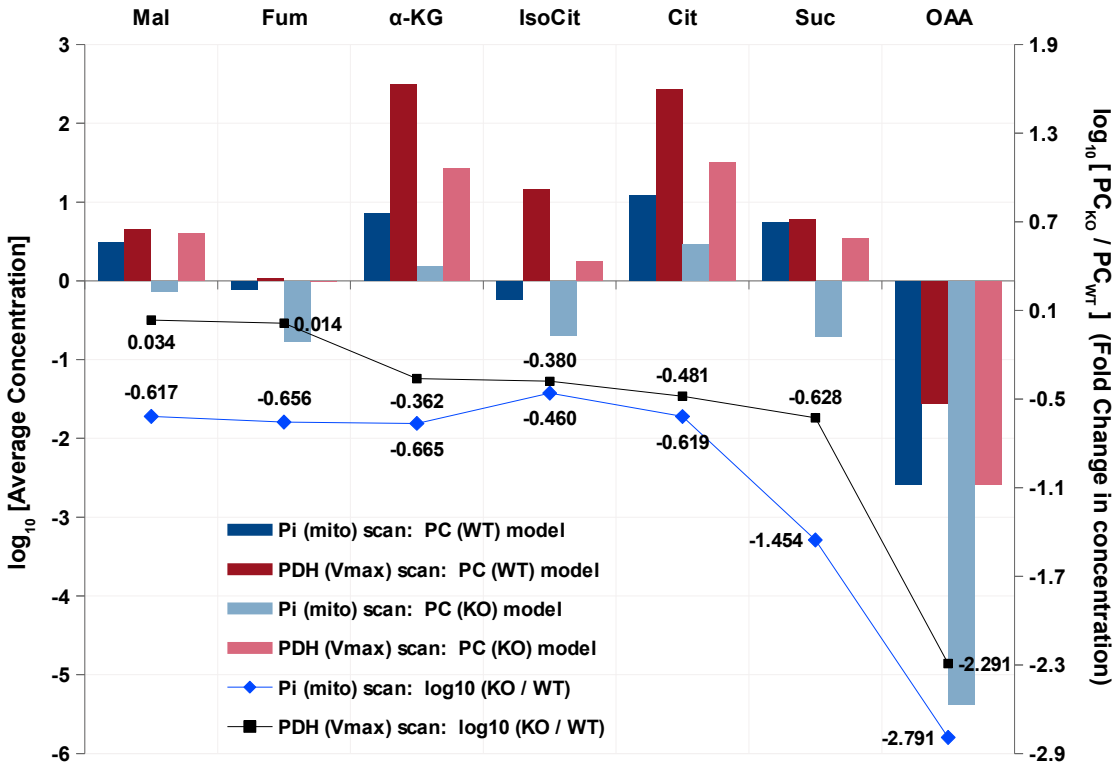

3.6.a. TCA cycle intermediate metabolites (TCAi)

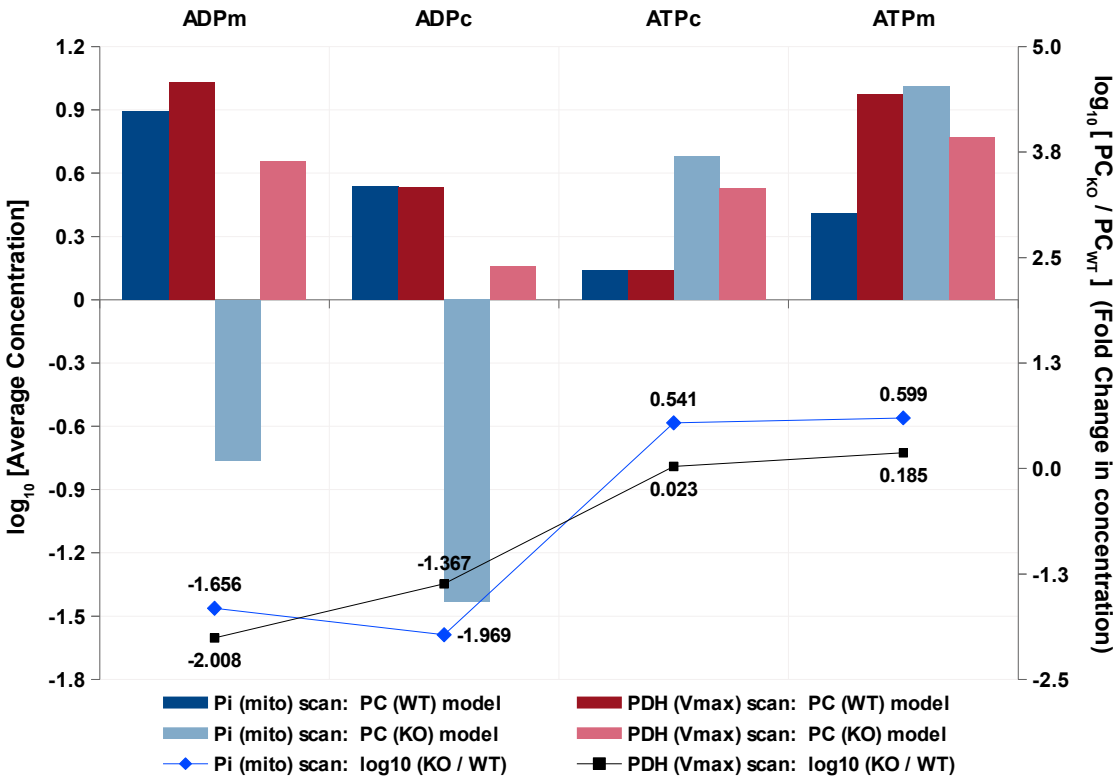

3.6.b. ATP−related metabolites

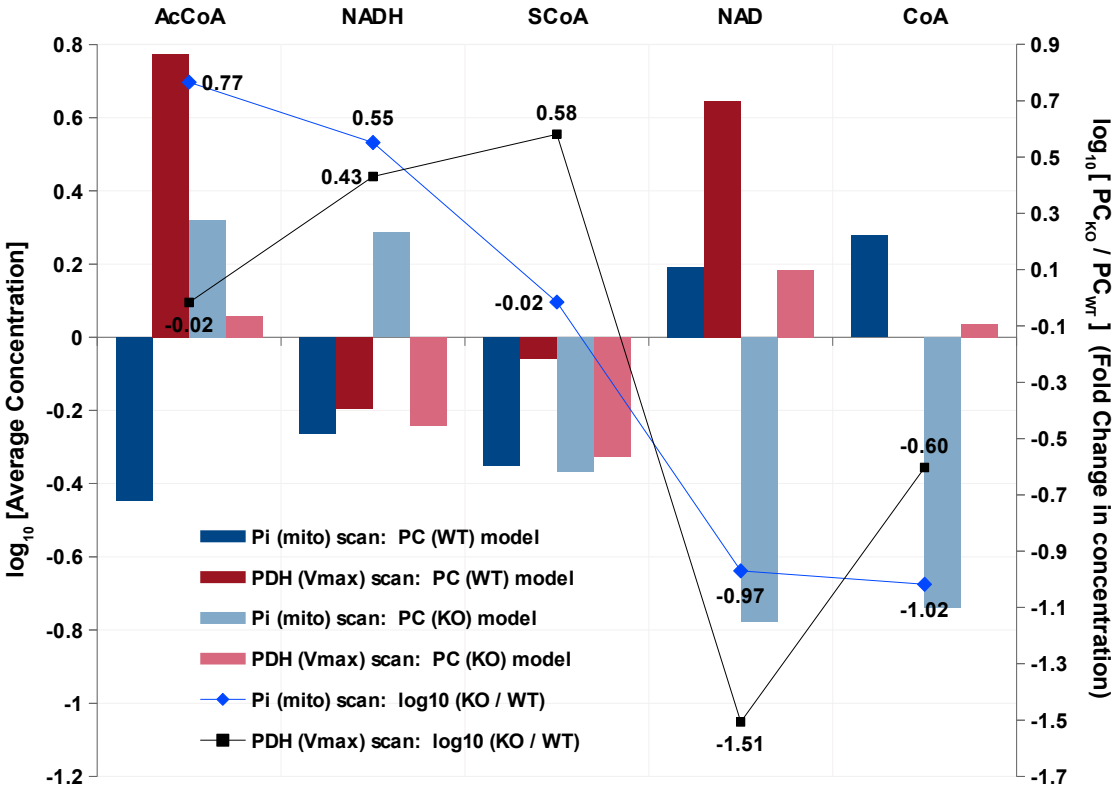

3.6.c. NAD- & CoA−related metabolites

▪ **Figure 3.6. Concentrations of TCAi's :** effect of PC *'knock-out'* (PC_{ko}) in comparison with the PC *'wild-type'* (PC_{wt} *i.e.* $LVR_{TCA}{}^{UPD}$).

▪ **This is a combined bar graph for the dynamic response of TCAi concentrations from PC_{wt} as well as PC_{ko} to changes in Pi_m concentration & the maximal activity of PDH (V_{max}^{PDH}), respectively. Four different bars represent four separate piece of data for the two liver TCA cycle models (*i.e.* PC_{wt} & PC_{ko}, respectively) – two each for [Pi_m] & V_{max}^{PDH}.**

▪ **Red bars** represent the steady-state data for change in V_{max}^{PDH}; whereas, **Blue bars** show the data for change in [Pi_m]. In both colours, *darker* bars represent the PC_{wt} data and *lighter* bars represent the PC_{ko} data, respectively.

▪ An average concentration value was calculated for each metabolite from all consecutive steady-state values per dataset. These were then used in the form of ***log_{10}*** values to generate the actual bar graph. For each common parameter, *i.e.* – [Pi_m] or V_{max}^{PDH}; a fold difference was calculated as –
[(avg. conc. in PC_{ko} model)/(avg. conc. in PC_{wt} model)] and was represented in the graph as –
log_{10}[(avg. conc. in PC_{ko} model)/(avg. conc. in PC_{wt} model)]

▪ ***Primary Y-axis (left) :*** log_{10}[average concentration] of TCAi's in logarithmic scale.

▪ ***Secondary Y-axis (right) :*** log_{10}[(avg. conc. in PC_{ko} model)/(avg. conc. in PC_{wt} model)] – fold difference of [(avg. conc. in PC_{ko} model)/(avg. conc. in PC_{wt} model)] in logarithmic scale.

▪ **Blue line** represents the *log_{10}[Fold difference] w.r.t.* the change in [Pi_m] and **Black line** represents the *log_{10}[Fold difference] w.r.t.* the change in V_{max}^{PDH}. *Both lines are drawn aligned to the 'Secondary Y-axis'.*

▪ ***Supplementary data for figs. 3.6a, 3.6b and 3.6c is shown in figs. II.1, II.2, II.3 and II.4 on pgs. XXIII to XXVI, respectively.***

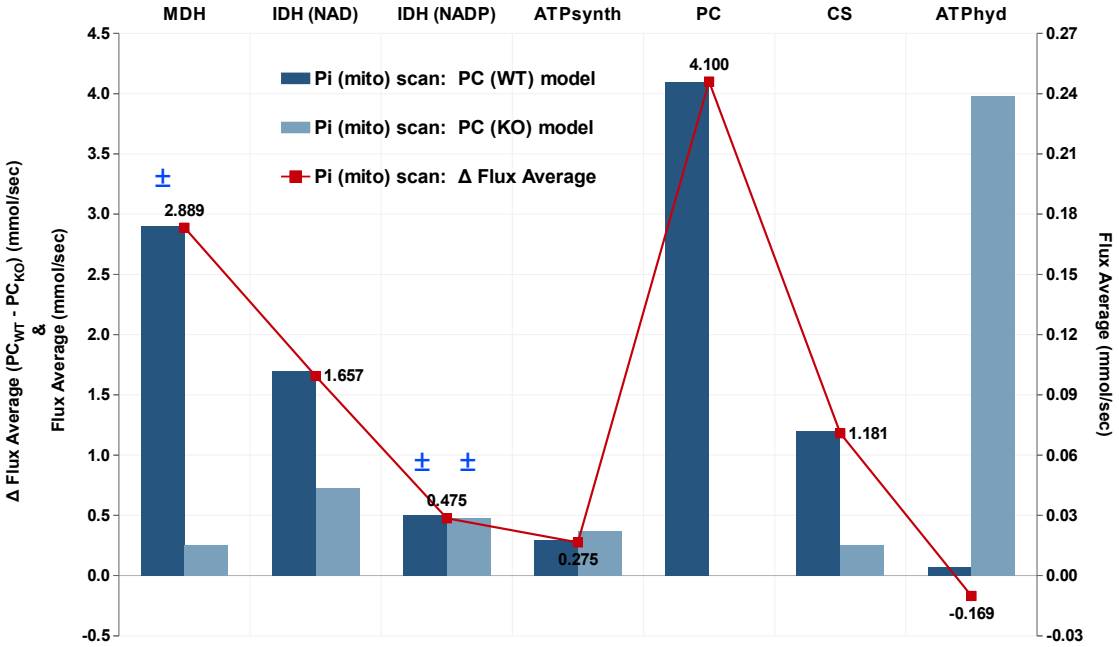

▪ **Figure 3.7. TCA cycle fluxes against increasing conc. of [Pi_m] :** effect of PC *'knock-out'* (PC_{ko}) in comparison with PC *'wild-type'* (PC_{wt} *i.e.* $LVR_{TCA}{}^{UPD}$).

▪ **This is a combined bar graph showing the dynamic response of key TCA cycle reaction fluxes from *PC_{wt}* as well as *PC_{ko}* to changes in Pi_m concentration.**

▪ **Dark Blue bars** represent the PC_{wt} steady-state data and the **Light Blue bars** represent the PC_{ko} steady-state data.

▪ An average flux value was calculated for each reaction from all consecutive steady-state values per dataset. These were then used to generate the actual bar graph. A difference of respective average flux values between the PC_{wt} & PC_{ko} models was calculated as – **Δ Flux Average (*PC_{wt}* - *PC_{ko}*)**.

▪ Since, in the case of a reaction flux, the negative sign signifies only the direction taken by a reaction in a steady-state; in this graph, the average flux value was considered as a positive number for those reactions that function in their respective reverse directions. **All such reactions are denoted by** ± .

▪ ***Primary Y-axis (left) :*** Average Flux & Δ Flux Average (PC_{wt} - PC_{ko}), mmol/sec.

▪ ***Secondary Y-axis (right) :*** Average Flux, mmol/sec.

▪ **Dark Blue bars** for the PC_{wt} model are aligned to the ***Primary Y-axis (left)***; whereas, **Light Blue bars** for the PC_{ko} model are aligned to the ***Secondary Y-axis (right)***.

▪ **Red line** represents the Δ Flux Average (PC_{wt} - PC_{ko}) and is drawn aligned to the ***Primary Y-axis (left)***.

▪ ***Supplementary data shown in fig. II.5 on pg. XXVII.***

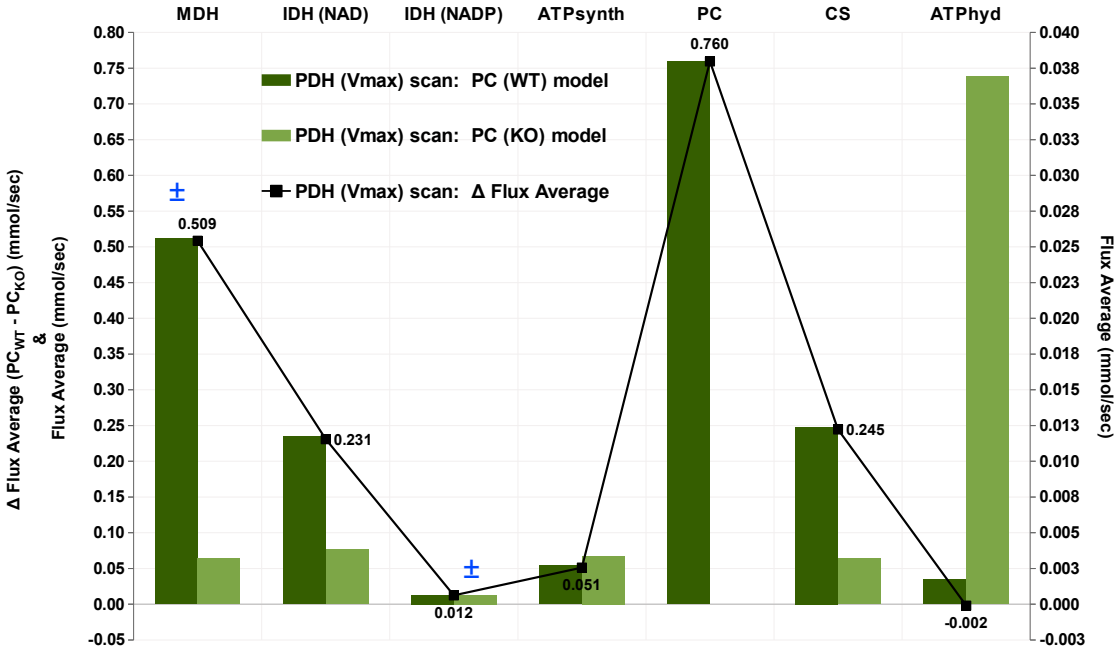

▪ **Figure 3.8.**
TCA cycle fluxes against the increasing maximal activity of PDH : effect of PC *'knock-out'* (PC_{ko}) in comparison with PC *'wild-type'* (PC_{wt} *i.e.* $LVR_{TCA}{}^{UPD}$).

▪ **This is a combined bar graph showing the dynamic response of key TCA cycle reaction fluxes from *PC_{wt}* as well as *PC_{ko}* to changes in V_{max}^{PDH}.**

▪ **Dark Green bars** represent the PC_{wt} steady-state data and the **Light Green bars** represent the PC_{ko} steady-state data.

▪ An average flux value was calculated for each reaction from all consecutive steady-state values per dataset. These were then used to generate the actual bar graph. A difference of respective average flux values between the PC_{wt} & PC_{ko} models was calculated as – **Δ Flux Average (*PC_{wt}* - *PC_{ko}*)**.

▪ Since, in the case of a reaction flux, the negative sign signifies only the direction taken by a reaction in a steady-state; in this graph, the average flux value was considered as a positive number for those reactions that function in their respective reverse direction s. **All such reactions are denoted by** ± .

▪ ***Primary Y-axis (left) :*** Average Flux & Δ Flux Average (PC_{wt} - PC_{ko}), mmol/sec.

▪ ***Secondary Y-axis (right) :*** Average Flux, mmol/sec.

▪ **Dark Green bars** for the PC_{wt} model are aligned to the ***Primary Y-axis (left)***; whereas, **Light Green bars** for the PC_{ko} model are aligned to the ***Secondary Y-axis (right)***.

▪ **Black line** represents the Δ Flux Average (PC_{wt} - PC_{ko}) and is drawn aligned to the ***Primary Y-axis (left)***.

▪ ***Supplementary data shown in fig. II.5 on pg. XXVII.***

From figs. 3.6 to 3.8 (see, pgs. 131 to 133), following observations can be made:

1. In PC_{wt} as well as PC_{ko}, excluding the 9 metabolites involved in 4 conservation relationships described in the earlier chapter (see tbl. 2.5 on pg. 34), remaining 7

TCAi's are not conserved within the system and act as free variables. In the PC_{wt} model, PC & MC together represent a large influx–outflux subsystem (see fig. 2.18 on pg. 59); which in theory, allows for relatively large variations in TCAi's compared to that in PC_{ko}. However, whether a particular metabolite concentration exhibits such variations is entirely dependent on how the control of a given metabolite concentration (*i.e.*, concentration control coefficient (C^S)) is shared between all TCA cycle enzymes. In the PC_{ko} model, in absence of PC and a virtually non-existent MC, the allowable variability in metabolite concentrations is significantly reduced compared to the PC_{wt} model. Moreover, the TCA cycle flux (flux through CS) in PC_{ko} is significantly smaller compared to that in PC_{wt}; which could potentially translate to relatively lower steady-state concentrations of individual TCA cycle intermediates. Therefore, mostly as a consequence of the altered structural properties, the difference in relative variations of individual metabolite concentrations between the two models is likely to be substantial in certain cases.

For instance, if we consider the average concentration value of a given metabolite in PC_{wt} as 100% for each steady-state scan dataset (*i.e.*, against the increasing $[\mathrm{Pi_m}]$ or $\mathrm{V_{max}^{PDH}}$, as represented in figs. 3.6 to 3.8), then the average concentration of any PC_{ko} metabolite can be expressed in terms of – *'percent of PC_{wt} concentration'*. PC_{ko} fluxes as well as the total metabolite content (sum of all internal metabolite concentrations) can be expressed similarly. Figures 3.9 and 3.10 (see, pgs. 135 and 136) illustrate the individual PC_{ko} concentrations and fluxes as *'% PC_{wt} concentration/ flux'*, respectively, for the same datasets represented earlier (see, figs. 3.6 to 3.8 on pgs. 131 to 133, respectively).

2. From fig. 3.9, we can observe that for a given parameter scan (across $[\mathrm{Pi_m}]$ or PDH activity), the average total metabolite content of PC_{ko} is reduced by a factor of 25 to 50 % of that in the PC_{wt} model. In fact, even when the two models are simulated at their respective initial conditions, the resultant total metabolite content of PC_{ko}, at *initial steady-state* , shows a 17% decrease compared to that in PC_{wt} (*i.e.*, if we add and compare all TCAi concentrations shown in fig. 3.4 on pg. 127, between the two models); which means that the relative difference in respective TCAi concentrations between these two models exists independent of any further changes in their respective initial conditions and could be due to the factors explained earlier.

3. From this graph, we can also observe that [oxaloacetate] shows the highest percentage reduction in PC_{ko} and considering its initial model value (4.05E-04 mM) as well as the absence of PC in this model, it doesn't seem so unreasonable.

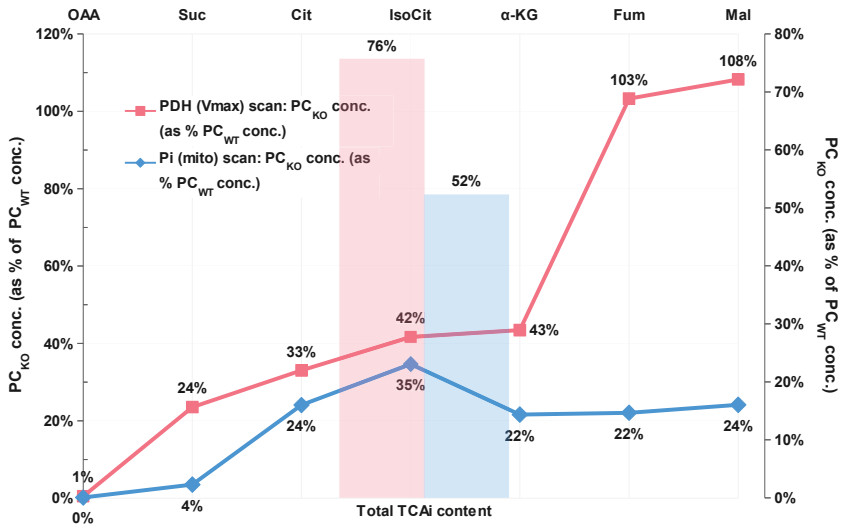

▪ **Figure 3.9. Concentrations of TCAi's in PC_{ko} :** as *'percent of PC_{wt} concentration'* for each metabolite, per dataset (*i.e.*, against $[Pi_m]$ or V_{max}^{PDH}).

▪ **This is a combined graph for the dynamic response of PC_{ko} TCAi concentrations to changes in $[Pi_m]$ & V_{max}^{PDH}, respectively.**

▪ This graph includes only 7 out of 16 TCAi's that are not conserved within the system and act as free variables. Also, this graph shows the same data presented earlier in fig. 3.6 (see, pg. 131), in terms of percentage changes.

▪ **Red line & Red bar :** V_{max}^{PDH} scan data; and **Blue line & Blue bar :** $[Pi_m]$ scan data.

▪ The bars in the background represent the 'Total TCAi content' calculated for each dataset. The total TCAi content is calculated as a sum total of average concentration values for all PC_{ko} TCAi's and not just the 7 TCAi's shown here. The total TCAi content is then represented as '% PC_{wt} concentration' per dataset, same as rest of the data included in this graph.

▪ ***Primary Y-axis (left) :*** PC_{ko} average conc. values, in percent (as % PC_{wt} conc.).

▪ ***Secondary Y-axis (right) :*** PC_{ko} total TCAi content, in percent (as % PC_{wt} conc.).

4. Between the V_{max}^{PDH} & $[Pi_m]$ scans, metabolites from the first half of the TCA cycle (*i.e.*, Cit_m, $Isocit_m$, & αKG_m) show the percentage concentration values within a short range of 20 to 40%; whereas, metabolites from the latter half of the cycle (*i.e.*, Fum_m & Mal_m) show the percentage concentration values within a much larger range of 20 to 110%. The overall reduction in PC_{ko} metabolites is significantly larger for the $[Pi_m]$ scan in comparison with the V_{max}^{PDH} scan; which can be explained based on the fact that increase in $[Pi_m]$ causes the rate of ATP synthase to increase, thereby increasing the TCA cycle substrate utilization and the percentage flux values given in fig. 3.10 (see, pg. 136) agree with this reasoning.

5. The PC_{ko} % flux values described in fig. 3.10, show a significantly larger reduction in almost all fluxes, by nearly 90 – 99% that of the respective PC_{wt} fluxes; except in the case of ATPhyd, which actually increases by 6% against V_{max}^{PDH} and by 244% against $[Pi_m]$. In the absence of PC, PC_{ko} contains a single ATP hydrolysing reaction in the form of ATPhyd and therefore, in this PC_{ko} system, its flux is increased in response to the change in ATP demand.

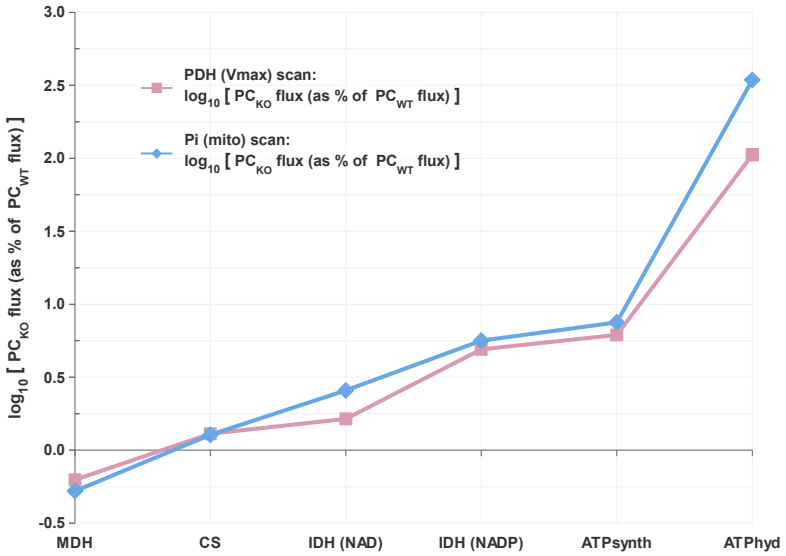

▪ **Figure 3.10.** ***PC$_{ko}$* TCA cycle fluxes :** as *'percent of PC$_{wt}$ flux'* for each TCA cycle reaction flux, per dataset (*i.e.*, against [Pi$_m$] or V_{max}^{PDH}).

▪ **This is a combined graph for the dynamic response of *PC$_{ko}$* fluxes to changes in [Pi$_m$] & V_{max}^{PDH}, respectively.** Also, it shows the same data presented earlier in figs. 3.7 and 3.8, as percentage changes.

▪ Since, in the case of a reaction flux, a negative sign signifies only the steady-state direction of a reaction; therefore, in this graph, the average flux value was considered as a positive number for those reactions that function in their respective reverse directions, before calculating the percentage values. Please refer to figs. 3.7 and 3.8; wherein, all such reactions are denoted by $\pm$.

▪ **Red line :** V_{max}^{PDH} scan data; and **Blue line :** [Pi$_m$] scan data.

▪ ***Y-axis :*** *PC$_{ko}$* average flux values, in percent (as % *PC$_{wt}$* flux), in logarithmic scale.

6. As shown in fig. 3.10, the TCA cycle flux in PC_{ko} is only 1.3% of that in the PC_{wt} model and thus strongly supports the observations made earlier regarding the relative percentage reduction in PC_{ko} metabolite concentrations.

7. From these graphs, we can observe that MDH shows the highest difference in flux between the two models. In fact, the PC_{ko} MDH flux is only 0.5–0.6% that of the PC_{wt} MDH flux in both scans (see, fig. 3.10). However, it is mostly because of the structural difference between these models. Since, MDH acts in the forward direction in PC_{ko} and at a same rate as the TCA cycle flux or 'ESS #1'; whereas in PC_{wt}, it acts as an *independent reaction* that operates in its reverse direction and at a rate higher than the TCA cycle flux.

Despite such detailed analysis, it is important to note that the quantitative aspect of the data shown here essentially highlights the broad qualitative differences between these models; since, they are basically the same model (see, note on pg. 126). Qualitatively, this analysis shows the effects of *zero pyruvate carboxylase activity* on liver TCA cycle metabolites & fluxes, as well as points towards the urgent need for an alternative anaplerotic mechanism in the heart TCA cycle prototype, based on the significantly reduced [oxaloacetate] in PC_{ko}, as shown in fig. 3.9.

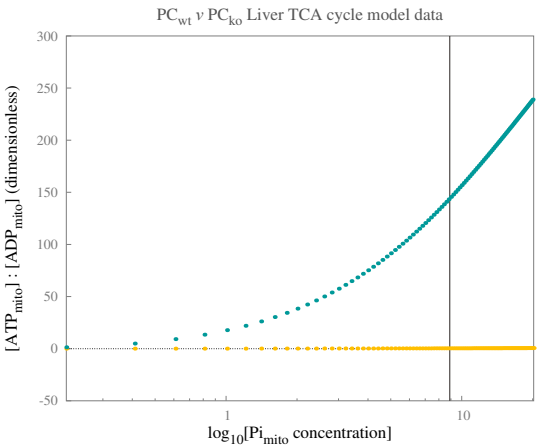

3.11.a. $[ATP/ADP]_m$

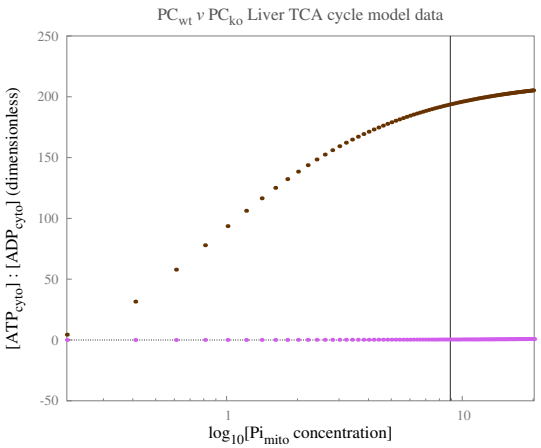

3.11.b. $[ATP/ADP]_c$

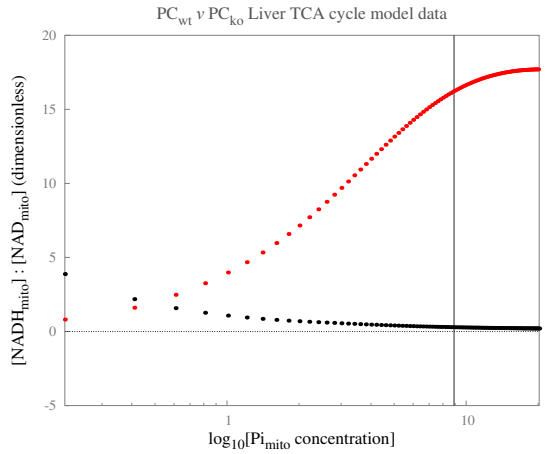

3.11.c. $[NADH/NAD^+]_m$

Median values		
NADH$_m$ / NAD$_m$	Updated model	0.3
	Original model	0.2
ATP$_m$ / ADP$_m$	Updated model	0.4
	Original model	3.5
ATP$_c$ / ADP$_c$	Updated model	0.4
	Original model	2.2

3.11.d. Median values

▪ **Figure 3.11. Variations in the 'Energy status' of the liver TCA cycle models:** $[ATP/ADP]$ & $[NADH/NAD^+]$ ratios across the increasing concentration of $[Pi_m]$.

- Key for figs. 3.11a to 3.11c is as follows :
  - **$[ATP/ADP]_m$:** PC *'wild-type'* (PC_{wt}) ; PC *'knock-out'* (PC_{ko})
  - **$[ATP/ADP]_c$:** PC *'wild-type'* (PC_{wt}) ; PC *'knock-out'* (PC_{ko})
  - **$[NADH/NAD^+]_m$:** PC *'wild-type'* (PC_{wt}) ; PC *'knock-out'* (PC_{ko})

For figs. 3.11a to 3.11c :

- *X-axis* : $\log_{10}[Pi_m]$ – concentration of mitochondrial inorganic phosphate (Pi_m) in logarithmic scale.
- *Y-axis* : Ratio of concentrations (dimensionless).
- The vertical black line represents the initial model value. At this point on the *X-axis*, $[Pi_m] = 8.9$ mM.
- A dotted, black, horizontal line represents the *"zero-axis"* in each figure.
- ***Supplementary data for figs. 3.11a, 3.11b and 3.11c is shown in figs. II.2c, II.2d, II.3c and II.3d on pgs. XXIV to XXV, respectively.***

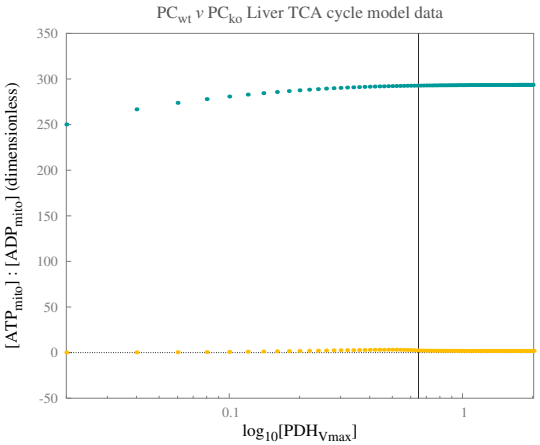

3.12.a. $[ATP/ADP]_m$

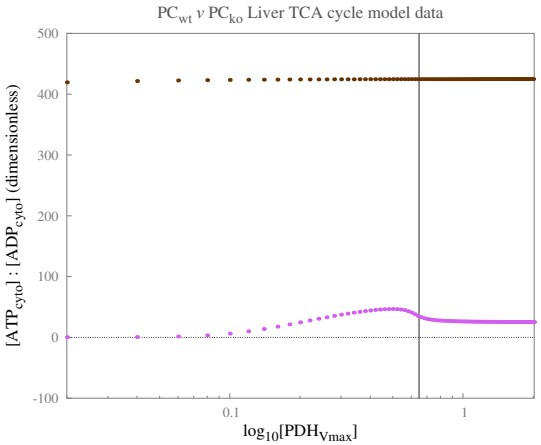

3.12.b. $[ATP/ADP]_c$

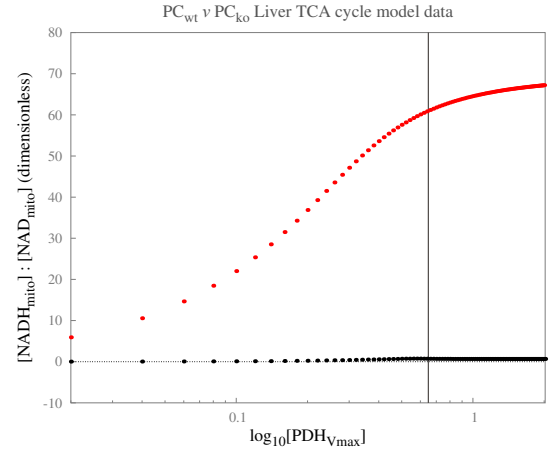

3.12.c. $[NADH/NAD^+]_m$

Median values		
NADH$_m$ / NAD$_m$	PC $_{WT}$ model	0.3
	PC $_{KO}$ model	65.0
ATP$_m$ / ADP$_m$	PC $_{WT}$ model	1.0
	PC $_{KO}$ model	293.0
ATP$_c$ / ADP$_c$	PC $_{WT}$ model	2.3
	PC $_{KO}$ model	425.0

3.12.d. Median values

▪ **Figure 3.12. Variations in the 'Energy status' of the liver TCA cycle models:** [ATP/ADP] & [NADH/NAD$^+$] ratios across increasing maximal activity of PDH (V^{PDH}_{max}).

▪ Key for figs. 3.12a to 3.12c is as follows :

- **[ATP/ADP]$_m$:** PC *'wild-type'* (*PC$_{wt}$*) ; PC *'knock-out'* (*PC$_{ko}$*)
- **[ATP/ADP]$_c$:** PC *'wild-type'* (*PC$_{wt}$*) ; PC *'knock-out'* (*PC$_{ko}$*)
- **[NADH/NAD$^+$]$_m$:** PC *'wild-type'* (*PC$_{wt}$*) ; PC *'knock-out'* (*PC$_{ko}$*)

For figs. 3.12a to 3.12c : ▪ *X-axis* : $\log_{10}[V^{PDH}_{max}]$ – PDH maximal activity in logarithmic scale. ▪ *Y-axis* : Ratio of concentrations (dimensionless). ▪ The vertical black line represents the initial model value. At this point on the *X-axis*, $V^{PDH}_{max} = 0.648$ mM/sec. ▪ A dotted, black, horizontal line represents the *"zero-axis"* in each figure. ▪ ***Supplementary data for figs. 3.12a, 3.12b and 3.12c is shown in figs. II.2a, II.2b, II.3a and II.3b on pgs. XXIV to XXV, respectively.***

The variation in the *'energy status'* of the two models, as seen in figs. 3.11 and 3.12 (see, pgs. 137 and 138), is in agreement with earlier made observations for the respective initial steady-states of these models on pg. 129.

Across [Pi$_m$] as well as V^{PDH}_{max}, the $[NADH/NAD^+]_m$ ratio between the *PC$_{wt}$* & *PC$_{ko}$*, shows a qualitative switch in the redox states. Across both parameters, the *PC$_{ko}$* model becomes further reduced; whereas, the *PC$_{wt}$* model exists in a comparatively more oxidised state.

Also, the $[ATP/ADP]_m$ & $[ATP/ADP]_c$ ratios for the PC_{ko} model show that there is significantly more ATP in the system, as compared to that in the PC_{wt} model. As mentioned earlier in the discussion for the initial steady-states, such a qualitative shift in the ATP/ADP ratios could be due to the PC removal and MDH operating in the forward direction in the PC_{ko} model.

Thus, identifying the properties of the PC_{ko} model and its differences with the PC_{wt} model, has been helpful to learn about the overall qualitative nature of the structural as well as kinetic properties of a mammalian heart- or skeletal muscle- specific TCA cycle model.

3.3.4 Metabolic Control Analysis (MCA) of the heart TCA cycle prototype

In this section, we'll see the results of *Metabolic Control Analysis (MCA)*, when applied to heart TCA cycle model prototype by observing the distribution of flux control coefficient (C^J).

3.3.4.1 Flux control coefficient analysis of the heart TCA cycle prototype

Figure 3.13, describes the control of flux through citrate synthase (CS), using the flux control coefficients (C^J) of all the PC_{ko} enzymes.

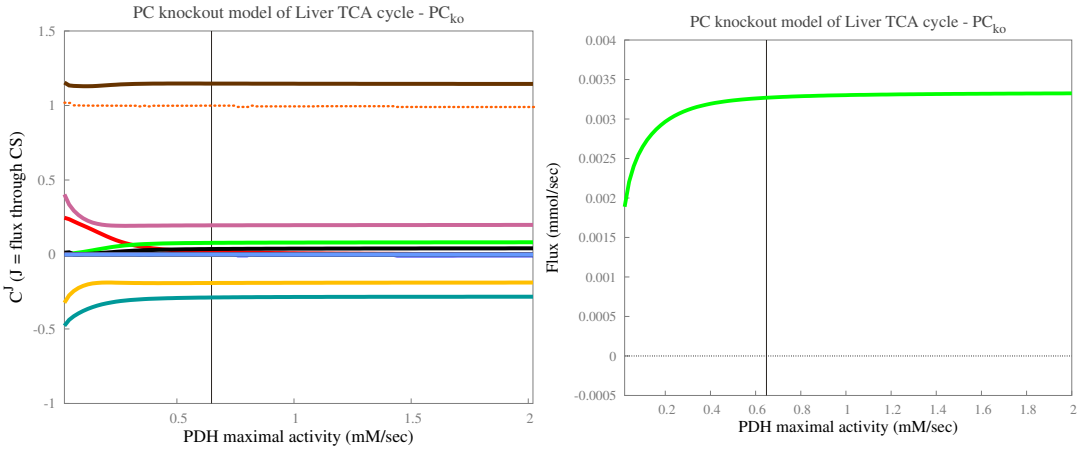

3.13.a. C^J, PC_{ko} model **3.13.b.** CS flux, PC_{ko} model

▪ **Figure 3.13. Control of TCA cycle flux in the 'PC knock-out' (PC_{ko}) model:** against the PDH maximal activity.

▪ Key for fig. 3.13a is as follows :

PDH ; CS ; ACO ; IDHa ; α-KGDH ; SCS;
SDH ; FM ; MDH ; ATPsynth ; ANT ; ATPhyd;
IDHb ; Total Sum (dotted line)

▪ The vertical black line represents the initial model value. At this point, in figs. 3.13a and 3.13b, $V_{max}^{PDH} = 0.648$ mM/sec, respectively. ▪ ***Orange dotted line*** shows the *Summation theorem* result.

Figure 3.13 (see, pg. 139) shows the distribution of flux control coefficients (C^J) calculated for the control of TCA cycle flux (flux through CS), for all enzymes of the PC_{ko} model, across the increasing maximal activity of PDH (V_{max}^{PDH}). These flux control coefficient plots are presented alongside a corresponding steady-state plot of citrate synthase (CS) flux (the reaction *'J'* on which the coefficient, *'C^J'* is calculated) across the same parameter range. In fig. 3.13, the flux control coefficients are distributed between the range of -0.5 to 1.2 (unitless). In these plots, result of the *summation theorem* is also included using a dotted line. For the corresponding flux control coefficient plot computed for the PC_{wt} model (*i.e.* updated liver TCA cycle model), please refer to fig. 2.25b (see, pg. 74) of the previous chapter on liver TCA cycle models.

The comparison of these two flux control coefficient plots reveals that the removal of PC from the PC_{ko} model, has nearly eliminated the complex pattern of C^J variation that was observed in the PC_{wt} model (see, fig. 2.25b). In PC_{wt} model, the control of TCA cycle flux is largely distributed between PDH, PC, ATPsynth, SDH, α-KGDH, & IDHa, with a rapid exchange of the majority of control between PDH and the other key enzymes. However, in the PC_{ko} model (see, fig. 3.13), the C^J distribution against V_{max}^{PDH} is fairly linear, without any rapid exchange between enzymes and distributed between ATPhyd, α-KGDH, ATPsynth, & IDHa, with ATPhyd sharing the majority of control. Citrate synthase (CS) also shares a minute amount of control in PC_{ko} (with an average C^J value of 0.07–0.08). Also, in PC_{ko}, IDHa & ATPsynth have a moderate but notable negative flux control coefficients, as shown in fig. 3.13.

The negative C^J value for IDHa indicates that an increase in the IDHa activity causes a modest decrease in the TCA cycle flux. This may initially seem counter-intuitive, but an increase in the IDHa activity increases the α-ketoglutarate concentration and thus its availability for the IDHb; which in turn increases the IDHb reverse flux, thereby counteracting and occasionally, even over-compensating for the greater IDHa activity.

Also, the negative C^J value of ATPsynth in fig. 3.13 may appear counter-intuitive, as well. In fact, in the liver TCA cycle model it shares a strongly positive value, as seen in fig. 2.25b (see, pg. 74). As described in the earlier chapter on liver TCA cycle models (see, pg. 75), based on the *Supply-demand analysis* put forward by Hofmeyr and Cornish-Bowden (2000), we may say that ATP synthase & ATP hydrolysis form a *demand block* within the heart TCA cycle prototype, whereas other reactions of the cycle represent the *supply block*. Accordingly, we may also expect that the flux control coefficient of ATPsynth for the control of TCA cycle flux to be on the positive side. However, with the notable exception of PC_{wt} results, flux control distribution in the PC_{ko} model doesn't agree with this observation and we believe that the reason for these counter-intuitive results lies in the *supply block* of the heart TCA cycle prototype.

The negative C^J value for ATPsynth indicates that an increase in the ATPsynth activity causes a modest decrease in the TCA cycle flux. In the PC_{ko} model, considering the absence of PC & extremely limited supply of oxaloacetate (with an initial model value of 4.05E-04 mM & an initial steady-state value of 1.2E-06 mM), the TCA cycle flux can increase only within a limited range and soon hits a plateau within a short range of change in enzyme activity, as seen in figs. II.5b, II.5d and 3.13b (see, pg. XXVII & pg. 139, respectively). Any significant increase in the ATPsynth activity also means a substantial increase in $NADH_m$ demand. Since, 3 out of 4 NAD- dependent dehydrogenases in PC_{ko} constitute 'ESS #1' along with CS (since, IDHa is an independent reaction), the $NADH_m$ supply is subjected to the same restrictions as that of the TCA cycle flux. Such limitations on the supply of reduced substrate for the synthesis of ATP is likely to impact the TCA cycle flux negatively, resulting into a negative C^J value of ATPsynth for the control of PC_{ko} TCA cycle flux.

Since, PC is absent in the heart TCA cycle prototype, ATPhyd becomes the only *ATP-hydrolysing reaction* in the model and therefore the only reaction that sets the *ATP-demand* in this system. From literature, we already know that in mammalian tissues such as heart and skeletal-muscle, the mitochondrial carbon metabolism is highly demand-driven and the high share of control exhibited by ATPhyd for the control of PC_{ko} TCA cycle flux, is in good agreement with the published data.

In the liver TCA cycle model, SDH shared a prominent share of control after the *'rapid-exchange phase'*, along with ATPsynth, PC, & α-KGDH. In the heart TCA cycle prototype however, it shares no discernible share of control. In fact in fig. 3.13, the average C^J value for SDH is as low as -0.002. As explained in the chapter on liver TCA cycle models (see, pg. 76), one of the major factors influencing the amount of control shared by SDH, was the interruption of its enzyme subset ('ESS #2') by the independent reactions (MDH, IDHa, and IDHb), causing the two halves of the subset to form a linear and a branched reaction sequence, respectively. The branched reaction sequence included FM, MC & MDH and it was formed due to MDH operating in its reverse direction. In the heart TCA cycle prototype, since PC was deleted and since, MC is essentially a *dead reaction* (against increasing V_{max}^{PDH}, its average steady-state value is 2.0E-12 mmol/sec), the branched reaction sequence from PC_{wt} is no longer operational in PC_{ko}, thereby causing SDH to lose its prominent share of control in this system.

Overall, even in response to change in other enzyme activities or metabolite concentrations, the distribution of flux control between the PC_{ko} TCA cycle enzymes is found to be roughly within the same range as that seen in fig. 3.13 and displays a qualitatively similar pattern of C^J distribution.

3.4 Discussion & Conclusions

The idea of a *"PC knock-out"* model was first born during the Metabolic Control Analysis of liver TCA cycle models as a simple yet elegant way to study the dynamic properties of a metabolic system that is more akin to the mammalian heart TCA cycle, *a priori*. So far, the structural as well as kinetic analysis of the *"PC knock-out"* model or the heart TCA cycle prototype has already provided valuable insights regarding the plausible behaviour of a mammalian heart or skeletal muscle-specific TCA cycle and they are as follows:

1. The *"PC knock-out"* model demonstrates that by removing the most influential, mammalian liver-specific anaplerotic reaction (*i.e.*, pyruvate carboxylase) from the updated liver TCA cycle model, we can isolate only those elementary modes that describe the core structural aspects of a mammalian heart or skeletal muscle-specific TCA cycle model and thereby transforming the liver-specific model into an archetypical heart-specific TCA cycle model. From a novice modeller's perspective, it is an important lesson in understanding how to isolate a desired subsystem that exists as an integral part of a larger system by simply analysing the model using structural analysis tools.

2. The elementary modes analysis of the PC_{ko} model suggests that the internal substrate cycle between the NAD^+-dependent isocitrate dehydrogenase and the $NADP^+$-dependent isocitrate dehydrogenase that operates in the updated liver TCA cycle model is likely to exist in a mammalian heart-specific TCA cycle model as well, provided it follows a similar structural definition as that of the PC_{ko} model. In fact, there is enough literature evidence to support the existence of such a cycle in heart tissue (Huang and Colman, 2005; Londesborough and Dalziel, 1968; McCormack and Denton, 1981; Rutter and Denton, 1988; Sazanov and Jackson, 1993).

3. The elementary modes analysis of the PC_{ko} model also shows that a theoretically ideal version of TCA cycle, often described in biochemistry textbooks, that produces 11 molecules of ATP_m & 3 molecules of CO_2 per pyruvate, can be built from this model by removing the $NADP^+$-dependent isocitrate dehydrogenase from PC_{ko} to further isolate $ElMo_{[2]}$ described in tbs. 3.1 and 3.2 (see, pg. 124). This TCA cycle model would then contain only a single elementary mode ($ElMo_{[2]}$), which would also be the only enzyme subset that comprises all 12 reactions of this model.

4. As mentioned in the earlier chapter, the moderate degree of control shared by ATPsynth in this model, indicates the importance of including a fully developed module of the Electron transport chain (ETC). The possible inclusion of an expanded ETC module would also include the oxygen consumption reaction; which would make the heart-specific model further aligned with the experimental observations.

5. The high degree of control shared by ATPhyd in this model, indicates the importance of ATP-demanding reactions such as ATPhyd in a heart-specific TCA cycle model. Currently, it is defined as an irreversible, simple first-order reaction flux. Considering its importance in this system, it might be appropriate to include a further detailed description of ATP hydrolysis. For instance, currently, both ATP_c & ADP_c represent an example of poorly constrained concentrations in a metabolic model and are likely to cause locally confined mathematical anomalies in certain special cases.

6. As mentioned in the earlier chapter, expanding the model to reflect PDH regulation by covalent modification would be a worthwhile addition to the heart-specific TCA cycle model, as it may help to facilitate a dynamic balance between the demands of gluconeogenesis and ATP production.

7. The absence of pyruvate carboxylase and the extremely low steady-state concentration of oxaloacetate in the PC_{ko} model, points towards an alternative anaplerotic mechanism that, at least in theory, is expected to provide additional routes into and out of the mitochondrial TCAi pool and the 'Malate-aspartate shuttle (MAS)' is one such mechanism that operates in mammalian heart or skeletal-muscle mitochondria. Possible inclusion of malate-aspartate shuttle in the heart-specific TCA cycle model, would be another useful modification to align this model further in agreement with the published data.

8. Overall analysis of the *"PC knock-out"* model, highlights the qualitative realignment of structural as well as dynamic properties of liver TCA cycle model towards a metabolic system that roughly describes a specific subset of metabolic characteristics that are in agreement with general experimental observations of a heart or skeletal muscle-specific TCA cycle. More importantly, obtaining an abstract picture for plausible metabolic characteristics of a heart-specific TCA cycle model, during the early stages of model development is extremely useful in optimising the entire development process, particularly the phase of *'data collection'*, for collecting the relevant enzyme kinetics data.

Chapter 4

The Heart TCA cycle model

4.1 Overview

In the previous chapter, dynamic properties of the mammalian liver-specific tricarboxylic acid cycle model developed within the Cell Systems Modelling Group (CSMG) (Brightman et al., 2010, *unpublished manuscript*) were studied extensively. The understanding and the knowledge of various modelling processes as well as the tissue-specific TCA cycle model itself, acquired during this study proved to be most helpful at the beginning stages of this project and formed the core base of all future development. In this chapter, we will be studying the modification of the existing liver TCA cycle model to a heart or skeletal muscle-specific TCA cycle model, as well as the resultant properties of the newly created system.

The structure of the existing liver TCA cycle model was modified in terms of reactions to be included in the resultant heart-specific model. Moreover, for the selected set of reactions, the mammalian heart-specific enzyme kinetics data was collected from published literature and applied to the model. Also, as mentioned in the earlier chapter, we have followed the same modelling strategy used to define individual reactions of the liver TCA cycle model, to construct a 'consensus' kinetic model of TCA cycle in mammalian heart or skeletal muscle mitochondria, which is neither over-simplified nor too complex in terms of rate equations, reversibility of reactions and regulatory interactions.

In Section 4.2, we shall discuss the definition & construction of heart TCA cycle model ($\mathrm{HRT}_{\mathrm{TCA}}$) in further detail. Section 4.3: Results for the heart TCA cycle model on pg. 150, describes an in-depth analysis of the emergent dynamic properties of this model.

4.2 Methods: Model design and definition

As mentioned earlier, the Heart TCA cycle model (HRT_{TCA}) representing the operation of heart or skeletal muscle-specific TCA cycle was manually constructed by modifying the existing liver TCA cycle model using ScrumPy. The model in ScrumPy format is available in Appendix F (see, pg. 241) and is illustrated in fig. 4.1 (see, pg. 145). The final version of the updated model contains 13 reactions and 24 metabolites.

4.2.1 Model definition

Since, this model is based on the liver TCA cycle model, it follows the same design choices in terms of individual enzyme rate equations that are represented using the simplified, generic, reversible bi-substrate equation (Chassagnole et al., 2001b; Rohwer et al., 2006), as explained in the earlier chapter (see, pg. 19).

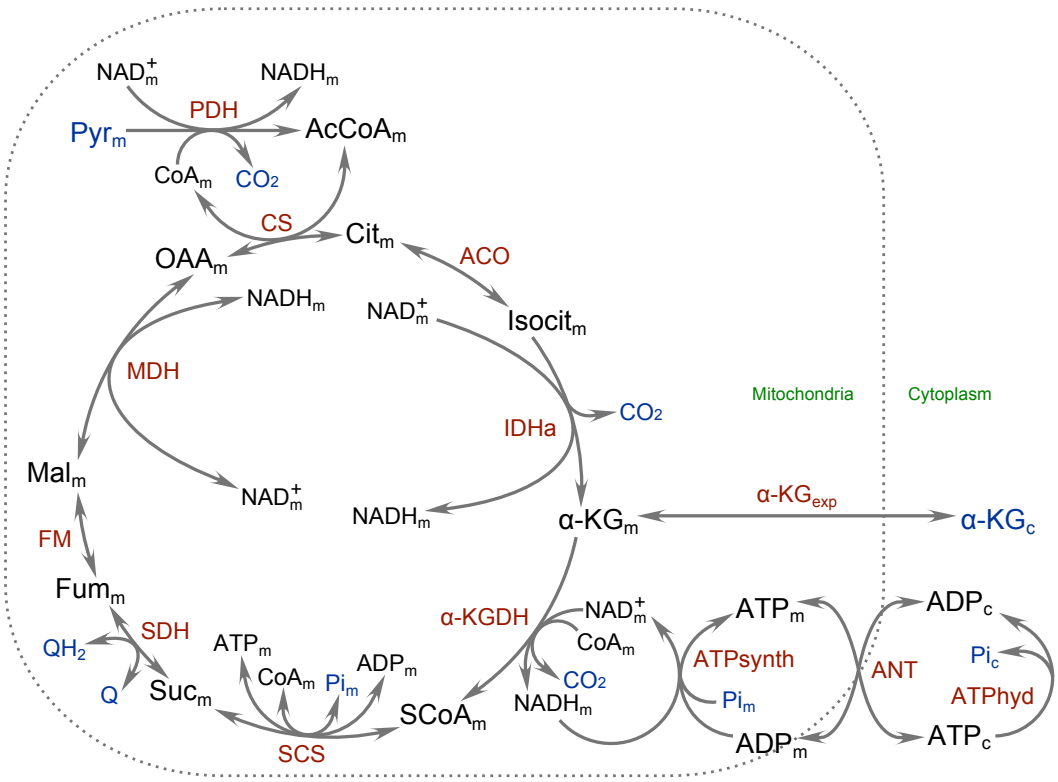

▪ **Figure 4.1.** Schematic illustrating the TCA cycle reactions participating in the heart TCA cycle model.

▪ Internal metabolites: in *Black*; external metabolites: in *Blue*; reaction/ enzyme names: in *Red*.

▪ Reaction with double arrowheads is assumed to be reversible and reaction with single arrowhead is assumed to be irreversible.

As illustrated in Figure 4.1, the model includes eight canonical (non-tissue-specific) TCA cycle reactions including the reaction catalysed by pyruvate dehydrogenase (PDH), a hypothetical, reversible transport reaction that transports α-ketoglutarate in and out of the mitochondria and three ATP/ADP−linked reactions that include an abstracted representation of oxidative phosphorylation, cytosolic ATP hydrolysis (ATPhyd), along with an adenine-nucleotide exchange with the cytosol catalysed by ANT. The two liver tissue-specific reactions (MC & PC) are absent in this model, since in mammalian heart as well as skeletal muscle tissue, literature evidence suggests that the anaplerotic contribution of PC to the total flux through the TCA cycle is insignificant as compared to that in liver (Gibala, 2003; Gibala et al., 2000; Owen et al., 2002; Scrutton and Utter, 1968). Also, there is very little evidence that would suggest any significant activity of MC in heart or skeletal muscle tissue (Chappell, 1968; Fiermonte et al., 1999; Klingenberg, 1970; LaNoue and Schoolwerth, 1979; Palmieri, 1994; Sluse et al., 1971). Furthermore, since the anaplerotic contribution of PC is minimal in mammalian heart as well as skeletal muscle tissue, in its absence, other anaplerotic pathways such as the malate-aspartate shuttle need to be considered in the model, in order to to maintain the oxaloacetate concentration at levels sufficient enough to sustain the physiological rates of citrate synthesis in these tissues (Garland et al., 1969; LaNoue et al., 1970; LaNoue et al., 1972; Srere, 1974; Williamson et al., 1972). A similar observation was made in the earlier chapter, during the analysis of concentration control coefficients for the liver TCA cycle model (see, pg. 108).

However, since it was crucial to first study the basic heart TCA cycle model before including the malate-aspartate shuttle reactions; a hypothetical, simplified reversible transport reaction, α-ketoglutarate transporter ($\alpha\text{-KG}_{\text{exp}}$) was included in the model and it follows a reversible uni-uni kinetic model (Segel, 1993). $\alpha\text{-KG}_{\text{exp}}$ is *not* a one-step representation for the actual function of malate-aspartate shuttle in mammalian heart or skeletal muscle tissue, but is intended only as a pointer or a placeholder to be replaced later by a set of reactions representing the malate-aspartate shuttle in these tissues. Also, during the development process, it was discovered that this model requires a small amount of outflow to achieve a stable steady-state and since MC is no longer present in this model, the required outflow reaction was chosen to be shown in the form of $\alpha\text{-KG}_{\text{exp}}$, which may also be viewed as only a partial representation of malate-oxoglutarate transporter (MOTx) – an integral transport reaction of the Malate-Aspartate shuttle. The enzyme rate equation for $\alpha\text{-KG}_{\text{exp}}$ is shown in eq. E.7 in Appendix E (see, pg. 240).

Initially, during the development of heart TCA cycle model, $NADP^+$-dependent isocitrate dehydrogenase (IDHb) was included in this system along with NAD^+-dependent isocitrate dehydrogenase (IDHa), similar to what we have already seen in the liver TCA cycle model. However, during steady-state analysis of this early version of the model, it

was discovered that both reactions act in the forward direction to produce α-ketoglutarate from isocitrate and that IDHb is almost entirely responsible for whatever amount of αKG_m is produced through these reactions; while IDHa carries only an infinitesimally small flux, which is nearly 1.5E+04 times lower than that of the flux through IDHb. In liver TCA cycle model, due to its specific structural properties and the amount of flux carried by pyruvate carboxylase (3-4 times the TCA cycle flux) and also the fact that the only available outflow in that model was at the level of malate, both IDHa & IDHb were functional and carried significant amount of flux, albeit in opposite directions. However, in the case of heart TCA cycle model, the significant amount of influx via PC is absent and the only outflow in this model is at the level of α-ketoglutarate, in the form of $\alpha\text{-}KG_{exp}$. In our view, it is possible that in such a system, the resultant TCA cycle flux requires and is sufficient to support only one reaction that converts isocitrate to αKG_m and based on the degrees of freedom associated with either of these reactions, the model tends to allow IDHb to carry most of the flux; since it utilises $NADP^+$ as a co-substrate, which along with NADPH is an external metabolite and more freely available than NAD^+_m or $NADH_m$. Therefore, until the present heart TCA cycle model is extended to include the malate-aspartate shuttle reactions, we decided that the basic heart TCA cycle model in its current form should only contain NAD^+-dependent isocitrate dehydrogenase (IDHa).

Therefore, in summary, other than these four changes to the liver TCA cycle model, other reactions remain unchanged in the heart TCA cycle model, except their corresponding model parameters and variables, which are updated according to the enzyme kinetics data specific to the mammalian heart or skeletal muscle tissue. For ANT & ATPsynth, original enzyme kinetics data from the liver TCA cycle model is kept as is, due to the unavailability of satisfactory estimates in mammalian heart or skeletal muscle tissue. The values of all updated model parameters (external metabolites & kinetic/ thermodynamic constants) are provided in the supplementary material, in Table III.2 (see, pg. XXIX). Also, complete details for the α-ketoglutarate transporter ($\alpha\text{-}KG_{exp}$) reaction added to the heart TCA cycle model are shown in eq. E.7 in Appendix E (see, pg. 240). For full details regarding net stoichiometric equations as well as enzyme rate equations of the remaining 12 reactions, please refer to Appendix B (see, pg. 223).

The heart TCA cycle model includes the same 16 variables (internal metabolites) as that of the liver TCA cycle model and they describe the concentrations of TCA cycle intermediates, and of acetyl-CoA, CoA_m, adenine nucleotides, NAD^+_m, & $NADH_m$. Each of these variables in the model is assigned an initial value, based on literature data. Also, this model includes 8 parameters that describe fixed quantities (external metabolites) of model input (pyruvate), enzyme cofactors/ effectors (Q/ QH_2 & Ca^{2+}), inorganic phosphates (Pi_m & Pi_c), and system outputs (CO_2 & αKG_c). For most of these 24

metabolites, a range of values, largely from rat heart or skeletal muscle tissue were found and a median value was used in the model. However, in the case of metabolites for which satisfactory estimates could not be found in the literature, the original liver-specific values were retained. Table 4.1 (see, pg. 149) shows the values of all the model variables (internal metabolites & key fluxes) in heart or skeletal muscle tissue, taken from the literature and compares them to the corresponding values predicted by the model at initial steady-state.

The heart TCA cycle model consists of a system of 12 non-linear ordinary differential equations, similar to the liver TCA cycle model, each of which describes the evolution of one of the model variables (concentrations of internal metabolites) over time, from their respective initial model values. However, due to the specific differences between these two models, 5 out of 12 equations are slightly altered (*viz.,* equations for – Isocit_m, αKG_m, Mal_m, OAA_m, and ATP_m) and are described in Appendix E (see eqs. E.1 to E.5 on pg. 240). The 4 algebraic expressions that additionally define the concentrations of conserved moieties have been removed from the heart TCA cycle model; due to their redundancy with respect to the ScrumPy -specific, default internal parameters that are assigned to each of the conserved totals by default, at model simulation (for further details, please refer to pg. 22 from the liver TCA cycle model chapter).

■ **Table 4.1.** Values of TCA cycle variables in heart tissue taken from the literature and predicted by the model [a,b]

Fluxes are in units of mmol/sec and concentrations in mM.

Variable	Literature Values		Model Values
	Range	Median	
TCA cycle (CS) flux	0.03 – 0.08	0.06	4.33E-03
$[CoA_m]$	0.01 – 0.08	0.046	2.05E-03
$[AcCoA_m]$	0.02 – 0.33	0.18	0.25
$[Cit_m]$	0.03 – 4.0	2.01	0.49
$[Isocit_m]$	0.03 – 0.12	0.08	3.32E-02
$[\alpha KG_m]$	0.01 – 0.8	0.4	6.00E-03
$[Suc_m]$	0.06 – 3.9	2.0	4.27E-02
$[SCoA_m]$	0.01 – 0.29	0.15	1.55E-04
$[Fum_m]$	6.9E-03 – 0.26	0.13	3.65E-02
$[Mal_m]$	0.16 – 1.88	1.02	0.16
$[OAA_m]$	0.002 – 0.062	0.032	1.44E-05
$[NAD^+_m]$	0.56 – 1.36	0.96	0.6
$[NADH_m]$	0.1 – 1.0	0.53	0.094
$[ADP_m]$			0.88
$[ATP_m]$	Same as the liver		9.52
Free [c] $[ADP_c]$	TCA cycle model		4.47E-02
Free [c] $[ATP_c]$			4.77

[a] The predicted model values are obtained at steady-state, upon simulating the Heart TCA cycle model. These are the same values shown in the analysis of initial steady-state of the model, in the results section.

[b] An expanded version of this table, containing details of the source references for the literature data, is provided in the supplementary material (see, Table III.1 on pg. XXVIII).

[c] Not bound to fixed sites; in the case of ATP, fixed-site binding is negligible.

4.3 Results for the heart TCA cycle model

In this section, various kinetic as well as structural properties of the heart TCA cycle model are studied using various methods of analysis, such as – *'Elementary modes analysis', 'Enzyme subset analysis', 'Steady-state analysis', 'Metabolic Control Analysis', etc.* Similar to the liver TCA cycle model analysis, we will primarily focus on physiologically significant key findings, in order to present a more thorough discussion of the presented data.

Briefly, the following types of results will be presented:

1. Elementary modes analysis (see sec. 4.3.1 on pg. 150)
2. Enzyme subset analysis (see sec. 4.3.2 on pg. 152)
3. Initial steady-state data & Steady-state analysis (see sec. 4.3.3 on pg. 153)
4. Metabolic Control Analysis (MCA) results (see sec. 4.3.5 on pg. 170)
   - 4.(*a.*) Flux control coefficient analysis results (see sec. 4.3.5.1 on pg. 170)
   - 4.(*b.*) Concentration control coefficient analysis results (see sec. 4.3.5.2 on pg. 176)
   - 4.(*c.*) Elasticity coefficient analysis results (see sec. 4.3.5.3 on pg. 184)

4.3.1 Elementary modes analysis of the heart TCA cycle model

The heart TCA cycle model contains a single elementary mode which consumes one molecule of pyruvate to produce 3 CO_2 molecules and 11 mitochondrial ATP that are consequently utilised to produce 11 cytosolic ADP & Pi. In summary, the present heart TCA cycle model performs optimally to produce a maximum possible amount of mitochondrial ATP by an ideal/ textbook TCA cycle. Table 4.2 shows this single elementary mode alongside its corresponding net stoichiometry.

	Heart TCA cycle reactions										*ATP/ ADP- linked reactions*		
Modes	**PDH**	**CS**	**ACO**	**IDHa**	**α-KGDH**	**SCS**	**SDH**	**FM**	**MDH**	**α-KG_{exp}**	**ATPsynth**	**ATPhyd**	**ANT**
ElMo 0	1	1	1	1	1	1	1	1	1	*0*	1	11	11

4.2.a

	Reactants			Products	
ElMo 0 :	11 Pi_m + Pyr_m + Q	⟶		3 CO_2 + QH_2 + 11 Pi_c	(1)

4.2.b

- **Table 4.2.** A table showing elementary modes for heart TCA cycle model.

- Table 4.2a shows the only elementary mode for the heart TCA cycle model; whereas, tbl. 4.2b shows its corresponding net stoichiometry.
- In tbs. 4.2a and 4.2b, fractions have been converted to decimals.
- All metabolites in tbl. 4.2b are, by necessity, external in the modelling sense.

This elementary mode is similar to $ElMo_{[3]}$ & $ElMo_{[2]}$ of the updated liver TCA cycle model and the *"PC knock-out"* model, respectively (see tbs. 2.3 and 3.1 on pgs. 33 and 124, respectively). Figure 4.3 shows a detailed account of the net mitochondrial ATP_m and $NADH_m$ production for this mode.

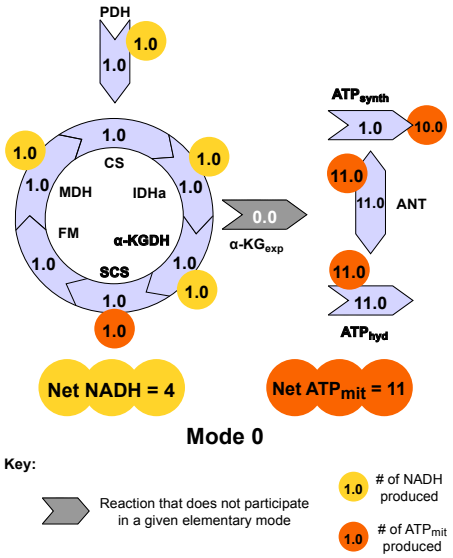

▪ **Figure 4.3.** Infographics showing the stoichiometric account of the net mitochondrial ATP_m and $NADH_m$ production for the heart TCA cycle model elementary mode.

- All the heart TCA cycle model reactions are represented in their minimal form. Only the absolutely essential metabolites & co-factors are included in this diagram.
- In this figure, the arrowheads point towards the respective forward or reverse directions of the participating reactions, specific to the elementary mode.
- Reactions shown in Grey, do not participate in the elementary mode. Whereas, reactions shown in light Blue, function in their respective forward directions.
- Numbers within the arrows represent the respective reaction strengths (see tbl. 4.2a on pg. 150).
- ATP_m is represented by a small Yellow circle and $NADH_m$ by a small Orange circle. Numbers within these circles represent the number of molecules produced by the corresponding reaction. For any reaction, the production of a metabolite is shown using a positive number and the consumption using a negative number.
- Net $NADH_m$ production = ${NADH_m}^{PDH} + {NADH_m}^{IDHa} + {NADH_m}^{\alpha\text{-}KGDH} + {NADH_m}^{MDH}$
- Net ATP_m production = ${ATP_m}^{ATPsynth} + {ATP_m}^{SCS}$

In the previous chapter, analysis of liver TCA cycle model elementary modes revealed that in the absence of PC & MC, MDH would operate in its respective forward direction and tbl. 4.2a and fig. 4.3 illustrate the same in the case of heart TCA cycle model (see fig. 2.6 on pg. 38). The internal substrate cycle between IDHa & IDHb that exists in the liver TCA cycle models is absent in this model, as it currently does not include the $NADP^+$-dependent isocitrate dehydrogenase reaction. As mentioned earlier in Methods (see, pg. 147), IDHb will be included in the heart TCA cycle model after it is extended to incorporate the malate-aspartate shuttle (MAS) reactions.

Table 4.3 illustrates the moiety conservation of ATP, NAD & CoA–related metabolites in the heart TCA cycle model. The conservation relationships in the heart TCA cycle model are exactly the same as they exist in the updated liver TCA cycle model (see tbl. 2.5 on pg. 34).

	Heart TCA cycle model
1	ATP_c : ADP_c
2	ATP_m : ADP_m
3	$NADH_m$: NAD_m
4	$AcCoA_m$: ($SCoA_m$, CoA_m)

- **Table 4.3.** Moiety conservation in heart TCA cycle model

Therefore, this elementary modes analysis shows that we have successfully isolated the 9 canonical TCA cycle reactions along with 3 ATP/ADP–linked reactions from the updated liver TCA cycle model and the resulting structural framework appropriately defines a mammalian heart or skeletal muscle-specific TCA cycle model.

4.3.2 Enzyme subset analysis of the heart TCA cycle model

The heart TCA cycle model contains a single enzyme subset that includes 12 out of 13 possible reactions in the model and tbl. 4.2a (see, pg. 150) shows the composition of this enzyme subset, which is also the only elementary mode present in the heart TCA cycle model. α-KG_{exp} is a structurally dead reaction, since it carries an infinitesimally small amount of flux. However, as mentioned earlier in Methods, it is nonetheless required for the kinetic stability of the heart TCA cycle model.

Also, this enzyme subset analysis reveals that in the absence of PC & MC or any other non-canonical TCA cycle reaction, the heart TCA cycle model enzyme subset is devoid of any interruption between two participating reactions and includes all TCA cycle reactions along with 3 ATP/ADP–linked reactions, unlike that of the liver TCA cycle model (see fig. 2.8 on pg. 43). In future, after the introduction of malate-aspartate shuttle reactions to the heart TCA cycle model, this enzyme subset is likely to break at junctions where the two pathways interact with each other.

In the following sections, we look at kinetic/ dynamic properties of the heart TCA cycle model and in some cases establish appropriate links with its structural properties as well.

4.3.3 Steady-state analysis of the heart TCA cycle model

The heart TCA cycle model was solved with the 'initially defined' values of all the parameters & variables presented in Methods to obtain the *'initial steady-state'* of the model (see tbs. III.1 and III.2 on pg. XXIX & pg. XXVIII, respectively). Figures 4.4 and 4.5 respectively show the reaction fluxes & metabolite concentrations in the heart TCA cycle model, at initial steady-state.

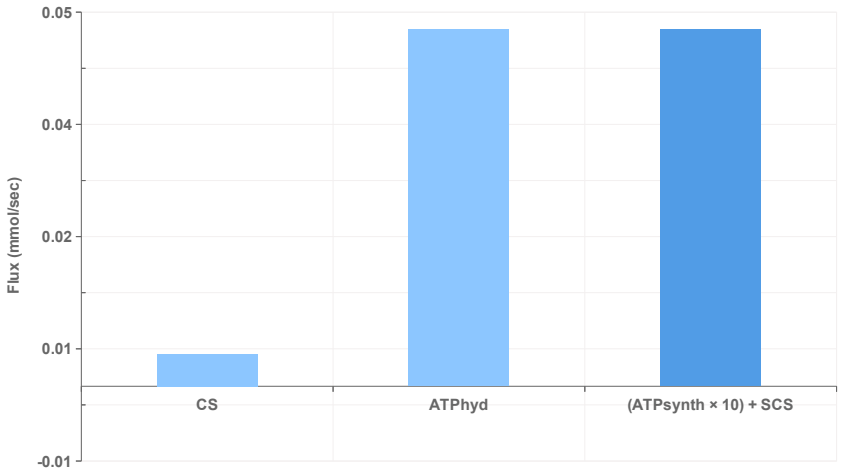

- **Figure 4.4.** Fluxes for the heart TCA cycle model, at initial steady-state.

- In the heart TCA cycle model, since there is a single enzyme subset, we have represented the flux through TCA cycle in the form of citrate synthase (CS) flux.
- In this graph, the light blue bar for ATPhyd represents total ATP_m consumption and the dark blue bar represents total ATP_m production by the heart TCA cycle model, at initial steady-state.
- In order to calculate the total ATP_m production flux in this model, the initial steady-state value for ATP synthase (ATPsynth) flux have been scaled by a factor of 10; due to the difference in respective reaction stoichiometries between ATPsynth (in mitochondria) and ATPhyd (in cytosol) and the initial steady-state value of SCS flux is then added to it, in order to account for substrate-level phosphorylation.

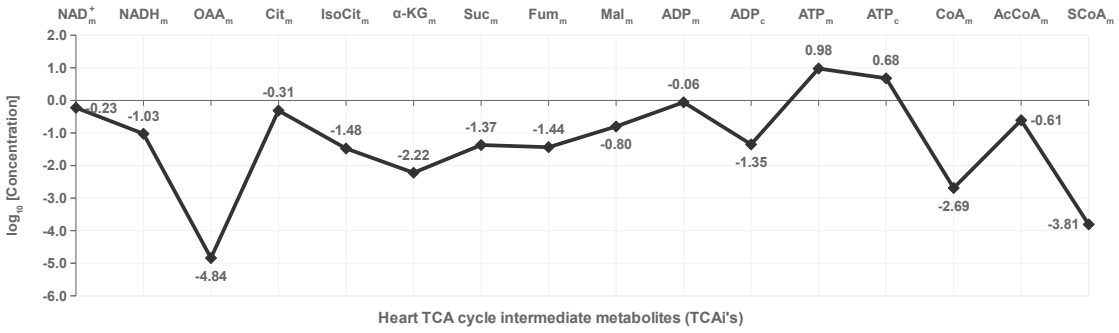

- **Figure 4.5.** A graph of TCA cycle intermediate metabolite concentrations for the heart TCA cycle model, at initial steady-state.

- *Y-axis* : Metabolite concentration in logarithmic scale.

Figure 4.4 (see, pg. 153) shows the magnitude of fluxes in the heart TCA cycle model, at initial steady-state. Since, all 12 out of 13 reactions in this model comprise a single enzyme subset, we have represented the flux through the TCA cycle in the form of citrate synthase (CS) flux. This graph also shows that the total ATP production (ATPsynth) & consumption (ATPhyd) fluxes in the heart TCA cycle model are well balanced, by accounting for the stoichiometric difference between them, as well as considering the substrate-level phosphorylation (SCS).

In the absence of anaplerotic contribution by pyruvate carboxylase, the initial steady-state TCA cycle flux (flux through CS) in the heart TCA cycle model is *approx.* 1.4% that of the updated liver TCA cycle model (see fig. 2.9 on pg. 46). Also, ATP synthase flux in the heart TCA cycle model is *approx.* 7.0% that of the updated liver TCA cycle model. However, at initial steady-state, the heart TCA cycle model ATP hydrolysis flux is *approx.* 33.0% more than that of the updated liver TCA cycle model. As already mentioned, lack of pyruvate carboxylase in the heart TCA cycle model is one of the most important factors due to which this model exhibits such significantly altered initial steady-state fluxes; however, the mammalian heart-specific enzyme kinetics data as well as the mammalian heart-specific metabolite concentration values used in this model could also be a factor, in part. Moreover, in the absence of PC, lack of malate-aspartate shuttle reactions in the heart TCA cycle model could also be partly responsible for a relatively lower TCA cycle flux than that of the liver TCA cycle model.

Figure 4.5 (see, pg. 153) shows the heart TCA cycle intermediate metabolites, at initial steady-state. Among all heart TCA cycle intermediates, oxaloacetate initial steady-state concentration is the lowest (1.4E-05 mM), followed by SCoA (1.6E-04 mM), CoA (2.0E-03 mM) and α-ketoglutarate (6.0E-03 mM). However, without any basis of comparison, it is rather difficult to elaborate on these results any further.

Therefore, in fig. 4.6 (see, pg. 155) we calculate the initial steady-state concentrations of all TCAi's as *% initial model values* and represent them as *% change in the initial model values* by subtracting 100% (initial model value) from the calculated value (please refer to the Y-axis scale in fig. 4.6). In other words, we calculate by how much any given TCAi concentration has increased or decreased from its corresponding initial model value, as the model achieves an initial steady-state, in percent. For better comparison, we performed these calculations with the initial steady-state concentrations of all TCAi's from the liver TCA cycle model & the *"PC knock-out"* model, as well (see figs. 2.10 and 3.4 on pgs. 47 and 127, respectively). Thus, fig. 4.6 compares the liver, PC_{ko} & heart TCA cycle model TCAi concentrations at initial steady-state, by representing them as % change in their corresponding initial model values from a given model.

Figure 4.6 shows that in the heart TCA cycle model, the respective initial steady-

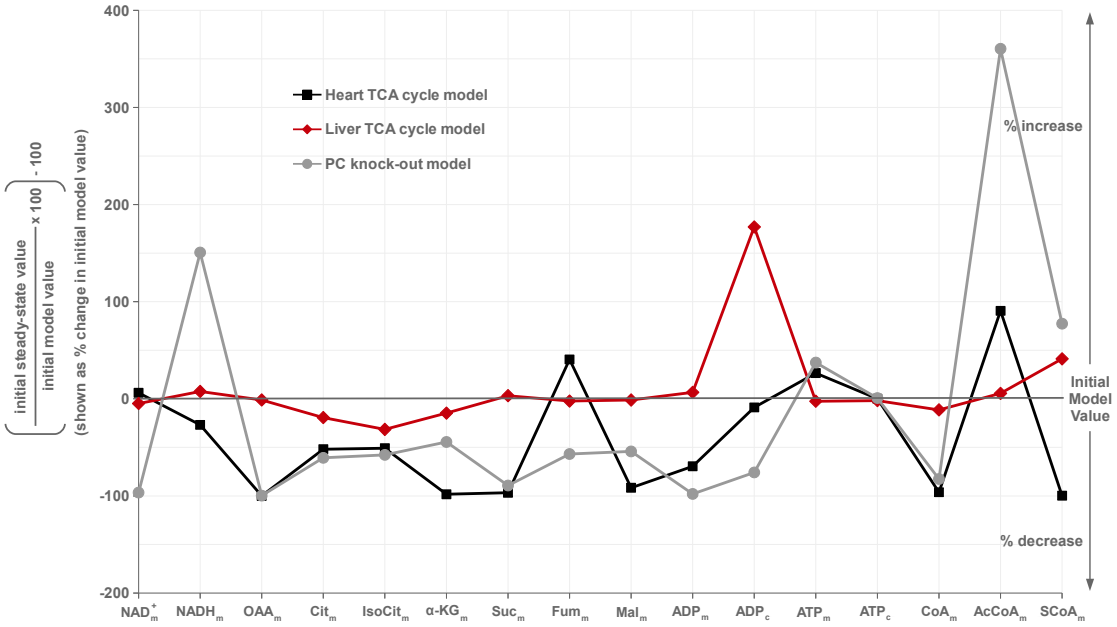

▪ **Figure 4.6.** Comparison of the liver, PC_{ko} & heart TCA cycle model TCAi concentrations in the form of 'percent change in initial model values', at initial steady-state.

▪ *Y-axis* : The initial steady-state TCAi concentrations represented as the '% change in their corresponding initial model values', per model.

▪ : Red line represents the '% change in initial model values' in the liver TCA cycle model initial steady-state; Grey line represents the '% change in initial model values' in the PC_{ko} initial steady-state; and Black line shows the '% change in initial model values' in the heart TCA cycle model initial steady-state.

▪ : *Zero-axis* represents the initial model value of a given TCAi, in a given model.

▪ : Values along the *positive Y-axis* show '% increase in the initial model value', whereas values along the *negative Y-axis* show '% decrease in the initial model value', per metabolite in a given model.

state concentrations of oxaloacetate, α-ketoglutarate, succinate, malate, coenzyme A and succinyl-CoA decrease by *approx.* 90% – 99% that of their corresponding initial model values. In the updated liver TCA cycle model, these TCAi's decrease only by *approx.* 1% – 15% that of their corresponding initial model values; except succinyl-CoA, which increases by *approx.* 40%. In the PC_{ko} model, these TCAi's decrease moderately by *approx.* 40% – 99% that of their corresponding initial model values; except succinyl-CoA, which increases by *approx.* 75%. Also, between all 3 models, citrate and isocitrate decrease by *approx.* 20% – 60% that of their corresponding initial model values.

In this graph, acetyl-CoA shows significant increase in all 3 models by *approx.* 5% – 350% that of its corresponding initial model values in these models. In the heart TCA cycle as well as the PC_{ko} model, the initial steady-state concentration of mitochondrial ATP increases by *approx.* 25% – 35% that of its corresponding initial model value; whereas it decreases by *approx.* 3% in the liver TCA cycle model. The cytosolic ATP concentration follows a similar pattern of changes between the 3 models. In the heart

TCA cycle model, initial steady-state concentration of NADH decreases by *approx.* 25% compared to its corresponding initial model value and NAD increases by *approx.* 5%; whereas the other two models show an exactly opposite pattern of change.

Overall, fig. 4.6 shows that there exists a significant qualitative as well as quantitative difference between the respective initial steady-state behaviours of the liver and the heart TCA cycle models. It also shows that although a *'zero PC activity'* in the PC_{ko} model allows for a qualitatively similar behaviour as that of the heart TCA cycle model, in part; it is nonetheless an approximation that utilises mammalian liver-specific enzyme kinetics & metabolite concentration data. Therefore, through the comparison between these three models, fig. 4.6 illustrates the importance of mammalian heart-specific enzyme kinetics & metabolite concentration data applied to the heart TCA cycle model, over any probable effects due to the absence of anaplerotic mechanisms in this model.

4.3.4 Dynamic responses of the heart TCA cycle model to the variations in TCA cycle enzyme activities

In this section, successive steady-states of the heart TCA cycle model are analysed in detail, in response to the variations in TCA cycle enzyme activities. Considering the flux control coefficient distribution for the PC_{ko} model presented earlier (see fig. 3.13 on pg. 139), ATPhyd appears to be the most controlling enzyme in a TCA cycle system that lacks the pyruvate carboxylase activity. Also, as seen earlier, the respective flux control coefficient distributions for the updated liver TCA cycle model, PC_{kd} model, as well as the reduced liver TCA cycle model, show that PDH is one of the key TCA cycle enzymes that shares a majority of the TCA cycle flux control before rapidly exchanging it with PC. Therefore, due to the absence of PC activity in the heart TCA cycle model, ATPhyd as well as PDH are suspected to be key factors in controlling the flux through the TCA cycle. Hence, from this analysis, we have presented steady-state data for a wide range of variations in the respective activities of ATPhyd & PDH.

Since for both enzymes, we have covered a wide range of activity variations (a total of six variations, ranging from *weak* to *overload*), we show the average steady-state behaviour of the model at every activity variation in the form of a bar graph. Also, since it is impossible to include such a large number of plots corresponding to each activity variation per enzyme, the original steady-state analysis plots are not shown in the supplementary material.

Figures 4.7 to 4.10 (see, pgs. 157 to 160, respectively) show the average steady-state behaviour of the heart TCA cycle model, when ATP hydrolysis activity is varied between 0.1x (*weak*) and 500x (*overload*), where 'x' is the initial model value for the ATP hydrolysis activity (where, 'x' = 0.01 mM/sec; termed here as – *basal activity*).

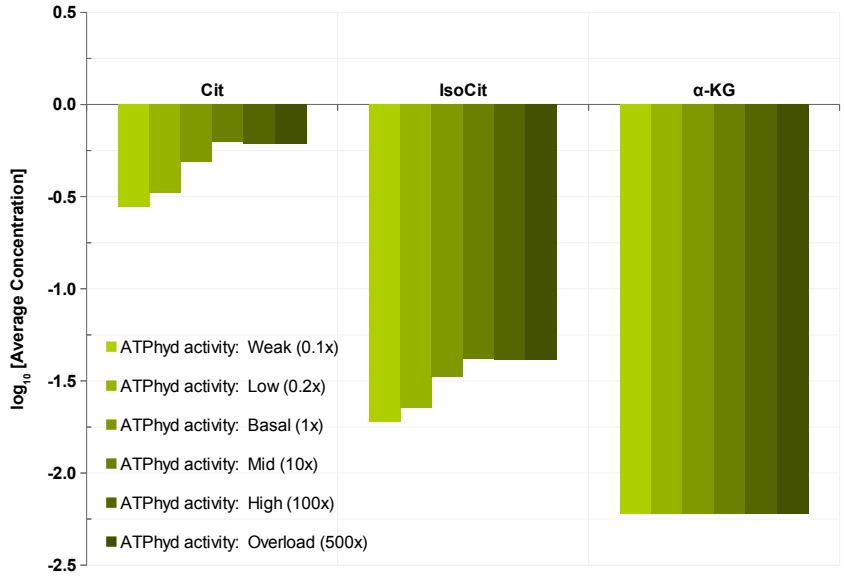

4.7.a. TCA cycle intermediate metabolites (TCAi) – Part 1

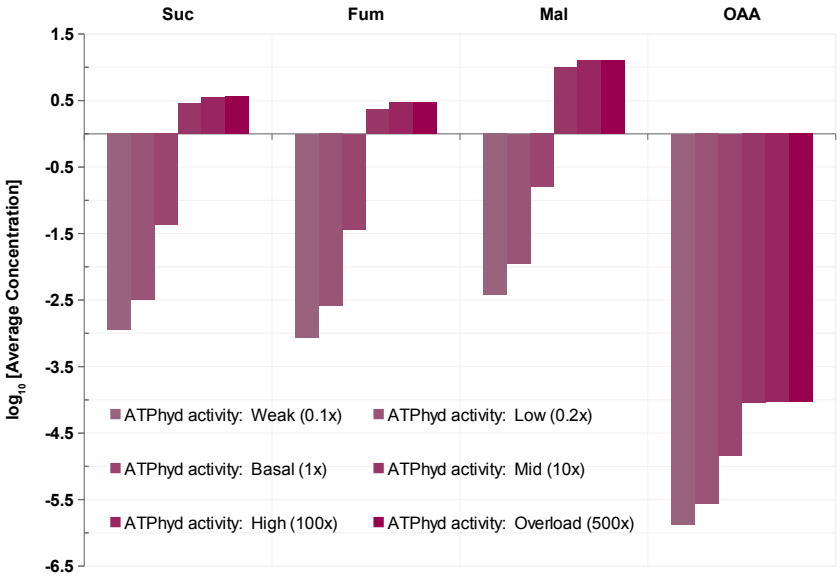

4.7.b. TCA cycle intermediate metabolites (TCAi) – Part 2

▪ **Figure 4.7.** The effect of a wide range of ATP hydrolysis activity variations on TCAi concentrations, against the change in ANT maximal activity.

▪ Six bars for every metabolite or reaction represent six ATPhyd activity variations, shown in light-to-dark colour shades, indicating *'weak'* to *'overload'* ATPhyd activities.

▪ An average concentration or flux value was calculated for each metabolite or reaction, from all consecutive steady-state values per dataset. They were then used as $\boldsymbol{log_{10}}$ values to generate the bar graph.

▪ The initial model value for ATPhyd activity in the heart TCA cycle model is 0.01 mM/sec and in this graph, it is represented as the *'basal activity'* or '1x'. ATPhyd activities included in this graph are as follows:

- Weak ATPhyd activity (0.1x) = 0.01 mM/sec (1x) ÷ 10 = 0.001 mM/sec
- Low ATPhyd activity (0.2x) = 0.01 mM/sec (1x) ÷ 5 = 0.002 mM/sec
- Basal ATPhyd activity (1x) = 0.01 mM/sec (1x)
- Mid/Moderate ATPhyd activity (10x) = 0.01 mM/sec (1x) × 10 = 0.1 mM/sec
- High ATPhyd activity (100x) = 0.01 mM/sec (1x) × 100 = 1.0 mM/sec
- Overload ATPhyd activity (500x) = 0.01 mM/sec (1x) × 500 = 5.0 mM/sec

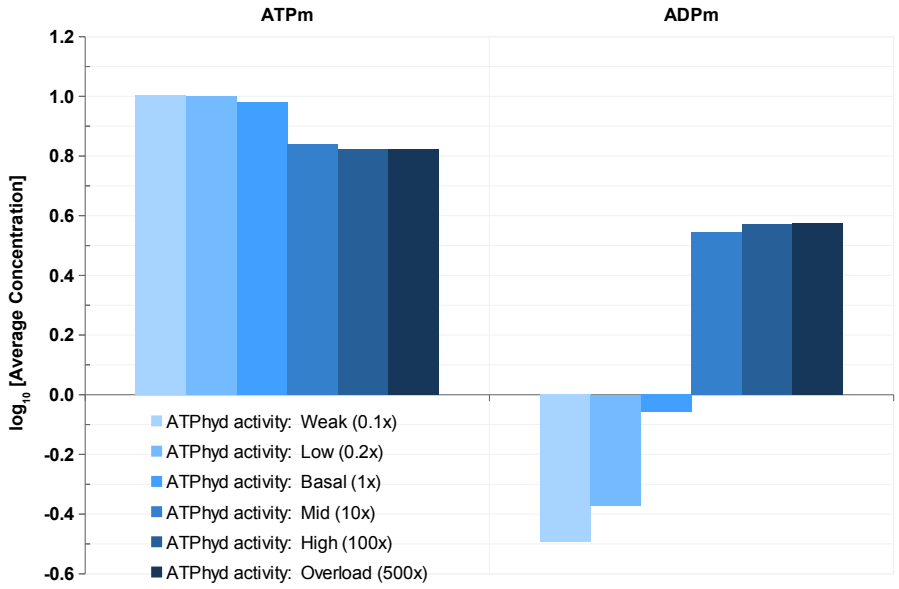

4.8.a. Mitochondrial adenine nucleotides

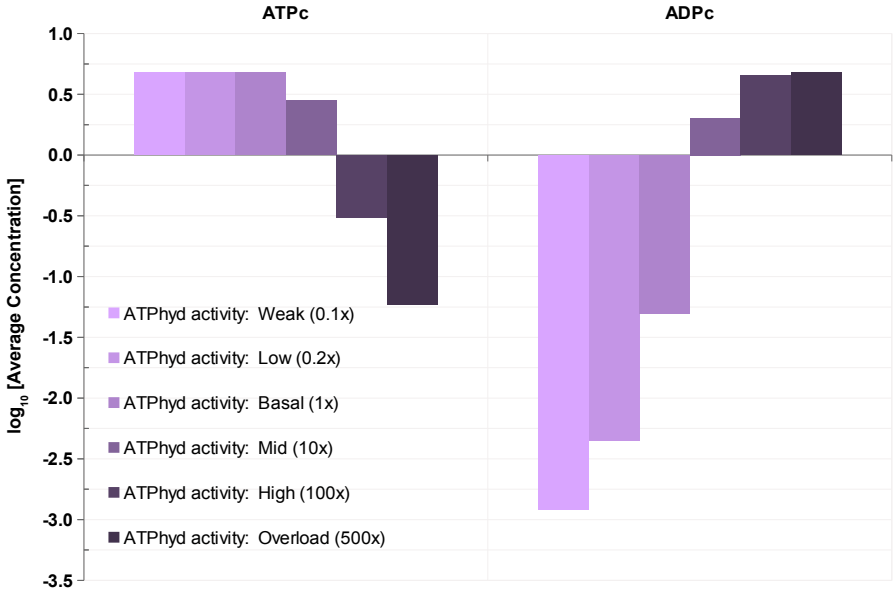

4.8.b. Cytosolic adenine nucleotides

▪ **Figure 4.8.** The effect of a wide range of ATP hydrolysis activity variations on mitochondrial & cytosolic adenine nucleotides, against the change in ANT maximal activity.

▪ For conditions, see fig. 4.7 on pg. 157.

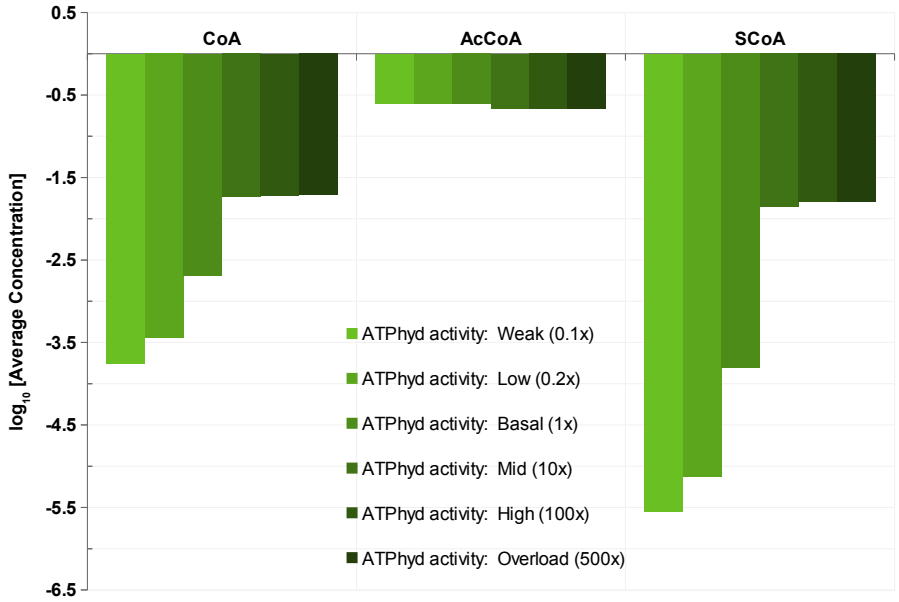

4.9.a. CoA−related metabolites

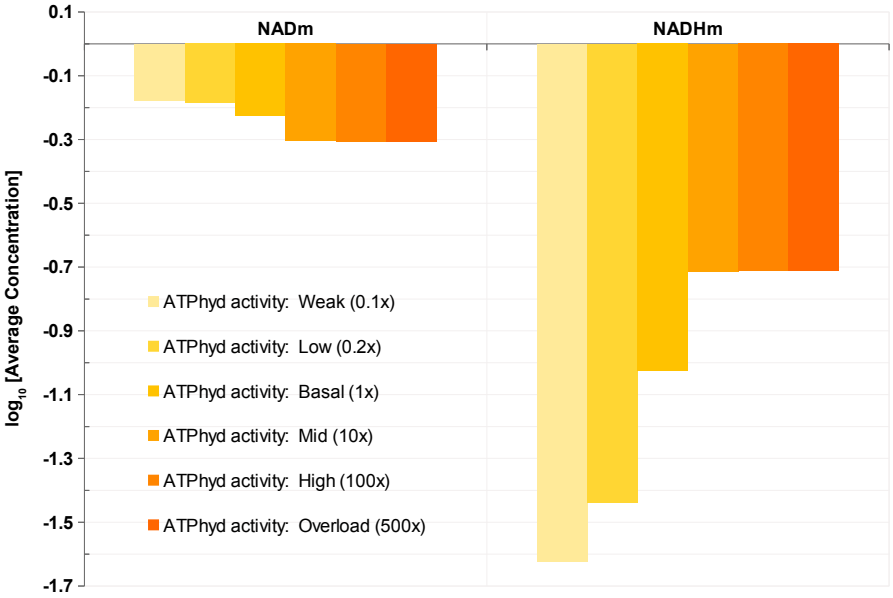

4.9.b. NAD−related metabolites

▪ **Figure 4.9.** The effect of a wide range of ATP hydrolysis activity variations on CoA− & NAD−related metabolites, against the change in ANT maximal activity.

▪ For conditions, see fig. 4.7 on pg. 157.

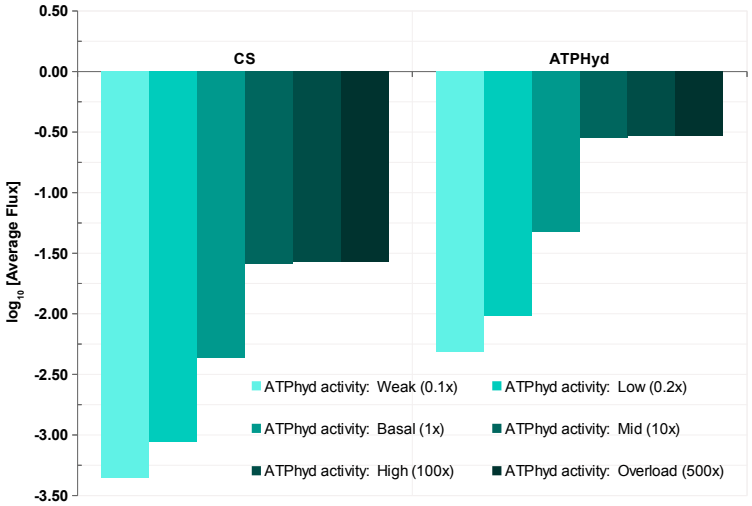

- **Figure 4.10.** The effect of a wide range of ATP hydrolysis activity variations on enzyme subset fluxes, against the change in ANT maximal activity.
- For conditions, see fig. 4.7 on pg. 157.

From the literature, we know that the cardiac or skeletal muscle are highly energy demanding tissues and their cellular metabolism is accordingly optimised to respond to any changes in the ATP demand. Therefore, in this analysis we test the heart TCA cycle model (HRT_{TCA}) against a wide range of energy demand by simulating the model at various levels of ATP hydrolysis activity, from *'weak'* (0.1x) to *'overload'* (500x). Thereby, we have attempted to study the steady-state behaviour of this model at 2 ATPhyd activity values that are lower than its *'basal'* activity or initial model value (*'weak' & 'low'*), as well as at 3 activity values that are higher than its *'basal'* activity (*'mid', 'high' & 'overload'*). Figures 4.7 to 4.10 (see, pgs. 157 to 160, respectively) illustrate the average steady-state behaviour of the heart TCA cycle model against a wide range of ATP hydrolysis activity. In all bar graphs presented here, bar representing the initial model value or the *'basal'* activity for a given parameter (*e.g.* ATPhyd) is always placed in the middle, surrounded by bars representing other activity values.

Overall, these graphs show that after the mid-level increase in the ATPhyd activity (10x), the heart TCA cycle model soon achieves a plateau phase, where any successive increase in the ATPhyd activity (100x & 500x) has a minimal effect on the average metabolite concentrations or reaction fluxes. However, in the case of ATP_c (see fig. 4.8b on pg. 158), these activity changes seem to have a significant effect on its average steady-state concentration, which decreases further as the ATPhyd activity is increased from 10x to 500x. In fact, at activities as high as that of 100 to 500 times the basal activity of ATPhyd, fig. 4.10 (see, pg. 160) shows that the flux through TCA cycle as well as ATPhyd does not change significantly, thus limiting the ANT flux as well, which allows the ATP_c concentration to fall significantly.

However, the heart TCA cycle model responds very well to ATPhyd activity changes in the range of weak (0.1x) to mid-level (10x) increase, around its basal level of activity.

Figure 4.10 (see, pg. 160) shows that the flux through TCA cycle as well as ATPhyd increases significantly as the ATP hydrolysis activity is increased from 0.001 mM/sec (weak) to 0.1 mM/sec (moderate). Literature evidence from enzymatic equilibrium studies on perfused hearts *in vitro* and NADH fluorescence studies on intact hearts, indicate that with increased workloads, net oxidation of mitochondrial NADH increases along with increase in the TCA cycle turnover rate (Kobayashi and Neely, 1983; Neely et al., 1972a; Nishiki et al., 1978; Williamson et al., 1976). Hence, the observed increase in the TCA cycle flux in response to increased ATP hydrolysis activity in the heart TCA cycle model, is in good agreement with the published experimental studies. Within this range, all TCA cycle intermediate metabolites increase significantly as the ATPhyd activity increases (see fig. 4.7 on pg. 157); except α-ketoglutarate, which falls sharply across all ATPhyd activities (see, fig. 4.7a). Compared to all TCA cycle intermediates, metabolites from the second half of TCA cycle such as, Suc_m, Fum_m, & Mal_m, all appear to accumulate in the system with increase in the ATPhyd activity (see, fig. 4.7b). Lack of transport reactions such as malate transporter, as well as the absence of malate-aspartate shuttle reactions could be some of the reasons for such accumulation of TCAi's.

Figure 4.9b (see, pg. 159) shows that within the range of 0.1x to 10x ATPhyd activity, NAD−related metabolites exhibit significant changes in their average steady-state concentrations, especially that of $NADH_m$; which increases sharply as the ATPhyd activity is increased. However, as mentioned earlier, both NAD^+_m as well as $NADH_m$ concentrations appear to stabilise beyond this range. Figure 4.9a shows that the CoA −related metabolites too respond similarly. Figure 4.8a (see, pg. 158) shows that the concentration of mitochondrial ATP decreases in a relatively buffered fashion as the ATPhyd activity is increased within this range, beyond which it stabilises. However, we feel that this buffered behaviour could partly be due to the respective initial model values of ATP−related metabolites, as these are the same values used in the liver TCA cycle model. Therefore, this analysis shows that the heart TCA cycle model (HRT_{TCA}) shows a consistent steady-state behaviour across a wide range of ATP hydrolysis activity or energy demand. Although, a 500 times increase in the ATPhyd activity can be considered a physiologically extreme situation or even a disease condition, this heart TCA cycle model performs robustly even at such physiological extremes.

If ATP hydrolysis represents the *demand* reaction in the heart TCA cycle model, pyruvate dehydrogenase represents the *supply* or *input* reaction. Therefore, in the following bar graphs we'll test the heart TCA cycle model against a wide range of increase in PDH maximal activity. Figures 4.11 to 4.14 (see, pgs. 162 to 165, respectively) show the average steady-state behaviour of the heart TCA cycle model, when pyruvate dehydrogenase activity is varied between 0.04x (*weak*) and 50x (*overload*), where 'x' is the initial model value for the pyruvate dehydrogenase activity (where, 'x' = 0.1885 mM/sec; termed here as – *basal activity*).

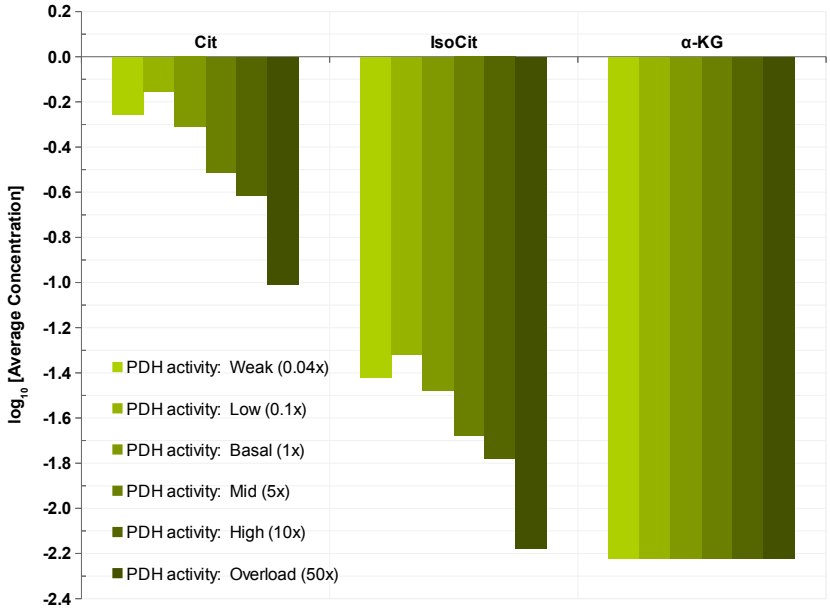

4.11.a. TCA cycle intermediate metabolites (TCAi) – Part 1

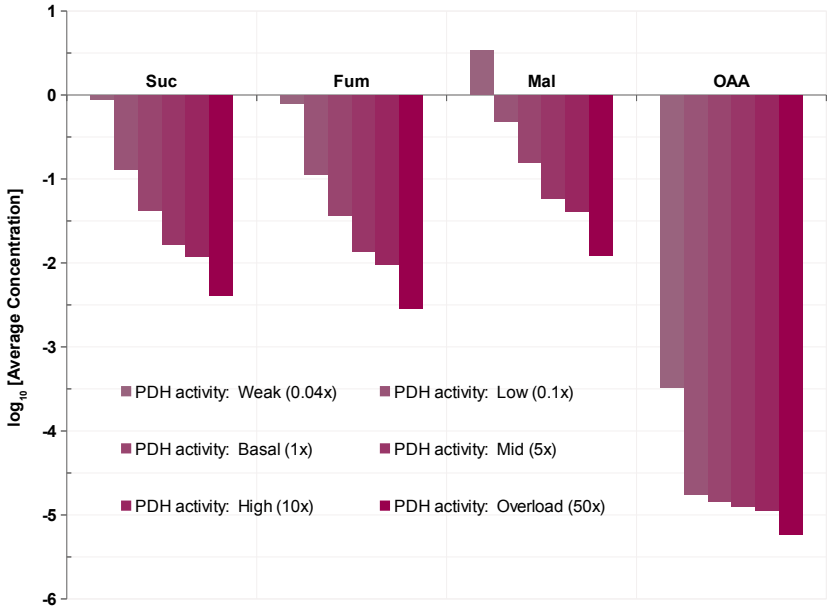

4.11.b. TCA cycle intermediate metabolites (TCAi) – Part 2

- **Figure 4.11.** The effect of a wide range of pyruvate dehydrogenase activity variations on TCAi concentrations, against the change in ANT maximal activity.

- Six bars for every metabolite or reaction represent six PDH activity variations, shown in light-to-dark colour shades, indicating *'weak'* to *'overload'* PDH activities.
- An average concentration or flux value was calculated for each metabolite or reaction, from all consecutive steady-state values per dataset. They were then used as $\boldsymbol{log_{10}}$ values to generate the bar graph.
- The initial model value for PDH activity in the heart TCA cycle model is 0.1885 mM/sec and in this graph, it is represented as the *'basal activity'* or '1x'. PDH activities included in this graph are as follows:
  - Weak PDH activity (0.04x) = 0.1885 mM/sec (1x) ÷ 25 = 0.00754 mM/sec
  - Low PDH activity (0.1x) = 0.1885 mM/sec (1x) ÷ 10 = 0.01885 mM/sec
  - Basal PDH activity (1x) = 0.1885 mM/sec (1x)
  - Mid/Moderate PDH activity (5x) = 0.1885 mM/sec (1x) × 5 = 0.9425 mM/sec
  - High PDH activity (10x) = 0.1885 mM/sec (1x) × 10 = 1.885 mM/sec
  - Overload PDH activity (50x) = 0.1885 mM/sec (1x) × 50 = 9.425 mM/sec

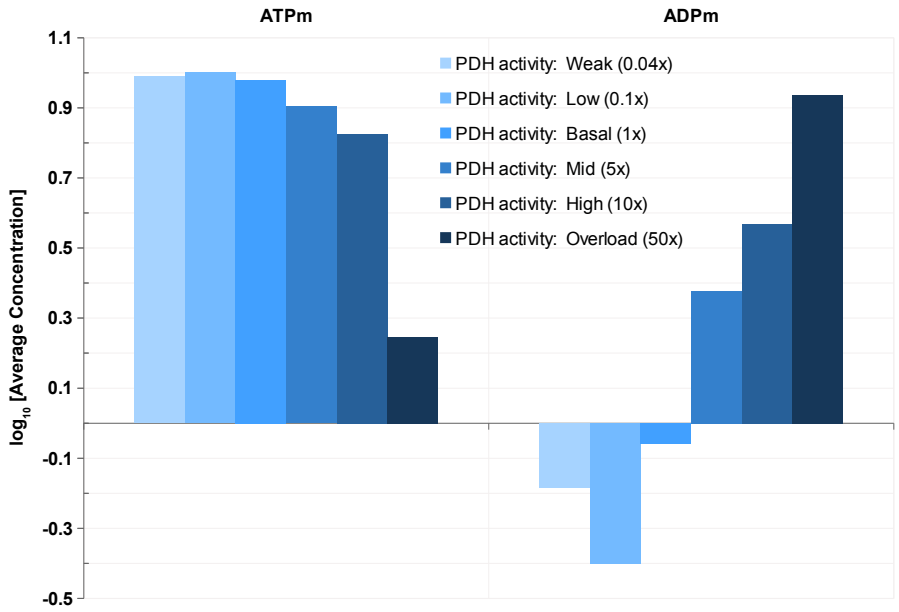

4.12.a. Mitochondrial adenine nucleotides

4.12.b. Cytosolic adenine nucleotides

▪ **Figure 4.12.** The effect of a wide range of pyruvate dehydrogenase activity variations on mitochondrial & cytosolic adenine nucleotides, against the change in ANT maximal activity.

▪ For conditions, see fig. 4.11 on pg. 162.

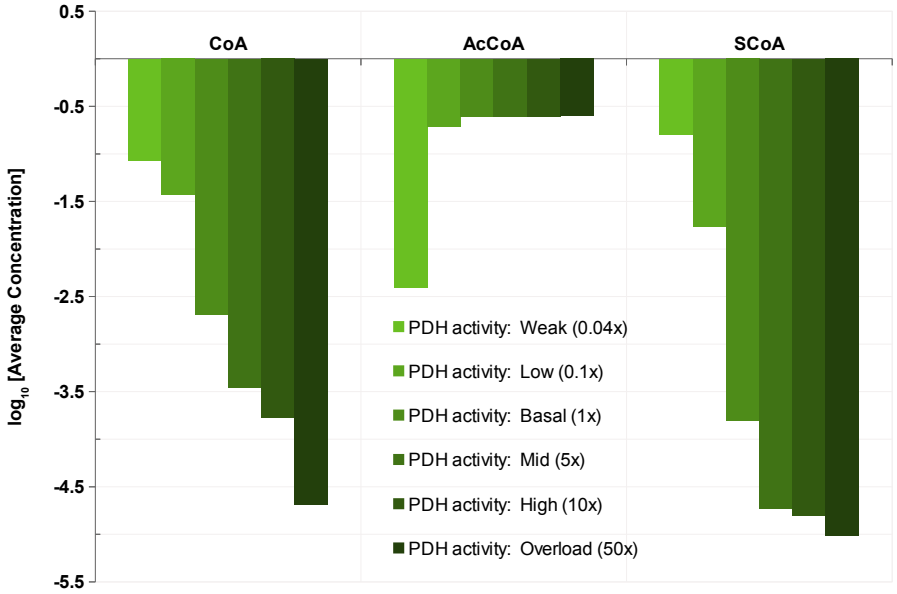

4.13.a. CoA−related metabolites

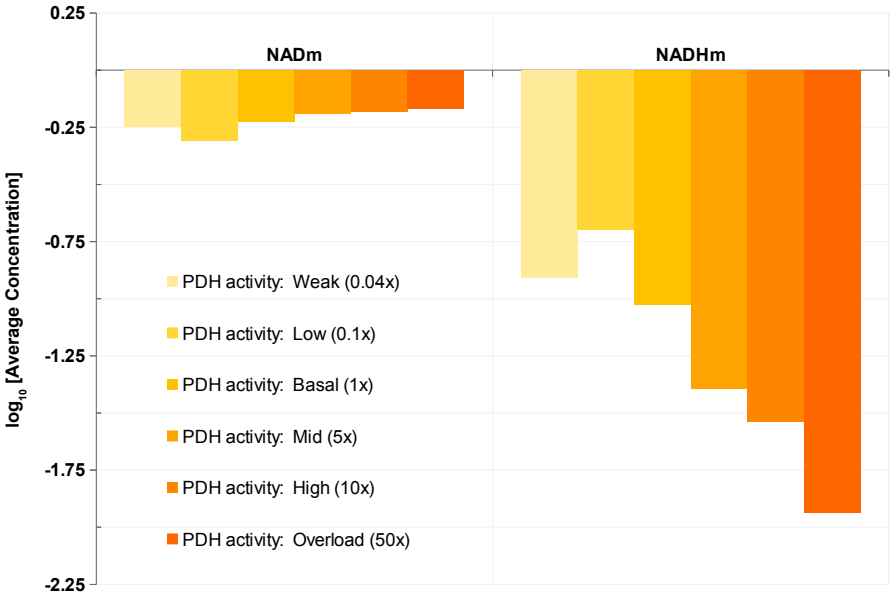

4.13.b. NAD−related metabolites

▪ **Figure 4.13.** The effect of a wide range of pyruvate dehydrogenase activity variations on CoA– & NAD−related metabolites, against the change in ANT maximal activity.

▪ For conditions, see fig. 4.11 on pg. 162.

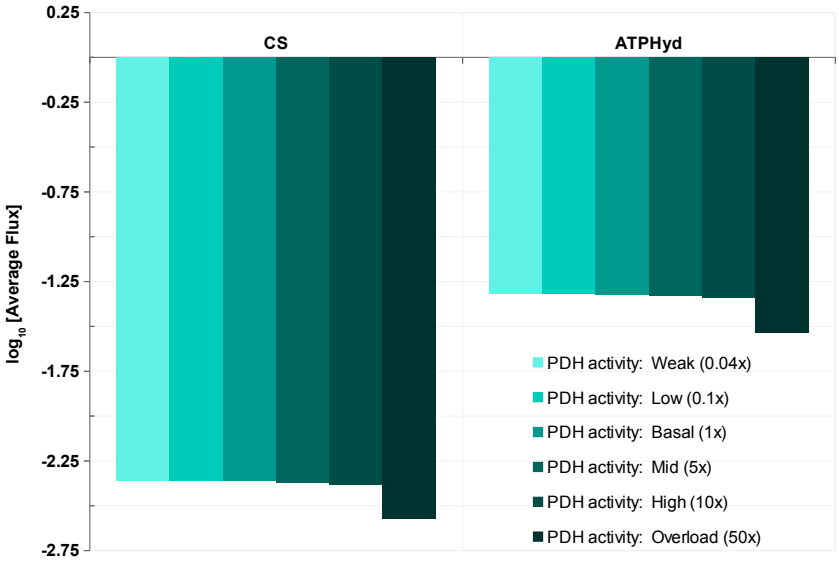

▪ **Figure 4.14.** The effect of a wide range of pyruvate dehydrogenase activity variations on enzyme subset fluxes, against the change in ANT maximal activity.

▪ For conditions, see fig. 4.11 on pg. 162.

From the literature, we know that the cellular pyruvate dehydrogenase activity levels are regulated through a complex interaction of covalent modification via pyruvate dehydrogenase kinase (PDHK) & pyruvate dehydrogenase phosphatase (PDHP), as well as allosteric effectors, depending on varying metabolic situations, such as feeding and fasting states. Therefore, in this analysis we test the heart TCA cycle model (HRT_{TCA}) against a wide range of acetyl-CoA supply by simulating the model at various levels of pyruvate dehydrogenase activity, from *'weak'* (0.04x) to *'overload'* (50x). Thus, we have studied the steady-state behaviour of this model at 2 PDH activity values that are lower than its *'basal'* activity or initial model value (*'weak' & 'low'*), as well as at 3 activity values that are higher than its *'basal'* activity (*'mid', 'high' & 'overload'*). Figures 4.11 to 4.14 (see pgs. 162 to 165, respectively) illustrate the average steady-state behaviour of the heart TCA cycle model against a wide range of pyruvate dehydrogenase activity.

Overall, these graphs show that most TCA cycle intermediates in this model decrease sharply in response to the increasing PDH activity or acetyl-CoA supply, except at the *'weak'* level (0.04x); where, citrate, isocitrate, acetyl-CoA, $NADH_m$, & ATP_m, all show significant decrease relative to their corresponding levels at the *'low'* (0.1x) PDH activity. It is possible that at 0.04x (0.00754 mM/sec), the pyruvate dehydrogenase activity is insufficient to supply adequate amount of acetyl-CoA, due to which the resting concentrations of TCA cycle intermediates fall. However, fig. 4.14 shows that the flux through TCA cycle as well as ATPhyd remains fairly unchanged throughout the range of increasing PDH activities, except at 50x activity of PDH (*'overload'*); where both these fluxes drop significantly. We may look at this situation as an *'over-driven'* state,

where other TCA cycle processes play catch-up with highly active PDH and fall short, thereby causing a reduction in the total TCA cycle flux, exemplified by a severe drop in the respective concentrations of most TCA cycle intermediates, such as – citrate, isocitrate, coenzyme A, $NADH_m$, ATP_m etc. (see figs. 4.11a, 4.12a and 4.13 on pgs. 162, 163 and 164, respectively).

As shown in fig. 4.14 (see, pg. 165), the insignificant increase in the TCA cycle flux achieved by increasing the PDH maximal activity is quite similar to the 'single gene modification experiments' carried out by biotechnologists, in hope of increasing the chosen metabolic pathway flux significantly by engineering an increase in a single target enzyme (Fell, 1997). However, such attempts rarely succeed, because the *'flux-enzyme relationship'* discovered by Small and Kacser (1993), implies that changing the amount of a single enzyme will have limited effects on the pathway flux, unless the flux control coefficient is greater than 0.5 to start with (Fell, 1997).

This analysis shows that although most of the TCA cycle intermediates show significant changes as the supply of acetyl-CoA or the PDH activity increases, the total flux through TCA cycle remains fairly unchanged. However, as noted in the previous chapter (see, pg. 80), a PDH maximal activity of 0.65 mM/sec (Fahien and Teller, 1992) represents the active PDH fraction under physiological conditions, which has been reported to be between 50% and 100% in perfused rat heart (Dennis et al., 1979; Olson et al., 1978; Reed et al., 1972). In the heart TCA cycle model, the initial model value for PDH V_{max} is even lower (0.1885 mM/sec; Kerbey et al., 1976; Kohn et al., 1979b). Therefore, at 50x increase in the PDH maximal activity (9.425 mM/sec), the PDH activity level falls well beyond physiological limits. Hence, the steady-state behaviour of the heart TCA cycle model at such non-physiological values of PDH activity is unlikely to have any physiological significance whatsoever.

Both the ATPhyd as well as PDH activity analyses shall be discussed further using the metabolite ratio profiles presented in figs. 4.15 and 4.16 on pgs. 167 and 168, respectively. Figures 4.15 and 4.16 describe the *'energy status'* of heart TCA cycle model in terms of key ratios like – $[ATP/ADP]_m$, $[ATP/ADP]_c$ & $[NADH/NAD^+]_m$, against a wide range of ATPhyd as well as PDH activities. Figures 4.15d and 4.16d provide a list of median values for these ratios.

Note: In figs. 4.15a to 4.15c (see, pg. 167), the partial absence of data-points at the 'weak' (0.1x; 0.001 mM/sec) level of ATP hydrolysis activity signifies that at such a low level of ATPhyd activity, the heart TCA cycle model is unable to find a stable steady-state; which is acceptable because this level of activity is at least 10 times lower than the physiological resting level of ATP demand reported in Rabbit skeletal muscle (Lambeth and Kushmerick, 2002).

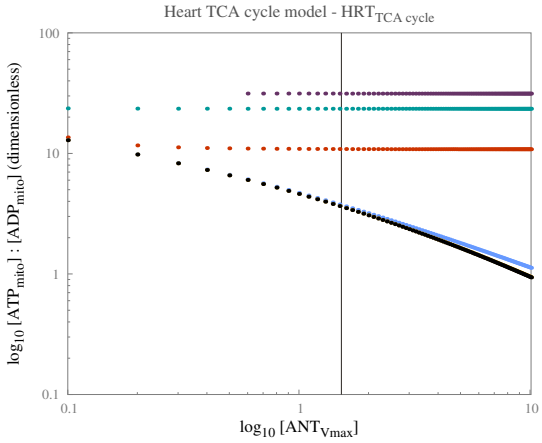

4.15.a. $[ATP/ADP]_m$

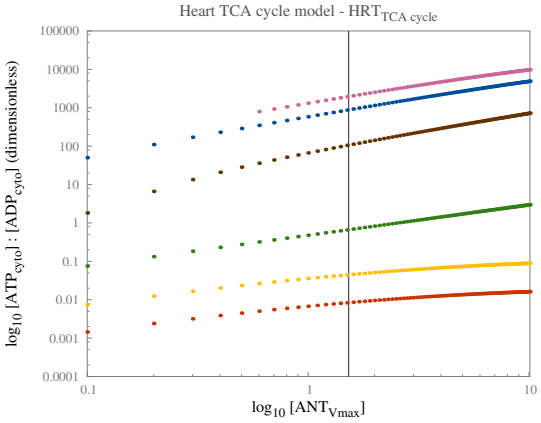

4.15.b. $[ATP/ADP]_c$

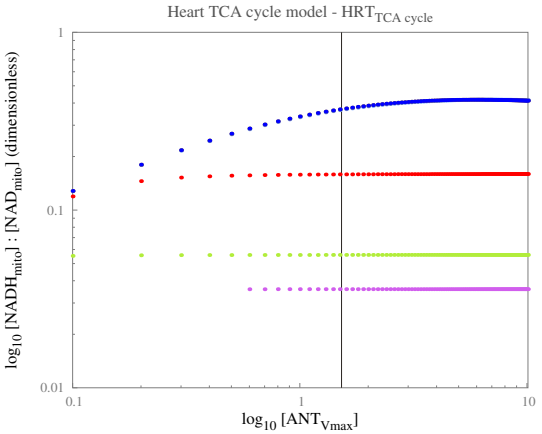

4.15.c. $[NADH/NAD^+]_m$

Median values

	Weak	Low	Basal	Mid	High	Very High
$NADH_m$ / NAD_m	0.04	0.06	0.16	0.4	0.4	0.4
ATP_m / ADP_m	31.35	23.45	10.8	1.7	1.56	1.55
ATP_c / ADP_c	6030.2	2867.4	390.2	1.8	0.08	0.01

4.15.d. Median values

▪ **Figure 4.15. Variations in the 'Energy status' of heart TCA cycle model:** $[ATP/ADP]$ & $[NADH/NAD^+]$ ratios against ATPhyd activity variations, across the change in ANT maximal activity.

▪ Key for figs. 4.15a to 4.15c is as follows :

- **$[ATP/ADP]_m$:** Weak (0.1x); Low (0.2x); Basal (1.0x); Mid (10.0x); High (100.0x); Overload (500.0x)
- **$[ATP/ADP]_c$:** Weak (0.1x); Low (0.2x); Basal (1.0x); Mid (10.0x); High (100.0x); Overload (500.0x)
- **$[NADH/NAD^+]_m$:** Weak (0.1x); Low (0.2x); Basal (1.0x); Mid (10.0x); High (100.0x); Overload (500.0x)

For figs. 4.15a to 4.15c :

▪ *X-axis* : $\log_{10}[V_{max}^{ANT}]$ – ANT maximal activity in logarithmic scale.

▪ *Y-axis* : Ratio of concentrations in logarithmic scale.

▪ The vertical black line represents the initial model value. At this point on the *X-axis*, $V_{max}^{ANT} = 1.52646$ mM/sec in logarithmic scale.

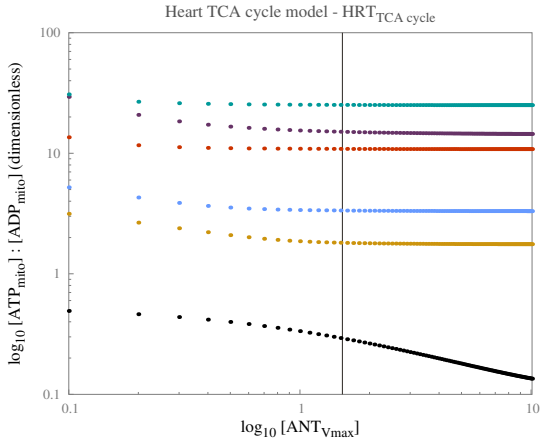

4.16.a. $[ATP/ADP]_m$

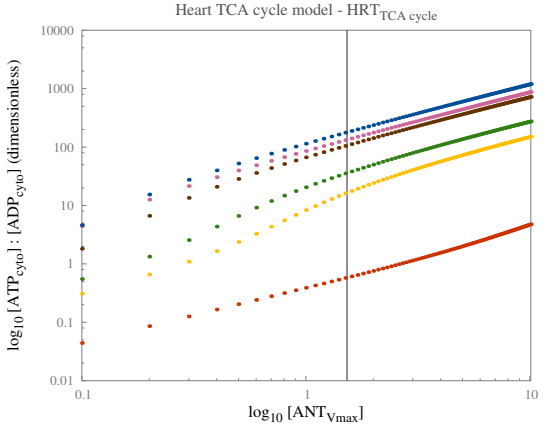

4.16.b. $[ATP/ADP]_c$

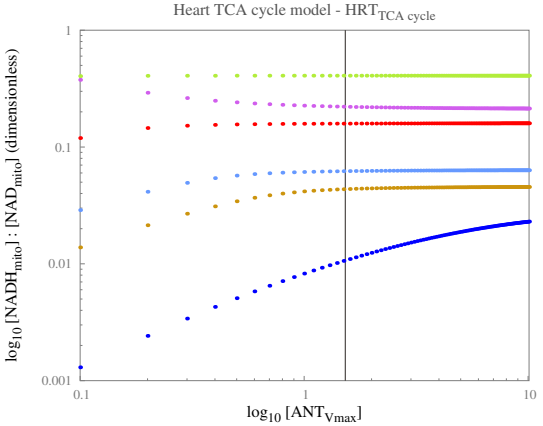

4.16.c. $[NADH/NAD^+]_m$

Median values						
	Weak	**Low**	**Basal**	**Mid**	**High**	**Very High**
$NADH_m$ / NAD_m	0.21	0.41	0.16	0.06	0.045	0.02
ATP_m / ADP_m	14.56	25.1	10.8	3.3	1.77	0.17
ATP_c / ADP_c	475.2	644.4	390.2	146.8	78.5	2.17

4.16.d. Median values

▪ **Figure 4.16. Variations in the 'Energy status' of heart TCA cycle model:** $[ATP/ADP]$ & $[NADH/NAD^+]$ ratios against PDH activity variations, across the change in ANT maximal activity.

▪ Key for figs. 4.16a to 4.16c is as follows :

- **$[ATP/ADP]_m$:** Weak; Low; Basal; Mid; High; Overload
- **$[ATP/ADP]_c$:** Weak; Low; Basal; Mid; High; Overload
- **$[NADH/NAD^+]_m$:** Weak; Low; Basal; Mid; High; Overload

▪ *X-axis* : $\log_{10}[V^{ANT}_{max}]$ – ANT maximal activity in logarithmic scale. ▪ *Y-axis* : Ratio of concentrations in logarithmic scale. ▪ The vertical black line represents the initial model value. At this point on the *X-axis*, $V^{ANT}_{max} = 1.52646$ mM/sec in logarithmic scale.

Overall, figs. 4.15 and 4.16 (see pgs. 167 and 168, respectively) show that through all variations of ATPhyd as well as PDH activities, metabolite ratio profiles of the heart TCA cycle model follow a similar qualitative course of change. However, as shown in fig. 4.15a, at *'mid'* (10x), *'high'* (100x) & *'overload'* (500x) levels of ATPhyd activities, the $[ATP/ADP]_m$ ratio drops significantly compared to the lower levels of ATPhyd activity, as the ANT maximal activity is incremented further. Figure 4.15d clearly distinguishes these levels of ATPhyd activity from others through their significantly lower median values, *viz.*– 1.7, 1.56, & 1.55 for 10x, 100x, & 500x of ATPhyd maximal activity, respectively. This distinction between the levels of ATPhyd activity can also be

seen in fig. 4.8a (see, pg. 158), in terms of the average steady-state concentrations of ATP_m & ADP_m respectively, albeit not as clearly. Also, at these same levels of ATPhyd activities (*i.e.* mid, high, & overload), fig. 4.15c shows that the respective $[NADH/NAD^+]_m$ ratio profiles follow the same qualitative course of increase. Figure 4.15d shows a common median value of 0.4 for the $[NADH/NAD^+]_m$ ratio at all three activities of ATP hydrolysis. Figure 4.9b (see, pg. 159) also shows this quantitatively in terms of the average steady-state concentrations of NAD^+_m & $NADH_m$, respectively.

As illustrated in fig. 4.16 (see, pg. 168), at *'overload'* (50x; 9.425 mM/sec) level of PDH activity, both the $[ATP/ADP]_m$ as well as $[NADH/NAD^+]_m$ ratio profiles show characteristically different course of change than that at other PDH activities; wherein, the $[ATP/ADP]_m$ ratio drops further as the ANT maximal activity is incremented (see, fig. 4.16a) and the $[NADH/NAD^+]_m$ ratio attempts to recover from a severe initial drop in its value (see, fig. 4.16c). In fact, as shown in fig. 4.16d, the corresponding median value for the $[ATP/ADP]_m$ ratio (*i.e.* 0.17), signifies that at such a high level of PDH activity, this ratio reverses and makes the system more 'ADP_m-rich'; which can also be observed in fig. 4.12a (see, pg. 163) in terms of the average steady-state concentrations of ATP_m & ADP_m, respectively. Also, at this high level of PDH activity, fig. 4.16d shows a corresponding median value of 0.02 for the $[NADH/NAD^+]_m$ ratio, which isn't that distinct from that of 0.045 at *'high'* PDH activity and doesn't really reflect the characteristically different qualitative course of change taken by this ratio at the *'overload'* level of PDH activity. However, this significant difference in the $[NADH/NAD^+]_m$ ratio between 50x activity and other levels of PDH activities, can be observed in fig. 4.13b (see, pg. 164) in terms of the average steady-state concentrations of NAD^+_m & $NADH_m$, respectively. Regardless, as mentioned earlier on pg. 166, since this level of pyruvate dehydrogenase activity (50x) should be considered physiologically anomalous, any further discussion about the model behaviour at this level of PDH activity is futile.

As mentioned earlier, against the increased ATP-demand set by higher values of ATPhyd activity, at *'mid'* (10x), *'high'* (100x) & *'overload'* (500x) levels, the mitochondrial redox ($[NADH/NAD^+]_m$) as well as the energy ($[ATP/ADP]_m$) states exhibit fairly stabilised changes in their respective values, compared to those at lower levels of ATPhyd activity (see fig. 4.15d on pg. 167). Incidentally, the experimental evidence from *workload intensity transition studies* in intact mammalian hearts *in vivo*, also suggest of almost constant [ADP], [PCr] (Phosphocreatine), [Pi] and $NADH/NAD^+$ during workload transitions (Balaban et al., 1986; Heineman and Balaban, 1993; Katz et al., 1987, 1989b; Sharma et al., 2005). On the other hand, with increasing workloads, experimental studies have reported larger changes in [ADP], [PCr], [Pi] and $NADH/NAD^+$ in perfused heart (From et al., 1990) and in isolated cardiac myocytes (White and Wittenberg, 1993) than those in intact heart *in vivo*. Also, Heineman and Balaban (1990) in their excellent

review paper include further evidence supporting the net oxidation of mitochondrial NADH with increased workloads, by citing *enzymatic equilibrium studies* on perfused hearts *in vitro* (Kobayashi and Neely, 1983; Neely et al., 1972a; Nishiki et al., 1978), as well as *NADH fluorescence studies* on intact hearts (Williamson et al., 1976). Therefore, the fairly stabilised redox & energy states in the heart TCA cycle model at 'moderate' to 'very high' ATP-demands, apparently reflect a similar physiological behaviour observed in intact mammalian hearts *in vivo*, at increased workloads.

Moreover, in isolated rat heart mitochondria, using a wide variety of respiratory substrates, NADH/NAD^+ ratio was found to vary between 0.02 (with no substrate added to the incubation medium) to 2.62 (with addition of 5 mM succinate to the incubation medium) (Kerbey et al., 1976). The variation in $[NADH/NAD^+]_m$ ratio observed during both studies with increased maximal activities of ATPhyd as well as PDH in the heart TCA cycle model (see figs. 4.15d and 4.16d on pgs. 167 and 168, respectively), is well within this range of reported values. Overall, the median values shown in figs. 4.15d and 4.16d for all variations in the respective maximal activities of ATPhyd & PDH, illustrate the significant quantitative difference in the *'energy status'* of the heart TCA cycle model, when subjected to large changes in key enzyme activities. It also highlights the robustness of the metabolic system represented by this model; which is a good indicator of its predictive capabilities, especially when combined with the malate-aspartate shuttle reactions in the near future.

Now, in the following sections, we shall discuss the control properties of the heart TCA cycle model in terms of the *flux control coefficients, concentration control coefficients, & elasticity coefficients.*

4.3.5 Metabolic Control Analysis of the heart TCA cycle model

In this section, we'll see the results of Metabolic Control Analysis (MCA) when applied to the heart TCA cycle model, by observing the distribution of flux control coefficient (C^J), concentration control coefficient (C^S) and elasticity coefficient (ε_S).

4.3.5.1 Flux control coefficient analysis for the heart TCA cycle model

Since, the heart TCA cycle model contains a single enzyme subset comprising all TCA cycle reactions, we'll analyse the control of flux through CS as a representation of the flux through TCA cycle. As the enzyme activities or metabolite concentrations vary, their corresponding degree of control varies as well. Hence, we examined how the pattern of control changed as these parameters were varied over a fixed range.

Figures 4.17 to 4.19 (see pgs. 171 to 173, respectively), show the flux control coefficients (C^J) calculated for the TCA cycle flux, for all enzymes in heart TCA cycle model, across a fixed range of increasing maximal activities (ANT, ATPhyd, & PDH) or metabolite concentrations (Pi_m, $cAdN_{csum}$, & αKG_c). These C^J plots are presented alongside a corresponding steady-state plot of CS flux across the same fixed range of a given parameter (*here, CS is the reaction 'J' on which C^J is calculated*). In each plot, result of the *summation theorem* is also included using a dotted line. In these plots, the flux control coefficients are distributed between the range of −0.8 to 1.2 (unitless).

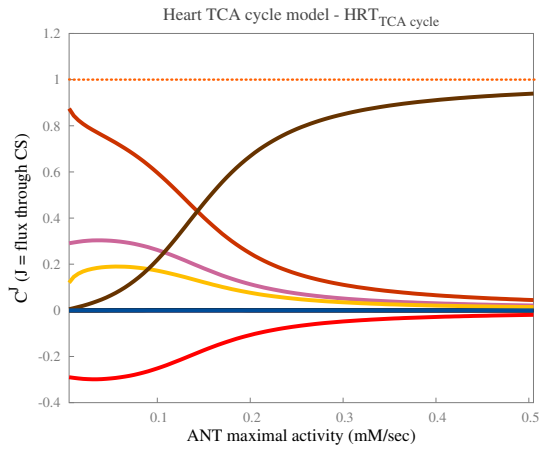

4.17.a. C^J *vs* ANT maximal activity

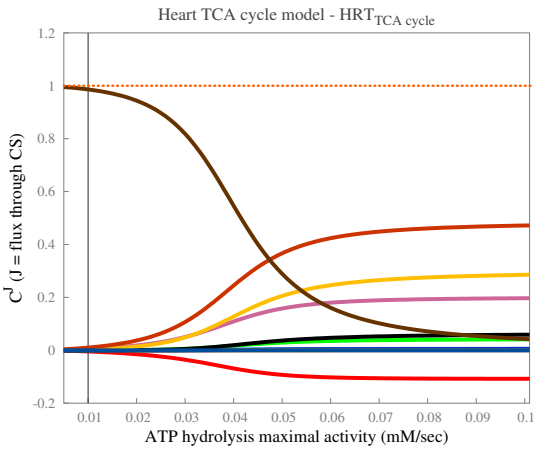

4.17.b. C^J *vs* ATPhyd maximal activity

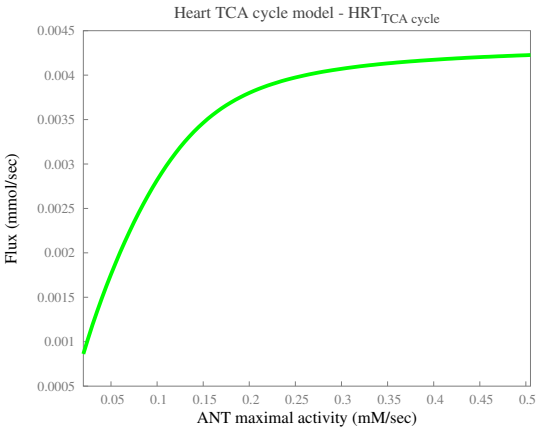

4.17.c. CS flux *vs* ANT activity

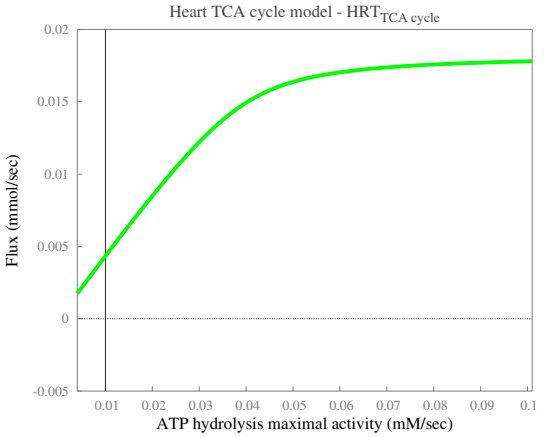

4.17.d. CS flux *vs* ATPhyd activity

- **Figure 4.17. Control of TCA cycle flux in the heart TCA cycle model:** against the activities of ANT & ATPhyd.

- Key for figs. 4.17a and 4.17b is as follows :

PDH ; CS ; ACO ; IDHa ; α-KGDH ; SCS;
SDH ; FM ; MDH ; ATPsynth ; ANT ; ATPhyd;
α-KG_{exp} ; Total Sum (dotted line)

- The vertical black line represents the initial model value. At this point, in figs. 4.17a and 4.17c, $V_{max}^{ANT} = 1.52646$ mM/sec and in figs. 4.17b and 4.17d, $V_{max}^{ATP_{hyd}} = 0.01$ mM/sec, respectively. However, in figs. 4.17a and 4.17c, the presented range of ANT maximal activity is only between 0.0 to 0.5 mM/sec and therefore, V_{max}^{ANT} initial model value is out of range in these plots.
- ***Orange dotted line*** shows the *Summation theorem* result across the entire range.

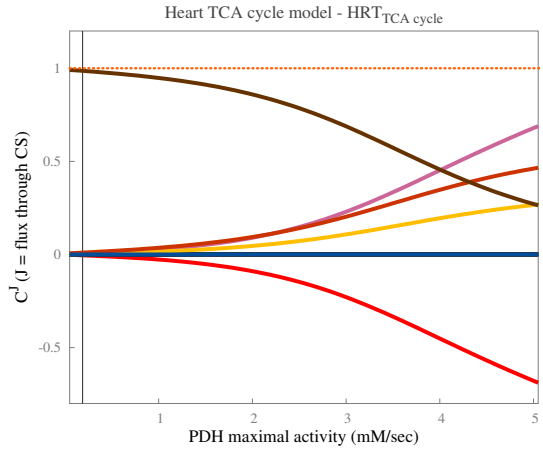

4.18.a. C^J *vs* PDH maximal activity

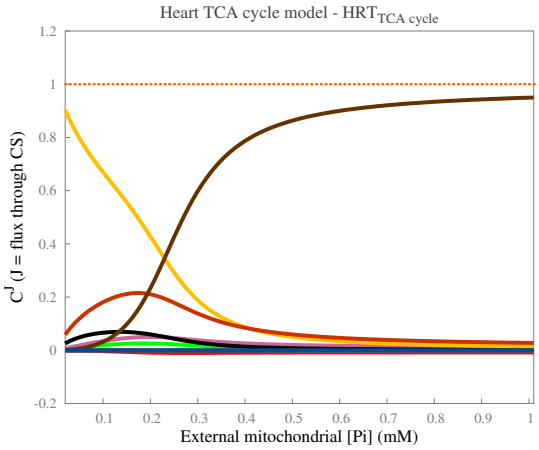

4.18.b. C^J *vs* Pi_m concentration

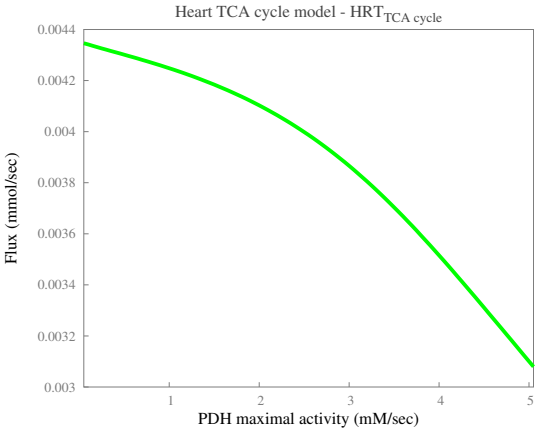

4.18.c. CS flux *vs* PDH activity

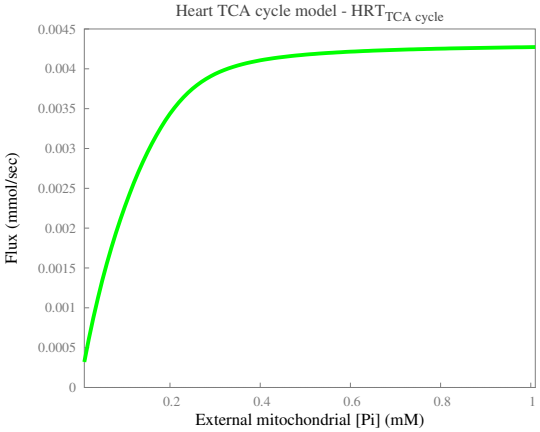

4.18.d. CS flux *vs* Pi_m concentration

▪ **Figure 4.18. Control of TCA cycle flux in the heart TCA cycle model:** against changing PDH maximal activity & Pi_m concentration.

▪ Key for figs. 4.18a and 4.18b is as follows :

PDH ; CS ; ACO ; IDHa ; α-KGDH ; SCS;
SDH ; FM ; MDH ; ATPsynth ; ANT ; ATPhyd;
α-KG_{exp} ; Total Sum (dotted line)

▪ The vertical black line represents the initial model value. At this point, in figs. 4.18a and 4.18c, $V_{max}^{PDH} = 0.1885$ mM/sec and in figs. 4.18b and 4.18d, $[Pi_m] = 8.9$ mM, respectively. However, in figs. 4.18b and 4.18d, the presented range of Pi_m concentration is only between 0.0 to 1.0 mM and therefore, $[Pi_m]$ initial model value is out of range in these plots.

▪ ***Orange dotted line*** shows the *Summation theorem* result across the entire range.

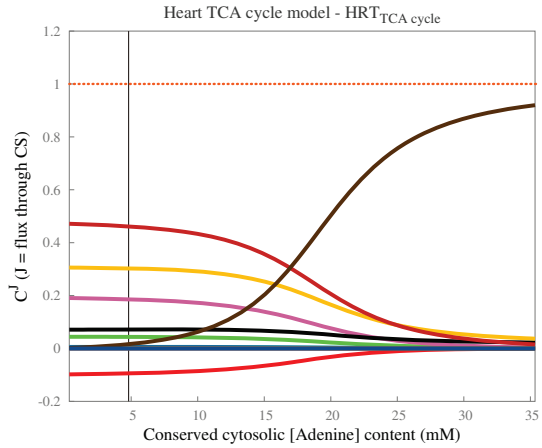

4.19.a. C^J *vs* $cAdN_{csum}$ total

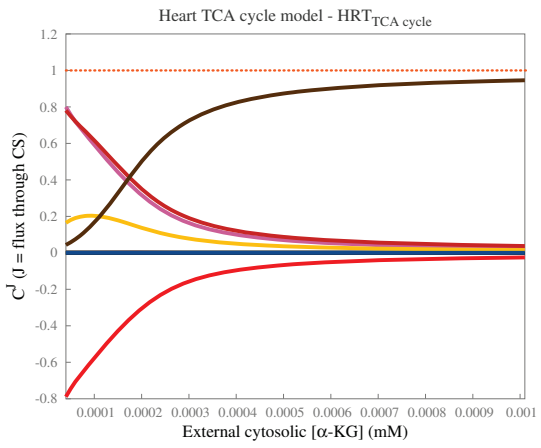

4.19.b. C^J *vs* αKG_c concentration

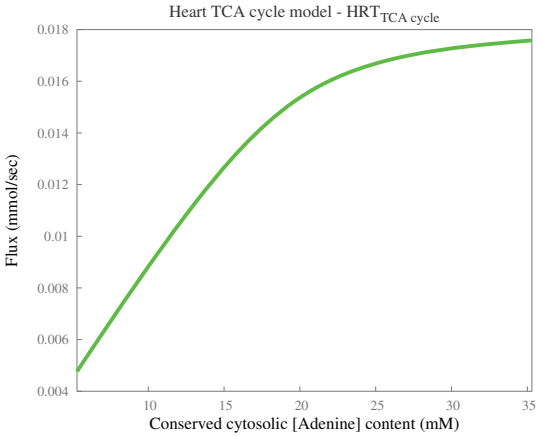

4.19.c. CS flux *vs* $cAdN_{csum}$ total

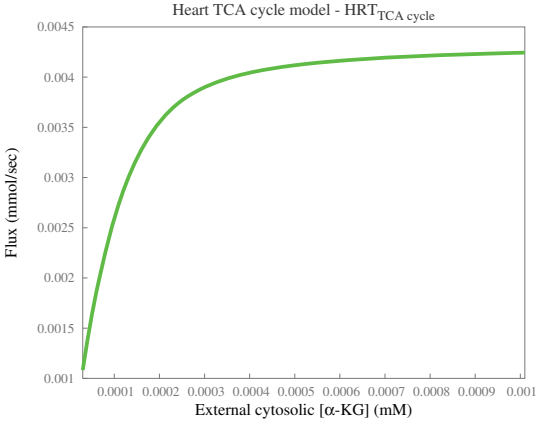

4.19.d. CS flux *vs* αKG_c concentration

▪ **Figure 4.19. Control of TCA cycle flux in the heart TCA cycle model:** against $cAdN_{csum}$ total & αKG_c concentration.

▪ Key for figs. 4.19a and 4.19b is as follows :

PDH ; CS ; ACO ; IDHa ; α-KGDH ; SCS;
SDH ; FM ; MDH ; ATPsynth ; ANT ; ATPhyd;
α-KG_{exp} ; Total Sum (dotted line)

▪ The vertical black line represents the initial model value. At this point, in figs. 4.19a and 4.19c, $cAdN_{csum}$ total = 4.81 mM and in figs. 4.19b and 4.19d, $[\alpha KG_c]$ = 0.006 mM, respectively. However, in figs. 4.19b and 4.19d, the presented range of αKG_c concentration is only between 0.0 to 0.001 mM and therefore, $[\alpha KG_c]$ initial model value is out of range in these plots.

▪ ***Orange dotted line*** shows the *Summation theorem* result across the entire range.

A plot of C^J against the enzyme maximal activity or concentration would normally be expected to be hyperbolic, however for the heart TCA cycle model, the C^J distribution pattern shown in figs. 4.17 to 4.19 (see pgs. 171 to 173, respectively) is distinctly sigmoidal. An in-depth discussion from the previous chapter (see, pg. 94), suggests that it is due to the saturation of one or more TCA cycle enzymes and if these enzyme(s) are desaturated with respect to their corresponding substrate(s), a nearly-hyperbolic pattern of C^J distribution can be restored.

As predicted correctly through the control analysis of the PC_{ko} model (see, pg. 141), in the absence of PC, the control of TCA cycle flux (flux through CS) in the heart TCA cycle model is dominated largely by ATP hydrolysis. From figs. 4.17 to 4.19, it is evident that ATPhyd has a relatively greater control of the TCA cycle flux; however, the control is also distributed between PDH, α-KGDH, ATPsynth, & ANT. In most cases, the control shared by ATPhyd increases or decreases to or from nearly a unity and the amount of control shared by other four enzymes changes accordingly, across the given parameter range. For instance in fig. 4.17a, C^J for ATPhyd increases gradually from zero to nearly a unity as the ANT maximal activity is increased and accordingly, the extent of control shared by the other four enzymes becomes minimal. On the contrary, in fig. 4.17b, C^J for ATPhyd decreases gradually from unity to nearly zero as the ATPhyd maximal activity is increased and accordingly, the extent of control shared by the other four enzymes increases to account for the loss of control by ATPhyd. Unlike that of the liver TCA cycle models, in this model the exchange of control between ATPhyd and the other 4 enzymes is quite gradual and occurs over nearly 30% – 50% of the given parameter range.

In these plots, pyruvate dehydrogenase shares a moderately negative flux control coefficient value, which appears counter-intuitive. However, in the absence of PC, it is the only *input* reaction in the heart TCA cycle model that supplies TCA cycle carbon in the form of acetyl-CoA and constitutes the *'supply block'*, according to the *'supply-demand analysis'* put forward by Hofmeyr and Cornish-Bowden (2000) (see, pg. 75). Also, structurally, all TCA cycle reactions of this model form a single enzyme subset that includes PDH as well as 3 ATP/ADP–linked reactions; which makes PDH a branch reaction in the linear sequence of other TCA cycle reactions. As a consequence of these factors, a moderately negative flux control coefficient for PDH may seem appropriate.

Also, as discussed in Fell (1997), according to the supply-demand analysis of metabolic control structures, the pathway flux can be controlled by the *'demand block'* (in this case, ATPhyd), only if $C^J_{HYD} \gg C^J_{PDH}$; where, J is the flux through CS. However, it requires that the elasticity for the metabolite (M) supplied (*i.e.* $AcCoA_m$) with respect to the *'supply block'* (*i.e.* PDH) must exceed its elasticity with respect to the *'demand block'* (*i.e.* ATPhyd) or $|\mathcal{E}^{PDH}_{AcCoA}| \gg \mathcal{E}^{HYD}_{AcCoA}$; which is true in this case, since $\mathcal{E}^{PDH}_{AcCoA} = -0.3$ and $\mathcal{E}^{HYD}_{AcCoA} = 0.0$ (as shown later, in fig. 4.25 on pg. 185). However, as the heart TCA cycle model is extended to include the malate-aspartate shuttle reactions in near future, we suspect that this negative coefficient value would disappear due to the additional branch points being introduced downstream of PDH.

Similarly, based on the same concept, moderately high C^J values for ANT & ATPsynth, as well as the significantly high control coefficient for ATPhyd can be explained on the basis that these reactions comprise the *'demand block'* of the heart

TCA cycle model. Also, α-KGDH, despite being highly regulated, shares a small but notable flux control coefficient with ANT & ATPsynth in the heart TCA cycle model.

At *initial conditions* of the heart TCA cycle model, figs. 4.17 to 4.19 show that the flux through TCA cycle is controlled entirely by ATP hydrolysis; except in the case of fig. 4.19a. In this particular case (see, fig. 4.19a), the control of TCA cycle flux is distributed uniformly between ANT, ATPsynth, α-KGDH, MDH, CS, & PDH, at initial conditions of the $\mathrm{cAdN_{csum}}$ total. In figs. 4.17a, 4.18b and 4.19b, though the respective initial model values of ANT maximal activity, $\mathrm{Pi_m}$ concentration, and $\mathrm{\alpha KG_c}$ concentration are out of the presented range, it is clear from their respective C^J distribution patterns that at initial conditions, the control of TCA cycle flux will be dominated by ATPhyd alone.

Also, fig. 4.18a (see, pg. 172) provides a further explanation for the insignificant increase in TCA cycle flux, during the steady-state analysis at various levels of pyruvate dehydrogenase activity (see fig. 4.14 on pg. 165). As shown in fig. 4.18a, with increase in the PDH maximal activity, C^J for ATPhyd begins to drop from unity and C^J for PDH becomes further negative. At the initial model value of PDH maximal activity or at *'basal'* activity of PDH (*i.e.* = 0.1885 mM/sec; 1.0x), the control of TCA cycle flux rests entirely in ATPhyd. Figure 4.18a shows that C^J for ATPhyd dominates even when the PDH maximal activity is increased by 5x (*i.e.* = 0.9425 mM/sec; *'moderate'*) or 10x (*i.e.* = 1.885 mM/sec; *'high'*). It also shows that with increase in PDH maximal activity, the significant loss of control shared by ATPhyd is picked up by α-KGDH, ANT & ATPsynth. Moreover, when the PDH maximal activity is increased beyond 2.5 mM/sec, the extent of control shared by ATPhyd is lost rapidly and gets counter-balanced by a further negative C^J for PDH, along with a corresponding increase in the control shared by α-KGDH, ANT & ATPsynth.

Therefore, fig. 4.18a shows that at very high activities of pyruvate dehydrogenase (*i.e.* = 9.425 mM/sec; *'overload'*; 50x), the control shared by ATPhyd would be close to zero, C^J for PDH would be highly negative and the control of TCA cycle flux would be distributed uniformly between α-KGDH, ANT, ATPsynth, & PDH (negative). Furthermore, fig. 4.18c (see, pg. 172) shows that a large increase in the PDH maximal activity actually causes a marginal decrease in the TCA cycle flux (*please note the Y-axis*); which means that further increase in PDH maximal activity (*e.g.* a 50x increase) would actually reduce the TCA cycle flux even further.

In conclusion, this analysis suggests that in order to achieve a significant increase in the TCA cycle flux at higher activities of pyruvate dehydrogenase, the activity of at least one of the other controlling enzymes (*i.e.* α-KGDH, ANT & ATPsynth) must also be increased simultaneously. During the discussion on steady-state analysis results shown

in figs. 4.11 to 4.14 (see pgs. 162 to 165, respectively), we arrived at a similar conclusion (see, pg. 166) and therefore the C^J distribution shown in fig. 4.18a lends further support to our well-founded suspicion.

Also, fig. 4.19b (see, pg. 173) shows the distribution of flux control coefficients against the increasing concentration of cytosolic α-ketoglutarate ([αKG_c]) in the heart TCA cycle model. It shows that with increase in [αKG_c], the TCA cycle flux is largely controlled by ATPhyd with minor extent control shared between PDH, ATPsynth, α-KGDH, & ANT; which diminishes as the αKG_c concentration is increased further. Although, the initial model value of [αKG_c] (0.006 mM) is beyond the range of concentration presented in this plot, it is clear that at this value, C^J for ATPhyd would be close to unity; which means that at and beyond the initial model value of [αKG_c], the TCA cycle flux would be controlled by ATPhyd alone. Figure 4.19d shows that the TCA cycle flux is increased moderately by 3-fold, with increase in [αKG_c]. It indicates that extending the heart TCA cycle model by including the malate-aspartate shuttle reactions might help in improving the flux through the TCA cycle, provided that the extended model results in net exchange of mitochondrial α-ketoglutarate.

Also, figs. 4.17d and 4.19c (see, pgs. 171 and 173) show that the TCA cycle flux is increased significantly, by nearly 3- to 4-times, with increase in the ATP hydrolysis activity, as well as the conserved total of cytosolic adenine nucleotides ($cAdN_{csum}$) (*please note the Y-axis from both plots*).

Therefore, overall, the emergent flux control properties of the heart TCA cycle model adequately reflect the energy-demand driven nature of the myocardial metabolism, qualitatively.

4.3.5.2 Concentration control coefficient analysis for the heart TCA cycle model

In this section, we shall analyse the *concentration control coefficients* (C^S) of TCA cycle intermediate metabolites, calculated with respect to all enzymes in the model. The heart TCA cycle model contains 16 internal metabolites, all of which can be analysed using the concentration control coefficients. However, in this section, we have presented data for only a selected group of metabolites, *viz.*– OAA_m, Cit_m, $AcCoA_m$, $NADH_m$, ATP_m, ATP_c, & Mal_m. These metabolites were selected based on the same reasons given in the previous chapter (see, pg. 100). Figures 4.20 to 4.23 (see, pgs. 177 to 180, respectively) show the distribution of concentration control coefficients for the selected TCA cycle intermediate metabolites, against the change in ATP hydrolysis activity. Also, fig. 4.24 (see, pg. 181), provides a qualitative overview of the control distribution for all 16 internal metabolites in the heart TCA cycle model, against the change in ATP hydrolysis activity.

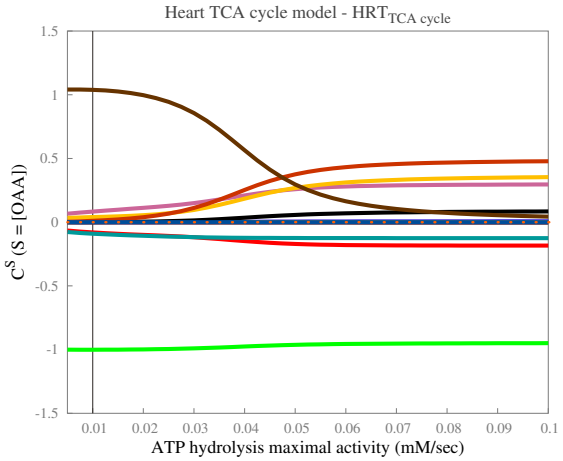

4.20.a. C^{OAA} *vs* ATPhyd maximal activity

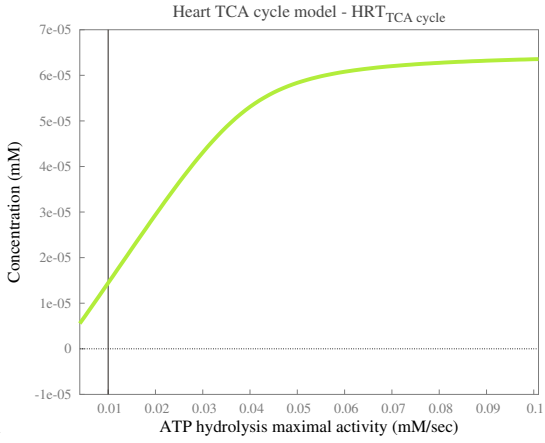

4.20.b. [OAA] *vs* ATPhyd activity

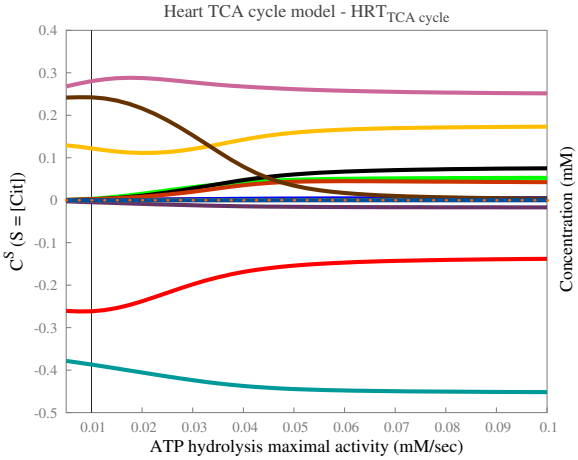

4.20.c. C^{Cit} *vs* ATPhyd maximal activity

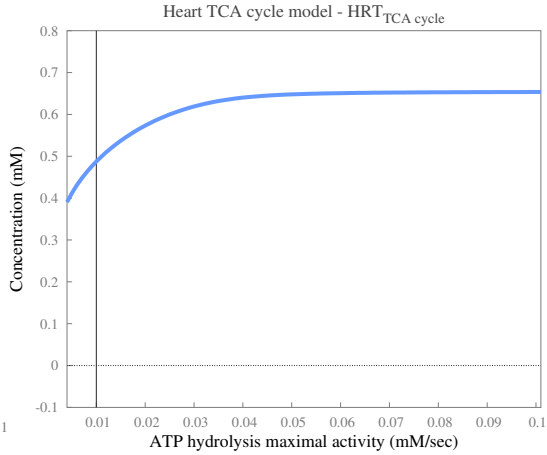

4.20.d. [Citrate] *vs* ATPhyd activity

- **Figure 4.20. Control of TCA cycle intermediate metabolites:** Distribution of concentration control coefficients calculated for the respective concentrations of OAA & Citrate, against the changing maximal activity of ATPhyd.

- Key for figs. 4.20a and 4.20c is as follows :

PDH ; CS ; ACO ; IDHa ; α-KGDH ; SCS;
SDH ; FM ; MDH ; ATPsynth ; ANT ; ATPhyd;
α-KG$_{exp}$; Total Sum (dotted line)

- The vertical black line represents the initial model value. At this point, in figs. 4.20a to 4.20d, $V_{max}^{ATP_{hyd}} = 0.01$ mM/sec.

- ***Orange dotted line*** shows the *Summation theorem* result across the entire range. For concentration control coefficients, since the sum is equal to zero, the dotted line is not easily visible.

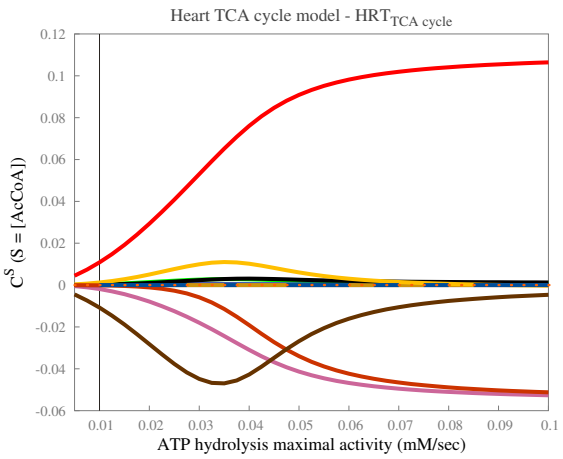

4.21.a. C^{AcCoA} *vs* ATPhyd maximal activity

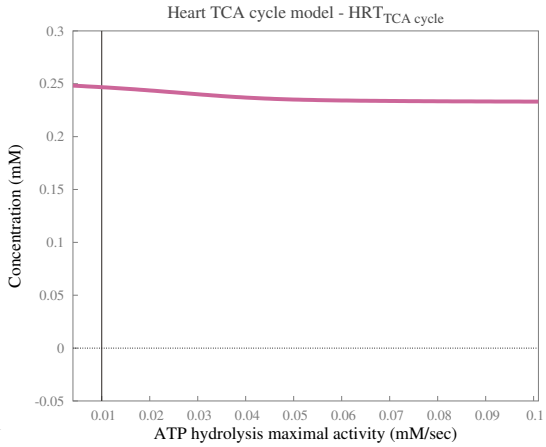

4.21.b. [AcCoA] *vs* ATPhyd activity

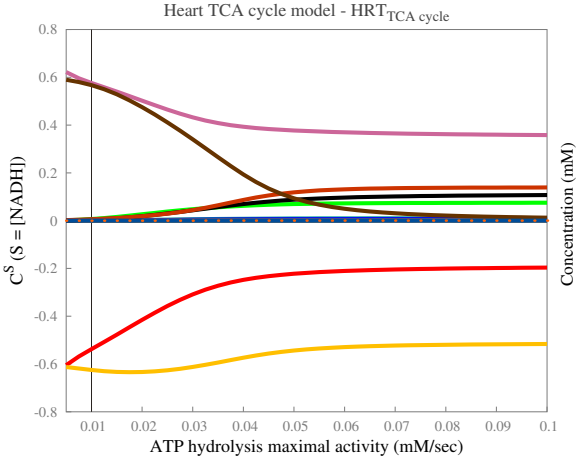

4.21.c. C^{NADH} *vs* ATPhyd maximal activity

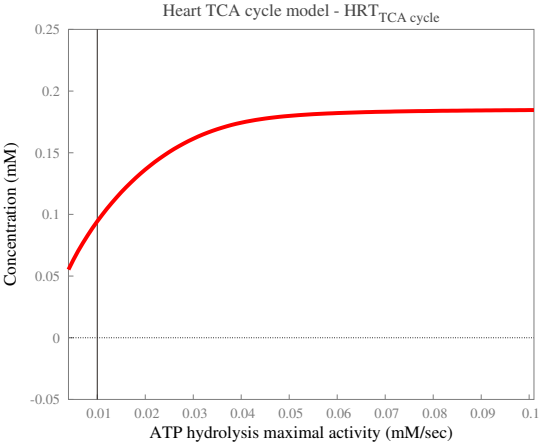

4.21.d. [NADH] *vs* ATPhyd activity

▪ **Figure 4.21. Control of CoA- & NAD−related metabolites:** Distribution of concentration control coefficients calculated for the respective concentrations of AcCoA & NADH, against the changing maximal activity of ATPhyd.

▪ Key for figs. 4.21a and 4.21c is as follows :

PDH ; CS ; ACO ; IDHa ; α-KGDH ; SCS;
SDH ; FM ; MDH ; ATPsynth ; ANT ; ATPhyd;
α-KG$_{exp}$; Total Sum (dotted line)

▪ The vertical black line represents the initial model value. At this point, in figs. 4.21a to 4.21d, $V_{max}^{ATP_{hyd}} = 0.01$ mM/sec.

▪ ***Orange dotted line*** shows the *Summation theorem* result across the entire range. For concentration control coefficients, since the sum is equal to zero, the dotted line is not easily visible.

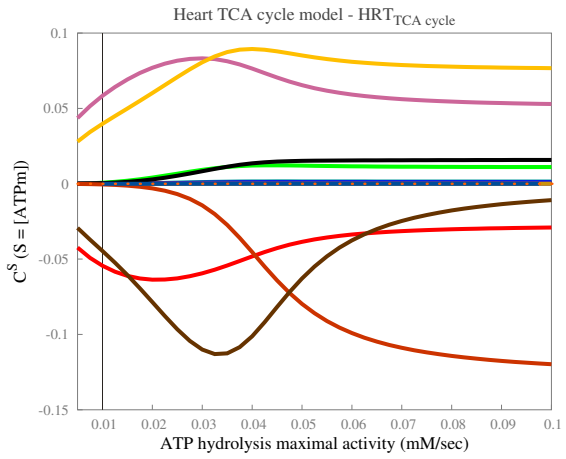

4.22.a. C^{ATP_m} *vs* ATPhyd maximal activity

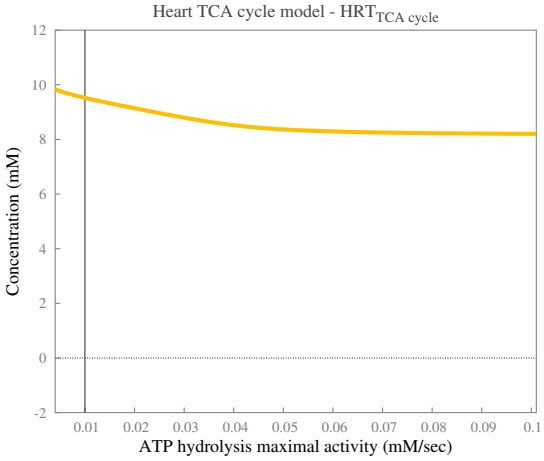

4.22.b. [ATP_m] *vs* ATPhyd activity

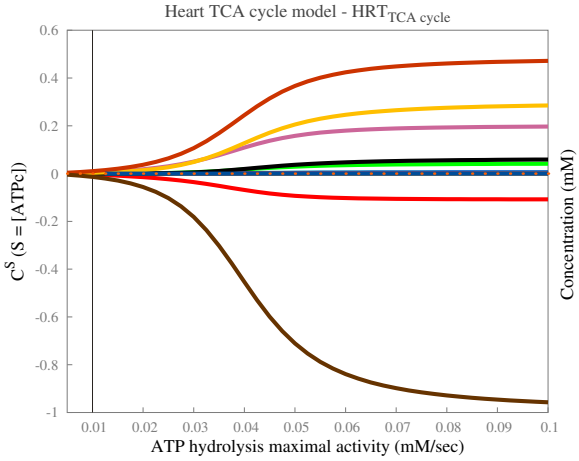

4.22.c. C^{ATP_c} *vs* ATPhyd maximal activity

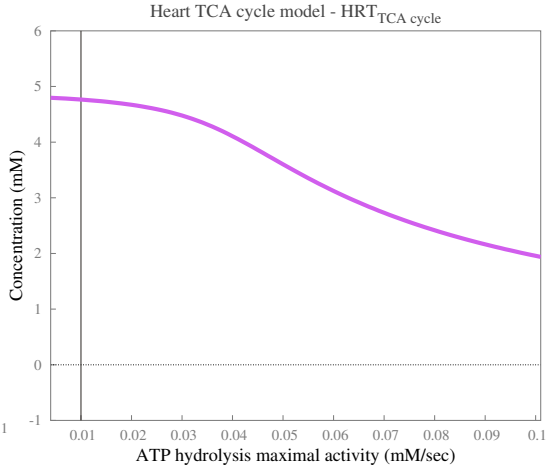

4.22.d. [ATP_c] *vs* ATPhyd activity

▪ **Figure 4.22. Control of ATP–related metabolites:** Distribution of concentration control coefficients calculated for the respective concentrations of ATP_m & ATP_c, against the changing maximal activity of ATPhyd.

▪ Key for figs. 4.22a and 4.22c is as follows :

PDH ; CS ; ACO ; IDHa ; α-KGDH ; SCS;
SDH ; FM ; MDH ; ATPsynth ; ANT ; ATPhyd;
α-KG_{exp} ; Total Sum (dotted line)

▪ The vertical black line represents the initial model value. At this point, in figs. 4.22a to 4.22d, $V_{max}^{ATP_{hyd}} = 0.01$ mM/sec.

▪ ***Orange dotted line*** shows the *Summation theorem* result across the entire range. For concentration control coefficients, since the sum is equal to zero, the dotted line is not easily visible.

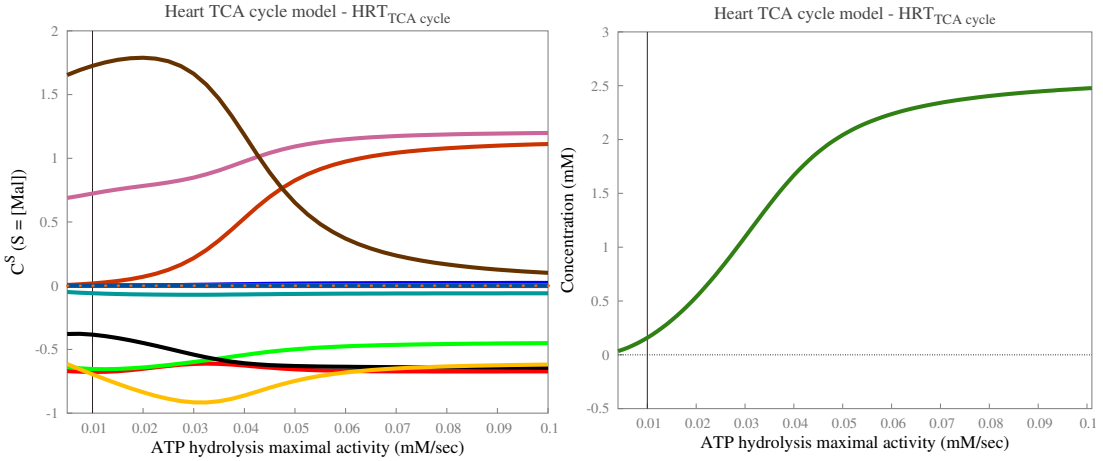

4.23.a. C^{Mal} *vs* ATPhyd maximal activity **4.23.b.** [Malate] *vs* ATPhyd activity

▪ **Figure 4.23. Control of TCA cycle intermediate metabolites:** Distribution of concentration control coefficients calculated for the malate concentration, against the changing maximal activity of ATPhyd.

▪ Key for fig. 4.23a is as follows :

PDH ; CS ; ACO ; IDHa ; α-KGDH ; SCS;
SDH ; FM ; MDH ; ATPsynth ; ANT ; ATPhyd;
α-KG$_{exp}$; Total Sum (dotted line)

▪ The vertical black line represents the initial model value. At this point, in figs. 4.23a and 4.23b, $V_{max}^{ATP_{hyd}} = 0.01$ mM/sec.

▪ ***Orange dotted line*** shows the *Summation theorem* result across the entire range. For concentration control coefficients, since the sum is equal to zero, the dotted line is not easily visible.

Figures 4.20 to 4.23 (see pgs. 177 to 180, respectively) show the concentration control coefficients (C^S) of OAA_m, Cit_m, $AcCoA_m$, $NADH_m$, ATP_m, ATP_c, & Mal_m against the change in ATP hydrolysis maximal activity. These concentration control coefficient plots are presented alongside a steady-state plot of the corresponding metabolite concentration, across the same parameter range (the metabolite concentration *'S'* for which the coefficient, *'C^S'* is calculated). In these plots, concentration control coefficients are distributed between the overall range of -1.5 to 2.0 (unitless). In each plot, a *summation theorem* result is also shown using a dotted line; however, for concentration control coefficients, since the sum is equal to zero, the dotted line coincides with the zero-axis and hence may not be easily visible. Also in these plots, the emergent pattern of distribution for concentration control coefficients is distinctively sigmoidal, like that of the flux control coefficient distributions seen earlier in figs. 4.17 to 4.19 (see pgs. 171 to 173, respectively).

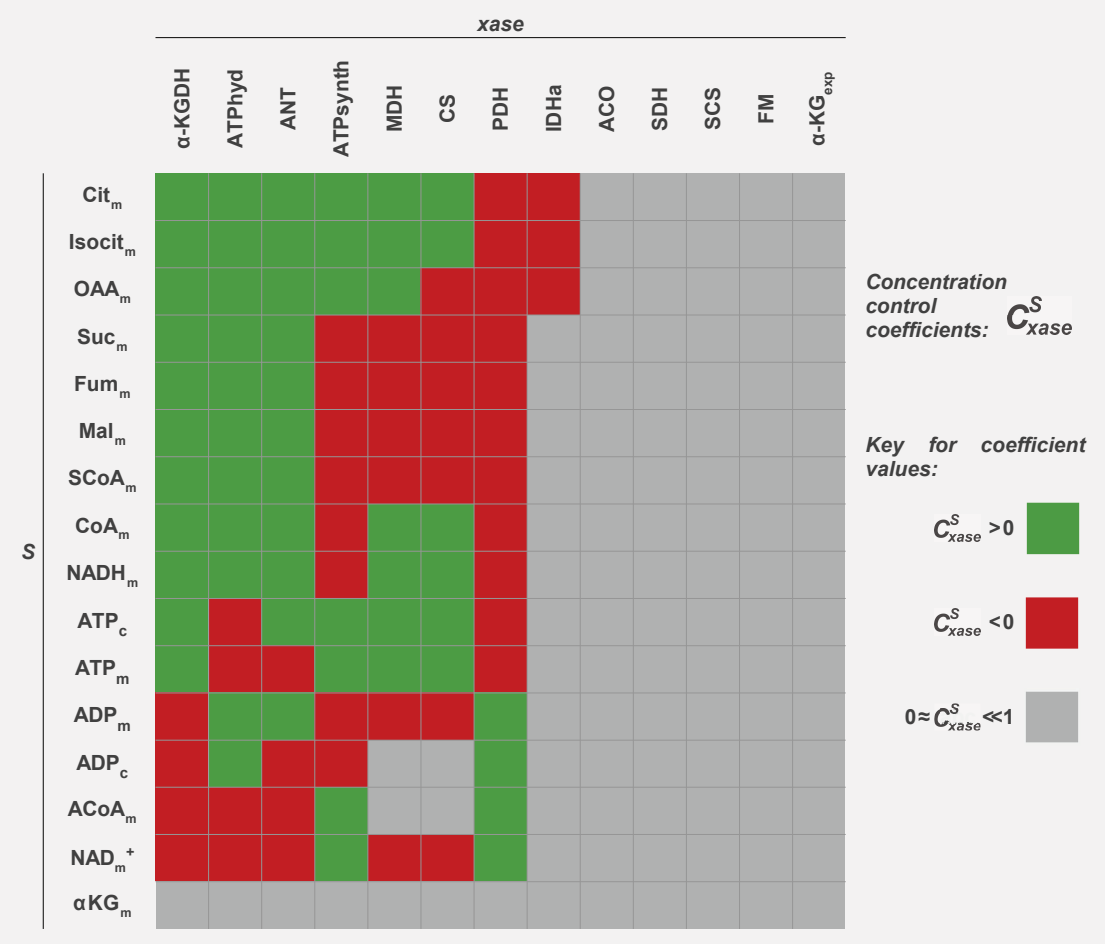

- **Figure 4.24. Control of TCAi's:** An overview of C^S distribution, against $V_{max}^{ATP_{hyd}}$.
- This figure shows the overall distribution of concentration control coefficients for all TCA cycle intermediate metabolites, with respect to all enzymes that share a moderate-to-high degree of control of the respective concentrations; against the change in ATPhyd maximal activity.
- Enzymes shaded in *grey* have either no control of the respective metabolite concentrations, or an infinitesimally small share of the overall control.
- This figure is based on the qualitative nature of the coefficient values (*i.e.* < 0, > 0, or ≈ 0) and does not reflect the actual quantitative data.

From these plots, it is evident that the overall control of TCA cycle intermediates is uniformly distributed between ATPhyd, ATPsynth, ANT, α-KGDH, & PDH, the same overall set of enzymes that control the TCA cycle flux in this model. Figure 4.24 (see, pg. 181), provides a qualitative overview of the control distribution for all 16 internal metabolites in the heart TCA cycle model, against the change in ATP hydrolysis activity. It shows the overall distribution of concentration control coefficients in the form of a *'heat-map'*, by considering all TCA cycle enzymes, for which the corresponding coefficient values are: > 0 or < 0; and not $\ll 1$ or ≈ 0. Therefore, for a given metabolite, all enzymes that have positive coefficients (> 0) are shaded in *green* and those that have negative coefficients (< 0) are shaded in *red*; whereas, enzymes with infinitesimally small coefficients ($\ll 1$ or ≈ 0) are shaded in *grey*.

From fig. 4.24 we may observe that, there are overall 5 distinct groups of TCA cycle intermediates that exhibit a similar qualitative pattern of concentration control in terms of the participating enzymes and they are as follows —

1. *Group A* contains citrate, isocitrate, & oxaloacetate and it shows positive coefficients for α-KGDH, ATPhyd, ANT, ATPsynth, MDH, & CS (except, OAA_m has a negative C^S for CS); whereas negative coefficients for PDH & IDHa.
2. *Group B* contains 4 TCA cycle intermediates from the second half of the TCA cycle – succinate, fumarate, malate, & succinyl-CoA and it shows positive coefficients for α-KGDH, ATPhyd, & ANT; whereas negative coefficients for ATPsynth, MDH, CS, & PDH.
3. *Group C* contains CoA_m & $NADH_m$ and it shows positive coefficients for α-KGDH, ATPhyd, ANT, MDH, & CS; whereas negative coefficients for ATPsynth & PDH.
4. *Group D* contains ATP–related metabolites – ATP_c, ATP_m, ADP_m, & ADP_c. Since, this is a group of conserved moieties, the constituent metabolites show a mirror-like pattern of the overall qualitative distribution of concentration control. ATP_c & ATP_m show positive coefficients for α-KGDH, MDH, & CS; whereas negative coefficients for ATPhyd & PDH. Additionally, ATP_c has a positive coefficient for ANT; whereas, ATP_m has a negative coefficient for ANT. On the other hand, ADP_m shows an exact mirror image of the corresponding concentration control pattern for ATP_m. ADP_c also shows a mirror image of the corresponding control pattern for ATP_c; however, in this case, the individual coefficients for MDH & CS are infinitesimally small, unlike in the case of ATP_c, where they are distinctly positive.
5. *Group E* contains acetyl-CoA & NAD^+_m and it is nearly an exact complement of the qualitative control pattern observed for the *Group C* metabolites, CoA_m & $NADH_m$. For acetyl-CoA, the individual coefficients for MDH & CS are infinitesimally small, unlike in the case of CoA_m, where they are distinctly positive. Other than that, the individual control patterns shown by $AcCoA_m$ & NAD^+_m are exact mirror images of the individual control patterns for CoA_m & $NADH_m$, respectively. Therefore, they both exhibit positive coefficients for ATPsynth & PDH; whereas negative coefficients for α-KGDH, ATPhyd, & ANT. Additionally, NAD^+_m also shows negative coefficients for MDH & CS.

Figure 4.24 also shows that the individual concentration control coefficients for ACO, SDH, SCS, FM, & $\alpha\text{-}KG_{exp}$ are either infinitesimally small or zero, for all 16 TCA cycle intermediates of the heart TCA cycle model; which means that they have minimal influence on the individual concentrations of all 16 TCA cycle intermediates. This figure also shows that apart from the 3 *Group A* metabolites (Cit_m, $Isocit_m$, & OAA_m), IDHa does not control the other 13 metabolite concentrations in the heart TCA cycle model.

α-ketoglutarate (αKG_m) shows infinitesimally small or zero coefficients for all 13 TCA cycle enzymes. Another observation that emerges from this qualitative analysis is that, α-KGDH, ATPhyd, & ANT have positive coefficients for all TCA cycle intermediates through groups *'A' to 'C'*; whereas, PDH shows negative coefficients for all TCA cycle intermediates through groups *'A' to 'C'*, plus ATP_c & ATP_m from *Group D*. Overall, fig. 4.24 shows that in the heart TCA cycle model, 3 TCA cycle metabolite concentrations are controlled by at least 8 enzymes (Cit_m, $Isocit_m$, & OAA_m), 10 concentrations are controlled by at least 7 enzymes and 2 concentrations are controlled by at least 5 enzymes (ADP_c & $AcCoA_m$).

Figure 4.20a (see, pg. 177) shows that against the change in ATPhyd maximal activity, the control of oxaloacetate concentration ($[OAA_m]$) is uniformly distributed between CS, ATPhyd, ANT, ATPsynth, α-KGDH, MDH, PDH, IDHa; however, throughout the entire range, citrate synthase maintains a nearly complete negative control of its concentration. Moreover, at the initial model value of ATPhyd maximal activity (*i.e.* = 0.01 mM/sec), $[OAA_m]$ is mainly controlled by ATPhyd & CS, with marginal contributions from other enzymes; where, C^S for ATPhyd is slightly more than +1 and C^S for CS is exactly −1. As a result, as shown in fig. 4.20b, the oxaloacetate concentration increases to 7-fold with increase in ATPhyd activity.

Figure 4.20c (see, pg. 177) shows that against the change in ATPhyd maximal activity, the control of citrate concentration ($[Cit_m]$) is uniformly distributed between α-KGDH, ATPsynth, ATPhyd, PDH, IDHa, MDH, CS, & ANT; with moderately negative coefficients for PDH & IDHa throughout the given range (*please note the Y-axis*). A negative C^S for PDH can be explained on the basis that in the heart TCA cycle model, it represents the only branch point in otherwise linear sequence of TCA cycle enzymes (for further explanation, please refer to pg. 174). Moreover, at the initial model value of ATPhyd maximal activity, $[Cit_m]$ is mainly controlled by α-KGDH, ATPsynth, ATPhyd, PDH, & IDHa. Also, across the given range of ATPhyd activity, since the sum of positive coefficients is more than that of the negative coefficients, citrate concentration increases to 1.75-fold (as shown in fig. 4.20d).

Figure 4.21a (see, pg. 178) shows that against the change in ATPhyd maximal activity, the acetyl-CoA concentration ($[AcCoA_m]$) is mainly controlled by PDH, ATPhyd, α-KGDH, & ANT. However, in this case, the positive (PDH) & negative coefficients (ATPhyd, α-KGDH, & ANT) are so finely balanced that the acetyl-CoA concentration does not change much throughout the range of ATPhyd activities (see, fig. 4.21b). Moreover, this observation provides a further explanation for the insignificant changes observed in the average steady-state concentration of acetyl-CoA, during the steady-state analysis at varying ATPhyd activities (see fig. 4.9a on pg. 159).

Figure 4.22a (see, pg. 179) shows that against the change in ATPhyd maximal activity, the concentration of mitochondrial ATP ($[ATP_m]$) is controlled by ATPsynth, α-KGDH, CS, MDH, ANT, ATPhyd, & PDH in a complicated pattern of exchange of control between individual enzymes. At the initial model value of ATPhyd maximal activity (*i.e.* = 0.01 mM/sec), $[ATP_m]$ is controlled by two pairs of enzymes, each with positive (ATPsynth & α-KGDH) and negative coefficients (ATPhyd & PDH). On the other hand, at 10x activity (*i.e.* = 0.1 mM/sec), $[ATP_m]$ is controlled by all 7 enzymes. The resultant effect of such a complicated pattern of control is that the mitochondrial ATP concentration is reduced moderately, as the ATPhyd activity increases from 0.01 to 0.1 mM/sec (see, fig. 4.22b).

Figure 4.23a (see, pg. 180) shows that against the change in ATPhyd maximal activity, the control of malate concentration ($[Mal_m]$) is distributed uniformly between ATPhyd, α-KGDH, ANT, CS, PDH, MDH, ATPsynth, & IDHa. In this case, ATPhyd, α-KGDH, & ANT show large positive coefficients and CS, PDH, MDH, & ATPsynth show moderately negative coefficients (*please note the Y-axis*). IDHa has a marginal negative coefficient throughout the given range of ATPhyd activity. Since, malate transporter is absent in the heart TCA cycle model, a collection of strong, positive control coefficients overcomes the negative control exerted by enzymes that directly or indirectly consume either malate or $NADH_m$; which allows the malate concentration to increase to 250-fold above its starting value (see, fig. 4.23b). Moreover, this observation provides a further explanation for the significant accumulation of malate, observed during the steady-state analysis at varying ATPhyd activities (see fig. 4.7a on pg. 157).

Therefore, overall, the emergent concentration control properties of the heart TCA cycle model, highlight the fact that most metabolite concentrations in this model show significant changes in their respective concentrations, only if either or all of the *'demand block'* enzymes are in control and thus reflect the energy-demand driven nature of this model, qualitatively.

4.3.5.3 Elasticity coefficient analysis for the heart TCA cycle model

In this section, we shall analyse the *elasticity coefficients* (ε_S) of heart TCA cycle model, calculated for all enzymes, with respect to all internal as well as external metabolites in the model. Figure 4.25 (see, pg. 185) shows the distribution of elasticity coefficients for the heart TCA cycle model, for all 15 enzymes in the model, calculated with respect to 28 metabolites that include internal as well as external metabolites. Figure 4.26 (see, pg. 186) shows the connectivity theorem result that links the elasticity coefficients ($\mathcal{E}_S^{xase}$) shown in fig. 4.25 and flux control coefficients (C_{xase}^J) computed at initial steady-state of the heart TCA cycle model (see tbl. 4.4 on pg. 185).

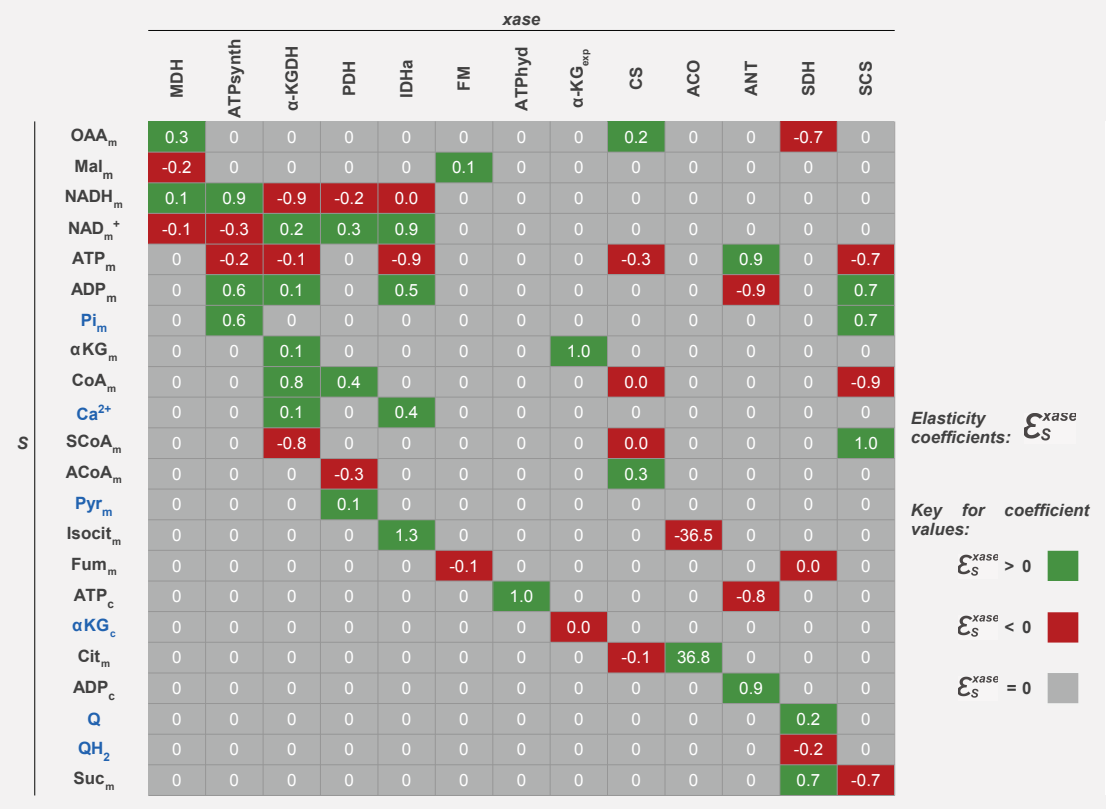

▪ **Figure 4.25. Local properties of the heart TCA cycle enzymes:** The distribution of elasticity coefficients in the heart TCA cycle model.

- In this figure, positive $\mathcal{E}_S$ values are shown in *green* and negative $\mathcal{E}_S$ values are shown in *red*.
- Enzymes that are not affected by a given metabolite (*'S'*), have elasticity values equal to zero and in this figure, they are shaded in *grey*.
- All internal metabolites are shown in *black* and external metabolites are shown in *blue*.

	C^J
MDH	-0.00003
ATP$_{synth}$	0.0028
α-KGDH	0.0049
PDH	-0.0031
IDHa	0.0007
FM	0.0000
ATP$_{hyd}$	0.9862
α-KG$_{exp}$	-0.0001
CS	0.0001
ACO	0.0004
ANT	0.0152
SDH	-0.0004
SCS	0.0002
Summation	1.007

▪ **Table 4.4. C^J, computed at the *initial steady-state* of heart TCA cycle model.**

- These flux control coefficients are used in fig. 4.26 (see, pg. 186) for calculating the *connectivity theorem*.
- Here, *'J'* represents the TCA cycle flux.
- All numbers in this table are rounded-up.

S	xase: MDH	ATPsynth	α-KGDH	PDH	IDHa	FM	ATPhyd	α-KG$_{exp}$	CS	ACO	ANT	SDH	SCS	Summation
OAA$_m$	0	0	0	0	0	0	0	0	0.00	0	0	0.00	0	0.00
Mal$_m$	0	0	0	0	0	0	0	0	0	0	0	0	0	0
¶ NAD^+_m	0	0	0	0	0	0	0	0	0	0	0	0	0	0
¶ ATP$_m$	0	0	0	0	0	0	0	0	0	0	0.00	0	0	0.00
Pi$_m$	0	0.00	0	0	0	0	0	0	0	0	0	0	0	0.00
αKG$_m$	0	0	0.00	0	0	0	0	0.00	0	0	0	0	0	0.00
¶ CoA$_m$	0	0	0	0	0	0	0	0	0	0	0	0	0	0
Ca^{2+}	0	0	0.00	0	0.00	0	0	0	0	0	0	0	0	0.00
Pyr$_m$	0	0	0	0.00	0	0	0	0	0	0	0	0	0	0.00
Isocit$_m$	0	0	0	0	0	0	0	0	0	-0.01	0	0	0	-0.01
Fum$_m$	0	0	0	0	0	0	0	0	0	0	0	0	0	0
¶ ATP$_c$	0	0	0	0	0	0	0	0	0	0	0.00	0	0	0.00
αKG$_c$	0	0	0	0	0	0	0	0	0	0	0	0	0	0
Cit$_m$	0	0	0	0	0	0	0	0	0	0.01	0	0	0	0.01
Q	0	0	0	0	0	0	0	0	0	0	0	0	0	0
QH$_2$	0	0	0	0	0	0	0	0	0	0	0	0	0	0
Suc$_m$	0	0	0	0	0	0	0	0	0	0	0	0.00	0.00	0.00

- **Figure 4.26. Connectivity relationships in the heart TCA cycle model:** Connectivity theorem result involving the elasticity coefficients ($\mathcal{E}^{xase}_{S}$) shown in fig. 4.25 (pg. 185) and flux control coefficients (C^{J}_{xase}) computed at initial steady-state (see tbl. 4.4 on pg. 185), such that for a given metabolite *'S'*, the total sum of all products of $\mathcal{E}^{xase}_{S}$ & C^{J}_{xase}, calculated for each enzyme, should be equal to zero.

- ¶ : These metabolites are conserved within this system, which means their connectivity equations are more complicated compared to the other metabolites in the system. For further explanation, please see pg. 113. These rows represent combined connectivity equations of conserved metabolites in the liver TCA cycle models; which also means that a number of individual equations are reduced compared to the total number of metabolites in the model.

- Zeros with blueish background indicate numbers that are smaller than ±0.01 and range between ±1.0E-05 to ±1.0E-03.

Figure 4.26 (see, pg. 186) shows the result of *connectivity theorem equations* for elasticities given in fig. 4.25. This result was obtained by multiplying flux control coefficients calculated at initial steady-state, by individual enzyme elasticities calculated for all metabolites in the model and ultimately adding all such products to get a sum total. This figure shows that the calculated flux control coefficients & individual enzyme elasticities satisfy the *connectivity theorem* (Kacser and Burns, 1973), within acceptable limits. According to the ratio form of connectivity theorem, flux control coefficients on a particular pathway flux (*'J'*), and elasticity coefficients on a given metabolite (*'S'*), calculated for each enzyme affected by *'S'*, are inversely proportional to each other (Fell, 1997); which means that enzymes with high flux control coefficient values have smaller elasticities and *vice versa*. *For further details regarding the calculation of connectivity theorem results, please refer to pg. 113.*

However in the heart TCA cycle model, since at *initial conditions*, the TCA cycle flux is almost entirely controlled by ATPhyd, all other enzymes show minimal flux control coefficient values (see tbl. 4.4 on pg. 185). Therefore, in fig. 4.25, it is rather difficult to spot the aforementioned inverse relationship between the flux control coefficients and elasticities. Nonetheless, SDH, SCS, & IDHa are some of the more easily observable examples that show high elasticity values with respect to their individual substrates; which indicates that they have minimal flux control coefficient values. Since, ATP hydrolysis is defined as a simple, irreversible mass-action reaction, it shows an elasticity coefficient of 1 for ATP_c, despite having a nearly complete control of TCA cycle. α-KG_{exp} is defined as a reversible mass-action reaction and it shows an elasticity coefficient of 1 for α-ketoglutarate and a minimal negative coefficient for αKG_c (shown as 0, in red); because its flux control coefficient is minimal. It shows a minimal negative ε_S for αKG_c because, elasticities are calculated *instantaneously* (*i.e.* without simulating the model) and such computation shows a relatively large positive flux value of α-KG_{exp} (*i.e.* 0.334 mmol/sec); which means that at *instantaneous* calculation, α-KG_{exp} mainly allows the pool of TCAi to equilibrate with cytosolic α-ketoglutarate via its forward reaction. Also, at *instantaneous* computation of fluxes, MDH & FM appear to carry fluxes in the opposite direction of TCA cycle and therefore, their respective substrate and product elasticities are reversed.

In fig. 4.25 aconitate hydratase (ACO) shows a large elasticity coefficient that is far greater than 1. This enzyme represents a near-equilibrium reaction and for such reactions, the elasticities with respect to substrate and product are mostly determined by the degree of displacement of the reaction from equilibrium (or the disequilibrium ratio (ρ)) rather than by their kinetic details, which can lead to much larger elasticity values than that of the non-equilibrium reactions (Fell, 1997; Groen et al., 1982a; Kacser and Burns, 1973; Westerhoff et al., 1984).

Between the three dehydrogenase reactions, *i.e.*, α-KGDH, PDH, & IDHa, the product inhibition by $NADH_m$ appears to be *strong*, *moderate* and *minimal* respectively; which means that the respective rates of these dehydrogenases respond to changes in the $NADH_m$ concentration, in that order. A similar case can be made for the ATP-mediated inhibition of IDHa, CS, & α-KGDH; where, their respective rates are 90%, 30%, & 10% responsive to changes in the ATP_m concentration, assuming 100% as a maximum possible response of an enzyme to changes in effector concentration. In the case of pyruvate dehydrogenase, product inhibition by both $NADH_m$ as well as $AcCoA_m$ appears to be fairly moderate in the heart TCA cycle model, based on their respective elasticity coefficients; however according to Bremer, variations in the $NADH/NAD^+$ ratio might prove to be a more direct regulator of the PDH activity than the AcCoA/CoA ratio, in general (Bremer, 1969). In the liver TCA cycle model, as shown in the earlier chapter (see, pg. 113), based on its elasticity (-0.5), the rate of liver pyruvate dehydrogenase was found to be substantially more responsive to changes in the concentration of NADH than that of acetyl-CoA.

Therefore, a system-wide analysis of flux control coefficients, concentration control coefficients, & elasticity coefficients illustrated how various metabolites, effectors and enzymes interact with each other in the heart TCA cycle model at *local* as well as *system* level. It also showed how the *local* and *system* level properties of this model are related to each other and how one can predict certain systemic or localised effects based on the relation between the two types of control properties for a given system. The flux control coefficient and concentration control coefficient analyses also helped in explaining some of the confounding observations seen during the steady-state analyses carried out at increasing activities of ATPhyd or PDH. Thus, our discussion on these analyses shows that Metabolic Control Analysis (MCA) is an immensely important and useful quantitative tool, without which we would be left with vague concepts of enzyme response to a metabolite that are often used for qualitative explanations of metabolic regulation in several biochemistry textbooks.

4.4 Discussion & Conclusions

The heart TCA cycle model was defined and built based on the valuable insights gained from the analysis of liver TCA cycle model as well as the *"PC knock-out"* model, by applying mammalian heart- or skeletal muscle-specific enzyme kinetics data to a selected set of reactions from the liver TCA cycle model. This nascent version of the heart TCA cycle model then went through a few iterations of troubleshooting, optimisation & modifications to find stable steady-state solutions of the model, when simulated. Some of the earlier versions of this model contained a few errors such as – NAD, NADH & OAA concentrations, as well as the ATP hydrolysis activity still operated with liver-specific values; and an oxaloacetate import reaction was added to stabilise the OAA concentration and thereby the model itself ... *etc.* Such errors were corrected and progressively updated versions of the model were created and analysed further.

The oxaloacetate import reaction added in the earlier versions of the model was physiologically unfounded as well as unreliable in terms of the model stability and therefore had to be replaced with a better alternative solution. Analyses of liver, PC_{ko} as well as the incipient versions of the heart TCA cycle models, constantly indicated towards the inclusion of malate-aspartate shuttle reactions in the heart-specific TCA cycle model and therefore, such an addition was planned as a future enhancement to this model. However, until such enhancement can be made, a stopgap solution was devised in the form of an α-ketoglutarate transporter reaction (α-KG_{exp}), that partially represented the abstract function of the malate-oxoglutarate transporter reaction (MOTx) from malate-aspartate shuttle (*see, Methods, for further details of* α-KG_{exp}). Moreover, based on the preliminary analysis of this modified model, the $NADP^+$-dependent isocitrate dehydrogenase reaction (IDHb) was also removed from the model (*see, Methods, for further details*). Thus formed, a corrected, modified and optimised version of the heart TCA cycle model was then thoroughly analysed and upon confirming its results, the model was finalised and frozen as a stable version, until future enhancements.

The final analysis of the heart TCA cycle model presented earlier, offered some unique and valuable perspective on the physiological characteristics of a heart-specific TCA cycle system, in terms of its structural, dynamic as well as control properties. Some of the key findings are as follows:

1. Our decision to remove the $NADP^+$-dependent isocitrate dehydrogenase reaction (IDHb) from the heart TCA cycle model is described earlier in the Methods section. However, from previous chapters we know that the internal substrate cycle between IDHa & IDHb exists and is operational in heart mitochondria, as well (Sazanov and Jackson, 1993; *for further details as well as refs., please see earlier*). We believe that

the redundancy and errors it created in the heart TCA cycle model were specific to its peculiar structure and given that this structural definition is subject to change as a result of the proposed model enhancement with malate-aspartate shuttle, it is likely to be reintroduced in the extended model in order to realign it, physiologically. We suspect that its reintroduction in the extended heart TCA cycle model, would restore the interrupted TCA cycle *'spans'* observed in the liver TCA cycle model and allow the IDHa & IDHb reactions to function as *'independent reactions'*. Moreover, with the addition of malate-aspartate shuttle to the extended model, mitochondrial malate dehydrogenase is also likely to act as an *'independent reaction'*.

Therefore, provided that the interrupted TCA cycle *'spans'* as well as the *independent reactions* are restored in the extended heart TCA cycle model, we believe that the negative control coefficient values that were observed earlier for pyruvate dehydrogenase (see figs. 4.17 to 4.23 on pgs. 171 to 180, respectively) would also disappear, due to additional branching of TCA cycle and that PDH would assume a more *'positive'* role, in terms of allowing the TCA cycle flux to increase rather than decrease.

2. Although compared to the liver TCA cycle model, the emerged pattern of control distributions in the heart TCA cycle model is quite straightforward, given that this model is going to be extended further, it once again reiterates the need of constructing simplified mathematical models that are capable of representing the fundamental physiological characteristics of real metabolic systems. Keeping the proposed model extensions in mind, we have to be very careful while designing such kinetic models by avoiding any non-essential kinetic information; because with the integration of multiple small models, the model complexity can reach critical levels very quickly!

Therefore, we must develop future heart-specific models with great care to avoid model complexity, by including only those reactions or processes that are absolutely essential for the overall biochemical function of the larger metabolic network in mammalian myocardial mitochondria.

3. Structurally, the heart TCA cycle model is a theoretically ideal version of TCA cycle, often described in biochemistry textbooks, that produces 11 molecules of ATP_m & 3 molecules of CO_2 per pyruvate. This model contains a single elementary mode, which is also an enzyme subset. Compared to the structure of liver TCA cycle model, this is a relatively simple model and yet, the kinetic properties that emerge from such a simple structure are quite complex in terms of the dynamic interactions between its components. Even its control properties require a careful second look, in order to correctly asses their significance with respect to the overall function of the TCA cycle described in this model.

Therefore, this TCA cycle model is a perfect example that shows the real limitations of a *classical reductionist approach* used in most biochemistry textbooks to describe the physiological workings of an *'ideal'* TCA cycle.

4. Structurally, the α-ketoglutarate transporter reaction (α-KG_{exp}) is identified as a *'dead reaction'*. Also, the steady-state obtained by simulating the heart TCA cycle model at *initial conditions*, shows that the flux through α-KG_{exp} is infinitesimally small and therefore it is almost inconsequential to the normal function of this model. However, it is essential to stabilise this model and therefore retained. Nonetheless, as described earlier, it represents a partially approximated form of the malate-oxoglutarate transporter reaction (MOTx) and thereby creates an in-built point of integration within the present heart TCA cycle model, for the proposed enhancement with malate-aspartate shuttle reactions.

Moreover, fig. 4.19b (see, pg. 173) shows the distribution of control on TCA cycle flux for a hypothetical situation, where cytosolic α-ketoglutarate concentration increases incrementally. Although hypothetical for this model, such a situation is within the realm of physiological probabilities and in the presence of a fully functional malate-aspartate shuttle, under favourable conditions, it might even be a distinct possibility. This particular situation is of special significance with respect to the proposed extension of heart TCA cycle model because, fig. 4.19d shows that the TCA cycle flux is increased moderately by 3-fold, with increase in [αKG_c]. It thus illustrates that if the extended model results in a net exchange of mitochondrial α-ketoglutarate, then it is likely that we would see some improvement in the flux through the TCA cycle.

5. The steady-state analysis at *initial conditions* of the heart TCA cycle model shows that the TCA cycle flux (flux through CS) in this model is at least 100 times less than that in the liver TCA cycle model. We believe that there are at least two factors that are responsible for such a small amount of flux through the TCA cycle and they are as follows —

5.(*a.*) The pyruvate carboxylase (PC) reaction is absent in the heart TCA cycle model; whereas, as shown in the previous chapter, it makes a significant anaplerotic contribution to the overall flux in liver TCA cycle models. Also, in the present heart TCA cycle model, other anaplerotic reactions such as those from the malate-aspartate shuttle are absent as well. Therefore, in this model, apart from PDH, there is no other *input* reaction to incorporate any additional carbon into the TCA cycle.

5.(***b.***) The selected set of heart-specific enzyme kinetics data applied to the heart TCA cycle model is also an important factor, which most certainly affects the overall flux in this model. However, changing one or more enzyme kinetics parameters in the model can alter the already established steady-state behaviour to a variable degree. Changing the model parameters could also affect the control of flux, due to change in the *local properties* or *elasticities* of individual enzyme(s), according to the *connectivity theorem* from Metabolic Control Analysis (Kacser and Burns, 1973); since, the ratio form of this theorem shows that elasticities and flux control coefficients are inversely proportional to each other (Fell, 1997). Therefore, it is prudent to commit any parameter changes to the model, only after thoroughly assessing their quantitative impact on a given system, based on their respective elasticities as well as response coefficients (R^{J}_{P}; where, P is the model parameter & J is the pathway flux; Fell, 1997; Westerhoff and Kell, 1987).

However, experimental data from published literature suggests that in mammalian heart, the actual physiological range of TCA cycle flux isn't far off from the initial steady-state value of TCA cycle flux in this model. In perfused rat hearts, the TCA cycle flux has been estimated to be in the range of 0.035 to 0.12 mmol/sec, using ^{13}C NMR spectra (Chance et al., 1983; Tran-Dinh et al., 1998; Weiss et al., 1995) and enzymatic assay techniques (Safer and Williamson, 1973; Sundqvist et al., 1989). ^{13}C NMR studies in perfused rabbit hearts, show that the TCA cycle flux ranges between 0.042 to 0.06 mmol/sec (Yu et al., 1995). A ^{13}C NMR spectroscopic evaluation of the TCA cycle flux in pig heart tissue shows that it varies between 0.034 to 0.053 mmol/sec, depending on experimental conditions (Panchal et al., 2000, 2001). Whereas, a classical study using enzymatic assay techniques in isolated rat heart mitochondria, shows a much wider range of variation for the flux through TCA cycle, between 0.017 to 0.231 mmol/sec (LaNoue and Williamson, 1971).

6. The steady-state analysis at various increasing levels of ATPhyd activities showed that the redox and energy states of the heart TCA cycle model respond in a fairly stabilised fashion at *'moderate'* (10x) to *'very high'* (500x) ATP-demands. However, the model appears to respond well between the lower range of ATPhyd activities from *'weak'* (0.1x) to *'moderate'* (10x). This is somewhat similar to a rectangular hyperbolic curve observed in enzyme kinetics; where there are *lag, exponential & plateau* phases of the curve.

This was a rather surprising result. Moreover, it even finds sufficient literature evidence, which suggests that this particular model behaviour is similar to the observations made in intact mammalian hearts *in vivo*, at increased workloads. However, we

believe that such a response could partly be due to the respective initial model values of ATP−related metabolites, as these are the same values used in the liver TCA cycle model. Also, after extending the model with malate-aspartate shuttle reactions, there is a possibility that this model behaviour could entirely disappear.

Nonetheless, for any mathematical model describing the cardiac or skeletal muscle metabolism, it is extremely important that the model responds robustly across a wide range of ATP-demands, due to the highly demand-based metabolic characteristics of these tissues. Therefore, this entire analysis using a wide array of ATP hydrolysis activities, is an important point of validation for the heart TCA cycle model, one that better aligns this model with respect to the cardiac mitochondrial physiology.

7. At a glance, comparing the control properties between the mammalian liver- & heart-specific models shows significant differences between the two model systems that arise mainly due to structural (removal of PC, MC & IDHb) as well as kinetic changes (application of heart-specific enzyme kinetics data). For instance, if we compare the *'heat-maps'* for the qualitative distribution of concentration control coefficients between the two models, we can quickly visualise how the same metabolite concentrations are controlled in a significantly different pattern of control distribution. It not only highlights the fact that flux or concentration control coefficients of enzymes is a *system property* of a given metabolic system, but also indicates the ability of mathematical models to differentiate between tissue-specific metabolic characteristics using different sets of enzyme kinetics data.

Therefore, using the knowledge and valuable insights gained from analysing the already established liver TCA cycle model, we successfully built a 'consensus' kinetic model of TCA cycle in mammalian heart or skeletal muscle mitochondria. For this model, our design strategies were predicated on building a separate, standalone model of the malate-aspartate shuttle, which would be combined later with this TCA cycle model. Therefore, given this understanding, we constructed a heart-specific TCA cycle model that is neither over-simplified nor too complex in terms of rate equations, reversibility of reactions and regulatory interactions. A thorough analysis of this model resulted in several significant findings, specific to the cardiac mitochondrial physiology. Now, it would be interesting to find out how this model responds after it is combined with the malate-aspartate shuttle reactions. However before we do that, in the following chapter, we'll first take a quick look at the standalone model of malate-aspartate shuttle.

Chapter 5

The Malate-aspartate shuttle model

5.1 Overview

Throughout previous chapters on the liver TCA cycle model, PC_{ko} model and the heart TCA cycle model, we have been talking about the malate-aspartate shuttle and how the newly built heart TCA cycle model may need the additional anaplerotic input provided by the shuttle reactions, especially in the absence of pyruvate carboxylase. We have also talked about the limited availability of mitochondrial oxaloacetate ($\mathrm{OAA_m}$) and how it affects the TCA cycle flux and how the malate-aspartate shuttle reactions could help in maintaining the mitochondrial oxaloacetate concentration within physiological range. Therefore, we set about constructing a heart-specific malate-aspartate shuttle model ($\mathrm{HRT_{MAS}}$) based on the same modelling strategy we have followed so far. This a second in the series of three heart-specific standalone models, where the heart TCA cycle model was the first model built.

To begin with, we constructed a structural model comprising the TCA cycle reactions, including the ATP/ADP−linked reactions, plus reactions from the malate-aspartate shuttle. Elementary modes were computed for this structural model and then analysed in detail. The elementary modes analysis suggested a single elementary mode that contained a minimal possible set of reactions that result in a fully functional malate-aspartate shuttle. Thus, this elementary mode was isolated as a separate model and converted to a kinetic model by including appropriate rate equations based on the simplified, generic, reversible bi-substrate equation (Chassagnole et al., 2001b; Rohwer et al., 2006). The rate equation parameters and the model variables were initiated based on the published literature data from heart mitochondria (preferably rat). This newly created malate-aspartate shuttle model was then analysed in detail using structural as well as kinetic analyses.

However, in the context of this report, since the dynamic behaviour of the malate-aspartate shuttle in the fully extended, heart integrated TCA cycle model ($\text{HRT}_{\text{TCA+}}$) is of more importance to us than its performance as a standalone model, we shall restrict our discussion regarding the specific properties of this standalone malate-aspartate shuttle model to an absolute minimum.

In Section 5.2, we shall discuss the definition & construction of the malate-aspartate shuttle model (HRT_{MAS}), in further detail. Section 5.3: Results for the Malate-Aspartate shuttle model on pg. 197, describes a quick analytical overview of the emergent dynamic properties of this model.

5.2 Methods: Model design and definition

As mentioned earlier, the Malate-aspartate shuttle model (HRT_{MAS}) representing the operation of heart or skeletal muscle-specific malate-aspartate shuttle was manually constructed using ScrumPy, by modifying the isolated elementary mode from a structural model built earlier. The model in ScrumPy format is available in Appendix G (see, pg. 244) and is illustrated in fig. 5.1 (see, pg. 196). The final version of the updated model contains 9 reactions and 21 metabolites.

5.2.1 Model definition

Since, this model is based on the same modelling strategy as that of the earlier models, it follows the same design choices in terms of individual enzyme rate equations that are represented using the generic reversible bi-substrate equation (Chassagnole et al., 2001b; Rohwer et al., 2006), as explained in the earlier chapter.

As illustrated in Figure 5.1, the malate-aspartate shuttle model includes nine reactions, comprising six malate-aspartate shuttle reactions, *viz.*– mitochondrial malate dehydrogenase (mMDH), cytosolic malate dehydrogenase (cMDH), mitochondrial glutamate-oxoglutarate transaminase (mGOT), cytosolic glutamate-oxoglutarate transaminase (cGOT), malate-oxoglutarate transporter (MOTx), & glutamate-aspartate transporter (GATx); as well as three ATP/ADP–linked reactions, *viz.*– adenine-nucleotide translocase (ANT), ATP synthase (ATPsynth), & ATP hydrolysis (ATPhyd). Except for ATPsynth & ATPhyd, all other reactions in this model are defined as reversible. The three ATP/ADP–linked reactions retain their original definitions from the earlier models. The malate-aspartate shuttle reactions are mainly defined as reversible bi-substrate equations with product inhibition and the already well defined mitochondrial malate dehydrogenase reaction was used as an example equation.

The malate-aspartate shuttle model includes 16 variables (internal metabolites) that

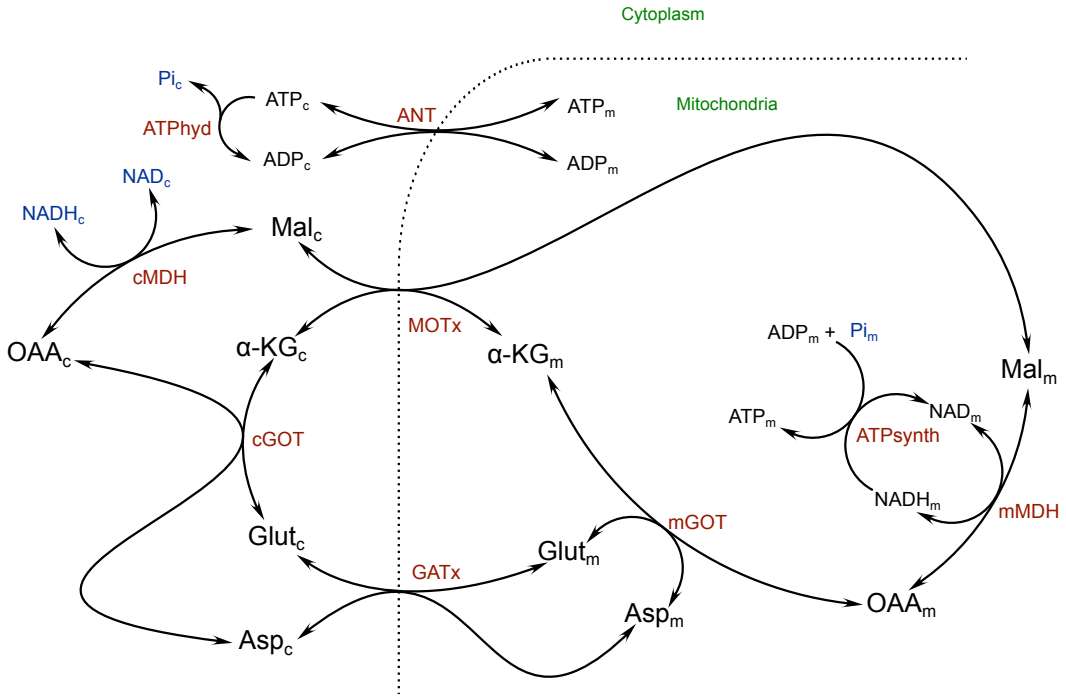

- **Figure 5.1.** Schematic illustrating the standlone malate-aspartate shuttle model.
- Internal metabolites: in *Black*; external metabolites: in *Blue*; reaction/ enzyme names: in *Red*.
- Reaction with double arrowheads is assumed to be reversible and reaction with single arrowhead is assumed to be irreversible.

describe the concentrations of *viz.*– NAD^+_m, $NADH_m$, adenine nucleotides, as well as mitochondrial α-ketoglutarate (αKG_m), malate (Mal_m), oxaloacetate (OAA_m), aspartate (Asp_m), & glutamate ($Glut_m$); and their corresponding cytosolic metabolites (αKG_c, Mal_c, OAA_c, Asp_c, $Glut_c$). Also, this model includes 8 parameters that describe fixed quantities (external metabolites) of inorganic phosphates (Pi_m & Pi_c) and cytosolic NAD & NADH (NAD^+_c & $NADH_c$). For most of these 21 metabolites, a range of values, largely from rat heart or skeletal muscle tissue were found and a median value was used in the model as an initial model value. Both the cytosolic as well as mitochondrial NAD & NADH concentrations are based on the published data from Kobayashi and Neely (1979).

In the malate-aspartate shuttle model, ATP hydrolysis is the only cytosolic reaction that utilises ATP_c and in the mitochondria, mMDH is the only dehydrogenase that produces $NADH_m$, which is consequently used by ATPsynth to produce ATP_m. However, compared to 3 or 4 dehydrogenase reactions of the TCA cycle model, the rate of ATP production in this standlone malate-aspartate shuttle model is far too less and causes model instability. Therefore, to stabilise the mitochondrial as well as the cytosolic concentrations of adenine nucleotides in this model, the ANT reaction is slowed down by *100x* and the ATPhyd reaction is sped up by *10x*. Although, such alterations are unphysiological, in a standlone model such as this, which does not have any additional carbon input in the form of pyruvate or amino acids, such steps are necessary to stabilise the model and to find a stable steady-state solution upon model simulation.

5.3 Results for the Malate-Aspartate shuttle model

In this section, we shall take a quick look at the significant properties of the standalone malate-aspartate shuttle model (HRT_{MAS}); since, we are more interested in finding out how this model works in the fully extended form when combined with the heart TCA cycle model, in the heart integrated TCA cycle model (HRT_{TCA+}).

5.3.1 Elementary modes analysis of Malate-Aspartate shuttle model

The malate-aspartate shuttle model contains a single elementary mode which consumes one molecule of $NADH_c$ to produce 2.5 mitochondrial ATP molecules via mitochondrial malate dehydrogenase, that are consequently utilised to produce 2.5 cytosolic ADP & Pi. Figure 5.2 shows this single elementary mode with its corresponding net stoichiometry, alongside each reaction.

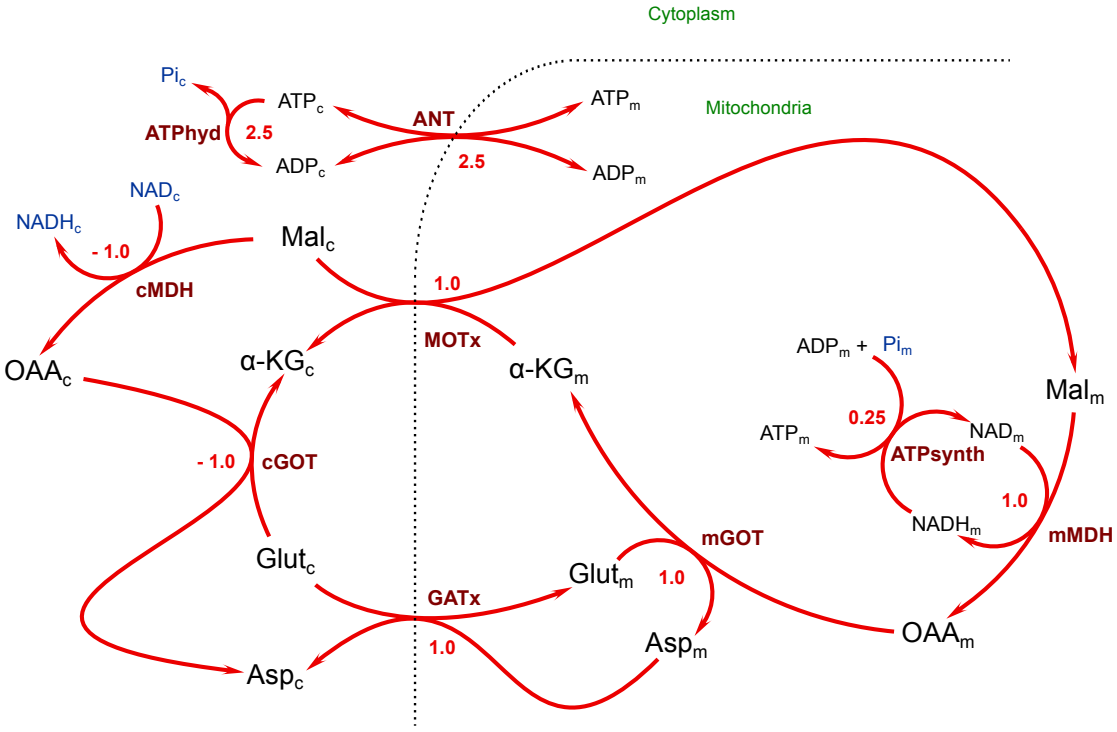

- **Figure**

5.2. Schematic illustrating the elementary modes of Malate-Aspartate shuttle model.

- Internal metabolites: in *Black*; external metabolites: in *Blue*; reaction/ enzyme names: in *Red*.
- The corresponding net stoichiometry is broken down and shown alongside each reaction in the elementary mode.

This elementary mode is exactly the same as the original elementary mode from which this model was initiated, by isolating a single elementary mode from the structural model containing TCA cycle & the malate-aspartate shuttle reactions. This mode shows that in this standalone form, the malate-aspartate shuttle is not open-ended and that it begins at the cytosolic malate dehydrogenase (cMDH) reaction by consuming $NADH_c$ (which is a fixed quantity in this model). Also, in this model, since the cMDH is defined in the same direction as that of the mitochondrial malate dehydrogenase (mMDH), it functions in reverse direction in this mode, which actually is the physiological correct direction for the cytosolic malate dehydrogenase.

In this elementary mode, since, cMDH reverses itself, the cytosolic glutamate-oxoglutarate transaminase (cGOT) reaction reverses its direction as well and forms cytosolic α-ketoglutarate & cytosolic aspartate; which tend to accumulate in this system. The accumulation of αKG_c & Asp_c is caused by the positive directions of glutamate-aspartate transporter (GATx) and malate-oxoglutarate transporter (MOTx) which transport mitochondrial aspartate (Asp_m) & mitochondrial α-ketoglutarate (αKG_m) into the cytosol, respectively. This is a reason why in the fully expanded model, we needed *sink* reactions that would transport the excess amino acids to the blood stream (to fixed quantities).

The malate-oxoglutarate transporter reaction imports cytosolic malate (Mal_c) into the mitochondria; which is utilised by the mitochondrial malate dehydrogenase to produce one molecule of $NADH_m$ and mitochondrial oxaloacetate (OAA_m). ATP synthase (ATPsynth) then utilises this single molecule of $NADH_m$ to produce 2.5 molecules of mitochondrial ATP that are then consequently transported to the cytosol and hydrolysed by ATPhyd.

5.3.2 Flux control coefficient analysis for the Malate-Aspartate shuttle model

In this section, we'll see the results of Metabolic Control Analysis (MCA) when applied to the malate-aspartate shuttle model, by observing the distribution of flux control coefficient.

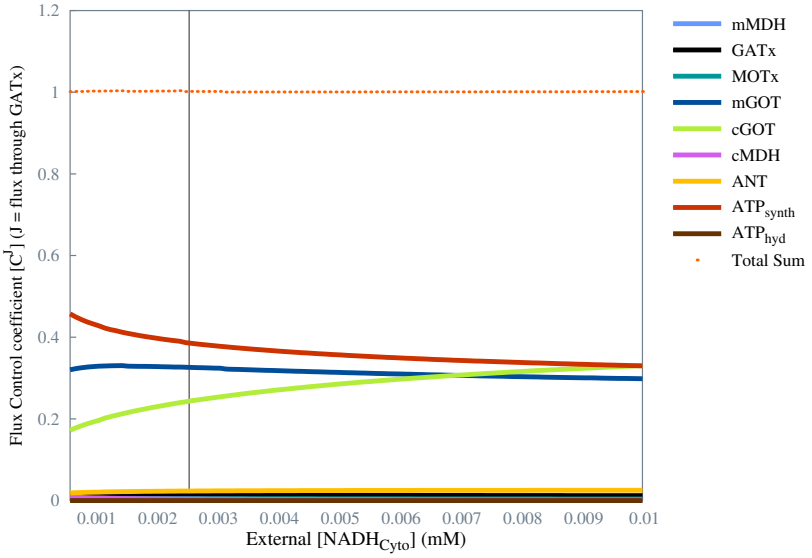

5.3.a. C^J *vs* $NADH_c$ conc.

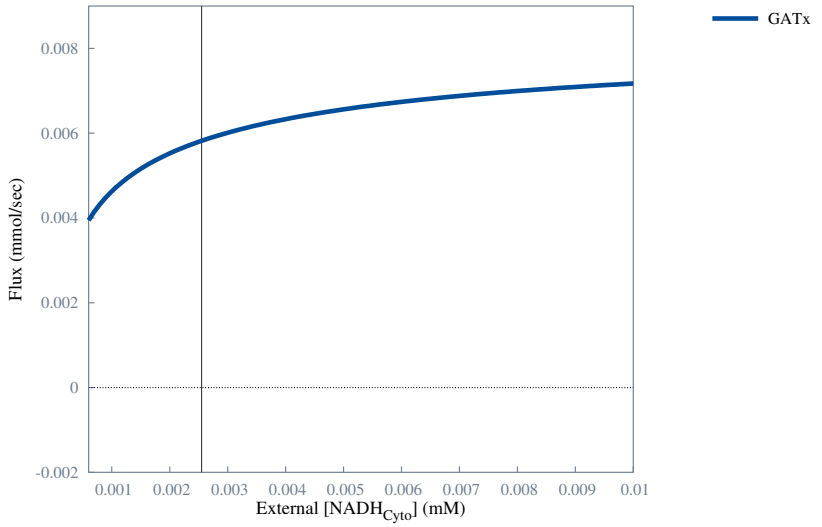

5.3.b. GATx flux *vs* $NADH_c$ conc.

▪ **Figure 5.3. Control of malate-aspartate shuttle flux in the malate-aspartate shuttle model:** against the changing $NADH_c$ concentration.

- Key for figs. 5.3a and 5.3b is given in the plots.
- The vertical black line represents the initial model value. At this point, in figs. 5.3a and 5.3b, $[NADH_c] = 0.00255$ mM.
- In the malate-aspartate shuttle model, the cytosolic NAD & NADH are fixed quantities.
- ***Orange dotted line*** shows the *Summation theorem* result across the entire range.

Figure 5.3 (see, pg. 199) shows the distribution of flux control coefficients for the malate-aspartate shuttle flux (here, represented in the form of GATx flux; since there is a single enzyme subset which contains all reactions of the model), against the increasing concentration of $NADH_c$ (which is an external metabolite in this model). The C^J plot is presented alongside a steady-state plot of the glutamate-aspartate transporter flux across the same given range of $NADH_c$ concentration.

Figure 5.3 shows that the control of malate-aspartate shuttle flux is uniformly distributed between ATPsynth, mitochondrial glutamate-oxoglutarate transaminase (mGOT) and cytosolic glutamate-oxoglutarate transaminase (cGOT); whereas, other enzymes share a minimal control of the flux. It also shows that the share of control gets exchanged between ATPsynth & cGOT at high $NADH_c$ concentrations (almost 5 times higher than its initial model value).

Moreover, fig. 5.3b shows that the flux through the malate-aspartate shuttle increases with increase in the $NADH_c$ concentration. As shown earlier in the elementary modes analysis, the malate-aspartate shuttle begins by consuming $NADH_c$ and therefore, this result shows that if in the fully extended model, we can achieve a dynamic increase of the $NADH_c$ concentration, the malate-aspartate shuttle flux also likely to increase. Therefore, this result calls for the internalisation of cytosolic NAD & NADH by including another pathway such as *glycolysis* to generate the cytosolic redox species dynamically within the boundaries of the heart integrated TCA cycle model (HRT_{TCA+}).

5.4 Discussion & Conclusions

In previous sections we saw a quick overview of the significant properties of a standalone malate-aspartate shuttle model. The combination of elementary modes analysis results as well as the analysis of flux control coefficients showed that the model responds adequately to the variations in its *input* (*i.e.* $NADH_c$). However, $NADH_c$ is an external metabolite or a *fixed quantity* in this model and combining this model as is with the heart TCA cycle model would mean that the transfer of reduction potential from cytosol to the mitochondria would be external to the resulting system; which isn't really helpful. Therefore, we should find a way to internalise the cytosolic redox couple within the system defined by the malate-aspartate shuttle reactions.

The need to transform the cytosolic redox couple into internal metabolites, called for the incorporation of another pathway or a reaction that would dynamically cycle between the cytosolic NAD & NADH. Therefore, we thought of incorporating a glycolytic pathway into the extended model. In the following chapter, we describe this newly built heart-specific glycolysis model.

Chapter 6

The Heart glycolysis model

6.1 Overview

In the previous chapter on the malate-aspartate shuttle model (HRT_{MAS}), we talked about the need to generate cytosolic redox species (*i.e.* NAD^+_c & $NADH_c$) dynamically within the boundaries of the extended model of the TCA cycle, upon its integration with the malate-aspartate shuttle model. Therefore, instead of representing the said reaction in an *assumed* fashion, we decided to build a proper heart glycolysis model (HRT_{Glc}) that would contain all the reactions in their fully functional form. Also, a lot of the published literature data was already available in publications such as Kashiwaya et al. (1994) and Kobayashi and Neely (1979); which made the process of model building a bit easier. Moreover, building a full glycolysis model had another advantage in that, the cytosolic adenine nucleotides (*i.e.* ATP_c & ADP_c) were highly constrained in the TCA cycle models seen earlier, due to a single reaction consuming and producing them and with the addition of glycolytic reactions in the cytosol, we hoped that these constrains would be comparatively less severe. Therefore, we set about constructing a heart glycolysis model (HRT_{Glc}) based on the same modelling strategy we have followed so far. This the last in the series of three heart-specific standalone models, where the heart TCA cycle model was the first model built.

Similar to the strategy followed during the construction of the malate-aspartate shuttle model, we started with a structural model and then isolated the elementary mode that represented a complete function of *canonical* glycolytic pathway, comprising a minimal set of reactions. Thus, this elementary mode was isolated as a separate model and converted to a kinetic model by including appropriate rate equations based on the simplified, generic, reversible bi-substrate equation (Chassagnole et al., 2001b; Rohwer

et al., 2006). The rate equation parameters and the model variables were initiated based on the published literature data from heart mitochondria (preferably rat). This newly created heart glycolysis model was then analysed in detail using structural as well as kinetic analyses.

However, in the context of this report, since the dynamic behaviour of glycolysis in the fully extended, heart integrated TCA cycle model ($\mathrm{HRT}_{\mathrm{TCA+}}$) is of more importance to us than its performance as a standalone model, we shall restrict our discussion regarding the specific properties of this standalone heart glycolysis model to an absolute minimum.

In Section 6.2, we shall discuss the definition & construction of the heart glycolysis model ($\mathrm{HRT}_{\mathrm{Glc}}$), in further detail. Section 6.3: Results for the Heart Glycolysis model on pg. 206, describes a quick analytical overview of the emergent dynamic properties of this model.

6.2 Methods: Model design and definition

As mentioned earlier, the Heart glycolysis model ($\mathrm{HRT}_{\mathrm{Glc}}$) representing the operation of heart or skeletal muscle-specific glycolysis was manually constructed using ScrumPy, by modifying the isolated elementary mode from a structural model built earlier. The model in ScrumPy format is available in Appendix H (see, pg. 247) and is illustrated in fig. 6.1 (see, pg. 203). The final version of the updated model contains 17 reactions and 22 metabolites.

6.2.1 Model definition

Since, this model is based on the same modelling strategy as that of the earlier models, it follows the same design choices in terms of individual enzyme rate equations that are represented using the generic reversible bi-substrate equation (Chassagnole et al., 2001b; Rohwer et al., 2006), as explained in the earlier chapter.

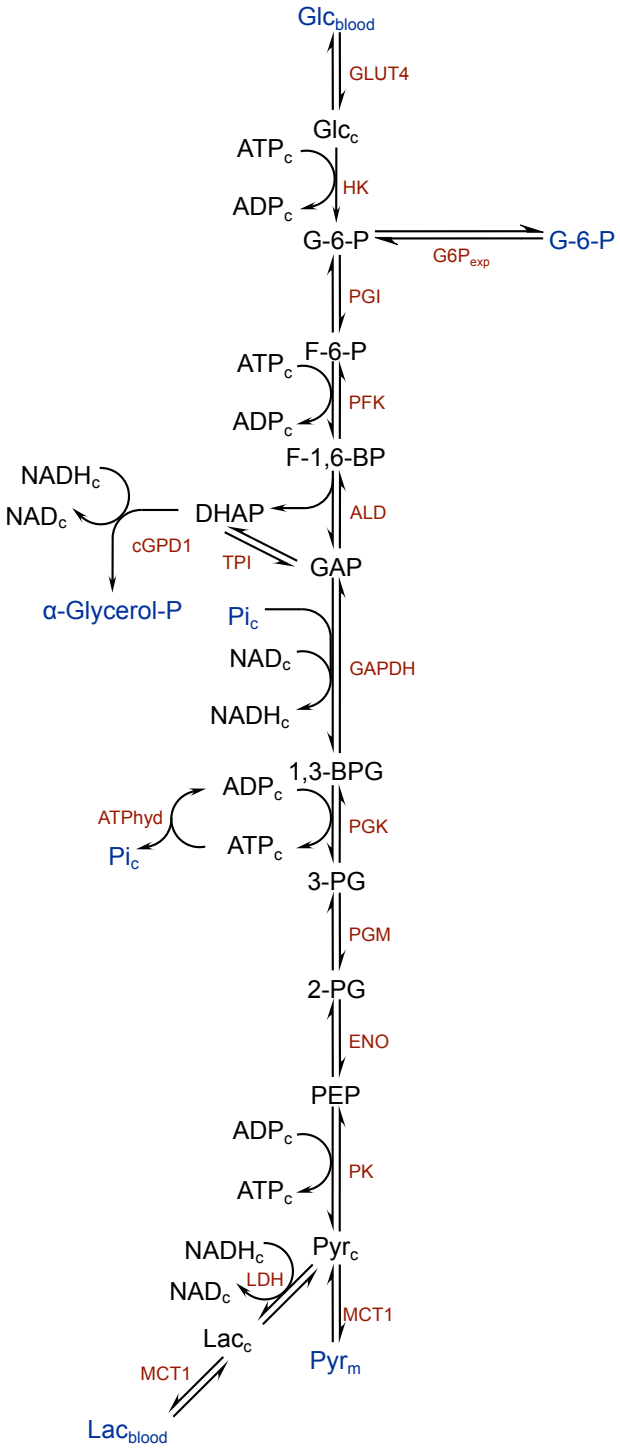

- **Figure 6.1.** Schematic illustrating the standalone heart glycolysis model.

- Internal metabolites: in *Black*; external metabolites: in *Blue*; reaction/ enzyme names: in *Red*.
- Reaction with double arrowheads is assumed to be reversible and reaction with single arrowhead is assumed to be irreversible.

As illustrated in Figure 6.1, the heart glycolysis model includes 17 reactions as follows:

1. Ten *canonical* glycolysis reactions : hexokinase (HK), phosphoglucose isomerase (PGI), phosphofructokinase (PFK), aldolase (ALD), triosephosphate isomerase (TPI), glyceraldehyde phosphate dehydrogenase (GAPDH), phosphoglycerate kinase (PGK), phosphoglycerate mutase (PGM), enolase (ENO), & pyruvate kinase (PK)
2. A reaction catalysed by lactate dehydrogenase (LDH)
3. A ATP hydrolysis (ATPhyd) reaction
4. Four transport reactions : glucose 6-phosphate export ($G6P_{exp}$), glucose transporter type 4 (GLUT4), monocarboxylate transporter type 1 (mito. memb.) (MCT1Mm), & monocarboxylate transporter type 1 (cell memb.) (MCT1Pm)
5. A reaction catalysed by cytosolic α-glycerol phosphate dehydrogenase type 1 (cGPD1)

Except for HK, cGPD1 & ATPhyd, all other reactions in this model are defined as reversible. The ATP hydrolysis reaction retains its original definition from the earlier models. The heart glycolysis model reactions are mainly defined as reversible bi-substrate equations with product inhibition, where appropriate.

The heart glycolysis model includes 16 variables (internal metabolites) that describe the concentrations of *viz.*–

1. glucose (Glc), lactate (Lac), & pyruvate (Pyr_m)
2. glucose 6-phosphate (G6P), fructose 6-phosphate (F6P), fructose 1,6-bisphosphate (F16BP), glyceraldehyde 3-phosphate (GAP), & dihydroxyacetone phosphate (DHAP)
3. 1,3-bisphosphoglycerate (13BPG), 3-phosphoglycerate (3PG), 2-phosphoglycerate (2PG), & phosphoenolpyruvate (PEP)
4. NAD^+_c, $NADH_c$, ADP_c, & ATP_c

Also, this model includes 6 parameters that describe fixed quantities (external metabolites), *viz.*–

1. blood pyruvate (Pyr_{bL}), blood glucose (Glc_{bL}), & blood lactate (Lac_{bL})
2. Pi_c, α-glycerol 3-phosphate (α-GLYp), & glucose 6-phosphate (external) (G6Px)

For most of these 22 metabolites, a range of values, largely from rat heart or skeletal muscle tissue were found and a median value was used in the model as an initial model value. Both the cytosolic as well as mitochondrial NAD & NADH concentrations are

based on the published data from Kobayashi and Neely (1979).

In this model, the GLUT4 reaction is modelled as a simple reversible reaction with product inhibition and the other complexities that exist in different types of glucose transporters are overlooked to maintain the simplicity of this model. The hexokinase is defined in the form of a irreversible reaction with product inhibition. The glucose 6-phosphate export reaction was added to the model at a later stage, during the model stabilisation; however, it also signifies the point of exchange with glycogenolysis and glycogen synthesizing reactions and in terms of glycogen utilisation by the heart muscle during fasting stage it is quite relevant. It has assumed enzyme kinetics. The cytosolic α-glycerol phosphate dehydrogenase type 1 (cGPD1) reaction was again added as another model stabilisation reaction during optimisation and a physiologically relevant reaction such as cGPD1 was chosen, because we wanted the material to leave the glycolytic pathway based on the constraints enforced by the cytosolic redox couple, so that the material leaves the pathway in a more physiologically aligned manner and ends up as α-glycerol 3-phosphate (α-GLYp) (which is a fixed quantity). This reaction also signifies the exit from glycolysis and formation of glycerol precursors. This reaction can be supported on the basis of flux distribution going from DHAP to glycerol production (Achs and Garfinkel, 1977; Kashiwaya et al., 1994). Also, based on its equilibrium constant (*i.e.* K_{eq} = 14000 unitless) in the direction of α-GLYp formation, it is physiologically unlikely that it would go reverse, therefore it was modelled as an irreversible reaction. Also, the activity of α-Glycerol 3-Phosphate oxidase is extremely low in heart muscle to be considered (*i.e.* 8 µmol/min/mg mitochondrial protein) and therefore it was not considered alongside the dehydrogenase reaction in this model (Kashiwaya et al., 1994).

The cytosolic pyruvate transport to mitochondria and the lactate transport to blood are represented by the monocarboxylate transporter type 1 (MCT1). Also, unlike the malate-aspartate shuttle model, this model uses the basal value of ATP hydrolysis activity that was established in the heart TCA cycle model (*i.e.* 0.01 mM/sec).

Thus established, we studied the structural as well as kinetic properties of this model and in the following section, we shall take a quick look at some of the significant properties of this mammalian heart-specific glycolytic system.

6.3 Results for the Heart Glycolysis model

In this section, we shall take a quick look at the significant properties of the standalone heart glycolysis model (HRT_{Glc}); since, we are more interested in finding out how this model works in the fully extended form when combined with the heart TCA cycle model, in the heart integrated TCA cycle model (HRT_{TCA+}).

6.3.1 Elementary modes analysis of Heart Glycolysis model

The heart glycolysis model contains three elementary modes and they are shown in tbl. 6.1.

Modes	GLUT4	HK	$G6P_{exp}$	PGI	PFK	ALD	TPI	cGPD1	GAPDH	PGK	PGM	ENO	PK	$MCT1M_m$	LDH	$MCT1P_m$	ATPhyd
ElMo 0	0	0	-0.5	0.5	0.5	0.5	-0.5	0	1	1	1	1	1	0	1	1	1.5
ElMo 1	1	1	0	1	1	1	0	1	1	1	1	1	1	1	0	0	0
ElMo 2	0	0	-1	1	1	1	0.5	1.5	0.5	0.5	0.5	0.5	0.5	1.5	-1	-1	0
ElMo 3	1.5	1.5	1	0.5	0.5	0.5	-0.5	0	1	1	1	1	1	0	1	1	0
ElMo 4	0.5	0.5	0	0.5	0.5	0.5	-0.5	0	1	1	1	1	1	0	1	1	1
ElMo 5	0	0	-1	1	1	1	0	1	1	1	1	1	1	1	0	0	1

- **Table 6.1.** A table showing elementary modes for the heart glycolysis model.
- In this table, fractions have been converted decimals.

The three elementary modes shown in tbl. 6.1 are as follows:

1. $ElMo_{[0]}$: This mode results in lactate formation with carbon coming from G6Px (or glycogenolysis) and ends up with no glycerol precursors.
2. $ElMo_{[1]}$: This elementary mode results in pyruvate formation with carbon coming from blood glucose and also forms α-glycerol 3-phosphate.
3. $ElMo_{[2]}$ & $ElMo_{[5]}$: These modes form pyruvate with the carbon that arrives from G6Px (or glycogenolysis) as well as blood lactate and also forms α-GLYp.
4. $ElMo_{[3]}$ & $ElMo_{[4]}$: These modes form lactate with the carbon coming from blood glucose with no glycerol precursors. Also, $ElMo_{[3]}$ exports some material out to the G6Px; whereas, $ElMo_{[4]}$ doesn't.

Therefore, the elementary modes analysis shows that both the pyruvate as well as lactate formations are possible with this model, where the carbon originates from two to three different sources available in the model.

6.3.2 Enzyme subset analysis of Heart Glycolysis model

The heart glycolysis model contains five enzyme subsets and they are shown in fig. 6.2.

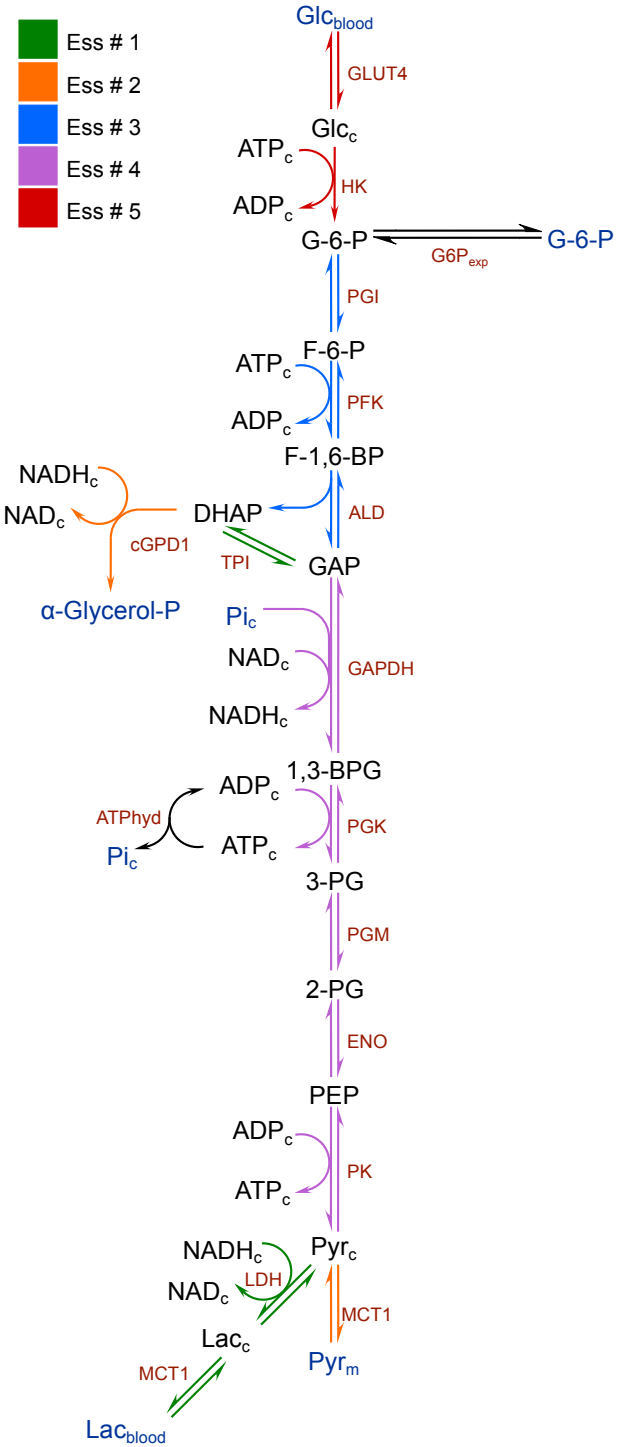

- **Figure 6.2.** Schematic illustrating the enzyme subsets in heart glycolysis model.
- Internal metabolites: in *Black*; external metabolites: in *Blue*; reaction/ enzyme names: in *Red*.
- Reaction with double arrowheads is assumed to be reversible and reaction with single arrowhead is assumed to be irreversible.

Figure 6.2 (see, pg. 207) shows that the heart glycolysis model contains 5 enzyme subsets; wherein, the enzyme subsets for the *"preparatory phase"* (ESS#3) and the *"pay-off phase"* (ESS#4) emerge as a result of this model's structural definition. This is a significant result of this structural analysis. Also, cGPD1 & MCT1Mm form a common enzyme subset (ESS#2) and $G6P_{exp}$ functions as an *independent reaction*. The model also contains GLUT4 -based (ESS#5) and LDH -based (ESS#1) enzyme subsets.

6.3.3 Flux control coefficient analysis for the Heart Glycolysis model

In this section, we'll see the results of Metabolic Control Analysis (MCA) when applied to the heart TCA cycle model, by observing the distribution of flux control coefficient (C^J).

Figure 6.3 (see, pg. 209) shows the distribution of flux control coefficients for the glyceraldehyde phosphate dehydrogenase flux (ESS#4 flux), against the increasing activity of hexokinase (which is an external metabolite in this model). The C^J plot is presented alongside a steady-state plot of the glyceraldehyde phosphate dehydrogenase flux across the same given range of hexokinase activity.

Figure 6.3 shows that the control of glyceraldehyde phosphate dehydrogenase flux is uniformly distributed between GLUT4, ATP hydrolysis (ATPhyd) and hexokinase (HK); whereas, other enzymes share a minimal control of the flux. It also shows that the share of control gets exchanged between GLUT4 & HK much before the initial model value of HK activity.

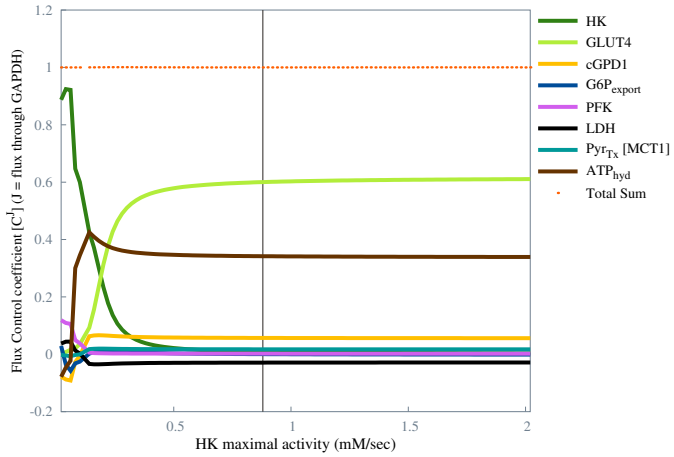

6.3.a. C^J GAPDH *vs* HK activity

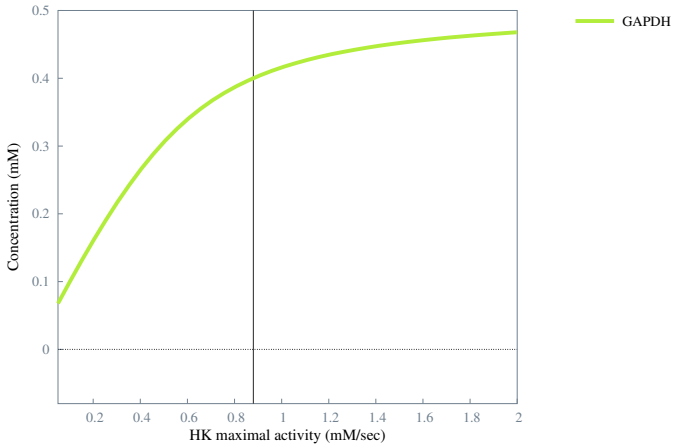

6.3.b. GAPDH flux *vs* HK activity

▪ **Figure 6.3. Control of glyceraldehyde phosphate dehydrogenase flux in the heart glycolysis model:** against the hexokinase activity.

- Key for figs. 6.3a and 6.3b is given in the plots.
- The vertical black line represents the initial model value. At this point, in figs. 6.3a and 6.3b, hexokinase activity = 0.88 mM/sec.
- ***Orange dotted line*** shows the *Summation theorem* result across the entire range.

6.4 Discussion & Conclusions

In previous sections we saw a quick overview of the significant properties of a standalone heart glycolysis model. The combination of elementary modes analysis results, enzyme subset results and the analysis of flux control coefficients showed that the model responds adequately to the variations in the activities of key enzymes.

Therefore, it was concluded that this model is ready to be integrated with the heart TCA cycle model as well as the malate-aspartate shuttle model. Thus, in the following chapter, we describe the fully integrated model containing all three standalone models.

Chapter 7

The Heart integrated TCA cycle model

7.1 Overview

In this heart integrated TCA cycle model ($\text{HRT}_{\text{TCA+}}$) the three previously seen heart-specific models were combined to form an integrated system containing 37 reactions. In the following section, we see its final composition.

7.2 Methods: Model design and definition

As mentioned earlier, the Heart integrated TCA cycle model ($\text{HRT}_{\text{TCA+}}$) representing the operation of heart or skeletal muscle-specific TCA cycle, malate-aspartate shuttle and glycolysis was manually constructed using ScrumPy, by integrating these three standalone models built earlier. The model in ScrumPy format is available in the standalone form as presented earlier and is illustrated in fig. 7.1 (see, pg. 211). The final version of the updated model contains 37 reactions and 54 metabolites.

7.2.1 Model definition

In addition to the reactions from these three standalone models, some *sink* reactions were required for the removal of excess pyruvate, cytosolic glutamate and cytosolic aspartate; therefore the required reactions were added in the form of reversible transport reactions. The final result of the model definition is shown in fig. 7.1 (see, pg. 211). Also, for the positive directions of the reactions as they are defined in the model, please refer to fig. 7.2 (see, pg. 212).

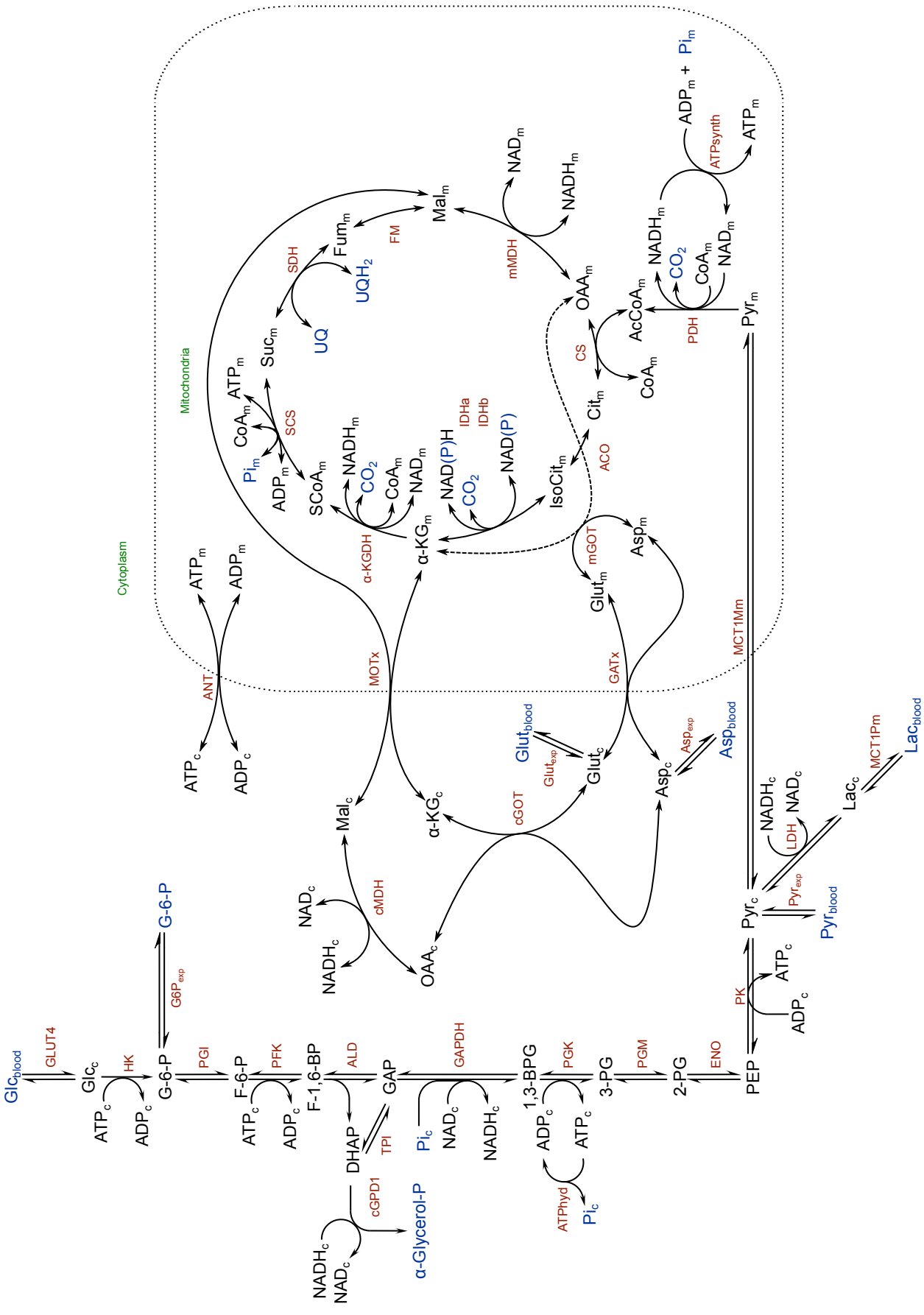

Figure 7.1. Schematic illustrating the heart integrated TCA cycle model.

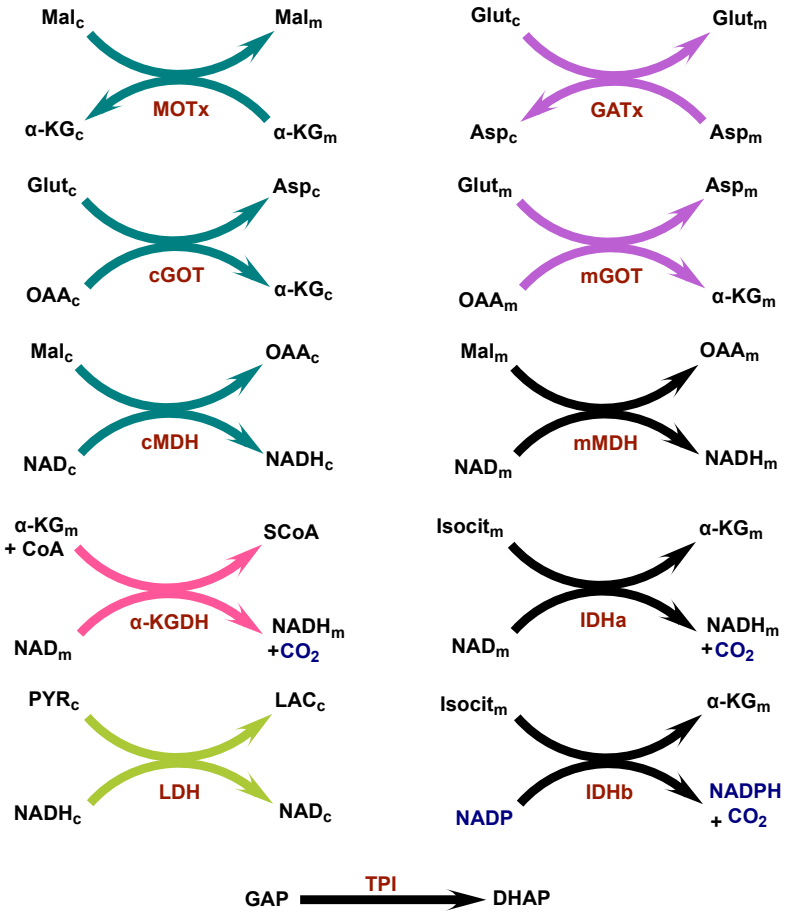

▪ **Figure 7.2.**
Schematic illustrating the positive reaction directions heart integrated TCA cycle model.

7.3 Results for the Heart integrated model

In this section, we shall take a quick look at the significant properties of the heart integrated TCA cycle model ($\mathrm{HRT}_{\mathrm{TCA}+}$).

7.3.1 Elementary modes analysis & Enzyme subset analysis of Heart integrated model

The heart integrated TCA cycle model contains a total of 278 elementary modes and 9 enzyme subsets. The enzyme subsets of the heart integrated TCA cycle model are shown in fig. 7.3 on pg. 213.

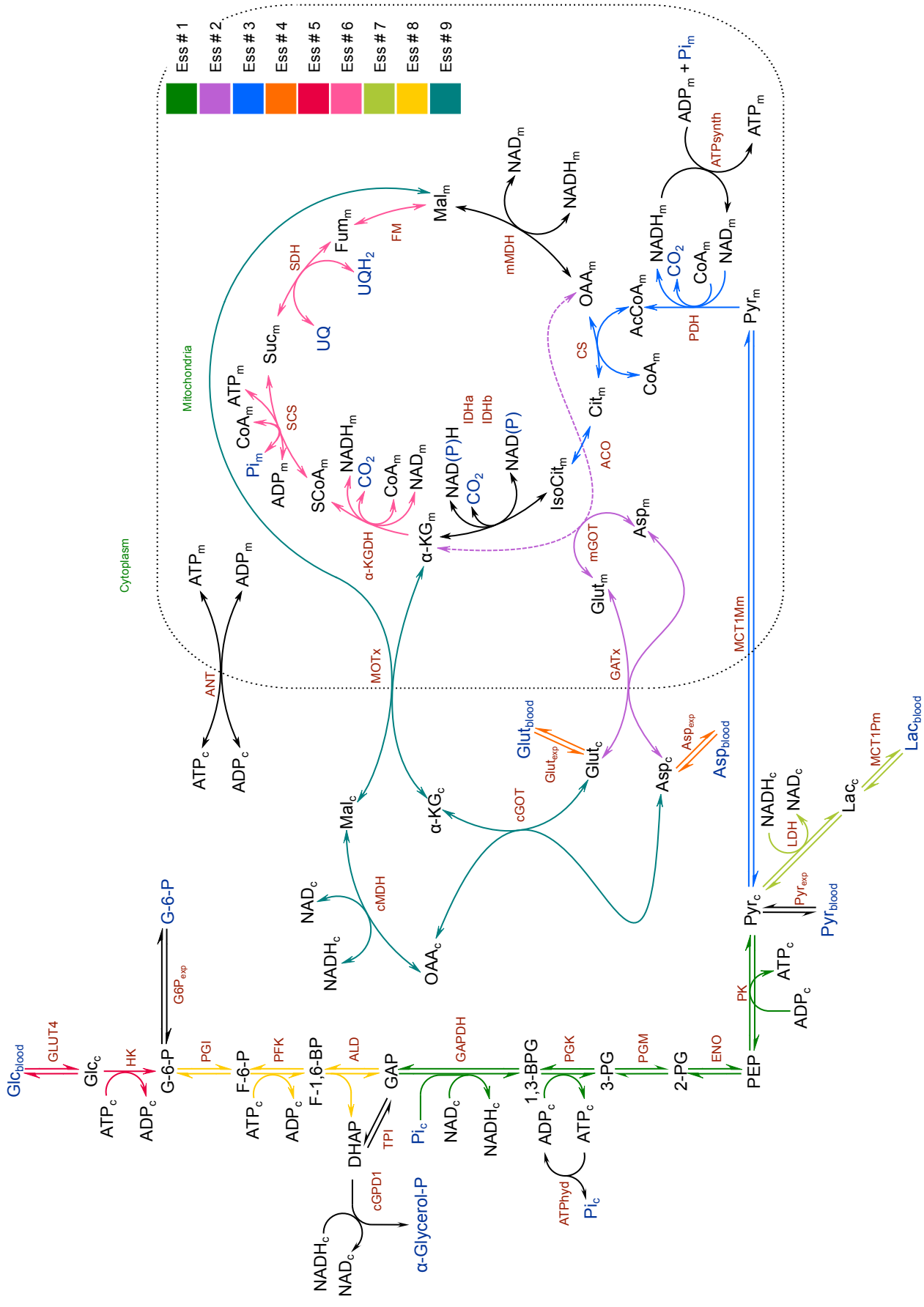

Figure 7.3. Schematic illustrating the heart integrated TCA cycle model enzyme subsets.

7.3.2 Steady-state analysis for the Heart integrated model

In this section, we'll see the results of steady-state analysis in the form of *'percentage response plots'*; wherein, all the fluxes in the model at a given steady-state (*e.g.* initial steady-state of the model or any other steady-state at differnt enzyme activity), are recalculated in terms of percentages with respect to GLUT4 as 100% . These schematics thus show us the flow of carbon through the integrated maze of reactions in this enhanced model.

First, we show the 'percentage response plot' at the initial steady-state of the model fig. 7.4, and then at a steady-state obtained by increasing the ATP hydrolysis activity by 10x fig. 7.5.

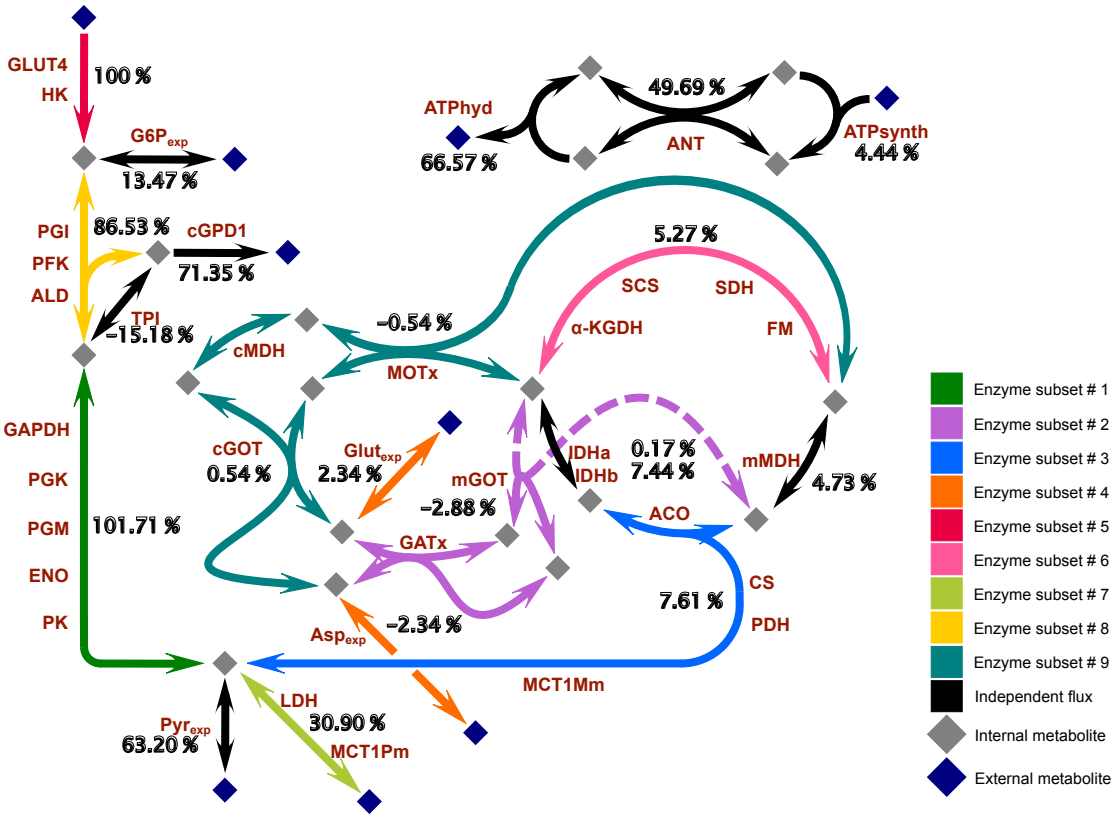

▪ **Figure 7.4.** Schematic illustrating the 'percentage response plot' at the initial steady-state of the heart integrated TCA cycle model.

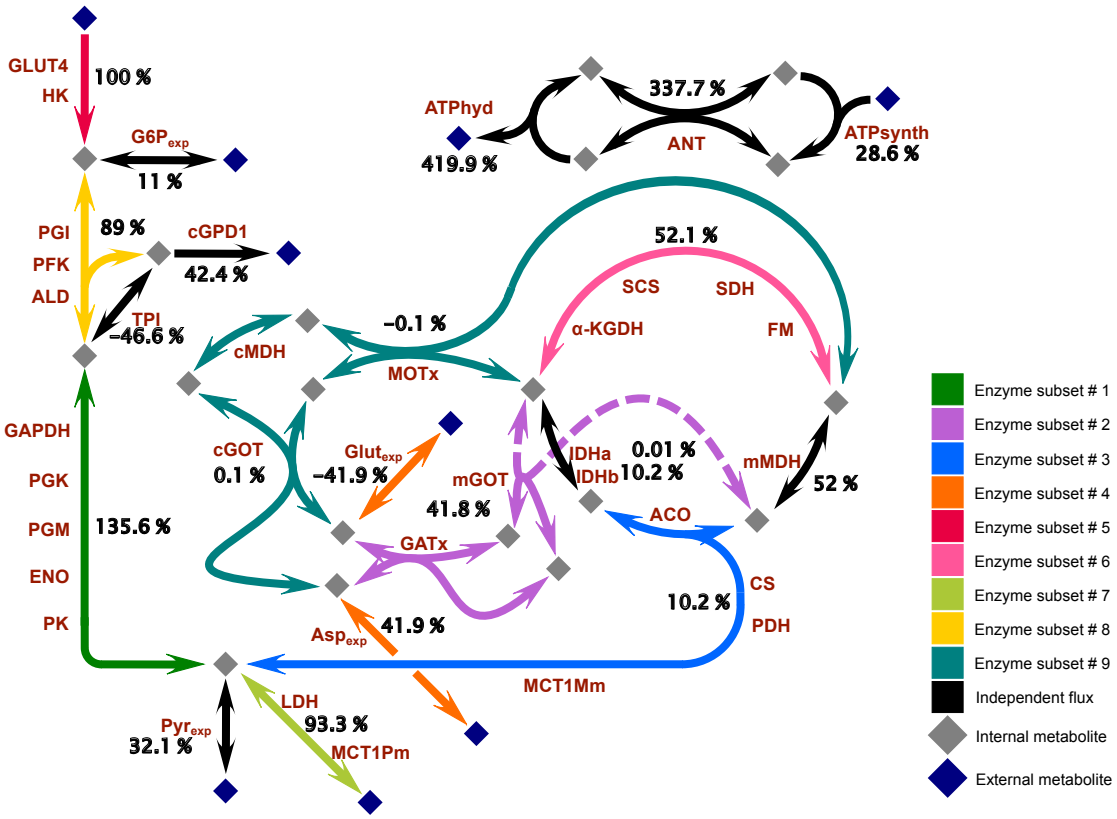

▪ **Figure 7.5.** Schematic illustrating the 'percentage response plot' at steady-state, at 10x ATPhyd activity in the heart integrated TCA cycle model.

7.4 Discussion & Conclusions

At the beginning of this project, the basic idea involved developing a mammalian heart-specific TCA cycle model that is both comprehensive in its ability to illustrate the physiological behaviour of the pathway in tissues such as the mammalian heart or skeletal-muscle as well as simple enough to include all the key biochemical interactions in the pathway. As mentioned earlier, we started with the well established model of TCA cycle in mammalian liver, developed within the CSMG. Analysis of this model helped us understand the tissue-specific interactions in the TCA cycle, as well as the overall physiological behaviour of the pathway and how to properly analyse it in detail going forward. With the help of this understanding, we developed the mammalian heart-specific TCA cycle model, which did not include the liver-specific reactions like pyruvate carboxylase and malate carrier (malate-phosphate transporter). Also, due to the structural limitations of this model, we decided to exclude the $NADP^+$-dependent isocitrate dehydrogenase from this model, pending further investigation.

Analysis of the heart TCA cycle model revealed that in the absence of a large anaplerotic input from the pyruvate carboxylase reaction, the model requires a similar anaplerotic input from the reactions involving malate-aspartate shuttle, otherwise the TCA cycle flux falls way below the physiologically expected range of values. Therefore, the heart TCA cycle model analysis confirmed what we had suspected all along, that it would need to be integrated with a model describing the malate-aspartate shuttle reactions and therefore we went ahead with the development of malate-aspartate shuttle model. This model was constructed using the same design principles as that of the previously built TCA cycle models and was based on the simplified, generic, reversible bi-substrate equation (Chassagnole et al., 2001b; Rohwer et al., 2006), modified where necessary to account for more than two substrates and/or products. Equations of this form are simple enough to include a limited number of parameters that are easily determined, and do not require additional explicit assumptions to be made, yet adequately describe the response of an enzyme to changes in both substrate and product concentrations within the physiological range (Chassagnole et al., 2001b). By default, this equation assumes competitive product inhibition with respect to the corresponding substrate (*e.g.* ADP competitive with ATP), and non-competitive inhibition for unrelated substrate-product pairs in multi-substrate reactions. Additional effector interactions are also considered when necessary. In all cases, the simplest expression that adequately represents the key kinetic properties of the enzyme is used. Throughout the models described in this work, nearly all rate equations are based on such a simplified bi-substrate equation, as it allowed us to maintain the model complexity to a bare minimum, while making the models neither too complicated nor overly simplified.

The standalone malate-aspartate shuttle model analysis revealed its ability to respond adequately in response to the change in its input, *i.e.* $NADH_c$. When combined with the already established heart TCA cycle model, the resultant system showed that the inclusion of malate-aspartate shuttle does in fact improve the overall TCA cycle flux. However, the malate-aspartate shuttle model in its standalone format included the cytosolic NAD and NADH species as external metabolites or as *fixed quantities*, since the malate-aspartate shuttle reactions in the cytosol do not recycle these species back to their oxidised form, in the absence of other cytoplasmic reactions (*e.g.* glycolysis). It meant that combining this model with the heart TCA cycle model, without any further modifications, would have caused the factors influencing the transfer of reduction potential between the cytosol and mitochondria to be external to the resulting system, which would have been counterintuitive. This particular observation suggested that the cytosolic redox couple should be internalised within the system defined by the malate-aspartate shuttle reactions, by further modifications to this system. It called for the incorporation of another pathway or a reaction that would dynamically cycle between the cytosolic NAD and NADH. Therefore, we decided to develop a standalone model of

the mammalian heart-specific glycolytic pathway and to incorporate into the extended model. The decision to develop a full glycolytic model instead of including a single-step, abstracted representation of glycolysis was based on the fact that the solution required to address this problem had to be relevant to the cardiac physiology and the fact that most of the required kinetic data in this tissue was already readily available.

Thus the heart integrated TCA cycle model ($\mathrm{HRT}_{\mathrm{TCA+}}$) was formed by combining three standalone models, *viz.*– the heart TCA cycle model ($\mathrm{HRT}_{\mathrm{TCA}}$), the malate-aspartate shuttle model ($\mathrm{HRT}_{\mathrm{MAS}}$), and the heart glycolysis model ($\mathrm{HRT}_{\mathrm{Glc}}$). Also, three *sink* reactions were added to this extended model in the form of reversible transport reactions in order to remove the excess pyruvate, cytosolic glutamate and cytosolic aspartate from the system. As discussed earlier in the heart TCA cycle model chapter (see, pg. 147), the NADP^{+}-dependent isocitrate dehydrogenase (IDHb) reaction was reintroduced into this extended model. Also, certain kinetic parameters were tweaked during the final optimisation process in order to achieve a stable steady-state solution for this integrated model of the heart TCA cycle.

This fully extended heart TCA cycle model was analysed in great detail and its observed pattern of behaviour was studied against the standalone TCA cycle model as a point of reference. The structural analysis of the heart integrated TCA cycle model showed that there are 278 elementary modes and 9 enzyme subsets in the model. The shortest elementary mode describes the futile cycle between IDHa and IDHb and consists of 5 reactions. The other two relatively shorter modes contain 7 & 11 reactions out of the possible 37 reactions in this model. The longest elementary modes of this integrated model contain a total of 30 reactions; which means that a group of 7 reactions do not participate in these modes. There are 10 such modes in this model, 5 of those are based on IDHa and the other 5 are their respective IDHb complements, similar to what we observed earlier in the case of TCA cycle models. All 10 modes utilise glucose as the sole carbon input and the pyruvate formed as a result of glycolysis feeds into either a fully functioning TCA cycle with malate-aspartate shuttle or the MDH-deficient TCA cycle with malate-aspartate shuttle. In all of these ten modes, at least 50% of the total incoming glucose gets converted to lactate and the rest of it to pyruvate, which then enters mitochondria to form citrate via the TCA cycle. However, a handful of these longest elementary modes produce only a fractional amount of ATP that can be hydrolysed in the cytosol via ATPhyd. Analysis of all 278 elementary modes reveals that in order to maximise the ATP production in this integrated system, the optimal number of reactions participating in a given elementary mode must be no less that 28 and no more 29, barring a single exception. However, the solitary exceptional mode lacks entire glycolysis and produces pyruvate via external lactate, thus allowing the TCA cycle to function. The elementary mode containing 29 reactions converts glucose to

pyruvate without any lactate, G6Px (assumed here as an exit from glycolysis to glycogen synthesis), or α-glycerol 3-phosphate (α-GLYp); resulting in a total of 14.5 molecules of ATP. Whereas, the elementary mode consisting 28 reactions produces pyruvate from G6Px (assumed here as an entry into glycolysis via glycogenolysis) without any lactate or α-GLYp production; thereby resulting in a total of 15 molecules of ATP. Interestingly, in both these cases, mitochondrial MDH (mMDH) is positive and carries exactly twice the amount of flux through the TCA cycle or malate-aspartate shuttle.

The 9 enzyme subsets of this integrated model includes 4 subsets in glycolysis, 2 in the TCA cycle, 2 in malate-aspartate shuttle, and the remaining subset describes the exchange of excess cytosolic amino acids with external media (*i.e.* blood). The 4 glycolytic subsets comprise of glucose entry and phosphorylation via hexokinase, "preparatory" and "pay-off" phases, and a lactate production subset. The two TCA cycle subsets include a subset of pyruvate entry into the mitochondria and its conversion to isocitrate and a subset comprising the decarboxylative reduction of α-ketoglutarate to malate. Whereas, the two malate-aspartate shuttle enzyme subsets include one containing GATx and mGOT, while the other containing MOTx, cGOT, and cMDH. The TCA cycle as well as the glycolytic enzyme subsets of this integrated system are identical to those observed in the standalone liver TCA cycle model and the mammalian heart-specific glycolysis model, respectively.

Steady-state analysis of the heart integrated TCA cycle model shows the dynamic responses of this system to changes in various enzyme activities. For instance, in the case of increasing ATPhyd activity or the ATP-demand, the model shows higher TCA cycle activity corresponding to increased amino acid import and higher mGOT/GATx activity, with comparatively increased amount of lactate production. While several such interesting steady-state as well as control coefficient distribution scenarios were tested for this extended model, the detailed analysis and discussion of which remains open to interpretaion depending on the exact nature of inquiry, since such large metabolic systems often tend to be highly complex in terms of their analysis.

Therefore in conclusion, the heart integrated TCA cycle model ($\mathrm{HRT}_{\mathrm{TCA+}}$) was successfully created and analysed. The model shows adequate responses aginst changes in enzyme activities or metabolite concentrations. The heart integrated TCA cycle model offers several key physiologically relevant end-points against which it can be validated, some of these end-points include, *viz.*– blood glucose, blood lactate, blood pyruvate *etc.* and yet, the model shows that its function can be enhanced with the help of additional biochemical pathways, such as the creatine - creatine phosphate shuttle and an enhanced version of the electron transport chain.

Appendix A: Differential and Algebraic Equations for liver TCA cycle models

$$\frac{d[\,\mathrm{AcCoA_m}\,]}{dt} = \nu_{\mathrm{PDH}} - \nu_{\mathrm{CS}} \tag{A.1}$$

$$\frac{d[\,\mathrm{Cit_m}\,]}{dt} = \nu_{\mathrm{CS}} - \nu_{\mathrm{ACO}} \tag{A.2}$$

$$\frac{d[\,\mathrm{Isocit_m}\,]}{dt} = \nu_{\mathrm{ACO}} - \nu_{\mathrm{IDHa}} - \nu_{\mathrm{IDHb}} \tag{A.3}$$

$$\frac{d[\,\alpha\mathrm{KG_m}\,]}{dt} = \nu_{\mathrm{IDHa}} + \nu_{\mathrm{IDHb}} - \nu_{\alpha\mathrm{KGDH}} \tag{A.4}$$

$$\frac{d[\,\mathrm{SCoA_m}\,]}{dt} = \nu_{\alpha\mathrm{KGDH}} - \nu_{\mathrm{SCS}} \tag{A.5}$$

$$\frac{d[\,\mathrm{Suc_m}\,]}{dt} = \nu_{\mathrm{SCS}} - \nu_{\mathrm{SDH}} \tag{A.6}$$

$$\frac{d[\,\mathrm{Fum_m}\,]}{dt} = \nu_{\mathrm{SDH}} - \nu_{\mathrm{FM}} \tag{A.7}$$

$$\frac{d[\,\mathrm{Mal_m}\,]}{dt} = \nu_{\mathrm{FM}} - \nu_{\mathrm{MDH}} - \nu_{\mathrm{MC}} \tag{A.8}$$

$$\frac{d[\,\mathrm{OAA_m}\,]}{dt} = \nu_{\mathrm{PC}} + \nu_{\mathrm{MDH}} - \nu_{\mathrm{CS}} \tag{A.9}$$

$$\frac{d\left[\,\mathrm{NAD_m^+}\,\right]}{dt} = 4 \cdot \nu_{\mathrm{ATP_{synth}}} - \nu_{\mathrm{PDH}} - \nu_{\mathrm{IDHa}} - \nu_{\alpha\mathrm{KGDH}} - \nu_{\mathrm{MDH}} \tag{A.10}$$

$$\frac{d[\,\mathrm{ATP_m}\,]}{dt} = 10 \cdot \nu_{\mathrm{ATP_{synth}}} + \nu_{\mathrm{SCS}} - \nu_{\mathrm{PC}} - \nu_{\mathrm{ANT}} \tag{A.11}$$

$$\frac{d[\,\mathrm{ATP_c}\,]}{dt} = \nu_{\mathrm{ANT}} - \nu_{\mathrm{ATP_{hyd}}} \tag{A.12}$$

$$[\,\mathrm{CoA_m}\,] = [\,\mathrm{CoA_{Tot_m}}\,] - [\,\mathrm{AcCoA_m}\,] - [\,\mathrm{SCoA_m}\,] \tag{A.13}$$

$$[\,\mathrm{NADH_m}\,] = [\,\mathrm{N_{Tot}}\,] - \left[\,\mathrm{NAD_m^+}\,\right] \tag{A.14}$$

$$[\,\mathrm{ADP_m}\,] = [\,\mathrm{A_{Tot_m}}\,] - [\,\mathrm{ATP_m}\,] \tag{A.15}$$

$$[\,\mathrm{ADP_c}\,] = [\,\mathrm{A_{Tot_c}}\,] - [\,\mathrm{ATP_c}\,] \tag{A.16}$$

Appendix B: Rate Equations for the liver TCA cycle reactions

B.1 Pyruvate Carboxylase

Pyruvate carboxylase (PC) catalyses the following net reaction:

$$\text{Pyruvate} + \text{ATP}_\text{m} + \text{HCO}_3^- \rightleftharpoons \text{Oxaloacetate} + \text{ADP}_\text{m} + \text{Pi}_\text{m} \qquad \text{(B.1)}$$

Although acetyl-CoA is not an absolute requirement for catalytic activity of mammalian PC (McClure et al., 1971), it is an effective allosteric activator of the enzyme. Acetyl-CoA reduces the apparent K_m values of both pyruvate and bicarbonate, but also increases the average maximal activity by around a factor of five (Ashman et al., 1972; Scrutton, 1974; Scrutton and White, 1972). At low acetyl-CoA (< 0.25 µM), the K_m values of pyruvate and bicarbonate decrease markedly and PC maximal activity shows little change; whereas, at concentrations that approach or exceed the apparent K_a of acetyl-CoA (> 0.25 µM) this pattern is reversed, with changes in maximal activity being more pronounced than those in the substrate K_m values (Scrutton and White, 1972). However, it seems unlikely that acetyl-CoA is responsible for any significant regulation of PC activity within the physiological context, since the mitochondrial concentration of acetyl-CoA is at least a factor of ten higher than the apparent K_a (Kimmich and Rasmussen, 1969). Mg^{2+} in excess of ATP also activates PC, by increasing the maximal activity only (Keech and Barritt, 1967; McClure and Lardy, 1971). In contrast to acetyl-CoA, the mitochondrial free Mg^{2+} concentration is in the region of the K_a, and hence this is suggested to represent an important regulatory interaction (Blair, 1969).

At physiological pyruvate concentration, both ADP and Pi are competitive inhibitors with respect to ATP (McClure et al., 1971). Ca^{2+} is also a potent inhibitor, possibly at least partly through competition with free Mg^{2+} (Kimmich and Rasmussen, 1969). However, these interactions have been suggested to have little physiological relevance (McClure and Lardy, 1971). The mitochondrial concentration of ATP is proposed to

be sufficient to maintain PC activity, irrespective of small changes in ADP and Pi concentrations. Furthermore, the K_a for Ca^{2+} is around 100 times greater than the mitochondrial Ca^{2+} concentration, while the free Mg^{2+} concentration would seem to be sufficiently high to counteract competitive inhibition by Ca^{2+}. At physiological pH, the affinity for acetyl-CoA is dependent upon pyruvate concentration; this dependence is particularly notable at low pyruvate (concentrations less than 0.5 mM) (Scrutton, 1974). Both ATP and bicarbonate increase the affinity of each other; similarly ADP and Pi each enhance the binding of the other (McClure et al., 1971).

In liver TCA cycle models, given the complexity of the regulatory interactions of PC, the inter-dependence of substrate and effector affinities has not been modelled explicitly; instead, the effects are approximated through use of K_m values. However in these models, the apparent maximal activity of PC is defined as a function of Mg^{2+} and acetyl-CoA concentrations; which is determined dynamically through a separate algebraic expression and substituted into the rate equation during simulation of the model.

PC kinetics are modelled using an extended version of the generic rate equation that allows for three substrates/ products. Terms for product inhibition by oxaloacetate, ADP and Pi are included in the expression by default, but additional competitive inhibition by Ca^{2+} is not considered, given that this seems unlikely to be physiologically relevant.

$$\nu_{\mathrm{PC}} = \frac{1}{\left[\left\{K_{\mathrm{ATP_m}}\left(1+\frac{[\mathrm{ADP_m}]}{K_{\mathrm{ADP_m}}}\right)\left(1+\frac{[\mathrm{Pi_m}]}{K_{\mathrm{Pi_m}}}\right)\right\}+[\mathrm{ATP_m}]\right]} \times \frac{V_{\mathrm{PC,\,app}}\left([\mathrm{Pyr_m}]\cdot[\mathrm{HCO_3^-}]\cdot[\mathrm{ATP_m}]-\frac{[\mathrm{OAA_m}]\cdot[\mathrm{ADP_m}]\cdot[\mathrm{Pi_m}]}{K_{\mathrm{eq}}}\right)}{\left[\left(K_{\mathrm{Pyr_m}}\cdot K_{\mathrm{HCO_3^-}}\right)\left\{\left(1+\frac{[\mathrm{Pyr_m}]}{K_{\mathrm{Pyr_m}}}\right)\left(1+\frac{\left[\mathrm{HCO_3^-}\right]}{K_{\mathrm{HCO_3^-}}}\right)+\left(\frac{[\mathrm{OAA_m}]}{K_{\mathrm{OAA_m}}}\right)\right\}\right]} \tag{B.2}$$

Where, $$V_{\mathrm{PC,\,app}} = V_{\mathrm{PC,\,min}} + \left(V_{\mathrm{PC,\,max}} - V_{\mathrm{PC,\,min}}\right)\cdot\alpha\cdot\beta \tag{B.3}$$

and, $$\alpha = \frac{[\mathrm{AcCoA_m}]^n}{\left(K_{\mathrm{AcCoA_m}} + [\mathrm{AcCoA_m}]\right)^n} \tag{B.4}$$

$$\beta = \frac{\left[\mathrm{Mg^{2+}}\right]}{K_{\mathrm{Mg^{2+}}} + \left[\mathrm{Mg^{2+}}\right]} \tag{B.5}$$

B.2 Pyruvate Dehydrogenase

The pyruvate dehydrogenase (PDH) complex catalyses the following net reaction:

$$\text{Pyruvate} + \text{NAD}^+_\text{m} + \text{CoA}_\text{m} + \text{H}_2\text{O} \longrightarrow \text{Acetyl-CoA} + \text{NADH}_\text{m} + \text{CO}_2 \tag{B.6}$$

Given the magnitude of the equilibrium constant for the forward reaction (K_eq = 1.2E+06 at pH 8.0; Alberty 2003b), this step is treated as irreversible.

PDH activity is regulated through covalent modification, *i.e.* through phosphorylation and dephosphorylation by pyruvate dehydrogenase kinase (PDHK) and pyruvate dehydrogenase phosphatase (PDHP) (Holness and Sugden, 2003). However, as a simplification, the apparent maximal activity of PDH is taken to be constant and these interactions are not currently represented in the model.

An irreversible form of the generic rate equation, modified to account for three substrates/ products, is used to represent PDH kinetics. Product inhibition by acetyl-CoA and NADH_m, competitive with respect to CoA_m and NAD^+_m, respectively (Tsai et al., 1973) is considered. CO_2 is assumed not to affect the rate of the reaction.

$$\begin{aligned}\nu_\text{PDH} &= \frac{1}{\left(K_{\text{Pyr}_\text{m}} + [\text{Pyr}_\text{m}]\right)} \\ &\times \frac{V_\text{PDH}\left([\text{Pyr}_\text{m}] \cdot \left[\text{NAD}^+_\text{m}\right] \cdot [\text{CoA}_\text{m}]\right)}{\left[K_{\text{NAD}^+_\text{m}}\left(1 + \frac{[\text{NADH}_\text{m}]}{K_{\text{NADH}_\text{m}}}\right) + \left[\text{NAD}^+_\text{m}\right]\right]\left[K_{\text{CoA}_\text{m}}\left(1 + \frac{[\text{AcCoA}_\text{m}]}{K_{\text{AcCoA}_\text{m}}}\right) + [\text{CoA}_\text{m}]\right]}\end{aligned} \tag{B.7}$$

B.3 Citrate Synthase

Citrate synthase (CS) catalyses the following net reaction:

$$\text{Oxaloacetate} + \text{Acetyl-CoA} + \text{H}_2\text{O} \rightleftharpoons \text{Citrate} + \text{CoA}_\text{m} \tag{B.8}$$

Although this step is generally regarded as irreversible, due to a large equilibrium constant for the forward reaction (K_eq = 1.13E+09 at pH 8.0; Alberty 2003b); when considered as a coupled system with the reaction catalysed by MDH, the overall equilibrium constant indicates a reversible process (Srere, 1972).

Succinyl-CoA and ATP are apparently the most significant effectors of purified rat liver CS, acting as a competitive inhibitors with respect to acetyl-CoA (Shepherd and Garland, 1969; Smith and Williamson, 1971). At low Mg^{2+} concentration (< 1 mM), it seems that unchelated ATP is the inhibitor. However, at higher Mg^{2+} concentrations, such as that within the mitochondrion, the Mg-ATP complex may also be inhibitory (Shepherd and Garland, 1969). Currently, in liver TCA cycle models, the Mg^{2+} concentration is fixed at 0.37 mM (Corkey et al., 1986).

The generic rate equation, modified to include terms representing competitive inhibition by both succinyl-CoA and Mg-ATP in addition to product inhibition by citrate, is used to model CS kinetics.

$$\begin{aligned} \nu_{\mathrm{CS}} &= \frac{1}{\left[K_{\mathrm{OAA_m}}\left(1+\frac{\left[\mathrm{Cit_m}\right]}{K_{\mathrm{Cit_m}}}\right)+\left[\mathrm{OAA_m}\right]\right]} \\ &\times \frac{V_{\mathrm{CS}}\left(\left[\mathrm{OAA_m}\right]\cdot\left[\mathrm{AcCoA_m}\right]-\frac{\left[\mathrm{Cit_m}\right]\cdot\left[\mathrm{CoA_m}\right]}{K_{\mathrm{eq}}}\right)}{\left[K_{\mathrm{AcCoA_m}}\left(1+\frac{\left[\mathrm{SCoA_m}\right]}{K_{\mathrm{SCoA_m}}}+\frac{\left[\mathrm{ATP_m}\right]}{K_{\mathrm{ATP_m}}}+\frac{\left[\mathrm{CoA_m}\right]}{K_{\mathrm{CoA_m}}}\right)+\left[\mathrm{AcCoA_m}\right]\right]} \end{aligned} \tag{B.9}$$

B.4 Aconitase

Aconitate hydratase (ACO) catalyses the following net reaction:

$$\mathrm{Citrate} \rightleftharpoons \mathrm{Isocitrate} + \mathrm{H_2O} \tag{B.10}$$

A reversible uni-uni rate law (Segel, 1993), with product inhibition by isocitrate, is used to represent this step.

$$\nu_{\mathrm{ACO}} = \frac{V_{\mathrm{ACO}}\left(\left[\mathrm{Cit_m}\right]-\frac{\left[\mathrm{Isocit_m}\right]}{K_{\mathrm{eq}}}\right)}{K_{\mathrm{Cit_m}}\left(1+\frac{\left[\mathrm{Isocit_m}\right]}{K_{\mathrm{Isocit_m}}}\right)+\left[\mathrm{Cit_m}\right]} \tag{B.11}$$

B.5 NAD$^+$-Dependent Isocitrate Dehydrogenase

NAD$^+$-dependent isocitrate dehydrogenase (IDHa) catalyses the following net reaction:

$$\text{Isocitrate} + \text{NAD}^+_\text{m} + \text{H}_2\text{O} \longrightarrow \alpha\text{-ketoglutarate} + \text{NADH}_\text{m} + \text{CO}_2 \qquad \text{(B.12)}$$

Although the reaction is in principle reversible, due to inadequate binding of both α-ketoglutarate and CO_2, this has not been observed in practice (Plaut, 1970), and therefore for the purposes of modelling we have considered the step to be effectively irreversible.

For the activity of IDHa, a low concentration of either Mg^{2+} (Gabriel and Plaut, 1982), Mn^{2+} or Co^{2+} is required, and in fact, Mg-isocitrate is more likely to be the physiological substrate (Plaut et al., 1974). Since Mg^{2+} is in excess within the mitochondrion, activation by this ion is not explicitly represented in the model. For the heart enzyme, the binding of isocitrate is cooperative however, under typical mitochondrial conditions, the Hill coefficient is near unity (Gabriel and Plaut, 1982; Plaut et al., 1974); whereas, Michaelis-Menton kinetics have been observed for the liver enzyme (Plaut and Aogaichi, 1968).

Both heart and liver NAD$^+$-dependent isocitrate dehydrogenase are activated by ADP, but inhibited by ATP; the former effector reduces the apparent K_m for isocitrate, while the latter is competitive with respect to NAD^+_m (Chen and Plaut, 1963; Plaut and Aogaichi, 1968). Some other TCA cycle models have assumed that unchelated ADP and ATP are the true effectors (Bazil et al., 2010; Kohn et al., 1979a; Wu et al., 2007). However, on the basis of the available experimental data, it is not possible to exclude inhibition by chelated ATP (Chen and Plaut, 1963; Plaut and Aogaichi, 1968), although the Mg-ADP complex is apparently inactive (Plaut et al., 1974). In practice, the distinction between unchelated and Mg-complexed ADP is relatively unimportant, since the mitochondrial concentrations are similar (Akerboom et al., 1978; Magnus and Keizer, 1997). Finally, Ca^{2+} also binds to mammalian IDHa, having a modest activating effect within a physiological concentration range (Rutter and Denton, 1988).

NAD$^+$-dependent isocitrate dehydrogenase kinetics are modelled using a modified, irreversible form of the generic rate equation. Product inhibition by $NADH_m$ is considered, but α-ketoglutarate and CO_2 are assumed to have no influence on reaction rate (Chen and Plaut, 1963; Plaut and Aogaichi, 1968). The expression also takes into account the activation of the enzyme by unchelated ADP and Ca^{2+}, as well as competitive inhibition by the Mg-ATP complex.

$$\nu_{\mathrm{IDHa}} = \frac{1}{\left[\left\{\left(K_{\mathrm{Isocit_m}}\right)^n \Big/ \left(1+\frac{\left[\mathrm{ADP_m^{3-}}\right]}{K_{\mathrm{ADP_m^{3-}}}}\right)\left(1+\frac{\left[\mathrm{Ca^{2+}}\right]}{K_{\mathrm{Ca^{2+}}}}\right)\right\} + \left[\mathrm{Isocit_m}\right]^n\right]} \times \frac{V_{\mathrm{IDHa}}\left(\left[\mathrm{Isocit_m}\right]^n \cdot \left[\mathrm{NAD_m^+}\right]\right)}{\left[K_{\mathrm{NAD_m^+}}\left(1+\frac{\left[\mathrm{ATP_m}\right]}{K_{\mathrm{ATP_m}}}+\frac{\left[\mathrm{NADH_m}\right]}{K_{\mathrm{NADH_m}}}\right)+\left[\mathrm{NAD_m^+}\right]\right]} \tag{B.13}$$

Where, $$\left[\mathrm{ADP_m^{3-}}\right] = f_{\mathrm{ADP_m^{3-}}} \cdot \left[\mathrm{ADP_m}\right] \tag{B.14}$$

The conversion factor $f_{\mathrm{ADP_m^{3-}}}$ gives the fraction of total mitochondrial ADP that is unchelated, and hence ionized (Magnus and Keizer, 1997), and is defined in the supplementary material (see tbl. I.2 on pg. III).

B.6 NADP$^+$-Dependent Isocitrate Dehydrogenase

NADP$^+$-dependent isocitrate dehydrogenase (IDHb) catalyses the following net reaction:

$$\text{Isocitrate} + \mathrm{NADP^+} + \mathrm{H_2O} \rightleftharpoons \alpha\text{-ketoglutarate} + \mathrm{NADPH} + \mathrm{CO_2} \tag{B.15}$$

Although the NADP$^+$-dependent enzyme from liver mitochondria represents only 25% of the cellular complement (Lowenstein, 1967), and is responsible for only 10–12% of total tissue isocitrate dehydrogenase (IDH) activity, the maximal catalytic capability is apparently up to 14 times greater than that of the NAD$^+$-dependent form (Smith and Plaut, 1979). Considering the apparent irreversibility of the NAD$^+$-dependent isocitrate dehydrogenase, Sazanov and Jackson (1994) have proposed the operation of a substrate cycle in which α-ketoglutarate ($\alpha\mathrm{KG_m}$) generated by IDHa is converted back to isocitrate by IDHb, which thus contributes to regulation of the TCA cycle. Evidence for the existence of such a cycle has been provided by mass isotopomer distribution studies in both heart and liver (Comte et al., 1997, 2002; Des Rosiers et al., 1994).

Unlike its NAD$^+$-associated counterpart, IDHb is not allosteric, but is subject to product inhibition by both α-ketoglutarate and NADPH, and by either CO_2 or bicarbonate; NADPH is competitive with NADP$^+$, but the reported kinetics of inhibition by α-ketoglutarate and CO_2 are more complex (Uhr et al., 1974). For the purposes of liver TCA cycle models, α-ketoglutarate is assumed to be competitive with respect to isocitrate and CO_2 is taken to be a non-competitive inhibitor.

The extended, generic rate equation is used to represent NADP$^+$-dependent isocitrate dehydrogenase kinetics. The expression includes an additional term representing non-competitive inhibition by CO_2.

$$\nu_{\text{IDHb}} = \frac{1}{\left(1+\frac{[\text{CO}_2]}{K_{\text{CO}_2}}\right)} \times \frac{V_{\text{IDHb}}\left([\text{Isocit}_\text{m}]\cdot[\text{NADP}^+] - \frac{[\alpha\text{KG}_\text{m}]\cdot[\text{NADPH}]}{K_{\text{eq}}}\right)}{\left[K_{\text{Isocit}_\text{m}}\left(1+\frac{[\alpha\text{KG}_\text{m}]}{K_{\alpha\text{KG}_\text{m}}}\right)+[\text{Isocit}_\text{m}]\right]\left[K_{\text{NADP}^+}\left(1+\frac{[\text{NADPH}]}{K_{\text{NADPH}}}\right)+[\text{NADP}^+]\right]} \quad \text{(B.16)}$$

B.7 α-Ketoglutarate Dehydrogenase

α-ketoglutarate dehydrogenase (α-KGDH) catalyses the following net reaction:

$$\alpha\text{-ketoglutarate} + \text{NAD}^+_\text{m} + \text{CoA}_\text{m} + \text{H}_2\text{O} \longrightarrow \text{Succinyl-CoA} + \text{NADH}_\text{m} + \text{CO}_2 \quad \text{(B.17)}$$

Given the magnitude of the equilibrium constant for the forward reaction (K_{eq} = 1.72E+07 at pH 8.0; Alberty 2003b), this step is treated as irreversible.

α-KGDH is activated by both ADP and Ca^{2+}, which independently reduce the apparent K_m for α-ketoglutarate without affecting the maximal rate (McCormack and Denton, 1979). Conversely, ATP inhibits the enzyme, increasing the apparent K_m for α-ketoglutarate (McCormack and Denton, 1979). The effects of ADP and ATP were determined in the presence of Mg^{2+} (McCormack and Denton, 1979). Product inhibition by succinyl-CoA is competitive with respect to CoA_m. Inhibition by NADH_m was originally described as non-competitive (Smith et al., 1974), but has been treated as competitive in other TCA cycle models (Bazil et al., 2010; Wu et al., 2007). In fact, latest analysis of the original data (Smith et al., 1974), indicates that competition by NADH_m is mixed with respect to both α-ketoglutarate and NAD^+_m, although competition between NAD^+_m and NADH_m is the more important component of the inhibition.

α-KGDH kinetics are modelled using an irreversible, modified form of the generic rate equation that takes into account activation by ADP and Ca^{2+}, competitive inhibition by ATP and succinyl-CoA, and mixed inhibition by NADH_m with respect to NAD^+_m.

$$\nu_{\alpha\mathrm{KGDH}} = \frac{1}{\left[\left\{\dfrac{K_{\alpha\mathrm{KG_m}}\left(1+\dfrac{[\mathrm{ATP_m}]}{K_{\mathrm{ATP_m}}}\right)}{\left(1+\dfrac{[\mathrm{ADP_m}]}{K_{\mathrm{ADP_m}}}\right)\left(1+\dfrac{[\mathrm{Ca^{2+}}]}{K_{\mathrm{Ca^{2+}}}}\right)}\right\}+[\alpha\mathrm{KG_m}]\right]}$$

$$\times \frac{\left\{V_{\alpha\mathrm{KGDH}}\Big/\left(1+\dfrac{[\mathrm{NADH_m}]}{K_{\mathrm{NADH_{m,\,u}}}}\right)\right\}\cdot\left([\alpha\mathrm{KG_m}]\cdot\left[\mathrm{NAD^+_m}\right]\cdot[\mathrm{CoA_m}]\right)}{\left[\left\{\dfrac{K_{\mathrm{NAD^+_m}}\left(1+\dfrac{[\mathrm{NADH_m}]}{K_{\mathrm{NADH_{m,\,c}}}}\right)}{\left(1+\dfrac{[\mathrm{NADH_m}]}{K_{\mathrm{NADH_{m,\,u}}}}\right)}\right\}+\left[\mathrm{NAD^+_m}\right]\right]\left[K_{\mathrm{CoA_m}}\left(1+\dfrac{[\mathrm{CoA_m}]}{K_{\mathrm{SCoA_m}}}\right)+[\mathrm{CoA_m}]\right]} \tag{B.18}$$

B.8 Succinyl-CoA Synthetase

Succinyl-CoA synthetase (SCS) catalyses the following net reaction:

$$\text{Succinyl-CoA} + \text{GDP} + \mathrm{Pi_m} \rightleftharpoons \text{Succinate} + \mathrm{CoA_m} + \text{GTP} \tag{B.19}$$

SCS kinetics are represented by an extended version of the generic rate equation. Competitive binding between GTP and Pi has been reported (Cha and Parks, 1964), and this is represented in addition to product inhibition by succinate and $\mathrm{CoA_m}$. Since the apparent equilibrium constant for the interconversion of adenine and guanine nucleotides is likely to be close to unity (Alberty, 2003b), ADP and ATP are substituted for GDP and GTP in the expression.

$$\nu_{\mathrm{SCS}} = \frac{1}{\left[\left\{K_{\mathrm{SCoA_m}}\left(1+\dfrac{[\mathrm{Suc_m}]}{K_{\mathrm{Suc_m}}}\right)\left(1+\dfrac{[\mathrm{CoA_m}]}{K_{\mathrm{CoA_m}}}\right)\right\}+[\mathrm{SCoA_m}]\right]}$$

$$\times \frac{V_{\mathrm{SCS}}\left([\mathrm{SCoA_m}]\cdot[\mathrm{ADP_m}]\cdot[\mathrm{Pi_m}]-\dfrac{[\mathrm{Suc_m}]\cdot[\mathrm{CoA_m}]\cdot[\mathrm{ATP_m}]}{K_{\mathrm{eq}}}\right)}{\left[\left(K_{\mathrm{ADP_m}}\cdot K_{\mathrm{Pi_m}}\right)\left\{\left(1+\dfrac{[\mathrm{ADP_m}]}{K_{\mathrm{ADP_m}}}\right)\left(1+\dfrac{[\mathrm{Pi_m}]}{K_{\mathrm{Pi_m}}}\right)+\left(\dfrac{[\mathrm{ATP_m}]}{K_{\mathrm{ATP_m}}}\right)\right\}\right]} \tag{B.20}$$

B.9 Succinate Dehydrogenase

Succinate dehydrogenase (SDH) catalyses the following net reaction:

$$\text{Succinate} \quad + \quad \text{Q} \quad \rightleftharpoons \quad \text{Fumarate} \quad + \quad \text{QH}_2 \tag{B.21}$$

The generic rate equation is used to model SDH kinetics. In addition to being subject to product inhibition by fumarate and QH_2, the reaction is inhibited by oxaloacetate, which is competitive with respect to succinate (Hatefi and Stiggall, 1976).

$$\begin{aligned} \nu_{\text{SDH}} \quad = \quad & \frac{1}{\left[K_{\text{Q}} \left(1 + \frac{\left[\text{QH}_2 \right]}{K_{\text{QH}_2}} \right) + \left[\text{Q} \right] \right]} \\ & \times \frac{V_{\text{SDH}} \left(\left[\text{Suc}_\text{m} \right] \cdot \left[\text{Q} \right] - \frac{\left[\text{Fum}_\text{m} \right] \cdot \left[\text{QH}_2 \right]}{K_{\text{eq}}} \right)}{\left[K_{\text{Suc}_\text{m}} \left(1 + \frac{\left[\text{OAA}_\text{m} \right]}{K_{\text{OAA}_\text{m}}} + \frac{\left[\text{Fum}_\text{m} \right]}{K_{\text{Fum}_\text{m}}} \right) + \left[\text{Suc}_\text{m} \right] \right]} \end{aligned} \tag{B.22}$$

B.10 Fumarase

Fumarate hydratase (FM) catalyses the following net reaction:

$$\text{Fumarate} \quad \rightleftharpoons \quad \text{Malate} \tag{B.23}$$

The rate equation used is a reversible uni-uni rate law (Segel, 1993), with product inhibition by malate.

$$\nu_{\text{FM}} \quad = \quad \frac{V_{\text{FM}} \left(\left[\text{Fum}_\text{m} \right] - \frac{\left[\text{Mal}_\text{m} \right]}{K_{\text{eq}}} \right)}{K_{\text{Fum}_\text{m}} \left(1 + \frac{\left[\text{Mal}_\text{m} \right]}{K_{\text{Mal}_\text{m}}} \right) + \left[\text{Fum}_\text{m} \right]} \tag{B.24}$$

B.11 Malate Dehydrogenase

Mitochondrial malate dehydrogenase (MDH) catalyses the following net reaction:

$$\text{Malate} \quad + \quad \text{NAD}^+_\text{m} \quad \rightleftharpoons \quad \text{Oxaloacetate} \quad + \quad \text{NADH}_\text{m} \tag{B.25}$$

The standard generic rate equation is used for this step, with product inhibition by oxaloacetate and NADH_m.

$$\begin{aligned} \nu_\text{MDH} \;=\; & \frac{1}{\left[K_{\text{Mal}_\text{m}}\left(1+\frac{[\text{OAA}_\text{m}]}{K_{\text{OAA}_\text{m}}}\right)+[\text{Mal}_\text{m}]\right]} \\ & \times \frac{V_\text{MDH}\left([\text{Mal}_\text{m}]\cdot\left[\text{NAD}^+_\text{m}\right]-\frac{[\text{OAA}_\text{m}]\cdot[\text{NADH}_\text{m}]}{K_\text{eq}}\right)}{\left[K_{\text{NAD}^+_\text{m}}\left(1+\frac{[\text{NADH}_\text{m}]}{K_{\text{NADH}_\text{m}}}\right)+\left[\text{NAD}^+_\text{m}\right]\right]} \end{aligned} \tag{B.26}$$

B.12 Adenine-Nucleotide Translocase

The adenine-nucleotide translocase (ANT) is an ATP/ ADP co-transporter that exchanges endogenous and exogenous ionized adenine nucleotides across the inner mitochondrial membrane:

$$\text{ATP}^{4-}_\text{m} \quad + \quad \text{ADP}^{3-}_\text{c} \quad \longleftrightarrow \quad \text{ATP}^{4-}_\text{c} \quad + \quad \text{ADP}^{3-}_\text{m} \tag{B.27}$$

The standard generic rate equation is used for this step.

$$\begin{aligned} \nu_\text{ANT} \;=\; & \frac{1}{\left[K_{\text{ADP}^{3-}_\text{c}}\left(1+\frac{\left[\text{ATP}^{4-}_\text{c}\right]}{K_{\text{ATP}^{4-}_\text{c}}}\right)+\left[\text{ADP}^{3-}_\text{c}\right]\right]} \\ & \times \frac{V_\text{ANT}\left(\left[\text{ATP}^{4-}_\text{m}\right]\cdot\left[\text{ADP}^{3-}_\text{c}\right]-\frac{\left[\text{ADP}^{3-}_\text{m}\right]\cdot\left[\text{ATP}^{4-}_\text{c}\right]}{K_\text{eq}}\right)}{\left[K_{\text{ATP}^{4-}_\text{m}}\left(1+\frac{\left[\text{ADP}^{3-}_\text{m}\right]}{K_{\text{ADP}^{3-}_\text{m}}}\right)+\left[\text{ATP}^{4-}_\text{m}\right]\right]} \end{aligned} \tag{B.28}$$

Where,

$$\left[\mathrm{ATP}_\mathrm{m}^{4-}\right] = f_{\mathrm{ATP}_\mathrm{m}^{4-}} \cdot \left[\mathrm{ATP}_\mathrm{m}\right] \tag{B.29}$$

$$\left[\mathrm{ADP}_\mathrm{m}^{3-}\right] = f_{\mathrm{ADP}_\mathrm{m}^{3-}} \cdot \left[\mathrm{ADP}_\mathrm{m}\right] \tag{B.30}$$

$$\left[\mathrm{ATP}_\mathrm{c}^{4-}\right] = f_{\mathrm{ATP}_\mathrm{c}^{4-}} \cdot \left[\mathrm{ATP}_\mathrm{c}\right] \tag{B.31}$$

$$\left[\mathrm{ADP}_\mathrm{c}^{3-}\right] = f_{\mathrm{ADP}_\mathrm{c}^{3-}} \cdot \left[\mathrm{ADP}_\mathrm{c}\right] \tag{B.32}$$

The conversion factors $f_{\mathrm{ATP}_\mathrm{m}^{4-}}$, $f_{\mathrm{ADP}_\mathrm{m}^{3-}}$, $f_{\mathrm{ATP}_\mathrm{c}^{4-}}$ and $f_{\mathrm{ADP}_\mathrm{c}^{3-}}$ give the fractions of the respective total adenine nucleotides that are ionized (Magnus and Keizer, 1997), and are defined in the supplementary material (see tbl. I.2 on pg. III).

B.13 Malate-Phosphate Exchange

The malate carrier (malate-phosphate transporter) (MC) exchanges endogenous and exogenous malate and inorganic phosphate (Pi) across the inner mitochondrial membrane:

$$\mathrm{Mal_m} \quad + \quad \mathrm{Pi_c} \quad \longleftrightarrow \quad \mathrm{Mal_c} \quad + \quad \mathrm{Pi_m} \tag{B.33}$$

The standard generic rate equation is used for this step.

$$\nu_\mathrm{MC} = \frac{V_\mathrm{MC}\left(\left[\mathrm{Mal_m}\right]\cdot\left[\mathrm{Pi_c}\right] - \dfrac{\left[\mathrm{Pi_m}\right]\cdot\left[\mathrm{Mal_c}\right]}{K_\mathrm{eq}}\right)}{\left[K_{\mathrm{Mal_m}}\left(1 + \dfrac{\left[\mathrm{Pi_m}\right]}{K_{\mathrm{Pi_m}}}\right) + \left[\mathrm{Mal_m}\right]\right]\left[K_{\mathrm{Pi_c}}\left(1 + \dfrac{\left[\mathrm{Mal_c}\right]}{K_{\mathrm{Mal_c}}}\right) + \left[\mathrm{Pi_c}\right]\right]} \tag{B.34}$$

B.14 ATP Synthesis

ATP synthesis is represented as a simple, single-step process that converts $\mathrm{NADH_m}$ generated via the TCA cycle to ATP:

$$10\ \mathrm{ADP_m} \quad + \quad 10\ \mathrm{Pi_m} \quad + \quad 4\ \mathrm{NADH_m} \quad \longrightarrow \quad 10\ \mathrm{ATP_m} \quad + \quad 4\ \mathrm{NAD_m^+} \tag{B.35}$$

The stoichiometry of the process reflects the total number of protons used in the generation of one molecule of ATP; *i.e.* by both ATP synthase and Pi import into the matrix. The process is assumed to be saturable and irreversible, and hence is modelled with an extended, irreversible form of the generic rate equation.

$$\nu_{\mathrm{ATP_{synth}}} = \frac{1}{\left[K_{\mathrm{NADH_m}} \left(1 + \frac{\left[\mathrm{NAD^+_m}\right]}{K_{\mathrm{NAD^+_m}}} \right) + \left[\mathrm{NADH_m}\right] \right]}$$

$$\times \frac{V_{\mathrm{ATP_{synth}}} \left(\left[\mathrm{NADH_m}\right] \cdot \left[\mathrm{ADP_m}\right] \cdot \left[\mathrm{Pi_m}\right] \right)}{\left[\left(K_{\mathrm{ADP_m}} \cdot K_{\mathrm{Pi_m}} \right) \left\{ \left(1 + \frac{\left[\mathrm{ADP_m}\right]}{K_{\mathrm{ADP_m}}} \right) \left(1 + \frac{\left[\mathrm{Pi_m}\right]}{K_{\mathrm{Pi_m}}} \right) + \left(\frac{\left[\mathrm{ATP_m}\right]}{K_{\mathrm{ATP_m}}} \right) \right\} \right]} \tag{B.36}$$

B.15 ATP Hydrolysis

Cytosolic ATP demand is modelled as a simple first-order flux:

$$\mathrm{ATP_c} \longrightarrow \mathrm{ADP_c} + \mathrm{Pi_c} \tag{B.37}$$

$$\nu_{\mathrm{ATP_{hyd}}} = f_{\mathrm{ATP_{hyd}}} \cdot \left[\mathrm{ATP_c^{4-}}\right] \tag{B.38}$$

Appendix C: The updated liver TCA cycle model in ScrumPy format

- **Listing C.1.** ScrumPy code for the updated liver TCA cycle model.

```
                    ####  All metabolites are in mM ####

               ####  External metabolites (Model Parameters) ####

    x_CO2 = 1.63   x_Pyr = 0.2   x_Q = 0.24   x_QH2 = 0.27   x_NADPH = 1.85
    x_Ca2p = 0.006     x_NADP = 0.31     x_HCO3 = 21.2     x_Malc = 0.47
    x_Mg2p = 0.37     x_Pim = 8.9     x_Pic = 4.2

                 #### Conserved totals (Model Parameters) ####

    N_Tot = 2.1     Adn_Totm = 10.4     Adn_Totc = 4.81     CoA_Tot = 2.7

               ####  Internal metabolites (Model Variables)  ####

    AcCoA = 0.33   Cit = 4.42   OAA = 0.00041   IsoCit = 0.28   aKG = 1.57
    Suc = 1.59   Fum = 0.35   Malm = 1.43   ATPm = 7.53   NADH = N_Tot - NAD
    NAD = 1.28     ATPc = 4.761     SCoA = 0.48     ADPm = Adn_Totm - ATPm
    CoA = CoA_Tot - (AcCoA + SCoA)     ADPc = Adn_Totc - ATPc

                       ####  TCA Cycle Reactions ####

                    ####  Pyruvate Dehydrogenase (PDH)  ####
PDH:

    x_Pyr + NAD + CoA -> x_CO2 + NADH + AcCoA

    (V_PDH * x_Pyr * NAD * CoA)/((K_PDH_Pyr + x_Pyr) * (K_PDH_NAD * (1 +
    NADH/K_PDH_NADH) + NAD) * (K_PDH_CoA * (1 + AcCoA/K_PDH_AcCoA) + CoA))

    V_PDH=0.648     K_PDH_Pyr=0.01     K_PDH_NAD=0.064     K_PDH_CoA = 0.012
    K_PDH_NADH=0.044     K_PDH_AcCoA=0.029

                       ####  Citrate synthase (CS) ####
CS:

    OAA + AcCoA <> Cit + CoA

    (V_CS * ((OAA * AcCoA) - ((Cit * CoA)/Keq_CS)))/ ((K_CS_OAA * (1 + Cit
    /K_CS_Cit) + OAA) * ((K_CS_AcCoA *(1 + (SCoA/K_CS_SCoA)
    + (ATPm/K_CS_ATPm) + (CoA/K_CS_CoA)))+ AcCoA))

    V_CS=13.75     Keq_CS=1.13e+09     K_CS_OAA=0.002     K_CS_Cit=1.6
    K_CS_AcCoA=0.016     K_CS_SCoA=0.14     K_CS_ATPm=0.55     K_CS_CoA=0.067

                           ####  Aconitase (ACO) ####
ACO:

    Cit <> IsoCit

    (V_ACO*(Cit-(IsoCit/Keq_ACO)))/((K_ACO_Cit*(1+IsoCit/K_ACO_IsoCit))+Cit)

    V_ACO=1.674     Keq_ACO=0.0685     K_ACO_Cit=0.62     K_ACO_IsoCit=0.2
```

```
            ####  NAD+-dependent Isocitrate Dehydrogenase (IDHa)  ####
IDHa:

    IsoCit + NAD -> aKG + NADH + x_CO2

    (V_IDHa*(IsoCit**n_IDHa)*NAD)/((((K_IDHa_IsoCit**n_IDHa)/((1+(ADPm
    *f_IDHa_ADPm)/K_IDHa_ADPm)*(1 + x_Ca2p/K_IDHa_Ca2p)))+(IsoCit**n_IDHa))
    *((K_IDHa_NAD*(1+(ATPm/K_IDHa_ATPm)+(NADH /K_IDHa_NADH)))+NAD))

    V_IDHa=1.58     n_IDHa=1     K_IDHa_IsoCit=0.56     f_IDHa_ADPm=0.818
    K_IDHa_ADPm=0.05     K_IDHa_Ca2p=0.00112     K_IDHa_NAD=0.07
    K_IDHa_ATPm=0.118     K_IDHa_NADH=0.029

            ####  NADP+-dependent Isocitrate Dehydrogenase (IDHb) ####
IDHb:

    IsoCit + x_NADP <> aKG + x_NADPH + x_CO2

    (V_IDHb * ((IsoCit * x_NADP) - (aKG * x_NADPH/Keq_IDHb)))
    /(((K_IDHb_IsoCit * (1 + aKG/K_IDHb_aKG)) + IsoCit) * ((K_IDHb_NADP
    * (1 + x_NADPH/K_IDHb_NADPH)) + x_NADP) * (1 + x_CO2/K_IDHb_CO2))

    V_IDHb=5.4188     Keq_IDHb=43.8     K_IDHb_CO2=3.8     K_IDHb_aKG=0.44
    K_IDHb_NADP=0.0056     K_IDHb_NADPH=0.0056     K_IDHb_IsoCit=0.0084

              ####  alpha-Ketoglutarate Dehydrogenase (aKGDH) ####
aKGDH:

    aKG + NAD + CoA -> x_CO2 + NADH + SCoA

    ((V_aKGDH * aKG * NAD * CoA)/(1 + NADH/K_NADH_u))/((((K_aKGDH_aKG
    * (1 + ATPm/K_aKGDH_ATPm))/((1 + ADPm/K_aKGDH_ADPm) * (1 + x_Ca2p
    /K_aKGDH_Ca2p))) + aKG) * (((K_aKGDH_NAD * (1 + NADH/K_NADH_c))/(1 +
    NADH/K_NADH_u)) + NAD) * ((K_aKGDH_CoA * (1 + SCoA/K_aKGDH_SCoA)) + CoA))

    V_aKGDH=27     K_NADH_u=0.0258     K_aKGDH_aKG=0.126     K_aKGDH_ADPm=0.1
    K_aKGDH_Ca2p=0.0012     K_aKGDH_ATPm=0.1     K_aKGDH_NAD=0.01932
    K_NADH_c=0.00354     K_aKGDH_CoA=0.025     K_aKGDH_SCoA=0.0069

                    ####  Succinyl-CoA synthetase (SCS) ####
SCS:

    SCoA + ADPm + x_Pim <> Suc + CoA + ATPm

    (V_SCS*((SCoA*ADPm*x_Pim)-((Suc*CoA*ATPm)/Keq_SCS)))/(((K_SCS_SCoA*(1+
    Suc/K_SCS_Suc)*(1+CoA/K_SCS_CoA))+SCoA)*(K_SCS_ADPm*K_SCS_Pim)*(((1+
    ADPm/K_SCS_ADPm)*(1+x_Pim/K_SCS_Pim))+(ATPm/K_SCS_ATPm)))

    V_SCS=4.2     Keq_SCS=1.3     K_SCS_SCoA=0.011     K_SCS_Suc=70
    K_SCS_CoA=0.02     K_SCS_ADPm=0.002     K_SCS_Pim=0.15     K_SCS_ATPm=0.005

                    ####  Succinate Dehydrogenase (SDH) ####
SDH:

    Suc + x_Q <> Fum + x_QH2

    (V_SDH*((Suc*x_Q)-((Fum*x_QH2)/Keq_SDH)))/((K_SDH_Suc*(1+(OAA/K_SDH_OAA)
    +(Fum/K_SDH_Fum))+Suc)*((K_SDH_Q*(1+x_QH2/K_SDH_QH2))+x_Q))

    V_SDH=0.48     Keq_SDH=1.01     K_SDH_Suc=0.13     K_SDH_OAA=0.0015
    K_SDH_Fum=1.3     K_SDH_Q=0.0003     K_SDH_QH2=0.0015

####
```

```
                              ####  Fumarase (FM) ####
FM:

    Fum <> Malm

    (V_FM * (Fum - Malm/Keq_FM))/((K_FM_Fum * (1 + Malm/K_FM_Malm)) + Fum)

    V_FM=7.696     Keq_FM=4.34     K_FM_Fum=0.015     K_FM_Malm=0.18

                     ####  Malate Dehydrogenase (MDH)  ####
MDH:

    Malm + NAD <> OAA + NADH

    (V_MDH * ((Malm * NAD) - ((OAA * NADH)/Keq_MDH)))/(((K_MDH_Malm * (1 +
    OAA/K_MDH_OAA)) + Malm) * ((K_MDH_NAD * (1 + NADH/K_MDH_NADH)) + NAD))

    V_MDH=26.752     Keq_MDH=0.000125     K_MDH_Malm=1.1     K_MDH_NAD=0.114
    K_MDH_OAA=0.0055     K_MDH_NADH=0.005

                       ####  ATP synthesis (ATPsynth)  ####
ATPsynth:

    4 NADH + 10 ADPm + 10 x_Pim -> 4 NAD + 10 ATPm

    (V_ATPsynth * NADH * ADPm * x_Pim)/(((K_ATPsynth_NADH * (1 + NAD
    /K_ATPsynth_NAD)) + NADH) * (K_ATPsynth_ADPm * K_ATPsynth_Pim) * (((1 +
    ADPm/K_ATPsynth_ADPm)*(1+x_Pim/K_ATPsynth_Pim))+(ATPm/K_ATPsynth_ATPm)))

    V_ATPsynth=0.886637     K_ATPsynth_NADH=0.88     K_ATPsynth_NAD=1.2
    K_ATPsynth_ADPm=3.1     K_ATPsynth_Pim=8.9     K_ATPsynth_ATPm=7.3

                ####  Adenine Nucleotide Translocase (ANT)  ####
ANT:

    ATPm + ADPc <> ADPm + ATPc

    (V_ANT*((f_ANT_ATPm*ATPm*f_ANT_ADPc*ADPc)-((f_ANT_ATPm*ADPm*f_ANT_ATPc
    *ATPc)/Keq_ANT)))/(((K_ANT_ATPm*(1+((f_ANT_ADPm*ADPm)/K_ANT_ADPm)))
    +(f_ANT_ATPm*ATPm))*((K_ANT_ADPc*(1+((f_ANT_ATPc * ATPc)/K_ANT_ATPc)))
    +(f_ANT_ADPc * ADPc)))

    V_ANT=1.52646     f_ANT_ATPm=0.0526     f_ANT_ADPc=0.45     Keq_ANT=118
    f_ANT_ADPm=0.818     f_ANT_ATPc=0.05     K_ANT_ATPm=0.03     K_ANT_ADPm=0.02
    K_ANT_ADPc=0.02     K_ANT_ATPc=0.03

                       ####  ATP Hydrolysis (ATPhyd) ####
ATPhyd:

    ATPc -> ADPc + x_Pic

    V_ATPhyd * ATPc

    V_ATPhyd = 0.00769203

          ####  Malate-Phosphate transporter (Malate Carrier) (MC)  ####
MC:

    Malm + x_Pic <> x_Pim + x_Malc

    (V_MC * ((Malm * x_Pic) - ((x_Pim * x_Malc)/Keq_MC)))/(((K_MC_Malm * (1 +
    x_Pim/K_MC_Pim)) + Malm) * ((K_MC_Pic * (1 + x_Malc/K_MC_Malc)) + x_Pic))

    V_MC=23.2574     Keq_MC=1.52     K_MC_Malm=0.9     K_MC_Pim=0.72
    K_MC_Pic=0.76     K_MC_Malc=0.2
```

```
                    ####  Pyruvate Carboxylase (PC) ####
PC:

    x_Pyr + x_HCO3 + ATPm <> OAA + ADPm + x_Pim

    V_coeff*((Vmin_PC+(Vmax_PC-Vmin_PC)*(AcCoA**n_PC/(Km_AcCoA_PC + AcCoA)
    **n_PC)*(x_Mg2p/(x_Mg2p+Km_Mg2p_PC)))   #---- (see, [1] given below)
    *((x_Pyr*x_HCO3*ATPm)-((OAA*ADPm*x_Pim)/Keq_PC))/((K_PC_Pyr*K_PC_HCO3)
    *(((1+x_Pyr/K_PC_Pyr)*(1+x_HCO3/K_PC_HCO3))+(OAA/K_PC_OAA))
    *((K_PC_ATPm*(1+ADPm/K_PC_ADPm)*(1+x_Pim/K_PC_Pim))+ATPm)))

    n_PC=2    Keq_PC=10.98    K_PC_Pyr=0.14    K_PC_HCO3=3    K_PC_OAA=0.1
    K_PC_ATPm=0.134    K_PC_ADPm=0.35    K_PC_Pim=6     Vmin_PC=1.02
    Vmax_PC=Vmin_PC*5     Km_AcCoA_PC=0.06     Km_Mg2p_PC=0.5    V_coeff=1.0

# 'V_coeff' is only a rate multiplication factor, as it multiplies the entire
# rate equation by 1. For analyses, to change the maximal rate of PC, the
# user must vary the value of 'V_coeff' within a permissible range.

########

# A function that dynamically calculates the value of 'Vapp_PC' at model
# simulation

#    Vmin_PC+(Vmax_PC-Vmin_PC)*(AcCoA**n_PC/(Km_AcCoA_PC+AcCoA)**n_PC)
#    *(x_Mg2p/(x_Mg2p+Km_Mg2p_PC)) = Vapp_PC                  #--------- [1]

#    Vmin_PC = 1.02

#    Vmax_PC = Vmin_PC * 5

#    Vm_AcCoA = (AcCoA**n_PC) / ((Km_AcCoA_PC + AcCoA)**n_PC)

#    Vm_Mg2p = (x_Mg2p) /(x_Mg2p + Km_Mg2p_PC)

#    Km_AcCoA_PC = 0.06
#    Km_Mg2p_PC = 0.5

#    Vapp_PC = 1.02 +(4.08 * (AcCoA**2 / (Km_AcCoA_PC + AcCoA)**2)
#   * (x_Mg2p /(x_Mg2p + Km_Mg2p_PC)))

########
```

Appendix D: A *Python* function to compute the overall variability in the apparent maximal activity of PC (V_{app}^{PC})

As discussed earlier on pg. 28, in order to produce a single dataset/ plot comprising all possible variations of the V_{app}^{PC} value, we designed a specifically-modified *Python* function. It can compute the value of V_{app}^{PC} within a given range of enzyme activity/ metabolite concentration, between two fixed points (a *'low'* & a *'high'* point) that are *'X'* multiples of the original activity/ concentration; and it performs separate simulations for every key enzyme or metabolite.

Therefore in this function, for every key enzyme or metabolite, its maximal activity/ metabolite concentration was changed from $1/5^{th}$ (0.2X) the initial model value (X) to 5–times the initial model value (5X). For example, in the liver TCA cycle model, the initial model value of PDH maximal activity is 0.65 mM/sec (X). So, using this method, PDH maximal activity was changed ranging from 0.13 (0.2X) to 3.25 mM/sec (5X). Thus, in a separate simulation for every key enzyme or metabolite, the value of V_{app}^{PC} was computed against increasing enzyme activity/ metabolite concentration that ranged between 0.2X and 5X. When the data from each simulation was combined in a common dataset, a *'dummy range'* from 1 to 50 arbitrary units was created specifically for plotting purposes; thereby creating a dataset that contained a single column of the *dummy range* and a column each for the computed V_{app}^{PC} values against key TCA cycle enzyme activities/ metabolite concentrations.

Therefore, if we assume a dataset with 50 rows (i_0 *to* i_{49}) & 4 columns (j_0 *to* j_3) :

- j_0 **:** a column for *'dummy range'* (*X-axis*)
- j_1 **:** a column for V_{app}^{PC} values against PDH maximal activity (*Y-axis*)
- j_2 **:** a column for V_{app}^{PC} values against ATPsynth maximal activity (*Y-axis*)
- j_3 **:** a column for V_{app}^{PC} values against some other key enzyme activity (*Y-axis*)

Then in this dataset,

- $\boldsymbol{i_0 j_0}$ **:** a point on X-axis at enzyme activity = 0.2X (= 1 in arbitrary units)

  (where, $V_{max}^{PDH} = 0.13$ mM/sec or $V_{max}^{ATP_{synth}} = 0.18$ mM/sec)

- $\boldsymbol{i_{49} j_0}$ **:** a point on X-axis at enzyme activity = 5X (= 50 in arbitrary units)

  (where, $V_{max}^{PDH} = 3.25$ mM/sec or $V_{max}^{ATP_{synth}} = 4.5$ mM/sec)

Also,

- $\boldsymbol{i_0 j_1}$ **:** a point on Y-axis representing the value of V_{app}^{PC} computed at,

  $V_{max}^{PDH} = 0.2X = 0.2 \times 0.65 = 0.13$ mM/sec

- $\boldsymbol{i_{49} j_1}$ **:** a point on Y-axis representing the value of V_{app}^{PC} computed at,

  $V_{max}^{PDH} = 5X = 5 \times 0.65 = 3.25$ mM/sec

Similarly, $\boldsymbol{i_0 j_2}$ & $\boldsymbol{i_{49} j_2}$ can be explained *w.r.t.* $V_{max}^{ATP_{synth}}$ and $\boldsymbol{i_0 j_3}$ & $\boldsymbol{i_{49} j_3}$ can be explained *w.r.t.* some other key enzyme activity/ metabolite concentration.

Thus, in a single plot, we were able to combine all computed variations in the apparent maximal activity of PC against change in key TCA cycle enzyme activities/ metabolite concentrations.

Listing D.1 shows the original code for this function implemented in Python.

- **Listing D.1.** A Python code for computing the V_{app}^{PC} variability.

```
from Data import DataSets# Map parameter names to the initial model values

InitVals = {"V_PDH":(0.65),"V_aKGDH":(27),"x_Pyr":(0.2),"x_Mg2p":(0.37)}

def StepScan(m, axis=InitVals, PName="V_PDH", Model=
          "_PCwt_LVRv6", Xval=5, nP=100, Tincr=100, SimT=500, Tolr=1.0E-07):

    nSt = nP-1          # Number of divisions to be made of the given range
    m.SSTol = Tolr      # Set the steady-state tolerance level

    InitState = m.GetState()      # Fetch initial state in 'InitState'

    m.Simulate(Tincr,SimT)        # Time-simulation.
    m.FindSS()                    # Steady-state search
    m.IsOK()                      # Check the steady-state validity
    ssState = m.GetState()        # Fetch initial steady-state in 'ssState'
```

```
18      m.SetFromState(InitState)     # Load the values stored in 'InitState'

20      Pini = axis.get(PName)        # Fetch "init" value for selected parameter
21      Plow = Pini/Xval              # Calc. "low" value for selected parameter
22      Phi = Pini*Xval               # Calc. "high" value for selected parameter
23      incr = (Phi - Plow)/nSt       # Calculate the increment size

25      print "Scanning x-axis: ", PName, "with : Xlow at - ", Plow,
26            " and Xhi at - ", Phi, "\n"

28      ds = m.NewDataSet(UpdateIfNotOK="Zero")     # Define a new, empty dataset
29      tmp = DataSets.DataSet()      # Define another empty dataset.
30      dout = []                     # A list to store "VappPC" values

32      m.SetFromState(ssState)       # Load the values stored in 'ssState'
33      Pstart = Plow - incr
34      m[PName] = Pstart             # Re-initiate the parameter's value

36      print "Starting the scan from Steady state. \n"
37      print "Initialized the model value of ", PName, " at ", Pstart, "\n"

39      FILE = PName + "_VappPCvalScn_LowHiXval_" + str(Xval) + "_Frm_" +
40      str(Plow) + "_To_" + str(Phi) + Model + ".txt"

42      for n in range(nP):                 # Start the "for-loop"
43          m[PName] += incr                # Increment the value of PName
44          m.FindSS()                      # Steady-state search
45          if not m.IsOK():                # If "valid" SS = false, pre-simulate
46              m.Simulate(Tincr, SimT)     # Pre-simulation to help find SS
47              m.FindSS()                  # Steady-state search
48          if m.IsOK():                    #  If "valid" SS = true:

50              Vapp_PC = m["Vmin_PC"] +(m["Vmax_PC"] - m["Vmin_PC"])
51              * (m["AcCoA"]**m["n_PC"] / (m["Km_AcCoA_PC"] + m["AcCoA"])
52              **m["n_PC"]) * (m["x_Mg2p"] /(m["x_Mg2p"] + m["Km_Mg2p_PC"]))

54                                  # "VappPC" function as defined in the model

56              dout.append(Vapp_PC)      # Add the calc. "VappPC" value to list
57              ds.Update()               # Update the empty dataset {ds}
58          else:                         # else, do nothing & exit loop

60      ds.MakeFirstCol(PName)            # Manipulate {ds} as needed
61      ds.DelCol(1)

63      tmp.NewCol(ds.GetCol(0), PName)   # Add info. to other dataset from {ds}
64      tmp.NewCol(dout, "Vapp_PC")       # Add the list of "VappPC" values

66      tmp.WriteFile(FILE)               # Save the dataset

68      m.SetFromState(InitState)         # Reload the values from 'InitState'

70      print "Initial state restored with [SetFromState]. \n"
71      print "Data saved in : ", FILE, "\n"
```

Appendix E: Differential and Rate equations: heart TCA cycle model

E.1 Differential equations for the heart TCA cycle model

As mentioned in the heart TCA cycle model chapter, only those Differential equations that are different between the heart & liver-specific TCA cycle models are shown here.

$$\frac{d[\,\mathrm{Isocit_m}\,]}{dt} = \nu_{\mathrm{ACO}} - \nu_{\mathrm{IDHa}} \tag{E.1}$$

$$\frac{d[\,\alpha\mathrm{KG_m}\,]}{dt} = \nu_{\mathrm{IDHa}} - \nu_{\alpha\mathrm{KGDH}} - \nu_{\alpha\mathrm{KG_{exp}}} \tag{E.2}$$

$$\frac{d[\,\mathrm{Mal_m}\,]}{dt} = \nu_{\mathrm{FM}} - \nu_{\mathrm{MDH}} \tag{E.3}$$

$$\frac{d[\,\mathrm{OAA_m}\,]}{dt} = \nu_{\mathrm{MDH}} - \nu_{\mathrm{CS}} \tag{E.4}$$

$$\frac{d[\,\mathrm{ATP_m}\,]}{dt} = 10 \cdot \nu_{\mathrm{ATP_{synth}}} + \nu_{\mathrm{SCS}} - \nu_{\mathrm{ANT}} \tag{E.5}$$

E.2 Rate equations for the heart TCA cycle model

As mentioned in the heart TCA cycle model chapter, details for only the newly added α-ketoglutarate transporter reaction (α-$\mathrm{KG_{exp}}$) are shown here.

E.2.1 α-ketoglutarate transporter

α-ketoglutarate transporter (α-$\mathrm{KG_{exp}}$) catalyses the following net reaction:

$$\alpha\mathrm{KG_m} \rightleftharpoons \alpha\mathrm{KG_c} \tag{E.6}$$

A reversible uni-uni rate law (Segel, 1993) is used to represent this step.

$$\nu_{\alpha\mathrm{KG_{exp}}} = V_{\alpha\mathrm{KG_{exp}}} \left(\left[\alpha\mathrm{KG_m}\right] - \frac{\left[\alpha\mathrm{KG_c}\right]}{K_{\mathrm{eq}}} \right) \tag{E.7}$$

Appendix F: The heart TCA cycle model in ScrumPy format

- **Listing F.1.** ScrumPy code for the heart TCA cycle model.

```
                    ####  All metabolites are in mM ####

               ####  External metabolites (Model Parameters) ####

     x_CO2 = 1.63   x_Pyr = 0.2   x_Q = 0.24   x_QH2 = 0.27   x_Ca2p = 0.006
     x_aKGc = 0.006     x_Pim = 8.9     x_Pic = 4.2

               ####  Internal metabolites (Model Variables)  ####

     AcCoA = 0.12947   Cit = 1.01379   OAAm = 0.034   IsoCit = 0.067586
     Suc = 1.3   Fum = 0.026   Malm = 1.88   ATPm = 7.53   NADHm = 0.129
     aKGm = 0.34 NADm = 0.56     ATPc = 4.761     SCoA = 0.066
     CoA = 0.0535     ADPc = 0.049     ADPm = 2.87

                       ####  TCA Cycle Reactions ####

                    ####  Pyruvate Dehydrogenase (PDH)  ####
PDH:

     x_Pyr + NADm + CoA -> x_CO2 + NADHm + AcCoA

     (V_PDH * x_Pyr * NADm * CoA)/((K_PDH_Pyr + x_Pyr) * (K_PDH_NADm * (1 +
     NADHm/K_PDH_NADHm) + NADm) * (K_PDH_CoA * (1 + AcCoA/K_PDH_AcCoA) + CoA))

     V_PDH=0.1885     K_PDH_Pyr=0.028     K_PDH_NADm=0.0607     K_PDH_CoA =
          0.006
     K_PDH_NADHm=0.044     K_PDH_AcCoA=0.029

                       ####  Citrate synthase (CS) ####
CS:

     OAAm + AcCoA <> Cit + CoA

     (V_CS * ((OAAm * AcCoA) - ((Cit * CoA)/Keq_CS)))/ ((K_CS_OAAm * (1 + Cit
     /K_CS_Cit) + OAAm) * ((K_CS_AcCoA *(1 + (SCoA/K_CS_SCoA)
     + (ATPm/K_CS_ATPm) + (CoA/K_CS_CoA)))+ AcCoA))

     V_CS=2.5433     Keq_CS=1.01e+06     K_CS_OAAm=0.005     K_CS_Cit=1.6
     K_CS_AcCoA=0.005     K_CS_SCoA=0.13     K_CS_ATPm=0.7     K_CS_CoA=0.067

                           ####  Aconitase (ACO) ####
ACO:

     Cit <> IsoCit

     (V_ACO*(Cit-(IsoCit/Keq_ACO)))/((K_ACO_Cit*(1+IsoCit/K_ACO_IsoCit))+Cit)

     V_ACO=2.27     Keq_ACO=0.0685     K_ACO_Cit=0.62     K_ACO_IsoCit=0.2

####
####
```

```
            ####  NAD+-dependent Isocitrate Dehydrogenase (IDHa)  ####
IDHa:

    IsoCit + NADm -> aKGm + NADHm + x_CO2

    (V_IDHa*(IsoCit**n_IDHa)*NADm)/((((K_IDHa_IsoCit**n_IDHa)/((1+(ADPm
    *f_IDHa_ADPm)/K_IDHa_ADPm)*(1 + x_Ca2p/K_IDHa_Ca2p)))+(IsoCit**n_IDHa))
    *((K_IDHa_NADm*(1+(ATPm/K_IDHa_ATPm)+(NADHm /K_IDHa_NADHm)))+NADm))

    V_IDHa=1.371     n_IDHa=2.7     K_IDHa_IsoCit=0.557     f_IDHa_ADPm=0.818
    K_IDHa_ADPm=0.05     K_IDHa_Ca2p=0.00112     K_IDHa_NADm=0.074
    K_IDHa_ATPm=0.091     K_IDHa_NADHm=0.029

            ####  alpha-Ketoglutarate Dehydrogenase (aKGDH) ####
aKGDH:

    aKGm + NADm + CoA -> x_CO2 + NADHm + SCoA

    ((V_aKGDH * aKGm * NADm * CoA)/(1 + NADHm/K_NADHm_u))/((((K_aKGDH_aKGm
    * (1 + ATPm/K_aKGDH_ATPm))/((1 + ADPm/K_aKGDH_ADPm) * (1 + x_Ca2p
    /K_aKGDH_Ca2p))) + aKGm) * (((K_aKGDH_NADm * (1 + NADHm/K_NADHm_c))/(1 +
    NADHm/K_NADHm_u)) + NADm) * ((K_aKGDH_CoA * (1 + SCoA/K_aKGDH_SCoA)) +
         CoA))

    V_aKGDH=7.4426     K_NADHm_u=0.0258     K_aKGDH_aKGm=0.08
         K_aKGDH_ADPm=0.1
    K_aKGDH_Ca2p=0.0012     K_aKGDH_ATPm=0.1     K_aKGDH_NADm=0.01932
    K_NADHm_c=0.00354     K_aKGDH_CoA=0.025     K_aKGDH_SCoA=0.0069

                ####  Succinyl-CoA synthetase (SCS) ####
SCS:

    SCoA + ADPm + x_Pim <> Suc + CoA + ATPm

    (V_SCS*((SCoA*ADPm*x_Pim)-((Suc*CoA*ATPm)/Keq_SCS)))/(((K_SCS_SCoA*(1+
    Suc/K_SCS_Suc)*(1+CoA/K_SCS_CoA))+SCoA)*(K_SCS_ADPm*K_SCS_Pim)*(((1+
    ADPm/K_SCS_ADPm)*(1+x_Pim/K_SCS_Pim))+(ATPm/K_SCS_ATPm)))

    V_SCS=3.1082     Keq_SCS=0.78     K_SCS_SCoA=0.011     K_SCS_Suc=70
    K_SCS_CoA=0.02     K_SCS_ADPm=0.002     K_SCS_Pim=0.15     K_SCS_ATPm=0.005

                ####  Succinate Dehydrogenase (SDH) ####
SDH:

    Suc + x_Q <> Fum + x_QH2

    (V_SDH*((Suc*x_Q)-((Fum*x_QH2)/Keq_SDH)))/((K_SDH_Suc*(1+(OAAm/K_SDH_OAAm
         )
    +(Fum/K_SDH_Fum))+Suc)*((K_SDH_Q*(1+x_QH2/K_SDH_QH2))+x_Q))

    V_SDH=0.4792     Keq_SDH=1.01     K_SDH_Suc=0.13     K_SDH_OAAm=0.0015
    K_SDH_Fum=1.3     K_SDH_Q=0.0003     K_SDH_QH2=0.0015

                        ####  Fumarase (FM) ####
FM:

    Fum <> Malm

    (V_FM * (Fum - Malm/Keq_FM))/((K_FM_Fum * (1 + Malm/K_FM_Malm)) + Fum)

    V_FM=7.9252     Keq_FM=4.34     K_FM_Fum=0.00174     K_FM_Malm=0.00379

####
####
```

```
                    ####  Malate Dehydrogenase (mMDH) ####
mMDH:

    Malm + NADm <> OAAm + NADHm

    (V_mMDH * ((Malm * NADm) - ((OAAm * NADHm)/Keq_mMDH)))/(((K_mMDH_Malm *
         (1 +
    OAAm/K_mMDH_OAAm)) + Malm) * ((K_mMDH_NADm * (1 + NADHm/K_mMDH_NADHm)) +
         NADm))

    V_mMDH=1.0266668     Keq_mMDH=0.000023     K_mMDH_Malm=1.1
         K_mMDH_NADm=0.3
    K_mMDH_OAAm=0.0055     K_mMDH_NADHm=0.005

                    ####  ATP synthesis (ATPsynth)  ####
ATPsynth:

    4 NADHm + 10 ADPm + 10 x_Pim -> 4 NADm + 10 ATPm

    (V_ATPsynth * NADHm * ADPm * x_Pim)/(((K_ATPsynth_NADHm * (1 + NADm
    /K_ATPsynth_NADm)) + NADHm) * (K_ATPsynth_ADPm * K_ATPsynth_Pim) * (((1 +
    ADPm/K_ATPsynth_ADPm)*(1+x_Pim/K_ATPsynth_Pim))+(ATPm/K_ATPsynth_ATPm)))

    V_ATPsynth=0.886637     K_ATPsynth_NADHm=0.88     K_ATPsynth_NADm=1.2
    K_ATPsynth_ADPm=3.1     K_ATPsynth_Pim=8.9     K_ATPsynth_ATPm=7.3

                ####  Adenine Nucleotide Translocase (ANT)  ####
ANT:

    ATPm + ADPc <> ADPm + ATPc

    (V_ANT*((f_ANT_ATPm*ATPm*f_ANT_ADPc*ADPc)-((f_ANT_ATPm*ADPm*f_ANT_ATPc
    *ATPc)/Keq_ANT)))/(((K_ANT_ATPm*(1+((f_ANT_ADPm*ADPm)/K_ANT_ADPm)))
    +(f_ANT_ATPm*ATPm))*((K_ANT_ADPc*(1+((f_ANT_ATPc * ATPc)/K_ANT_ATPc)))
    +(f_ANT_ADPc * ADPc)))

    V_ANT=1.52646     f_ANT_ATPm=0.0526     f_ANT_ADPc=0.45     Keq_ANT=118
    f_ANT_ADPm=0.818     f_ANT_ATPc=0.05     K_ANT_ATPm=0.03     K_ANT_ADPm=0.02
    K_ANT_ADPc=0.02     K_ANT_ATPc=0.03

                    ####  ATP Hydrolysis (ATPhyd) ####
ATPhyd:

    ATPc -> ADPc + x_Pic

    V_ATPhyd * ATPc

    V_ATPhyd = 0.01   #ATP demand at rest (Low)

##    V_ATPhyd = 0.10167  #ATP demand (Moderate)
##    V_ATPhyd = 0.97333  #ATP demand during exercise (High)
##    V_ATPhyd = 5.0    #ATP demand (Hypothetical Test!) (Overload)

##    These values are for Rabbit skeletal muscle from PMID: 12220081.

        ####  alpha-Ketoglutarate transporter (aKG_exp) ####
aKGmFlush:

    aKGm <> x_aKGc

    V_aKGmFlush * (aKGm - (x_aKGc/Keq_aKGmFlush))

    V_aKGmFlush = 1.0     Keq_aKGmFlush = 1.0
```

Appendix G: The Malate-Aspartate shuttle model in ScrumPy format

- **Listing G.1.** ScrumPy code for the Malate-Aspartate shuttle model.

```
                    ####  All metabolites are in mM ####

               ####  External metabolites (Model Parameters) ####

    x_Pim = 8.9     x_Pic = 4.2   x_NADHc = 0.00255   x_NADtot = 1.03755
    x_NADc = x_NADtot - x_NADHc

               ####  Internal metabolites (Model Variables)  ####

    NADm = 0.56   NADHm = 0.129   ATPm = 7.53   ADPm = 2.87
    Aspc = 3.42   Glutc = 6.78   Malc = 0.024   aKGc = 0.004   OAAc = 0.002
    Malm = 1.88 aKGm = 0.34     Aspm = 1.564     Glutm = 2.5
    OAAm = 0.034     ATPc = 4.761     ADPc =  0.049

                       ####  TCA Cycle Reactions ####

               ####  mitochondrial malate dehydrogenase (mMDH) ####
mMDH:

    Malm + NADm <> OAAm + NADHm

    (V_mMDH * ((Malm * NADm) - ((OAAm * NADHm)/Keq_mMDH)))/(((K_mMDH_Malm *
  (1 + OAAm/K_mMDH_OAAm)) + Malm) * ((K_mMDH_NADm * (1 + NADHm
  /K_mMDH_NADHm)) + NADm))

  V_mMDH = 25.66667 Keq_mMDH = 0.000023 K_mMDH_Malm = 1.1
  K_mMDH_OAAm = 0.0055  K_mMDH_NADm = 0.3 K_mMDH_NADHm = 0.005

                       ####  ATP synthesis (ATPsynth)  ####
ATPsynth:

    4 NADHm + 10 ADPm + 10 x_Pim -> 4 NADm + 10 ATPm

    (V_ATPsynth * NADHm * ADPm * x_Pim)/(((K_ATPsynth_NADHm * (1 + NADm
    /K_ATPsynth_NADm)) + NADHm) * (K_ATPsynth_ADPm * K_ATPsynth_Pim) * (((1 +
    ADPm/K_ATPsynth_ADPm)*(1+x_Pim/K_ATPsynth_Pim))+(ATPm/K_ATPsynth_ATPm)))

    V_ATPsynth=0.886637     K_ATPsynth_NADHm=0.88     K_ATPsynth_NADm=1.2
    K_ATPsynth_ADPm=3.1     K_ATPsynth_Pim=8.9     K_ATPsynth_ATPm=7.3

              ####  Adenine Nucleotide Translocase (ANT)  ####
ANT:

    ATPm + ADPc <> ADPm + ATPc

    (V_ANT*((f_ANT_ATPm*ATPm*f_ANT_ADPc*ADPc)-((f_ANT_ATPm*ADPm*f_ANT_ATPc
    *ATPc)/Keq_ANT)))/(((K_ANT_ATPm*(1+((f_ANT_ADPm*ADPm)/K_ANT_ADPm)))
    +(f_ANT_ATPm*ATPm))*((K_ANT_ADPc*(1+((f_ANT_ATPc * ATPc)/K_ANT_ATPc)))
    +(f_ANT_ADPc * ADPc)))

    V_ANT=1.52646/100 f_ANT_ATPm=0.0526     f_ANT_ADPc=0.45     Keq_ANT=118
    f_ANT_ADPm=0.818    f_ANT_ATPc=0.05    K_ANT_ATPm=0.03    K_ANT_ADPm=0.02
```

```
    K_ANT_ADPc=0.02     K_ANT_ATPc=0.03

                        ####  ATP Hydrolysis (ATPhyd) ####
ATPhyd:

    ATPc -> ADPc + x_Pic

    V_ATPhyd * ATPc

    V_ATPhyd = 0.10167    #ATP demand (Moderate)

##    V_ATPhyd = 0.01   #ATP demand at rest (Low)
##    V_ATPhyd = 0.97333  #ATP demand during exercise (High)
##    V_ATPhyd = 5.0    #ATP demand (Hypothetical Test!) (Overload)

##    These values are for Rabbit skeletal muscle from PMID: 12220081.

                        ####  Malate-Aspartate Shuttle (MAS)  ####

           ####  glutamate-aspartate transporter (GATx)  ####
GATx:

  Glutc + Aspm <> Glutm + Aspc

  (V_GATx * ((Aspm * Glutc) - ((Aspc * Glutm)/Keq_GATx)))/
  (((Km_GATx_Aspm * (1 + (Glutm / Km_GATx_Glutm))) + Aspm)
  *((Km_GATx_Glutc * (1 + (Aspc /Km_GATx_Aspc))) + Glutc))

  V_GATx = 5.0E-01  Keq_GATx = 118  Km_GATx_Aspm = 0.055
  Km_GATx_Glutm = 0.5 Km_GATx_Glutc = 3.0 Km_GATx_Aspc = 3.5

           ####  malate-oxoglutarate transporter (MOTx)  ####
MOTx:

  Malc + aKGm <> Malm + aKGc

  (V_MOTx * ((aKGm * Malc) - (aKGc * Malm)))/(((Km_MOTx_aKGm *
  (1 + (Malm / Km_MOTx_Malm))) + aKGm)*((Km_MOTx_Malc *
  (1 + (aKGc /Km_MOTx_aKGc))) + Malc))

  V_MOTx = 14.266 Km_MOTx_Malm = 1.30 Km_MOTx_aKGm = 1.29
  Km_MOTx_Malc = 0.21 Km_MOTx_aKGc = 0.0135

           ####  mitochondrial glutamate-oxoglutarate transaminase (mGOT)
          ####
mGOT:

  OAAm + Glutm <> aKGm + Aspm

  (V_mGOT * ((OAAm * Glutm) - ((aKGm * Aspm)/Keq_mGOT)))/
  (((Km_mGOT_OAAm * (1 + (aKGm / Km_mGOT_aKGm))) + OAAm)
  *((Km_mGOT_Glutm * (1 + (Aspm /Km_mGOT_Aspm))) + Glutm))

  V_mGOT = 0.11667/10 Keq_mGOT = 7.1428
  Km_mGOT_OAAm = 0.088  Km_mGOT_aKGm = 0.43
  Km_mGOT_Glutm = 8.9 Km_mGOT_Aspm = 3.9

           ####  cytosolic glutamate-oxoglutarate transaminase (cGOT)  ####
cGOT:

  OAAc + Glutc <> aKGc + Aspc

  (V_cGOT * ((OAAc * Glutc) - ((aKGc * Aspc)/Keq_cGOT)))/
  (((Km_cGOT_OAAc * (1 + (aKGc / Km_cGOT_aKGc))) + OAAc)
  *((Km_cGOT_Glutc * (1 + (Aspc /Km_cGOT_Aspc))) + Glutc))
```

```
118     V_cGOT = 0.069*10 Keq_cGOT = 0.3  Km_cGOT_OAAc = 0.095
119     Km_cGOT_aKGc = 0.38 Km_cGOT_Glutc = 9.6 Km_cGOT_Aspc = 4.4

121             ####  cytosolic malate dehydrogenase (cMDH) ####
122   cMDH:

124     Malc + x_NADc  <> OAAc + x_NADHc

126     (V_cMDH * ((Malc * x_NADc) - ((OAAc * x_NADHc)/Keq_cMDH)))/
127     (((K_cMDH_Malc * (1 + (OAAc/K_cMDH_OAAc))) + Malc)
128     * ((K_cMDH_NADc * (1 + (x_NADHc/K_cMDH_NADHc))) + x_NADc))

130     V_cMDH = 0.57 Keq_cMDH = 0.000023 K_cMDH_Malc = 1.3
131     K_cMDH_OAAc = 0.09  K_cMDH_NADc = 0.16  K_cMDH_NADHc = 0.019
```

Appendix H: The Heart Glycolysis model in ScrumPy format

- **Listing H.1.** ScrumPy code for the Heart Glycolysis model.

```
                    ####  All metabolites are in mM ####

               ####  External metabolites (Model Parameters) ####

    x_GLCb = 4.2   x_LACb = 0.7   x_PYRm = 0.2   x_Pic = 4.2
    x_G6P = 0.00270 x_aGlycerol3P = 0.125

               ####  Internal metabolites (Model Variables)  ####

    Glc = 2.251 G6P = 0.270 F6P = 0.066 F16BP = 0.056
    GAP = 2.592 DHAP = 0.058  B13PG = 1.39  P3G = 0.114
    P2G = 0.014 PEP = 0.021 PYRc = 0.088  Lac = 1.093
    FreeATPc = 4.761  FreeADPc =  0.049 NADc = 1.035
    NADHc = 0.00255

                    ####  Glycolysis Model (Heart/ Skeletal Muscle) ####

                    ####  Blood Export Reactions  ####
MCT1Pm:

    Lac <> x_LACb

    (V_MCT1Pm * (Lac - (x_LACb / Keq_MCT1Pm))) / ((K_MCT1Pm_Lac *
    (1 + (x_LACb / K_MCT1Pm_xLACb))) + Lac)

    V_MCT1Pm = 1.1  Keq_MCT1Pm = 1.0  K_MCT1Pm_Lac = 2.27
    K_MCT1Pm_xLACb = 2.27

                       ####  Glycolysis Reactions  ####

GLUT4:

    x_GLCb <> Glc

    (V_GLUT4 * (x_GLCb - (Glc / Keq_GLUT4))) / ((K_GLUT4_xGLCb *
    (1 + (Glc / K_GLUT4_Glc))) + x_GLCb)

    V_GLUT4 = 0.10667 Keq_GLUT4 = 1.0 K_GLUT4_xGLCb = 2.0
    K_GLUT4_Glc = 2.0

HK:

    Glc + FreeATPc -> G6P + FreeADPc

    (V_HK * Glc * FreeATPc)/((K_HK_FreeATPc + FreeATPc)* (K_HK_Glc *
    (1 + (G6P / K_HK_G6P)) + Glc))

    V_HK = 0.88 K_HK_Glc = 0.072  K_HK_FreeATPc = 0.236
    K_HK_G6P = 0.253

PGI:
```

```
    G6P <> F6P

    (V_PGI * (G6P - (F6P / Keq_PGI))) / ((K_PGI_G6P * (1 + (F6P /
    K_PGI_F6P))) + G6P)

    V_PGI = 16.10667  Keq_PGI = 0.3 K_PGI_G6P = 0.425
    K_PGI_F6P = 0.031

G6PExp:

    G6P <> x_G6P

    V_G6PExp * (G6P - (x_G6P / Keq_G6PExp))

    V_G6PExp = 0.3  Keq_G6PExp = 1.0

PFK:

    F6P + FreeATPc <> F16BP + FreeADPc

    (V_PFK * (F6P * FreeATPc) - ((F16BP * FreeADPc) / Keq_PFK)) /
    (((K_PFK_F6P * (1 + (F16BP / K_PFK_F16BP))) + F6P)
    * ((K_PFK_FreeATPc * (1 + (FreeADPc / K_PFK_FreeADPc))) + FreeATPc))

    V_PFK = 2.12533 Keq_PFK = 1320.0  K_PFK_F16BP = 4.02
    K_PFK_F6P = 0.224 K_PFK_FreeATPc = 0.127  K_PFK_FreeADPc = 2.71

ALD:

    F16BP <> GAP + DHAP

    (V_ALD * (F16BP - ((GAP * DHAP) / Keq_ALD))) / ((K_ALD_F16BP *
    (1 + ((GAP / K_ALD_GAP) + (DHAP / K_ALD_DHAP)))) + F16BP)

    V_ALD = 1.58667 Keq_ALD = 0.0987  K_ALD_F16BP = 0.038
    K_ALD_GAP = 1.1 K_ALD_DHAP = 2.1

TPI:

    GAP <> DHAP

    (V_TPI * (GAP - (DHAP / Keq_TPI))) / ((K_TPI_GAP * (1 +
    (DHAP / K_TPI_DHAP))) + GAP)

    V_TPI = 61.0  Keq_TPI = 22.0  K_TPI_GAP = 0.32
    K_TPI_DHAP = 0.61

####

cGPD1:

    DHAP + NADHc -> x_aGlycerol3P + NADc

    (V_cGPD1 * (DHAP / K_cGPD1_DHAP) * (NADHc / K_cGPD1_NADHc)) /
    ((1 + (DHAP / K_cGPD1_DHAP)) * (1 + (NADHc / K_cGPD1_NADHc)))

    V_cGPD1 = 0.11  K_cGPD1_DHAP = 0.192535 K_cGPD1_NADHc = 0.001

GAPDH:

    GAP + NADc + x_Pic <> B13PG + NADHc

    (V_GAPDH * ((GAP * NADc) - ((B13PG * NADHc) / Keq_GAPDH))) /
    (((K_GAPDH_GAP * (1 + (B13PG / K_GAPDH_B13PG))) + GAP)
    * ((K_GAPDH_NADc * (1 + (NADHc / K_GAPDH_NADHc))) + NADc) *
```

```
118     (1 + (x_Pic / K_GAPDH_xPic)))

120     V_GAPDH = 8.56  Keq_GAPDH = 0.604 K_GAPDH_GAP = 0.042
121     K_GAPDH_B13PG = 0.0008  K_GAPDH_NADc = 0.058  K_GAPDH_xPic = 1.42
122     K_GAPDH_NADHc = 0.0033

124 PGK:

126     B13PG + FreeADPc <> P3G + FreeATPc

128     (V_PGK * ((B13PG * FreeADPc) - ((P3G * FreeATPc) / Keq_PGK))) /
129     (((K_PGK_B13PG * (1 + (P3G / K_PGK_P3G))) + B13PG)
130     * ((K_PGK_FreeADPc * (1 + (FreeATPc / K_PGK_FreeATPc))) + FreeADPc))

132     V_PGK = 401.60  Keq_PGK = 3767.0  K_PGK_B13PG = 0.021
133     K_PGK_P3G = 1.2 K_PGK_FreeADPc = 0.008  K_PGK_FreeATPc = 0.565

135 PGM:

137     P3G <> P2G

139     (V_PGM * (P3G - (P2G / Keq_PGM))) / ((K_PGM_P3G * (1 +
140     (P2G / K_PGM_P2G))) + P3G)

142     V_PGM = 17.9733 Keq_PGM = 0.11  K_PGM_P3G = 0.145
143     K_PGM_P2G = 0.014

145 ENO:

147     P2G <> PEP

149     (V_ENO * (P2G - (PEP / Keq_ENO))) / ((K_ENO_P2G *
150     (1 + (PEP / K_ENO_PEP))) + P2G)

152     V_ENO = 2.96  Keq_ENO = 4.0 K_ENO_P2G = 0.045
153     K_ENO_PEP = 0.37

155 PK:

157     PEP + FreeADPc <> PYRc + FreeATPc

159     (V_PK * ((PEP * FreeADPc) - ((PYRc * FreeATPc) / Keq_PK))) /
160     (((K_PK_PEP * (1 + (PYRc / K_PK_PYRc))) + PEP)
161     * ((K_PK_FreeADPc * (1 + (FreeATPc / K_PK_FreeATPc))) + FreeADPc))

163     V_PK = 15.09333 Keq_PK = 12000.0  K_PK_PEP = 0.11
164     K_PK_FreeADPc = 0.268 K_PK_PYRc = 7.05
165     K_PK_FreeATPc = 0.82

167 LDH:

169     PYRc + NADHc <> Lac + NADc

171     (V_LDH * ((PYRc * NADHc) - ((Lac * NADc) / Keq_LDH))) /
172     (((K_LDH_PYRc * (1 + (Lac / K_LDH_Lac))) + PYRc)
173     * ((K_LDH_NADHc * (1 + (NADc / K_LDH_NADc))) + NADHc))

175     V_LDH = 9.9 Keq_LDH = 78500.0 K_LDH_PYRc = 0.125
176     K_LDH_NADHc = 0.001 K_LDH_Lac = 0.17  K_LDH_NADc = 0.253

178 MCT1Mm:

180     PYRc <> x_PYRm

182     (V_MCT1Mm * (PYRc - (x_PYRm / Keq_MCT1Mm))) /
```

```
183       ((K_MCT1Mm_PYRc * (1 + (x_PYRm / K_MCT1Mm_xPYRm))) + PYRc)

185       V_MCT1Mm = 0.079  Keq_MCT1Mm = 1.0  K_MCT1Mm_PYRc = 0.15
186       K_MCT1Mm_xPYRm = 0.4

188   ATPhyd:

190       FreeATPc -> FreeADPc + x_Pic

192       V_ATPhyd * FreeATPc

194       V_ATPhyd = 0.01   #ATP demand at rest (Low)

196   ##    V_ATPhyd = 0.10167  #ATP demand (Moderate)
197   ##    V_ATPhyd = 0.97333  #ATP demand during exercise (High)

199   ##    These values are for Rabbit skeletal muscle from PMID: 12220081.
```

References

1. M.J. Achs and D. Garfinkel. Computer simulation of rat heart metabolism after adding glucose to the perfusate. *Am. J. Physiol.*, 232(5):R175–R184, 1977. URL http://www.ncbi.nlm.nih.gov/pubmed/16503.

2. T.P.M. Akerboom, H. Bookelman, P.F. Zuurendonk, R. van der Meer, and J.M. Tager. Intramitochondrial and extramitochondrial concentrations of adenine nucleotides and inorganic phosphate in isolated hepatocytes from fasted rats. *Eur. J. Biochem./FEBS*, 84(2):413–420, March 1978. URL http://www.ncbi.nlm.nih.gov/pubmed/639797.

3. K.R. Albe and B.E. Wright. Systems analysis of the tricarboxylic acid cycle in Dictyostelium discoideum. II. Control analysis. *J. Biol. Chem.*, 267(5):3106–3114, February 1992. URL http://www.ncbi.nlm.nih.gov/pubmed/1737767.

4. R.A. Alberty. *Thermodynamics of Biochemical Reactions*. John Wiley & Sons, Inc., Hoboken, N.J., U.S.A., 2003a. URL http://www.worldcat.org/oclc/51242181.

5. R.A. Alberty. Thermodynamics of Biochemical Reactions at Specified pH. In *Thermodynamics of Biochemical Reactions*, chapter 4, pages 57–87. John Wiley & Sons, Inc., Hoboken, N.J., U.S.A., 2003b. URL http://www.worldcat.org/oclc/51242181.

6. L.K. Ashman, D.B. Keech, J.C. Wallace, and J. Nielsen. Sheep kidney pyruvate carboxylase. Studies on its activation by acetyl coenzyme A and characteristics of its acetyl coenzyme A independent reaction. *J. Biol. Chem.*, 247(18):5818–5824, 1972. URL http://www.ncbi.nlm.nih.gov/pubmed/5057085.

7. B.M. Bakker, P.A. Michels, F.R. Opperdoes, and H.V. Westerhoff. What controls glycolysis in bloodstream form Trypanosoma brucei? *J. Biol. Chem.*, 274(21):14551–14559, May 1999. URL http://www.ncbi.nlm.nih.gov/pubmed/10329645.

8. R.S. Balaban. Cardiac Energy Metabolism Homeostasis: Role of Cytosolic Calcium. *J. Mol. Cell. Cardiol.*, 34(10):1259–1271, October 2002. URL http://www.ncbi.nlm.nih.gov/pubmed/12392982.

9. R.S. Balaban, H.L. Kantor, L.A. Katz, and R.W. Briggs. Relation between work and phosphate metabolite in the in vivo paced mammalian heart. *Science*, 232(4754):1121–1123, May 1986. URL http://www.ncbi.nlm.nih.gov/pubmed/3704638.

10. J. M. Baranyai and J. J. Blum. Quantitative analysis of intermediary metabolism in rat hepatocytes incubated in the presence and absence of ethanol with a substrate mixture including ketoleucine. *Biochem. J.*, 258:121–140, 1989. URL http://www.ncbi.nlm.nih.gov/pubmed/2930501.

11. J.N. Bazil, G.T. Buzzard, and A.E. Rundell. Modelling mitochondrial bioenergetics with integrated volume dynamics. *PLoS comput. biol.*, 6(1):e1000632, January 2010. URL http://www.ncbi.nlm.nih.gov/pubmed/20052270.

12. B.D. Bennett, E.H. Kimball, M. Gao, R. Osterhout, S.J. Van Dien, and J.D. Rabinowitz. Absolute metabolite concentrations and implied enzyme active site occupancy in *Escherichia coli*. *Nat. Chem. Biol.*, 5 (8):593–599, August 2009. URL http://www.ncbi.nlm.nih.gov/pubmed/19561621.

13. M. Beylot, M.V. Soloviev, F. David, B.R. Landau, and H. Brunengraber. Tracing Hepatic Gluconeogenesis Relative to Citric Acid Cycle Activity in Vitro and in Vivo: Comparisons In The Use of [3-C]Lactate, [2-C]Acetate, and α-Keto[3-C]Isocaproate. *J. Biol. Chem.*, 270(4):1509–1514, 1995. URL http://www.ncbi.nlm.nih.gov/pubmed/7829478.

14. R.J. Bing. Cardiac metabolism. *Physiol. Rev.*, 45:171–213, 1965. URL http://www.ncbi.nlm.nih.gov/pubmed/14302909.

15. J.A. Bittl and J.S. Ingwall. Reaction rates of creatine kinase and ATP synthesis in the isolated rat heart. A ^{31}P NMR magnetization transfer study. *J. Biol. Chem.*, 260(6):3512–3517, March 1985. URL http://www.ncbi.nlm.nih.gov/pubmed/3972835.

16. J.M. Blair. A reinterpretation of the kinetics of pyruvate carboxylase. *FEBS lett.*, 2(4):245–247, February 1969. URL http://www.ncbi.nlm.nih.gov/pubmed/11946324.

17. S. Bose, S. French, F.J. Evans, F. Joubert, and R.S. Balaban. Metabolic network control of oxidative phosphorylation: multiple roles of inorganic phosphate. *J. Biol. Chem.*, 278(40):39155–39165, October 2003. URL http://www.ncbi.nlm.nih.gov/pubmed/12871940.

18. J.L. Bowtell, S. Marwood, M. Bruce, D. Constantin-Teodosiu, and P.L. Greenhaff. Tricarboxylic acid cycle intermediate pool size: functional importance for oxidative metabolism in exercising human skeletal muscle. *Sports Medicine*, 37(12):1071–1088, 2007. URL http://www.ncbi.nlm.nih.gov/pubmed/18027994.

19. M.D. Brand, M.E. Harper, and H.C. Taylor. Control of the effective P/O ratio of oxidative phosphorylation in liver mitochondria and hepatocytes. *Biochem. J.*, 291 (Pt 3):739–748, May 1993. URL http://www.ncbi.nlm.nih.gov/pubmed/8489502.

20. J. Bremer. In H. Peeters, editor, *Protides of the biological fluids : [Proceedings of the Fifteenth Colloquium, Bruges]*, volume XV, pages 185–189, Amsterdam, London, New York, Princeton., 1967. Elsevier Publishing Co. URL http://books.google.co.uk/books?id=QNwyAAAAIAAJ.

21. J. Bremer. Pyruvate dehydrogenase, substrate specificity and product inhibition. *Eur. J. Biochem./ FEBS*, 8(4):535–540, 1969. URL http://www.ncbi.nlm.nih.gov/pubmed/4307688.

22. J. Bremer and M. Aas. Mitochondria: structure and function. In L. Ernster and Z. Drahota, editors, *Federation of European Biochemical Societies, Symposium at the 5th Meeting, Prague, July 1968*, [FEBS Symposium: Vol.17], page 393. Academic Press, New York And London, 1969. URL http://www.worldcat.org/oclc/310882710.

23. F.A. Brightman, M. Heiske, A. Ghaisas, C. Nazaret, J.-P. Mazat, and D.A. Fell. Control of flux in a model of the mammalian liver tricarboxylic acid cycle. Unpublished manuscript, available at: `http://mudshark.brookes.ac.uk/Publications/articles`, 2010.

24. J.T. Brosnan and I.B. Fritz. The permeability of mitochondria to carnitine and acetylcarnitine. *Biochem. J.*, 125(4):94P–95P, May 1971. URL http://www.ncbi.nlm.nih.gov/pubmed/5144261.

25. G.C. Brown. Control of respiration and ATP synthesis in mammalian mitochondria and cells. *Biochem. J.*, 284 (Pt 1):1–13, May 1992. URL http://www.ncbi.nlm.nih.gov/pubmed/1599389.

26. S. Cha and R.E. Jr. Parks. Succinic thiokinase. II. Kinetic studies: initial velocity, product inhibition, and effect of arsenate. *J. Biol. Chem.*, 239(6):1968–1977, 1964. URL http://www.ncbi.nlm.nih.gov/pubmed/14213385.

27. E.M. Chance, S.H. Seeholzer, K. Kobayashi, and J.R. Williamson. Mathematical analysis of isotope labeling in the citric acid cycle with applications to ^{13}C NMR studies in perfused rat hearts. *J. Biol. Chem.*, 258(22):13785–13794, November 1983. URL http://www.ncbi.nlm.nih.gov/pubmed/6643454.

28. J.B. Chappell. Systems used for the transport of substrates into mitochondria. *Brit. Med. Bull.*, 24(2): 150–157, May 1968. URL http://www.ncbi.nlm.nih.gov/pubmed/5649935.

[29.] J.B. Chappell and A.R. Crofts. Ion Transport and Reversible Volume Changes of Isolated Mitochondria : [proceedings of the Symposium on the Regulation of Metabolic Processes in Mitochondria ; held in Bari on April 26 - May 1, 1965]. In J.M. Tager, S. Papa, E. Quagliariello, and E.C. Slater, editors, *Regulation of Metabolic Processes in Mitochondria*, volume XII of *Biochimica et biophysica acta ; 7*, pages 293–316, Amsterdam, Holland., 1966. Elsevier Publishing Co. URL http://www.worldcat.org/oclc/490004785.

[30.] J.B. Chappell and K. Haarhoff. *The Biochemistry of Mitochondria (Slater, E.C., Kaniuga, Z., and Wojtczak, L., eds)*. Academic Press Inc., Ltd., London, U.K., 1967.

[31.] C. Chassagnole, D. A. Fell, B. Rais, B. Kudla, and J.-P. Mazat. Control of the threonine-synthesis pathway in Escherichia coli: a theoretical and experimental approach. *Biochem. J.*, 356(Pt 2):433–444, 2001a. URL http://www.ncbi.nlm.nih.gov/pubmed/11368770.

[32.] C. Chassagnole, B. Rais, E. Quentin, D. A. Fell, and J.-P. Mazat. An integrated study of threonine-pathway enzyme kinetics in Escherichia coli. *Biochem. J.*, 356:415–423, 2001b. URL http://www.ncbi.nlm.nih.gov/pubmed/11368768.

[33.] R.F. Chen and G.W. Plaut. Activation and Inhibition of DPN-Linked Isocitrate Dehydrogenase of Heart By Certain Nucleotides. *Biochemistry*, 2(5):1023–1032, 1963. URL http://www.ncbi.nlm.nih.gov/pubmed/14087354.

[34.] R.F. Colman. Mechanisms for the oxidative decarboxylation of isocitrate: Implications for control. *Adv. Enzyme Regul.*, 13(1):413–433, January 1975. URL http://www.ncbi.nlm.nih.gov/pubmed/1977.

[35.] B. Comte, G. Vincent, B. Bouchard, and C. Des Rosiers. Probing the Origin of Acetyl-CoA and Oxaloacetate Entering the Citric Acid Cycle from the ^{13}C Labeling of Citrate Released by Perfused Rat Hearts. *J. Biol. Chem.*, 272(42):26117–26124, 1997. URL http://www.ncbi.nlm.nih.gov/pubmed/9334176.

[36.] B. Comte, G. Vincent, B. Bouchard, M. Benderdour, and C. Des Rosiers. Reverse flux through cardiac $NADP^+$-isocitrate dehydrogenase under normoxia and ischemia. *Am. J. Physiol.*, 283(4):H1505–H1514, 2002. URL http://www.ncbi.nlm.nih.gov/pubmed/12234803.

[37.] R.J. Connett. Analysis of metabolic control: new insights using scaled creatine kinase model. *Am. J. Physiol.*, 254(6, Pt 2):R949–R959, June 1988. URL http://www.ncbi.nlm.nih.gov/pubmed/2837918.

[38.] COPASI project. Section: Mass Conservations in *Copasi User Manual (HTML version)*, 2009a. URL http://www.copasi.org/tiki-index.php?page=OD.Mass.Conservations&structure=User_Manual. [Last Modification: Friday 20 of March, 2009 10:13:22 EDT].

[39.] COPASI project. Section: Global Quantities in *Copasi User Manual (HTML version)*, 2009b. URL http://www.copasi.org/tiki-index.php?page=OD.Global.Quantities. [Last Modification: Tuesday 31 of March, 2009 14:01:05 EDT].

[40.] B.E. Corkey, J. Duszynski, T. L. Rich, B. Matschinsky, and J. R. Williamson. Regulation of free and bound magnesium in rat hepatocytes and isolated mitochondria. *J. Biol. Chem.*, 261(6):2567–2574, 1986. URL http://www.ncbi.nlm.nih.gov/pubmed/3081495.

[41.] A. Cornish-Bowden. *Fundamentals of Enzyme Kinetics*. Wiley-Blackwell, Weinheim, Germany, 4th edition, 2012. URL http://www.worldcat.org/oclc/795334653.

[42.] A. Cornish-Bowden and M.L. Cárdenas. Information transfer in metabolic pathways. Effects of irreversible steps in computer models. *Eur. J. Biochem./FEBS*, 268(24):6616–6624, December 2001. URL http://www.ncbi.nlm.nih.gov/pubmed/11737216.

[43.] S. Cortassa, M.A. Aon, E. Marbán, R.L. Winslow, and B. O'Rourke. An integrated model of cardiac mitochondrial energy metabolism and calcium dynamics. *Biophys. J.*, 84(4):2734–2755, April 2003. URL http://www.ncbi.nlm.nih.gov/pubmed/12668482.

[44.] S. Cortassa, B. O'Rourke, R.L. Winslow, and M.A. Aon. Control and regulation of mitochondrial energetics in an integrated model of cardiomyocyte function. *Biophys. J.*, 96(6):2466–2478, March 2009. URL http://www.ncbi.nlm.nih.gov/pubmed/19289071.

45. B. Crabtree and E.A. Newsholme. The derivation and interpretation of control coefficients. *Biochem. J.*, 247(1):113–120, 1987. URL http://www.ncbi.nlm.nih.gov/pubmed/3689338.

46. S.C. Dennis, A. Padmas, M.S. DeBuysere, and M.S. Olson. Studies on the regulation of pyruvate dehydrogenase in the isolated perfused rat heart. *J. Biol. Chem.*, 254(4):1252–1258, 1979. URL http://www.ncbi.nlm.nih.gov/pubmed/216689.

47. R.M. Denton and J.G. McCormack. Fuel selection at the level of mitochondria in mammalian tissues. *Proc. Nutr. Soc.*, 54(1):11–22, March 1995. URL http://www.ncbi.nlm.nih.gov/pubmed/7568246.

48. R.M. Denton, J.G. McCormack, and N.J. Edgell. Role of calcium ions in the regulation of intramitochondrial metabolism. Effects of Na^+, Mg^{2+} and ruthenium red on the Ca^{2+}-stimulated oxidation of oxoglutarate and on pyruvate dehydrogenase activity in intact rat heart mitochondria. *Biochem. J.*, 190(1):107–117, 1980. URL http://www.ncbi.nlm.nih.gov/pubmed/6160850.

49. C. Depre, J.L. Vanoverschelde, and H. Taegtmeyer. Glucose for the heart. *Circulation*, 99(4):578–588, February 1999. URL http://www.ncbi.nlm.nih.gov/pubmed/9927407.

50. C. Des Rosiers, C.A. Fernandez, F. David, and H. Brunengraber. Reversibility of the mitochondrial isocitrate dehydrogenase reaction in the perfused rat liver. Evidence from isotopomer analysis of citric acid cycle intermediates. *J. Biol. Chem.*, 269(44):27179–27182, November 1994. URL http://www.ncbi.nlm.nih.gov/pubmed/7961626.

51. C. Des Rosiers, L. Di Donato, B. Comte, A. Laplante, C. Marcoux, F. David, C.A. Fernandez, and H. Brunengraber. Isotopomer analysis of citric acid cycle and gluconeogenesis in rat liver. Reversibility of isocitrate dehydrogenase and involvement of ATP-citrate lyase in gluconeogenesis. *J. Biol. Chem.*, 270: 10027–10036, 1995. URL http://www.ncbi.nlm.nih.gov/pubmed/7730304.

52. L. Di Donato, C. Des Rosiers, J.A. Montgomery, F. David, M. Garneau, and H. Brunengraber. Rates of gluconeogenesis and citric acid cycle in perfused livers, assessed from the mass spectrometric assay of the ^{13}C labelling pattern of glutamate. *J. Biol. Chem.*, 268(6):4170–4180, 1993. URL http://www.ncbi.nlm.nih.gov/pubmed/8095046.

53. J. Dzbek and B. Korzeniewski. Control over action potential, calcium peak and average fluxes in the cyclic quasi-steady-state ion transport system in cardiac myocytes: in silico studies. *Biochem. J.*, 404(2): 227–233, June 2007. URL http://www.ncbi.nlm.nih.gov/pubmed/17284165.

54. J. Dzbek and B. Korzeniewski. Control over the contribution of the mitochondrial membrane potential (ΔPsi) and proton gradient (ΔpH) to the protonmotive force (Δp). In silico studies. *J. Biol. Chem.*, 283 (48):33232–33239, November 2008. doi: 10.1074/jbc.M802404200. URL http://www.ncbi.nlm.nih.gov/pubmed/18694940.

55. M. Erecinska, M. Stubbs, Y. Miyata, C.M. Ditre, and D.F. Wilson. Regulation of cellular metabolism by intracellular phosphate. *Biochim. Biophys. Acta. - Bioenergetics*, 462(1):20–35, October 1977. URL http://www.ncbi.nlm.nih.gov/pubmed/199253.

56. M. Erecinska, D.F. Wilson, and K. Nishiki. Homeostatic regulation of cellular energy metabolism: experimental characterization in vivo and fit to a model. *Am. J. Physiol. Cell Physiol.*, 234(3):C82–C89, March 1978. URL http://www.ncbi.nlm.nih.gov/pubmed/204196.

57. L. Ernster and F. Navazio. Studies on TPN-linked oxidations. *Biochim. Biophys. Acta.*, 26(2):408–415, November 1957. URL http://www.ncbi.nlm.nih.gov/pubmed/13499379.

58. L.A. Fahien and J.K. Teller. Glutamate-malate metabolism in liver mitochondria. A model constructed on the basis of mitochondrial levels of enzymes, specificity, dissociation constants, and stoichiometry of hetero-enzyme complexes. *J. Biol. Chem.*, 267(15):10411–10422, May 1992. URL http://www.ncbi.nlm.nih.gov/pubmed/1350279.

59. D.A. Fell. *Understanding the Control of Metabolism*. Portland press, London, 1997. URL http://www.worldcat.org/oclc/36267572.

60. D.A. Fell and H.M. Sauro. Metabolic control analysis. Additional relationships between elasticities and control coefficients. *Eur. J. Biochem./FEBS*, 148(1):555–561, 1985. URL http://www.ncbi.nlm.nih.gov/pubmed/3996393.

61. D.A. Fell and S. Thomas. Physiological control of metabolic flux: the requirement for multisite modulation. *Biochem. J.*, 311 (Pt 1):35–39, October 1995. URL http://www.ncbi.nlm.nih.gov/pubmed/7575476.

62. D.A. Fell, S. Thomas, and M.G. Poolman. *Plant Carbohydrate Biochemistry*, chapter Modelling metabolic pathways and analysing control., page 17. Experimental biology reviews. BIOS Scientific Pusblishers Ltd., Oxford, 1999. URL http://www.worldcat.org/oclc/807880646.

63. G. Fiermonte, V. Dolce, R. Arrigoni, M.J. Runswick, J.E. Walker, and F. Palmieri. Organization and sequence of the gene for the human mitochondrial dicarboxylate carrier: evolution of the carrier family. *Biochem. J.*, 344(Pt 3):953–960, 1999. URL http://www.ncbi.nlm.nih.gov/pubmed/10585886.

64. A.J. Fritzen, N. Grunnet, and B. Quistorff. Flux control analysis of mitochondrial oxidative phosphorylation in rat skeletal muscle: pyruvate and palmitoyl-carnitine as substrates give different control patterns. *Eur. J. Appl. Physiol.*, 101(6):679–689, December 2007. URL http://www.ncbi.nlm.nih.gov/pubmed/17717681.

65. A.H. From, S.D. Zimmer, S.P. Michurski, P. Mohanakrishnan, V.K. Ulstad, W.J. Thoma, and K. Uğurbil. Regulation of the oxidative phosphorylation rate in the intact cell. *Biochemistry*, 29(15):3731–3743, April 1990. URL http://www.ncbi.nlm.nih.gov/pubmed/2340268.

66. J.L. Gabriel and G.W.E. Plaut. Specific site inhibitors of NAD^+-specific isocitrate dehydrogenase from bovine heart. *J. Biol. Chem.*, 257(14):8021–8029, July 1982. URL http://www.ncbi.nlm.nih.gov/pubmed/6177694.

67. P.B. Garland, D. Shepherd, and D.W. Yates. Steady-state concentrations of coenzyme A, acetyl-coenzyme A and long-chain fatty acyl-coenzyme A in rat-liver mitochondria oxidizing palmitate. *Biochem. J.*, 97(2):587–594, November 1965. URL http://www.ncbi.nlm.nih.gov/pubmed/16749169.

68. P.B. Garland, D. Shepherd, D.G. Nicholls, D.W. Yates, and P.A. Light. Interactions between fatty acid oxidation and the tricarboxylic acid cycle. In J.M. Lowenstein, editor, *Citric Acid Cycle: Control and Compartmentation*, pages 163–212. Marcel Dekker, New York, 1969. URL http://www.ncbi.nlm.nih.gov/nlmcatalog/217042.

69. M.J. Gibala. Anaplerosis of the muscle tricarboxylic acid cycle pool during contraction: does size matter? *J. Physiol.*, 548(Pt 2):334, April 2003. URL http://www.ncbi.nlm.nih.gov/pubmed/12611921.

70. M.J. Gibala, D.A. MacLean, T.E. Graham, and B. Saltin. Anaplerotic processes in human skeletal muscle during brief dynamic exercise. *J. Physiol.*, 502 (Pt 3):703–713, August 1997. URL http://www.ncbi.nlm.nih.gov/pubmed/9279819.

71. M.J. Gibala, M.E. Young, and H. Taegtmeyer. Anaplerosis of the citric acid cycle: role in energy metabolism of heart and skeletal muscle. *Acta Physiol. Scand.*, 168(4):657–665, April 2000. URL http://www.ncbi.nlm.nih.gov/pubmed/10759602.

72. C. Giersch. Concerning the measurement of flux control coefficients by enzyme titration. Steady states, quasi-steady-states, and the role of time in control analytical experiments. *Eur. J. Biochem.*, 231(3):587–592, August 1995a. URL http://www.ncbi.nlm.nih.gov/pubmed/7649157.

73. C. Giersch. Determining elasticities from multiple measurements of flux rates and metabolite concentrations. Application of the multiple modulation method to a reconstituted pathway. *Eur. J. Biochem.*, 227 (1-2):194–201, January 1995b. URL http://www.ncbi.nlm.nih.gov/pubmed/7851386.

74. N.L. Greenbaum and D.F. Wilson. The distribution of inorganic phosphate and malate between intra- and extramitochondrial spaces. Relationship with the transmembrane pH difference. *J. Biol. Chem.*, 260(2): 873–879, January 1985. URL http://www.ncbi.nlm.nih.gov/pubmed/2857172.

75. J.L. Griffin, J.M. O'Donnell, L.T. White, R.J. Hajjar, and E.D. Lewandowski. Postnatal expression and activity of the mitochondrial 2-oxoglutarate-malate carrier in intact hearts. *Am. J. Physiol.*, 279(6): C1704–C1709, 2000. URL http://www.ncbi.nlm.nih.gov/pubmed/11078684.

76. A.K. Groen, R. van der Meer, H.V. Westerhoff, T.P.M. Akerboom, J.M. Tager, and R.J.A. Wanders. In H. Sies, editor, *Metabolic compartmentation*, pages 9–37. Academic Press, London & New York, illustrated edition, 1982a. URL http://www.worldcat.org/oclc/489706487.

77. A.K. Groen, R.J.A. Wanders, H.V. Westerhoff, R. Van der Meer, and J.M. Tager. Quantification of the contribution of various steps to the control of mitochondrial respiration. *J. Biol. Chem.*, 257(6):2754–2757, April 1982b. URL http://www.ncbi.nlm.nih.gov/pubmed/7061448.

78. B.A. Haddock, D.W. Yates, and P.B. Garland. The localization of some coenzyme A-dependent enzymes in rat liver mitochondria. *Biochem. J.*, 119(3):565–573, September 1970. URL http://www.ncbi.nlm.nih.gov/pubmed/5500317.

79. R.P. Hafner, G.C. Brown, and M.D. Brand. Analysis of the control of respiration rate, phosphorylation rate, proton leak rate and protonmotive force in isolated mitochondria using the 'top-down' approach of metabolic control theory. *Eur. J. Biochem./FEBS*, 188(2):313–319, March 1990. URL http://www.ncbi.nlm.nih.gov/pubmed/2156698.

80. R.G. Hansford and R.N. Johnson. The steady state concentrations of coenzyme A-SH and coenzyme A thioester, citrate, and isocitrate during tricarboxylate cycle oxidations in rabbit heart mitochondria. *J. Biol. Chem.*, 250(21):8361–8375, 1975. URL http://www.ncbi.nlm.nih.gov/pubmed/1194259.

81. Y. Hatefi and D.L. Stiggall. Metal-Containing Flavoprotein Dehydrogenases. In P.D. Boyer, editor, *The Enzymes*, volume XIII, chapter 4, pages 175–297. Academic Press, New York, San Francisco & London, 3rd edition, 1976. URL http://www.sciencedirect.com/science/article/pii/S1874604708602425.

82. F.W. Heineman and R.S. Balaban. Control of mitochondrial respiration in the heart in vivo. *Annu. Rev. Physiol.*, 52(1):523–542, 1990. URL http://www.ncbi.nlm.nih.gov/pubmed/2158767.

83. F.W. Heineman and R.S. Balaban. Effects of afterload and heart rate on NAD(P)H redox state in the isolated rabbit heart. *Am. J. Physiol.*, 264(2 (Pt 2)):H433–H440, 1993. URL http://www.ncbi.nlm.nih.gov/pubmed/8447459.

84. R. Heinrich and T.A. Rapoport. A linear steady-state treatment of enzymatic chains. General properties, control and effector strength. *Eur. J. Biochem.*, 42(1):89–95, 1974. URL http://www.ncbi.nlm.nih.gov/pubmed/4830198.

85. R. Heinrich and S. Schuster. *The Regulation of Cellular Systems*. Chapman and Hall, New York, N.Y., 1996. URL http://books.google.co.uk/books?id=LUQSSDViXX0C.

86. R. Heinrich and S. Schuster. The modelling of metabolic systems. Structure, control and optimality. *Biosystems*, 47(1–2):61–77, 1998. URL http://www.ncbi.nlm.nih.gov/pubmed/9715751.

87. J.B. Hoek, N.E. Lofrumento, A.J. Meyer, and J.M. Tager. Phosphate transport in rat-liver mitochondria. *Biochim. Biophys. Acta. - Bioenergetics*, 226(2):297–308, March 1971. URL http://www.ncbi.nlm.nih.gov/pubmed/5575160.

88. J.S. Hofmeyr and A. Cornish-Bowden. Regulating the cellular economy of supply and demand. *FEBS lett.*, 476(1-2):47–51, June 2000. URL http://www.ncbi.nlm.nih.gov/pubmed/10878248.

89. M.J. Holness and M.C. Sugden. Regulation of pyruvate dehydrogenase complex activity by reversible phosphorylation. *Biochem. Soc. Trans.*, 31(Pt 6):1143–1151, December 2003. URL http://www.ncbi.nlm.nih.gov/pubmed/14641014.

90. S. Hoops, S. Sahle, R. Gauges, C. Lee, J. Pahle, N. Simus, M. Singhal, L. Xu, P. Mendes, , and U. Kummer. COPASI – a COmplex PAthway SImulator. *Bioinformatics*, 22(24):3067–3074, 2006. URL http://www.ncbi.nlm.nih.gov/pubmed/17032683.

91. Y.C. Huang and R.F. Colman. Location of the coenzyme binding site in the porcine mitochondrial $NADP^+$-dependent isocitrate dehydrogenase. *J. Biol. Chem.*, 280(34):30349–30353, August 2005. URL http://www.ncbi.nlm.nih.gov/pubmed/15975917.

92. N.J. Hutson, A.L. Kerbey, P.J. Randle, and P.H. Sugden. Conversion of inactive (phosphorylated) pyruvate dehydrogenase complex into active complex by the phosphate reaction in heart mitochondria is inhibited by alloxan-diabetes or starvation in the rat. *Biochem. J.*, 173(2):669–680, August 1978. URL http://www.ncbi.nlm.nih.gov/pubmed/212016.

93. B.M. Jucker, J.Y. Lee, and R.G. Shulman. In vivo ^{13}C NMR measurements of hepatocellular tricarboxylic acid cycle flux. *J. Biol. Chem.*, 273(20):12187–12194, May 1998. URL http://www.ncbi.nlm.nih.gov/pubmed/9575166.

94. H. Kacser and J.A. Burns. The control of flux. *Symp. Soc. Exp. Biol.*, 27:65–104, 1973. URL http://www.ncbi.nlm.nih.gov/pubmed/7672373.

95. H. Kacser and J.A. Burns. The molecular basis of dominance. *Genetics*, 97(3-4):639–666, 1981. URL http://www.ncbi.nlm.nih.gov/pubmed/7297851.

96. Y. Kashiwaya, K. Sato, N. Tsuchiya, S. Thomas, D.A. Fell, R.L. Veech, and J.V. Passonneau. Control of glucose utilization in working perfused rat heart. *J. Biol. Chem.*, 269(41):25502–25514, October 1994. URL http://www.ncbi.nlm.nih.gov/pubmed/7929251.

97. L.A. Katz, A.P. Koretsky, and R.S. Balaban. Respiratory control in the glucose perfused heart. A ^{31}P NMR and NADH fluorescence study. *FEBS lett.*, 221(2):270–276, September 1987. URL http://www.ncbi.nlm.nih.gov/pubmed/3622766.

98. L.A. Katz, J.A. Swain, M.A. Portman, and R.S. Balaban. Relation between phosphate metabolites and oxygen consumption of heart in vivo. *Am. J. Physiol.*, 256(1, Pt 2):H265–H274, January 1989a. URL http://www.ncbi.nlm.nih.gov/pubmed/2912189.

99. L.A. Katz, J.A. Swain, M.A. Portman, and R.S. Balaban. Relation between phosphate metabolites and oxygen consumption of heart in vivo. *Am. J. Physiol.*, 256(1 (Pt 2)):H265–H274, January 1989b. URL http://www.ncbi.nlm.nih.gov/pubmed/2912189.

100. B. Keech and G.J. Barritt. Allosteric Activation of Sheep Kidney Pyruvate Carboxylase by the Magnesium Ion (Mg^{2+}) and the Magnesium Adenosine Triphosphate Ion ($MgATP^{2-}$). *J. Biol. Chem.*, 242(9): 1983–1987, May 1967. URL http://www.ncbi.nlm.nih.gov/pubmed/6022848.

101. A.L. Kerbey, P.J. Randle, R.H. Cooper, S. Whitehouse, H.T. Pask, and R.M. Denton. Regulation of pyruvate dehydrogenase in rat heart. Mechanism of regulation of proportions of dephosphorylated and phosphorylated enzyme by oxidation of fatty acids and ketone bodies and of effects of diabetes: role of coenzyme A, acetyl-coenzyme A and reduced and oxidized nicotinamide-adenine dinucleotide. *Biochem. J.*, 154(2):327–348, February 1976. URL http://www.ncbi.nlm.nih.gov/pubmed/180974.

102. B. Kiens. Skeletal muscle lipid metabolism in exercise and insulin resistance. *Physiol. Rev.*, 86(1): 205–243, 2006. URL http://www.ncbi.nlm.nih.gov/pubmed/16371598.

103. G.A. Kimmich and H. Rasmussen. Regulation of pyruvate carboxylase activity by calcium in intact rat liver mitochondria. *J. Biol. Chem.*, 244(1):190–199, January 1969. URL http://www.ncbi.nlm.nih.gov/pubmed/5773282.

104. P. Kingsley-Hickman, E.Y. Sako, P.A. Andreone, J.A. St. Cyr, S. Michurski, J.E. Foker, A.H.L. From, M. Petein, and K. Ugurbil. ^{31}P NMR measurement of ATP synthesis rate in perfused intact rat hearts. *FEBS lett.*, 198(1):159–163, 1986. URL http://www.ncbi.nlm.nih.gov/pubmed/2869973.

105. S. Klamt and E.D. Gilles. Minimal cut sets in biochemical reaction networks. *Bioinformatics*, 20(2): 226–234, 2004. URL http://www.ncbi.nlm.nih.gov/pubmed/14734314.

106. M. Klingenberg. Mitochondria metabolite transport. *FEBS lett.*, 6(3):145–154, 1970. URL http://www.ncbi.nlm.nih.gov/pubmed/11947361.

[107.] M. Klingenberg and E. Pfaff. Structural and functional compartmentation in mitochondria : [proceedings of the Symposium on the Regulation of Metabolic Processes in Mitochondria ; held in Bari on April 26 - May 1, 1965]. In J.M. Tager, S. Papa, E. Quagliariello, and E.C. Slater, editors, *Regulation of Metabolic Processes in Mitochondria*, volume XII of *Biochimica et biophysica acta ; 7*, page 180, Amsterdam, Holland., 1966. Elsevier Publishing Co. URL http://www.worldcat.org/oclc/490004785.

[108.] K. Kobayashi and J.R. Neely. Control of maximum rates of glycolysis in rat cardiac muscle. *Circ. Res.*, 44(2):166–175, 1979. URL http://www.ncbi.nlm.nih.gov/pubmed/216503.

[109.] K. Kobayashi and J.R. Neely. Mechanism of Pyruvate Dehydrogenase Activation by Increased Cardiac Work. *J. Mol. Cell. Cardiol.*, 15(6):369–382, 1983. URL http://www.ncbi.nlm.nih.gov/pubmed/6876186.

[110.] M.C. Kohn, M.J. Achs, and D. Garfinkel. Computer simulation of metabolism in pyruvate-perfused rat heart. II. Krebs cycle. *Am. J. Physiol.*, 237(3):R159–R166, 1979a. URL http://www.ncbi.nlm.nih.gov/pubmed/224718.

[111.] M.C. Kohn, M.J. Achs, and D. Garfinkel. Computer simulation of metabolism in pyruvate-perfused rat heart. III. Pyruvate dehydrogenase. *Am. J. Physiol.*, 237(3):R167–173, 1979b. URL http://www.ncbi.nlm.nih.gov/pubmed/474788.

[112.] H.L. Kornberg. Anaplerotic sequences and their role in metabolism. In P.N. Campbell and G.D. Greville, editors, *Essays in Biochemistry*, volume 2, pages 1–31. Academic Press, London, U.K. and New York, N.Y., 1966.

[113.] B. Korzeniewski and W. Froncisz. An extended dynamic model of oxidative phosphorylation. *Biochim. Biophys. Acta.*, 1060(2):210–223, October 1991. URL http://www.ncbi.nlm.nih.gov/pubmed/1657162.

[114.] B. Korzeniewski and J.-P. Mazat. Theoretical studies on the control of oxidative phosphorylation in muscle mitochondria: application to mitochondrial deficiencies. *Biochem. J.*, 319(Pt 1):143–148, 1996a. URL http://www.ncbi.nlm.nih.gov/pubmed/8870661.

[115.] B. Korzeniewski and J.-P. Mazat. Theoretical studies on control of oxidative phosphorylation in muscle mitochondria at different energy demands and oxygen concentrations. *Acta Biotheor.*, 44(3–4):263–269, 1996b. URL http://www.ncbi.nlm.nih.gov/pubmed/8953212.

[116.] B. Korzeniewski, M.E. Harper, and M.D. Brand. Proportional activation coefficients during stimulation of oxidative phosphorylation by lactate and pyruvate or by vasopressin. *Biochim. Biophys. Acta.*, 1229(3): 315–322, May 1995. URL http://www.ncbi.nlm.nih.gov/pubmed/7748883.

[117.] B. Korzeniewski, V. Deschodt-Arsac, G. Calmettes, J.M. Franconi, and P. Diolez. Physiological heart activation by adrenaline involves parallel activation of ATP usage and supply. *Biochem. J.*, 413(2):343–347, July 2008. URL http://www.ncbi.nlm.nih.gov/pubmed/18377364.

[118.] H.A. Krebs and R.L. Veech. Equilibrium relations between pyridine nucleotides and adenine nucleotides and their roles in the regulation of metabolic processes. *Adv. Enzyme Regul.*, 7(1):397–413, 1969. URL http://www.ncbi.nlm.nih.gov/pubmed/4391643.

[119.] M.J. Lambeth and M.J. Kushmerick. A computational model for glycogenolysis in skeletal muscle. *Ann. Biomed. Eng.*, 30(6):808–827, 2002. URL http://www.ncbi.nlm.nih.gov/pubmed/12220081.

[120.] K.F. LaNoue and A.C. Schoolwerth. Metabolite transport in mitochondria. *Annu. Rev. Biochem.*, 48 (1):871–922, February 1979. URL http://www.ncbi.nlm.nih.gov/pubmed/38739.

[121.] K.F. LaNoue and J.R. Williamson. Interrelationships between malate-aspartate shuttle and citric acid cycle in rat heart mitochondria. *Metabolism*, 20(2):119–140, February 1971. URL http://www.ncbi.nlm.nih.gov/pubmed/4322086.

[122.] K.F. LaNoue, W.J. Nicklas, and J.R. Williamson. Control of citric acid cycle activity in rat heart mitochondria. *J. Biol. Chem.*, 245(1):102–111, 1970. URL http://www.ncbi.nlm.nih.gov/pubmed/4312474.

123. K.F. LaNoue, J. Bryla, and J.R. Williamson. Feedback interactions in the control of citric acid cycle activity in rat heart mitochondria. *J. Biol. Chem.*, 247(3):667–679, 1972. URL http://www.ncbi.nlm.nih.gov/pubmed/4333508.

124. K.F. LaNoue, E.I. Walajtys, and J.R. Williamson. Regulation of glutamate metabolism and interactions with the citric acid cycle in rat heart mitochondria. *J. Biol. Chem.*, 248(20):7171–7183, 1973. URL http://www.ncbi.nlm.nih.gov/pubmed/4355202.

125. S.H. Lee and E.J. Davis. Carboxylation and decarboxylation reactions. Anaplerotic flux and removal of citrate cycle intermediates in skeletal muscle. *J. Biol. Chem.*, 254(2):420–430, 1979. URL http://www.ncbi.nlm.nih.gov/pubmed/762069.

126. A. L. Lehninger. *Biochemistry.* Worth Publishers Inc., New York, N.Y., 1977. URL http://books.google.co.uk/books?id=5Ek9J4p3NfkC.

127. A. L. Lehninger, D.L. Nelson, and M.M. Cox. *Principles of Biochemistry*. Worth Publishers Inc., New York, N.Y.), 2nd edition, 1993. ISBN 0-87901-500-4. URL http://books.google.co.uk/books?id=5Ek9J4p3NfkC.

128. T. Letellier, R. Heinrich, M. Malgat, and J.-P. Mazat. The kinetic basis of threshold effects observed in mitochondrial diseases: a systemic approach. *Biochem. J.*, 302(Pt 1):171–174, August 1994. URL http://www.ncbi.nlm.nih.gov/pubmed/8068003.

129. P. Liguzinski and B. Korzeniewski. Metabolic control over the oxygen consumption flux in intact skeletal muscle: in silico studies. *Am. J. Physiol. Cell Physiol.*, 291(6):C1213–C1224, December 2006. URL http://www.ncbi.nlm.nih.gov/pubmed/16760266.

130. J.C. Londesborough and K. Dalziel. The equilibrium constant of the isocitrate dehydrogenase reaction. *Biochem. J.*, 110(2):217–222, November 1968. URL http://www.ncbi.nlm.nih.gov/pubmed/4387224.

131. J.M. Lowenstein. The Tricarboxylic Acid Cycle. In D.M. Greenberg, editor, *Metabolic Pathways: Energetics, Tricarboxylic Acid Cycle, and Carbohydrates*, volume I, chapter 4, pages 147–267. Academic Press, Inc., New York & London, 3rd edition, 1967. URL http://www.worldcat.org/oclc/900886404.

132. G.W. Magnus. *A mitochondria-based model for bursting and its D-glucose dependence in the pancreatic beta cell.* Ph.D. thesis, University of California, Davis, 1995. Degree granted in Chemistry.

133. G.W. Magnus and J. Keizer. Minimal model of beta-cell mitochondrial Ca^{2+} handling. *Am. J. Physiol. Cell Physiol.*, 273(2):C717–C733, August 1997. URL http://www.ncbi.nlm.nih.gov/pubmed/9277370.

134. I. Magnusson, W.C. Schumann, G.E. Bartsch, V. Chandramouli, K. Kumaran, J. Wahren, and B.R. Landau. Non-invasive tracing of Krebs cycle metabolism in liver. *J. Biol. Chem.*, 266(11):6975–6984, 1991. URL http://www.ncbi.nlm.nih.gov/pubmed/2016309.

135. W.R. McClure and H.A. Lardy. Rat liver pyruvate carboxylase. IV. Factors affecting the regulation in vivo. *J. Biol. Chem.*, 246(11):3591–3596, 1971. URL http://www.ncbi.nlm.nih.gov/pubmed/5103844.

136. W.R. McClure, H.A. Lardy, and H.P. Kneifel. Rat liver pyruvate carboxylase. I. Preparation, properties, and cation specificity. *J. Biol. Chem.*, 246(11):3569–3578, June 1971. URL http://www.ncbi.nlm.nih.gov/pubmed/5578910.

137. W.R. McClure, H.A. Lardy, M. Wagner, and W.W. Cleland. Rat liver pyruvate carboxylase. II. Kinetic studies of the forward reaction. *J. Biol. Chem.*, 246(11):3579–83, June 1971. URL http://www.ncbi.nlm.nih.gov/pubmed/5103842.

138. J.G. McCormack and R.M. Denton. The effects of calcium ions and adenine nucleotides on the activity of pig heart 2-oxoglutarate dehydrogenase complex. *Biochem. J.*, 180(3):533–544, June 1979. URL http://www.ncbi.nlm.nih.gov/pubmed/39549.

139. J.G. McCormack and R.M. Denton. A comparative study of the regulation of Ca^{2+} of the activities of the 2-oxoglutarate dehydrogenase complex and NAD^{+}-isocitrate dehydrogenase from a variety of sources. *Biochem. J.*, 196(2):619–624, May 1981. URL http://www.ncbi.nlm.nih.gov/pubmed/7032511.

140. E. Mogilevskaya, O. Demin, and I. Goryanin. Kinetic model of mitochondrial krebs cycle: unravelling the mechanism of salicylate hepatotoxic effects. *J. Biol. Phys.*, 32(3-4):245–271, 2006. URL http://www.ncbi.nlm.nih.gov/pubmed/19669466.

141. R. Moreno-Sánchez, R. Encalada, A. Marín-Hernández, and E. Saavedra. Experimental validation of metabolic pathway modelling. *FEBS J.*, 275(13):3454–3469, July 2008. URL http://www.ncbi.nlm.nih.gov/pubmed/18510554.

142. C. Nazaret, M. Heiske, K. Thurley, and J.-P. Mazat. Mitochondrial energetic metabolism: a simplified model of TCA cycle with ATP production. *J. Theor. Biol.*, 258(3):455–464, 2009. URL http://www.ncbi.nlm.nih.gov/pubmed/19007794.

143. J.R. Neely and H.E. Morgan. Relationship between carbohydrate and lipid metabolism and the energy balance of heart muscle. *Annu. Rev. Physiol.*, 63:413–459, 1974. URL http://www.ncbi.nlm.nih.gov/pubmed/19400669.

144. J.R. Neely, R.M. Denton, P.J. England, and P.J. Randle. The effects of increased heart work on the tricarboxylate cycle and its interactions with glycolysis in the perfused rat heart. *Biochem. J.*, 128(1):147–159, June 1972a. URL http://www.ncbi.nlm.nih.gov/pubmed/5085551.

145. J.R. Neely, R.M. Denton, P.J. England, and P.J. Randle. The effects of increased heart work on the tricarboxylate cycle and its interactions with glycolysis in the perfused rat heart. *Biochem. J.*, 128(1):147–159, 1972b. URL http://www.ncbi.nlm.nih.gov/pubmed/5085551.

146. C.K. Ng, S.C. Huang, H.R. Schelbert, and D.B. Buxton. Validation of a model for [1-11C]acetate as a tracer of cardiac oxidative metabolism. *Am. J. Physiol.*, 266(4, Pt 2):H1304–H1315, 1994. URL http://www.ncbi.nlm.nih.gov/pubmed/8184908.

147. K. Nishiki, D.F. Wilson, and M. Erecinska. Energy relationships between cytosolic metabolism and mitochondrial respiration in rat heart. *Am. J. Physiol. Cell Physiol.*, 234(3):C73–C81, March 1978. URL http://www.ncbi.nlm.nih.gov/pubmed/204195.

148. J.M. O'Donnell, C. Doumen, K.F. LaNoue, L.T. White, X. Yu, N.M. Alpert, and E.D. Lewandowski. Dehydrogenase regulation of metabolite oxidation and efflux from mitochondria in intact hearts. *Am. J. Physiol.*, 274(2, Pt 2):H467–H476, February 1998. URL http://www.ncbi.nlm.nih.gov/pubmed/9486249.

149. M.S. Olson and J.R. Williamson. Regulation of citrate synthesis in isolated rat liver mitochondria. *J. Biol. Chem.*, 246(24):7794–7803, 1971. URL http://www.ncbi.nlm.nih.gov/pubmed/5135321.

150. M.S. Olson, S.C. Dennis, M.S. DeBuysere, and A. Padma. The Regulation of Pyruvate Dehydrogenase in the Isolated Perfused Rat Heart. *J. Biol. Chem.*, 253(20):7369–7375, 1978. URL http://www.ncbi.nlm.nih.gov/pubmed/701258.

151. L.H. Opie. *Heart Physiology: From Cell to Circulation*. Lippincott-Raven Publishers, Philadelphia, 1998. URL http://books.google.co.uk/books?id=CPVSg69CPMsC.

152. J.F. Oram, S.L. Bennetch, and J.R. Neely. Regulation of fatty acid utilization in isolated perfused rat hearts. *J. Biol. Chem.*, 248(15):5299–5309, August 1973. URL http://www.ncbi.nlm.nih.gov/pubmed/4768902.

153. O.E. Owen, S.C. Kalhan, and R.W. Hanson. The key role of anaplerosis and cataplerosis for citric acid cycle function. *J. Biol. Chem.*, 277(34):30409–30412, August 2002. URL http://www.ncbi.nlm.nih.gov/pubmed/12087111.

154. F. Palmieri. Mitochondrial carrier proteins. *FEBS lett.*, 346(1):48–54, June 1994. URL http://www.ncbi.nlm.nih.gov/pubmed/8206158.

155. A.R. Panchal, B. Comte, H. Huang, T. Kerwin, A. Darvish, C. Des Rosiers, H. Brunengraber, and W.C. Stanley. Partitioning of pyruvate between oxidation and anaplerosis in swine hearts. *Am. J. Physiol. Heart Circ. Physiol.*, 279(5):H2390–H2398, November 2000. URL http://www.ncbi.nlm.nih.gov/pubmed/11045976.

156. A.R. Panchal, B. Comte, H. Huang, B. Dudar, B. Roth, M. Chandler, C. Des Rosiers, H. Brunengraber, and W.C. Stanley. Acute hibernation decreases myocardial pyruvate carboxylation and citrate release. *Am. J. Physiol. Heart Circ. Physiol.*, 281(4):H1613–H1620, October 2001. URL http://www.ncbi.nlm.nih.gov/pubmed/11557551.

157. D.F. Parsons, G.R. Williams, and B. Chance. Characteristics of isolated and purified preparations of the outer and inner membranes of mitochondria. *Ann. N. Y. Acad. Sci.*, 137(2):643–666, July 1966. URL http://www.ncbi.nlm.nih.gov/pubmed/4290884.

158. S. Passarella, A. Atlante, D. Valenti, and L. de Bari. The role of mitochondrial transport in energy metabolism. *Mitochondrion*, 2(5):319–343, April 2003. URL http://www.ncbi.nlm.nih.gov/pubmed/16120331.

159. K.J. Peuhkurinen, T.E. Takala, E.M. Nuutinen, and I.E. Hassinen. Tricarboxylic acid cycle metabolites during ischemia in isolated perfused rat heart. *Am. J. Physiol.*, 244(2):H281–H288, February 1983. URL http://www.ncbi.nlm.nih.gov/pubmed/6824095.

160. E. Pfaff, M. Klingenberg, E. Ritt, and W. Vogell. [Correlation of the unspecific permeable mitochondrial space with the "intermembrane space"]. *Eur. J. Biochem.*, 5(2):222–232, July 1968. URL http://www.ncbi.nlm.nih.gov/pubmed/4299136. [Article in German].

161. T. Pfeiffer, I. Sánchez-Valdenebro, J.C. Nuño, F. Montero, and S. Schuster. METATOOL: for studying metabolic networks. *Bioinformatics*, 15(3):251–257, 1999. URL http://www.ncbi.nlm.nih.gov/pubmed/10222413.

162. G.W.E. Plaut. DPN-linked Isocitrate Dehydrogenase of animal tissues. In B.L. Horecker and E.R. Stadtman, editors, *Curr. Top. Cell. Regul.*, volume 2, chapter 1, pages 1–27. Academic Press, New York & London, 1970. URL http://books.google.co.in/books?id=HzmaBQAAQBAJ&pg=PA1.

163. G.W.E. Plaut and T. Aogaichi. Purification and properties of diphosphopyridine nucleotide-linked isocitrate dehydrogenase of mammalian liver. *J. Biol. Chem.*, 243(21):5572–5583, 1968. URL http://www.ncbi.nlm.nih.gov/pubmed/4387006.

164. G.W.E. Plaut, V.L. Schramm, and T. Aogaichi. Action of magnesium ion on diphosphopyridine nucleotide-linked isocitrate dehydrogenase from bovine heart. Characterization of the forms of the substrate and the modifier of the reaction. *J. Biol. Chem.*, 249(6):1848–1856, 1974. URL http://www.ncbi.nlm.nih.gov/pubmed/4361827.

165. M.G. Poolman. ScrumPy: Metabolic modelling with Python. *IEE Proc. Syst. Biol.*, 153:375–378, 2006. URL http://www.ncbi.nlm.nih.gov/pubmed/16986321.

166. M.G. Poolman, H. Ölçer, J.C. Lloyd, C.A. Raines, and D.A. Fell. Computer modelling and experimental evidence for two steady states in the photosynthetic Calvin cycle. *Eur. J. Biochem.*, 268(10):2810–2816, 2001. URL http://www.ncbi.nlm.nih.gov/pubmed/11358496.

167. M.G. Poolman, D.A. Fell, and C.A. Raines. Elementary modes analysis of photosynthate metabolism in the chloroplast stroma. *Eur. J. Biochem.*, 270(3):430–439, 2003. URL http://www.ncbi.nlm.nih.gov/pubmed/12542693.

168. M.G. Poolman, C. Sebu, M.K. Pidcock, and D.A. Fell. Modular decomposition of metabolic systems via null-space analysis. *J. Theor. Biol.*, 249(4):691–705, 2007. URL http://www.ncbi.nlm.nih.gov/pubmed/17949756.

169. L. Pritchard and D.B. Kell. Schemes of flux control in a model of Saccharomyces cerevisiae glycolysis. *Eur. J. Biochem.*, 269(16):3894–3904, August 2002. URL http://www.ncbi.nlm.nih.gov/pubmed/12180966.

170. M. Rabkin and J. J. Blum. Quantitative analysis of intermediary metabolism in hepatocytes incubated in the presence and absence of glucagon with a substrate mixture containing glucose, ribose, fructose, alanine and acetate. *Biochem. J.*, 225:761–786, 1985. URL http://www.ncbi.nlm.nih.gov/pubmed/3919712.

171. P.J. Randle, P.J. England, and R.M. Denton. Control of the tricarboxylate cycle and its interactions with glycolysis during acetate utilization in rat heart. *Biochem. J.*, 117(4):677–695, May 1970. URL http://www.ncbi.nlm.nih.gov/pubmed/5449122.

172. B.B. Rasmussen and R.R. Wolfe. Regulation of fatty acid oxidation in skeletal muscle. *Annu. Rev. Nutr.*, 19(1):463–484, 1999. URL http://www.ncbi.nlm.nih.gov/pubmed/10448533.

173. C. Reder. Metabolic control theory: a structural approach. *J. Theor. Biol.*, 135(2):175–201, 1988. URL http://www.ncbi.nlm.nih.gov/pubmed/3267767.

174. L.J. Reed, T.C. Linn, F.H. Pettit, R.M. Oliver, F. Hucho, J.W. Pelley, D.D. Randall, and T.E. Roche. Pyruvate Dehydrogenase Complex: Structure, Function, and Regulation : [proceedings of Metabolic Regulation: Energy metabolism and the Regulation of Metabolic Processes in Mitochondria ; held at University of Nebraska Medical School Omaha, Nebraska on May 3-4, 1971]. In M.A. Mehlman and R.W. Hanson, editors, *Energy metabolism and the Regulation of Metabolic Processes in Mitochondria*, Symposia on Metabolic Regulation, pages 253–270, New York, N.Y. and London, U.K., 1972. Academic Press. URL http://www.sciencedirect.com/science/article/pii/B9780124878501500191.

175. J. M. Rohwer, A. J. Hanekom, C. Crous, J. L. Snoep, and J. H. Hofmeyr. Evaluation of a simplified generic bi-substrate rate equation for computational systems biology. *Syst. Biol. (Stevenage).*, 153:338–341, 2006. URL http://www.ncbi.nlm.nih.gov/pubmed/16986312.

176. J.M. Rohwer and F.C. Botha. Analysis of sucrose accumulation in the sugar cane culm on the basis of in vitro kinetic data. *Biochem. J.*, 358(Pt 2):437–445, 2001. URL http://www.ncbi.nlm.nih.gov/pubmed/11513743.

177. R.R. III Russell and H. Taegtmeyer. Pyruvate carboxylation prevents the decline in contractile function of rat hearts oxidizing acetoacetate. *Am. J. Physiol.*, 261(6, Pt 2):H1756–H1762, December 1991. URL http://www.ncbi.nlm.nih.gov/pubmed/1750532.

178. G.A. Rutter and R.M. Denton. Regulation of NAD^+-linked isocitrate dehydrogenase and 2-oxoglutarate dehydrogenase by Ca^{2+} ions within toluene-permeabilized rat heart mitochondria. Interactions with regulation by adenine nucleotides and $NADH/NAD^+$ ratios. *Biochem. J.*, 252(1):181–189, May 1988. URL http://www.ncbi.nlm.nih.gov/pubmed/3421900.

179. B. Safer and J.R. Williamson. Mitochondrial-cytosolic interactions in perfused rat heart. Role of coupled transamination in repletion of citric acid cycle intermediates. *J. Biol. Chem.*, 248(7):2570–2579, 1973. URL http://www.ncbi.nlm.nih.gov/pubmed/4349041.

180. B. Safer, C.M. Smith, and J.R. Williamson. Control of the transport of reducing equivalents across the mitochondrial membrane in perfused rat heart. *J. Mol. Cell. Cardiol.*, 2(2):111–124, June 1971. URL http://www.ncbi.nlm.nih.gov/pubmed/4329775.

181. L.A. Sazanov and J.B. Jackson. Possible functions of the NADP-linked isocitrate dehydrogenase and H(+)-transhydrogenase in heart mitochondria. *Biochem. Soc. Trans.*, 21(3, Pt 3):260S, August 1993. URL http://www.ncbi.nlm.nih.gov/pubmed/8224412.

182. L.A. Sazanov and J.B. Jackson. Proton-translocating transhydrogenase and NAD- and NADP-linked isocitrate dehydrogenases operate in a substrate cycle which contributes to fine regulation of the tricarboxylic acid cycle activity in mitochondria. *FEBS lett.*, 344(2-3):109–116, May 1994. URL http://www.ncbi.nlm.nih.gov/pubmed/8187868.

183. L.A. Sazanov and J.B. Jackson. Cyclic reactions catalysed by detergent-dispersed and reconstituted transhydrogenase from beef-heart mitochondria; implications for the mechanism of proton translocation. *Biochim. Biophys. Acta.*, 1231(3):304–312, October 1995. URL http://www.ncbi.nlm.nih.gov/pubmed/7578218.

184. C.H. Schilling, S. Schuster, B.Ø. Palsson, and R. Heinrich. Metabolic pathway analysis: basic concepts and scientific applications in the post-genomic era. *Biotechnol. Prog.*, 15(3):296–303, 1999. URL http://www.ncbi.nlm.nih.gov/pubmed/10356246.

185. S. Schuster and C. Hilgetag. On Elementary Flux Modes in Biochemical Systems at Steady State. *J. Biol. Syst.*, 2(2):165–182, 1994. URL http://dx.doi.org/10.1142/S0218339094000131.

186. S. Schuster, T. Dandekar, and D.A. Fell. Detection of Elementary Flux Modes in Biochemical Networks: a Promising Tool for Pathway Analysis and Metabolic Engineering. *Trends. Biotech.*, 17(2):53–60, 1999. URL http://www.ncbi.nlm.nih.gov/pubmed/10087604.

187. S. Schuster, D.A. Fell, and T. Dandekar. A general definition of metabolic pathways useful for systematic organization and analysis of complex metabolic networks. *Nat. biotech.*, 18(3):326–332, March 2000. URL http://www.ncbi.nlm.nih.gov/pubmed/10700151.

188. S. Schuster, C. Hilgetag, J.H. Woods, and D.A. Fell. Reaction routes in biochemical reaction systems: algebraic properties, validated calculation procedure and example from nucelotide metabolism. *J. Math. Biol.*, 45:153–181, 2002a. URL http://www.ncbi.nlm.nih.gov/pubmed/12181603.

189. S. Schuster, S. Klamt, W. Weckwerth, F. Moldenhauer, and T. Pfeiffer. Use of network analysis of metabolic systems in bioengineering. *Bioproc. Biosys. Eng.*, 24(6):363–372, 2002b. URL http://link.springer.com/article/10.1007/s004490100253.

190. W.D. Schwenke, S. Soboll, H.J. Seitz, and H. Sies. Mitochondrial and cytosolic ATP/ADP ratios in rat liver in vivo. *Biochem. J.*, 200(2):405–408, November 1981. URL http://www.ncbi.nlm.nih.gov/pubmed/7340839.

191. M.C. Scrutton. Pyruvate carboxylase. Studies of activator-independent catalysis and of the specificity of activation by acyl derivatives of coenzyme A for the enzyme from rat liver. *J. Biol. Chem.*, 249(22): 7057–7067, 1974. URL http://www.ncbi.nlm.nih.gov/pubmed/4612033.

192. M.C. Scrutton and M.F. Utter. Pyruvate carboxylase. IX. Some properties of the activation by certain acyl derivatives of coenzyme A. *J. Biol. Chem.*, 242(8):1723–1735, 1967. URL http://www.ncbi.nlm.nih.gov/pubmed/6024765.

193. M.C. Scrutton and M.F. Utter. The Regulation of Glycolysis and Gluconeogenesis in Animal Tissues. *Annu. Rev. Biochem.*, 37(1):249–302, June 1968. URL http://www.annualreviews.org/doi/abs/10.1146/annurev.bi.37.070168.001341.

194. M.C. Scrutton and M.D. White. Pyruvate carboxylase from rat liver: catalytic properties in the absence, and at low concentrations, of acetyl-CoA. *Biochem. Biosys. Res. Commun.*, 48(1):85–93, 1972. URL http://www.ncbi.nlm.nih.gov/pubmed/5041883.

195. I.H. Segel. *Enzyme Kinetics: Behavior and Analysis of Rapid Equilibrium and Steady-State Enzyme Systems*, volume 44 of *Wiley Classics Library*. John Wiley & Sons Inc., New York, illustrated edition, 1993. URL http://www.worldcat.org/oclc/865328408.

196. N. Sharma, I.C. Okere, D.Z. Brunengraber, T.A. McElfresh, K.L. King, J.P. Sterk, H. Huang, M.P. Chandler, and W.C. Stanley. Regulation of pyruvate dehydrogenase activity and citric acid cycle intermediates during high cardiac power generation. *J. Physiol.*, 562(Pt 2):593–603, January 2005. URL http://www.ncbi.nlm.nih.gov/pubmed/15550462.

197. D. Shepherd and P.B. Garland. The kinetic properties of citrate synthase from rat liver mitochondria. *Biochem. J.*, 114(3):597–610, September 1969. URL http://www.ncbi.nlm.nih.gov/pubmed/5820645.

198. E. A. Siess, D. G. Brocks, and O. H. Wieland. In H. Sies, editor, *Metabolic compartmentation*, pages 235–257. Academic Press, London & New York, illustrated edition, 1982a. URL http://www.worldcat.org/oclc/489706487.

199. E.A. Siess and O.H. Wieland. Regulation of pyruvate dehydrogenase interconversion in isolated hepatocytes by the mitochondrial ATP/ADP ratio. *FEBS lett.*, 52(2):226–230, April 1975. URL http://www.ncbi.nlm.nih.gov/pubmed/1132478.

200. E.A. Siess and O.H. Wieland. Phosphorylation state of cytosolic and mitochondrial adenine nucleotides and of pyruvate dehydrogenase in isolated rat liver cells. *Biochem. J.*, 156(1):91–102, April 1976. URL http://www.ncbi.nlm.nih.gov/pubmed/133678.

201. E.A. Siess, D.G. Brocks, and O.H. Wieland. Subcellular distribution of key metabolites in isolated liver cells from fasted rats. *FEBS lett.*, 69(1-2):265–271, 1976. URL http://www.ncbi.nlm.nih.gov/pubmed/992036.

202. E.A. Siess, R.I. Kientsch-Engel, and O.H. Wieland. Role of free oxaloacetate in ketogenesis. Derivation from the direct measurement of mitochondrial [β-hydroxybutyrate]/[acetoacetate] ratio in hepatocytes. *Eur. J. Biochem./FEBS*, 121(3):493–499, January 1982b. URL http://www.ncbi.nlm.nih.gov/pubmed/7056252.

203. F.E. Sluse, A.J. Meijer, and J.M. Tager. Anion translocators in rat-heart mitochondria. *FEBS lett.*, 18(1):149–153, October 1971. URL http://www.ncbi.nlm.nih.gov/pubmed/11946108.

204. J.R. Small and H. Kacser. Responses of metabolic systems to large changes in enzyme activities and effectors. 1. The linear treatment of unbranched chains. *Eur. J. Biochem./FEBS*, 213(1):613–624, April 1993. URL http://www.ncbi.nlm.nih.gov/pubmed/8477732.

205. C.M. Smith and G.W.E. Plaut. Activities of NAD^+-specific and $NADP^+$-specific isocitrate dehydrogenases in rat-liver mitochondria. Studies with D-threo-alpha-methylisocitrate. *Eur. J. Biochem./FEBS*, 97 (1):283–295, 1979. URL http://www.ncbi.nlm.nih.gov/pubmed/38961.

206. C.M. Smith and J.R. Williamson. Inhibition of citrate synthase by succinyl-CoA and other metabolites. *FEBS lett.*, 18(1):35–38, October 1971. URL http://www.ncbi.nlm.nih.gov/pubmed/11946076.

207. C.M. Smith, J. Bryla, and J.R. Williamson. Regulation of mitochondrial α-ketoglutarate metabolism by product inhibition at α-ketoglutarate dehydrogenase. *J. Biol. Chem.*, 249(5):1497–1505, 1974. URL http://www.ncbi.nlm.nih.gov/pubmed/4361738.

208. S. Soboll, R. Scholz, and H.W. Heldt. Subcellular Metabolite Concentrations. Dependence of Mitochenodrial and Cytosolic ATP Systems on the Metabolic State of Perfuse Rat Liver. *Eur. J. Biochem.*, 87(2):377–390, June 1978. URL http://www.ncbi.nlm.nih.gov/pubmed/668699.

209. S. Soboll, T.P.M. Akerboom, W.D. Schwenke, R. Haase, and H. Sies. Mitochondrial and cytosolic ATP/ADP ratios in isolated hepatocytes. A comparison of the digitonin method and the non-aqueous fractionation procedure. *Biochem. J.*, 192(3):951–954, 1980. URL http://www.ncbi.nlm.nih.gov/pubmed/7236247.

210. G.L. Sottocasa, B. Kuylenstierna, L. Ernster, and A. Bergstrand. Separation and some enzymatic properties of the inner and outer membranes of rat liver mitochondria. *Meth. Enzymol.*, 10(1):448–463, 1967. URL http://www.sciencedirect.com/science/article/pii/0076687967100773.

211. R.G. Spencer, J.A. Balschi, J.S. Leigh Jr., and J.S. Ingwall. ATP synthesis and degradation rates in the perfused rat heart. ^{31}P-nuclear magnetic resonance double saturation transfer measurements. *Biophys. J.*, 54(5):921–929, November 1988. URL http://www.ncbi.nlm.nih.gov/pubmed/3242635.

212. P.A. Srere. Is there an organization of Krebs cycle enzymes in the mitochondrial matrix? : [proceedings of Metabolic Regulation: Energy metabolism and the Regulation of Metabolic Processes in Mitochondria ; held at University of Nebraska Medical School Omaha, Nebraska on May 3-4, 1971]. In M.A. Mehlman and R.W. Hanson, editors, *Energy metabolism and the Regulation of Metabolic Processes in Mitochondria*, Symposia on Metabolic Regulation, pages 79–91, New York, N.Y. and London, U.K., 1972. Academic Press. URL http://www.sciencedirect.com/science/article/pii/B9780124878501500117.

213. P.A. Srere. Controls of citrate synthase activity. *Life Sci.*, 15(10):1695–1710, 1974. URL http://www.ncbi.nlm.nih.gov/pubmed/4621239.

[214.] W.C. Stanley, F.A. Recchia, and G.D. Lopaschuk. Myocardial substrate metabolism in the normal and failing heart. *Physiol. Rev.*, 85(3):1093–1129, 2005. URL http://www.ncbi.nlm.nih.gov/pubmed/15987803.

[215.] G. Stephanopoulos and J.J. Vallino. Network rigidity and metabolic engineering in metabolite overproduction. *Science*, 252(5013):1675–1681, 1991. URL http://www.ncbi.nlm.nih.gov/pubmed/1904627.

[216.] M. Stitt, W.P. Quick, U. Schurr, E.-D. Schulze, S.R. Rodermel, and L. Bogorad. Decreased ribulose-1,5-bisphosphate carboxylase-oxygenase in transgenic tobacco transformed with 'antisense' rbcS : II. Flux-control coefficients for photosynthesis in varying light, CO_2, and air humidity. *Planta*, 183(4):555–566, 1991. URL http://www.ncbi.nlm.nih.gov/pubmed/24193849.

[217.] S. Strumiło. Short-term regulation of the mammalian pyruvate dehydrogenase complex. *Acta biochimica Polonica*, 52(4):759–764, January 2005. URL http://www.ncbi.nlm.nih.gov/pubmed/16025163.

[218.] L. Stryer. *Biochemistry*. W. H. Freeman, New York, N.Y., 2002. URL http://books.google.co.uk/books?id=pLBpAAAAMAAJ.

[219.] M. Stubbs, R.L. Veech, and H.A. Krebs. Control of the redox state of the nicotinamide-adenine dinucleotide couple in rat liver cytoplasm. *Biochem. J.*, 126(1):59–65, January 1972. URL http://www.ncbi.nlm.nih.gov/pubmed/4342386.

[220.] J.W. Stucki and P. Walter. Pyruvate metabolism in mitochondria from rat liver. Measured and computer-simulated fluxes. *Eur. J. Biochem.*, 30(1):60–72, 1972. URL http://www.ncbi.nlm.nih.gov/pubmed/4263926.

[221.] J.W. Stucki, F. Brawand, and P. Walter. Regulation of pyruvate metabolism in rat-liver mitochondria by adenine nucleotides and fatty acids. *Eur. J. Biochem./FEBS*, 27(1):181–191, May 1972. URL http://www.ncbi.nlm.nih.gov/pubmed/5049053.

[222.] K.E. Sundqvist, J.K. Hiltunen, and I.E. Hassinen. Pyruvate carboxylation in the rat heart. Role of biotin-dependent enzymes. *Biochem. J.*, 257(3):913–916, February 1989. URL http://www.ncbi.nlm.nih.gov/pubmed/2930495.

[223.] H. Taegtmeyer, Razeghi P Wilson CR, and Sharma S. Myocardial substrate metabolism in the normal and failing heart. *Physiol. Rev.*, 85:1093–1129, 2005.

[224.] M.E. Tischler, P. Hecht, and J.R. Williamson. Effect of ammonia on mitochondrial and cytosolic NADH and NADPH systems in isolated rat liver cells. *FEBS lett.*, 76(1):99–104, April 1977. URL http://www.ncbi.nlm.nih.gov/pubmed/15869.

[225.] N.V. Torres, F. Mateo, E. Meléndez-Hevia, and H. Kacser. Kinetics of metabolic pathways. A system in vitro to study the control of flux. *Biochem. J.*, 234(1):169–174, February 1986. URL http://www.ncbi.nlm.nih.gov/pubmed/3707539.

[226.] N.V. Torres, R. Souto, and E. Meléndez-Hevia. Study of the flux and transition time control coefficient profiles in a metabolic system in vitro and the effect of an external stimulator. *Biochem. J.*, 260(3):763–769, June 1989. URL http://www.ncbi.nlm.nih.gov/pubmed/2764903.

[227.] S. Tran-Dinh, J.A. Hoerter, P. Mateo, F. Bouet, and M. Herve. A Simple Mathematical Model and Practical Approach for Evaluating Citric Acid Cycle Fluxes in Perfused Rat Hearts by ^{13}C-NMR and ^{1}H-NMR Spectroscopy. *Eur. J. Biochem./FEBS*, 245(2):497–504, April 1997. URL http://www.ncbi.nlm.nih.gov/pubmed/9151985.

[228.] S. Tran-Dinh, J.A. Hoerter, P. Mateo, F. Gyppaz, and M. Herve. ^{13}C-NMR spectroscopic evaluation of the citric acid cycle flux in conditions of high aspartate transaminase activity in glucose-perfused rat hearts. *Biochimie*, 80(12):1013–1024, December 1998. URL http://www.ncbi.nlm.nih.gov/pubmed/9924979.

[229.] C.T. Trinh, A. Wlaschin, and F. Srienc. Elementary mode analysis: a useful metabolic pathway analysis tool for characterizing cellular metabolism. *Appl. Microbiol. Biotechnol.*, 81(5):813–826, 2009. URL http://www.ncbi.nlm.nih.gov/pubmed/19015845.

[230.] C.S. Tsai, M.W. Burgett, and L.J. Reed. α-Keto acid dehydrogenase complexes. XX. A kinetic study of the pyruvate dehydrogenase complex from bovine kidney. *J. Biol. Chem.*, 248(24):8348–8352, 1973. URL http://www.ncbi.nlm.nih.gov/pubmed/4357736.

[231.] M.L. Uhr, V.W. Thompson, and W.W. Cleland. The kinetics of pig heart triphosphopyridine nucleotide-isocitrate dehydrogenase. I. Initial velocity, substrate and product inhibition, and isotope exchange studies. *J. Biol. Chem.*, 249(9):2920–2927, 1974. URL http://www.ncbi.nlm.nih.gov/pubmed/4151308.

[232.] R.R. Vallabhajosyula, V. Chickarmane, and H.M. Sauro. Conservation analysis of large biochemical networks. *Bioinformatics*, 22(3):346–353, February 2006. URL http://www.ncbi.nlm.nih.gov/pubmed/16317075.

[233.] R.L. Veech, L.V. Eggleston, and H.A. Krebs. The redox state of free nicotinamide-adenine dinucleotide phosphate in the cytoplasm of rat liver. *Biochem. J.*, 115(4):609–619, December 1969. URL http://www.ncbi.nlm.nih.gov/pubmed/4391039.

[234.] G. von Glutz and P. Walter. Compartmentation of acetyl-CoA in rat-liver mitochondria. *Eur. J. Biochem./FEBS*, 60(1):147–152, December 1975. URL http://www.ncbi.nlm.nih.gov/pubmed/1204636.

[235.] G. von Glutz and P. Walter. Regulation of pyruvate carboxylation by acetyl-CoA in rat liver mitochondria. *FEBS lett.*, 72(2):299–303, December 1976. URL http://www.ncbi.nlm.nih.gov/pubmed/16386045.

[236.] R.G. Weiss, M.D. Stern, C.P. de Albuquerque, K. Vandegaer, V.P. Chacko, and G. Gerstenblith. Consequences of altered aspartate aminotransferase activity on ^{13}C-glutamate labelling by the tricarboxylic acid cycle in intact rat hearts. *Biochim. Biophys. Acta.*, 1243(3):543–548, April 1995. URL http://www.ncbi.nlm.nih.gov/pubmed/7727532.

[237.] H.V. Westerhoff and D.B. Kell. Matrix method for determining steps most rate-limiting to metabolic fluxes in biotechnological processes. *Biotechnol. Bioeng.*, 30(1):101–107, July 1987. URL http://www.ncbi.nlm.nih.gov/pubmed/18576589.

[238.] H.V. Westerhoff, A.K. Groen, and R.J.A. Wanders. Modern theories of metabolic control and their applications. *Biosci. Rep.*, 4(1):1–22, 1984. URL http://www.ncbi.nlm.nih.gov/pubmed/6365197.

[239.] R.L. White and B.A. Wittenberg. NADH fluorescence of isolated ventricular myocytes: effects of pacing, myoglobin, and oxygen supply. *Biophys. J.*, 65(1):196–204, July 1993. URL http://www.ncbi.nlm.nih.gov/pubmed/8369428.

[240.] O.H. Wieland. The mammalian pyruvate dehydrogenase complex: structure and regulation. *Rev. Physiol. Biochem. Pharmacol.*, 96(1):123–170, 1983. URL http://www.ncbi.nlm.nih.gov/pubmed/6338572.

[241.] D.H. Williamson and J.T. Brosnan. Concentrations of Metabolites in Animal Tissues. *Meth. Enzym. Anal.*, 4(1):2266–2302, 1974. URL http://www.sciencedirect.com/science/article/pii/B9780120913046500938.

[242.] D.H. Williamson, P. Lund, and H.A. Krebs. The Redox State of Free Nicotinamide-Adenine Dinucleotide in the Cytoplasm and Mitochondria of Rat Liver. *Biochem. J.*, 103(2):514–527, May 1967a. URL http://www.ncbi.nlm.nih.gov/pubmed/4291787.

[243.] J.R. Williamson. In S. Papa, J.M. Tager, E. Quagliariello, and E.C. Slater, editors, *The Energy Level and Metabolic Control in Mitochondria : [proceedings of the Round Table Discussion on the Energy Level and Metabolic Control in Mitochondria ; organized by the Department of Biochemistry, University of Bari (Italy) and the Laboratory of Biochemistry, University of Amsterdam (The Netherlands), held in Polignaro a Mare, May 13-16, 1968]*, volume XV, pages 385–400, Bari, Italy, 1969. Adriatica Editrice. URL http://www.worldcat.org/oclc/67268.

[244.] J.R. Williamson. Mitochondrial function in the heart. *Annu. Rev. Physiol.*, 41(1):485–506, 1979. URL http://www.ncbi.nlm.nih.gov/pubmed/373602.

245. J.R. Williamson and R.H. Cooper. Regulation of the citric acid cycle in mammalian systems. *FEBS lett.*, 117(Suppl.):K73–K85, 1980. URL http://www.ncbi.nlm.nih.gov/pubmed/6998729.

246. J.R. Williamson and B.E. Corkey. Assays of intermediates of the citric acid cycle and related compounds by fluorometric enzyme methods. *Meth. Enzymol.*, 13(1):434–513, 1969. URL http://www.sciencedirect.com/science/article/pii/0076687969130724.

247. J.R. Williamson and M.S. Olson. Control of citrate and acetoacetate synthesis in rat liver. *Biochem. Biosys. Res. Commun.*, 32(5):794–799, 1968. URL http://www.ncbi.nlm.nih.gov/pubmed/5682303.

248. J.R. Williamson, M.S. Olson, B.E. Herczeq, and H.S. Coles. Control of citrate formation in rat liver mitochondria. *Biochem. Biosys. Res. Commun.*, 27(5):595–600, 1967b. URL http://www.ncbi.nlm.nih.gov/pubmed/6033144.

249. J.R. Williamson, E.T. Browning, and M.S. Olson. Interrelations between fatty acid oxidation and the control of gluconeogenesis in perfused rat liver. *Adv. Enzyme Regul.*, 6(1):67–100, 1968. URL http://www.ncbi.nlm.nih.gov/pubmed/5721291.

250. J.R. Williamson, R. Scholz, and E.T. Browning. Control mechanisms of gluconeogenesis and ketogenesis. II. Interactions between fatty acid oxidation and the citric acid cycle in perfused rat liver. *J. Biol. Chem.*, 244(17):4617–4627, 1969a. URL http://www.ncbi.nlm.nih.gov/pubmed/5808508.

251. J.R. Williamson, R. Scholz, E.T. Browning, R.G. Thurman, and M.H. Fukami. Metabolic effects of ethanol in perfused rat liver. *J. Biol. Chem.*, 244(18):5044–5054, September 1969b. URL http://www.ncbi.nlm.nih.gov/pubmed/4390471.

252. J.R. Williamson, C.M. Smith, K.F. LaNoue, and J. Bryla. Feedback Control of The Citric Acid Cycle : [proceedings of Metabolic Regulation: Energy metabolism and the Regulation of Metabolic Processes in Mitochondria ; held at University of Nebraska Medical School Omaha, Nebraska on May 3-4, 1971]. In M.A. Mehlman and R.W. Hanson, editors, *Energy metabolism and the Regulation of Metabolic Processes in Mitochondria*, Symposia on Metabolic Regulation, pages 185–210, New York and London, 1972. Academic Press. URL http://www.sciencedirect.com/science/article/pii/B9780124878501500166.

253. J.R. Williamson, B. Safer, K.F. LaNoue, C.M. Smith, and E. Walajtys. Mitochondrial-cytosolic interactions in cardiac tissue: role of the malate-aspartate cycle in the removal of glycolytic NADH from the cytosol. In D.D. Davis, editor, *Symposia of the Society for Experimental Biology*, volume 27, pages 241–281, Oxford, 1973. Cambridge University Press.

254. J.R. Williamson, C. Ford, J. Illingworth, and B. Safer. Coordination of citric acid cycle activity with electron transport flux. *Circ. Res.*, 38(5 (Suppl 1)):I39–I51, May 1976. URL http://www.ncbi.nlm.nih.gov/pubmed/1269091.

255. H. Wohlrab. Molecular aspects of inorganic phosphate transport in mitochondria. *Biochim. Biophys. Acta.*, 853(2):115–134, 1986. URL http://www.ncbi.nlm.nih.gov/pubmed/3548824.

256. A.B. Wojtczak. Control of acetoacetate and β-hydroxybutyrate production in rat liver mitochondria. *Biochem. Biosys. Res. Commun.*, 31(4):634–640, May 1968. URL http://www.ncbi.nlm.nih.gov/pubmed/5656251.

257. H.G. Wood, J.J. Davis, and H. Lochmüller. The Equilibria of Reactions Catalyzed by Carboxytransphosphorylase, Carboxykinase, and Pyruvate Carboxylase and the Synthesis of Phosphoenolpyruvate. *J. Biol. Chem.*, 241(23):5692–5704, 1966. URL http://www.ncbi.nlm.nih.gov/pubmed/4288897.

258. F. Wu, F. Yang, K.C. Vinnakota, and D.A. Beard. Computer modelling of mitochondrial tricarboxylic acid cycle, oxidative phosphorylation, metabolite transport, and electrophysiology. *J. Biol. Chem.*, 282(34): 24525–24537, 2007. URL http://www.ncbi.nlm.nih.gov/pubmed/17591785.

259. D.W. Yates and P.B. Garland. The partial latency and intramitochondrial distribution of carnitine-palmitoyltransferase (E.C.2.3.1.-), and the CoASH and carnitine permeable space of rat liver mitochondria. *Biochem. Biosys. Res. Commun.*, 23(4):460–465, May 1966. URL http://www.ncbi.nlm.nih.gov/pubmed/5962271.

260. X. Yu, L.T. White, C. Doumen, L.A. Damico, K.F. LaNoue, N.M. Alpert, and E.D. Lewandowski. Kinetic analysis of dynamic ^{13}C NMR spectra: metabolic flux, regulation, and compartmentation in hearts. *Biophys. J.*, 69(5):2090–2102, November 1995. URL http://www.ncbi.nlm.nih.gov/pubmed/8580353.

261. K. Yugi and M. Tomita. A general computational model of mitochondrial metabolism in a whole organelle scale. *Bioinformatics*, 20(11):1795–1796, July 2004. URL http://www.ncbi.nlm.nih.gov/pubmed/14962921.

262. S. Zhao, W. Xu, W. Jiang, W. Yu, Y. Lin, T. Zhang, J. Yao, L. Zhou, Y. Zeng, H. Li, Y. Li, J. Shi, W. An, S.M. Hancock, F. He, L. Qin, J. Chin, P. Yang, X. Chen, Q. Lei, Y. Xiong, and K.-L. Guan. Regulation of cellular metabolism by protein lysine acetylation. *Science*, 327(5968):1000–1004, February 2010. URL http://www.ncbi.nlm.nih.gov/pubmed/20167786.

263. J.L. Zweier and W.E. Jacobus. Substrate-induced alterations of high energy phosphate metabolism and contractile function in the perfused heart. *J. Biol. Chem.*, 262(17):8015–8021, June 1987. URL http://www.ncbi.nlm.nih.gov/pubmed/3597359.

Supplement I: Liver TCA cycle models

I.1 Suppl. data : Model definition for liver TCA model

▪ **Supplemental Table I.1.** Values of TCA cycle variables in liver tissue taken from the literature and predicted by the model [j,k,l,m,n]

Fluxes are in units of mmol/sec and concentrations in mM.

Variable	Literature Values		Model Values	Reference
	Range	Median		
TCA cycle (CS) flux	0.04 – 0.48	0.24	0.27	(9; 11; 13; 24; 30; 32; 41; 55; 104; 121)
PC flux	0.05 – 4.5 [b]	0.70 [b]	0.82	(9; 13; 30; 32; 83; 104)
MDH flux	−0.63 – −4.0E-04 [c]	−0.07	−0.55	(9; 30; 104)
MC flux	0.03 – 1.0 [d]	0.34	0.82	(9; 30; 104)
$[CoA_m]$ [a]	0.31 – 1.93	1.92	1.67	(152; 154)
$[AcCoA_m]$	0.14 – 0.49	0.25	0.35	(38; 118; 152; 154)
$[Cit_m]$	1.7 – 5.5	3.73	3.57	(2; 58; 116; 118; 165)
$[Isocit_m]$	0.14 – 0.62	0.15	0.19	(58; 116; 152)
$[\alpha KG_m]$	0.38 – 2.8	1.3	1.34	(58; 116; 118; 121)
$[Suc_m]$	1.5	– [h]	1.64	(118)
$[SCoA_m]$	0.30 – 1.4	– [h]	0.68	(123)
$[Fum_m]$	–	– [h]	0.34	–
$[Mal_m]$	0.23 – 2.5	1.26	1.41	(36; 58; 68; 118; 151; 152)
$[OAA_m]$	4.0E-05 – 2.71E-02	2.26E-03	4.05E-04	(36; 118; 121; 126; 151; 152)
$[NAD^+_m]$	0.41 – 1.93	1.25	1.22 [i]	(48; 103; 117; 152)
$[NADH_m]$	0.20 – 1.25	0.51	0.88 [i]	(48; 103; 117; 122; 152)
$[ADP_m]$	3.11 – 9.0 [e]	6.12 [e]	3.06	(2; 82; 111; 118; 133; 165)
$[ATP_m]$	3.19 – 13.65 [f]	7.64 [f]	7.34	(2; 58; 82; 111; 118; 133; 165)
Free [g] $[ADP_c]$	0.04 – 0.20	0.17	0.14	(21; 26; 94; 139)
Free [g] $[ATP_c]$	2.62 – 7.4	4.76	4.67	(2; 22; 31; 111; 118; 133; 136)

[a] In the original liver TCA cycle model, CoA_m was a fixed parameter. In the updated liver TCA cycle model, it has been correctly re-defined as a model variable.

[b] PC flux apparently ranges between 1.3 and 9.4 times TCA cycle flux in liver, and is on average around three times TCA cycle flux (Baranyai and Blum, 1989; Beylot et al., 1995; Des Rosiers et al., 1995; Di Donato et al., 1993; Magnusson et al., 1991; Rabkin and Blum, 1985).

[c] MDH flux apparently ranges between −1.3 and −0.01 times TCA cycle flux in liver, and is on average around −0.3 times TCA cycle flux (Baranyai and Blum, 1989; Des Rosiers et al., 1995; Rabkin and Blum, 1985).

[d] MC flux apparently ranges between 0.67 and 2.1 times TCA cycle flux in liver, and is on average around 1.4 times TCA cycle flux (Baranyai and Blum, 1989; Des Rosiers et al., 1995; Rabkin and Blum, 1985).

[e] Calculated from reported total mitochondrial ADP concentrations, assuming that $\left[\mathrm{MgADP}\right]$ is approximately 55% of total free $[\mathrm{ADP_m}]$ (Akerboom et al., 1978; Magnus and Keizer, 1997).

[f] Calculated from reported total mitochondrial ATP concentrations, assuming that $\left[\mathrm{MgATP}\right]$ is approximately 95% of total free $[\mathrm{ATP_m}]$ (Akerboom et al., 1978; Magnus and Keizer, 1997).

[g] Not bound to fixed sites; in the case of ATP, fixed-site binding can be viewed as negligible (Magnus and Keizer, 1997).

[h] Fewer than three reported values, hence a median value was not determined.

[i] Total liver tissue mitochondrial $[\mathrm{NAD^+_m}] + [\mathrm{NADH_m}]$ apparently varies between 0.75 and 3.0 mM, and is on average 2.1 mM (Hawtrey, 1962; Purvis, 1960; Siess et al., 1982a; Williamson, 1969).

[j] The predicted model values are obtained at steady-state, upon simulating the updated liver TCA cycle model. These are the same values shown in the analysis of initial initial steady-state of the model, in the results section.

[k] Table I.1 is reproduced from the main text of the article and expanded to include the sources of the literature data.

[l] Metabolite and effector concentrations reported in units of moles per gram of wet or dry tissue weight were converted to units of mM assuming a liver tissue dry/wet weight ratio of 0.26 (Söling, 1982) and a cell volume/weight ratio of 2.1 ml g^{-1} dry weight (Siess et al., 1982b).

[m] Concentrations reported in units of moles per gram of mitochondrial protein were similarly converted assuming a mitochondrial protein density of 272500 mg l^{-1} (Vinnakota and Bassingthwaighte, 2004).

[n] In determining mitochondrial fluxes and concentrations, the mitochondrial/cell volume ratio for liver tissue was taken to be 0.1 (Söling, 1982).

Parameter values are largely derived from the literature, and unless otherwise specified are for mammalian (predominantly rat) liver mitochondria. Wherever possible, values determined under conditions approximating the in vivo mitochondrial environment are used; a mitochondrial matrix pH of 8 is assumed (Abad et al., 2004; Lambert and Brand, 2004; Llopis et al., 1998; Matsuyama et al., 2000; Wiederkehr et al., 2009). Concentrations were converted to units of mM, and from cellular/ cytosolic to mitochondrial, using the conversion factors listed above.

- **Supplemental Table I.2.** Parameter Values for the Liver TCA cycle model

Equation	Parameter	Value	Units	Reference
A.16	$[A_{Tot_c}]$	4.81 [b,d]	mM	(2; 21; 118; 133; 139) (22; 26; 31; 94; 136)
B.13 & B.18	$[Ca^{2+}]$ [a]	6.0E-03	mM	(22)
B.16	$[CO_2]$	1.63	mM	(139)
A.13	$[CoA_{Tot_m}]$	2.7	mM	–
B.2	$[HCO^{3-}]$	21.2	mM	(139)
B.34	$[Mal_c]$	0.47 [b]	mM	(36; 118; 152)
B.5	$[Mg^{2+}]$ [a]	0.37	mM	(22)
A.15	$[A_{Tot_m}]$	10.4 [b,c]	mM	(2; 111; 118; 133; 165)
B.16	[NADP]	0.31 [b]	mM	(48; 117; 118; 152)
	[NADPH]	1.85 [b]	mM	(48; 117; 118; 122; 152)
A.14	$[N_{Tot}]$	2.1 [b,g]	mM	(48; 103; 117; 118; 122; 152)
B.2, B.20, B.34 & B.36	$[Pi_m]$	8.9	mM	(118)
B.34	$[Pi_c]$	4.2 [b]	mM	(2; 31; 118; 129)
B.2 & B.7	$[Pyr_m]$	0.2 [e]	mM	(68; 118)
B.22	[Q]	0.24 [f]	mM	(11; 12)
	$[QH_2]$	0.27	mM	(11; 12)
B.2	K_{eq}	10.98 [h]	unitless	(158)
	K_{Pyr_m}	0.14	mM	(87)
	$K_{HCO^{3-}}$	3.0	mM	(113)
	K_{ATP_m}	0.134 [i]	mM	(6)

(*Continued on next page . . .*)

B.2	$K_{\mathrm{OAA_m}}$	0.1	mM	(87)
	$K_{\mathrm{ADP_m}}$	0.35	mM	(89)
	$K_{\mathrm{Pi_m}}$	6.0	mM	(89)
B.3	$V_{\mathrm{PC_{min}}}$	1.02 [j]	mM/sec	(6; 35; 112; 113)
	$V_{\mathrm{PC_{max}}}$	5.1 [k,l]	mM/sec	(35)
B.4	$K_{\mathrm{AcCoA_m}}$	0.06	mM	(87)
	n	2.0	–	(88)
B.5	$K_{\mathrm{Mg^{2+}}}$	0.5	mM	(87)
B.7	V_{PDH}	0.648 [k,m]	mM/sec	(35)
	$K_{\mathrm{Pyr_m}}$	0.01	mM	(114)
	$K_{\mathrm{NAD^+_m}}$	0.064	mM	(106)
	$K_{\mathrm{CoA_m}}$	0.012 [n]	mM	(130)
	$K_{\mathrm{NADH_m}}$	0.044 [o]	mM	(5)
	$K_{\mathrm{AcCoA_m}}$	0.029 [p]	mM	(5)
B.9	V_{CS}	13.75 [k]	mM/sec	(35)
	K_{eq}	1.13E+09 [q]	unitless	(4)
	$K_{\mathrm{OAA_m}}$	2.0E-03	mM	(115)
	$K_{\mathrm{AcCoA_m}}$	0.016	mM	(115)
	$K_{\mathrm{Cit_m}}$	1.6 [n]	mM	(123)
	$K_{\mathrm{CoA_m}}$	0.067 [n]	mM	(123)
	$K_{\mathrm{SCoA_m}}$	0.14	mM	(123)
	$K_{\mathrm{ATP_m}}$	0.55	mM	(115)
B.11	V_{ACO}	1.674 [k,r]	mM/sec	(34; 42; 142)
	K_{eq}	0.0685 [q]	unitless	(4)
	$K_{\mathrm{Cit_m}}$	0.62 [s]	mM	(143)
	$K_{\mathrm{Isocit_m}}$	0.2 [s]	mM	(143)
B.13	V_{IDHa}	1.58 [k]	mM/sec	(35)
	n	1.0	–	(101)
	$K_{\mathrm{NAD^+_m}}$	0.07 [n]	mM	(102)

(*Continued on next page . . .*)

	$K_{\mathrm{NADH_m}}$	0.029 [b]	mM	(23; 100; 101)
	$K_{\mathrm{ATP_m}}$	0.118 [n]	mM	(102)
B.13	$K_{\mathrm{Isocit_m}}$	0.56 [p]	mM	(107)
	$K_{\mathrm{ADP^{3-}_m}}$	0.05 [n]	mM	(102)
	$K_{\mathrm{Ca^{2+}}}$	1.12E-03 [p]	mM	(91)
B.14 & B.29	$f_{\mathrm{ADP^{3-}_m}}$	0.818 [t]	unitless	(82)
	V_{IDHb}	5.419 [k]	mM/sec	(35)
	K_{eq}	43.8 [u]	unitless	(68; 77)
	$K_{\mathrm{Isocit_m}}$	8.4E-03 [s]	mM	(51)
B.16	K_{NADP}	5.6E-03 [s]	mM	(51)
	$K_{\alpha\mathrm{KG_m}}$	0.44 [n]	mM	(78)
	K_{NADPH}	5.6E-03 [n]	mM	(78)
	$K_{\mathrm{CO_2}}$	3.8 [n]	mM	(78)
	$V_{\alpha\mathrm{KGDH}}$	27.0	mM/sec	(35)
	$K_{\mathrm{CoA_m}}$	0.025 [s]	mM	(46)
	$K_{\mathrm{NADH,c}}$	3.54E-03 [s,v]	mM	(124)
	$K_{\mathrm{SCoA_m}}$	6.9E-03 [s]	mM	(124)
	$K_{\mathrm{ATP_m}}$	0.1 [s]	mM	(90)
B.18	$K_{\mathrm{NADH,u}}$	0.0258 [s,v]	mM	(124)
	$K_{\alpha\mathrm{KG_m}}$	0.126 [s,v]	mM	(124)
	$K_{\mathrm{ADP_m}}$	0.1 [s]	mM	(90)
	$K_{\mathrm{Ca^{2+}}}$	1.2E-03 [p]	mM	(107)
	$K_{\mathrm{NAD^+_m}}$	0.0193 [s,v]	mM	(124)
	V_{SCS}	4.2 [k,w]	mM/sec	(8; 19; 35)
	K_{eq}	1.3 [q]	unitless	(4)
	$K_{\mathrm{SCoA_m}}$	0.011 [s]	mM	(18)
B.20	$K_{\mathrm{ADP_m}}$	2.0E-03 [s]	mM	(18)
	$K_{\mathrm{Pi_m}}$	0.15 [s]	mM	(18)
	$K_{\mathrm{Suc_m}}$	70.0 [s]	mM	(18)
	$K_{\mathrm{CoA_m}}$	0.02 [s]	mM	(18)

(*Continued on next page . . .*)

B.20	$K_{\mathrm{ATP_m}}$	5.0E-03 [s]	mM	(18)
B.22	V_{SDH}	0.48 [k,s]	mM/sec	(3; 140)
	K_{eq}	1.01 [q]	unitless	(4)
	$K_{\mathrm{Suc_m}}$	0.13 [n]	mM	(40)
	K_{Q}	3.0E-04 [n]	mM	(40)
	$K_{\mathrm{Fum_m}}$	1.3 [s]	mM	(29)
	$K_{\mathrm{QH_2}}$	1.5E-03 [n]	mM	(40)
	$K_{\mathrm{OAA_m}}$	1.5E-03 [n]	mM	(29; 162)
B.24	V_{FM}	7.696 [k]	mM/sec	(35)
	K_{eq}	4.34 [b]	unitless	(4; 14; 15; 67)
	$K_{\mathrm{Fum_m}}$	0.015	mM	(62)
	$K_{\mathrm{Mal_m}}$	0.18	mM	(62)
B.26	V_{MDH}	26.752 [k]	mM/sec	(35)
	K_{eq}	1.25E-04 [n]	unitless	(49)
	$K_{\mathrm{Mal_m}}$	1.1	mM	(25)
	$K_{\mathrm{NAD^+_m}}$	0.114	mM	(25)
	$K_{\mathrm{OAA_m}}$	5.5E-03 [n]	mM	(49)
	$K_{\mathrm{NADH_m}}$	5.0E-03 [s]	mM	(57)
B.28	V_{ANT}	1.527 [x]	mM/sec	–
	K_{eq}	118.0 [y]	unitless	(50; 60; 92)
	$K_{\mathrm{ATP^{4-}_m}}$	0.03 [b]	mM	(33; 59; 66; 92; 157)
	$K_{\mathrm{ADP^{3-}_c}}$	0.02 [b]	mM	(33; 59; 66; 92; 141; 157)
	$K_{\mathrm{ADP^{3-}_m}}$	0.02 [b]	mM	(33; 59; 66; 92; 157)
	$K_{\mathrm{ATP^{4-}_c}}$	0.03 [b]	mM	(33; 59; 66; 92; 141; 157)
B.29	$f_{\mathrm{ATP^{4-}_m}}$	5.26E-02 [z]	unitless	(82)
	$f_{\mathrm{ATP^{4-}_c}}$	0.05	unitless	(82)
	$f_{\mathrm{ADP^{3-}_c}}$	0.45	unitless	(82)
B.34	V_{MC}	23.257 [x]	mM/sec	–
	K_{eq}	1.52	unitless	(53)

(*Continued on next page . . .*)

B.34	$K_{\mathrm{Mal_m}}$	0.9	mM	(53)
	$K_{\mathrm{Pi_c}}$	0.76	mM	(53)
	$K_{\mathrm{Pi_m}}$	0.72	mM	(53)
	$K_{\mathrm{Mal_c}}$	0.2	mM	(53)
B.36	$V_{\mathrm{ATP_{synth}}}$	0.887 [x]	mM/sec	–
	$K_{\mathrm{NADH_m}}$	0.88 [aa]	mM	–
	$K_{\mathrm{ADP_m}}$	3.1 [aa]	mM	–
	$K_{\mathrm{Pi_m}}$	8.9 [aa]	mM	–
	$K_{\mathrm{NAD^+_m}}$	1.2 [aa]	mM	–
	$K_{\mathrm{ATP_m}}$	7.3 [aa]	mM	–
B.38	$f_{\mathrm{ATP_{hyd}}}$	7.69E-03 [x]	sec^{-1}	–

[a] Refers to free concentration.

[b] Average of reported values.

[c] Sum of the reported Mg-ADP and Mg-ATP concentrations, assuming that the magnesium-complexed species represent 55% and 95% of free ADP and ATP, respectively (Magnus and Keizer, 1997).

[e] Within range of reported values.

[f] Calculated from total ubiquinone concentration, assuming $[QH_2] = 0.27$ mM (Benard, 2006; Benard et al., 2006).

[g] Sum of reported NAD and NADH concentrations.

[h] The value represents the K_{eq} taking $[HCO_3^-]$ as the substrate, calculated from the K_{eq} for total $[CO_2]$ reported in the source (Wood et al., 1966).

[i] Determined in sheep kidney; determined in chicken liver.

[j] The basal activity of PC is *approx.* 20% of the activity of the maximally activated enzyme (Ashman et al., 1972; Fahien and Teller, 1992; Scrutton, 1974; Scrutton and White, 1972).

[k] Calculated from the reported mitochondrial concentration and specific activity, taking into account the number of active sites within the holoenzyme.

[l] Assumed to represent the activity of the maximally activated enzyme.

[m] Assumed to represent the physiological level of activation.

[n] Determined in bovine heart.

[o] Determined in rat kidney.

[p] Determined in rat heart.

[q] Calculated from the thermodynamic properties of the species involved in the reaction (Alberty, 2003).

[r] Enzyme concentration estimated from the specific activities of the crude extract and the purified enzyme from rat liver (Eprintsev et al., 2002; Guarriero-Bobyleva et al., 1973), according to the methodology of Albe et al., 1990; specific activity determined in pig heart (Villafranca and Mildvan, 1971b).

[s] Determined in pig heart.

[t] $f_{ADP_m^{3-}} = 0.45/0.55$, assuming $[ADP^{3-}] = 0.45 \times [ADP]$ (total free ADP), and $[ADP] = [ADP^{3-}] + [MgADP]$ (Magnus and Keizer, 1997).

[u] At a fixed total mitochondrial $[CO_2]$ concentration of 22.8 mM (Veech et al., 1979).

[v] Original data (Smith et al., 1974) re-fitted to a mixed inhibition model.

[w] Specific activity determined in pig heart (Cha and Parks, 1964b).

[x] Fitted value.

[y] Calculated from the Nernst equation (Metelkin et al., 2006), assuming that the membrane potential provides 85% of the driving force for nucleotide translocation (Klingenberg and Rottenberg, 1977), and taking Ψ to be 150 mV (Holian and Wilson, 1980; Klingenberg and Rottenberg, 1977).

[z] $f_{ATP_m^{4-}} = 0.05/0.95$, assuming $[ATP^{4-}] = 0.05 \times [ATP]$ (total free ATP), and $[ATP] = [ATP^{4-}] + [MgATP]$ (Magnus and Keizer, 1997).

[aa] Set equal to the steady-state concentration of the metabolite.

I.2 Suppl. data : Steady-state analysis of liver model

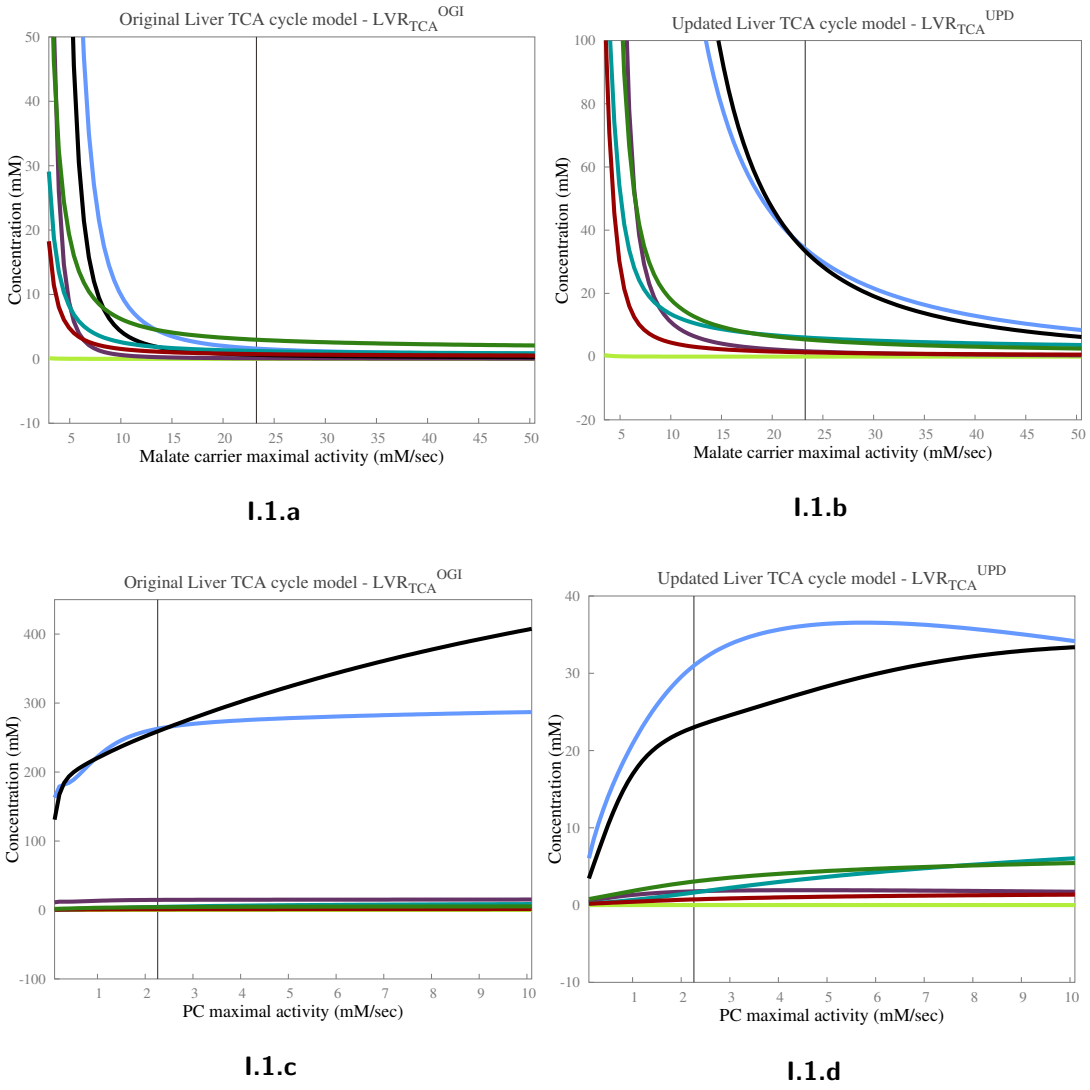

- **Supplemental Figure I.1. Change in the metabolic status of CoA between the two liver TCA cycle models:** Effect on TCAi concentrations against the change in maximal activities of MC & PC, respectively.

- Key for figs. I.1a to I.1d is as follows :

OAA_m ; Cit_m ; $Isocit_m$; αKG_m ; Suc_m ; Fum_m ; Mal_m

- ***Supplementary data for fig. 2.16a on pg. 54.***

- The vertical black line represents the initial model value. At this point, in figs. I.1a and I.1b, $V_{max}^{MC} = 23.2574$ mM/sec and in figs. I.1c and I.1d, $V_{max}^{PC} = 2.26234$ mM/sec (apparent velocity).

- *Y-axes* for figs. I.1a and I.1b have been set within a limited range of concentration values (in mM), to avoid the possible plot-line compression due to extreme values.

- Note the substantially different *Y-axis* scales between figs. I.1a and I.1c compared with figs. I.1b and I.1d, respectively.

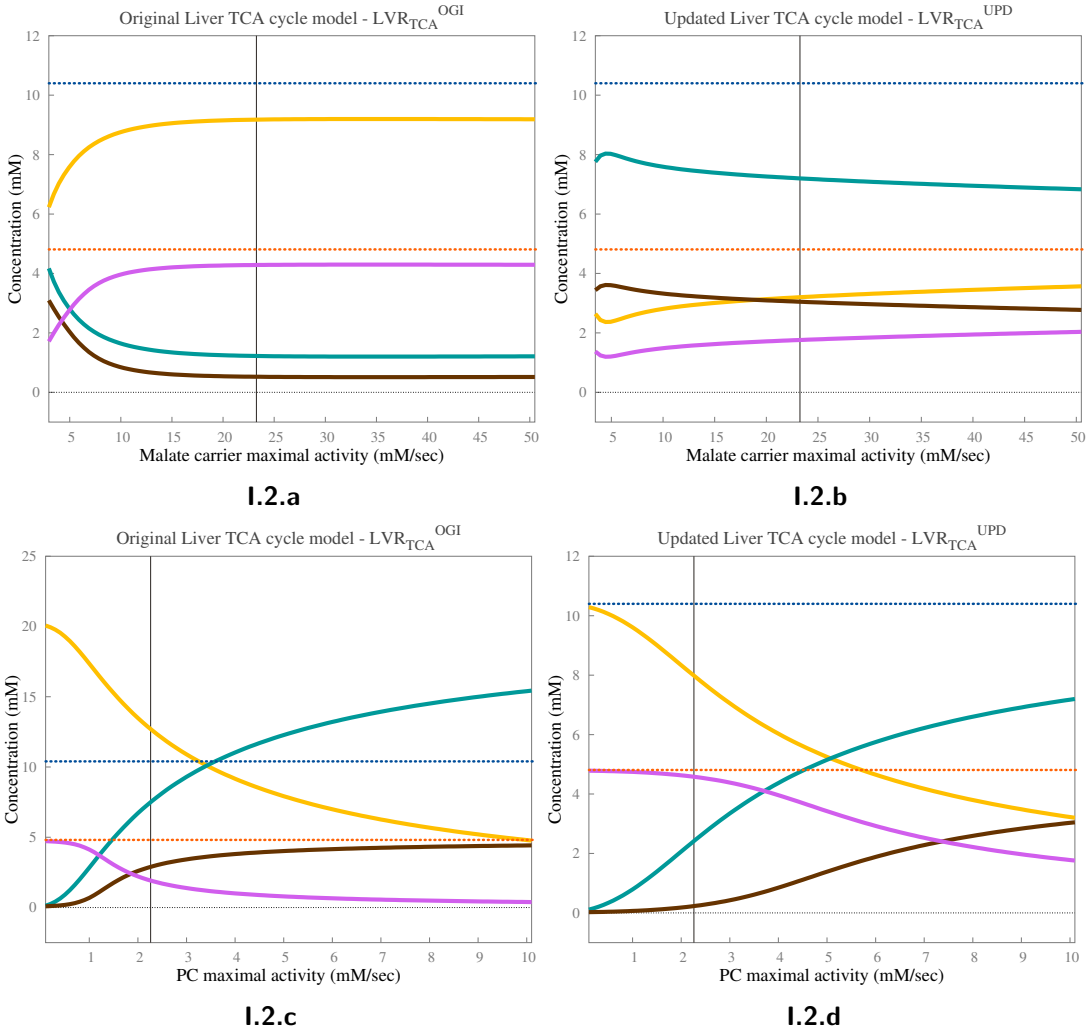

▪ **Supplemental Figure I.2. Change in the metabolic status of CoA between the two liver TCA cycle models:** Effect on mitochondrial & cytosolic ATP/ADP concentrations against the change in maximal activities of MC & PC, respectively.

▪ Key for figs. I.2a to I.2d is as follows :

ATP_m ; ADP_m ; ATP_c ; ADP_c
mitochondrial ATP+ADP (total) ; cytosolic ATP+ADP (total)

▪ ***Supplementary data for fig. 2.16b on pg. 54 and for figs. 2.22a and 2.22b on pg. 68.***

▪ The vertical black line represents the initial model value. At this point, in figs. I.2a and I.2b, V_{max}^{MC} = 23.2574 mM/sec and in figs. I.2c and I.2d, V_{max}^{PC} = 2.26234 mM/sec (apparent velocity), respectively.

▪ Note the substantially different *Y-axis* scales between figs. I.2c and I.2d.

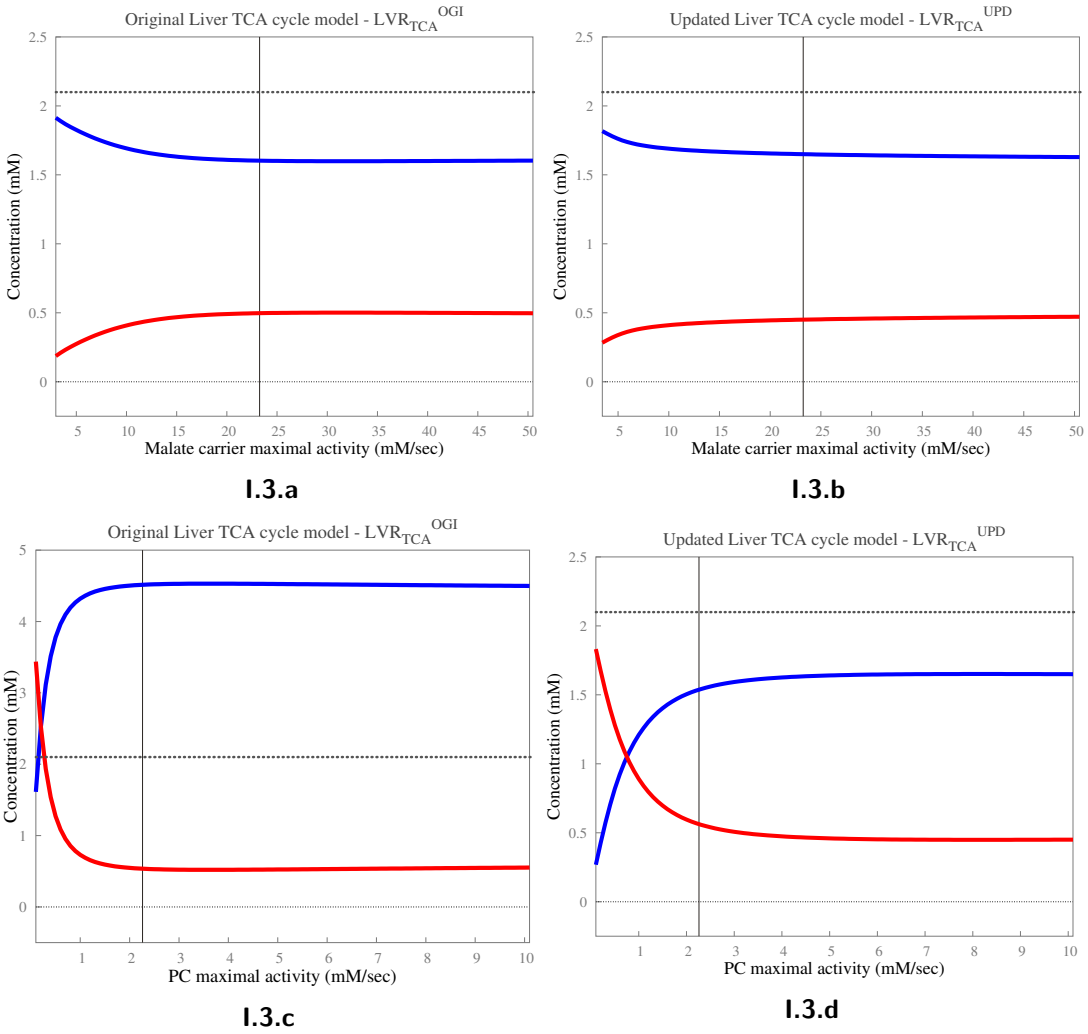

- **Supplemental Figure I.3. Change in the metabolic status of CoA between the two liver TCA cycle models:** Effect on mitochondrial NAD^+/ NADH concentrations against the change in maximal activities of MC & PC, respectively.

- Key for figs. I.3a to I.3d is as follows :

  NAD_m^+ ; $NADH_m$; mitochondrial NAD^+/ NADH (total)

- ***Supplementary data for fig. 2.16c on pg. 55 and for fig. 2.22c on pg. 68.***

- The vertical black line represents the initial model value. At this point, in figs. I.3a and I.3b, $V_{max}^{MC} = 23.2574$ mM/sec and in figs. I.3c and I.3d, $V_{max}^{PC} = 2.26234$ mM/sec (apparent velocity), respectively.

- Note the substantially different *Y-axis* scales between figs. I.3c and I.3d.

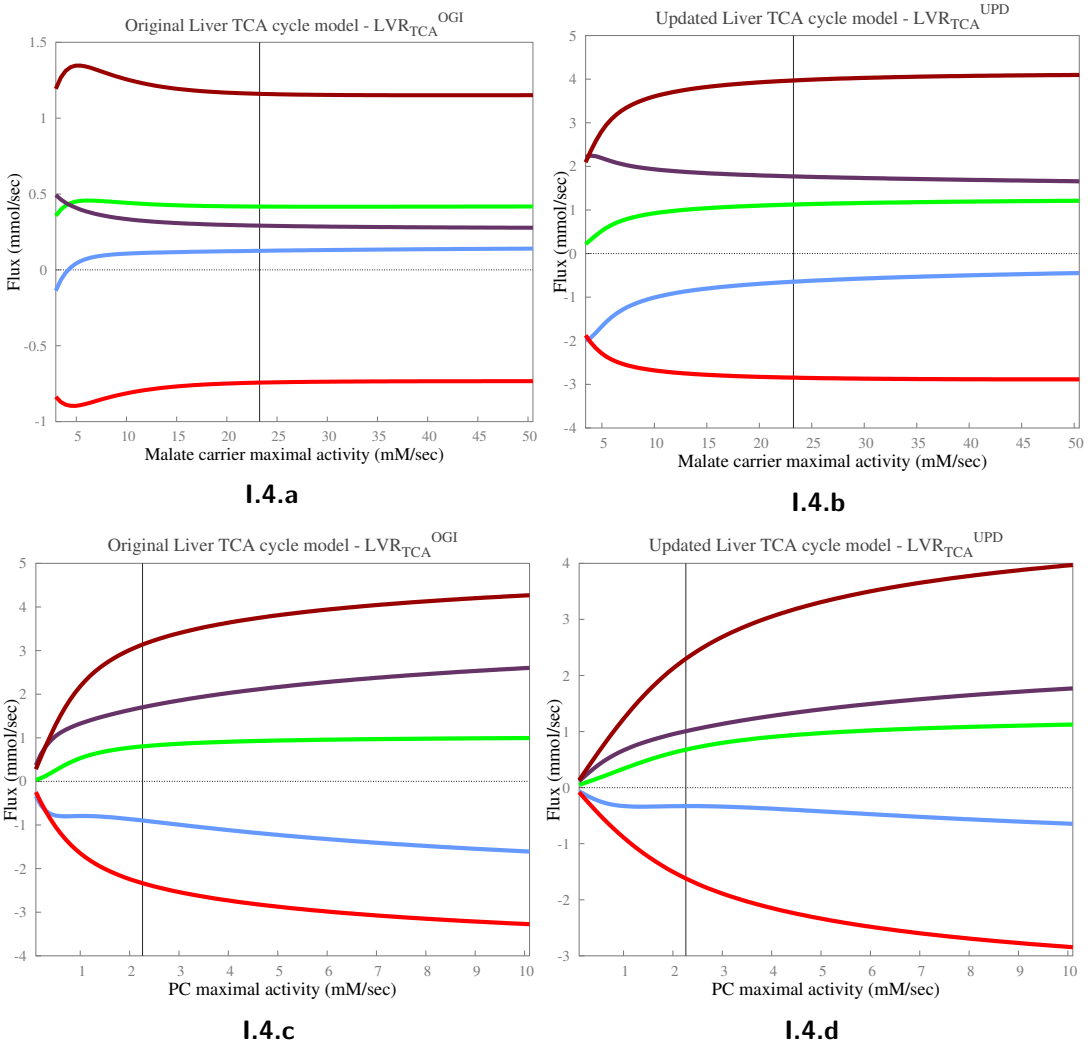

- **Supplemental Figure I.4. Change in the metabolic status of CoA between the two liver TCA cycle models:** Effect on key Liver TCA cycle fluxes against the change in maximal activities of MC & PC, respectively.

- Key for figs. I.4a to I.4d is as follows :

IDHa ; CS ; IDHb ; PC ; MDH

- ***Supplementary data for fig. 2.17 on pg. 56.***

- The vertical black line represents the initial model value. At this point, in figs. I.4a and I.4b, $V_{max}^{MC} = 23.2574$ mM/sec and in figs. I.4c and I.4d, $V_{max}^{PC} = 2.26234$ mM/sec (apparent velocity), respectively.

- Note the substantially different *Y-axis* scales between figs. I.4a and I.4c compared with figs. I.4b and I.4d, respectively.

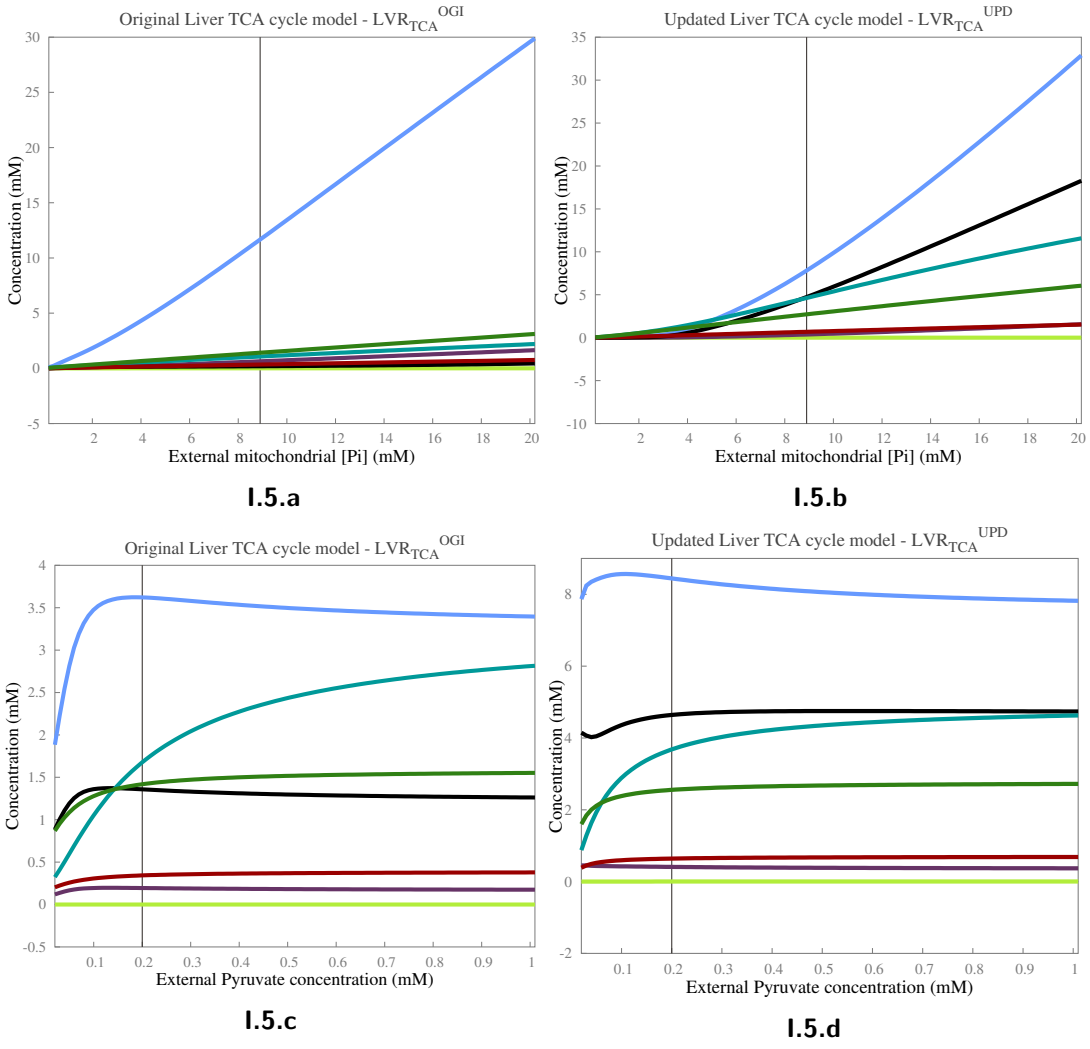

- **Supplemental Figure I.5. Change in the metabolic status of CoA between the two liver TCA cycle models:** Effect on TCAi concentrations against the change in concentrations of Pi_m & Pyr_m, respectively.

- Key for figs. I.5a to I.5d is as follows :

OAA_m ; Cit_m ; $Isocit_m$; αKG_m ; Suc_m ; Fum_m ; Mal_m

- ***Supplementary data for fig. 2.19a on pg. 62.***

- The vertical black line represents the initial model value. At this point, in figs. I.5a and I.5b, $[Pi_m] = 8.9$ mM and in figs. I.5c and I.5d, $[Pyr_m] = 0.2$ mM, respectively.

- Note the substantially different *Y-axis* scales between figs. I.5a and I.5c compared with figs. I.5b and I.5d, respectively.

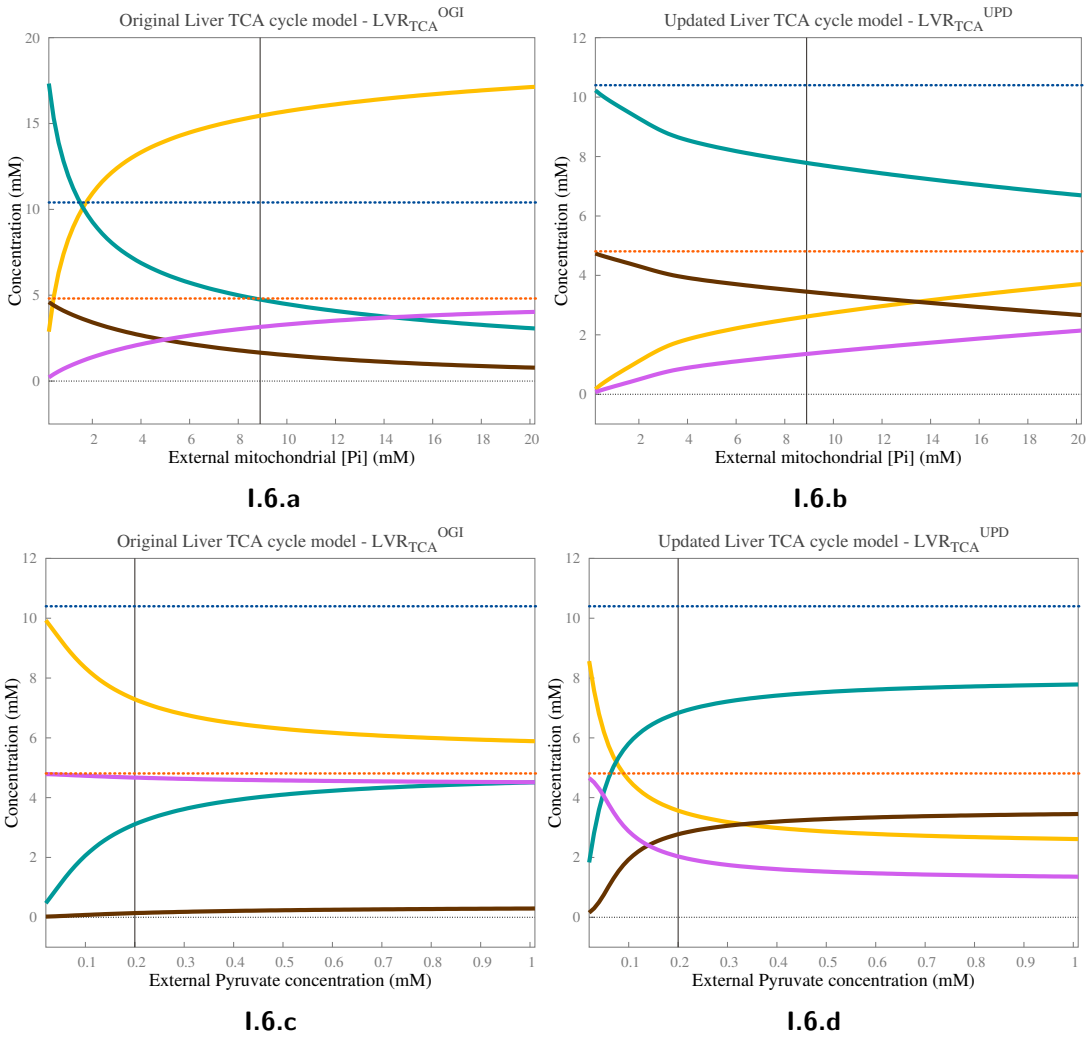

- **Supplemental Figure I.6. Change in the metabolic status of CoA between the two liver TCA cycle models:** Effect on mitochondrial & cytosolic ATP/ ADP concentrations against the change in concentrations of Pi_m & Pyr_m, respectively.

- Key for figs. I.6a to I.6d is as follows :

ATP_m ; ADP_m ; ATP_c ; ADP_c

mitochondrial ATP+ADP (total) ; cytosolic ATP+ADP (total)

- ***Supplementary data for fig. 2.19b on pg. 62 and for figs. 2.23a, 2.23b, 2.24a and 2.24b on pgs. 69 and 70.***

- The vertical black line represents the initial model value. At this point, in figs. I.6a and I.6b, $[Pi_m] = 8.9$ mM and in figs. I.6c and I.6d, $[Pyr_m] = 0.2$ mM, respectively.

- Note the substantially different *Y-axis* scales between figs. I.6a and I.6b.

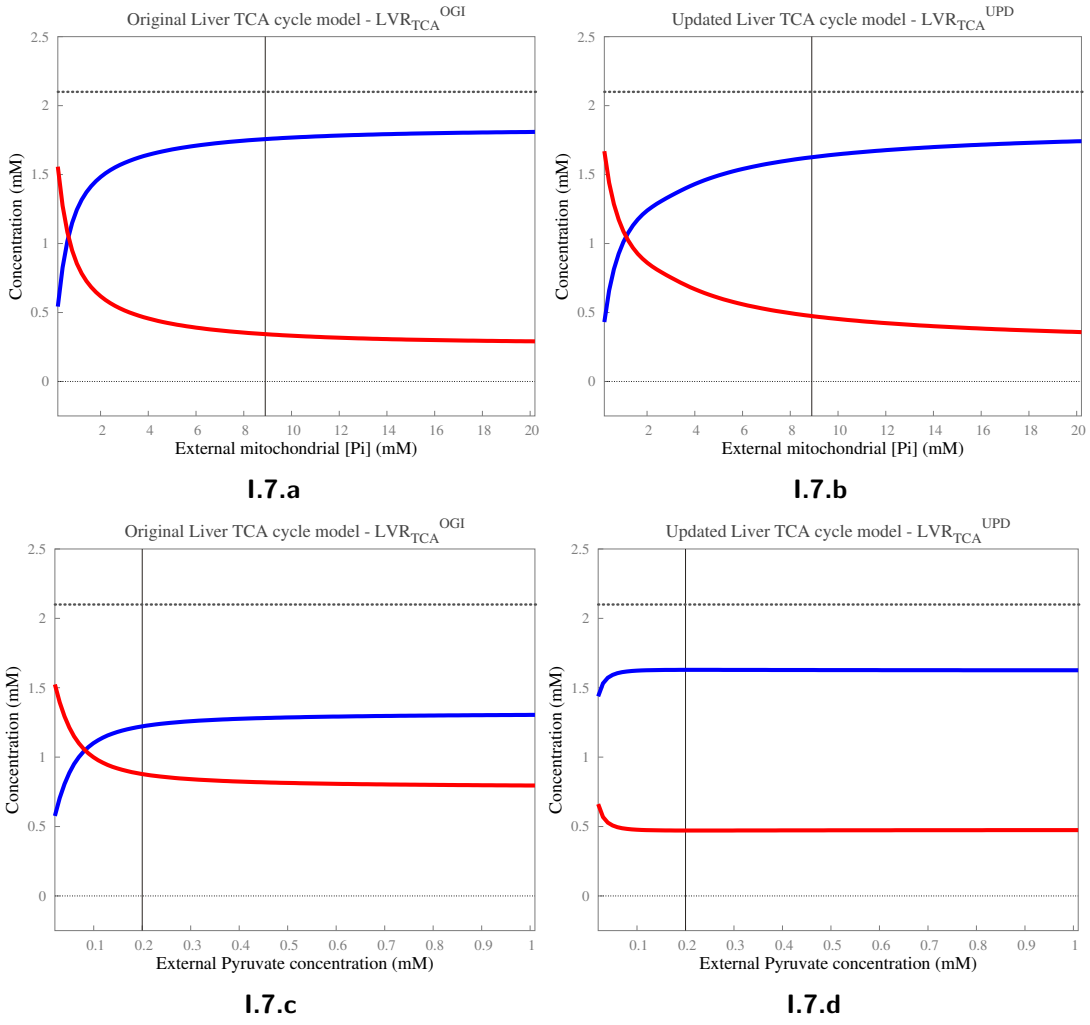

- **Supplemental Figure I.7. Change in the metabolic status of CoA between the two liver TCA cycle models:** Effect on mitochondrial NAD^+/ NADH concentrations against the change in concentrations of Pi_m & Pyr_m, respectively.

- Key for figs. I.7a to I.7d is as follows :

NAD^+_m ; $NADH_m$; mitochondrial NAD^+/ NADH (total)

- ***Supplementary data for fig. 2.19c on pg. 63 and for figs. 2.23c and 2.24c on pgs. 69 and 70.***

- The vertical black line represents the initial model value. At this point, in figs. I.7a and I.7b, $[Pi_m] = 8.9$ mM and in figs. I.7c and I.7d, $[Pyr_m] = 0.2$ mM, respectively.

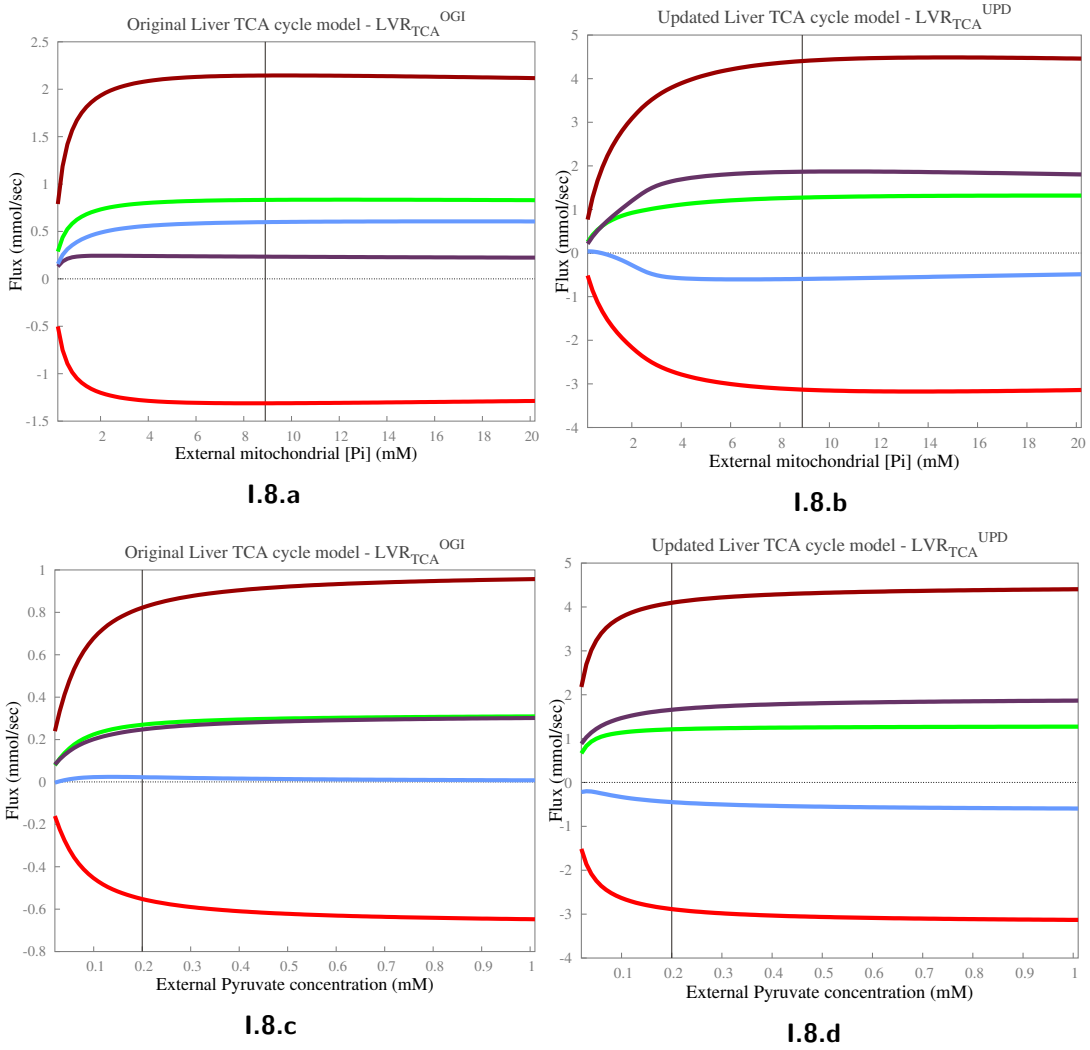

- **Supplemental Figure I.8. Change in the metabolic status of CoA between the two liver TCA cycle models:** Effect on key Liver TCA cycle fluxes against the change in concentrations of Pi_m & Pyr_m, respectively.

- Key for figs. I.8a to I.8d is as follows :

IDHa ; CS ; IDHb ; PC ; MDH

- ***Supplementary data for fig. 2.20 on pg. 64.***

- The vertical black line represents the initial model value. At this point, in figs. I.8a and I.8b, $[Pi_m] = 8.9$ mM and in figs. I.8c and I.8d, $[Pyr_m] = 0.2$ mM, respectively.

- Note the substantially different *Y-axis* scales between figs. I.8a and I.8c compared with figs. I.8b and I.8d, respectively.

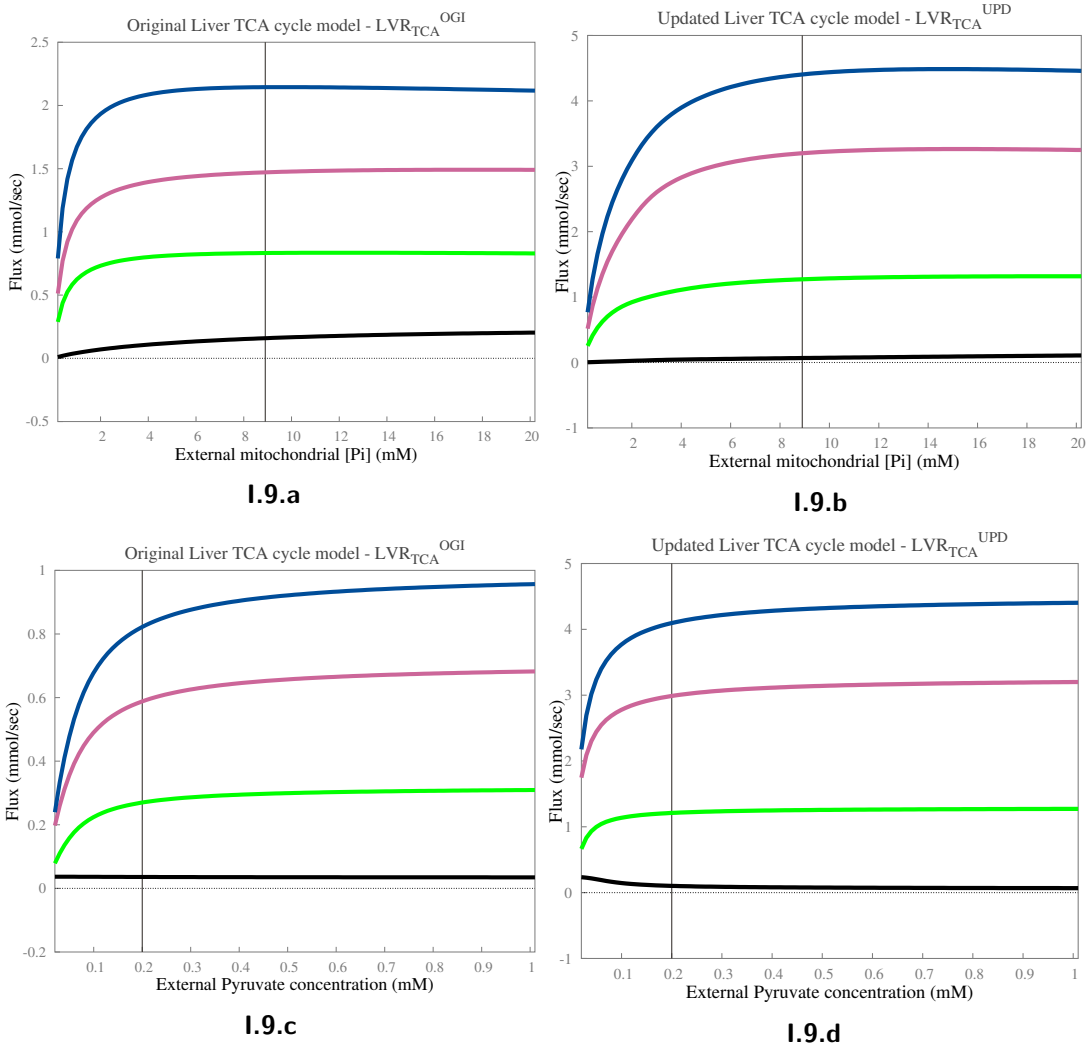

- **Supplemental Figure I.9. Change in the metabolic status of CoA between the two liver TCA cycle models:** Effect on ATP/ADP-linked fluxes against the change in concentrations of Pi_m & Pyr_m, respectively.

- Key for figs. I.9a to I.9d is as follows :

  ATPsynth ; SCS ; ATPhyd ; PC

- ***Supplementary data for fig. 2.21 on pg. 65.***

- The vertical black line represents the initial model value. At this point, in figs. I.9a and I.9b, $[Pi_m] = 8.9$ mM and in figs. I.9c and I.9d, $[Pyr_m] = 0.2$ mM, respectively.

- Note the substantially different *Y-axis* scales between figs. I.9a and I.9c compared with figs. I.9b and I.9d, respectively.

- **In this figure, the ATP synthase (ATPsynth) flux have been scaled by a factor of 10; due to the difference in respective reaction stoichiometries between ATPsynth (in mitochondria) and ATPhyd (in cytosol).**

I.3 Suppl. data : C^J's for the liver TCA cycle model

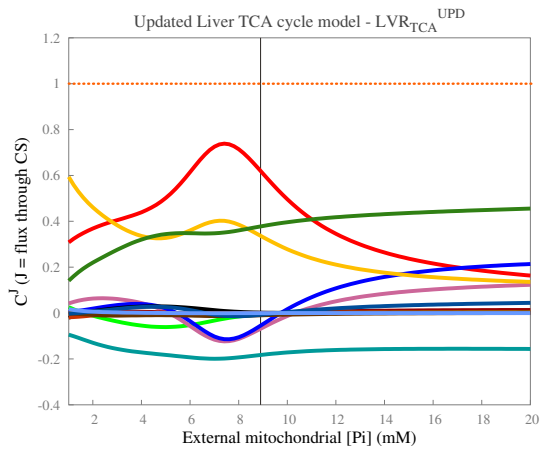

I.10.a. C^J, Updated model

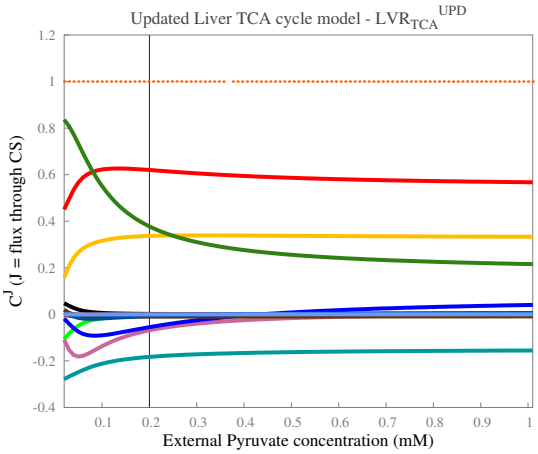

I.10.b. C^J, Updated model

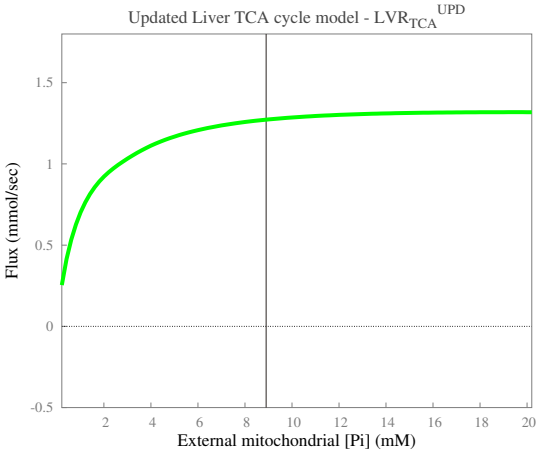

I.10.c. CS flux, Updated model

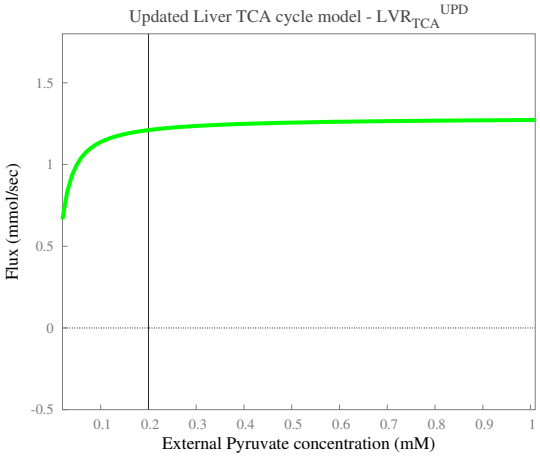

I.10.d. CS flux, Updated model

- **Supplemental Figure**

I.10. Control of the TCA cycle flux: Distribution of flux control coefficients calculated for the flux through CS, against the change in concentrations of Pi_m & Pyr_m, respectively.

- Key for figs. I.10a and I.10b is as follows :

PDH ;	CS ;	ACO ;	IDHa ;	α-KGDH ;	SCS;
SDH ;	FM ;	MDH ;	ATPsynth ;	ANT ;	ATPhyd;
PC ;	MC ;	IDHb ;	Total Sum (dotted line)		

- The vertical black line represents the initial model value. At this point, in figs. I.10a and I.10c, $[Pi_m] = 8.9$ mM and in figs. I.10b and I.10d, $[Pyr_m] = 0.2$ mM, respectively.

- Figure I.10b: The ***Orange dotted line*** that represents the Summation theorem result, shows some dropouts. This is due to an erroneous Summation theorem result (less than or greater than unity) at that point; which in turn is a result of an unstable steady-state. ***Hence, such data points are excluded from these plots.***

- ***Corresponding flux control coefficient plots for the original liver TCA cycle model are both qualitatively as well as quantitatively similar to the data shown above and therefore not included here.***

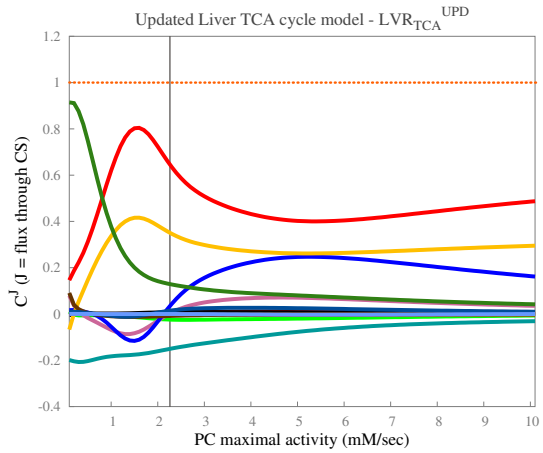

I.11.a. C^J, Updated model

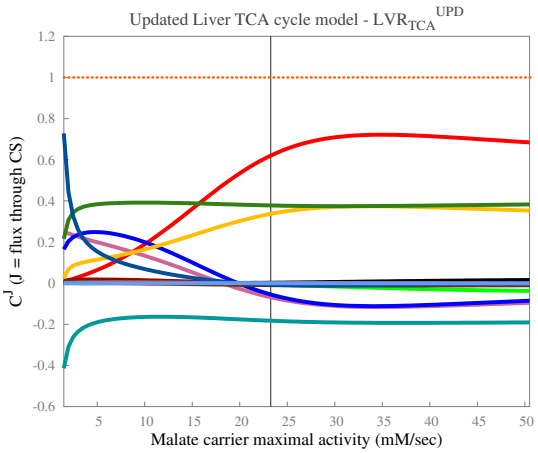

I.11.b. C^J, Updated model

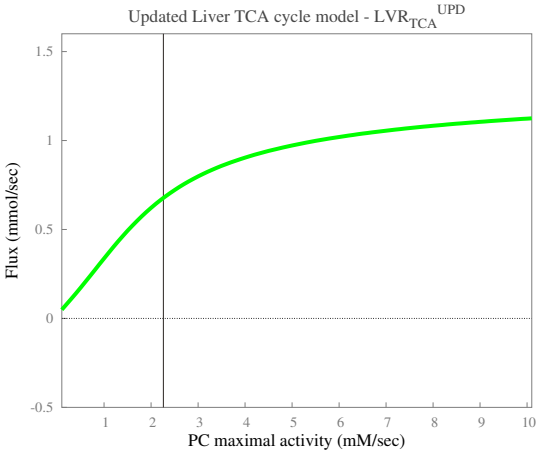

I.11.c. CS flux, Updated model

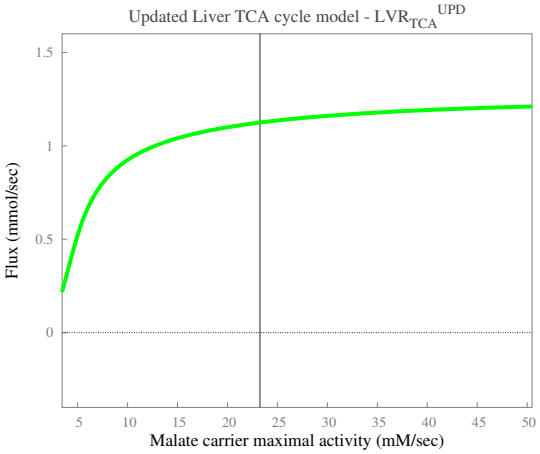

I.11.d. CS flux, Updated model

- **Supplemental Figure**

I.11. Control of the TCA cycle flux: Distribution of flux control coefficients calculated for the flux through CS, against the change in maximal activities of PC & MC, respectively.

- Key for figs. I.11a and I.11b is as follows :

PDH ;	CS ;	ACO ;	IDHa ;	α-KGDH ;	SCS;
SDH ;	FM ;	MDH ;	ATPsynth ;	ANT ;	ATPhyd;
PC ;	MC ;	IDHb ;	Total Sum (dotted line)		

- The vertical black line represents the initial model value. At this point, in figs. I.11a and I.11c, $V_{max}^{PC} = 2.26234$ mM/sec (apparent velocity) and in figs. I.11b and I.11d, $V_{max}^{MC} = 23.2574$ mM/sec, respectively.

- ***Orange dotted line*** shows the *Summation theorem* result across the entire range.

- ***Corresponding flux control coefficient plots for the original liver TCA cycle model are both qualitatively as well as quantitatively similar to the data shown above and therefore not included here.***

I.4 Suppl. data : C^S's for the liver TCA cycle model

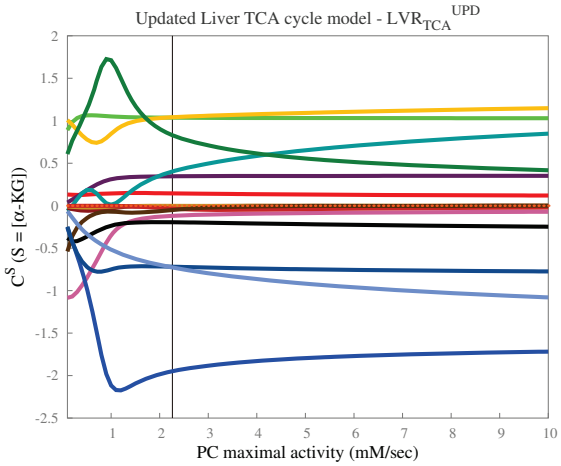

I.12.a. $C^{\alpha KG}$, Updated model

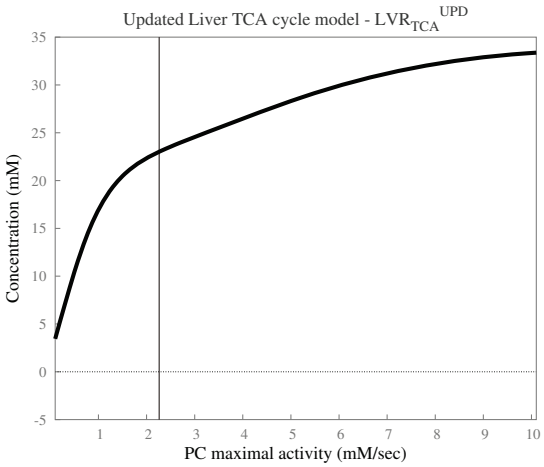

I.12.b. [αKG], Updated model

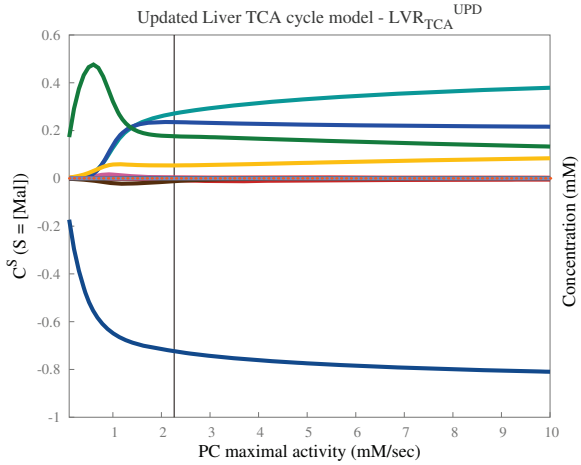

I.12.c. C^{Mal}, Updated model

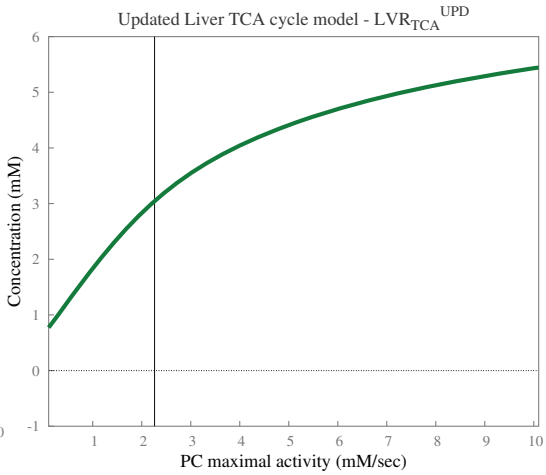

I.12.d. [Malate], Updated model

- **Supplemental Figure I.12. Control of TCA cycle intermediate metabolites:** Distribution of concentration control coefficients calculated for the respective concentrations of – αKG & Malate; against the changing maximal activity of pyruvate carboxylase.

- Key for figs. I.12a and I.12c is as follows :

PDH ; CS ; ACO ; IDHa ; α-KGDH ; SCS;
SDH ; FM ; MDH ; ATPsynth ; ANT ; ATPhyd;
PC ; MC ; IDHb ; Total Sum (dotted line)

- The vertical black line represents the initial model value. At this point, in figs. I.12a to I.12d, $V_{max}^{PC} = 2.26234$ mM/sec (apparent velocity).

- ***Orange dotted line*** shows the *Summation theorem* result across the entire range. For concentration control coefficients, since the sum is equal to zero, the dotted line is not easily visible.

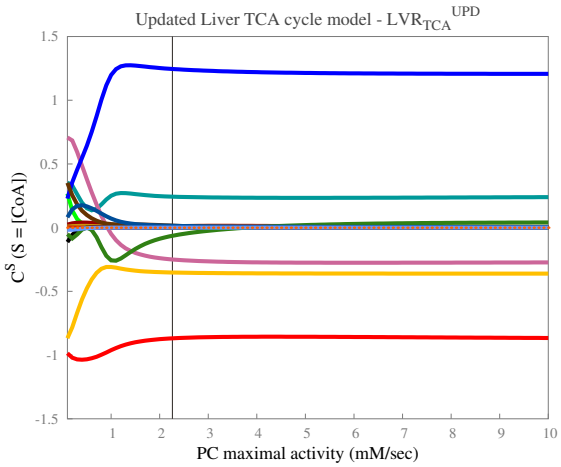

I.13.a. C^{CoA}, Updated model

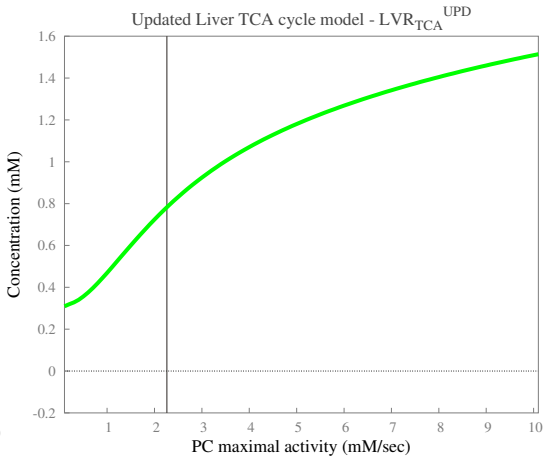

I.13.b. [CoA], Updated model

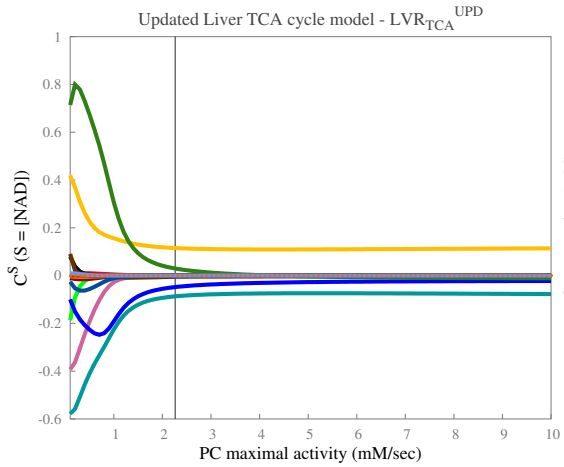

I.13.c. C^{NAD}, Updated model

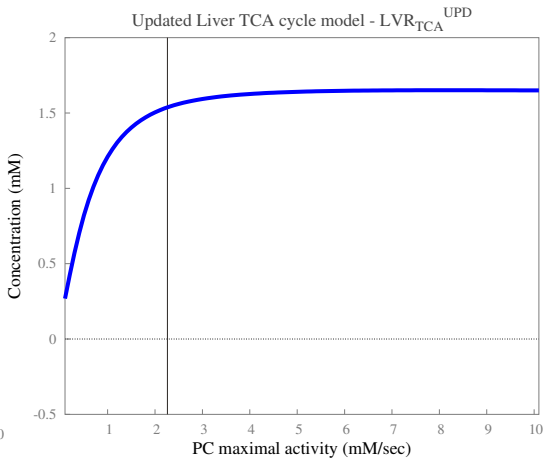

I.13.d. [NAD^+], Updated model

- **Supplemental Figure I.13. Control of CoA- & NAD−related metabolites:** Distribution of concentration control coefficients calculated for the respective concentrations of – CoA & NAD^+; against the changing maximal activity of pyruvate carboxylase.

- Key for figs. I.13a and I.13c is as follows :

PDH ;	CS ;	ACO ;	IDHa ;	α-KGDH ;	SCS;
SDH ;	FM ;	MDH ;	ATPsynth ;	ANT ;	ATPhyd;
PC ;	MC ;	IDHb ;	Total Sum (dotted line)		

- The vertical black line represents the initial model value. At this point, in figs. I.13a to I.13d, V_{max}^{PC} = 2.26234 mM/sec (apparent velocity).

- ***Orange dotted line*** shows the *Summation theorem* result across the entire range. For concentration control coefficients, since the sum is equal to zero, the dotted line is not easily visible.

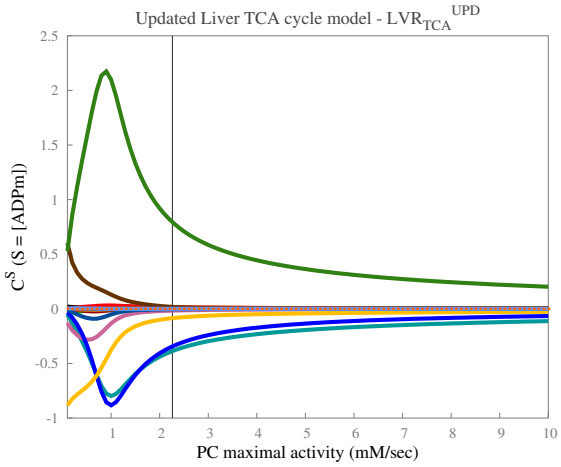

I.14.a. C^{ADP_m}, Updated model

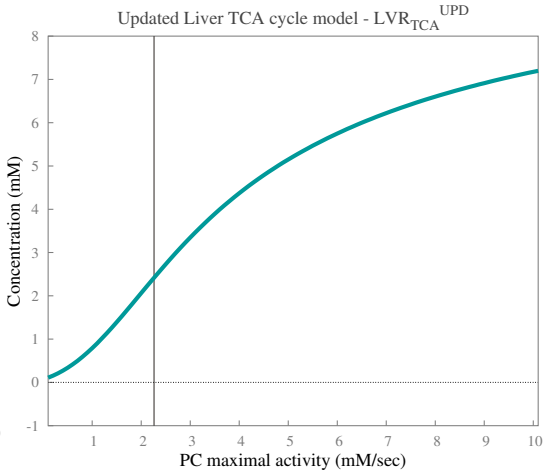

I.14.b. $[ADP_m]$, Updated model

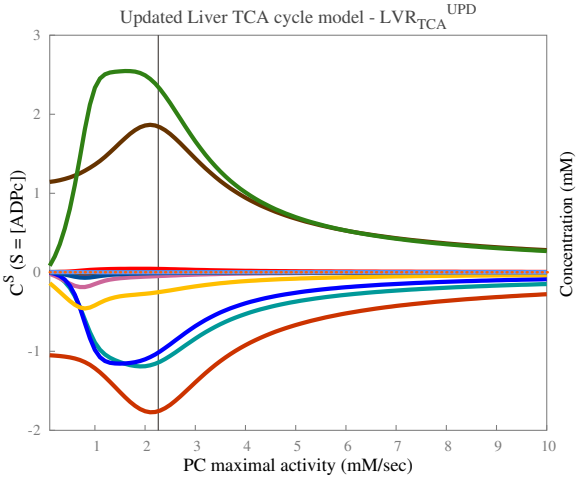

I.14.c. C^{ADP_c}, Updated model

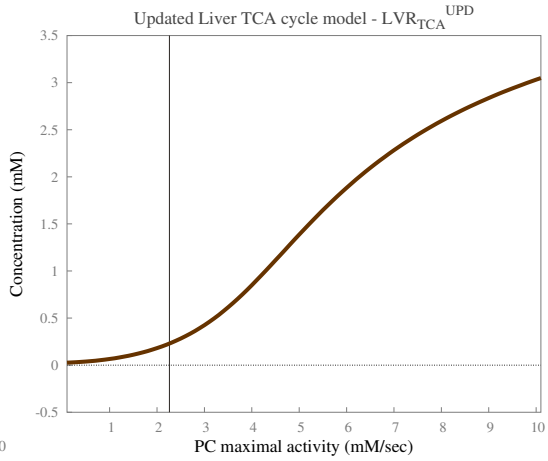

I.14.d. $[ADP_c]$, Updated model

- **Supplemental Figure I.14. Control of ADP-related metabolites:** Distribution of concentration control coefficients calculated for the respective concentrations of – ADP_m & ADP_c; against the changing maximal activity of pyruvate carboxylase.

- Key for figs. I.14a and I.14c is as follows :

PDH ;	CS ;	ACO ;	IDHa ;	α-KGDH ;	SCS;
SDH ;	FM ;	MDH ;	ATPsynth ;	ANT ;	ATPhyd;
PC ;	MC ;	IDHb ;	Total Sum (dotted line)		

- The vertical black line represents the initial model value. At this point, in figs. I.14a to I.14d, $V_{max}^{PC} = 2.26234$ mM/sec (apparent velocity).

- ***Orange dotted line*** shows the *Summation theorem* result across the entire range. For concentration control coefficients, since the sum is equal to zero, the dotted line is not easily visible.

Supplement II: *"PC knock-out"* model

II.1 Suppl. data : Steady-state analysis of PC_{ko} model

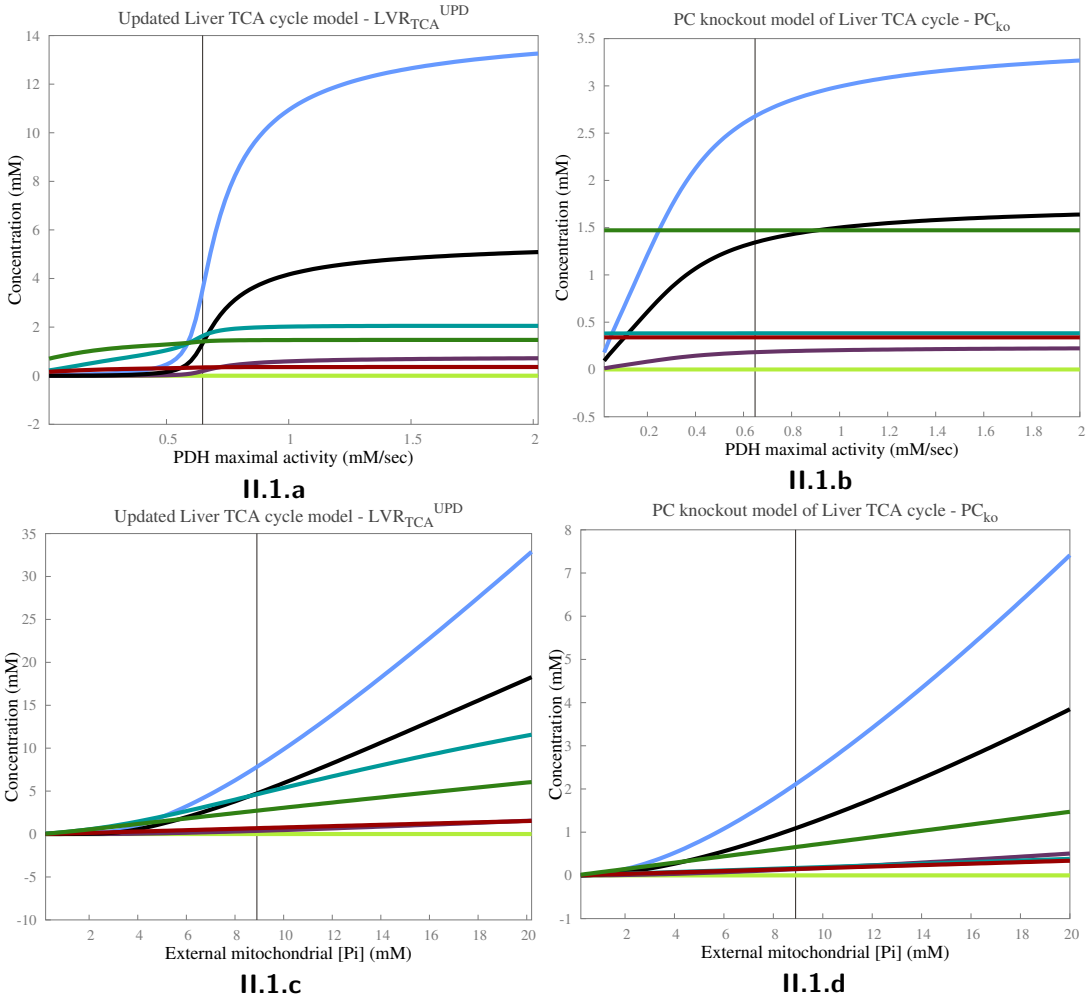

▪ **Supplemental Figure II.1. Concentrations of TCAi's :** effect of PC *'knock-out'* (PC_{ko}) in comparison with the PC *'wild-type'* (PC_{wt} *i.e.* $LVR_{TCA}{}^{UPD}$).

▪ Key for figs. II.1a to II.1d is as follows :

OAA_m; Cit_m; $Isocit_m$; αKG_m; Suc_m; Fum_m; Mal_m

▪ ***Supplementary data for the fig. 3.6a on pg. 130.***

▪ The vertical black line represents the initial model value. At this point, in figs. II.1a and II.1b, $V_{max}^{PDH} = 0.648$ mM/sec and in figs. II.1c and II.1d, $[Pi_m] = 8.9$ mM, respectively.

▪ Note the substantially different *Y-axis* scales between figs. II.1a and II.1c compared with figs. II.1b and II.1d, respectively.

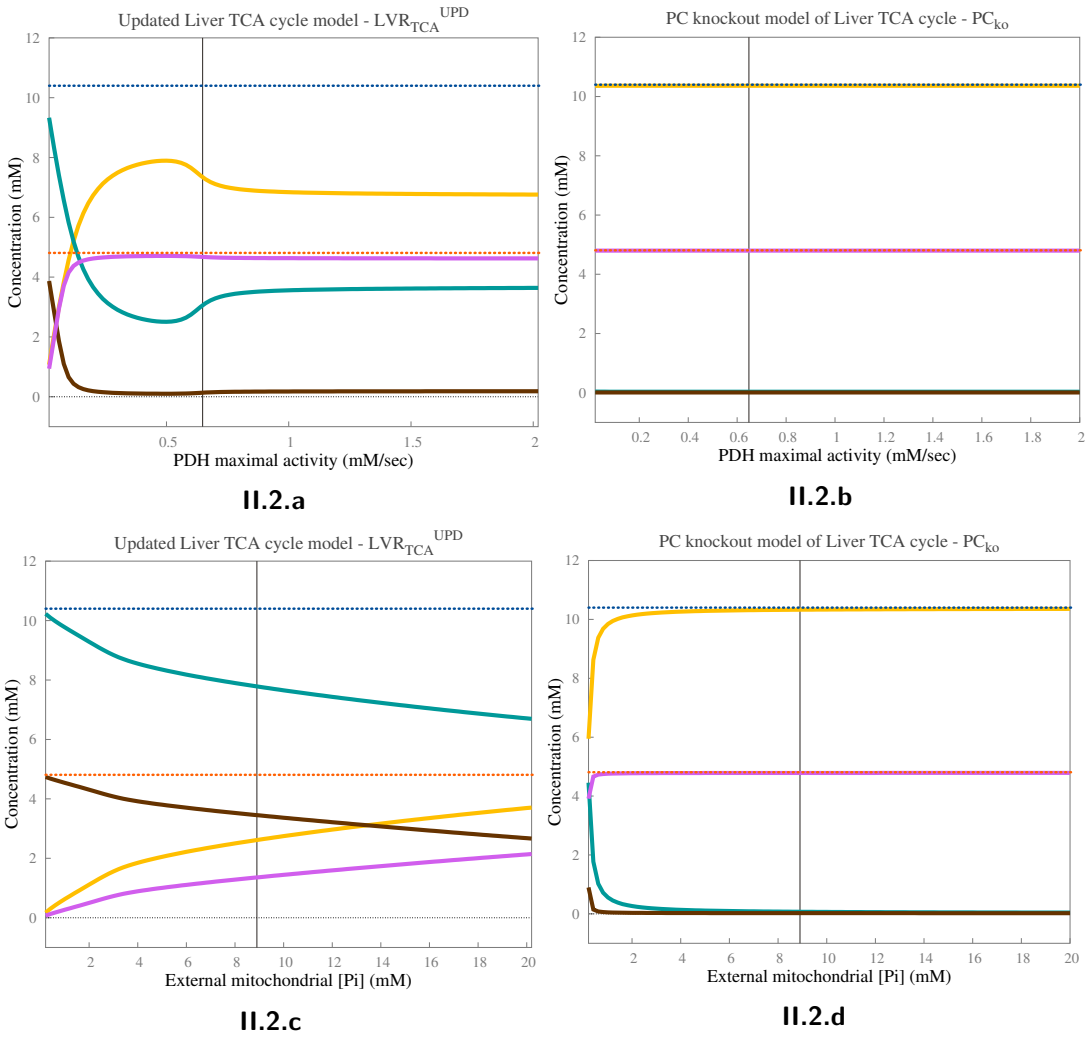

▪ **Supplemental Figure II.2. Concentrations of ATP−related metabolites:** effect of PC *'knock-out'* (PC_{ko}) in comparison with the PC *'wild-type'* (PC_{wt} *i.e.* LVR_{TCA}^{UPD}).

▪ Key for figs. II.2a to II.2d is as follows :

ATP_m ; ADP_m ; ATP_c ; ADP_c

mitochondrial ATP+ADP (total) ; cytosolic ATP+ADP (total)

▪ ***Supplementary data for fig. 3.6b on pg. 130 and for figs. 3.11a, 3.11b, 3.12a and 3.12b on pgs. 137 and 138.***

▪ The vertical black line represents the initial model value. At this point, in figs. II.2a and II.2b, V_{max}^{PDH} = 0.648 mM/sec and in figs. II.2c and II.2d, $[Pi_m]$ = 8.9 mM, respectively.

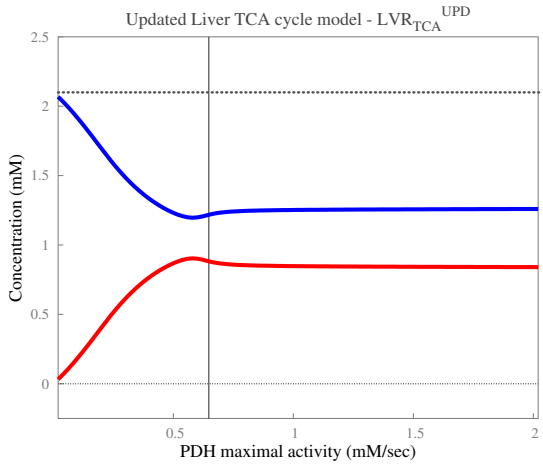

II.3.a

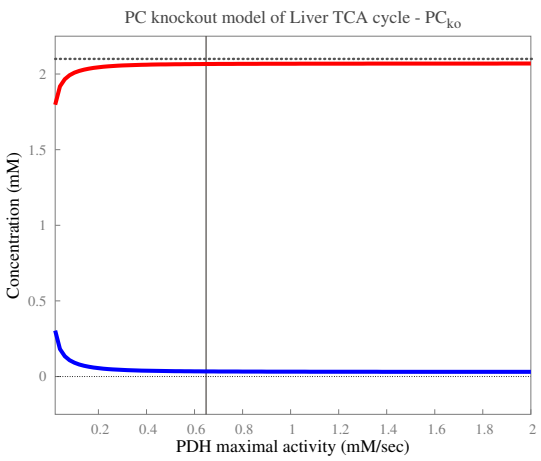

II.3.b

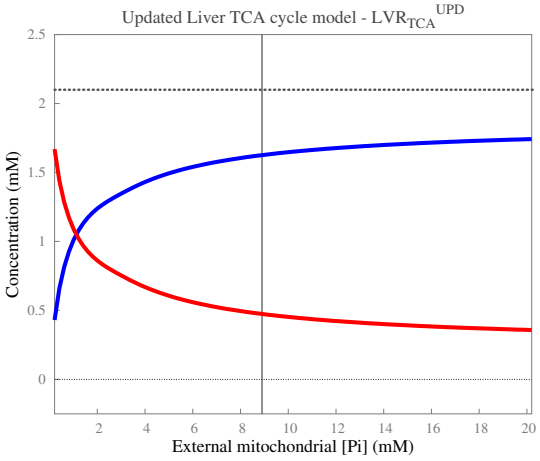

II.3.c

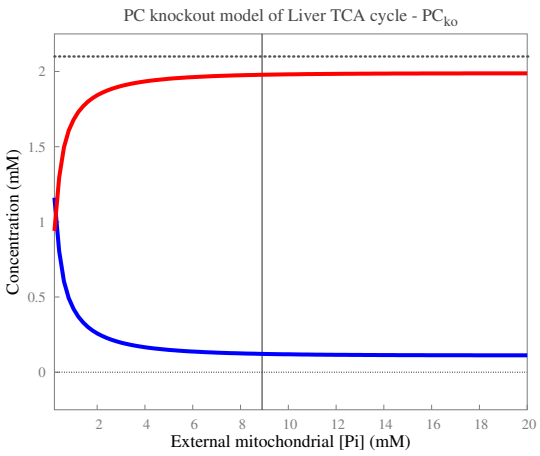

II.3.d

▪ **Supplemental Figure II.3. Concentrations of NAD−related metabolites:** effect of PC *'knock-out'* (PC_{ko}) in comparison with the PC *'wild-type'* (PC_{wt} *i.e.* LVR_{TCA}^{UPD}).

▪ Key for figs. II.3a to II.3d is as follows :

NAD_m^+ ; $NADH_m$; mitochondrial NAD^+/ NADH (total)

▪ ***Supplementary data for fig. 3.6c on pg. 131 and for figs. 3.11c and 3.12c on pgs. 137 and 138.***

▪ The vertical black line represents the initial model value. At this point, in figs. II.3a and II.3b, V_{max}^{PDH} = 0.648 mM/sec and in figs. II.3c and II.3d, [Pi_m] = 8.9 mM, respectively.

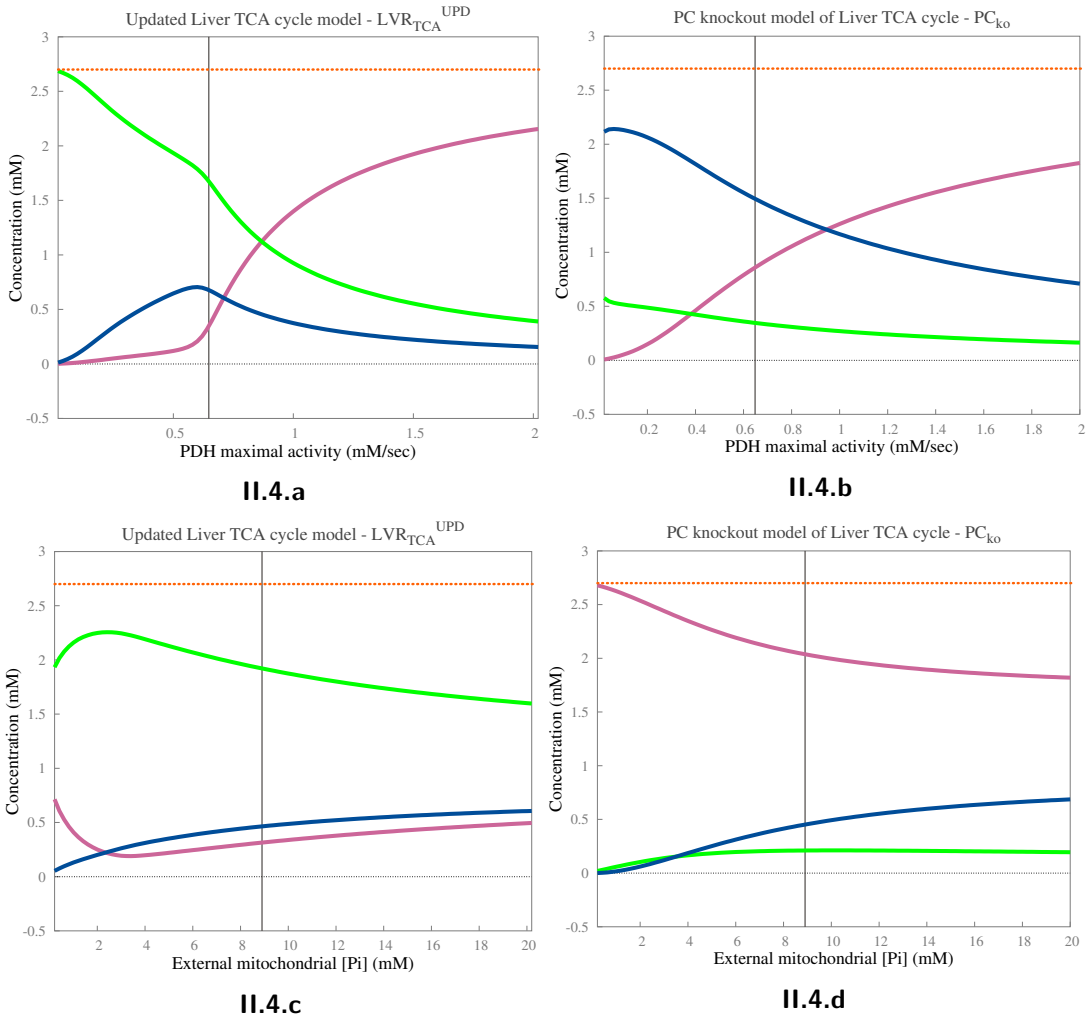

▪ **Supplemental Figure II.4. Concentrations of CoA−related metabolites:** effect of PC *'knock-out'* (PC_{ko}) in comparison with the PC *'wild-type'* (PC_{wt} *i.e.* LVR_{TCA}^{UPD}).

▪ Key for figs. II.4a to II.4d is as follows :

AcCoA$_m$; CoA$_m$; SCoA$_m$; *Total CoA content*

▪ ***Supplementary data for fig. 3.6c on pg. 131.***

▪ The vertical black line represents the initial model value. At this point, in figs. II.4a and II.4b, V_{max}^{PDH} = 0.648 mM/sec and in figs. II.4c and II.4d, [Pi$_m$] = 8.9 mM, respectively.

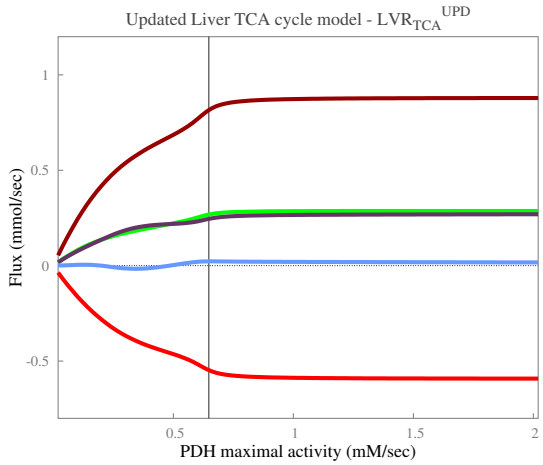

II.5.a

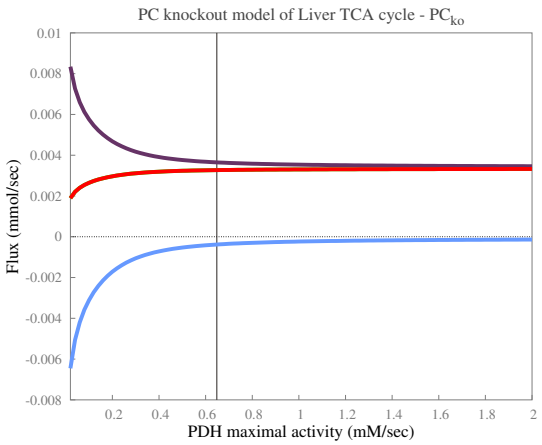

II.5.b

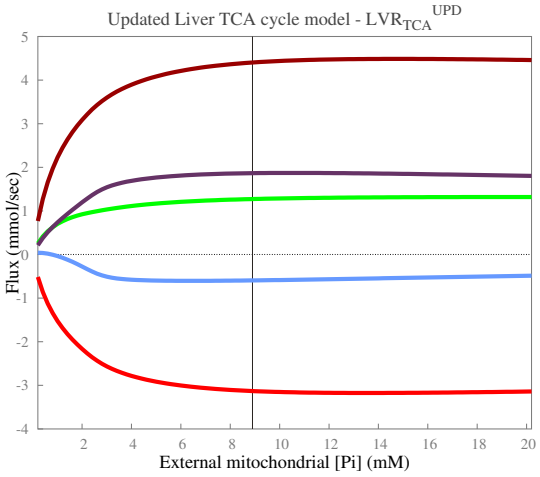

II.5.c

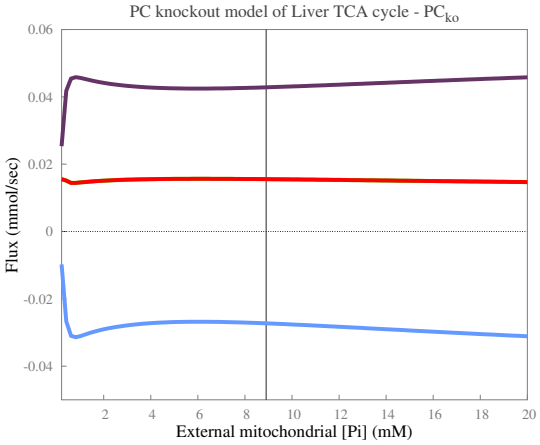

II.5.d

- **Supplemental Figure II.5. Liver TCA cycle fluxes against changes in Pi_m concentration & PDH maximal activity:** effect of PC *'knock-out'* (PC_{ko}) in comparison with the PC *'wild-type'* (PC_{wt} *i.e.* LVR_{TCA}^{UPD}).

- Key for figs. II.5a to II.5d is as follows :

IDHa; CS; IDHb; PC; MDH

- ***Supplementary data for the figs. 3.7 and 3.8 on pgs. 132 and 133.***

- The vertical black line represents the initial model value. At this point, in figs. II.5a and II.5b, V_{max}^{PDH} = 0.648 mM/sec and in figs. II.5c and II.5d, [Pi_m] = 8.9 mM, respectively.

Supplement III: Heart TCA cycle model

III.1 Suppl. data : Model definition for heart TCA model

▪ **Supplemental Table III.1.** Values of TCA cycle variables in heart tissue taken from the literature and predicted by the model [a,b,c]

Fluxes are in units of mmol/sec and concentrations in mM.

Variable	Literature Values		Model Values	Reference
	Range	Median		
TCA cycle (CS) flux	0.03 – 0.08	0.06	4.33E-03	(20; 72; 96; 97; 108; 132; 137; 145; 160)
$[CoA_m]$	0.01 – 0.08	0.046	2.05E-03	(3; 27; 37; 45; 127; 131; 150; 163)
$[AcCoA_m]$	0.02 – 0.33	0.18	0.25	(72; 99; 156; 160)
$[Cit_m]$	0.03 – 4.0	2.01	0.49	(3; 54; 73; 131; 150; 153; 164) (80; 84; 96; 105; 128; 132; 159) (97; 108; 109; 134; 156; 160; 163)
$[Isocit_m]$	0.03 – 0.12	0.08	3.32E-02	(54; 105; 153)
$[\alpha KG_m]$	0.01 – 0.8	0.4	6.00E-03	(47; 74; 80; 105; 108; 132; 160; 163) (3; 17; 54; 73; 109; 131; 156; 159)
$[Suc_m]$	0.06 – 3.9	2.0	4.27E-02	(17; 73; 80; 96; 97; 128; 131; 159; 163)
$[SCoA_m]$	0.01 – 0.29	0.15	1.55E-04	(44; 161; 163)
$[Fum_m]$	6.9E-03 – 0.26	0.13	3.65E-02	(17; 54; 80; 96; 97; 131)
$[Mal_m]$	0.16 – 1.88	1.02	0.16	(73; 80; 96; 105; 128; 131; 153; 159) (47; 97; 108; 109; 132; 134; 163)
$[OAA_m]$	0.002 – 0.062	0.032	1.44E-05	(39; 80; 105; 108; 134; 153; 156; 160; 163)
$[NAD^+_m]$	0.56 – 1.36	0.96	0.6	(61; 153; 163)
$[NADH_m]$	0.1 – 1.0	0.53	0.094	(61; 72; 93; 98; 153; 156; 163)
$[ADP_m]$			0.88	
$[ATP_m]$	Same as the liver		9.52	Same as the liver
Free [d] $[ADP_c]$	TCA cycle model		4.47E-02	TCA cycle model
Free [d] $[ATP_c]$			4.77	

[a] The predicted model values are obtained at steady-state, upon simulating the Heart TCA cycle model. These are the same values shown in the analysis of initial steady-state of the model, in the results section.

[b] Metabolite and effector concentrations reported in units of moles per gram of wet or dry tissue weight were converted to units of mM assuming a heart tissue dry/wet weight ratio of 0.2 (Lopaschuk et al., 1992) and a cell volume/weight ratio of 2.0 ml g^{-1} dry weight (Idell-Wenger et al., 1978; Yu et al., 1995).

[c] Concentrations reported in units of moles per gram of mitochondrial protein were similarly converted assuming a mitochondrial protein density of 272500 mg l^{-1} (Vinnakota and Bassingthwaighte, 2004).

[d] Not bound to fixed sites; in the case of ATP, fixed-site binding is negligible (Magnus and Keizer, 1997).

Parameter values are largely derived from the literature, and unless otherwise specified are for mammalian (predominantly rat) heart mitochondria. Wherever possible, values determined under conditions approximating the in vivo mitochondrial environment are used; a mitochondrial matrix pH of 8 is assumed (1; 70; 76; 86; 146). Concentrations were converted to units of mM, and from cellular/ cytosolic to mitochondrial, using the conversion factors listed above.

- **Supplemental Table III.2.** Parameter Values for the Heart TCA cycle model

Equation [I]	Parameter	Value	Units	Reference
E.7	$[\alpha KG_c]$	6.0E-03	mM	–
A.16	$[A_{Tot_c}]$			
B.13 & B.18	$[Ca^{2+}]$			
B.6, B.12 & B.17	$[CO_2]$			
A.15	$[A_{Tot_m}]$	*Same as the liver TCA cycle model*		
B.20 & B.36	$[Pi_m]$			
B.37	$[Pi_c]$			
B.7	$[Pyr_m]$			
B.22	$[Q]$			
	$[QH_2]$			
B.7	V_{PDH}	0.1885 [a,b]	mM/sec	(56; 65)
	K_{Pyr_m}	0.028	mM	(120; 147; 148)
	$K_{NAD^+_m}$	0.0607	mM	(10; 65; 106; 138; 149; 159)
	K_{CoA_m}	0.006	mM	(65; 148)
	K_{NADH_m}	*Same as the liver TCA cycle model*		
	K_{AcCoA_m}			
B.9	V_{CS}	2.5433 [a,c]	mM/sec	(95; 125)
	K_{eq}	1.01E+06 [d]	unitless	(43)
	K_{OAA_m}	5.0E-03	mM	(95; 125)
	K_{AcCoA_m}	5.0E-03	mM	(69; 95; 125)
	K_{SCoA_m}	0.13	mM	(10; 65; 123; 159)

(*Continued on next page . . .*)

B.9	$K_{\mathrm{ATP_m}}$	0.70	mM	(75; 95; 115)
	$K_{\mathrm{Cit_m}}$	*Same as the liver TCA cycle model*		
	$K_{\mathrm{CoA_m}}$			
B.11	V_{ACO}	2.27 [a,e]	mM/sec	(7; 125)
	K_{eq}	*Same as the liver TCA cycle model*		
	$K_{\mathrm{Cit_m}}$			
	$K_{\mathrm{Isocit_m}}$			
B.13	V_{IDHa}	1.371 [a,f]	mM/sec	(3; 7; 126)
	n	2.7	–	(28; 107)
	$K_{\mathrm{NAD^+_m}}$	0.074	mM	(63; 64; 65; 102; 159)
	$K_{\mathrm{ATP_m}}$	0.091	mM	(63; 64; 65; 159)
	$K_{\mathrm{Isocit_m}}$	*Same as the liver TCA cycle model*		
	$K_{\mathrm{NADH_m}}$			
	$K_{\mathrm{ADP^{3-}_m}}$			
	$K_{\mathrm{Ca^{2+}}}$			
B.14 & B.29	$f_{\mathrm{ADP^{3-}_m}}$			
E.7	$V_{\alpha\mathrm{KG_{exp}}}$	1.0	mM/sec	–
	K_{eq}	1.0	unitless	–
B.18	$V_{\alpha\mathrm{KGDH}}$	7.4426	mM/sec	(3; 85; 110)
	$K_{\alpha\mathrm{KG_m}}$	0.08 [g]	mM	(64; 155; 159)
	$K_{\mathrm{CoA_m}}$	*Same as the liver TCA cycle model*		
	$K_{\mathrm{NADH,c}}$			
	$K_{\mathrm{SCoA_m}}$			
	$K_{\mathrm{ATP_m}}$			
	$K_{\mathrm{NADH,u}}$			
	$K_{\mathrm{ADP_m}}$			
	$K_{\mathrm{Ca^{2+}}}$			
	$K_{\mathrm{NAD^+_m}}$			

(*Continued on next page . . .*)

B.20	V_{SCS}	3.1082 [a,h]	mM/sec	(3; 19; 93)
	K_{eq}	0.78	unitless	(81)
	K_{SCoA_m}			
	K_{ADP_m}			
	K_{Pi_m}			
	K_{Suc_m}	*Same as the liver TCA cycle model*		
	K_{CoA_m}			
	K_{ATP_m}			
B.22	V_{SDH}			
	K_{eq}			
	K_{Suc_m}			
	K_{Q}	*Same as the liver TCA cycle model*		
	K_{Fum_m}			
	K_{QH_2}			
	K_{OAA_m}			
B.24	V_{FM}	7.93 [a]	mM/sec	(7; 126)
	K_{Fum_m}	1.74E-03	mM	(16; 159)
	K_{Mal_m}	3.80E-03	mM	(16; 159)
	K_{eq}	*Same as the liver TCA cycle model*		
B.26	V_{MDH}	1.03 [a,i,j]	mM/sec	(57)
	K_{eq}	2.3E-05	unitless	(125)
	$K_{NAD^+_m}$	0.3	mM	(57; 135; 159)
	K_{Mal_m}			
	K_{OAA_m}	*Same as the liver TCA cycle model*		
	K_{NADH_m}			
B.28	V_{ANT}			
	K_{eq}	*Same as the liver TCA cycle model*		
	$K_{ATP^{4-}_m}$			
	$K_{ADP^{3-}_c}$			

(*Continued on next page . . .*)

B.28	$K_{\mathrm{ADP}_{\mathrm{m}}^{3-}}$ $K_{\mathrm{ATP}_{\mathrm{c}}^{4-}}$ $f_{\mathrm{ATP}_{\mathrm{m}}^{4-}}$	*Same as the liver TCA cycle model*		
B.29	$f_{\mathrm{ATP}_{\mathrm{c}}^{4-}}$ $f_{\mathrm{ADP}_{\mathrm{c}}^{3-}}$			
B.36	$V_{\mathrm{ATP}_{\mathrm{synth}}}$ $K_{\mathrm{NADH}_{\mathrm{m}}}$ $K_{\mathrm{ADP}_{\mathrm{m}}}$ $K_{\mathrm{Pi}_{\mathrm{m}}}$ $K_{\mathrm{NAD}_{\mathrm{m}}^{+}}$ $K_{\mathrm{ATP}_{\mathrm{m}}}$	*Same as the liver TCA cycle model*		
B.38	$f_{\mathrm{ATP}_{\mathrm{hyd}}}$	0.01 [k]	sec^{-1}	(71)

[a] Calculated from the reported mitochondrial concentration and specific activity, taking into account the number of active sites within the holoenzyme.

[b] Assumed to represent the physiological level of activation.

[c] Calculated using the rat heart enzyme, purified using a tris–HCl buffer maintained at pH 8.1 and at 28°C (Moriyama and Srere, 1971).

[d] Calculated from the thermodynamic properties of the species involved in the reaction. Calculated using the pig heart enzyme, purified at pH 7.0 and at 38°C (Guynn et al., 1973).

[e] Enzyme concentration estimated from the specific activities of the crude extract and the purified enzyme from rat liver (Eprintsev et al., 2002; Guarriero-Bobyleva et al., 1973), according to the methodology of Albe et al., 1990; specific activity determined in bovine heart (Bachmann et al., 1966; Srere, 1972a).

[f] The enzyme specific activity was determined in the bovine heart mitochondria.

[g] Calculated using the rat heart enzyme, purified using a tris–Cl buffer maintained at pH 7.2 and at 28°C (Williamson et al., 1973; Wu et al., 2007).

[h] Calculated using the specific activity of pig heart enzyme, purified using a potassium phosphate (KH_2PO_4) buffer maintained at pH 7.4 and at 30°C (Cha and Parks, 1964b; Mogilevskaya et al., 2006).

[i] Calculated using the specific activity of pig heart enzyme, purified using a tris–acetate buffer maintained at pH 8.0 and at 25°C (Kimball et al., 1979).

[j] The originally calculated V_{max} value of 25.66667 mM/sec was divided by a factor of 25 during the model optimisation process.

[k] Estimated rate of ATP demand at rest (basal activity), in the rabbit skeletal muscle (Lambeth and Kushmerick, 2002). The estimates at moderate and high level of ATP demand are also provided in the same citation.

[l] As mentioned in the heart TCA cycle model chapter, apart from the α-ketoglutarate transporter reaction (α-KG_{exp}), all the other enzymatic reactions are essentially common between the heart & the liver-specific TCA cycle models, in terms of their individual rate equations. Therefore in this table, only the αKG_c concentration parameter, as well as the rate parameters for α-KG_{exp} reaction point to the appropriate equation defined in the heart-specific model. All the remaining parameters listed in this table, point to the reaction equations included within the liver TCA cycle model chapter appendix (Please refer to Appendix B on pgs. pg. 221 to pg. 232).

Supplementary References

1. M.F. Abad, G. Di Benedetto, P.J. Magalhaes, L. Filippin, and T. Pozzan. Mitochondrial pH Monitored by a New Engineered Green Fluorescent Protein Mutant. *J. Biol. Chem.*, 279(12):11521–11529, March 2004. URL http://www.ncbi.nlm.nih.gov/pubmed/14701849.

2. T.P.M. Akerboom, H. Bookelman, P.F. Zuurendonk, R. van der Meer, and J.M. Tager. Intramitochondrial and extramitochondrial concentrations of adenine nucleotides and inorganic phosphate in isolated hepatocytes from fasted rats. *Eur. J. Biochem./FEBS*, 84(2):413–420, March 1978. URL http://www.ncbi.nlm.nih.gov/pubmed/639797.

3. K.R. Albe, M.H. Butler, and B.E. Wright. Cellular concentrations of enzymes and their substrates. *J. Theor. Biol.*, 143(2):163–95, March 1990. URL http://www.ncbi.nlm.nih.gov/pubmed/2200929.

4. R.A. Alberty. Thermodynamics of Biochemical Reactions at Specified pH. In *Thermodynamics of Biochemical Reactions*, chapter 4, pages 57–87. John Wiley & Sons, Inc., Hoboken, N.J., U.S.A., 2003. URL http://www.worldcat.org/oclc/51242181.

5. P.L. Altman and D.D. Katz. *Cell biology*. Biological handbooks, Vol. I. Federation of American Societies for Experimental Biology, Bethesda, Maryland, 1976. URL http://www.worldcat.org/oclc/3293807.

6. L.K. Ashman, D.B. Keech, J.C. Wallace, and J. Nielsen. Sheep kidney pyruvate carboxylase. Studies on its activation by acetyl coenzyme A and characteristics of its acetyl coenzyme A independent reaction. *J. Biol. Chem.*, 247(18):5818–5824, 1972. URL http://www.ncbi.nlm.nih.gov/pubmed/5057085.

7. E. Bachmann, D.W. Allmann, and D.E. Green. The membrane systems of the mitochondrion. I. The S fraction of the outer membrane of beef heart mitochondria. *Arch. Biochim. Biophys.*, 115(1):153–164, jul 1966. URL http://www.ncbi.nlm.nih.gov/pubmed/4226061.

8. D.J. Ball and J.S. Nishimura. Affinity chromatography and affinity labelling of rat liver succinyl-CoA synthetase. *J. Biol. Chem.*, 255(22):10805–10812, November 1980. URL http://www.ncbi.nlm.nih.gov/pubmed/7430155.

9. J. M. Baranyai and J. J. Blum. Quantitative analysis of intermediary metabolism in rat hepatocytes incubated in the presence and absence of ethanol with a substrate mixture including ketoleucine. *Biochem. J.*, 258:121–140, 1989. URL http://www.ncbi.nlm.nih.gov/pubmed/2930501.

10. J.N. Bazil, G.T. Buzzard, and A.E. Rundell. Modelling mitochondrial bioenergetics with integrated volume dynamics. *PLoS comput. biol.*, 6(1):e1000632, January 2010. URL http://www.ncbi.nlm.nih.gov/pubmed/20052270.

11. G. Benard. Ph.D. thesis, Université Victor Segalen Bordeaux 2, 2006.

12. G. Benard, B. Faustin, E. Passerieux, A. Galinier, C. Rocher, N. Bellance, J.P. Delage, L. Casteilla, T. Letellier, and R. Rossignol. Physiological diversity of mitochondrial oxidative phosphorylation. *Am. J. Physiol. Cell Physiol.*, 291(6):C1172–C1182, December 2006. URL http://www.ncbi.nlm.nih.gov/pubmed/16807301.

13. M. Beylot, M.V. Soloviev, F. David, B.R. Landau, and H. Brunengraber. Tracing Hepatic Gluconeogenesis Relative to Citric Acid Cycle Activity in Vitro and in Vivo: Comparisons In The Use of [3-C]Lactate, [2-C]Acetate, and α-Keto[3-C]Isocaproate. *J. Biol. Chem.*, 270(4):1509–1514, 1995. URL http://www.ncbi.nlm.nih.gov/pubmed/7829478.

14. J.S. Blanchard and W.W. Cleland. Use of isotope effects to deduce the chemical mechanism of fumarase. *Biochemistry*, 19(19):4506–4513, September 1980. URL http://www.ncbi.nlm.nih.gov/pubmed/7407088.

15. R.M. Bock and R.A. Alberty. Studies of the Enzyme Fumarase. I. Kinetics and Equilibrium. *J. Am. Chem. Soc.*, 75(8):1921–1925, 1953. URL http://pubs.acs.org/doi/abs/10.1021/ja01104a043.

16. D.A. Brant, L.B. Barnett, and R.A. Alberty. The Temperature Dependence of the Steady State Kinetic Parameters of the Fumarase Reaction. *J. Am. Chem. Soc.*, 85(15):2204–2209, 1963. URL http://pubs.acs.org/doi/abs/10.1021/ja00898a003.

17. R.A. Carvalho, P. Zhao, C.B. Wiegers, F.M. Jeffrey, C.R. Malloy, and A.D. Sherry. TCA cycle kinetics in the rat heart by analysis of ^{13}C isotopomers using indirect ^{1}H. *Am. J. Physiol. Heart Circ. Physiol.*, 281(3):H1413–H1421, 2001. URL http://www.ncbi.nlm.nih.gov/pubmed/11514314.

18. S. Cha and R.E. Jr. Parks. Succinic thiokinase. II. Kinetic studies: initial velocity, product inhibition, and effect of arsenate. *J. Biol. Chem.*, 239(6):1968–1977, 1964a. URL http://www.ncbi.nlm.nih.gov/pubmed/14213385.

19. S. Cha and R.E. Jr. Parks. Succinic thiokinase. I. Purification of the enzyme from pig heart. *J. Biol. Chem.*, 239(6):1961–1967, 1964b. URL http://www.ncbi.nlm.nih.gov/pubmed/14213384.

20. E.M. Chance, S.H. Seeholzer, K. Kobayashi, and J.R. Williamson. Mathematical analysis of isotope labeling in the citric acid cycle with applications to ^{13}C NMR studies in perfused rat hearts. *J. Biol. Chem.*, 258(22):13785–13794, November 1983. URL http://www.ncbi.nlm.nih.gov/pubmed/6643454.

21. S.M. Cohen. Simultaneous ^{13}C and ^{31}P NMR studies of perfused rat liver. Effects of insulin and glucagon and a ^{13}C NMR assay of free Mg^{2+}. *J. Biol. Chem.*, 258(23):14294–14308, December 1983. URL http://www.ncbi.nlm.nih.gov/pubmed/6358220.

22. B.E. Corkey, J. Duszynski, T. L. Rich, B. Matschinsky, and J. R. Williamson. Regulation of free and bound magnesium in rat hepatocytes and isolated mitochondria. *J. Biol. Chem.*, 261(6):2567–2574, 1986. URL http://www.ncbi.nlm.nih.gov/pubmed/3081495.

23. S. Cortassa, M.A. Aon, E. Marbán, R.L. Winslow, and B. O'Rourke. An integrated model of cardiac mitochondrial energy metabolism and calcium dynamics. *Biophys. J.*, 84(4):2734–2755, April 2003. URL http://www.ncbi.nlm.nih.gov/pubmed/12668482.

24. J.M. Crawford and J.J. Blum. Quantitative analysis of flux along the gluconeogenic, glycolytic and pentose phosphate pathways under reducing conditions in hepatocytes isolated from fed rats. *Biochem. J.*, 212(3):585–598, June 1983. URL http://www.ncbi.nlm.nih.gov/pubmed/6411069.

25. K.E. Crow, T.J. Braggins, R.D. Batt, and M.J. Hardman. Rat liver cytosolic malate dehydrogenase: purification, kinetic properties, role in control of free cytosolic NADH concentration. Analysis of control of ethanol metabolism using computer simulation. *J. Biol. Chem.*, 257(23):14217–14225, December 1982. URL http://www.ncbi.nlm.nih.gov/pubmed/7142202.

26. C.C. Cunningham, C.R. Malloy, and G.K. Radda. Effect of fasting and acute ethanol administration on the energy state of in vivo liver as measured by ^{31}P-NMR spectroscopy. *Biochim. Biophys. Acta. - Mol. Cell. Res.*, 885(1):12–22, January 1986. URL http://www.ncbi.nlm.nih.gov/pubmed/3942792.

27. M.S. DeBuysere and M.S. Olson. The analysis of acyl-Coenzyme A derivatives by reverse-phase high-performance liquid chromatography. *Anal. Biochem.*, 133(2):373–379, 1983. URL https://www.ncbi.nlm.nih.gov/pubmed/6638498.

28. R.M. Denton, D.A. Richards, and J.G. Chin. Calcium ions and the regulation of NAD^+-linked isocitrate dehydrogenase from the mitochondria of rat heart and other tissues. *Biochem. J.*, 176(3):899–906, dec 1978. URL http://www.ncbi.nlm.nih.gov/pubmed/218557.

29. D.V. DerVartanian and C. Veeger. Studies on succinate dehydrogenase: I. Spectral properties of the purified enzyme and formation of enzyme-competitive inhibitor complexes. *Biochim. Biophys. Acta.*, 92 (2):233–247, 1964. URL http://www.ncbi.nlm.nih.gov/pubmed/14249115.

30. C. Des Rosiers, L. Di Donato, B. Comte, A. Laplante, C. Marcoux, F. David, C.A. Fernandez, and H. Brunengraber. Isotopomer analysis of citric acid cycle and gluconeogenesis in rat liver. Reversibility of isocitrate dehydrogenase and involvement of ATP-citrate lyase in gluconeogenesis. *J. Biol. Chem.*, 270:10027–10036, 1995. URL http://www.ncbi.nlm.nih.gov/pubmed/7730304.

31. F. Desmoulin, P.J. Cozzone, and P. Canioni. Phosphorus-31 nuclear-magnetic-resonance study of phosphorylated metabolites compartmentation, intracellular pH and phosphorylation state during normoxia, hypoxia and ethanol perfusion, in the perfused rat liver. *Eur. J. Biochem.*, 162(1):151–159, January 1987. URL http://www.ncbi.nlm.nih.gov/pubmed/3816778.

32. L. Di Donato, C. Des Rosiers, J.A. Montgomery, F. David, M. Garneau, and H. Brunengraber. Rates of gluconeogenesis and citric acid cycle in perfused livers, assessed from the mass spectrometric assay of the ^{13}C labelling pattern of glutamate. *J. Biol. Chem.*, 268(6):4170–4180, 1993. URL http://www.ncbi.nlm.nih.gov/pubmed/8095046.

33. E.D. Duée and P.V. Vignais. Kinetics and specificity of the adenine nucleotide translocation in rat liver mitochondria. *J. Biol. Chem.*, 244(14):3920–3931, July 1969. URL http://www.ncbi.nlm.nih.gov/pubmed/4979771.

34. A.T. Eprintsev, E.V. Semenova, and V.N. Popov. Induction of Aconitate Hydratase in Hepatocytes of Starving Rats. *Biochemistry (Moscow)*, 67(7):795–801, 2002. URL http://www.ncbi.nlm.nih.gov/pubmed/12139479.

35. L.A. Fahien and J.K. Teller. Glutamate-malate metabolism in liver mitochondria. A model constructed on the basis of mitochondrial levels of enzymes, specificity, dissociation constants, and stoichiometry of hetero-enzyme complexes. *J. Biol. Chem.*, 267(15):10411–10422, May 1992. URL http://www.ncbi.nlm.nih.gov/pubmed/1350279.

36. A.J. Garber and R.W. Hanson. The interrelationships of the various pathways forming gluconeogenic precursors in guinea pig liver mitochondria. *J. Biol. Chem.*, 246(3):589–598, February 1971. URL http://www.ncbi.nlm.nih.gov/pubmed/5542673.

37. P.B. Garland and P.J. Randle. Control of pyruvate dehydrogenase in the perfused rat heart by the intracellular concentration of acetyl-coenzyme A. *Biochem. J.*, 91(1):6C–7C, 1964. URL http://www.ncbi.nlm.nih.gov/pubmed/5833391.

38. P.B. Garland, D. Shepherd, and D.W. Yates. Steady-state concentrations of coenzyme A, acetyl-coenzyme A and long-chain fatty acyl-coenzyme A in rat-liver mitochondria oxidizing palmitate. *Biochem. J.*, 97(2):587–594, November 1965. URL http://www.ncbi.nlm.nih.gov/pubmed/16749169.

39. M.J. Gibala, M.A. Tarnopolsky, and T.E. Graham. Tricarboxylic acid cycle intermediates in human muscle at rest and during prolonged cycling. *Am. J. Physiol.*, 272(2 (Pt 1)):E239–E244, 1997. URL http://www.ncbi.nlm.nih.gov/pubmed/9124329.

40. V.G. Grivennikova, E.V. Gavrikova, A.A. Timoshin, and A.D. Vinogradov. Fumarate reductase activity of bovine heart succinate-ubiquinone reductase. New assay system and overall properties of the reaction. *Biochim. Biophys. Acta.*, 1140(3):282–92, January 1993. URL http://www.ncbi.nlm.nih.gov/pubmed/8417779.

41. N. Grunnet and J. Katz. Effects of ammonia and norvaline on lactate metabolism by hepatocytes from starved rats. The use of 14C-labelled lactate in studies of hepatic gluconeogenesis. *Biochem. J.*, 172(3):595–603, June 1978. URL http://www.ncbi.nlm.nih.gov/pubmed/687361.

42. V. Guarriero-Bobyleva, M.A. Volpi-Becchi, and A. Masini. Parallel Partial Purification of Cytoplasmic and Mitochondrial Aconitate Hydratases from Rat Liver. *Eur. J. Biochem.*, 34(3):455–458, May 1973. URL http://www.ncbi.nlm.nih.gov/pubmed/4736701.

43. R.W. Guynn, H.J. Gelberg, and R.L. Veech. Equilibrium constants of the malate dehydrogenase, citrate synthase, citrate lyase, and acetyl coenzyme A hydrolysis reactions under physiological conditions. *J. Biol. Chem.*, 248(20):6957–6965, 1973. URL http://www.ncbi.nlm.nih.gov/pubmed/4743509.

44. J.L. Hall, G.D. Lopaschuk, A. Barr, J. Bringas, R.D. Pizzurro, and W.C. Stanley. Increased cardiac fatty acid uptake with dobutamine infusion in swine is accompanied by a decrease in malonyl CoA levels. *Cardiovasc. Res.*, 32(5):879–885, nov 1996a. URL http://www.ncbi.nlm.nih.gov/pubmed/8944819.

45. J.L. Hall, W.C. Stanley, G.D. Lopaschuk, J.A. Wisneski, R.D. Pizzurro, C.D. Hamilton, and J.G. Mccormack. Impaired pyruvate oxidation but normal glucose uptake in diabetic pig heart during dobutamine-induced work. *Am. J. Physiol.*, 271(6, Pt 2):H2320–H2329, 1996b. URL http://www.ncbi.nlm.nih.gov/pubmed/8997289.

46. M. Hamada, K. Koike, Y. Nakaula, T. Hiraoka, and M. Koike. A kinetic study of the alpha-keto acid dehydrogenase complexes from pig heart mitochondria. *J. Biochem.*, 77(5):1047–1056, May 1975. URL http://www.ncbi.nlm.nih.gov/pubmed/169232.

47. J.J. Hautecler, C.M. Sluse-Goffart, A. Evens, C. Duyckaerts, and F.E. Sluse. Effect of aspartate and glutamate on the oxoglutarate carrier investigated in rat heart mitochondria and inverted submitochondrial vesicles. *Biochim. Biophys. Acta.*, 1185(2):153–159, 1994. URL http://www.ncbi.nlm.nih.gov/pubmed/7909447.

48. A.O. Hawtrey. Studies on isocitrate oxidation in mitochondria of normal rat liver and azo-dye-induced hepatomas. *Biochem. J.*, 85:293–305, November 1962. URL http://www.ncbi.nlm.nih.gov/pubmed/14435366.

49. E. Heyde and S. Ainsworth. Kinetic Studies on the Mechanism of the Malate Dehydrogenase Reaction. *J. Biol. Chem.*, 243(9):2413–2423, 1968. URL http://www.ncbi.nlm.nih.gov/pubmed/4296842.

50. A. Holian and D.F. Wilson. Relationship of transmembrane pH and electrical gradients with respiration and adenosine 5'-triphosphate synthesis in mitochondria. *Biochemistry*, 19(18):4213–4221, September 1980. URL http://www.ncbi.nlm.nih.gov/pubmed/7417402.

51. Y.C. Huang and R.F. Colman. Location of the coenzyme binding site in the porcine mitochondrial $NADP^+$-dependent isocitrate dehydrogenase. *J. Biol. Chem.*, 280(34):30349–30353, August 2005. URL http://www.ncbi.nlm.nih.gov/pubmed/15975917.

52. J.A. Idell-Wenger, L.W. Grotyohann, and J.R. Neely. Coenzyme A and Carnitine Distribution in Normal and Ischemic Hearts. *J. Biol. Chem.*, 253(12):4310–4318, 1978. URL http://www.ncbi.nlm.nih.gov/pubmed/207696.

53. C. Indiveri, G. Prezioso, T. Dierks, R. Kramer, and F. Palmieri. Kinetic characterization of the reconstituted dicarboxylate carrier from mitochondria: a four-binding-site sequential transport system. *Biochim. Biophys. Acta. - Bioenergetics*, 1143(3):310–318, July 1993. URL http://www.ncbi.nlm.nih.gov/pubmed/8329439.

54. F.M. Jeffrey, A. Reshetov, C.J. Storey, R.A. Carvalho, A.D. Sherry, and C.R. Malloy. Use of a single ^{13}C NMR resonance of glutamate for measuring oxygen consumption in tissue. *Am. J. Physiol.*, 277(6, Pt 1):E1111–E1121, dec 1999. URL http://www.ncbi.nlm.nih.gov/pubmed/10600802.

55. B.M. Jucker, J.Y. Lee, and R.G. Shulman. In vivo ^{13}C NMR measurements of hepatocellular tricarboxylic acid cycle flux. *J. Biol. Chem.*, 273(20):12187–12194, May 1998. URL http://www.ncbi.nlm.nih.gov/pubmed/9575166.

56. A.L. Kerbey, P.J. Randle, R.H. Cooper, S. Whitehouse, H.T. Pask, and R.M. Denton. Regulation of pyruvate dehydrogenase in rat heart. Mechanism of regulation of proportions of dephosphorylated and phosphorylated enzyme by oxidation of fatty acids and ketone bodies and of effects of diabetes: role of coenzyme A, acetyl-coenzyme A and reduced and oxidized nicotinamide-adenine dinucleotide. *Biochem. J.*, 154(2):327–348, February 1976. URL http://www.ncbi.nlm.nih.gov/pubmed/180974.

57. D.F. Kimball, L. Peterson, D.J. McLoughlin, and R.G. Wolfe. Malate dehydrogenase. Kinetic studies with meso-tartrate and 2-keto-3-hydroxysuccinate, comparison of the mitochondrial and supernatant pig heart enzymes. *Arch. Biochim. Biophys.*, 195(1):66–73, 1979. URL http://www.ncbi.nlm.nih.gov/pubmed/475389.

58. G.A. Kimmich and H. Rasmussen. Regulation of pyruvate carboxylase activity by calcium in intact rat liver mitochondria. *J. Biol. Chem.*, 244(1):190–199, January 1969. URL http://www.ncbi.nlm.nih.gov/pubmed/5773282.

59. M. Klingenberg. The ADP-ATP translocation in mitochondria, a membrane potential controlled transport. *J. Memb. Biol.*, 56(2):97–105, 1980. URL http://www.ncbi.nlm.nih.gov/pubmed/7003152.

60. M. Klingenberg and H. Rottenberg. Relation between the gradient of the ATP/ADP ratio and the membrane potential across the mitochondrial membrane. *Eur. J. Biochem./FEBS*, 73(1):125–130, February 1977. URL http://www.ncbi.nlm.nih.gov/pubmed/14003.

61. K. Kobayashi and J.R. Neely. Control of maximum rates of glycolysis in rat cardiac muscle. *Circ. Res.*, 44(2):166–175, 1979. URL http://www.ncbi.nlm.nih.gov/pubmed/216503.

62. K. Kobayashi, T. Yamanishi, and S. Tuboi. Physicochemical, catalytic, and immunochemical properties of fumarases crystallized separately from mitochondrial and cytosolic fractions of rat liver. *J. Biochem.*, 89(6):1923–1931, June 1981. URL http://www.ncbi.nlm.nih.gov/pubmed/7287666.

63. M.C. Kohn and D. Garfinkel. Computer simulation of metabolism in palmitate-perfused rat heart. II. Behavior of complete model. *Ann. Biomed. Eng.*, 11(6):511–531, jan 1983. URL http://www.ncbi.nlm.nih.gov/pubmed/6391299.

64. M.C. Kohn, M.J. Achs, and D. Garfinkel. Computer simulation of metabolism in pyruvate-perfused rat heart. II. Krebs cycle. *Am. J. Physiol.*, 237(3):R159–R166, 1979a. URL http://www.ncbi.nlm.nih.gov/pubmed/224718.

65. M.C. Kohn, M.J. Achs, and D. Garfinkel. Computer simulation of metabolism in pyruvate-perfused rat heart. III. Pyruvate dehydrogenase. *Am. J. Physiol.*, 237(3):R167–173, 1979b. URL http://www.ncbi.nlm.nih.gov/pubmed/474788.

66. R. Kramer and M. Klingenberg. Electrophoretic control of reconstituted adenine nucleotide translocation. *Biochemistry*, 21(5):1082–1089, March 1982. URL http://www.ncbi.nlm.nih.gov/pubmed/6280754.

67. H.A. Krebs. The equilibrium constants of the fumarase and aconitase systems. *Biochem. J.*, 54(1):78–82, April 1953. URL http://www.ncbi.nlm.nih.gov/pubmed/13058835.

68. H.A. Krebs and R.L. Veech. Regulation of the Redox State of the Pyridine Nucleotides in Rat Liver. In H. Sund, editor, *Pyridine Nucleotide-Dependent Dehydrogenases: Proceedings of an Advanced Study Institute held at the University of Konstanz, Germany, September 15–20, 1969*, chapter 34, pages 413–438. Springer-Verlag, Berlin, Heidelberg, New York, 1 edition, 1970. URL https://books.google.co.in/books?id=PgH8CAAAQBAJ.

69. L.C. Kurz, S. Shah, C. Frieden, T. Nakra, R.E. Stein, G.R. Drysdale, C.T. Evans, and P.A. Srere. Catalytic Strategy of Citrate Synthase: Subunit Interactions Revealed as a Consequence of a Single Amino Acid Change in the Oxaloacetate Binding Site. *Biochemistry*, 34(41):13278–13288, 1995. URL http://www.ncbi.nlm.nih.gov/pubmed/7577912.

70. A.J. Lambert and M.D. Brand. Superoxide production by NADH:ubiquinone oxidoreductase (complex I) depends on the pH gradient across the mitochondrial inner membrane. *Biochem. J.*, 382(Pt 2):511–517, September 2004. URL http://www.ncbi.nlm.nih.gov/pubmed/15175007.

71. M.J. Lambeth and M.J. Kushmerick. A computational model for glycogenolysis in skeletal muscle. *Ann. Biomed. Eng.*, 30(6):808–827, 2002. URL http://www.ncbi.nlm.nih.gov/pubmed/12220081.

72. K.F. LaNoue and J.R. Williamson. Interrelationships between malate-aspartate shuttle and citric acid cycle in rat heart mitochondria. *Metabolism*, 20(2):119–140, February 1971. URL http://www.ncbi.nlm.nih.gov/pubmed/4322086.

73. K.F. LaNoue, W.J. Nicklas, and J.R. Williamson. Control of citric acid cycle activity in rat heart mitochondria. *J. Biol. Chem.*, 245(1):102–111, 1970. URL http://www.ncbi.nlm.nih.gov/pubmed/4312474.

74. K.F. LaNoue, E.I. Walajtys, and J.R. Williamson. Regulation of glutamate metabolism and interactions with the citric acid cycle in rat heart mitochondria. *J. Biol. Chem.*, 248(20):7171–7183, 1973. URL http://www.ncbi.nlm.nih.gov/pubmed/4355202.

75. L.P. Lee and G.W. Kosicki. Citrate synthase interaction with polyphosphate derivatives. *Biochim. Biophys. Acta.*, 139(1):195–198, May 1967. URL http://www.ncbi.nlm.nih.gov/pubmed/4382275.

76. J. Llopis, J.M. McCaffery, A. Miyawaki, M.G. Farquhar, and R.Y. Tsien. Measurement of cytosolic, mitochondrial, and Golgi pH in single living cells with green fluorescent proteins. *Proc. Natl. Acad. Sci. U.S.A.*, 95(12):6803–6808, June 1998. URL http://www.ncbi.nlm.nih.gov/pubmed/9618493.

77. J.C. Londesborough and K. Dalziel. The equilibrium constant of the isocitrate dehydrogenase reaction. *Biochem. J.*, 110(2):217–222, November 1968. URL http://www.ncbi.nlm.nih.gov/pubmed/4387224.

78. J.C. Londesborough and K. Dalziel. Kinetic studies of NADP-dependent isocitrate dehydrogenase from beef heart mitochondria. In H. Sund, editor, *Pyridine Nucleotide-Dependent Dehydrogenases: Proceedings of an Advanced Study Institute held at the University of Konstanz, Germany, September 15–20, 1969*, chapter 27, pages 315–324. Springer-Verlag, Berlin, Heidelberg, New York, 1 edition, 1970. URL https://books.google.co.in/books?id=PgH8CAAAQBAJ.

79. G.D. Lopaschuk, R.L. Collins-Nakai, and T. Itoi. Developmental changes in energy substrate use by the heart. *Cardiovasc. Res.*, 26(12):1172–1180, 1992. URL http://www.ncbi.nlm.nih.gov/pubmed/1288863.

80. M. Lu, L. Zhou, W.C. Stanley, M.E. Cabrera, G.M. Saidel, and X. Yu. Role of the malate-aspartate shuttle on the metabolic response to myocardial ischemia. *J. Theor. Biol.*, 254(2):466–475, sep 2008. URL http://www.ncbi.nlm.nih.gov/pubmed/18603266.

81. R. Lynn and R.W. Guynn. Equilibrium constants under physiological conditions for the reactions of succinyl coenzyme A synthetase and the hydrolysis of succinyl coenzyme A to coenzyme A and succinate. *J. Biol. Chem.*, 253(8):2546–2553, apr 1978. URL http://www.ncbi.nlm.nih.gov/pubmed/204656.

82. G.W. Magnus and J. Keizer. Minimal model of beta-cell mitochondrial Ca^{2+} handling. *Am. J. Physiol. Cell Physiol.*, 273(2):C717–C733, August 1997. URL http://www.ncbi.nlm.nih.gov/pubmed/9277370.

83. I. Magnusson, W.C. Schumann, G.E. Bartsch, V. Chandramouli, K. Kumaran, J. Wahren, and B.R. Landau. Non-invasive tracing of Krebs cycle metabolism in liver. *J. Biol. Chem.*, 266(11):6975–6984, 1991. URL http://www.ncbi.nlm.nih.gov/pubmed/2016309.

84. W.Z. Martini, W.C. Stanley, H. Huang, C.D. Rosiers, C.L. Hoppel, and H. Brunengraber. Quantitative assessment of anaplerosis from propionate in pig heart in vivo. *Am. J. Physiol. Endocrinol. Metab.*, 284 (2):E351–E356, feb 2003. URL http://www.ncbi.nlm.nih.gov/pubmed/12388135.

85. V. Massey. The composition of the ketoglutarate dehydrogenase complex. *Biochim. Biophys. Acta.*, 38:447–460, mar 1960. URL http://www.ncbi.nlm.nih.gov/pubmed/14422131.

86. S. Matsuyama, J. Llopis, Q.L. Deveraux, R.Y. Tsien, and J.C. Reed. Changes in intramitochondrial and cytosolic pH: early events that modulate caspase activation during apoptosis. *Nat. Cell. Biol.*, 2(6): 318–325, June 2000. URL http://www.ncbi.nlm.nih.gov/pubmed/10854321.

87. W.R. McClure and H.A. Lardy. Rat liver pyruvate carboxylase. IV. Factors affecting the regulation in vivo. *J. Biol. Chem.*, 246(11):3591–3596, 1971. URL http://www.ncbi.nlm.nih.gov/pubmed/5103844.

88. W.R. McClure, H.A. Lardy, and H.P. Kneifel. Rat liver pyruvate carboxylase. I. Preparation, properties, and cation specificity. *J. Biol. Chem.*, 246(11):3569–3578, June 1971. URL http://www.ncbi.nlm.nih.gov/pubmed/5578910.

89. W.R. McClure, H.A. Lardy, M. Wagner, and W.W. Cleland. Rat liver pyruvate carboxylase. II. Kinetic studies of the forward reaction. *J. Biol. Chem.*, 246(11):3579–83, June 1971. URL http://www.ncbi.nlm.nih.gov/pubmed/5103842.

90. J.G. McCormack and R.M. Denton. The effects of calcium ions and adenine nucleotides on the activity of pig heart 2-oxoglutarate dehydrogenase complex. *Biochem. J.*, 180(3):533–544, June 1979. URL http://www.ncbi.nlm.nih.gov/pubmed/39549.

91. J.G. McCormack and R.M. Denton. A comparative study of the regulation of Ca^{2+} of the activities of the 2-oxoglutarate dehydrogenase complex and NAD^{+}-isocitrate dehydrogenase from a variety of sources. *Biochem. J.*, 196(2):619–624, May 1981. URL http://www.ncbi.nlm.nih.gov/pubmed/7032511.

92. E. Metelkin, I. Goryanin, and O. Demin. Mathematical modelling of mitochondrial adenine nucleotide translocase. *Biophys. J.*, 90(2):423–432, January 2006. URL http://www.ncbi.nlm.nih.gov/pubmed/16239329.

93. E. Mogilevskaya, O. Demin, and I. Goryanin. Kinetic model of mitochondrial krebs cycle: unravelling the mechanism of salicylate hepatotoxic effects. *J. Biol. Phys.*, 32(3-4):245–271, 2006. URL http://www.ncbi.nlm.nih.gov/pubmed/19669466.

94. S. Morikofer-Zwez and P. Walter. Binding of ADP to rat liver cytosolic proteins and its influence on the ratio of free ATP/free ADP. *Biochem. J.*, 259(1):117–124, April 1989. URL http://www.ncbi.nlm.nih.gov/pubmed/2497727.

95. T. Moriyama and P.A. Srere. Purification of rat heart and rat liver Citrate Synthases. Physical, kinetic, and immunological studies. *J. Biol. Chem.*, 246(10):3217–3223, 1971. URL http://www.ncbi.nlm.nih.gov/pubmed/4995747.

96. A.R. Panchal, B. Comte, H. Huang, T. Kerwin, A. Darvish, C. Des Rosiers, H. Brunengraber, and W.C. Stanley. Partitioning of pyruvate between oxidation and anaplerosis in swine hearts. *Am. J. Physiol. Heart Circ. Physiol.*, 279(5):H2390–H2398, November 2000. URL http://www.ncbi.nlm.nih.gov/pubmed/11045976.

97. A.R. Panchal, B. Comte, H. Huang, B. Dudar, B. Roth, M. Chandler, C. Des Rosiers, H. Brunengraber, and W.C. Stanley. Acute hibernation decreases myocardial pyruvate carboxylation and citrate release. *Am. J. Physiol. Heart Circ. Physiol.*, 281(4):H1613–H1620, October 2001. URL http://www.ncbi.nlm.nih.gov/pubmed/11557551.

98. A.V. Panov and R.C. Jr. Scaduto. Influence of calcium on NADH and succinate oxidation by rat heart submitochondrial particles. *Arch. Biochim. Biophys.*, 316(2):815–820, 1995. URL http://www.ncbi.nlm.nih.gov/pubmed/7864638.

99. K.J. Peuhkurinen and I.E. Hassinen. Pyruvate carboxylation as an anaplerotic mechanism in the isolated perfused rat heart. *Biochem. J.*, 202(1):67–76, jan 1982. URL http://www.ncbi.nlm.nih.gov/pubmed/7082318.

100. G.W.E. Plaut. Isocitrate dehydrogenase (DPN-specific) from bovine heart. *Meth. Enzymol.*, 13(1):34–42, 1969. URL http://www.sciencedirect.com/science/article/pii/0076687969130724.

101. G.W.E. Plaut and T. Aogaichi. Purification and properties of diphosphopyridine nucleotide-linked isocitrate dehydrogenase of mammalian liver. *J. Biol. Chem.*, 243(21):5572–5583, 1968. URL http://www.ncbi.nlm.nih.gov/pubmed/4387006.

102. G.W.E. Plaut, C.P. Cheung, R.J. Suhadolnik, and T. Aogaichi. Cosubstrate and allosteric modifier activities of structural analogues of NAD and ADP for NAD-specific isocitrate dehydrogenase from bovine heart. *Biochemistry*, 18(15):3430–3438, July 1979. URL http://www.ncbi.nlm.nih.gov/pubmed/223632.

103. J.L. Purvis. Pyridine nucleotides in rat-liver mitochondria I. The demonstration of a new form of diphosphopyridine nucleotide and of triphosphopyridine nucleotide. *Biochim. Biophys. Acta.*, 38: 435–446, January 1960. URL http://www.ncbi.nlm.nih.gov/pubmed/14435366.

104. M. Rabkin and J. J. Blum. Quantitative analysis of intermediary metabolism in hepatocytes incubated in the presence and absence of glucagon with a substrate mixture containing glucose, ribose, fructose, alanine and acetate. *Biochem. J.*, 225:761–786, 1985. URL http://www.ncbi.nlm.nih.gov/pubmed/3919712.

105. P.J. Randle, P.J. England, and R.M. Denton. Control of the tricarboxylate cycle and its interactions with glycolysis during acetate utilization in rat heart. *Biochem. J.*, 117(4):677–695, May 1970. URL http://www.ncbi.nlm.nih.gov/pubmed/5449122.

106. T.E. Roche and R.L. Cate. Purification of porcine liver pyruvate dehydrogenase complex and characterization of its catalytic and regulatory properties. *Arch. Biochim. Biophys.*, 183(2):664–677, October 1977. URL http://www.ncbi.nlm.nih.gov/pubmed/200177.

107. G.A. Rutter and R.M. Denton. Regulation of NAD^+-linked isocitrate dehydrogenase and 2-oxoglutarate dehydrogenase by Ca^{2+} ions within toluene-permeabilized rat heart mitochondria. Interactions with regulation by adenine nucleotides and $NADH/NAD^+$ ratios. *Biochem. J.*, 252(1):181–189, May 1988. URL http://www.ncbi.nlm.nih.gov/pubmed/3421900.

108. B. Safer and J.R. Williamson. Mitochondrial-cytosolic interactions in perfused rat heart. Role of coupled transamination in repletion of citric acid cycle intermediates. *J. Biol. Chem.*, 248(7):2570–2579, 1973. URL http://www.ncbi.nlm.nih.gov/pubmed/4349041.

109. B. Safer, C.M. Smith, and J.R. Williamson. Control of the transport of reducing equivalents across the mitochondrial membrane in perfused rat heart. *J. Mol. Cell. Cardiol.*, 2(2):111–124, June 1971. URL http://www.ncbi.nlm.nih.gov/pubmed/4329775.

110. D.R. Sanadi. α-ketoglutarate dehydrogenase from pig heart. *Meth. Enzymol.*, 13(1):52–55, 1969. URL http://www.sciencedirect.com/science/article/pii/0076687969130153.

111. W.D. Schwenke, S. Soboll, H.J. Seitz, and H. Sies. Mitochondrial and cytosolic ATP/ADP ratios in rat liver in vivo. *Biochem. J.*, 200(2):405–408, November 1981. URL http://www.ncbi.nlm.nih.gov/pubmed/7340839.

112. M.C. Scrutton. Pyruvate carboxylase. Studies of activator-independent catalysis and of the specificity of activation by acyl derivatives of coenzyme A for the enzyme from rat liver. *J. Biol. Chem.*, 249(22): 7057–7067, 1974. URL http://www.ncbi.nlm.nih.gov/pubmed/4612033.

113. M.C. Scrutton and M.D. White. Pyruvate carboxylase from rat liver: catalytic properties in the absence, and at low concentrations, of acetyl-CoA. *Biochem. Biosys. Res. Commun.*, 48(1):85–93, 1972. URL http://www.ncbi.nlm.nih.gov/pubmed/5041883.

114. F. Seifert, R. Golbik, J. Brauer, L. Hauke, K. Schroder-Tittmann, E. Hinze, L.G. Korotchkina, M.S. Patel, and K. Tittmann. Direct Kinetic Evidence for Half-Of-The-Sites Reactivity in the E1 Component of the Human Pyruvate Dehydrogenase Multienzyme Complex through Alternating Sites Cofactor Activation. *Biochemistry*, 45(42):12775–12785, 2006. URL http://www.ncbi.nlm.nih.gov/pubmed/17042496.

115. D. Shepherd and P.B. Garland. The kinetic properties of citrate synthase from rat liver mitochondria. *Biochem. J.*, 114(3):597–610, September 1969. URL http://www.ncbi.nlm.nih.gov/pubmed/5820645.

116. H. Sies, T.P.M. Akerboom, and J.M. Tager. Mitochondrial and Cytosolic NADPH Systems and Isocitrate Dehydrogenase Indicator Metabolites during Ureogenesis from Ammonia in Isolated Rat Hepatocytes. *Eur. J. Biochem.*, 72(2):301–307, January 1977. URL http://www.ncbi.nlm.nih.gov/pubmed/13998.

117. E. A. Siess, D. G. Brocks, and O. H. Wieland. Nicotinamide nucleotide compartmentation. In H. Sies, editor, *Metabolic compartmentation*, pages 205–231. Academic Press, London & New York, illustrated edition, 1982a. URL http://www.worldcat.org/oclc/489706487.

118. E. A. Siess, D. G. Brocks, and O. H. Wieland. Subcellular distribution of adenine nucleotides and of metabolites of tricarboxylate cycle and gluconeogenesis in hepatocytes. In H. Sies, editor, *Metabolic compartmentation*, pages 235–257. Academic Press, London & New York, illustrated edition, 1982b. URL http://www.worldcat.org/oclc/489706487.

119. E.A. Siess and O.H. Wieland. Phosphorylation state of cytosolic and mitochondrial adenine nucleotides and of pyruvate dehydrogenase in isolated rat liver cells. *Biochem. J.*, 156(1):91–102, April 1976. URL http://www.ncbi.nlm.nih.gov/pubmed/133678.

120. E.A. Siess, S. Nimmannit, and O.H. Wieland. Kinetic and regulatory properties of pyruvate dehydrogenase from Ehrlich ascites tumor cells. *Cancer Res.*, 36(1):55–59, 1976. URL http://www.ncbi.nlm.nih.gov/pubmed/174813.

121. E.A. Siess, R.I. Kientsch-Engel, and O.H. Wieland. Concentration of free oxaloacetate in the mitochondrial compartment of isolated liver cells. *Biochem. J.*, 218(1):171–176, February 1984. URL http://www.ncbi.nlm.nih.gov/pubmed/6424654.

122. C.M. Smith and G.W.E. Plaut. Activities of NAD^+-specific and $NADP^+$-specific isocitrate dehydrogenases in rat-liver mitochondria. Studies with D-threo-alpha-methylisocitrate. *Eur. J. Biochem./FEBS*, 97(1):283–295, 1979. URL http://www.ncbi.nlm.nih.gov/pubmed/38961.

123. C.M. Smith and J.R. Williamson. Inhibition of citrate synthase by succinyl-CoA and other metabolites. *FEBS lett.*, 18(1):35–38, October 1971. URL http://www.ncbi.nlm.nih.gov/pubmed/11946076.

124. C.M. Smith, J. Bryla, and J.R. Williamson. Regulation of mitochondrial α-ketoglutarate metabolism by product inhibition at α-ketoglutarate dehydrogenase. *J. Biol. Chem.*, 249(5):1497–1505, 1974. URL http://www.ncbi.nlm.nih.gov/pubmed/4361738.

125. P.A. Srere. The citrate enzymes: their structures, mechanisms, and biological functions. *Curr. Top. Cell. Regul.*, 5:229–283, 1972a. URL http://www.ncbi.nlm.nih.gov/pubmed/4587829.

126. P.A. Srere. Is there an organization of Krebs cycle enzymes in the mitochondrial matrix? : [proceedings of Metabolic Regulation: Energy metabolism and the Regulation of Metabolic Processes in Mitochondria ; held at University of Nebraska Medical School Omaha, Nebraska on May 3-4, 1971]. In M.A. Mehlman and R.W. Hanson, editors, *Energy metabolism and the Regulation of Metabolic Processes in Mitochondria*, Symposia on Metabolic Regulation, pages 79–91, New York, N.Y. and London, U.K., 1972b. Academic Press. URL http://www.sciencedirect.com/science/article/pii/B9780124878501500117.

127. W.C. Stanley, L.A. Hernandez, D. Spires, J. Bringas, S. Wallace, and J.G. McCormack. Pyruvate dehydrogenase activity and malonyl CoA levels in normal and ischemic swine myocardium: effects of dichloroacetate. *J. Mol. Cell. Cardiol.*, 28(5):905–914, 1996. URL http://www.ncbi.nlm.nih.gov/pubmed/8762030.

128. W.C. Stanley, K.M. Kivilo, A.R. Panchal, P.H. Hallowell, C. Bomont, T. Kasumov, and H. Brunengraber. Post-ischemic treatment with dipyruvyl-acetyl-glycerol decreases myocardial infarct size in the pig. *Cardiovasc. Drugs. Ther.*, 17(3):209–216, 2003. URL https://www.ncbi.nlm.nih.gov/pubmed/14574079.

129. R. Stermann and K. Decker. Differential response of ATP and orthophosphate in cytosol and mitochondria of rat hepatocytes to treatment with Pi and d-galactosamine. *FEBS lett.*, 95(2):214–216, November 1978. URL http://www.ncbi.nlm.nih.gov/pubmed/720612.

130. S. Strumiło, M. Czygier, J. Kondracikowska, P. Dobrzyń, and J. Czerniecki. Kinetic and spectral investigation of allosteric interaction of coenzymes with 2-oxo acid dehydrogenase complexes. *J. Mol. Struc.*, 614(1-3):221–226, September 2002. URL http://www.sciencedirect.com/science/article/pii/S0022286002002557.

131. K.E. Sundqvist, K.J. Peuhkurinen, J.K. Hiltunen, and I.E. Hassinen. Effect of acetate and octanoate on tricarboxylic acid cycle metabolite disposal during propionate oxidation in the perfused rat heart. *Biochim. Biophys. Acta.*, 801(3):429–436, oct 1984. URL http://www.ncbi.nlm.nih.gov/pubmed/6487652.

132. K.E. Sundqvist, J.K. Hiltunen, and I.E. Hassinen. Pyruvate carboxylation in the rat heart. Role of biotin-dependent enzymes. *Biochem. J.*, 257(3):913–916, February 1989. URL http://www.ncbi.nlm.nih.gov/pubmed/2930495.

133. H. D. Söling. Species dependent compartmentation of guanine nucleotide metabolism in the vertebrate liver cell. In H. Sies, editor, *Metabolic compartmentation*, pages 123–146. Academic Press, London & New York, illustrated edition, 1982. URL http://www.worldcat.org/oclc/489706487.

134. H. Taegtmeyer. On the inability of ketone bodies to serve as the only energy providing substrate for rat heart at physiological work load. *Basic Res. Cardiol.*, 78(4):435–450, 1983. URL http://www.ncbi.nlm.nih.gov/pubmed/6626122.

135. M. Telegdi, D.V. Wolfe, and R.G. Wolfe. Malate Dehydrogenase. XII. Initial rate kinetic studies of substrate activation of porcine mitochondrial enzyme by malate. *J. Biol. Chem.*, 248(18):6484–6489, 1973. URL http://www.ncbi.nlm.nih.gov/pubmed/4354213.

136. M.E. Tischler, P. Hecht, and J.R. Williamson. Determination of mitochondrial/cytosolic metabolite gradients in isolated rat liver cells by cell disruption. *Arch. Biochim. Biophys.*, 181(1):278–292, May 1977. URL http://www.ncbi.nlm.nih.gov/pubmed/18107.

137. S. Tran-Dinh, J.A. Hoerter, P. Mateo, F. Gyppaz, and M. Herve. ^{13}C-NMR spectroscopic evaluation of the citric acid cycle flux in conditions of high aspartate transaminase activity in glucose-perfused rat hearts. *Biochimie*, 80(12):1013–1024, December 1998. URL http://www.ncbi.nlm.nih.gov/pubmed/9924979.

138. C.S. Tsai, M.W. Burgett, and L.J. Reed. α-Keto acid dehydrogenase complexes. XX. A kinetic study of the pyruvate dehydrogenase complex from bovine kidney. *J. Biol. Chem.*, 248(24):8348–8352, 1973. URL http://www.ncbi.nlm.nih.gov/pubmed/4357736.

139. R.L. Veech, J.W. Lawson, N.W. Cornell, and H.A. Krebs. Cytosolic phosphorylation potential. *J. Biol. Chem.*, 254(14):6538–6547, July 1979. URL http://www.ncbi.nlm.nih.gov/pubmed/36399.

140. C. Veeger, D.V. DerVartanian, and W.P. Zeylemaker. Succinate dehydrogenase: [EC 1.3.99.1 Succinate: (acceptor) oxidoreductase]. *Meth. Enzymol.*, 13(1):81–90, 1969. URL http://www.sciencedirect.com/science/article/pii/0076687969130207.

141. M. Vendelin, O. Kongas, and V.A. Saks. Regulation of mitochondrial respiration in heart cells analysed by reaction-diffusion model of energy transfer. *Am. J. Physiol. Cell Physiol.*, 278(4):C747–C764, 2000. URL http://www.ncbi.nlm.nih.gov/pubmed/10751324.

142. J.J. Villafranca and A.S. Mildvan. The Mechanism of Aconitase Action. I. Preparation, physical properties of the enzyme, and activation by iron(II). *J. Biol. Chem.*, 246(3):772–779, 1971a. URL http://www.ncbi.nlm.nih.gov/pubmed/5542689.

143. J.J. Villafranca and A.S. Mildvan. The Mechanism of Aconitase Action. II. Magnetic resonance studies of the complexes of enzyme, manganese(II), iron(II), and substrates. *J. Biol. Chem.*, 246(18):5791–5798, January 1971b. URL http://www.ncbi.nlm.nih.gov/pubmed/4328840.

144. K.C. Vinnakota and J.B. Bassingthwaighte. Myocardial density and composition: a basis for calculating intracellular metabolite concentrations. *Am. J. Physiol. Heart Circ. Physiol.*, 286(5):H1742–H1749, May 2004. URL http://www.ncbi.nlm.nih.gov/pubmed/14693681.

145. R.G. Weiss, M.D. Stern, C.P. de Albuquerque, K. Vandegaer, V.P. Chacko, and G. Gerstenblith. Consequences of altered aspartate aminotransferase activity on ^{13}C-glutamate labelling by the tricarboxylic acid cycle in intact rat hearts. *Biochim. Biophys. Acta.*, 1243(3):543–548, April 1995. URL http://www.ncbi.nlm.nih.gov/pubmed/7727532.

146. A. Wiederkehr, K.-S. Park, O. Dupont, N. Demaurex, T. Pozzan, G.W. Cline, and C.B. Wollheim. Matrix alkalinization: a novel mitochondrial signal for sustained pancreatic beta-cell activation. *The EMBO journal*, 28(4):417–428, February 2009. URL http://www.ncbi.nlm.nih.gov/pubmed/19165153.

147. O.H. Wieland, B. Von Jagow-Westermann, and B. Stukowski. Kinetic and regulatory properties of heart muscle pyruvate dehydrogenase. *Hoppe-Seyler's Z. Physiol. Chem.*, 350(3):329–334, March 1969. URL http://www.ncbi.nlm.nih.gov/pubmed/4306028.

148. O.H. Wieland, U. Hartmann, and E.A. Siess. Neurospora crassa pyruvate dehydrogenase: interconversion by phosphorylation and dephosphorylation. *FEBS lett.*, 27(2):240–244, 1972a. URL http://www.ncbi.nlm.nih.gov/pubmed/4352021.

149. O.H. Wieland, E.A. Siess, H. J. v. Funcke, C. Patzelt, A. Schirmann, G. Loffler, and L. Weiss. Regulation of the Mammalian Pyruvate Dehydrogenase Complex: Physiological Aspects and Characterization of PDH-Phosphatase from Pig Heart. In O.H. Wieland, E. Helmreich, and H. Holzer, editors, *Metabolic Interconversion of Enzymes: 2nd International Symposium on Metabolic Interconversion of Enzymes, 1971*, chapter 30, pages 293–309. Springer Berlin Heidelberg, Berlin, Heidelberg, 1 edition, 1972b. URL http://dx.doi.org/10.1007/978-3-662-37966-0{_}30.

150. D.H. Williamson and J.T. Brosnan. Concentrations of Metabolites in Animal Tissues. *Meth. Enzym. Anal.*, 4(1):2266–2302, 1974. URL http://www.sciencedirect.com/science/article/pii/B9780120913046500938.

151. D.H. Williamson, P. Lund, and H.A. Krebs. The Redox State of Free Nicotinamide-Adenine Dinucleotide in the Cytoplasm and Mitochondria of Rat Liver. *Biochem. J.*, 103(2):514–527, May 1967. URL http://www.ncbi.nlm.nih.gov/pubmed/4291787.

152. J.R. Williamson. In S. Papa, J.M. Tager, E. Quagliariello, and E.C. Slater, editors, *The Energy Level and Metabolic Control in Mitochondria : [proceedings of the Round Table Discussion on the Energy Level and Metabolic Control in Mitochondria ; organized by the Department of Biochemistry, University of Bari (Italy) and the Laboratory of Biochemistry, University of Amsterdam (The Netherlands), held in Polignaro a Mare, May 13-16, 1968]*, volume XV, pages 385–400, Bari, Italy, 1969. Adriatica Editrice. URL http://www.worldcat.org/oclc/67268.

153. J.R. Williamson and B.E. Corkey. Assays of intermediates of the citric acid cycle and related compounds by fluorometric enzyme methods. *Meth. Enzymol.*, 13(1):434–513, 1969. URL http://www.sciencedirect.com/science/article/pii/0076687969130724.

154. J.R. Williamson, E.T. Browning, and M.S. Olson. Interrelations between fatty acid oxidation and the control of gluconeogenesis in perfused rat liver. *Adv. Enzyme Regul.*, 6(1):67–100, 1968. URL http://www.ncbi.nlm.nih.gov/pubmed/5721291.

155. J.R. Williamson, B. Safer, K.F. LaNoue, C.M. Smith, and E. Walajtys. Mitochondrial-cytosolic interactions in cardiac tissue: role of the malate-aspartate cycle in the removal of glycolytic NADH from the cytosol. In D.D. Davis, editor, *Symposia of the Society for Experimental Biology*, volume 27, pages 241–281, Oxford, 1973. Cambridge University Press.

156. J.R. Williamson, C. Ford, J. Illingworth, and B. Safer. Coordination of citric acid cycle activity with electron transport flux. *Circ. Res.*, 38(5 (Suppl 1)):I39–I51, May 1976. URL http://www.ncbi.nlm.nih.gov/pubmed/1269091.

157. H.H. Winkler, F.L. Bygrave, and A.L. Lehninger. Characterization of the Atractyloside-sensitive Adenine Nucleotide Transport System in Rat Liver Mitochondria. *J. Biol. Chem.*, 243(1):20–28, January 1968. URL http://www.ncbi.nlm.nih.gov/pubmed/4966963.

158. H.G. Wood, J.J. Davis, and H. Lochmüller. The Equilibria of Reactions Catalyzed by Carboxytransphosphorylase, Carboxykinase, and Pyruvate Carboxylase and the Synthesis of Phosphoenolpyruvate. *J. Biol. Chem.*, 241(23):5692–5704, 1966. URL http://www.ncbi.nlm.nih.gov/pubmed/4288897.

159. F. Wu, F. Yang, K.C. Vinnakota, and D.A. Beard. Computer modelling of mitochondrial tricarboxylic acid cycle, oxidative phosphorylation, metabolite transport, and electrophysiology. *J. Biol. Chem.*, 282 (34):24525–24537, 2007. URL http://www.ncbi.nlm.nih.gov/pubmed/17591785.

160. X. Yu, L.T. White, C. Doumen, L.A. Damico, K.F. LaNoue, N.M. Alpert, and E.D. Lewandowski. Kinetic analysis of dynamic ^{13}C NMR spectra: metabolic flux, regulation, and compartmentation in hearts. *Biophys. J.*, 69(5):2090–2102, November 1995. URL http://www.ncbi.nlm.nih.gov/pubmed/8580353.

161. K. Yugi and M. Tomita. A general computational model of mitochondrial metabolism in a whole organelle scale. *Bioinformatics*, 20(11):1795–1796, July 2004. URL http://www.ncbi.nlm.nih.gov/pubmed/14962921.

162. W.P. Zeylemaker, A.D.M. Klaasse, E.C. Slater, and C. Veeger. Studies on succinate dehydrogenase. VI. Inhibition by monocarboxylic acids. *Biochim. Biophys. Acta. - Enzymology*, 198(3):415–422, March 1970. URL http://www.ncbi.nlm.nih.gov/pubmed/5461693.

163. L. Zhou, J.E. Salem, G.M. Saidel, W.C. Stanley, and M.E. Cabrera. Mechanistic model of cardiac energy metabolism predicts localization of glycolysis to cytosolic subdomain during ischemia. *Am. J. Physiol. Heart Circ. Physiol.*, 288(5):H2400–H2411, may 2005. URL http://www.ncbi.nlm.nih.gov/pubmed/15681693.

164. A. Zorzano, T.W. Balon, L.J. Brady, P. Rivera, L.P. Garetto, J.C. Young, M.N. Goodman, and N.B. Ruderman. Effects of starvation and exercise on concentrations of citrate, hexose phosphates and glycogen in skeletal muscle and heart. Evidence for selective operation of the glucose-fatty acid cycle. *Biochem. J.*, 232(2):585–591, dec 1985. URL http://www.ncbi.nlm.nih.gov/pubmed/4091810.

165. P. F. Zuurendonk. Ph.D. thesis, University of Amsterdam, 1978.